UNIVERSIDAD COMPLUTENSE DE MADRID

FACULTAD DE CIENCIAS FÍSICAS

TESIS DOCTORAL

Avances en la integración de las emisiones del tráfico en la modelización de la calidad del aire urbano a múltiples escalas: Aplicaciones seleccionadas

MEMORIA PARA OPTAR AL GRADO DE DOCTOR

PRESENTADA POR

Alejandro Rodríguez Sánchez

DIRIGIDA POR

Marta García Vivanco
José Luis Santiago del Río

Universidad Complutense de Madrid
Facultad de Ciencias Físicas
Programa de Doctorado en Fisica

TESIS DOCTORAL

Advances in the Integration of Traffic Emissions into Urban Air Quality Modeling at Multiple Scales: Selected Applications

Avances en la integración de las emisiones del tráfico en la modelización de la calidad del aire urbano a múltiples escalas: Aplicaciones seleccionadas

Alejandro Rodríguez Sánchez

Directores:
Dra. Marta García Vivanco
Dr. José Luis Santiago del Río

Agradecimientos

En primer lugar me gustaría agradecer a mis directores de tesis, Marta y José Luis, por haber confiado en mí y haberme dado esta oportunidad de aprender y formarme, y por transmitirme tantos conocimientos, y por su paciencia y apoyo constantes. También a Carlos, mi tutor académico, por su incondicional ayuda y su paciencia con mi caótica organización.

Por supuesto, también a todos mis compañeros y compañeras, a los que considero amigos y amigas, de UNIMA que desde el primer día me hicieron sentir como uno más y de los que también he aprendido más de lo que hubiera podido imaginar como persona ignorante que aún soy.

Gracias también a Fernando por acogerme en su coche para ir y volver al congreso HARMO en Aveiro, el primero en mi historial y del que guardo un recuerdo gratísimo desde el primer minuto del viaje hasta el último.

También quiero agradecer a Alberto toda la atención que me ha dedicado desde que nos conocimos, por estar siempre disponible para resolver mis dudas e inquietudes y por ser de tan gran ayuda en todas las facetas y alimentar mi motivación en la investigación.

Gracias también al Ayuntamiento de Zaragoza por facilitar todos los datos que han sido necesarios para llevar a cabo una parte fundamental de este trabajo. Y al CIEMAT por la financiación de este trabajo a través del proyecto Retos-Aire (RTI2018-099138-B-I00), y del proyecto TRANSAIRE.

No me quiero olvidar tampoco de todos mis amigos del grupo de Ecotoxicología de la Contaminación Atmosférica, que también me han tendido su ayuda y apoyo siempre que lo he necesitado, y me han adoptado como a uno más sin aún yo saber si lo he merecido. Gracias en especial a Raquel, Tania, Sara, Samu y Rocío por no dejar que me viniera abajo en los momentos más difíciles y siempre saber sacarme una sonrisa.

Me siento muy afortunado de tener muchos amigos a los que poder agradecer su apoyo y su paciencia conmigo en estos años. Gracias a todos, sin vosotros no hubiera sido posible haber llegado hasta aquí. En especial a Juanjo, Antonio y Andrea por brindarme momentos felices y la energía suficiente para llegar a estos agradecimientos cuando parecía que la tesis podría

conmigo. A Dani, "Compañero", por su amistad incondicional y su fe infinita en mí. Ya no queda nada para que cambies mi contacto en el móvil... A Weckx y a Cay, que como Dani, siempre he sabido que podía contar con ellos y me proporcionaban desahogo y distracción cuando lo necesitaba. A Javi, Jose, Rebollo y Josemi, que siempre han estado ahí cuando les he necesitado a pesar de la distancia que nos separa. A María Elena, que siempre sabe como hacer pasar un buen rato, que es fundamental para poder sacar adelante un trabajo como este, y por muchos más que vendrán. Y también a María y Abram, porque una amistad no siempre es más por antigua, sino por lo que representa para uno -que es muchísimo.

Esta tesis no hubiera sido posible sin mi familia, mis padres María José y Juan Carlos y mi hermana Paula. Muchas gracias por haberme hecho de mí lo que soy hoy en día, vuestra comprensión y vuestra paciencia en mis momentos más difíciles y vuestra ayuda incondicional y vuestros consejos cuando más perdido me sentía. A mis primos y tíos, por su interés incondicional en este trabajo y su comprensión. Gracias también a José Manuel, María y Miguel por su ayuda y consejos que tanto me han ayudado.

A mi abuelo, quién con tantas conversaciones sobre el tiempo y la naturaleza y paseos por el campo, sembró la semilla que hoy florece con este trabajo.

Y por último, quiero agradecer a la co-autora de este trabajo y de todos los que quedan por llegar, María, porque sin ti, sin tu espontaneidad, tu paciencia y tu comprensión este trabajo no hubiera sido posible.

A todos vosotros, a los que me he dejado por el camino y a los que ya no están, gracias de corazón.

¡Cuánta hambre se ha pasado!
Hambre por cada lado.
Hambre de paz, hambre de hombre honrado.

"Un millón de sueños". Cecilia, 1973.

Contents

Resumen

La calidad del aire es actualmente una preocupación medioambiental prioritaria en las ciudades. Elevados niveles de contaminación atmosférica han sido frecuentemente observados en las áreas urbanas, donde se concentran emisiones de contaminantes y población. En particular, el tráfico rodado es habitualmente la principal fuente de contaminación del aire en zonas urbanas. El NO_X, considerado como la suma de NO y NO_2, es el principal contaminante en forma gaseosa asociado al tráfico. A pesar de recientes mejoras en la calidad del aire de la Unión Europea (UE), gracias a la implementación de políticas medioambientales, los valores límites establecidos por la UE y por la Organización Mundial de la Salud (OMS) todavía no se cumplen en toda Europa. Recientemente, numerosas medidas relacionadas con el tráfico están siendo aplicadas en un intento por reducir la contaminación atmosférica en ciertas áreas. Pero la concentración de contaminantes está influenciada por fenómenos muy locales, y es conocido que se están produciendo superaciones de valores límite o situaciones de no cumplimiento sin ser detectadas por las Estaciones de Monitorización de la Calidad del Aire (EMCA). En este sentido, existe una falta de análisis de alta resolución del impacto de estas medidas, así como estimaciones de la influencia de factores externos, como las condiciones meteorológicas, en la efectividad de estas.

La modelización de la calidad del aire cubre un amplio rango de escalas y procesos. En áreas urbanas, el gran número de obstáculos (edificios, vegetación, vehículos, etc.) induce complejos patrones de flujo en las calles. Así, la heterogénea distribución de contaminantes entre los edificios solo puede ser capturada por medio de mapas de alta resolución espacial. En este sentido, los modelos CFD son poderosas herramientas para reproducir la dispersión de contaminantes considerando características realistas de los entornos urbanos. Otro factor responsable de los fuertes gradientes de contaminantes en zonas urbanas es la heterogeneidad de las emisiones de contaminantes, especialmente del tráfico rodado. En este contexto, una metodología para la estimación de emisiones a microescala es util para estimar adecuadamente su distribución espacial a alta resolución. Por otra parte, las emisiones de tráfico afectan a la calidad del aire a escala de toda la ciudad y regional, para lo cual los modelos de mesoscala son los más adecuados para modelizar el transporte, la transformación y el depósito de contaminantes. Estos modelos también pueden beneficiarse de la estimación

de emisiones detalladas.

En este trabajo, una metodología de estimación de emisiones a microescala, basada en una combinación adecuada de modelos de tráfico y emisión microscópicos, ha sido aplicada para obtener emisiones de tráfico a alta resolución- tanto espacial como temporal- para diferentes zonas urbanas. Estos modelos no solo describen el comportamiento de entidades individuales que definen el tráfico como los vehículos y sus interacciones, sino que también consideran las indicaciones de tráfico y cambios de carril de cada vehículo. Esto resulta en ciclos de parada y arrancada que producen patrones de frenado y aceleración que tienen una importante influencia en las emisiones. En una aplicación particular, esta metodología ha sido empleada para estimar emisiones en zonas urbanas para diferentes configuraciones de tráfico, y así evaluar el impacto de diversas medidas de tráfico dirigidas a reducir la contaminación atmosférica en una zona urbana. Con este fin, las emisiones fueron implementadas en un modelo CFD para simular su dispersión. Concentraciones de contaminantes para largos periodos de tiempo se estimaron usando una metodología que basa la estimación de valores horarios de concentración de contaminantes en un conjunto de simulaciones CFD de estado estacionario previamente computadas. Además, se ha estudiado exhaustivamente su sensibilidad a cambios en las condiciones meteorológicas. Para estimar el NO_2 a partir del NO_X calculado con esta metodología se ha desarrollado un método simple pero eficaz para estimar el impacto de la meteorología en las concentraciones de fondo ahorrando los costes computacionales que requeriría usar un modelo de mesoscala para este fin. Los resultados muestran que las distintas medidas de mitigación analizadas, junto a la renovación de la flota de vehículos ocurrida con el paso del tiempo, han ayudado a reducir las concentraciones de NO_X y NO_2 en el área de estudio. Pero también que su sensibilidad a la meteorología no debe ser despreciada. De hecho, localmente, un cambio en la meteorología puede tener mayor impacto en las concentraciones de contaminantes que la propia medida de mitigación. Aunque cuanto menor son las concentraciones de contaminantes menor es su sensibilidad a las condiciones meteorológicas, como se ha demostrado al analizar una medida de mitigación que reduce notablemente los valores de NO_X.

Asimismo, como parte de este trabajo se ha analizado el impacto de las restricciones derivadas de la pandemia de COVID-19 en las emisiones de contaminantes atmosféricos en Europa. Este estudio complementa las aplicaciones principales de la tesis al mostrar cómo una reducción abrupta de la movilidad y de las actividades económicas puede afectar significativamente a las emisiones de contaminantes, sirviendo como enlace a otros trabajos de la tesis al proporcionar un valor de referencia de reducción de emisiones a distintas medidas de mitigación como las estudiadas en algunos de los trabajos de esta tesis.

Por último, se ha desarrollado una metodología para usar un nuevo conjunto de emisiones detalladas en el modelo CHIMERE. Para ello, se ha creado una interfaz para facilitar la

implementación de las emisiones en el modelo sin perder las ventajas que aportan unas emisiones de alta resolución espacial y temporal. Este trabajo muestra como implementar emisiones detalladas en el modelo regional resulta en mejores estimaciones de concentraciones de distintos contaminantes. Como ejemplo de estas mejoras se demuestra la mejor estimación de parámetros legislados, lo que puede ser de notable utilidad para gestores.

Este trabajo contribuye a una mejora del entendimiento del impacto de las medidas de tráfico en zonas urbanas en la calidad del aire a largo plazo, así como de la influencia de las condiciones meteorológicas en la efectividad de estas medidas. Además, este trabajo facilita el estudio de medidas de tráfico a mesoescala proveyendo una interfaz para incluir estas emisiones en un modelo regional.

Abstract

Air quality is nowadays a priority environmental concern in the cities. High air pollution levels have been often observed in urban areas, where both pollutants emissions and population are concentrated. In particular, road transport is often the main source of air pollution in urban areas. The NO_X, namely NO and NO_2, are the primary traffic-related pollutants in gas-phase, albeit only the NO_2 is legislated given its harmful impacts on human health. Despite air quality has recently improved in the European Union (EU) due to the implementation of environmental policies, the limit values established by the EU and the World Health Organization (WHO) are still not fully met across Europe. Recently, numerous traffic measures are being applied as an attempt to reduce air pollution in certain areas. However, pollutant concentrations are influenced by very local phenomena, and exceedances or non-compliance situations are known to be occurring without being captured by the Air Quality Monitoring Stations (AQMS). In this sense, there is a lack of analysis of the impact of these applied measures at high-resolution, as well as estimations of the influence of external factors, such as meteorological conditions, on the effectiveness of these measures.

The air quality modelling covers a wide range of scales and processes. In urban areas, the vast number of obstacles (buildings, vegetation, vehicles, etc.) induce complex flow patterns in the streets. Hence the irregular distribution among buildings can only be captured by means of maps of high spatial resolution. In this sense, the Computational Fluid Dynamics (CFD) models are powerful tools for reproducing the dispersion of pollutants considering realistic features of urban environments. Another factor responsible of the strong gradients of air pollutants is the heterogeneity of pollutant emissions, mainly from road traffic. In this context, a microscale emissions' estimation methodology is a useful approach to properly estimate the spatial distribution of emissions at high-resolution. On the other hand, traffic emissions affect air quality at regional scales, for which mesoscale chemistry-transport models are best suitable for model the transport, transformations and deposition of pollutants. These models can also benefit from the estimation of detailed emissions.

In this work, a microscale emission estimation methodology, based on a suitable combination of traffic and emissions micro-simulation models, has been applied to obtain high-resolution

road traffic emissions in different urban areas. These models do not only describe the behaviour of the single entities which define the traffic such as individual vehicles and their interactions, but they also take into account traffic signs and lane changes for each vehicle. This results in stop & go cycles that produce braking-acceleration patterns with an important influence on emissions.

In a particular application, the aforementioned methodology was used to compute the emissions in an urban area for different traffic configurations, with the aim to evaluate the impact of several traffic measures oriented to reduce air pollution in an urban area. To that end, the emissions were implemented into a CFD model to simulate their dispersion in an urban area. Long-period concentrations of air pollutants were computed using a methodology that bases the computation of hourly air pollutants concentrations in a set of pre-computed steady-state CFD simulations. Furthermore, the influence of meteorological conditions on these measures has been extensively studied through the simulation of several meteorological conditions and their application to the aforementioned methodology. For the computation of NO_2, from the previously computed NO_X, an empirical approach has been followed, developing a simple methodology to assess the impact of meteorology on background concentrations saving the computational resources needed by a mesoscale air quality model to this end. It has been found that the analysed mitigation strategies, together with a renovation of the vehicle fleet which took place along time in the study area, have helped to reduce the levels of NO_X and NO_2 concentrations. Nonetheless, the influence of meteorological conditions cannot be neglected when analysing annual or monthly concentration values. In fact, at a local scale, the impact of a change of meteorological conditions on pollutants concentrations can overcome that of a mitigation strategy. Even though, the lower the air pollutant concentrations the lower their sensitivity to meteorological conditions, as it has been demonstrated when analysing a mitigation measure that notably reduces NO_X concentrations.

In addition, this work includes an analysis of the impact of the COVID-19 pandemic-related restrictions on air pollutant emissions in Europe. This study complements the main applications of the thesis, illustrating how a sudden reduction in mobility and economic activities can significantly affect pollutant emissions, serving as a link to other works in this thesis by providing a reference value of emissions reduction to diverse mitigation strategies, such as those analysed in some works of this thesis.

Lastly, it has been developed a methodology to use a new dataset of emissions calculated at street level resolution in CHIMERE regional chemistry-transport model. With this aim, in the scope of this work an interface has been developed to facilitate the implementation of emissions within the model, without losing the advantages that provide the high-resolution emissions. This work shows how the implementation of detailed emissions improves the

estimation of several pollutants in a regional CTM. As an example of those improvements, it has been showed how a detailed set of emissions contribute to a better estimation of legislated parameters, which can be of notable usefulness to policy makers.

This work contributes to a better understanding of the impact traffic measures in an urban area on long-period air quality, and of the influence of the meteorological conditions in the effectiveness of these measures at high resolution. Furthermore, this work facilitates the study of traffic measures at mesoscale by providing an interface to include those emissions in a regional CTM.

List of Symbols

a	Romberg formula regression parameter
b	Romberg formula regression parameter
C	Pollutant concentration
c	Romberg formula regression parameter
C_d	Air resistance coefficient
C_ε	Model constant for ε equation
C_μ	Model constant
C_{sim}	Pollutant concentration of CFD simulation
C_{mod}	Modelled concentration
D	Molecular diffusivity
F_{r_0}	Rolling resistance coefficient
F_{r_1}	Rolling resistance coefficient
F_{r_4}	Rolling resistance coefficient
G_k	Production of turbulent kinetic energy
g	Acceleration due to gravity
K_t	Turbulent or eddy diffusivity
k	Turbulent kinetic energy
m_{load}	Vehicle's load mass
$m_{vehicle}$	Vehicle's mass
P_d	Power demand
P_{rr}	Power needed to overcome the rolling resistance
P_{ar}	Power needed to overcome the air resistance
P_a	Power needed for desired acceleration
P_{grad}	Power needed to overcome the road slope
Pr_t	Turbulent Prandtl number
Re	Reynolds number
Ri	Richardson number
S	Mean strain-tensor
S_h	Source or sink of heat

S_k	Source or sink of turbulent kinetic energy
S_M	Source or sink of momentum
S_{veg,u_i}	Sink of momentum for vegetation modelling
$S_{veg,k}$	Sink of k for vegetation modelling
$S_{veg,\varepsilon}$	Sink of ε for vegetation modelling
S_ϕ	Source or sink of a scalar variable
Sc_t	Turbulent Schmidt number
t	Time
U	Mean velocity component
u	Instantaneous velocity
u'	Turbulent velocity component
u_*	Friction velocity
V_d	Deposition velocity
z	Height above a reference plane
z_0	Roughness length
β_p	Constant for vegetation modelling
β_d	Constant for vegetation modelling
$\eta_{gearbox}$	Efficiency of vehicle's gearbox
κ	Von Karman constant
μ	Dynamic viscosity
μ_t	Turbulent or eddy viscosity
ν	Kinematic viscosity
ν_t	Turbulent or eddy kinematic viscosity
ρ	Air density
σ_k	Turbulent Prandtl number for turbulent kinetic energy
σ_ε	Turbulent Prandtl number for turbulent dissipation energy
σ_θ	Turbulent Prandtl number for temperature
τ	Shearing stress
τ_0	Surface shear stress or drag
ϕ	Scalar variable
Φ	Mean scalar component
ϕ	Turbulent scalar component
As	Arsenic
CH_4	Methane
CO_2	Carbon dioxide
H_2O	Water
Hg	Mercury
N_2	Molecular Nitrogen

NH_3	Ammonia
Ni	Nickel
NO	Nitrogen monoxide
NO_2	Nitrogen dioxide
NO_X	Nitrogen oxides
O_3	Ozone
Pb	Lead
PM_{10}	Particulate Matter with aerodynamic diameter less than 10 μm
$PM_{2.5}$	Particulate Matter with aerodynamic diameter less than 2.5 μm
SO_2	Sulphure dioxide
SO_X	Sulphare oxides

List of acronyms

ABL	Atmospheric Boundary Layer
AQMS	Air Quality Monitoring Station
BAU	Business As Usual
BEP	Building Effect Parametrization
BEM	Building Energy Model
BEV	Battery Electric Vehicle
CEP	Characteristic Emission curves over Power
CFD	Computational Fluid Dynamics
CNG	Compressed Natural Gas
CO	Carbon monoxide
CORSIM	CORridor SIMulation
CRS	Coordinate Reference System
DNS	Direct Numerical Simulation
DPF	Diesel Particulate Filter
EEA	European Environmental Agency
EGR	Exhaust Gas Recirculation
EU	European Union
EV	Electric Vehicle
EZ	Entrainment Zone
FAC2	Factor 2
FAME	Fatty Acid Methyl Ester
FB	Fractional Bias
FC	Fuel Consumption
GTL	Gas-To-Liquid
HBEFA	Handbook of Emission Factors for Road Transport
HC	Hydrocarbon
HDV	Heavy Duty Vehicle
HEV	Hybrid Electric Vehicle
HFCV	Hydrogen Fuel Cell Vehicle

HOV	High Occupancy Vehicle
LAD	Leaf Area Density
LES	Large Eddy Simulation
LEZ	Low Emission Zone
LNG	Liquified Natural Gas
LNT	Lean NO_X Trap
LPG	Liquified Petroleum Gas
ML	Mixing Layer
MOST	Monin-Obukhov Similarity Theory
NAC	NO_X Adsorber Catalyst
NECD	New European Driving Cycle
NG	Natural Gas
NMSE	Normalized Mean Square Error
NMHC	Non-Methane Hydrocarbon
NMVOC	Non-Methane Volatile Organic Compound
NSL	Nocturnal Stable Layer
NSR	NO_X Storage Reduction
PBL	Planetary Boundary Layer
PEV	Plug-in Electric Vehicle
PHEV	Plug-in Hybrid Electric Vehicle
PM	Particulate Matter
R	Correlation coefficient
RANS	Reynolds-averaged Navier-Stokes
RL	Residual Layer
RSM	Reynolds Stress Model
RNG	Re-Normalisation Group
S	Sulphure
SCR	Selective Catalytic Reduction
SL	Surface Layer
SNAP	Selected Nomenclature for Air Pollution
SRA	Station Representativeness Area
SUMO	Simulation of Urban MObility
TEE	Traffic Energy and Emissions
TLS	Traffic Light Signal
UBL	Urban Boundary Layer
UCL	Urban Canopy Layer
VISSIM	Verkehr In Städten - SIMulation
VOC	Volatile organic compound

WA CFD-RANS	Weighted Average CFD-RANS methodology
WHO	World Health Organization
WLTP	World harmonized Light vehicles Test Procedure
WRF	Weather Research and Forcasting

List of Figures

List of Tables

Chapter 1

Introduction and research motivation

1.1 Air pollution

Despite ongoing overall improvements in air quality, air pollution is the main environmental health issue in Europe (EEA, 2024). According to the World Health Organisation – WHO – as for 2019, around 6.7 million premature deaths occur every year around the world due to air pollution. Of these, 4.2 million are related to ambient/outdoor air pollution (WHO, 2024).

The air pollutants can be directly emitted from both anthropogenic and natural sources, called primary pollutants, which in turn chemically react in the atmosphere forming secondary compounds. They are dispersed into the atmosphere influenced by meteorological conditions (wind speed and direction, temperature, humidity, solar radiation) that affect the chemical reactions. High pollution levels have often been observed in urban areas, where both emissions and population are concentrated. The interaction between the atmospheric processes and the morphology of a city, with its buildings and streets canyons, creates complex air flow patterns. This fact, joined to the heterogeneity of emissions inside a city (most of then coming from road traffic), generates strong spatial gradients in the concentration fields inside the urban canopy layer (Santiago et al., 2013).

In order to reduce the negative impacts of air pollution on human health, the EU and the WHO have established specific threshold values for several pollutants. In 22 September 2021, the WHO published an update on their Air Quality Guidelines which tightened the threshold limits for common pollutants such as particulated matter ($PM_{2.5}$ and PM_{10}), nitrogen dioxide (NO_2), and ozone (O_3) (Table 1.1). The **Directive 2024/2881** (Directive (EU) 2024/2881, 2024) is the reference norm at European level at the time this document was writing. It merges the two previous directives, **Directive 2008/50/EC** and **Directive 2004/107/EC** into one and guides provisions to clarify and simplify the rules, aligning 2030 EU air quality

standards more closely with the latest recommendations of the World Health Organization. The limit values for air pollutants established by this Directive are reference values to be complied by Member States by January 1st, 2030. Furthermore, Directive 2024/2881 states the need of modelling applications to interpret punctual data in terms of geographical distribution of concentration of pollutants, and to inform air quality plans and roadmaps, and to estimate the impact of short-term measures in air pollution.

Table 1.1: Limit values for several pollutants (Directive (EU) 2024/2881, 2024; WHO, 2018; WHO, 2021). All values in $\mu g \cdot m^{-3}$ except for CO, which are in $mg \cdot m^{-3}$

Pollutant	Averaging Time	2005 WHO AQGs	2021 WHO AQGs	EU 2008/50/EC	EU 2024/2881
$PM_{2.5}$	Annual	10	5	25	10
	24-hour	25	15 ($\leq 3d$)	-	25 ($\leq 18d$)
PM_{10}	Annual	20	15	40	20
	24-hour	50	45 ($\leq 3d$)	50 ($\leq 35d$)	45 ($\leq 18d$)
O_3	8-hour	100	100	120 ($\leq 25d$)	120 ($\leq 18d$)
NO_2	Annual	40	10	40	20
	24-hour	-	50 ($\leq 3d$)	-	50 ($\leq 18d$)
	1-hour	200 ($\leq 1h$)	200 ($\leq 18h$)	200 ($\leq 3h$)	
SO_2	Annual	-	-	-	20
	24-hour	20	40	125 ($\leq 3d$)	50 ($\leq 18d$)
	1-hour	-	-	350 ($\leq 24h$)	350 ($\leq 3h$)
CO	24-hour	-	4 ($\leq 3d$)	-	4 ($\leq 18d$)
	8-h max	10	10	10	10

At the moment this work was written, it does not yet exist in Spain a transposition to the national legal framework of the Directive 2024/2881 as this work is currently ongoing. The current legal base to the regulation of the air quality and atmospheric pollution in Spain is established by **Ley 34/2007**. It defines the environmental politics to follow in order to meet the the European Union standards established by the European Directive 2008/50/EC and 2004/107/EC. The Spanish Real Decreto **R.D. 102/2011** (Real Decreto 102/2011, 2011) (modified in **R.D. 39/2017** (Real Decreto 39/2017, 2017)) establishes air quality limit values for the main atmospheric pollutants.

Tackling the problematic of air pollution requires extensive knowledge of its causes. Therefore, more detailed studies are required to face the still high levels of harmful pollutants recorded at monitoring stations. Accordingly, a comprehensive study of the potential impacts of mitigation measures on air quality prior their implementation is essential.

1.2 Processes affecting air quality

The air quality is affected by several processes of different nature. First, emissions introduce pollutants into the air. Primary pollutants (NO_X or primary PM), those emitted directly

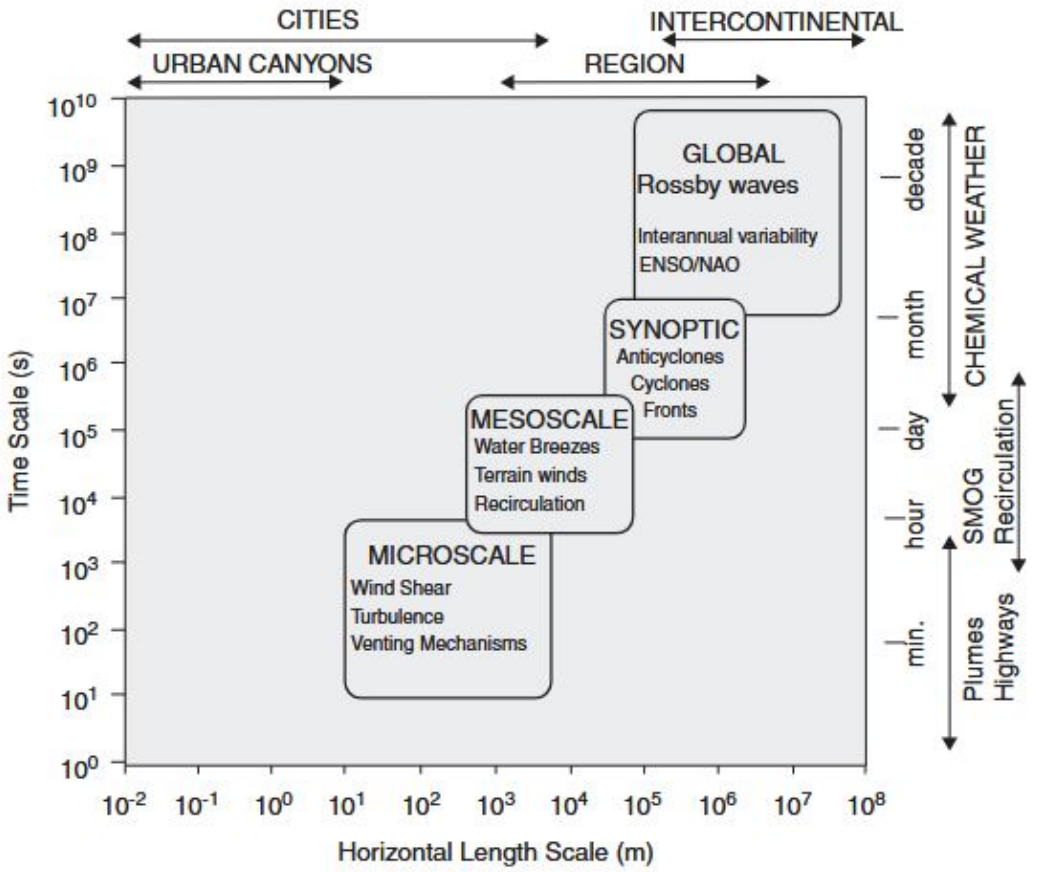

Figure 1.1: Time and spatial scales of chemical and dynamic processes in the urban atmosphere. Source: Salmond and McKendry (2009).

from a source, can be emitted by different sources of anthropogenic activity -such as road transport, industrial or agriculture activities- or by natural sources (i.e., volcanic activity or biogenic activity). Other pollutants, such as O_3 or secondary PM, form in the atmosphere due to chemical transformations of primary pollutants. These are called secondary pollutants. Moreover, the meteorological conditions affect the air quality by modifying the dispersion or by depositing them into surfaces. The deposition of pollutants is the direct transfer of the pollutants to any surface. Precipitation can help dissipating heavier pollutants by depositing them onto the surface, whereas wind can disperse lighter ones (Kassomenos et al., 1998, 2014). This kind of deposition, in which precipitation is the driver of the transfer, is called wet deposition. Deposition can also occur without precipitation, in that case its called dry deposition. Wet deposition is much more effective than dry deposition. Other parameters such as solar radiation and temperature can favour the removal or creation of pollutants by triggering chemical transformations of pollutants Latini et al., 2002. Finally, the topography or the morphology of an area can affect air quality at a local scale by creating conditions that favours the dispersion or accumulation of pollutants (Li et al., 2020).

Most of those processes occur in the lowest part of the atmosphere. The atmosphere is a layer of gases that surrounds the Earth's surface, attracted to it by the force of gravity. It can be classified in terms of the scales of motions, both spatially and temporally, into broad categories: microscale, mesoscale, synoptic and global (Arya, 2001). Figure 1.1 illustrates the temporal and spatial scales of those categories, as well as the main examples of phenomena occurring within them.

The atmosphere is composed of several layers, the lowest of them, the troposphere, is where all the emission processes and meteorological phenomena occur. In particular, the earth's surface is a boundary on the domain of the atmosphere, and it exercises a notable influence on the lowest 100 to 3000 m of the atmosphere, creating what is called the Planetary Boundary Layer (PBL), also known as Atmospheric Boundary Layer (ABL). Thus, the PBL can be defined as the part of the troposphere that results from the interaction with the underlying surface. In this layer, the atmospheric processes are mainly dominated by the exchanges of heat, mass and momentum between the atmosphere and the earth's surface (Stull, 1988).

Most pollutant sources are near surface, therefore most pollution is trapped in the PBL. Variations in the flow features of the PBL and its volume will have a significant impact on air quality. The thickness of the PBL is largely variable in time and space, and depends on several processes such as the rate of heating or cooling of the surface, the wind speed, and the surface roughness. Therefore, the variation of the PBL height is associated to atmospheric phenomena at different scales; from the synoptic weather conditions to the surface energy balance resulted from the interaction of the lower layer with the surface features (Arya, 2001). Furthermore, its temporal variability is closely related to the diurnal cycle as a result of the solar radiation-induced heating and cooling of the land surfaces.

Over an urban area, the flow features in the PBL are modified. The buildings and other structures increase the surface roughness and modify the surface-energy balance as well. Accordingly, the lowest part of the atmosphere over an urban area is also known as Urban Boundary Layer (UBL). Figure 1.2 shows the cross sections of the structure of the diurnal (upper figure) and nocturnal (lower) UBL. The UBL is divided into the Mixing Layer (ML), and the Surface Layer (SL). The SL comprises the lowest part of the UBL, and there the flow is dominated by friction with Earth's surface. The SL involves the Inertial Sublayer and the Roughness Sublayer, in which the Urban Canopy Layer (UCL) is found.

The ML is a more homogeneous area, usually convectively driven, where flows are well developed and pollutants are expected to be well mixed (Stull, 1988). On initially cloud-free days, ML growth is tied to solar heating of the ground. It starts to grow about a half hour after sunrise, reaching its maximum depth in late afternoon. The ML is topped by a stable layer, which acts as a lid to the rising thermals, thus restraining the domain of turbulence.

It is called the Entrainment Zone (EZ) because entrainment into the ML occurs there.

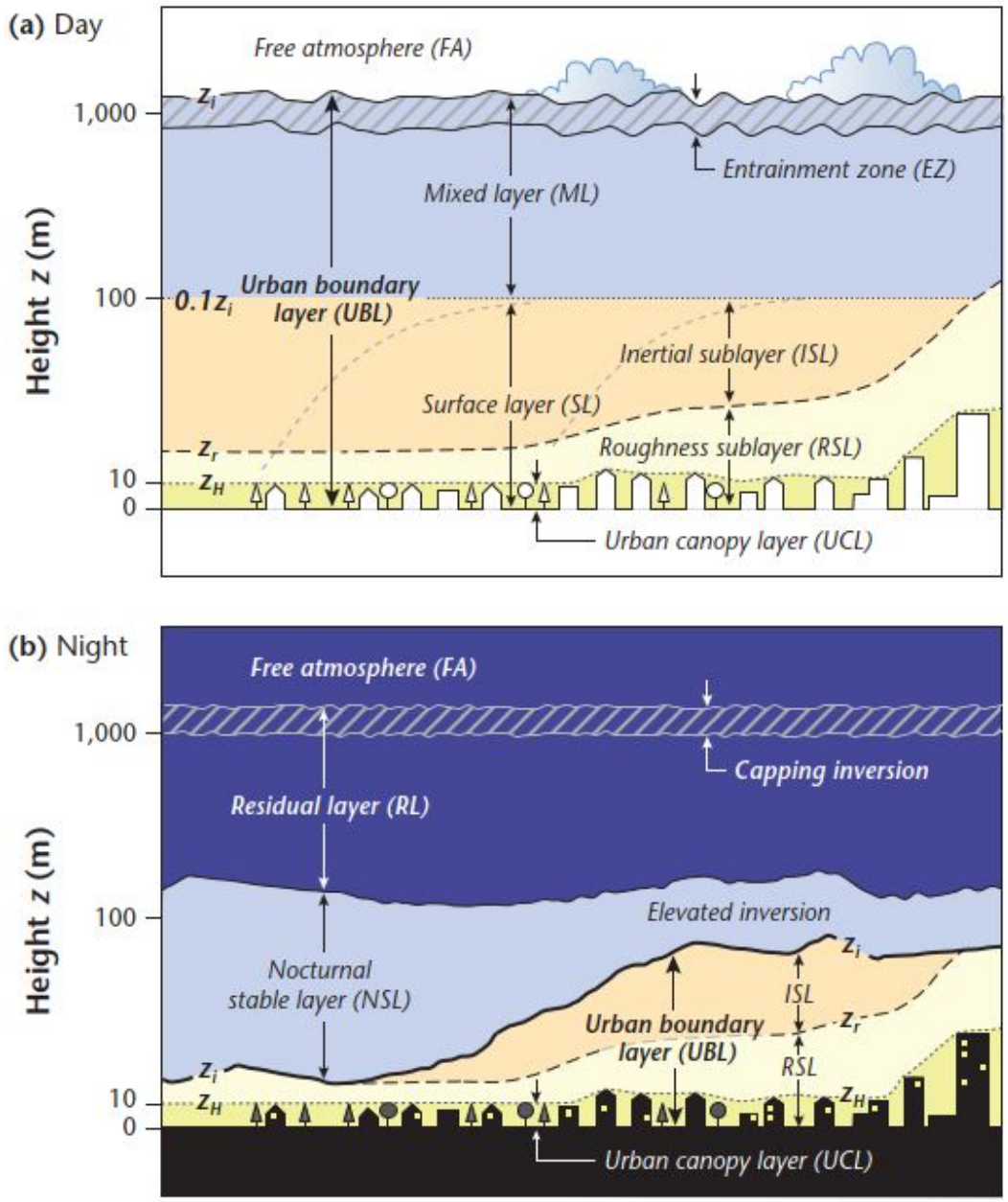

Figure 1.2: Structure of the Planetary Boundary Layer a) during the day; b) during the night. Source: Arya (2001).

At night, the UBL shrinks as cooling at Earth's surface usually creates a stable layer, about 200 to 400 m width, that suppress the turbulent vertical mixing (Oke, 1997). This is the so-called Nocturnal Stable Layer (NSL). Above the NSL, extending roughly up to the height of the daytime UBL, is a layer with properties conserved from the previous afternoon. This Residual Layer (RL) is capped by the inversion carried over from the daytime EZ. In urban areas, the heating of the surface due to the release of heat by the urban surfaces causes mixing, which together with the greater urban roughness cause the atmosphere over the city

to be better mixed at night, maintaining the daytime UBL, although with a much lower depth.

The Monin-Obukhov Similarity Theory (MOST) established an approach to describe the mean flow profiles in a horizontally homogeneous surface layer, by means of the atmospheric stability based on the scale variables of the length, velocity and temperature. The scale velocity is the so-called friction velocity (u_*), related to the surface drag (τ_0) through the relation $u_*^2 \equiv \tau_0/\rho$, where ρ is the air density. The surface kinematic heat flux ($H_0/\rho C_p$) is expressed as $H_0/\rho C_p \equiv -u_*/\theta_*$, where θ_* is the scale temperature; H_0 is the sensible heat flux at the surface and C_p is the specific heat at constant pressure. Accordingly, the stability parameter (z/L) is computed on the length scale L known as the Obukhov length, which is defined as:

$$L = -\frac{u_*^3}{\kappa(g/T_0)(H_0/\rho C_p)} \tag{1.1}$$

where κ is the von Karman constant, equal to 0.4; $g = 9.81\ m \cdot s^{-2}$ is the gravity acceleration and T_0 is the reference temperature. Therefore, g/T_0 is the buoyancy variable. In this way, the ratio z/L provides the relative importance of the buoyancy forces against the shear effects. Negative values of z/L stand for unstable atmospheric conditions, whereas positive values represent stable conditions.

Finally, the wind profiles over a homogeneous surface layer can be described by the following logarithmic vertical profile:

$$u(z) = \frac{u_*}{\kappa}\left[ln\left(\frac{z}{z_o}\right) + \psi(z/L)\right] \tag{1.2}$$

The expression $\psi(z/L)$ is the dimensionless function of the MOST, that is zero in neutral atmospheric conditions.

Most of the physical processes occurring in the lower atmosphere are involved within a turbulent flow regime with high Reynolds number (Re). This number is expressed as UL_{ref}/ν, where U and L_{ref} are the characteristic velocity and the length scale of the mean flow, respectively, and ν is the kinetic viscosity ($\nu = \mu/\rho$, where μ is the dinamic viscosity and ρ is the fluid's density). The turbulence can be generated either by the shear production that transforms the mean flow energy into turbulent kinetic energy (k) or by the buoyancy production due to the conversion of potential energy of unstable stratification into turbulent kinetic energy (similarly, stable stratification suppresses turbulence). The contribution of each process is determined by the Richardson number (Ri), expressed by the ratio of the

buoyancy and shear terms.

$$Ri = \frac{g}{T_0} \frac{\partial\theta/\partial z}{(\partial \mathbf{u}/\partial z)^2} \tag{1.3}$$

The turbulent flow is characterised to be highly irregular and rotational, as well as dissipative, because k is continuously dissipated by viscosity. Therefore, flow variables exhibit intermittent variations both in time and space. These fluctuations represent the turbulence contribution, which are commonly represented using the Reynolds decomposition (Reynolds, 1895). Thus, the instantaneous variable (ϕ) of a turbulent flow can be defined as the sum of its mean component ($\Phi = \overline{\phi}$) and its time fluctuation (ϕ'), resulting in $\phi = \Phi + \phi'$. Figure 1.3 illustrates the turbulent fluctuation of velocity at a local point.

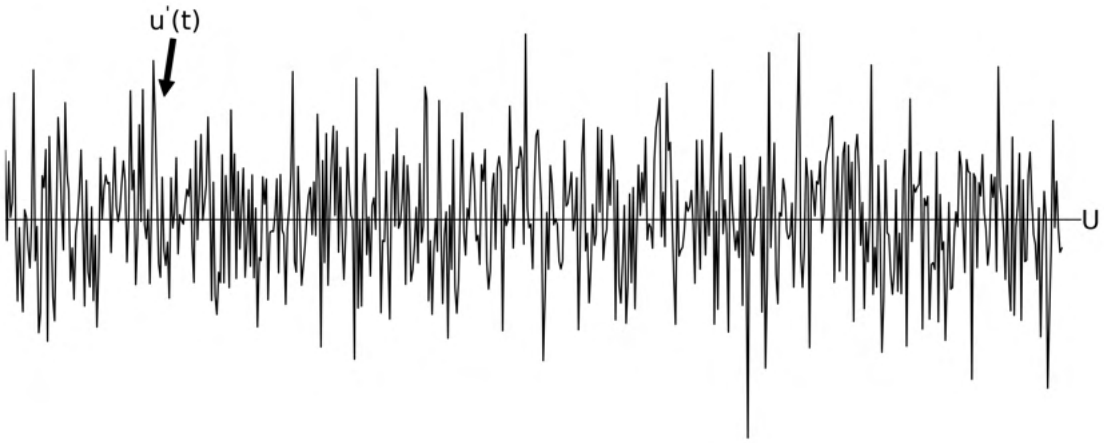

Figure 1.3: Representation of the turbulent component of the velocity at a local point.

Turbulent flows are highly rotational and involve three dimensional vortex-like structures called *eddies*. Turbulence consist on many different size eddies (whose size depend on Re) superimposed on each other. The relative strengths of these different scale eddies define the *turbulence spectrum*. Two broad categories can be distinguished in the turbulence spectrum. The large-eddy scale (l) and the small-eddy scale (η). The former receives the most energy from the mean flow and l is comparable to its characteristic scale without depending on the fluid properties. In contrast, the small-eddy scale is entirely dependent on the fluid viscosity and the energy dissipation rate (ϵ). From the Energy Cascade Hypothesis, the essential characteristic of the turbulence is based on a continuous energy transfer from the largest to the smallest scale of eddies. And, assuming the Kolmogorov Hypothesis, the small-scale length is exclusively dependent on $\eta = \nu^{3/4}\epsilon^{-1/4}$.

1.3 Traffic emissions

Studies on air quality in cities revealed that road transport is a main source of air pollution (EEA, 2025; Thunis et al., 2023), significantly affecting air quality in urban areas. In EU, transport sector is the largest emitter of nitrogen oxides (NO_X) and responsible of almost half of their total emissions in Europe. It is also an important emitter of particulate matter, representing a 12% of the total emissions for both $PM_{2.5}$ and PM_{10} (EEA, 2023). Many efforts have been aimed at reducing emissions from this sector since 1990, which has led to significant reductions in emissions of several pollutants. Compared to 2000, emissions in 2019 have decreased in average by: 40% in PM_{10}, 48% in NO_X, 53% in $PM_{2.5}$ and 71%, 75% and 77% in SO_X, CO and NMVOCs respectively. Nonetheless, these reductions in air pollutant emissions have been lower than expected (EEA, 2017) due to an increase in traffic volume of up to 22 % between 2000 and 2019 (EEA, 2023), which also has led to increased emissions of metals (Figure 1.4). The COVID-19 pandemic had an important impact on road transport emissions between 2020 and 2022 (Rodríguez-Sánchez et al., 2022). An extensive analysis of those changes in emissions is presented in Chapter 4.

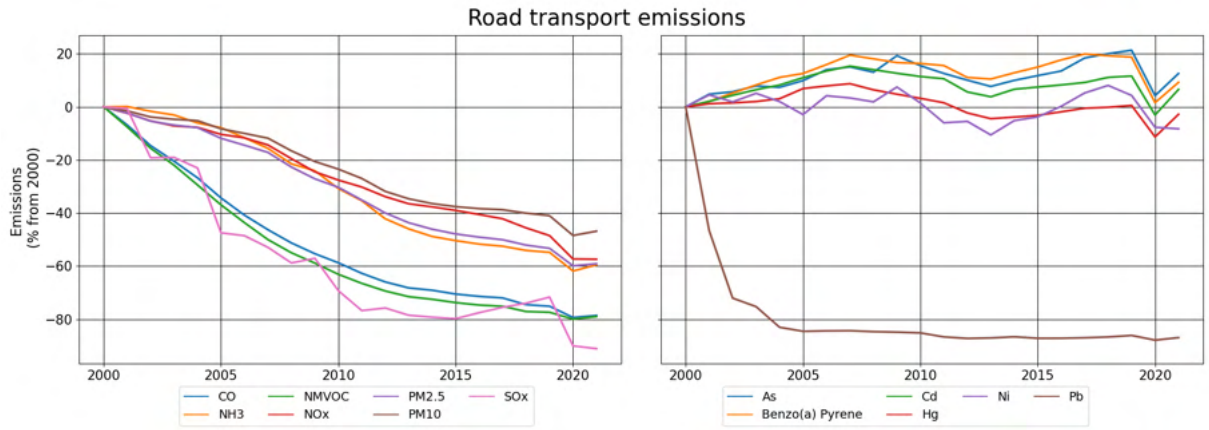

Figure 1.4: EU27 Road transport emissions evolution since 2000. Adapted from EEA (2025).

1.3.1 Main air pollutants from traffic

In the following paragraphs, the main pollutants emitted from road traffic are presented, some of which have been previously mentioned on this work:

1.3.1.1 Nitrogen oxides

The nitrogen oxides (NO_x) constitute a group of different chemicals which are all formed from the reaction of nitrogen with oxygen. Although this group includes several gases, the term 'nitrogen oxides' is usually used in atmospheric chemistry to refer to the mix of nitric oxide (NO), which is a colourless, odourless gas and nitrogen dioxide (NO_2), which

is a reddish-brown gas with a pungent odour. They are very toxic and reactive gases, with harmful environmental effects and health problems mainly for the respiratory system (Spirić et al., 2012).

1.3.1.2 Volatic organic compounds

Volatile organic compounds (VOCs) are a group of carbon-based chemicals that easily evaporate into the air. Many VOCs are released into the atmosphere through traffic emissions, especially from the incomplete combustion of gasoline and diesel fuels in vehicles. These emissions include a variety of hydrocarbons (HCs), such as benzene, toluene, ethylene, and xylene, which are among the most common VOCs found in urban air. VOCs contribute significantly to air pollution by reacting with nitrogen oxides (NO_X) in the presence of sunlight to form ground-level ozone and secondary organic aerosols, both of which are harmful to human health and the environment.

1.3.1.3 Carbon monoxide

The carbon monoxide (CO) is a colorless, odorless, tasteless gas mainly produced by the incomplete combustion of carbon-containing compounds. This happens when the carbon present in the fuel is only partially oxided, resulting in CO instead of CO_2. It is highly toxic. This gas can disrupt the transport of oxygen by the blood, leading to heart and health problems. It also contributes to the greenhouse effect -not directly, but indirectly by altering the abundance of greenhouse gases such as methane and carbon dioxide.

1.3.1.4 Particulate matter

Particulate matter (PM) are microscopic particles of solid or liquid matter suspended in the air. One main anthropogenic source of PM is the incomplete combustion of fossil fuels. PM can be classified by its origin in two categories: primary PM and secondary PM. 'Primary' PM is the fraction of PM that is emitted directly into the atmosphere (i.e. from the combustion processes inside a vehicles' motor), whereas 'secondary' PM forms in the atmosphere from the release of precursor gases (mainly sulphur dioxide (SO_2), nitrogen oxides (NO_X), ammonia (NH_3) and some VOCs). Depending on the size of the particles, they are also subdivided into PM_{10}, which are particles with less than 10 μm of diameter; and $PM_{2.5}$ (particles up to 2.5 μm). Regarding their effects in health, due to their small size they can penetrate into sensitive areas of the respiratory system causing or aggravating respiratory illnesses, specially on those people with existing heart or respiratory problems. But their risks are not limited to the cardiorespiratory system. They can also affect the central nervous system, the reproductive system and also can infer cancer producing premature deaths. PM can also impact the climate by altering the amount of incoming solar radiation and outgoing

terrestrial longwave radiation retained in the Earth's system.

1.3.1.5 Heavy metals

There has been an ongoing discussion with regards to the definition of the term 'heavy metals'. Nowadays, this word usually describes metallic chemical elements and metalloids. Some heavy metals such as cadmium (Cd), mercury (Hg) and lead (Pb) are toxic to human health, animals and plants. Heavy metal pollution has emerged in recent decades due to the anthropogenic activity, which is the prime cause of pollution (Briffa et al., 2020). The emissions of heavy metals are linked to specific industrial plants, being their main emitters the mining, smelting, foundries and other metal-based industries. Heavy metal use in the agricultural field has been the secondary source of heavy metal pollution. Heavy metals can be also emitted by natural processes such as volcanic activity, metal corrosion, metal evaporation from sol and water, sediment resuspension and soil erosion.

1.3.2 Traffic emission processes

Road traffic emissions can be classified into three different categories depending on the processes involved in their release to the atmosphere:

1.3.2.1 Exhaust emissions

Exhaust emissions are those produced primarily in the combustion of petroleum-based fuels (diesel, gasoline, natural gas (NG) and liquefied petroleum gas (LPG)). In a perfect engine, oxygen in the air would react in a combustion process with all of the hydrogen in the fuel to form water and with all of the carbon in the fuel to form CO_2, and the nitrogen in the air would remain unaffected. However, in reality no combustion process is perfect; thus, vehicle engines emit many different pollutants in addition to water, CO_2 and CO. The amount of exhaust emissions a vehicle releases into the atmosphere depends on several factors, which include the type of fuel used in the combustion process; the type of engine; the vehicle size, weight and maintenance; and the driving cycle. Emissions of gases such as NO_X and SO_2 are extremely dependant on the temperature and pressure conditions reached inside the combustion chamber. Due to the importance of temperature on exhaust emissions, it is particularly considered in the emission formation:

- Hot running emissions: exhaust emissions that occur under "hot stabilized" conditions, which means that the engine and the emission control system (e.g. catalytic converter) have reached their typical operating temperatures.
- Start "cold" emissions: exhaust emissions that occur in addition to hot running emissions because engines and catalysts are not (fully) warmed up and operate in

a non-optimal manner.

1.3.2.2 Non-exhaust emissions

Non-exhaust emissions are those which occur by other means than the combustion processes. They essentially affect to PM and some heavy metals, which are released to the atmosphere as a result of the abrasion and corrosion of the vehicle tyres, brakes and clutch, the road surface wear or the corrosion of the chasis, bodywork and other vehicle components. Non-exhaust emissions can be classified by the processes involved on their generation:

Brake and tyre wear

These emissions result from the frictional contact between the road and vehicle tyres, or between different elements of a vehicle. Break wear emissions are generated by the friction produced at the contact between brake system components during forced deceleration. On the other hand, tyre wear emissions are produced by the frictional contact between the road surface and the tyre tread. This friction results in the abrasion of the tyre tread that emits particles into the atmosphere (Thorpe and Harrison, 2008). There is a large number of factors that may affect the wear factor, that is the rate at which tyre wear emissions occur, such as the tyre characteristics (size, tread depth, pressure and temperature, etc.), the vehicle characteristics (such as weight and distribution of load, engine power, location of driving wheels), the road surface characteristics (material, texture pattern, porosity, condition, wetness, etc.) and the vehicle operation (speed, acceleration, frequency and extent of braking and cornering) (Boulter, 2005).

Road dust resuspension

Road dust resuspension. These emissions refer to the road surface deposited material that is resuspended into the air after the passing of a vehicle due to vehicle-generated turbulence.

Evaporative emissions

Evaporative emissions are the result of non-exhaust VOCs losses from the vehicle's fuel system. Those losses can happen by breathing losses through the tank vent or by fuel permeation through plastic and rubber components (EMEP/EEA, 2023). Gasoline fuel vapour contains a variety of different HCs, which can be emitted any time there is fuel in the tank, even when the vehicle is parked with its engine turned off. On the other hand, evaporative emissions from diesel vehicles are usually considered to be negligible due to the presence of heavier HC and the relatively low vapor pressure of diesel fuel. Three main factors contribute to the evaporative emissions:

- Ambient temperature. The increase in ambient temperature results in the thermal expansion of the fuel and vapour in the tank. In absence of an emission control system, some of the increased volume of fuel vapour is released to the atmosphere.
- Running losses. Those are the consequence of vapour generated in the fuel tank during vehicle operation. Driving style can have an important impact on running losses.
- Hot-soak emissions. Hoak-soak emissions are caused when a hot engine is turned off. Heat from the engine and exhaust system increases the temperature of the fuel in the system (which is no longer flowing) and some of it evaporates from the carburettor and from the fuel tank in carbureted vehicles, or from the fuel tank in fuel injected vehicles.

1.3.3 Traffic-related measures for improving air quality

Over recent years the number of policy actions undertaken in urban areas across Europe to specifically mitigate the negative impacts of air pollution on human health and vegetation due to traffic-related emissions. Those policy actions can be grouped into two major categories (Litman, 2013):

- Cleaner vehicles strategies oriented to reduce emission rates per vehicle-kilometre. These include the promotion of electric or more efficient and alternative fuel vehicles and fuel efficiency standards and initiative. Local and regional air quality management plans -including initiatives such as Low-Emission Zones (LEZ) - are now undertaken in many areas (Holman et al., 2015).
- Mobility management strategies that reduce total vehicle travel. These include cleaner transport options (transit, walking, cycling or High Occupancy Vehicle -HOV- priority lanes), incentives to choose more efficient options (parking pricing, transit encouragement, fuel tax increases or congestion charges) and land use management such as traffic calming measures.

In a more global sense, different legal mechanisms have been introduced such as setting limit values for ambient concentrations of pollutants and the regulation of road-transport related emissions by introducing more restringing emission standards or by setting requirements for fuel quality.

In the European Union, the legal framework that establishes emission standards from vehicles consists in a series of directives, each of them amendments to the 1970 **Directive 70/220/EEC**. A summary list of the standards for vehicle type passenger cars is shown in Table 1.2.

These standards, known as Euro norms, define the acceptable limits for exhaust emissions

Table 1.2: EU emission standards for passenger cars. Limit values for pollutants are given in g/km.

Fuel	Stage	EU legislation	Date	CO	HC	NO_X	PM	NMHC
Petrol	Euro1	D.91/441/EEC & D.93/59/EEC	1992.07	2.72	-	-	-	-
	Euro2	D.94/12/EC & D.96/69/EC	1996.01	2.2	-	-	-	-
	Euro3	D.98/69/EC	2005.01	1.0	0.10	0.08	-	-
	Euro4	D.98/69/EC & D.2002/80/EC	2009.09	1.0	0.10	0.06	0.005	0.068
	Euro5	715/2007/EC	2009.09	1.0	0.10	0.06	0.005	0.068
	Euro6	459/2012/EC	2014.09	1.0	0.10	0.06	0.005	0.068
Diesel	Euro1	D.91/441/EEC & D.93/59/EEC	1992.07	2.72	-	-	0.14	-
	Euro2	D.94/12/EC & D.96/69/EC	1996.01	1.0	-	-	0.08	-
	Euro3	D.98/69/EC	2005.01	0.64	-	0.50	0.05	-
	Euro4	D.98/69/EC & D.2002/80/EC	2009.09	0.50	-	0.25	0.025	-
	Euro5	715/2007/EC	2009.09	0.50	-	0.18	0.005	-
	Euro6	459/2012/EC	2014.09	0.50	-	0.08	0.005	-

(in pollutant mass by km driven) of new vehicles sold in the EU Member States according to standardised measurements in laboratories for standardized predefined driving cycles. It applies to passenger cars and light duty vehicles, two/three wheeled vehicles and the engines used in heavy duty vehicles (HDVs). Each type of vehicle has different emission limits and test procedures. The Euro norms are used as reference to establish local and regional policy actions to reduce air pollution levels.

1.3.3.1 Low-Emission Zones

Low-Emission Zones (LEZ) are areas with restricted access to certain vehicles based on their emissions. Generally, the restriction is based on the emission standard a vehicle was constructed to. In 2022, there were approximately 200 active LEZs in Europe (Holman et al., 2015). However, this number is in continuous change. In Spain, the Climate Change Act (Ley 7/2021, 2021) requires every municipality with more than 50.000 inhabitants to be equipped with a LEZ since 2023. This made the number of LEZs in Spain raise from 3 to 158 since January 2023. Similarly, the French Senate voted in favour of requiring municipalities with more than 150.000 inhabitants to have a LEZ. The original deadline was 2024 and some municipalities have implemented it. Nonetheless, in 2025 the French Senate voted in favour of revoking the obligatoriness of implementing a LEZ. Most LEZs are permanently active, but others are not. For example, the Lisbon LEZ works from 7h to 21h only on working days (Sadler Consultants, Ltd., 2025). However, as air quality improves, some municipalities have opted for removing their LEZs. That is the case for several municipalities in Germany such as Freiburg, Hannover and Karlsruhe among others.

LEZs are intended to improve air quality within their area of affectation by creating a step change of the vehicle fleet inside that area. Nonetheless, some studies question the efficiency

of already existing LEZ in Europe because most of them do not apply to most vehicles or their size is not big enough to dissuade people from using private transport (Holman et al., 2015; Moral-Carcedo, 2024). In addition, their evaluation has been frequently based on punctual AQMS measures before and after the implementation which may or may not be representative of the air quality of the area within the LEZ is located. Detailed studies are needed to fully understand the impacts of air mitigation strategies in urban areas, before and after their implementation, which is the main reason they will be studied in this PhD Thesis.

1.3.3.2 Alternative fuels and electric vehicles

Together with the LEZs, cleaner vehicles are becoming increasingly popular among Europe as an attempt to transition to a cleaner mobility. Those vehicles are powered by alternative fuels, which substitute oil-based fuels with the aim to reduce the CO_2 and pollutants emissions into the atmosphere. Alternative fuels can be classified in three distinct categories:

Alternative fossil fuels for a transitional phase

Those fuels are a low-carbon substitute to oil-based fuels oriented to facilitate the transition to zero-carbon fuels. They are considered only as a temporary solution as they still emit pollutants and CO_2. Examples of the alternative fossil fuels are the Liquified Natural Gas (LNG), the Compressed Natural Gas (CNG) and the Gas-To-Liquid (GTL). LNG with high energy density offers a cost-efficient alternative to diesel with lower pollutant and CO_2 emissions and higher energy efficiency. LNG is particularly suited to long-distance road freight transport for which alternatives to diesel are extremely limited. By using LNG, trucks might be able to meet the more stringent pollutant emission limits of future EURO VI standards cost efficiently.

Compressed natural gas (CNG) is a fuel gas mainly composed of methane (CH_4), compressed to less than 1% of the volume it occupies at standard atmospheric pressure. CNG vehicles have low pollutant emissions and have therefore rapidly gained ground in urban fleets of buses. In Madrid, more than the 82% of the bus fleet is composed of CNG-powered vehicles (Madrid-City-Council, 2025). Natural gas is lighter than air, meaning that it is quickly dispersed through the air avoiding high pollution events. However its main component, CH_4, is a powerful, short-lived greenhouse gas which can contribute to increase the intensity greenhouse effect.

Natural gas can also be transformed to a liquid fuel by first decomposing it to a 'synthesis gas', consisting of hydrogen and carbon monoxide, and then by refining to a synthetic fuel with the same technical characteristics as conventional fuels, fully compatible with existing combustion engines and fuel infrastructure. This process is called Gas-to-liquid (GTL).

Synthetic fuels can also be produced from waste feedstock. They improve the security of supply and reduce pollutant emissions of present vehicles.

Renewable fuels

As their name states, renewable fuels are fuels produced from renewable sources, such as organic waste. A representative example of renewable fuels are biofuels. Biofuels are liquid fuels for transport produced from biomass. Biofuels are classified into four generations (Alalwan et al., 2019). First generation biofuels use food crops as biomass feedstock, although several of them compete with global food needs. Second generation biofuels use non-food crops, although the cost-effectiveness is debated. Third and fourth generation biofuels are still in development and use microbiological methods, biotechnology and genetics. Liquid biofuels commercially available today are mainly 'first generation' biofuels. Blends with conventional fossil fuels are compatible with the existing fuel infrastructure, and most vehicles and vessels are compatible with the blends currently available (E10 – petrol with up to 10% bioethanol and diesel with up to 7% FAME biodiesel content).

Alternative fuels for zero-emission vehicles

Inside this category are the electric vehicles (EV), the hydrogen fuel cell vehicles (HFCV) and the ammonia-powered vehicles.

EV are powered by electricity, which can be produced from three main sources: fossil carbon, nuclear and renewable. As for 2022, 43.9% of electricity generated in the EU cam from fossil fuels, 34.5% from renewable sources (a 12.5% increase since 2012) and 21.4% from nuclear plants. The remaining 0.2% were generated by other sources (Eurostat, 2025). EVs can be supplied from this electricity by plugging them to the grid. EVs emit no pollutants and no noise and are therefore particularly suited for urban areas. EVs can be classified by their type of electric supply. The most commercialised types of EVs are:

- Battery Electric Vehicles (BEVs) uses electrical energy exclusively from an on-board battery pack to power one or more electric traction motors, on which the vehicle solely relies for propulsion.
- Hybrid Electric Vehicles (HEVs) combine a traditional internal combustion engine (ICE) with one or more electric engines. Modern HEVs use energy recovery technologies such as motor–generator units and regenerative braking to recycle the vehicle's kinetic energy to electric energy via an alternator, which is stored in a battery pack or a supercapacitor. Many HEVs reduce idle emissions by temporarily shutting down the combustion engine at idle (such as when waiting at the traffic light) and restarting it when needed; this is known as a start-stop system.

- Plug-in Electric Vehicles (PEVs) are the common terminology for plug-in hybrid electric vehicles (PHEVs) and 100% electric vehicles (BEVs).

Their relatively low autonomy, together with the lack of recharging points -with a common plug- is a major drawback of EVs (Pamidimukkala et al., 2024; European Institute of Innovation & Technology, 2025). They would need to be located at home, at the workplace and in public spaces. At present, most of the European Union Member States are catching up with the number of publicly accessible recharging points and announced policies to develop an adequate network of recharging facilities. In Spain, the legal framework that regulate the implementation of recharging facilities is the **Real Decreto-ley 29/2021** (Real Decreto-ley 29/2021, 2021). It establishes the minimum number of recharging facilities to be installed within residential parking zones with more than 20 parking places and in Stated-owned buildings. To facilitate their installation, a set of tax incentives are also defined within the text.

The hydrogen fuel cell vehicles (HFCV) are powered by hydrogen. HFCVs are like BEVs in that they are both electric vehicles that use an electric motor instead of an internal combustion engine to power the wheels. However, while BEVs run on batteries that are plugged in to recharge, HFCVs produce their electricity onboard (EPA, 2025). However, hydrogen (H_2) is a small molecule that is flammable and has the potential to leak, which makes it less safe than other alternatives. H_2 leak detection methods are in place to prevent leakes into the atmosphere. On the other hand, ammonia-powered vehicles has gained sifnificant attention an alternative to HFCVs due to ammonia's easy storage and transportation abilities, high energy density, and low production cost (Zhu et al., 2023).

1.4 Air quality modelling

The air quality modelling aims to estimate the concentrations of compounds in the atmosphere by resolving, using numerical methods, the equations that describe the processes occurring in the atmosphere. Depending on the definition of the reference system used, the air quality models can be classified on Lagrangian (which use a mobile reference system) or Eulerian (fixed reference system). The latter split the spatial domain in tridimensional cells, within the mass balance is resolved considering the different physical and chemical processes that affect it. The emission of pollutants, their transport through the atmosphere, the turbulent diffusion, the deposition processes and the chemical reactions will determine the evolution of any atmospheric pollutant.

The mass balance equation is given by the following expression (Seinfeld and Pandis, 1998):

$$\frac{\partial \overline{C}}{\partial t} = -\overline{v}\nabla\overline{C} - \nabla\overline{(v'C')} + Q + D + R \tag{1.4}$$

where $\overline{C}$ is the mean concentration of a certain gaseous air pollutant, $-\overline{v}\nabla\overline{C}$ represents the advection of the pollutant through the atmosphere, $-\nabla\overline{(v'C')}$ is the turbulent diffusion, Q is the emission rate of the pollutant, D the deposition term and R corresponds to the production or removal of that pollutant due to chemical reactions. For particulated pollutants other additional processes such as nucleation, coagulation and absorption must be considered.

Air quality models need of input data for a proper resolution of the Equation 1.4. Meteorological fields, given by meteorological models, land use and pollutants emissions are examples of the necessary information for resolving the mass balance equation. The utilities of the air quality models are numerous and varied, such as their contribution to air quality levels predictions, the assessment of environmental impacts or the evaluation of air pollution mitigation strategies.

But air quality models applications are not limited to the estimation of air pollutant concentrations. They are also useful to compute a temporal and spatial distribution of their concentrations when observational data is scarce or incomplete, and they also have unique applications that observations cannot perform. For example, with an air quality model it is possible to perform studies of source attribution of air pollutants arriving to a certain point, which is useful to develop air pollution mitigation strategies. In this sense, they are also useful to develop or/and evaluate abatement measures.

Air quality models can be classified, among other criteria, in terms of the spatial scale they are applied to:

- Large-scale models. They resolve phenomena with long wavelengths, affecting large areas -even the whole Earth's atmosphere. Their large scale represents a constrain within the current computational resources to their ability to resolve shorter wavelengths, therefore they cannot be used to characterise air quality due to local phenomena (i.e. traffic inside a street).

- Mesoscale models. Also known as limited-area models, they focus on a certain region of the atmosphere, generally no larger than a continent, and therefore they can resolve shorter wavelengths than a large-scale model. They are typically used for country-wide air quality estimations, but they are also useful for city-wide estimations. However, they cannot capture very local spatial gradients of air pollutant concentrations that usually occur between different streets -on even inside a sole street- in a city.

- Microscale models. These models, in contrast to the large-scale and mesoscale models, are focused into small areas (no more than a few docens of square kilometers) which

allows them to resolve the governing flow with a great level of detail, capturing very local phenomena.

The current Air Quality Directive ((Directive (EU) 2024/2881, 2024)) highlights the necessity and importance of "modelling applications" on estimating air quality and on the developing of mitigation strategies devoted to improve air quality where and when necessary. This Directive understands "modelling applications" as any application of a modelling system, understood as a chain of models and submodels, including all necessary input data, and any post-processing. Therefore, the works presented in this thesis, which are focused on high-resolution emissions and their application in several models are quite relevant under the scope of this Directive.

1.5 Thesis motivation and objectives

Reliable and versatile estimations of traffic emissions for air quality applications are a growing need. The spatial resolution of microscopic traffic simulations, coupled with an emissions model, provides detailed estimations of traffic emissions, needed for their applications in air quality modelling, with special relevance for studies of evaluation of impacts of traffic-related measures.

Pioneer studies used traffic simulations coupled with an emissions model in order to estimate high-resolution traffic emissions. Some studies have been focused on the behaviour of the vehicle's emissions in very localised points (Den Braven et al., 2012), whereas other studies have analysed real urban areas (Abou-Senna et al., 2013; Quaassdorff et al., 2016). In addition, studies have benefit of high-resolution emission estimations to perform detailed air quality estimations in urban areas with microscale models (Sanchez et al., 2017).

At the time being, there is a growing interest on traffic measures to mitigate the negative impacts of traffic emissions on air quality. These measures, however, are barely evaluated or they have been evaluated using in-situ measurements (Boogaard et al., 2012; Ellison et al., 2013; Panteliadis et al., 2014), whose spatial representativeness may be limited. To overcome that issue, a methodology that allows for an evaluation of these measures using high-resolution modelling techniques must be used. Furthermore, the evaluation of mitigation strategies requires to simulate large time periods, and larger domains than those previously modelled. The latter has the added difficulty of the uncertainty in simulated traffic flows in those areas without any kind of observations, which induce uncertainty into the emissions. Therefore, that uncertainty must be computed, which has not been done in aforementioned works.

In addition, mesoscale air quality models, which are essential to provide information about

the air quality to regional- to country-wise policy makers, should also benefit from the advantages of high-resolution emissions estimations, specially as Directive 2024/2881 requires the use of modelling applications to inform air quality plans and air quality roadmaps and to estimate the impacts of short-term measures, which requires a great level of detail. In the context of this thesis, as a previous step, an estimate of the emission changes for a macroscale emission scenario was done, by considering the COVID-19 lockdown of activities situation. In Rodríguez-Sánchez et al. (2022), the impact of the changes in emissions for each activity was estimated for several countries in order to provide emissions to a mesoscale chemical-transport model (CTM). This work was focused on the estimation of emission reductions, relative to an emission inventory considered as Business As Usual (BAU) conditions. Once the reductions were estimated, they were applied to a BAU emissions inventory. With that purpose, emission factors were computed for each sector of activity. For the road sector, country-wise data from TomTom and Google were used to estimate the changes in emissions. This study allowed the provision of emission data for the COVID-19 scenario, and could be applied to other type of measures. Nevertheless, the target CTM for this type of studies are those working at regional scales, as the reduction obtained at national level is applied to all the model grid-cells.

However, for urban areas a larger level of detail is needed to estimate the impacts of mitigation measures. In this sense, microscale traffic models linked to detailed emissions models represent a valuable tool for the Directive 2024/2881 requirements. These systems are useful to estimate the emissions of individual vehicles and the impact of traffic flows on air quality under different circumstances. Nonetheless and despite the more detailed emission estimates of detailed and complex emissions models, the sensitivity towards many factors would also create uncertainty due to the detailed input data required.

The general objective of this research is to provide reliable, high-resolution traffic emissions to different air quality models in order to study the impacts of traffic-related measures on air quality and the impact of meteorological conditions on their effectiveness using models at different scales. In addition, it aims to provide a development for allowing mesoscale models to benefit from high-resolution emissions estimations. With that purpose, a multi-model methodology which consists in the computation of traffic emissions through the coupling of a microscopic traffic simulation with an emissions model, is employed. Moreover, due to the emergence of the COVID-19 pandemic, an opportunity to estimate the impact of a global-scale lockdown in air pollutant emissions emerged. In the scope of this thesis, a simple and fast methodology to estimate that impact a macro scale was developed. The estimated emission reductions serve as reference for future mitigation strategies.

The main purpose of this thesis is achieved by fulfilling the following specific objectives:

1. *The estimation of a global-scale lockdown in emissions*: The emergence of the COVID-19 pandemic required the development of a methodology to estimate its impact on air pollutant emissions. In this work, a simple methodology based on a large range of openly available data is used to estimate the change in emissions during 2020 due to the pandemic-related lockdowns for several activity sectors, including road transport.

2. *The estimation of high-resolution emissions, and their uncertainty due to incertitude in vehicle's routes, for different traffic configurations*: A traffic simulator coupled with an instantaneous model emission is calibrated to estimate the emissions resulting from traffic flows, and their uncertainty due to the incertitude in traffic flows at streets without observed data, for different traffic configurations.

3. *The estimation of the impact of several measures on NO_X emissions*: A comprehensive analysis of the obtained emissions is performed to estimate the impacts of several measures on NO_X emissions. In addition, those impacts are compared with macroscale changes in emissions that took place due to the COVID-19 lockdown.

4. *The estimation of the impact of several traffic measures on NO_X concentrations*: The obtained emissions are used as inputs to a CFD model to compute the NO_X concentrations for each traffic configuration. The impact of several traffic measures is thoroughly analysed.

5. *The evaluation of the impact of meteorological conditions on air quality and the effectiveness of air pollution mitigation strategies*: Using the aforementioned computed emissions and different meteorological conditions obtained from simulations of a meteorological model, the impact of those conditions on the resulting air quality from the different emissions configurations can be assessed.

6. *The development of an interface to adapt high-resolution emissions to a mesoscale model*: A Python-based interface has been developed to adapt the emissions to the requirements of a mesoscale air quality model, in order to run this model using high-resolution emissions.

7. *The impact of detailed emissions on the performance of a mesoscale air quality model*: The impact of using high-resolution emissions as input data in a mesoscale model is exhaustively analysed.

The present work is divided into chapters which follow the achievement of the aforementioned objectives. A full description of the traffic simulation models and the emissions models, including the ones used in this work and their capabilities, is given in Chapter 2. Chapter 3 describes the available modelling techniques to estimate air quality at several scales, as well as other models needed for that purposes (i.e.,

meteorological models). Chapter 4 presents a work developed during the COVID-19 pandemic in which the impact of the pandemic in air pollutant emissions is computed for several European countries and activity sectors for the year 2020, including the road transport sector, using a fast and easily reproducible methodology. In Chapter 5, high-resolution emissions for different traffic conditions are estimated in order to perform an exhaustive analysis of the impacts on air quality of several mitigation strategies and their sensitivity to meteorological conditions in Plaza Elíptica, an urban hot-spot in southern Madrid. Chapter 6 presents the estimation of the impacts on NO_X emissions and air quality in an urban area of a planned mitigation strategy, as well as its sensitivity to meteorological conditions. Additionally, a comparison with an already-implemented strategy in that same area is provided. Finally, Chapter 7 presents a comprehensive analysis of the advantages of implementing high-resolution emissions into a mesoscale air quality model, through the development of a suitable interface.

Chapter 2

Road traffic emission modelling

Emissions represent the entry of pollutants into the atmosphere. Thus, their knowledge is fundamental to understand and handle the air pollution levels. They are, therefore, a key information for the air quality models.

The application of traffic simulators and emission models for traffic emission computation is becoming increasingly popular because of the necessity of accurate estimations and assessments of vehicle emissions for decision-making policies. These policies can be applied to different scales, from very local (i.e., a set of roads inside a city) to national or global scales. This chapter discusses the information needed to compute road-traffic emissions and the different traffic and emission model approaches available for different types of studies, depending on their scale. A more exhaustive review of the models employed in this thesis is presented in Chapter 3.

2.1 Traffic simulation approaches

Simulation modelling techniques are essential to produce the information needed by traffic emission models. Modelling techniques are classified into three scales depending on the level of detail they include: macroscopic, mesoscopic and microscopic.

Macroscopic models describe the most important properties of traffic flows, including formation and dissipation of queues, and they allow to compute travel-averaged values. That makes them useful for dynamic traffic management or to produce large-scale road traffic-related emission inventories (Rodriguez-Rey et al., 2021). Mesoscopic models are an in-between kind of model of macroscopic and microscopic models. They simulate individual vehicle behaviour but in a simplified way (for example, they do not consider interactions between vehicle and road network). Unlike microscopic simulation, vehicle data are not updated at every time step, but only when changes occur in the network or vehicle behaviour.

On the other hand, microscopic models consider individual vehicles and their interactions with other vehicles and the road network in full detail. In this kind of models, the behaviour of the vehicle depends on both the vehicle's physical abilities to move (for example, the maximum velocity a vehicle can reach) and the driver's controlling behaviour (for example, the ability of the driver to react to a sudden change of speed in the vehicle just in front of his). The driver's controlling behaviour covers every decision resulting from the interaction of the driver with the surrounding vehicles at every time step. The logics that govern this behaviour are the breaking-acceleration patterns; lane change logics (describe the decisions for a lane change considering driver preferences and the situation in both current and other lanes); and route selection logics (define the route a driver takes depending on external information such as the traffic state in the network). Very short time steps are used in microscopic models (as much as 0.1 seconds).

Examples of microscopic traffic simulation software include:

- CORSIM (McTrans Center, 2025) is a microscopic simulation software, designed for traffic planning and road network analysis. It consists of an integrated set of a surface-street traffic simulation model (NETSIM) and a freeway simulation model (FRESIM), which allows to represent the entire traffic environment as a whole system, including specific properties of the vehicle.

- SUMO (Alvarez Lopez et al., 2018) is a microscopic traffic simulator that allows to simulate the movement of a certain traffic demand through a road network by taking into account the interactions of the vehicles comprising the traffic demand between each other and with the elements of the road network. The interactions of each vehicle with its surroundings in SUMO are defined by the so-called car-following and lane-changing models. SUMO is designed to handle large networks and allows for multimodal simulations. SUMO also allows to generate the traffic demand for a simulation from activity-based data.

- Aimsun (Barceló et al., 1998) is an application that harmonizes all three levels of simulation: macroscopic, mesoscopic and microscopic in one application. As in the case of SUMO, the microscopic model was designed based on algorithms of gap detection, car-following models and lane-changing models and allows for multimodal simulations. It also can be used for large networks.

- VISSIM is another tool for microscale traffic simulations. It allows to generate detailed traffic scenarios for complex urban geometries using the link-connector system. VISSIM consists of two different programs that includes a signal state software to define traffic lights and a traffic flows simulation model that allows to simulate the interaction with pedestrian. As in the case of SUMO, it can be coupled with an emissions model to

compute traffic-related emissions (PTV Group, 2025).

- PARAMICS (Cameron et al., 1994) is a set of software models for microscopic traffic simulations that integrates every network sizes. It also allows to control traffic and information systems.

A summary of the most commonly used traffic simulation models and their main characteristics and features are shown in Table 2.1.

Table 2.1: Most commonly used traffic simulation models and their characteristics.

Model name	**Characteristics**	**Main Features/Capabilities**
AIMSUN	Microscopic, distributed computing technique	Surface streets, freeways, actuated signals, dynamic traffic assignment, variable message signs, 3-D animation, telematics.
CORSIM	Microscopic	Surface streets, freeways, actuated signals, weaving sections, incidents, variable message signs, 2-D animation.
INTEGRATION	Mesoscopic	Surface streets, freeways, traffic assigment, intelligent transportation system, toll plaza, vehicle emissions, HOV.
PARAMICS	Microscopic, distributed computing technique	Surface streets, freeways, transit operations, 3-D animation, roundabouts, congested networks.
SATURN	Microscopic	Individual junctions, traffic assignment.
SimTraffic	Microscopic	Surface streets, actuated signal, pedestrians, roundabouts, 3-D animation.
SUMO	Microscopic	Surface streets, freeways, ramp metering, large networks, pedestrians, bikes, 3-D animation, roundabouts, vehicle emissions, dynamic traffic assigment, activity-based traffic demand.
VISSIM	Microscopic	Surface streets, freeways, ramp metering, pedestrians, transit operations, 3-D animation.

2.1.1 Variables involved in traffic exhaust emissions calculation

Exhaust emissions from vehicles arise from the combustion of fuels inside internal combustion engines (EMEP/EEA, 2023). The generic methods employed to compute those emissions are usually based on a limited number of factors. Basically, the emission computation is based on emission factors which are the amount of pollutant emitted per distance unit (g/km), per time unit (g/s) or consumed fuel (g/kg) multiplied by the number of different vehicle types. However, the level of detail of the models largely influences these calculations (Smit et al., 2008). Usually, the factors that mostly influences the emission calculations are the main vehicle type (passenger car, light commercial vehicle, motorcycle, bus, articulated truck, etc.), fuel type (diesel, petrol, LPG, etc.) and the emission standard (Euro 1, Euro 2, Euro

3, etc.) (Smit et al., 2009).

The estimation of detailed and accurate exhaust emissions from road transport for real-driving conditions present several difficulties. These are related to the limited amount of direct measurements of exhaust emissions, which cannot cover a full vehicle fleet. For instance, in Europe all light-duty vehicles have to be tested on a *chassis dynamometer*, also known as roller bench. A chassis dynamometer allows to operate a vehicle in a lab to simulate real-world vehicle operation. To determine one vehicle's emissions, the vehicle follows a pre-defined driving cycle of accelerations, gear changes, steady speeds, deceleration and idling on the chassis dynamometer. While the vehicle is being driven on the roller bench, the emissions from the tailpipe (exhaust emissions) are collected and recirculated to a dilution tube where they are analysed (EEA, 2016). Until 2019, the pre-defined driving cycle used to test a vehicle was the so-called New European Driving Cycle (NECD). This driving cycle was first introduced in 1970 to represent typical driving conditions of busy European cities, and updated in both 1990 and 1997 in an attempt to better represent more demanding, high-speed driving modes. However, the NEDC was originally developed when vehicles were lighter and less powerful than those available nowadays and it is widely accepted that the NEDC is outdated. For that reason since September 2019, the NEDC was replaced by the Worldwide Harmonised Light Vehicles Test Procedure (WLTP) driving cycle (Tutuianu et al., 2015). The WLTP is more realistic for the current vehicle characteristics and driving conditions of global cities, including, among other changes, harder acceleration patterns and more time at high speeds. Figure 2.1 shows a comparison between the previous driving cycle (NECD), and the new one (WLTP).

The emissions obtained from the laboratory are the starting point for the computation of road transport emissions. The final emission values will depend on vehicle characteristics such as weight, model, size, fuel type and technology, and on driving conditions.

2.1.1.1 Vehicle characteristics

Emissions produced by a vehicle are influenced by the vehicle design and manufacturing technology. One of the most important parameters is the engine type since vehicles are still powered predominantly by combustion of fossil fuels in the form of petroleum products. The promotion of electric and alternative fuels powered vehicles (Directive 2014/23/EU, 2014) has enhanced the increase of electric and hybrid vehicles in the European vehicle fleet (European Alternative Fuels Observatory, 2025). Nonetheless, as it is shown in Figure 2.2, alternative fuels vehicles represent a low percentage of the total European vehicle fleet (lower than 8% by 2024), with gasoline and diesel continuing to be the most popular types by a large margin.

Diesel engines produce less CO and HC than gasoline engines without a catalyst. However,

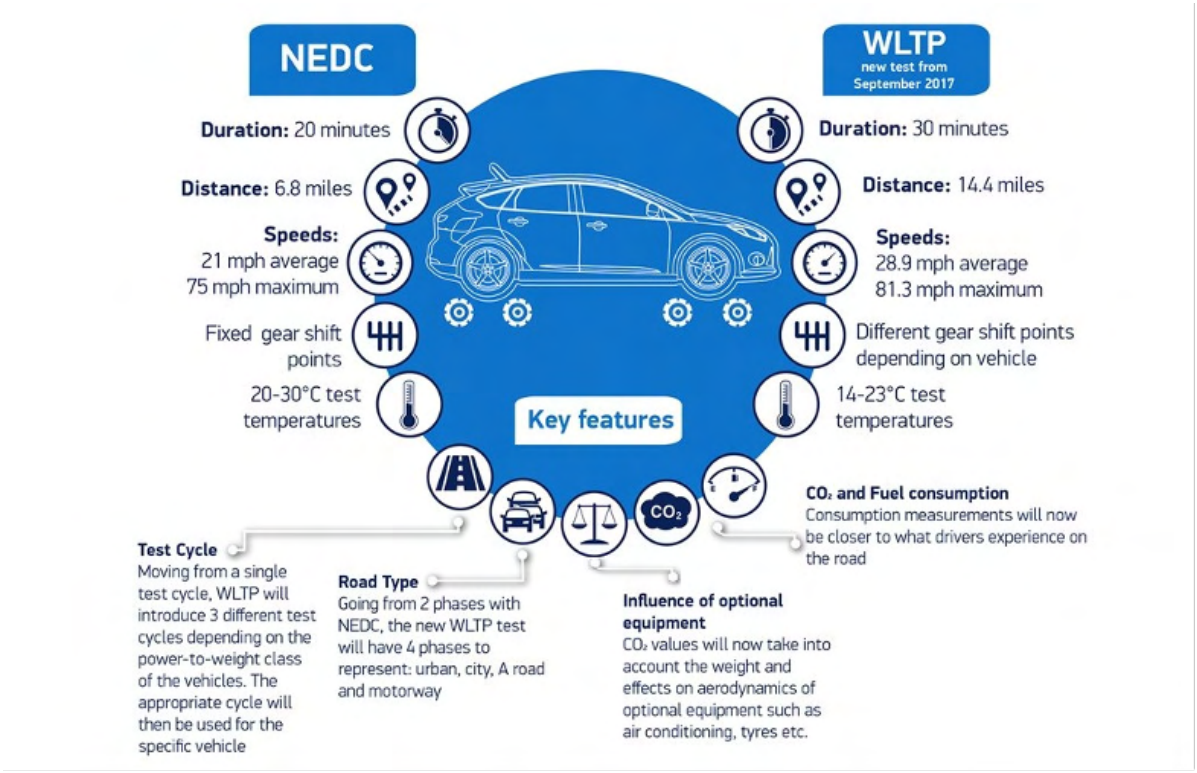

Figure 2.1: Comparison between NEDC and WLTP driving cycles. Source: European Commission (2025)

they produce much more NO_X and PM (Reşitoğlu et al., 2015). This fact is due to the fuel characteristics such as the vapor pressure and the sulphure (S) content, which have an impact on emissions. In addition, heavier vehicles require larger quantities of energy to propel them than lighter ones. This directly impacts the amount of fuel consumed by each vehicle type, which at the end affects air pollutant emissions. Other important factor to consider is the state of a vehicle. Analysis of on road vehicles reveal that large variations in emission levels appear for badly maintained vehicles which generate significantly higher emissions (Smit et al., 2017). In general, the distance travelled by a vehicle increases its deterioration. Vehicles with high mileages and those driven at higher speeds present higher emission rates for CO, NO_X and VOCs. However, deteriorating rates of the actual vehicles are still data that cannot be easily collected because they are highly dependent on driving conditions and maintenance levels. Nonetheless, an accurate description of the fleet composition and its evolution with the time is necessary for emission calculations.

Nevertheless, to meet certain standards vehicles may be equipped with emission exhaust after-treatment control systems to meet the corresponding emissions requirements. These systems allow to remove pollutants from the vehicle exhaust after it leaves the engine, just before they are emitted into the air. Newer emission standards include different exhaust after-treatments. The most common after-treatments to control NO_X emissions are Exhaust

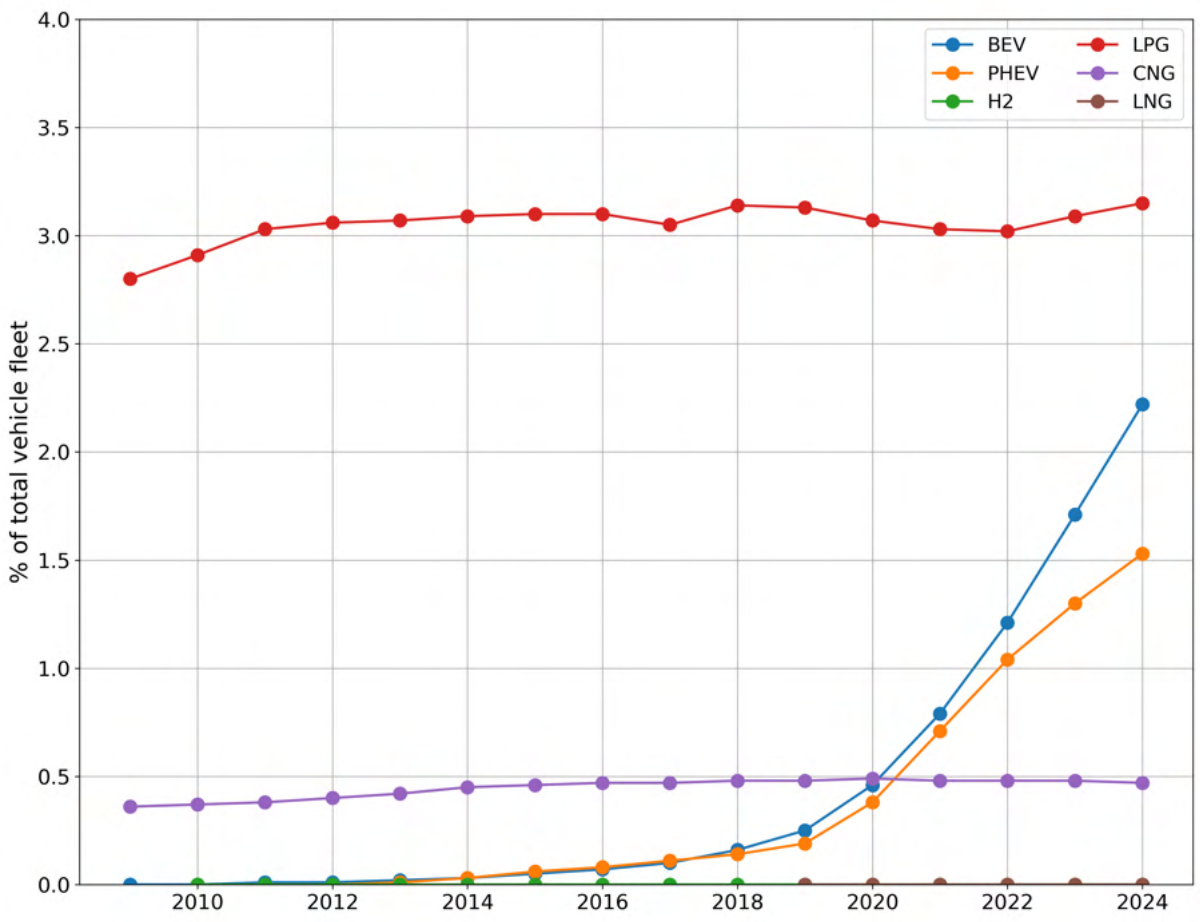

Figure 2.2: Evolution of alternative fuel vehicles in European Union as total percentage of the European vehicle fleet. Adapted from European Alternative Fuels Observatory (2025).

Gas Recirculation (EGR), Lean NO_X trap (LNT) and Selective Catalytic Reduction (SCR) and the 3-way catalyst (Reşitoğlu et al., 2015). EGR system is used in large diesel engines. CO_2-rich exhaust gases are recirculated back into the combustion chamber and mixed with fresh air. This turns out in lower combustion temperatures that reduce the thermal production of NO_X, although it may increase HC and CO emissions. LNT is also called NO_X Storage Reduction (NSR) or NO_X Adsorber Catalyst (NAC). This system stores NO_X on the catalyst under engine lean conditions. Then, under fuel-rich engine conditions it releases the trapped NO_X. SCR is reduction technology improved for heavy-duty vehicles and more and more common on light-duty vehicles (e.g. Euro 6 passenger cars). In this case NO_X emissions in the exhaust gas are minimized by a selective catalytic reduction in post-combustion reactor where ammonia (NH_3) or urea is used as a redactor agent. This system reduces NO_X on a continuous way and with high efficiency. Nevertheless, a negative impact of this after-treatment is the increase in NH_3 emissions, which affects negatively the air quality also by secondary aerosols formation through interaction with SO_X and NO_X. In addition, the sulphur content of the fuel may limit the applicability of this technology since it may degrade active sites within the catalytic converter, lowering the catalytic activity. The 3-way catalyst is used in gasoline fuelled vehicles to convert NO_X, CO and HC into less harmful substances (N_2, CO_2 and H_2O) by using a reduction catalyst (platinum and rhodium) and an oxidation catalyst (platinum and palladium) both with ceramic honeycomb structure. To control PM emissions the most used exhaust after-treatment is the Diesel Particulate Filter (DPF). In this technology emissions from the exhaust gas are removed by physical filtration. The plugged channels at each end of the device force the diesel particulates through the porous substrate walls. These walls act as very efficient mechanical filters and when the particles pass through it, they are transported into the pore walls by diffusion. As the filter becomes increasingly saturated, a layer of soot is formed on the surface of the channels walls. Nevertheless, excessive saturation must be prevented by regenerating the filter through pyrolysis of trapped PM (Reşitoğlu et al., 2015).

2.1.1.2 Driving conditions

A vehicle can produce quite different amount of emissions depending on the way it is used. Therefore, detailed and accurate knowledge about the driving cycles of a vehicle during a trip is fundamental for emissions estimations. Nonetheless, this type of data is usually limited to averaged speed values, with the loss of information it entails. Travels with frequent stops and start operations, accelerations and decelerations are more inefficient in fuel usage and present higher emissions. But the driving cycle is not the only factor affecting emissions from a vehicle. Other driving-related factors such as the driver characteristics (e.g., age, income, aggressivity), the trip (e.g., trip purpose, type of use), the local context (e.g., the origin and destination, residential area, city size) and the time (e.g., season, time of day or

day of the week) play also a relevant role in emissions produced by a vehicle. Considering those factors improves the emissions estimation (Quaassdorff, 2018).

2.1.2 Emission modelling approaches

Models for the estimation of road traffic-related emissions can be classified by their scale of application, the generic type of model, their emission calculation approach or the type of input data used to feed them (McCrae et al., 2006). Thus, model classification systems tend to be based upon a combination of the geographical scale of their application, the model generic type, the kind of input data and the emission computation approach.

2.1.2.1 Aggregated emission factor models

These models operate with a single emission factor representative of a specific vehicle type and a very general driving style (rural, urban or highway). The vehicle operation is only considered in a very rudimentary level, and its specifications neglected. Therefore, these models cannot be used to determine emissions for concrete situations. Instead, aggregated emission factor models are commonly used in large-scale applications such as the national and regional inventories (McCrae et al., 2006).

2.1.2.2 Average speed models

Average speed models are based upon the principle that the average emission factor for a specific vehicle type and a certain pollutant varies according the average speed during a trip. A good example of average speed model is COPERT (Ntziachristos et al., 2009). COPERT is integrated in the EMEP/EEA methodology for air pollutant computation and it is the reference for most European countries for reporting official emissions data.

These models are widely used for its relatively easy use (average speed modelling is a long-established method for emissions computation) and the existence of a close correspondence between the required model inputs and the data generally available to user. However, average speed models have several limitations including the neglecting of driving behaviours or the variability of vehicle operations. This can have a significant impact on the results at a local scale where those two factors represent an important component of traffic emissions (Negrenti, 1999; Ryu et al., 2015).

2.1.2.3 Traffic situation models

In contrast to average speed models, in traffic situation models the cycle average emission rates are not correlated with the trip average speed but instead with various driving cycle parameters. Those parameters are referenced to specific, pre-defined, traffic situations which

are known by the user. The traffic situation models incorporate the effects of traffic dynamics on an aggregated link level and distinguishes different road types; it incorporates both speed and traffic situation into emission estimation. These models are therefore better suited than the previously described ones for mesoscale applications, in which emission estimates are required for individual road links. An example of traffic situation model is the HBEFA (Handbook of Emission Factors for Road Transport) (Hausberger, 2009). In this model, the traffic situation (free-flow, heavy, saturated, stop & go) is identified by using a qualitative description of the speed variation. Then, at each road link an emission factor based on reference emission functions for a representative sample of several vehicle types is applied depending on the identified traffic situation. The obtained emission value must be weighted according to the traffic flow and composition. Other correction factors to consider the effects of cold starting, road gradient, altitude, special driving conditions and degradation of emission control systems are applied to the reference emission functions in order to generate appropriate emission estimates. The main limitations of the traffic situation models are related to the definition of the traffic situation which includes a subjective interpretation of the traffic definition, and also the universal applicability of the traffic situations is not resolved (McCrae et al., 2006).

2.1.2.4 Traffic variable models

These models generate simplified driving pattern data as a function of a number of traffic variables relating to traffic characteristics (traffic volume, average speed, traffic density, queue length) and road infrastructure characteristics (link length, number of lanes, free-flow speed, type of intersection, signal settings). These simplified driving patterns are combined with emission rates derived from other emission models.

An example of traffic variable models is the Traffic Energy and Emissions (TEE) model (Negrenti, 1999). It introduces a correction factor to the emission factor computed for a certain vehicle at a certain average speed in order to consider the impact of congestion on emissions at a certain average speed. This corrective factor is derived from average speed, green time percentage, link length and traffic density.

2.1.2.5 Cycle variable models

In these models, emission factors are function of various driving cycle variables, such as idle time or average speed at a high temporal resolution (from minutes to seconds). The temporal resolution depends on the length of the driving patterns on which the model is based.

VERSIT+ (Smit et al., 2007) is a representative example of this kind of models. It computes emission factors using multivariate regression functions based in a large sample of vehicles functioning in different driving cycles. Each one of the driving cycles is characterized

by a number of descriptive parameters (speed, acceleration, deceleration, etc.) and their derivatives. The model predicts, for each pollutant and vehicle category, the average emission values over the various driving cycles resulting in the determination of the descriptive variables which best predict the emissions. Its main limitation is the need of a detailed driving cycle which can be obtained only by microscale traffic simulation models.

2.1.2.6 Modal models

Modal models relate the emissions produced by a vehicle during a trip to the different modes of vehicle operation taking place during the trip. On simpler modal models, those modes of operation are reduced to idle, acceleration, deceleration and steady speed or cruise (McCrae et al., 2006). A complex extension are the so-called *instantaneous models*, whose purpose is to provide a more precise description of vehicle emission behaviour. In instantaneous models, emissions are modelled as a function of the engine power needed to propel a vehicle so that it is possible to calculate "continuous" emissions and fuel consumption for a particular vehicle type from a given driving cycle. The term "continuous" may be misleading as instantaneous models are discrete in time, higher in resolution than cycle-variable models with typical time steps being of the order of 1 second or less. Model variables used in the emissions computation include instantaneous speed and acceleration and vehicle variables such as engine capacity, vehicle mass, road gradient, aerodynamic drag coefficient and frontal area. More advanced instantaneous models take also into account transient driving cycle where engine load varies every second. The fundamental limitation is that this kind of models require a substantial amount of input data (vehicle specific parameters) which is very expensive to collect and also very detailed information on the operational profiles of vehicles (instantaneous second-by-second speed-time).

PHEM-light (Hausberger and Krajzewicz, 2014) is a simplified version of the European modal emission model PHEM (Hausberger, 2009). It offers a broad vehicle classification database which is based in the European fleet. PHEM-light retains relevant information of vehicle parameters and emission behaviour in Characteristic Emission curves over Power (CEP). These CEP curves define the emission amount (g/h) as function of the actual engine power. As a result, PHEM-light computes instantaneous fuel consumption, as well as CO_2, NO_X, CO, HC and PM_X emission quantities for given speed and acceleration demands.

2.2 Microscopic traffic simulations

In this thesis a microscale traffic model is used and applied to configure different traffic scenarios, coupled with a high resolution model emissions model. This system is adequate to be applied at different, complex urban configurations and changing traffic conditions. The

SUMO traffic simulator has been chosen to simulate the traffic patterns, coupled with the PHEM-light modal instantaneous model. SUMO has the advantage of being an open-source product with a large user community, which allows the user to contribute to the software development and to benefit from others' (users and developers) contributions. SUMO provides to PHEM-light model data of the individual vehicles present in the network at each timestep. Instantaneous models such as PHEM-light have been found useful to provide emissions with high spatial and temporal resolutions, suitable for microscale studies in local hot-spots (Bigazzi et al., 2010; Csikós and Varga, 2012; Quaassdorff et al., 2016). These results can also be used in mesoscale chemistry-transport models to assess the air quality at city or regional scales.

2.2.1 The SUMO traffic simulator

The SUMO microscale traffic simulator allows to simulate the movement of a certain traffic demand through a road network by taking into account the interactions of the vehicles comprising the traffic demand between each other and with the elements of the road network. The interactions of each vehicle with its surroundings in SUMO is defined by the so-called car-following models.

2.2.1.1 Car-following models in SUMO

The default car-following model used in SUMO is based on the Krauss model (Krauss, 1998). The Krauss main idea can be summarized with the following statement: "Let a vehicle drive as fast as it can while maintaining perfectly safe conditions". The safe conditions can be determined in terms of a "safe velocity". With that on mind, the former statement can be summarized in a simple formula:

$$v \leq v_{safe} \tag{2.1}$$

where v is the vehicle's velocity and v_{safe} the "safety velocity".

In addition, the Krauss model assumes that the maximum acceleration and deceleration of a vehicle in order to achieve safe conditions (i.e., to avoid a collision) is bounded:

$$-b \leq \frac{dv}{dt} \leq a \tag{2.2}$$

$$a, b > 0 \tag{2.3}$$

The definition of the safety velocity on the Krauss model is based on the actual and desired gaps between the vehicle and its leader (the vehicle in front of it). If one defines G as the

actual gap between a vehicle and its leader and G_{des} as the desired gap, and considers the model being discrete in time, the safety velocity of a certain vehicle at a given time is defined by the next equation:

$$v_{safe}(t) = v_l(t) + \frac{G(t) - G_{des}(t)}{\tau_b + \tau} \tag{2.4}$$

where $v_l(t)$ is the leader's velocity at a time "t", $\tau_b = \frac{\overline{v}}{b(\overline{v})}$ is a time scale given by the leader's and the follower's velocity and τ is the reaction time of the following driver.

As previously mentioned, the Krauss model is constructed under the assumption of letting a vehicle drive as fast as it can to maintain safety conditions. This velocity is defined by v_{safe}. Thus, the main formulas defining a vehicle's behaviour under the Krauss model are Equation 2.4 and:

$$v_{des}(t) = min[v_{max}, v(t) + a(v)\Delta t, v_{safe}(t)] \tag{2.5}$$

$$v(t + \Delta t) = max[0, v_{des}(t) - \eta] \tag{2.6}$$

$$x(t + \Delta t) = x(t) + v\Delta t \tag{2.7}$$

In Eq. 2.6, η represents a random perturbation constant to consider each driver's deviation from optimal driving.

SUMO uses by default the Krauss car-following model, but with some differences. In SUMO, different deceleration values are handled for each vehicle type (the vehicle's type is passed to SUMO through the parameter *vClass*). And SUMO includes a variation of the safe vehicle formula in order to maintain safety when using the Ballistic-position update, which considers the acceleration constant in a single timestep. The original Krauss formula is an Eulerian-based formula, which keeps velocity constant in a single timestep.

Several other variations of the Krauss model are considered within SUMO. For example, the *KraussPS* car-following model included in SUMO is based in the Krauss model but it is adapted in order to consider the road slope. This is the car-following model used in this work. The main parameters of the Krauss-based car-following models in SUMO are summarized in Appendix A.

Besides a vehicle's behaviour with respect to its leader on the same lane, SUMO also models the lane changing of a vehicle using a lane-changing model. Lane changing is useful in several cases. For example, a vehicle must require a lane changing when following a route that requires leaving or incorporating a motorway. Not in every moment of a simulation a lane changing is possible. It may happen that there is no enough space in the target lane.

In this case, no lane-changing is performed. The lane-changing model used by default in SUMO discriminates between four motivations for lane-changing:

The first motivation is the *strategic change*, which occurs when a vehicle must perform a lane change in order to be able to continue its current route. The second case of lane-changing is the so-called *cooperative change*, in which a vehicle changes from one lane to another in order to help another vehicle continue its travel without altering its speed. The opposite situation can also occur, in which a vehicle changes its lane in order to avoid a slow leader and therefore to keep its speed as constant as possible. This kind of lane changing is called *tactical change*. Finally, the *regulatory change* occurs in roads where the leftmost (or rightmost) lane is reserved to overtaking manoeuvres. In this case vehicles must leave this lane clear, changing lanes when an overtaking manoeuvre has finished.

The motivations described above are hierarchically ordered in the lane-changing model as follows. In every simulation step, each vehicle first considers changing to the right, and if no change to the right is performed, a change to the left is considered as well. Accordingly, the currently considered direction d is either right (-1) or left (1) according to the resulting change in lane index.

The parameters that regulate a vehicle's behaviour regarding the lane-changing process in SUMO are described in Appendix A.

2.2.2 Input data

To run a real-case simulation, three kind of input data are mandatory: a composition of the vehicle fleet of the study area; traffic count data in order to create the traffic demand; and a road network describing, at least, the roads and intersections where traffic shall transit.

2.2.2.1 Road network

SUMO road networks are composed of graphs and nodes. Nodes, usually named *junctions* in SUMO-context, represent intersections, and *edges* represent roads or streets. Edges can be composed of one or more *lanes*. In addition, several kind of edges are defined. *internal edges* are within a *junction* or intersection, and connect and incoming regular edge with an outgoing edge. The *regular edges* are every edge not belonging to an intersection. SUMO road networks are encoded as XML files. The contents are grouped by the instances in the following order:

- cartographic projection valid for this network.
- edges; at first, internal edges are given, then regular edges; each edge contains the list of lanes that belong to it.

- traffic light logics.
- junctions, including their right-of-way definitions; plain junctions first, then internal junctions connections, plain first, then internal.
- optionally roundabouts.

SUMO networks can be created or edited from a visual network editor provided within the simulator called **netedit**. Also, SUMO can import networks from other formats using the utility **netconvert**. Possible sources include OpenStreetMap, VISSUM, VISIM, MatSIM, OpenDRIVE and ArcView-data. In this research SUMO networks have been imported from OpenStreetMap data. OpenStreetMap data can be obtained from multiple sources such as Geofabrik. Geofabrik allows download large amount of OpenStreetMap raw data, most of them updated in a daily basis. The data downloaded from Geofabrik is then clipped to the desired extent of the domain area. Once the OpenStreetData file has the desired dimensions, must be converted to a SUMO-readable format. This is done with the **netconvert** script.

However, the resulting SUMO network can have errors and a pre-processing is needed in order to debug it. Typical errors include wrong lane connections inside an intersection, wrong number of lanes composing an edge and unrealistic traffic light cycles. Figure 2.3 illustrates an example of the debugging process. Figure 2.3a) shows a satellite image of Puerta del Carmen, an intersection in Zaragoza consisting on 3 lanes crossing from southeast to northwest, two lanes from northeast to southwest and other two from southwest to northeast. Figure 2.3b) shows the original representation of Puerta del Carmen within the SUMO network after importing it from OpenStreetMaps. In this representation, only one lane traverses the intersection from southeast to nortwest, and several forbidden connections are made. Figure 2.3c) shows the debugged network, which has been manually corrected using satellite and street-level images as reference.

The correction process for traffic lights is more complex in absence of detailed data of the real traffic lights. In those cases, a test simulation is performed to identify unrealistic behaviours. Those behaviours usually manifest in form of unexpected traffic jams when the traffic flow is low. Once an ill-regulated intersection is located, traffic lights are adjusted assuming that traffic lights inside the network try to optimise traffic flow. This can be manually or adjusting the TLS behaviour within the road network by activating the option that allows for dynamical traffic lights cycles duration.

2.2.2.2 Vehicle fleet composition

For realistic traffic simulations and emission estimations the description of the simulated vehicle fleet is important, as the traffic-related emissions depend on the vehicle classification (Quaassdorff et al., 2022). In SUMO, each vehicle inserted in the simulation must have

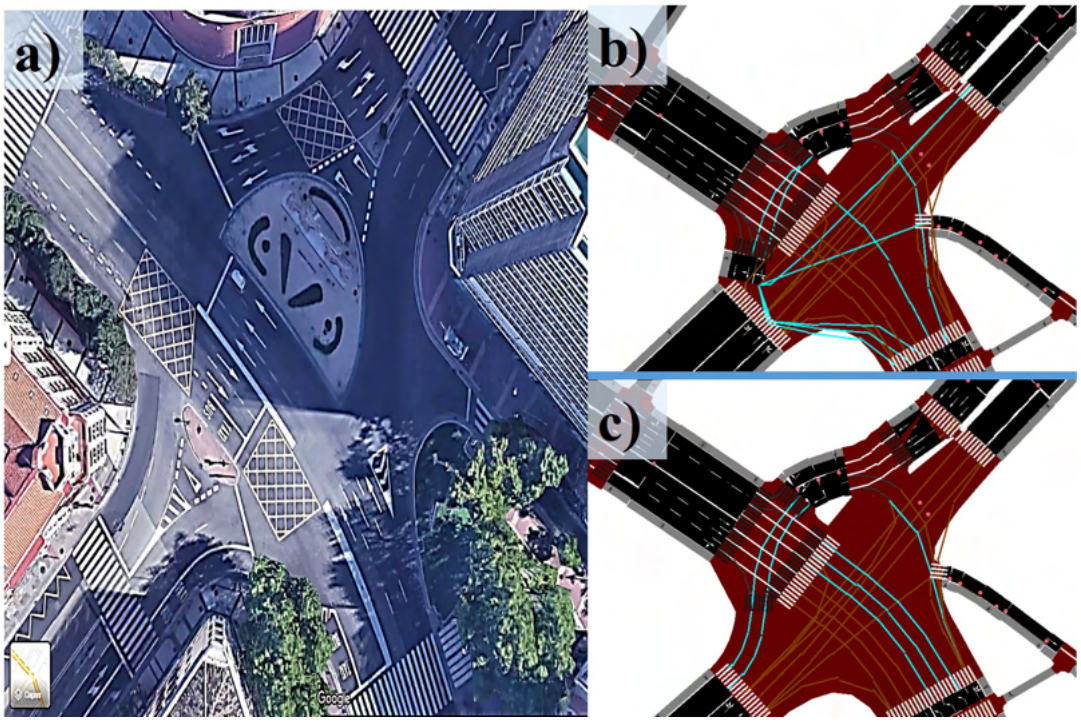

Figure 2.3: a) Satellital view of Puerta del Carmen (Zaragoza). Source: Google Maps. b) SUMO network original representation of Puerta del Carmen. c) SUMO network debugged representation of Puerta del Carmen. In b) and c), lane connections are represented with brown lines. Intervened lanes connections are highlighted in cyan.

associated a vehicle type. The vehicle type is defined by several physical attributes, the most relevant of them described in Appendix A, including the emissions class of the vehicle which defines its emissions behaviour.

Using this information a customized vehicle fleet composed of several vehicle types can be created by using the "vTypeDistribution" attribute:

```
    <routes>
        <vTypeDistribution id="typedist1">
            <vType id="type1" accel="0.8" length="5"
            maxSpeed="70" probability="0.9"/>
            <vType id="type2" accel="1.8" length="15"
            maxSpeed="50" probability="0.1"/>
        </vTypeDistribution>
</routes>
```

2.2.2.3 Traffic count data

Traffic count data is essential to perform a realistic traffic simulation, as it provides a reference to the algorithms which generate the traffic demand.

SUMO accepts traffic count data in ';'-separated csv files. These files must include, at least, the following information:

- A string containing the detector ID, which must match any ID included in the detectors file.
- The time period begin (since the start of the simulation period) that this entry describes, in minutes.
- The number of vehicles that drove over the detector within the time period describing this entry.

```
Detector;Time;qPass;qLDuty;qHDuty
det1;0;50;10;2
det1;15;70;16;4
det1;30;67;18;4
det2;0;13;5;1
det2;15;16;7;1
```

Figure 2.4: Example of traffic count data read by SUMO.

Additional columns must be added, for example, to define the number of several kind of vehicles that drove over a detector. This is useful for when a simulation should include several kind of vehicles. Figure 2.4 shows the first six lines of a possible traffic count data file suitable for SUMO to read. In this example, the first row is the header of the file, which is mandatory and indicates the name of the columns. $qPass$ indicates the number of passenger cars that drove over any detector present in the Detector column; $qLDuty$ the number of light duty vehicles; and $qHDuty$ the number of heavy duty vehicles. In this example can be seen that for detector "det1", 50 passenger vehicles, 10 light duty vehicles and 2 heavy duty vehicles entered at the time period beginning 0 minutes after the start of the simulation.

The location of the detectors included in the traffic count data file within the road network is provided to SUMO by means of a file of detectors. This file must include information about the detector ID, the lane within the network where it is located, and its position relative to the start point of the lane.

Once SUMO has information about the detectors location and the traffic flows driving over them, traffic demand can be generated through algorithms.

2.2.3 Routes computation and simulation

Routes in SUMO consist of a sequence of connected edges, with one starting and one ending, along a vehicle can travel. On the other hand, a trip is a vehicle movement from one place to another defined by the starting edge, the destination edge, and the departure time.

Considering this, the goal of a realistic traffic simulation is to assign routes to vehicles in order to match the traffic count data at every time interval.

In this research, trips are randomly generated using some constrains:

- Very short trips must be forbidden, in order to avoid over fitting in traffic counts.
- Trips must preferentially start and end in streets with a minimum length.
- If vehicle type is heavy duty, trips must start, when possible, near the limits of the simulation domain. This is done to avoid unrealistic amounts of heavy duty vehicles transiting the inner roads of the city.

Once the trips have been created, routes between trips can be constructed following several criteria. The approach followed in this research, in absence of information regarding trips such as origin/destination matrices (O/D matrices), was to create a set of random routes for each possible trip within the simulation. The possible trips for each vehicle within the simulation depends of the vehicle type, as different edges allows the circulation of different vehicle types. Once a random set of routes is created for each trip, an algorithm assigns a route to a vehicle using the available traffic count data as reference at the traffic detector locations. The process of route assignment for a vehicle consist on two steps:

- First, the algorithm selects a random traffic detector which has not reached its traffic count value for the working time interval.
- Then, a route passing that traffic detector is assign to that vehicle.

This iterative process continues until all counting locations have reached their measured count or there are no viable routes.

To calibrate the model stable conditions must have been reached. For that reason, a 1-h spin-up period were included in the simulations. This period has not been included in the validation of traffic flows.

2.3 Traffic-related emissions computation

Traffic-related emissions were computed during the simulation thanks to an on-line coupling between SUMO and the version 5 of the microscopic PHEM-light emissions model. For each timestep of the simulation, an emission value is obtained for each vehicle present in the simulation.

2.3.1 The PHEM-light emissions model

The PHEM-light model (Hausberger and Krajzewicz, 2014) is a simplification of the instantaneous emissions model PHEM is based in the European fleet for the vehicle classification.

PHEM calculates the engine power in 1 Hz based on the given courses of vehicle speed (the "driving cycle") and road gradient, the driving resistances and the losses in the transmission system. The 1 Hz course of engine speed is simulated based on the transmission ratios and a gear-shift model. Alternatively the course of engine load and/or engine speed can also directly be provided to the emission model. To take transient influences on the emission levels into consideration, the results from the emission maps are adjusted by means of transient correction functions (Hausberger, 2009).

The simplifications in PHEM-light with respect to PHEM include the no inclusion of transient dynamic corrections, temperature influences on after-treatment-systems and the driver gear shift model to compute engine speeds. This allows not to save the history driving trajectories (speed and acceleration), which is fundamental in order to save space and time for an on-line coupling with SUMO. PHEM-light retains relevant information of vehicle parameters and emission behaviour in Characteristic Emission curves over Power (CEP) for European vehicles. These CEP curves define the emission amount (g h^{-1}) as function of the actual engine power. As a result, PHEM-light compute instantaneous fuel consumption (FC) along with CO_2, NO_X, CO, Hydrocarbons (HC) and Particulate Matter (PM) emissions for a given speed and acceleration combination. The model requires an input file containing all vehicle speeds (1 Hz in km h^{-1}), accelerations (m^2 s^{-1}) and road gradient (%) information for one driving cycle. Vehicles speeds and accelerations at lower frequencies are readable by the model, which interpolates them to 1 Hz in order to perform the computations, and then extrapolates the result to the original frequency. Vehicle parameters such as vehicle mass, loading or engine rated power among others are divided into 131 classes that combines vehicle type (PC, LCV, HDV), vehicle size class (LCV I, II, III and HDV I and II) vehicle category (Rigid truck, Trailer Truck, Coach, City Bus), fuel (Diesel, Petrol, Battery Electric Vehicle – BEV –, Compressed Natural Gas – CNG –) and Euro standard (Euro0 to Euro6d). This information is then combined for the 1 Hz engine power computation of each individual vehicle over one driving cycle.

2.3.1.1 PHEM-light implementation

The implementation of PHEM-light can be divided in two parts: the transient computations of vehicle-related variables such as maximum acceleration and power demands, and the handling of emission and vehicle data (Hausberger and Krajzewicz, 2014).

Transient computations

The computation of maximum acceleration and power demands depend on the vehicle parameters (such as road load coefficients, mass, loading, etc.), speed, acceleration and road gradient. To the total power demand (P_d), four different demands contribute:

- Power needed to overcome the rolling resistance (P_{rr}).
- Power needed to overcome the air resistance (P_{ar})
- Power needed for desired acceleration (P_a)
- Power to overcome the road gradient (P_{grad}).

Those four different demands are given by the following formulas:

$$P_{rr} = (m_{vehicle} + m_{load}) \cdot g \cdot (Fr_0 + Fr_1 \cdot v + Fr_4 \cdot v^4) \cdot v \tag{2.8}$$

$$P_{ar} = \left(C_d \cdot A \cdot \frac{\rho}{2}\right) \cdot v^3 \tag{2.9}$$

$$P_a = (m_{vehicle} + m_{rot} + m_{load}) \cdot a \cdot v \tag{2.10}$$

$$P_{grad} = (m_{vehicle} + m_{load}) \cdot gradient \cdot 0.01 \cdot v \tag{2.11}$$

where, $m_{vehicle}$ is the vehicle weight in kg, m_{load} is the mass of the vehicle load also in kg. $g = 9.81\ m \cdot s^{-2}$ is the gravity acceleration, Fr_0 [adimensional], Fr_1 [$s\ m^{-1}$] and Fr_4 [$s^4\ m^{-4}$] are rolling resistance coefficients. The vehicle's velocity and acceleration are represented by v and a respectively. A is the cross sectional area of the vehicle, ρ is the air density, C_d is the air resistance coefficient and *gradient* is the road slope in %.

Then, the total power demand is computed as follows:

$$P_d = (P_{rr} + Par + P_a + P_{grad})/\eta_{gearbox} \tag{2.12}$$

where $\eta_{gearbox} = 0.95$ is the average efficiency.

Emission and vehicle data handling

Relevant information on vehicle parameters and emission behaviour are kept in so called CEP classes. Each PHEM emission class is associated to one CEP class. These classes compromise

information on emission data files and vehicle files, which are read upon the first usage of the corresponding PHEM emission class. Files not used during a simulation are not read, saving storage and computation time. Each CEP instance combines the information read from three files:

- Fuel consumption data file
- Emission data file
- Vehicle data file

The vehicle data file contains all relevant information on the vehicle (i.e., vehicle mass, engine rated power and road load coefficients). Unlike in PHEM, vehicles in PHEM-light are additionally classified as light or heavy vehicles.

The emission and fuel consumption data files contain emission and fuel consumption levels for the whole range of normalized power demands. These normalized power demands are de-normalize to absolute power levels in kW for the emissions computation. But this normalization process is required in order to combine several vehicles and emission behaviours into one average vehicle per PHEM emission class. Further, it allows varying vehicle weight, rated power and driving resistances without having to adapt the characteristic emission curve. This makes PHEM-light easily extendable to varying vehicle parameters. One feature of PHEM-light -which is even an extension to PHEM- is that the de-normalization process is done differently for heavy and light vehicles. The two different principles are:

1. Normalization over rated power (NRP)
2. Normalization over critical power (NCP)

For heavy vehicles, the NRP method is applied for the normalization. For light vehicles, the NRP is applied for CO_2 emissions, and the NCP for the rest of pollutants.

The availability of two normalization methods makes that emission data is read from two separate files, one for fuel consumption and one for other pollutants, in order to avoid reading different power ranges and emission levels from one file. Thus, the data loading process consists of the following steps:

1. Load vehicle file and asses if vehicle is light or heavy
2. Load fuel consumption file, de-normalize
3. Load other emission pollutant file, de-normalize using either NRP or NRC
4. Create CEP object that holds emission and vehicle data

The CEP class holds the emission and vehicle data. Emission data is hold in vector-like

structures. Due to the different power patterns which result from different de-normalization procedures, two separate structures for FC and other pollutants are held. An example for NO_X CEP data is given by Figure 2.5.

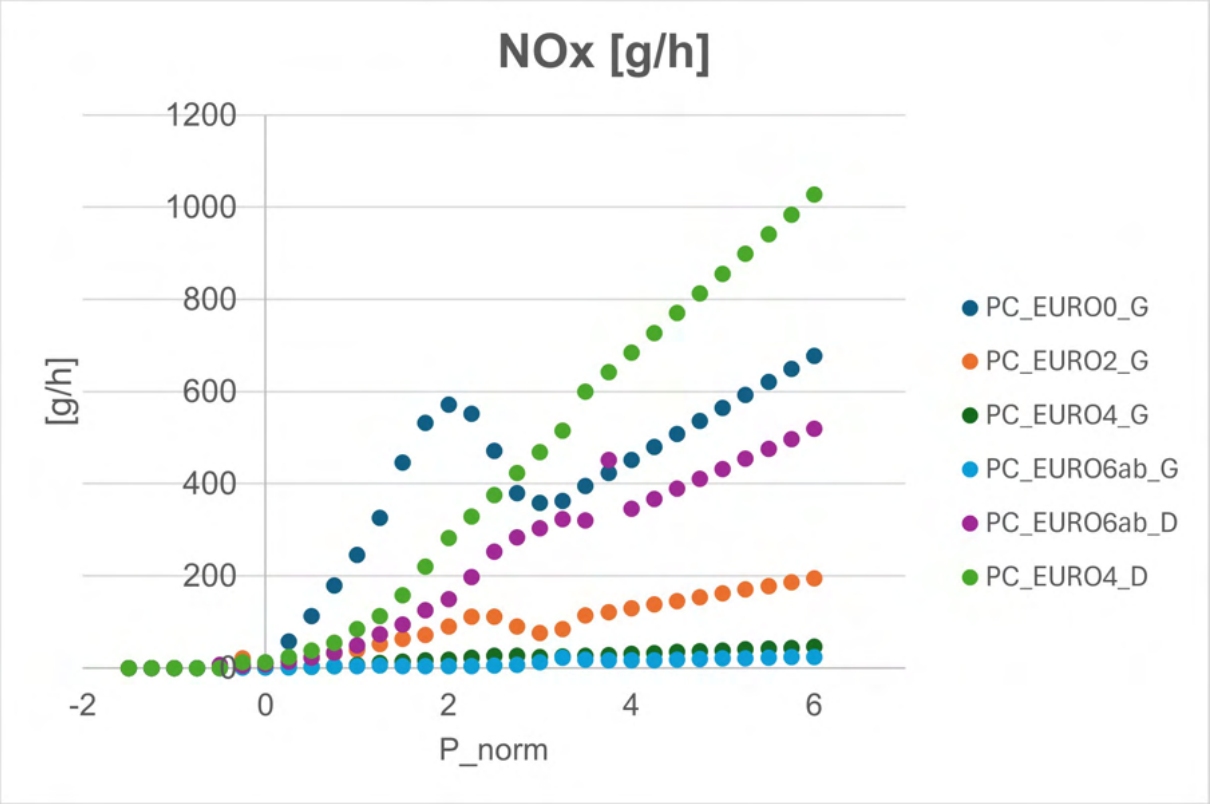

Figure 2.5: Emission factors for NO_X given by different passenger car CEP classes.

2.3.1.2 Implementation within SUMO

The PHEM-light model is on-line coupled with SUMO through a set of methods for retrieving emission levels and maximum acceleration for specific driving situations. Each vehicle in SUMO is assigned to a vehicle type, which contains information about the car-following and lane-change movement models, including physical parameters such as the vehicle's length, maximum velocity, loading, etc. It also describes an vehicle emission class, which must match one the PHEM emission classes. SUMO passes this emission class to the PHEM-light model, which reads the CEP class corresponding to that emission category in order to compute the power demand and emissions resulting for each vehicle given the situation of the vehicle at a certain time step, which is computed by SUMO. Figure 2.6 shows the overall structure of PHEM-light.

PHEM-light contains 200 definitions of CEP classes (50 for passenger cars, 77 for light duty vehicles, 22 for motorcycles and 51 for heavy duty vehicles, buses and coaches). The nomenclature of each CEP classes is a string structured in at least three parts: "AA_BB_CC".

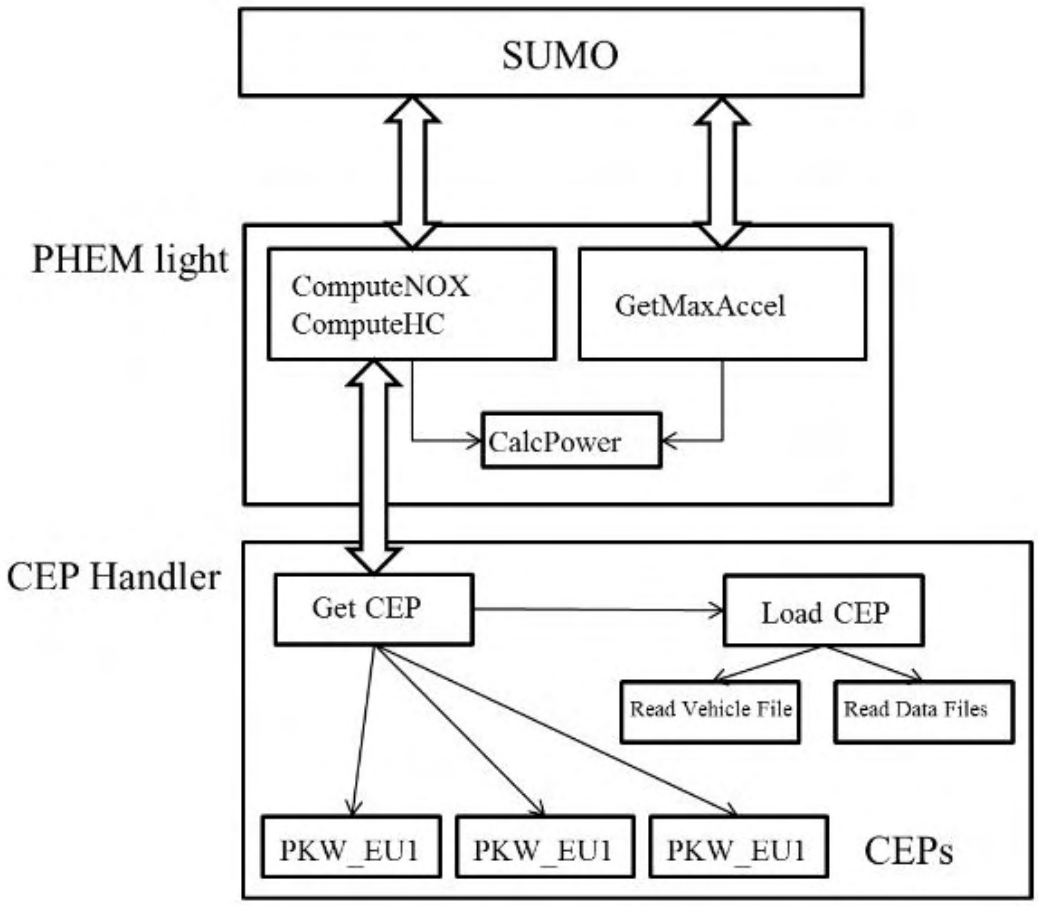

Figure 2.6: Structure of PHEM-light.

The first part of the string provides information about the vehicle class (passenger, light duty, heavy duty, motorbike, a city bus or a coach. The second part of the string provides the emission standard to which the vehicle is conformed. The third part of the string contains information about the vehicle's fuel type (gasoline, diesel, diesel with particle filter, diesel with software update, hybrid powertrain, battery electric). For light and heavy duty vehicles, a fourth label is mandatory, indicating the size class of the vehicle (I, II or III). For example, a passenger car equiped with a gasoline engine and conformed to Euro6 emissions standard will be named as **PC_EU6_G**. To compute the emissions for this vehicle type, this label must be passed to the "emissionClass" parameter in the definition of the SUMO's vehicle types, so SUMO passes it to the PHEM-light model which will read the CEP class corresponding to PC_EU6_G.

In this PhD thesis, the traffic-related emissions outputs are used as input for mesoscale and microscale air quality models. The emission outputs are stored in a file including large amounts of information for each vehicle at each timestep, including NO_X emissions. Thanks to the great amount of information present in the emission output files, this data can be treated in multiple forms for different purposes. For the emissions to be used within the air quality models, they can be aggregated in cells. For the microscale model, the emission data were aggregated in 5 m x 5 m cells, whereas for the mesoscale model the aggregation resolution was the resolution of each domain of the mesoscale model. The emissions can also be aggregated by vehicle type, by road network lane or by trip, among other possibilities.

2.3.2 Preparing SUMO emissions for CFD models

In order to compute air pollutants dispersion in urban areas at high-resolution, the SUMO emissions output were aggregated into cells of 5 m x 5 m and then processed to distribute the regular-gridded mass emissions into the irregular mesh of the CFD model as volumetric emissions. Once aggregated the emissions into regular cells of 5 m x 5 m, the regular-gridded emissions must be interpolated to the irregular mesh of the CFD model, and convert from mass emitted in regular grid to volumetric emissions in each CFD irregular cell. This is a non-trivial because, for different reasons, in the interpolation process it may happen that some CFD cells remain unassigned to the regular-gridded SUMO emissions. The process can be summarized as follows:

- First, a coordinate translation must be done to the CFD coordinate system. The STAR-CCM+ CFD model does not work with an official coordinate system. Instead, it defines the origin at the lower-left corner of the domain. The data coordinates obeys the metric system.

- In the interpolation process, if some SUMO emission cells does not correspond to

any CFD cell, the emission of those SUMO cells are distributed in the CFD cells corresponding to the same road.

- Finally, the volumetric emissions are imposed in the CFD cells considering that the total emissions are conserved.

Figure 2.7 shows the spatial distribution of traffic-related emissions inserted in the CFD for a specific scenario executed for the Plaza Elíptica square.

Figure 2.7: Spatial distribution of one set of the SUMO emissions regridded to the CFD mesh.

Chapter 3

Atmospheric modelling at different scales

3.1 Introduction

Air pollution modelling estimates the concentration of air pollutants. To do this, it uses fluid equations based on data about pollutant emissions. It also considers atmospheric and chemical processes that disperse, transport, convert, or remove pollutants by deposition. Air quality models can be classified by their spatial covering into several categories:

Models that cover the whole globe are called **global** models. Their resolution is typically of the order of 10 km x 10 km, as it is limited to the computational resources: the larger the area to model, the coarser the spatial resolution. Other models, however, are limited to a certain area. Depending on the size of the resolved area these models can be classified on **mesoscale** models or **microscale** models. The spatial resolution of these models also depends on the modelling domain extension. Mesoscale models can cover an area as big as a continent. In addition, several domains can be resolved, with the possibility of a domain being nested inside another with higher spatial resolutions. The typical horizontal spatial resolution of the mesoscale models is of several km^2. However, specially in the case of nested domains, a mesoscale domain can have a spatial resolution of up to tens of meters. Microscale models, on the contrary, are designed to study detailed processes at a street level. With the current computational capacities microscale model can cover an area of up to several tens of km^2 and their spatial resolution is of the order of 1 m x 1 m.

Depending on the modelling horizontal scale, different tools have been used in the scope of this Ph.D. thesis. The motivation behind the use of different scales lies in the purpose of each study case. In urban areas, the urban morphology interactions with the mean flow are important in determining the final distribution of the air pollutants concentrations.

In these cases, a model which resolves explicitly those interactions is needed to estimate accurately the distribution of air pollutants inside an urban areas, with its characteristic strong gradients. For those cases, a high-resolution modelling technique -such as microscale models- is necessary. However, these models needs refined input data, which is not always available, and a large amount of computational resources. Furthermore, chemical reactions are not usually considered in these models as they would further increase the computational load. However, as computational resources increase, chemical reactions are being introduced, although in a simplified form, in microscale models. This was done, for example, in Sanchez et al. (2016). In other cases when the interest resides in simulating a larger area, a compromise between spatial resolution and domain extension must be reached. In these cases, mesoscale models are the best option with the current availability of computational resources. In addition, the lower computational load required by mesoscale models facilitates the incorporation of chemical reactions in these models, needed for considering secondary pollutants in air quality studies.

Air quality modelling is a multi-scale problem. Pollutants emitted in cities can be transported and travel long distances affecting large areas. Similarly, air quality in cities can be affected by those pollutants arriving from remote areas. For that reason, different modelling techniques are necessary to fully understand the air pollution issue.

This chapter aims to present a brief review of the modelling techniques employed in this Ph.D. thesis. First, a brief review of the mesoscale CHIMERE model is presented. Subsequently, a description of the microscale models is presented, focused on CFD models and how they resolve the governing equations of fluid dynamics. The chapter finalizes with a detailed explanation of the methodology employed to estimate long-term air pollution using CFD simulations.

3.2 Mesoscale modelling

In this Ph.D. thesis, a mesoscale chemistry-transport model has been used to model the air quality at a regional scale, the **CHIMERE chemistry-transport model**.

3.2.1 The CHIMERE chemistry-transport model

CHIMERE is an Eulerian, limited-area, chemistry-transport model. It simulates the transport, turbulent mixing, chemical conversions and deposition of air pollutants to provide the concentrations of hundreds of gas-phase and aerosol species over local to continental domain. In order to do so, for a given chemical species, CHIMERE solves the mass balance equation given by Equation 1.4. To run CHIMERE external forcings are required: meteorological fields, primary pollutant emissions and chemical boundary conditions (Menut

et al., 2013). Meteorological conditions from any meteorological model can be used provided that all mandatory variables for the CHIMERE simulation are given in the appropriate format. The general principle of the CHIMERE chemistry-transport model is shown in Figure 3.1. In this research, the version 2013 of CHIMERE is used.

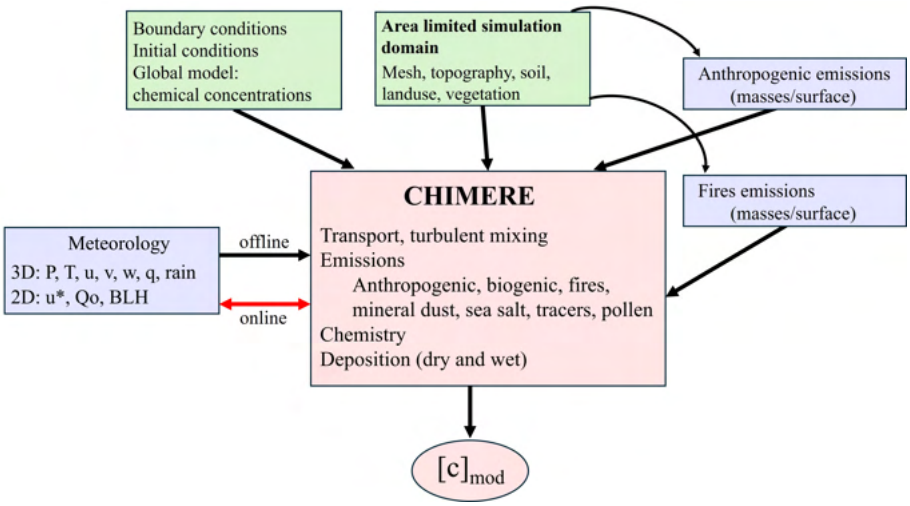

Figure 3.1: CHIMERE chemistry-transport model general principle. Adapted from LMD (2025).

Once the external forcings are prepared to be read by the model, CHIMERE is split into two main parts: an initialisation phase and the model integration phase. The initialisation phase consists on reading all input parameters as well as the preparation of the initial meteorological and chemical fields. The model integration phase is divided into three stages:

- An hourly time step to provide the forcings (meteorological conditions, chemical boundary conditions and emission fluxes).
- A user's defined coarse time step, named as "nphour", that corresponds to the time interpolation of parameters such as wind, temperature and reactions rates. CHIMERE, in order to prevent issues related to the violation of the Courant-Friedrich-Levy (CFL) criteria, dynamically estimates a recommended physical time step in the meteorological preprocessor. During the run, if the specified time step is longer that the recommended one, the recommended time step is used in model integrations.
- A chemical time step called "ichemstep". This corresponds to the integration of the chemical mechanism, including concentration increments due to all processes. In this case, it is possible to select one or two Gauss-Seidel iteration, but the use of two iterations is strongly recommended.

The numerical integration of all processes follows a production-loss budget approach. This means that all production and loss terms for each chemical species are computed simultaneously. This method avoids error propagations usually generated with operator-splitting techniques. In operator-splitting techniques, the concentration fields are updated

sequentially following the different processes affecting each chemical species. Both production-loss and operator-splitting approaches are illustrated in Figure 3.2.

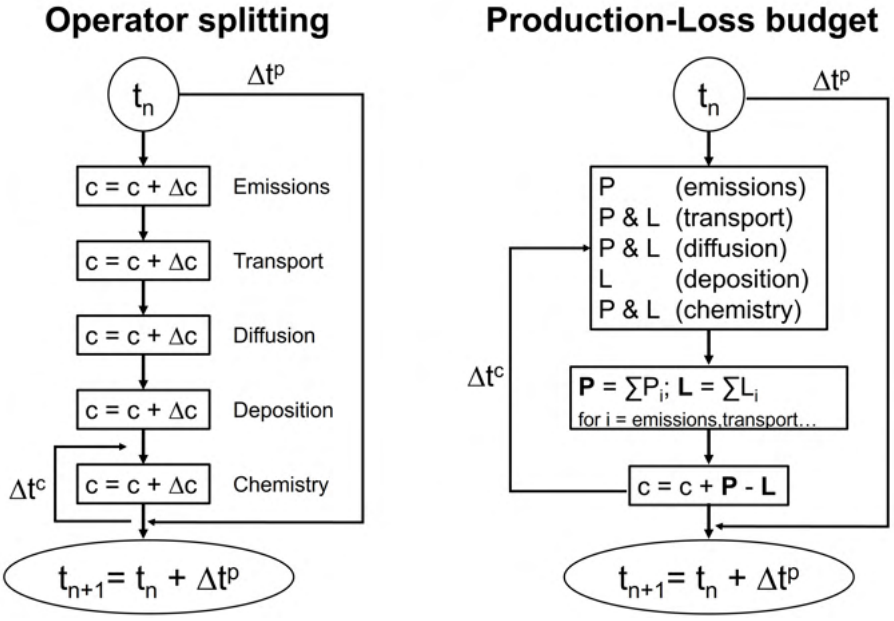

Figure 3.2: Integration operator techniques for chemistry-transport models. Adapted from Menut et al. (2013).

The numerical method used to estimate the temporal evolution of concentrations is adapted from the second-order TWOSTEP algorithm originally proposed by Verwer (1994) (Menut et al., 2013):

$$c^{n+1} = \frac{4}{3}c^n - \frac{1}{3}c^{n-1} + \frac{2}{3}\Delta t R(c^{n+1}) \tag{3.1}$$

where c^n represents the chemical concentrations of certain species at time t_n, Δt the time step leading from time t_n to t_{n+1}, and $R(c) = P(c) - L(c)$ the temporal evolution of the concentrations due to chemical production and emissions (P) and chemical loss and deposition (L). After rearranging and introducing the production and loss terms, Equation 3.1 can be written as follows:

$$c^{n+1} = \left(I + \frac{2}{3}\Delta t L(c^{n+1})\right)^{-1} \cdot \left(\frac{4}{3}c^n - \frac{1}{3}c^{n-1} + \frac{2}{3}\Delta t P(c^{n+1})\right) \tag{3.2}$$

where I is the identity matrix. The implicit non-linear system represented by Equation 3.2 can be solved with a Gauss-Seidel method (Verwer, 1994).

In CHIMERE, the production and loss terms P and L are modified in order to include the advection and diffusion effects. Therefore, in this model the terms P and L become $\widehat{P} = P + P_h + P_v$ and $\widehat{L} = L + L_h + L_v$ respectively. P_h and P_v represent the temporal

evolution of concentrations due to horizontal (only advection) and vertical (advection and diffusion) inflow into a given grid box whereas L_h and L_v denote the temporal evolution due to the respective outflow divided by the concentration itself.

Emissions

Emissions of pollutants have different origins and include a number of different gaseous and aerosol species, chemically reactive or not. Furthermore, the sources can be located at the surface (traffic, biogenic) or along vertical profiles (industrial emissions, biomass burning). In CHIMERE, these emissions are split into several families representing their origin:

- The **anthropogenic emissions** include all human activities (traffic, industries, agriculture, shipping, aviation...). The anthropogenic emissions must be provided within an activity sectors classification, such as the "Selected Nomenclature for Air Pollutants" (SNAP) nomenclature or the GNFR nomenclature.
- The biogenic emissions represent activities related to the vegetation. These emissions are computed using the global MEGAN (Model of Emissions of Gases and Aerosols from Nature) model (Guenther et al., 2006a).
- The mineral dust emissions represent the natural emissions of non-reactive particles, mainly generated by the surface layer dynamics (Menut et al., 2009).
- The fire emissions, which are more sporadic.

Anthropogenic emissions are key to study air pollutant mitigation strategies. For a realistic simulation, these emissions must be provided every hour for the specific species of the chemical mechanism used and projected over the gridded domain, regardless of the original data projection. From the raw data to the data required for a specific simulation, a sequence of preprocessing actions is necessary. In CHIMERE, this preprocessing is performed by the **EMISURF program**.

Since CHIMERE needs the emitted species to be in a specific format which means that usually, as explained above, a pre-processing to adapt the emissions from inventories to a CHIMERE-usable format is needed. The EMISURF program takes as inputs gridded emissions in a monthly or annual basis and, after a sequence of steps, converts them into hourly fluxes of model chemical species. In the version 2013, the emissions must be given on **SNAP nomenclature**. The SNAP nomenclature was created by the EMEP/CORINAIR project to group emissions by activity sector. It is a three-level hierarchical nomenclature composed of 11 sectors (level 1), 76 sub-sectors (level 2) and 375 activities (level 3). CHIMERE uses the first level of SNAP sectors to process the emissions. Table 3.1 summarizes the 11 sectors of activity included in the level 1 of the SNAP nomenclature.

Table 3.1: 11 sectors of activity included in the first level of the SNAP nomenclature and their description.

SNAP	Description
1	Energy industries (power plants and refineries)
2	Residential/Commercial combustion
3	Industrial combustion
4	Industrial processes
5	Extraction and distribution of fossil fuels
6	Solvent and other product use
7	Road transport
8	Non-road transport
9	Waste management
10	Agriculture
11	Biogenic emissions

Several steps are required to prepare emissions fulfilling the CHIMERE requirements:

First, an horizontal regridding of the original emissions to the CHIMERE simulation grid is done. To this end, several spatial proxies can be used (population density, road map, agriculture and wood-burning aerosol emissions from the residential sector) depending on the sector of the emissions considered. The landuse proxy is common for all sectors. For SNAP 7 (road transport), the emissions can be regridded using a road map, a population density map or a landuse map. SNAP7 emissions are regridded in EMISURF using the road proxy data. Figure 3.3 shows the road proxy distribution for Spain, with a zoom over Zaragoza city.

Another process is the application of chemical speciation profiles to map emissions from inventory pollutants to "model species". This process is applied to the NMVOCs, NO_X, carbonaceous pollutants and SO_X. For the case of NMVOCs, a disaggregation into 221 "real" compounds of the British PORG speciation is performed, depending on the SNAP updated in GNFR sector (Passant, 2002), that are then regrouped into a smaller set of VOC classes which correspond directly to the specific compounds of the MELCHIOR mechanism. The NO_X emissions are split into NO, NO_2 and HONO. In the version 2013 of CHIMERE, annual emissions of NO_X are speciated as 9.2% of NO_2, 0.8% of HONO and 90% of NO, following GENEMIS recommendations (Friedrich, 2000; Kurtenbach et al., 2001; Aumont et al., 2003). Emissions of SO_X are speciated as 99% of SO_2 and 1% of H_2SO_4. For the anthropogenic emissions of primary particles, H_2SO_4, PPM, OCAR, BCAR are split over three modes:

- XXX_fin for diameters $D_p < 2.5\ \mu m$.
- XXX_coa for $2.5 < D_p < 10\ \mu m$.

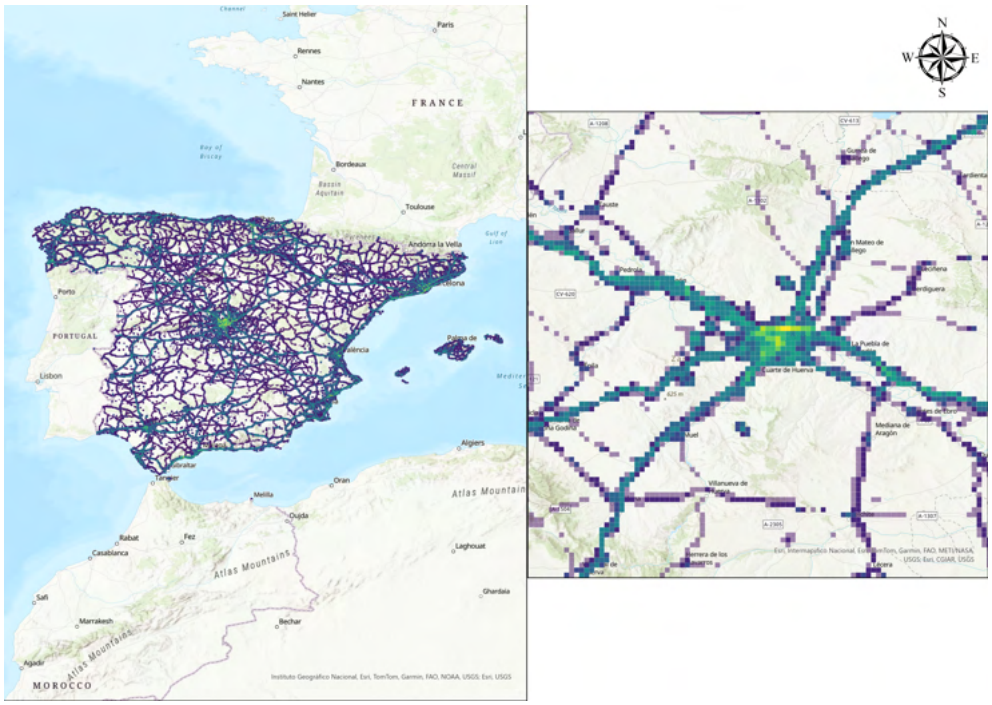

Figure 3.3: Road proxy used by the EMISURF program for Spain (left) and a zoom over Zaragoza city (left).

- XXX_big for $D_p > 10\ \mu m$.

Then, a distribution of emissions to vertical layers is performed to convert 2D fluxes from the inventories into 3D fluxes. This is done by using a typical vertical profile for the emissions of each sector of activity. The injection height profiles used in this Ph.D. thesis are based on the work from Bieser et al. (2011) and they are shown in Table 3.2.

Finally, temporal profiles are applied to refine the emission data from monthly or annual data to hourly fluxes. This process follow the guidelines provided by the Institute for Energy Economics and Rational Use of Energy, University of Stuttgart (Ebel et al., 1994). Hourly data are calculated in Menut et al. (2012).

- **Seasonal factors**: In the first place, a seasonal factor is applied to the annual data. Each model species has its own seasonal factor table, which depends on the country where the emission takes place and the sector of activity.

- **Weekly factors**: Identically as in the seasonal case, the weekly factors are country- and sector of activity-dependant. There is one file of weekly factors for each model species.

- **Hourly factors**: The final step of the temporal refining process is the application of hourly factors. The hourly factors consist on 24 numerical factors representing the daily evolution of an species emission. They are common to all species but each SNAP

Table 3.2: Fraction of total emissions injected along the injection profiles for each SNAP category.

Injection profiles for each SNAP category							
Injection height (m)	20	92	184	324	522	781	1106
SNAP 1	0	0	0.25	51	45.3	3.25	0.2
SNAP 2	100	0	0	0	0	0	0
SNAP 3	6	16	75	3	0	0	0
SNAP 4	5	15	70	10	0	0	0
SNAP 5	2	18	60	30	0	0	0
SNAP 6	100	0	0	0	0	0	0
SNAP 7	100	0	0	0	0	0	0
SNAP 8	100	0	0	0	0	0	0
SNAP 9	0	0	41	57	2	0	0
SNAP 10	100	0	0	0	0	0	0
SNAP 11	100	0	0	0	0	0	0

has its own hourly factors.

The EMISURF output file is a netCDF4 file for model species, domain and month of the year containing hourly fluxes of the model species emissions for each cell of the simulation domain. mission fluxes are 4-D variables, with 24-hours data at the time dimension corresponding to the hourly profile of the given weekday.

As aforementioned, the CHIMERE chemistry-transport model needs meteorological fields as forcing to compute the pollutants concentrations. In this research, the meteorological model employed it has been the **Weather Research and Forecasting model**.

3.2.2 The Weather Research and Forecasting model (WRF)

The WRF model (Skamarock and Klemp, 2008) is a numerical weather prediction system designed for both atmospheric research and operational forecasting applications. It is a fully compressible, 3D, Eulerian, nonhydrostatic model conservative for scalar variables. As a mesoscale model, it serves a wide range of meteorological applications across scales from tens of meters to thousands of kilometres. It uses a terrain following hybrid sigma-pressure vertical coordinate (Figure 3.4). The grid staggering is the Arakawa C-grid, and the same time step is used for all terms. The model dynamics conserves scalar quantities locally and globally. WRF allows multiple domain nesting. This kind of technique allows resolution to be enhanced over a region of interest by introducing an additional grid (or grids) into the simulation. When using nesting domains, the boundary conditions of the finer (nested) grid are provided by the interpolation of the coarse (parent) grid. The nesting can be a one-way nesting, in which information flows from the parent domain to the nested domain; and two-way nesting in which the information exchange flows in both directions where the nested

grid solution replaces the parent grid solution for those parent grid points that lie inside the nested domain grid. WRF is a limited area model (LAM), and such as it needs boundary conditions. Usually, boundary conditions for WRF are given by a global meteorological model. During the experiments performed in this work, the boundary conditions were given by the Global Forecasting System (GFS) model, a global meteorological model developed by the National Center for Environmental Prediction (NCEP) of NOAA (NCEP/NOAA, 2025). Processes within the sub-grid scale are parametrized.

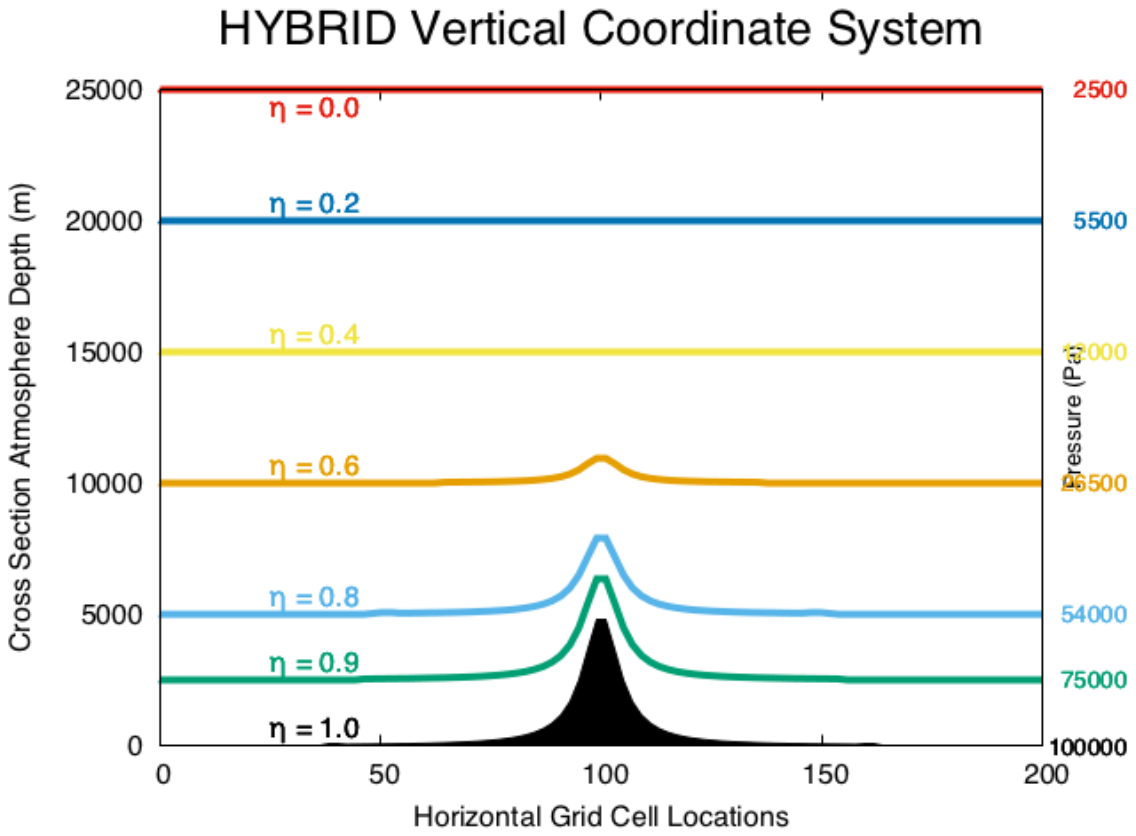

Figure 3.4: Hybrid terrain-following vertical coordinate system employed by WRF. Source: NCAR

The WRF model is composed of three components: the pre-processing system, in which boundary and initial conditions are defined; the initialization, which interpolates the initial and boundary conditions to each domain's grid; and the solver itself that contains all the information about the physics to compute the spatial and temporal variation of the atmospheric dynamics. It is necessary to provide the solver the information about the parametrizations of all the physical phenomena that occurs at sub-grid scale within the simulation domains.

When working with urban areas, as is the case of this thesis, is important to correctly assess the impact of their presence on the mesoscale circulation. The BEP+BEM parametrization (Martilli et al., 2002; Salamanca et al., 2010) simulates the local-scale meteorological effects

of the grid-average urban morphology within the WRF model. The BEP scheme takes into account the influence of buildings and urban heterogeneities on the UCL. In particular, it considers the impact of the drag induced by buildings on the momentum fluxes; the modification of the heat fluxes due to shadowing and radiation trapping effects; and the enhancement of the transformation of mean kinetic energy into turbulent kinetic energy. Moreover, BEM computes heat fluxes between the indoor and outdoor sides of each building. It considers diffusion of heat through walls, floors and roofs, the natural ventilation, and the radiation exchanged between the indoor surfaces. BEM also takes into account the presence of air conditioning systems (ACS), windows and equipment inside the buildings' rooms.

3.3 Microscale modelling

There exist different approaches at microscale air quality modelling. Some of them resolve the fundamental equations of fluid mechanics near complex geometries (i.e., Computational Fluids Dynamics models (CFD)); others are based on parameterizations of those processes involved (e.g. Gaussian models); and others are in-between such as Lagrangian models. Recently, artificial intelligence-based models have become very popular, which usually are trained with CFD modelling outputs. At microscale, Computational Fluid Dynamics (CFD) models have been widely used to assess pollutants dispersion within street-canyons (Santiago et al., 2007; Sanchez et al., 2017; Rivas et al., 2019). They accurately simulate the turbulent flow dynamics, and subsequent dispersion patterns, by solving the Navier-Stokes equations, and explicitly accounting for the complexity of the built-up environment. However, this level of detail requires also a large computational demand, which usually limits their use to short time periods.

3.3.1 The CFD-RANS model

Governing equations

CFD models are based on the governing equations for the fluid that represent the principles of conservation of mass, momentum and energy in terms of mathematical expressions. In this research, the simulated fluid is the air in the urban canopy. Considering the characteristics of the air, some assumptions can be made:

- Air is a Newtonian fluid, where the viscous stresses are proportional to the rates of deformation.
- Air, in the velocity range considered, behaves as an incompressible fluid where the density is constant. In addition, the dynamic viscosity is considered constant.

Considering those assumptions, the governing equations take the following forms (Versteeg and Malalasekera, 2007):

$$\frac{\partial u}{\partial x} + \frac{\partial v}{\partial y} + \frac{\partial \omega}{\partial z} = 0 \tag{3.3}$$

$$\frac{\partial u}{\partial t} + u\frac{\partial u}{\partial x} + v\frac{\partial u}{\partial y} + \omega\frac{\partial u}{\partial z} = -\frac{1}{\rho}\frac{\partial p}{\partial x} + \nu\nabla^2 u + S_{M_X} \tag{3.4}$$

$$\frac{\partial v}{\partial t} + u\frac{\partial v}{\partial x} + v\frac{\partial v}{\partial y} + \omega\frac{\partial v}{\partial z} = -\frac{1}{\rho}\frac{\partial p}{\partial y} + \nu\nabla^2 v + S_{M_Y} \tag{3.5}$$

$$\frac{\partial \omega}{\partial t} + u\frac{\partial \omega}{\partial x} + v\frac{\partial \omega}{\partial y} + \omega\frac{\partial \omega}{\partial z} = -\frac{1}{\rho}\frac{\partial p}{\partial z} + \nu\nabla^2 \omega + S_{M_Z} \tag{3.6}$$

$$\frac{\partial \theta}{\partial t} + u\frac{\partial \theta}{\partial x} + v\frac{\partial \theta}{\partial y} + \omega\frac{\partial \theta}{\partial z} = \alpha_h\nabla^2\theta + S_h \tag{3.7}$$

where ρ represents the air density, ν the fluid kinematic viscosity which is related to the dynamic viscosity (μ) through $\nu = \mu/\rho$, α_h is the thermal diffusivity. u, v and ω represent the three components x, y and z of the velocity vector, S_M the momentum source for each component and S_h is the source term of heat. Equation 3.3 represents the mass conservation principle, Equations 3.4-3.6 the momentum conservation and Equation 3.7 represents the energy conservation in terms of the transport of temperature.

Urban processes are characterised by the turbulent phenomena (Rotach, 1999; Roth, 2000; Britter and Hanna, 2003). There are several models that are able to resolve the turbulent flow equations:

- **The Direct Numerical Simulation (DNS) models**: The DNS models directly resolves the flow equations without considering any modelling assumptions. This means that both the mean flow and all turbulent components are computed, which in addition means that the whole range of spatial and temporal scales of the turbulence must be resolved. DNS simulations are, therefore, computationally very expensive which difficults its use in complex geometries as urban areas with the current resources.

- **The Large Eddy Simulation (LES) models**: The main idea behind the LES models is to reduce computational cost by ignoring the smallest length scales, based on the fact that most of the turbulent energy is carried by the largest scales. To this end, LES models perform a spatial filtering of the governing equations, resolving the mean flow and large eddies. The effects of the smaller eddies must not be neglected though, and is included by sub-grid scale models.

- **The Reynolds-Averaged Navier-Stokes (RANS) models** The RANS model is based on the Reynolds-Averaged Navier-Stokes equations, which consist on a temporal

average of the governing equations. The turbulent fluctuations of the equations appear as additional terms in the time-averaged flow equations, and they are not directly resolved. Instead, they are parametrized adding a turbulence closure.

The RANS model

A CFD-RANS model is construct around the Reynolds-averaged Navier-Stokes equations, which are based on the time average of the fluid dynamics equations. If one considers the time average of a variable ϕ as follows,

$$\Phi = \frac{1}{\Delta t}\int_0^{\Delta t} \phi(t) \cdot dt \tag{3.8}$$

then the flow variable ϕ can be decomposed into a mean component, Φ and a time-varying or turbulent component, ϕ', whose time average is zero.

$$\phi = \Phi + \phi' \tag{3.9}$$

This decomposition in mean and turbulent parts of a flow variable is called **Reynolds decomposition**. Using this decomposition, all variables are defined as follows:

$$u = U + u' \tag{3.10}$$

$$v = V + v' \tag{3.11}$$

$$\omega = W + \omega' \tag{3.12}$$

The RANS equations are based on this decomposition to extract the time-averaged equations of the fluid dynamics. When applying the Reynolds decomposition to the Navier-Stokes equations, and using Einstein notation (i=1,2,3 represents x, y and z directions respectively) for seek of simplification, the Navier-Stokes equations take the following forms:

$$\frac{\partial U_i}{\partial x_i} = 0 \tag{3.13}$$

$$\frac{\partial U_i}{\partial t} + U_j\frac{\partial U_i}{\partial x_j} = -\frac{1}{\rho}\frac{\partial P}{\partial x_i} + \frac{\partial}{\partial x_j}\left[\nu\frac{\partial U_i}{\partial x_j}\right] - \frac{1}{\rho}\frac{\partial \overline{u_i'u_j'}}{\partial x_j} + S_{M_{x_i}} \tag{3.14}$$

Equations 3.13 and 3.14 represent the fluid dynamics equations for the mean flows. The six additional terms in the momentum equations $\tau_{ij} = \rho\overline{u_i'u_j'}$ comprise the **Reynolds stress tensor**. Based on the Newton's law of viscosity, the viscous stress are taken to be proportional to the rate of deformation of fluid elements. Thus, the *Boussinesq hypothesis*

about eddy viscosity and eddy diffusivity proposed that the Reynolds stress are proportional to the mean strain-rate tensor (Arya, 2001).

$$\tau_{ij} = -\rho\overline{u_i' u_j'} = \mu_t \left(\frac{\partial U_i}{\partial x_j} + \frac{\partial U_j}{\partial x_i} \right) - \frac{2}{3}\rho k \delta_{ij} \tag{3.15}$$

where the **mean strain-rate tensor** (S_{ij}) is:

$$S_{ij} = \frac{1}{2} \left(\frac{\partial U_i}{\partial x_j} + \frac{\partial U_j}{\partial x_i} \right) \tag{3.16}$$

The **turbulent kinetic energy** (k) is defined as $k = \frac{1}{2}\overline{u_i' u_i'}$ and the **turbulent or eddy viscosity** (μ_t) is related to the turbulent or eddy kinematic viscosity as $\nu_t = \mu_t/\rho$, which needs to be determined.

For a scalar variable, the transport equation is expressed as follows:

$$\frac{\partial \Phi}{\partial t} + U_j \frac{\partial \Phi}{\partial x_j} = D \frac{\partial^2 \Phi}{\partial x_j \partial x_j} - \frac{\partial \overline{u_j' \phi'}}{\partial x_j} + S_\phi \tag{3.17}$$

The terms on the left-hand side represent the rate of change of the scalar variable and the convective term. On the right-hand side, the first term stands for the diffusive term, where D is the molecular diffusivity. The second term denotes the turbulent transport and the last one, S_ϕ, the source of the scalar. The turbulent fluxes of any scalar variable are considered proportional to the gradient of the mean value of the transported scalar.

$$-\overline{u_i' \phi'} = K_t \frac{\partial \Phi}{\partial x_i} \tag{3.18}$$

where K_t is the **turbulent or eddy diffusivity**. This parameter for heat and mass is expected to be analogous to the eddy viscosity μ_t for momentum since the turbulent transport of these variables are also controlled by same mechanism of eddy mixing. Therefore, the eddy diffusivity for mass and heat are defined as:

$$K_t = \frac{\mu_t}{\sigma_t} \tag{3.19}$$

where σ_t stands for the turbulent Prandtl number (Pr_t) for heat or the turbulent Schimdt number (Sc_t) for mass.

Therefore, the closure issue is reduced to solve the distribution of μ_t, for which is necessary a turbulence closure model. There exist several kinds of turbulence closure models. The simplest gradient-transport theories, which are based on the equations of mean motion, form

the basis of the so-called first-order closure models. Others more sophisticate higher-order closure models are based on the equations mean motion, turbulence variances, covariances and higher moments (Stull, 1988).

One first-order closure model is the so-called **mixing length model**. It is based in the assumption that the Reynolds strees has the same behaviour as the viscous stress, and so they are assumed to be proportional to the rate of deformation of fluid elements, with the turbulent viscosity (μ_t) being the proportionality constant. A more complex model is the **Reynolds Stress Model (RSM)**. This model computes the individual Reynolds stresses by resolving six additional equations, one for each element of the Reynolds stress tensor. In the middle between the simple mixing length model and the complex RSM are the $k-\varepsilon$ models. The $k-\varepsilon$ models only adds two more equations for the turbulent kinetic energy (k) and the turbulent dissipation rate (ε) that are solved together with the RANS equations (Versteeg and Malalasekera, 2007).

The $k-\varepsilon$ closure models

As the mixing length model, the $k-\varepsilon$ models assumes that the Reynolds stress is proportional to the rate of deformation of fluid elements and that the proportionality constant is the turbulent viscosity. The $k-\varepsilon$ model is based on modelling two additional transport equations, one for the turbulent kinetic energy and another for the turbulent dissipation rate. Several turbulence closures work on the basis of the $k-\varepsilon$ approach. The most common ones are the standard $k-\varepsilon$ (Launder and Spalding, 1974), the realizable $k-\varepsilon$ and the Re-Normalization Group (RNG) $k-\varepsilon$ (Yakhot and Orszag, 1986). The turbulence closure model used in this research is the **realizable** $k-\varepsilon$. The $k-\varepsilon$ models are commonly used for modelling urban air quality (Kim and Baik, 2004; Solazzo et al., 2008) and have a good reputation for reliability (Murakami, 1990). Of all the $k-\varepsilon$ models, the realizable $k-\varepsilon$ improves the standard $k-\varepsilon$ using the turbulent viscosity deduced by a new analytical expression and the ε equation is derived from an exact equation for the transport of the mean-square vorticity fluctuation (Shih et al., 1995).

The governing equations in the realizable $k-\varepsilon$ turbulence closure model are:

$$\frac{\partial k}{\partial t}+u_i\frac{\partial k}{\partial x_i}=\frac{1}{\rho}\frac{\partial}{\partial x_i}\left[\left(\mu+\frac{\mu_t}{\sigma_k}\right)\frac{\partial k}{\partial x_i}\right]+\frac{G_k}{\rho}-\varepsilon+S_k \tag{3.20}$$

$$\frac{\partial \varepsilon}{\partial t}+u_i\frac{\partial \varepsilon}{\partial x_i}=\frac{1}{\rho}\frac{\partial}{\partial x_i}\left[\left(\mu+\frac{\mu_t}{\sigma_\varepsilon}\right)\frac{\partial \varepsilon}{\partial x_i}\right]+C_1S_\varepsilon-C_2\frac{\varepsilon^2}{k+\sqrt{\nu\varepsilon}}+S_\varepsilon \tag{3.21}$$

where $C_1=max[0.43,\frac{\eta}{\eta+5}]$, with $\eta=S\frac{k}{\varepsilon}$. $\sigma_k=1.0$ and $\sigma_\varepsilon=1.2$ are turbulent Prandtl numbers for k and ε respectively and $C_2=1.9$ is a model constant. These values for the

model constants have been proved to be the most suitable for a wide range of turbulent flow at microscale (Launder and Spalding, 1974). The term G_k represents the production of turbulent kinetic energy and is defined as $G_k = \mu_t^2 S^2$ where S is the modulus of the mean strain-rate tensor ($S = \sqrt{2S_{ij}S_{ij}}$).

In other words, the terms on the left hand side of Equations 5.6 and 5.7 represent the rate of change and convective transport of k and ϵ respectively. On the right hand side, the first term represents the diffusive transport of those variables and the following two terms the production and destruction of k and ε. S_k and S_ε are the source terms for k and ε respectively.

Vegetation effects

Urban vegetation can also be considered within CFD models. In this sense, there are several possible approaches to simulate the urban vegetation within CFD models (Hefny Salim et al., 2015). An **implicit approach** consists on consider the impacts of vegetation implicitly by adjusting the roughness length (z_0) value on the surface grid cells where a tree is located. On the other hand, an strictly **explicit approach** would require vegetation to be resolved in all detail with a very fine grid, which eventually would lead to grid sizes of below a millimetre to resolve the size of a leaf. However, this is not feasible for large domains. For this reason, usually the followed approach consist on an in-between the implicit and explicit approaches. In this in-between approach the tree is considered as a porous media and additional terms are added to the momentum and turbulence equations to parametrize the additional mechanical production of turbulence due to the vegetation. The wind speed reduction resulting from the presence of vegetation is modelled by including a source term in the momentum equations:

$$S_{ui} = -c_d L(z) U u_i \tag{3.22}$$

where c_d is the drag coefficient (set to 0.2), $L(z)$ is the equivalent leaf-area density of the plant at height z, U is the mean wind speed at height z, and u_i is the wind velocity component.

In addition, the vegetation modifies the mean flow motion into wake turbulence, but the smaller length scale compared to turbulence generated by the shear induces a fast dissipation. Then, this process is usually parametrized as source and sink terms of turbulent kinetic energy (k) and turbulent dissipation rate (ε) (Buccolieri et al., 2018).

$$S_k = \rho L(z) c_d \cdot \left(\beta_p U^3 - \beta_d U k\right) \tag{3.23}$$

$$S_\epsilon = \rho L(z) c_d \cdot \left(C_{\varepsilon 4}\beta_p \frac{\varepsilon}{k} U^3 - C_{\varepsilon 5}\beta_d U \varepsilon\right) \tag{3.24}$$

where β_p is the fraction of mean kinetic energy converted into turbulent kinetic energy by means of drag and takes a value between 0 and 1; β_d is the dimensionless coefficient for the short-circuiting of the turbulence cascade; and $C_{\varepsilon 4}$ and $C_{\varepsilon 5}$ are model constants. Based on previous studies (Santiago et al., 2013, 2017b), β_p is equal to 1. The constant β_d is a dimensionless coefficient for the turbulence cascade short-circuiting and $C_{\varepsilon 4}$ and $C_{\varepsilon 5}$ ($C_{\varepsilon 4} = C_{\varepsilon 5}$) are based on the following analytical expressions (Sanz, 2003).

$$\beta_d = C_\mu^{1/2} \left(\frac{2}{\alpha}\right)^{2/3} \beta_p + \frac{3}{\sigma_k} \tag{3.25}$$

$$C_{\varepsilon 4}(= C_{\varepsilon 5}) = \sigma_k \left(\frac{2}{\sigma_\varepsilon} - \frac{C_\mu^{1/2}}{6} \left(\frac{2}{\alpha}\right)^{2/3} (C_{\varepsilon 2} - C_{\varepsilon 1})\right) \tag{3.26}$$

where α is a constant equal to 0.5 (Dalpé and Masson, 2009). The values of C_μ and $C_{\varepsilon 1}$ are regarded as constant values of 0.09 and 1.44 respectively.

In addition to the aerodynamical effects, the presence of vegetation removes pollutants from air by means of deposition on the leaves. In mesoscale models, this effect is normally parametrized by means of a downward flux:

$$F_{dep} = V_d(z) C(z) \tag{3.27}$$

where $V_d(z)$ is the deposition velocity at height z and $C(z)$ is the pollutant concentration at that same height.

However, since the resolution at the microscale is much finer and resolves the vegetation into several computational cells, urban vegetation has been modelled in CFD simulations as a volumetric sink term in the transport equation of pollutants:

$$S_d = -L(z) V_d C(x, y, z) \tag{3.28}$$

3.3.2 Modelling long periods using CFD simulations

Due to the high computational resources required for CFD simulations, it is not always feasible to perform long-period simulations. For that reason, a numerical methodology based on steady-state CFD simulations is used to estimate long time-series of air pollutants concentrations at microscale. In this methodology, called WA CFD-RANS (Parra et al., 2010; Santiago et al., 2013), the k-ε RANS model was used to perform 16 steady-state simulations corresponding to 16 different wind directions (sectors N, NNE, NE, ENE, E, ESE, SE, SSE,

S, SSW, SW, WSW, W, WNW, NW, and NNW). The inlet wind direction varies in steps of 22.5^{o} between simulations. For each one, inlet profiles for wind speed are logarithmic and for turbulent kinetic energy (k) and turbulence dissipation rate (ε) are computed by the following equations (Richards and Hoxey, 1993):

$$u(z) = \frac{u_*}{\kappa} ln\left(\frac{z + z_0}{z_0}\right) \tag{3.29}$$

$$k = \frac{u_*^2}{\sqrt{C_\mu}} \tag{3.30}$$

$$\epsilon = \frac{u_*^3}{\kappa(z + z_0)} \tag{3.31}$$

where u_* is the friction velocity, z_0 is the roughness length, $C_\mu = 0.09$ is a model constant and κ is the von Karman's constant ($\kappa = 0.4$).

These vertical profiles correspond to neutral atmospheric conditions. In these conditions, simulated pollutant concentrations are inversely proportional to wind speed, which allows to employ the proposed methodology.

Also for each simulation, the traffic emissions are provided through passive tracers near to the ground distributed by the domain cells corresponding to roads.

To estimate the evolution of the pollutant concentrations over time, the following steps are followed:

For each hour, the selection of the wind direction sector at every hour is derived from the outputs of meteorological mesoscale simulations. Likewise, the corresponding emission scenario is selected for that hour following the traffic flow pattern previously described. Thus, the initial concentration field of NO_X depends on the wind direction and the traffic scenario:

$$C_{sim}(t) = C_{sim}(WindSector(t), EmisScen(t)) \tag{3.32}$$

The second step is to transform the simulated concentration for the selected scenario according to the actual wind speed. On the basis that the thermal and the chemical effects are neglected, and of the logarithmic inlet wind profiles, the simulated concentration is inversely proportional to the actual wind speed (Parra et al., 2010). But in this Ph.D. thesis is used an approach similar to that proposed by Sanchez et al. (2017), in which $[NO_X]$ is transformed using the friction velocity as reference velocity instead of the wind speed:

$$C_{mod}(t) = \frac{u_{*,CFD}(t)}{u_{*,WRF}(t)} \cdot C_{sim}(t) \tag{3.33}$$

This is because at low wind speeds thermal effects become significant, failing the assumption of $[NO_X]$ being inversely proportional to wind speed and the use of the friction velocity minimizes this error. It is noteworthy that the value of the friction velocity is obtained from the mesoscale model and it accounts for not only dynamical effects of buildings but also thermal effects. Thus, several effects neglected in CFD simulations, such as the deviation from neutral conditions, are considered in a simplified way by means of this reference velocity, which is given by the following expression,

$$u_* = \left[\left(\overline{u'w'}\right)^2 + \left(\overline{v'w'}\right)^2 \right]^{0.25} \tag{3.34}$$

Whereas in Sanchez et al. (2017) the reference u_* value is considered at the roof height of the tallest building, in this work will be used the maximum friction velocity inside the planetary boundary layer (PBL). This is done in order to consider the variability on PBL height and improve the representation of the dispersion of pollutants.

However, when the friction velocity given by the mesoscale model is below a given threshold (in this work, 0.07 $m \cdot s^{-1}$) Equation 3.33 changes. In those cases, none specific wind direction is selected, as for very low wind speeds the wind direction is highly variable. Instead, an average of all 16 wind directions is taken and u_* is limited to 0.07 $m \cdot s^{-1}$. That is, for cases of very low wind velocities, Eq. 3.33 is converted to:

$$C_{mod}(t) = \frac{u_{*,CFD}(t)}{0.07} \cdot \overline{C_{sim}^{16WD}}(t) \tag{3.35}$$

where

$$\overline{C_{sim}^{16WD}}(t) = C_{sim}(EmisScen(t)) \tag{3.36}$$

Finally, the background concentrations at each time step must be added to compute the total air pollutant concentrations, as the CFD only computes the local contribution:

$$C_{mod}(t) = \frac{u_{*,CFD}(t)}{u_{*,WRF}} \cdot \overline{C_{sim}^{16WD}}(t) + C_{back}(t) \tag{3.37}$$

, where $u_{*,WRF} \geq 0.07\ m \cdot s^{-1}$, as mentioned above.

3.3.3 Transforming NO_X to NO_2 at microscale

In this thesis non-reactive pollutants are considered in the CFD simulations. This assumption allows the application of the WA CFD-RANS methodology. Since the CFD model configuration used in the scope of this thesis does not consider chemistry, a methodology to estimate NO_2 concentrations from NO_X is needed.

Empirical functions are widely used to parametrize the NO/NO_2 conversion (Düring et al., 2011). One of them is the so-called Romberg approach (Equation 3.38)

$$NO_2 = \frac{a \cdot NO_X}{NO_X + b} + c \cdot NO_X \tag{3.38}$$

where a, b and c are regression parameters. In this thesis, historical data from the selected AQMS is adjusted to Equation 3.38 in order to optimize the regression parameters. This approach has been followed in other works (Bachlin et al., 2006; Jurado et al., 2020) and also have been employed to compute NO_2 concentrations from CFD simulations (Reiminger et al., 2024). In this research, the criterion followed for the optimization is the maximization of the R-square parameter.

Chapter 4

Estimating the impacts on emissions of a global-scale lockdown[1]

4.1 Introduction

Since late February 2020, most European countries started to impose lockdowns and mobility restrictions in order to prevent further spread of the COVID-19 pandemic. All non-essential activities were paralysed for weeks in most countries at some point, resulting in a reduction in atmospheric anthropogenic emissions. As a result, a drop in atmospheric pollutant concentrations was observed in several countries both by in-situ (Burns et al., 2021; Putaud et al., 2021) and satellite-based observations (Sun et al., 2021; Fioletov et al., 2022). While these studies have assessed changes in pollutant concentrations, further understanding of the impacts of restriction measures upon air quality and climate requires the quantification of the reduction of anthropogenic emissions. In this sense, works such as Guevara et al. (2021) and Zheng et al. (2021) provide a look at the non-local quantification of emission changes due to the pandemic. The work of Guevara et al. (2021) is focused in Europe, and for the period between February 21st and July 31st 2020 -which does not cover emission variations due to changes in restrictions after the first COVID-19 outbreak, while Zheng et al. (2021) is focused in China. Neither covers a wide enough range to compare the 2020 emissions with previous years.

As Guevara et al. (2021) points out, understanding and quantifying the impact of the COVID-19 lockdowns on European emissions and air quality is a difficult task due to the heterogeneous implementation of restrictions across different countries, including

[1]The main contents of the chapter are included in the published research article: Rodríguez-Sánchez, A., Vivanco, M. G., Theobald, M. R and Martín, F.: Estimating the effect of the COVID-19 pandemic on pollutant emissions in Europe, *Atmospheric Pollution Research*, 13(5), 101388, DOI:10.1016/j.apr.2022.101388, 2022.

(i) different starting dates of the restrictions, (ii) diversity in the levels and type of restrictions, (iii) changes in time of the restriction levels, and (iv) different spontaneous responses by individuals. It is important to highlight that estimations of changes in anthropogenic emissions released to the atmosphere are required for diverse applications including economics and policy making (e.g. providing reference values for developing strategies), healthcare (e.g. for estimating health impacts of air pollution) and ecology (e.g. for estimating impacts to vegetation).

The chronology of national restriction levels in Europe is illustrated in Figure 4.1, which shows stringency index trends computed by the Oxford COVID-19 Government Response Tracker (OxCGRT) for selected countries (Hale et al., 2021). The stringency index reports how the response of governments varied by combining several indicators (e.g. school closures, restrictions in movement, implementation of economic policies). As it can be seen, there were two main periods when moderate or severe restrictions were imposed in all countries. In this work, those periods are referred to as "first wave" and "second wave". The first wave is considered as the period between February 21st, 2020 -when Italy impose strict restrictions- and July 1st, when all the countries have reduced stringency indexes. The start of the second wave is more difficult to define, due to lags between countries. Nevertheless, December 2020, January 2021 and February 2021 have significantly higher stringency indexes than previous months and therefore it can be considered that the second wave occurred during the winter months and the first three weeks of March 2021, after which the stringency index begins to drop in most countries.

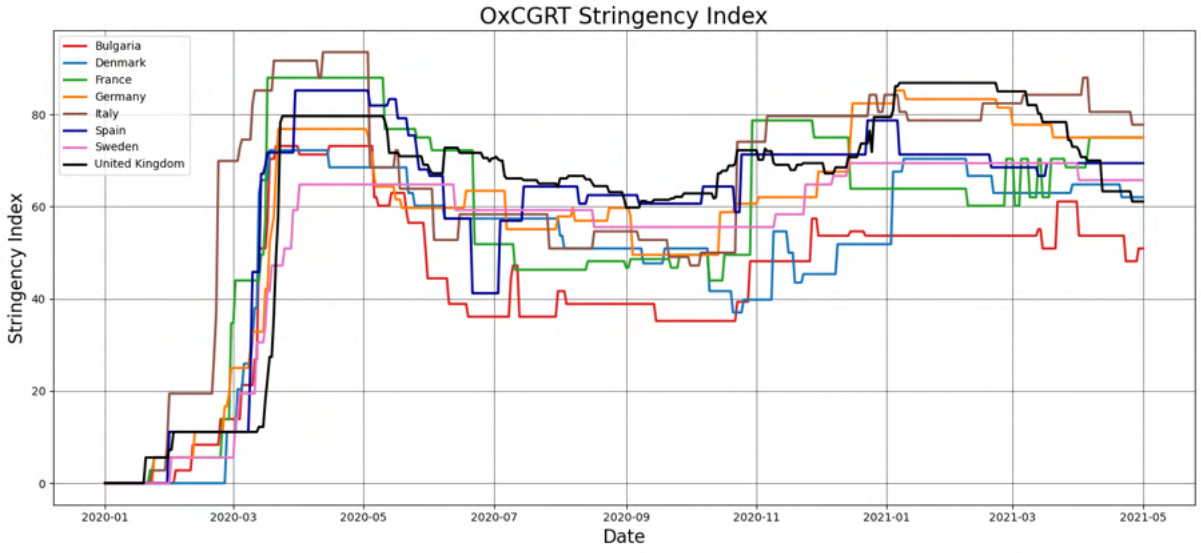

Figure 4.1: Evolution of the stringency index computed by the Oxford COVID-19 Government Response Tracker (OxCGRT) for the period January 1st, 2020 to May 1st, 2021 for seven selected countryies. Data available in Hale et al. (2021).

In this PhD thesis, a methodology to estimate day-, sector- and country-dependent emission

reduction factors for most European countries using open-source data is described. These factors are used to quantify European primary emission reductions and the associated impacts upon air quality. Those emission reduction factors are considered as a multiplicative factor to pre-pandemic emission values, and are calculated from data from a wide range of information sources, including open-access and near-real-time measured activity data, proxy indicators and other available reports. This work covers the whole of 2020 for the following anthropogenic source categories: energy industry, manufacturing industry, road transport, shipping and aviation. Furthermore, this study presents a faster, simpler and easily reproducible methodology as it does not use Machine Learning (ML) algorithms because, despite being widely used tools in scientific research, tuning a ML model can be a difficult and time-consuming task, thus complicating the emission reduction estimation process.

The main objective of the present work is to develop a methodology that allows the estimation of emission reductions due to the COVID-19 pandemic in an easy way, to provide a certain degree of independency to researchers that need this information for different purposes. The aim of this work is not to create an entirely new methodology buy to simplify existing ones and modify them when appropriate, avoiding both high computing resources and specific expertise in techniques such as ML.

4.2 Methodology

The approach followed to estimate emission reduction factors (ERFs) is based on that of Guevara et al. (2021). Data from a large range of information sources was gathered. As a result, a set of time- and sector-resolved ERFs for European countries for the year 2020 has been estimated, considering the Gridded Nomenclature For Reporting (GNFR) classification of emission source sectors. As in Guevara et al. (2021), we considered the following GNFR sectors:

- *GNFR_A*: Energy industry
- *GNFR_B*: Manufacturing industry
- *GNFR_F*: Road transport
- *GNFR_G*: Shipping
- *GNFR_C*: Other stationary combustion activities, specifically residential and commercial/institutional sectors

The ERFs for the GNFR_G activity sector are only time- and pollutant-dependent due to the lack of physical borders in the sea. In addition, some sectors such as agriculture, which is

considered part of the GNFR_C category, have been considered as essential activities during the pandemic because of their importance to provide necessary services to the community. Because of that, it has been assumed that emissions from these activities have not changed at all during the pandemic. Regarding the spatial coverage of the dataset, this work tries to include all the European countries with continuous data for the entire year of 2020. Subsection 4.2.1 provides further information about the data sources and the countries with available data for each activity source sector.

In this work, daily time series representing the main activities of each sector have been collected and processed, with the exception of GNFR_G (shipping), for which only weekly data were available. Then, the information was combined to derive daily ERFs as a function of country and sector.

4.2.1 Information sources and quality check

The constructed dataset includes information from a large variety of data sources. For estimating GNFR_A and GNFR_B ERFs, data from the ENTSO-E (European Network of Transmission System Operators for Electricity) transparency platform was used. ENTSO-E is the association for the cooperation of the European transmission system operators (TSOs) and is responsible for the secure and coordinated operation of Europe's electricity system (ENTSO-E, 2021). Hourly data of electricity demand for the EU-27 countries plus Norway and United Kingdom was collected for the years 2017-2020 and computed the daily total values. Days with no data were assumed to be days with no variations with respect to business-as-usual (BAU) values. Also, temperature data from the Copernicus Climate Change Service (Copernicus Climate Change Service (C3S), 2021) was used. Data from Switzerland was obtained from the national website. Another source of information was the Google Mobility database (Google, L.L.C., 2021). This dataset reports daily variations on mobility by country for different categories of places: public transport stations, grocery stores, parks, residential places, workplaces and recreation sites. Daily data for the EU-27 countries, Norway, North Macedonia, Turkey and United Kingdom was obtained for the period February 17th, 2020 to January 1st, 2021. Its values for the different places were adjusted using the criterion of Guevara et al. (2021). These data were used to estimate GNFR_C and GNFR_F emission reduction factors. Furthermore, daily local traffic data from the cities of Madrid (Madrid City-Council, 2025) and Dublin (TII, 2021) were used to improve the temporal resolution of TomTom based traffic ERFs. The emission reduction factors for the shipping sector were derived from the data on the impact of COVID-19 on European shipping traffic provided by EMSA, which starts at week 15 of 2020. These data are not country dependent but a single value for all European waters is given. Finally, the ERFs related to air traffic emissions during Landing and Take-Off cycles (LTO) in airports

were derived from daily statistics provided by EUROCONTROL (2021a,b)

4.2.2 Energy industry

Following the methodology of Guevara et al. (2021), it was assumed that energy from the industry sector follows the changes in electricity demand reported by ENTSO-E, under the hypothesis that changes in electricity demand are closely related to changes in electricity generation. ENTSO-E centralizes the collection and publication of the electricity generation for each European member state and the United Kingdom. However, unlike in Guevara et al. (2021), we have not used ML algorithms to weather-normalize the electricity demand. The use of electricity demand as an energy indicator is not a totally rigorous assumption, because other factors such as the use of heating or cooling systems also contribute to the demand (Botzen et al., 2021; De Cian et al., 2007). The use of those systems is directly related to the temperature; for this reason in this work electric demand data from a period with a similar meteorology to 2020 was used, in order to minimize the impact of heating or cooling systems, and attribute the differences to the effect of COVID-19 restrictions on electricity consumption. With this consideration, hourly data from 2018 and 2019 was collected for each country, since this is the period -since 1950- with average and seasonal average temperatures most similar to those of 2020 (Table 4.1). The season with the largest differences between 2020 and the 2018-2019 reference period is winter, as winter 2020 was an exceptionally warm one. However, this season is the one with least impact of temperature on electric demand, as heating systems in Europe use little electricity -barely a 5.9% of the energy used for heating is electricity (Odyssee-Mure, 2025). This means that it is expected that changes in emissions in winter 2020 due to restrictions related to the pandemic (especially in February) are notably larger than variations in emissions due to changes in meteorology. As a result, we assume that mean emissions of 2018 and 2019 are representative of the emissions for 2020 when considering only the effect of weather on the emissions.

Taking into account these considerations, the emission reduction factor for the energy industry were calculated as in Guevara et al. (2021), as:

$$ERF_{GNFR\_A} = \frac{ED_{2020}(d,c) - ED_{ref}(d,c)}{ED_{ref}(d,c)} \tag{4.1}$$

where $ERF_{GNFR\_A}(d,c)$ is the emission reduction factor for energy industry for day d and country c; $ED_{2020}(d,c)$ is the electric demand observed in 2020 for day d and country c; and $ED_{ref}(d,c)$ is the average of electric demand observed in 2018 and 2019 for day d and country c, as representative of BAU electric demand.

Figure 4.2 shows the difference between the computed ERFs using 2018 as reference year

Table 4.1: Variation of mean temperatures for 2018 and 2018-2019 with respect to 2020. DJF refers to the period December-January-February; MAM to March-April-May; JJA to June-July-August; and SON to September-October-November. Annual stands for the mean across all months.

	DJF	MAM	JJA	SON	Annual
$T_{2018-2019}$ minus T_{2020}	1.59	-0.21	-0.28	0.80	0.47
T_{2018} minus T_{2020}	2.44	-0.24	-0.48	0.60	0.58

and using 2018-2019 as reference period. Differences are generally small, but there are some notable exceptions. This is due to missing values, with Luxembourg and Cyprus being the countries with most missing data. For the days with missing data, the final ERF has been set to one (i.e., the same values as BAU values are considered for those days).

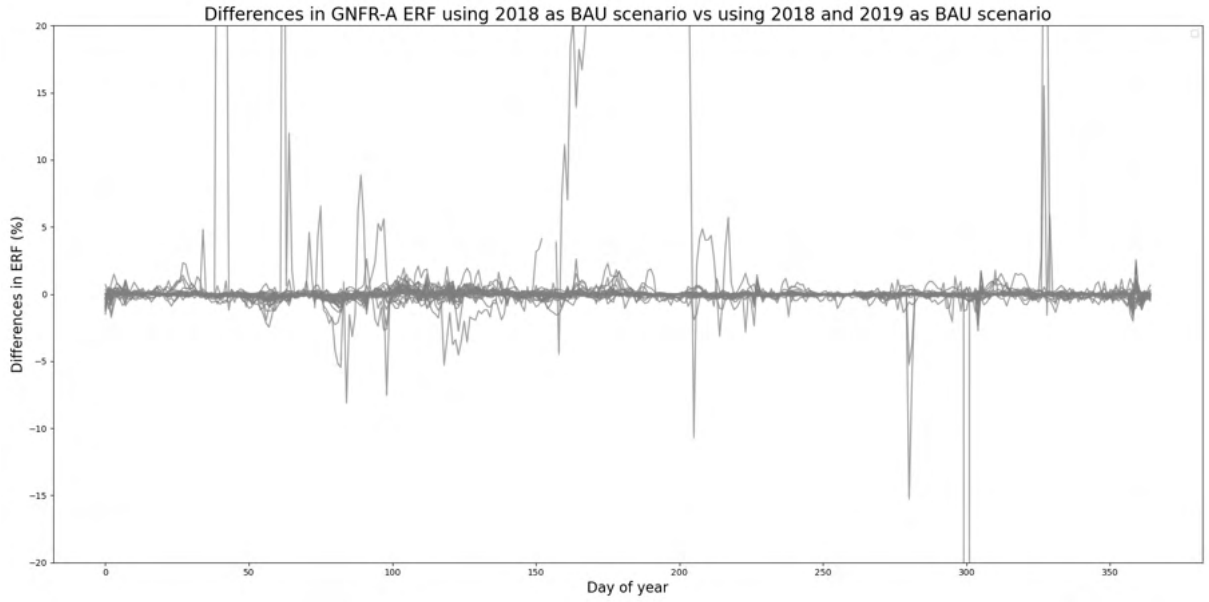

Figure 4.2: Timeseries of differences between the ERFs for the GNFR_A category computed using 2018 as reference year and those using 2018-2019 as reference period.

4.2.3 Manufacturing industry

The ERFs for the manufacturing industry (category GNFR_B) are based on those of the GNFR_A category. Following the criterion of Guevara et al. (2021), 25% of the total energy generation emissions reductions have been attributed to the manufacturing industry sector, which is consistent with the 27% decrease in electricity use by this sector reported by the electricity transmission system operator of France. The reduction of power demand attributable to the manufacturing industry sector was then translated into a total reduction in industrial activity using the national energy balances reported in Eurostat (2025):

$$ERF_{GNFR\_B}(d,c) = \frac{0.25 \cdot ERF_{GNFR\_A}(d,c)}{s(c)} \tag{4.2}$$

where $ERF_{GNFR\_B}(d,c)$ is the ERF for the manufacturing industry energy use for day d and country c, and $s(c)$ is the contribution of this sector to the total energy consumption for country c.

4.2.4 Road transport

In order to compare methodologies, the road transport sector have been computed using TomTom, N.V. (2025) monthly rush hour congestion data as well as the Google Mobility dataset (Google, L.L.C., 2021). Both procedures have been found to be fast and provide good results. Therefore, TomTom data could be an open-source to Google mobility data, which was not available to the general public before and after the pandemic, although the data for the pandemic is still publicly accessible. Furthermore, to improve temporal resolution, data from traffic counts have been included for countries where this type of data is freely available. To include these data, it has been assumed that reductions in road mobility in the main city or cities of a country contribute the most to national reductions and so it has been considered the traffic reductions in the most important cities of each country to be representative of the reductions for the entire country.

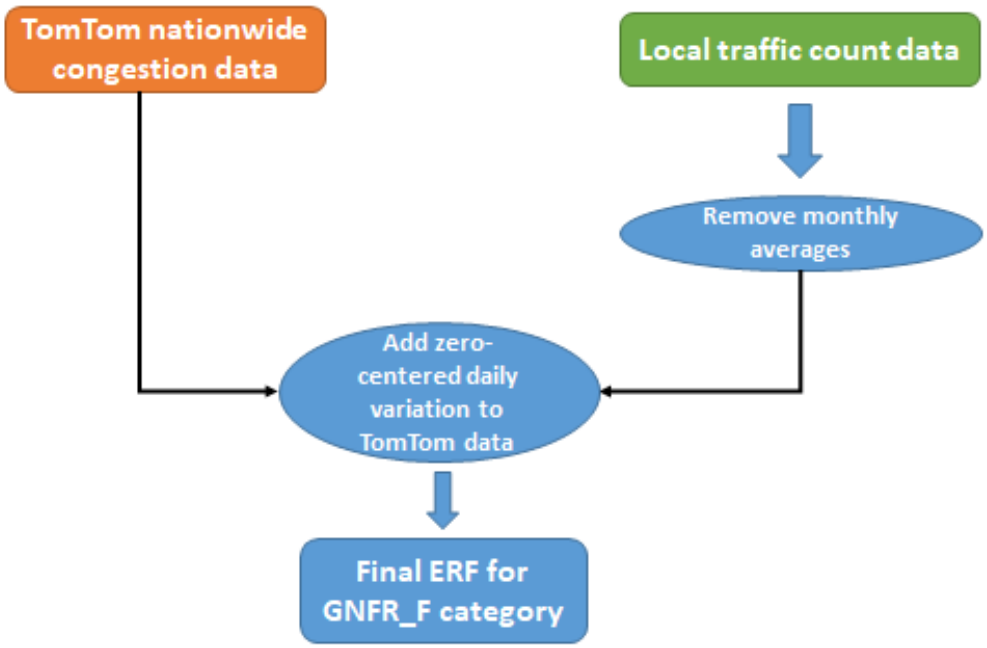

Figure 4.3: Procedure to improve temporal resolution of original GNFR_F ERFs for using daily traffic count data.

The procedure is illustrated in Figure 4.3. Once the monthly emission ERFs for the traffic sector are calculated using TomTom, N.V. (2025) monthly-based mobility data, their temporal resolution in a certain country is improved using the traffic count data from the main cities of the country. From the raw traffic count data, daily and monthly reductions of traffic flows in 2020 with BAU values are derived. The monthly reductions are then subtracted from the daily reductions in order to obtain the daily reductions with respect to the monthly mean values (zero-centered daily variations of traffic). Finally, those daily reductions with a mean value of zero are added to the previously computed monthly ERFs to obtain the definitive daily ERF for this country. The result is a time series with daily time resolution, but with a monthly mean equal to the monthly emission reduction factors derived from TomTom data. These series have a bias with respect Google mobility data that in part represents the contribution from the population of the rest of the country. This bias tends to be positive (i.e., in this work larger reductions than other works and Google data are estimated), in part since mobility reductions in villages and small towns are smaller than in larger cities due to the lower availability of essential services and the lower spread of COVID-19 in less populated areas, especially at advanced stages of an outbreak (Coşkun et al., 2021; Wong and Li, 2020). This approach works well for countries such as Spain and Ireland, as illustrated in Figures 4.4 and 4.5. Unfortunately, not all European countries had openly available traffic count data at the time this work was developed, and therefore most countries ERFs were calculated on a monthly basis.

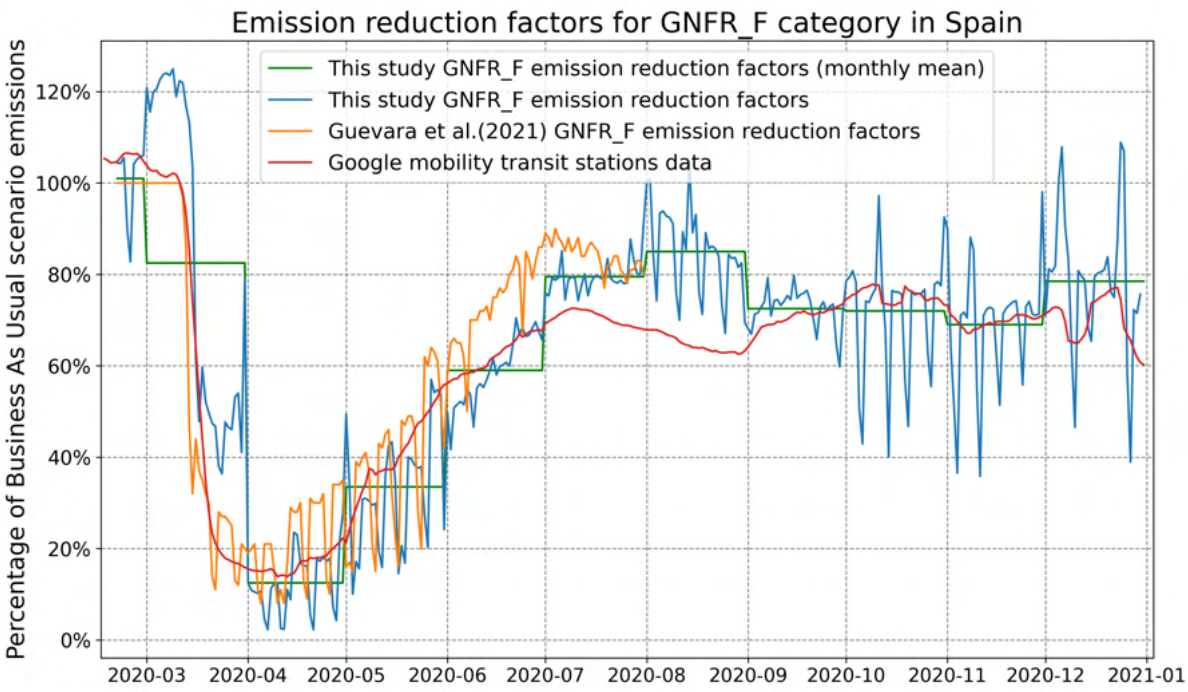

Figure 4.4: Daily emission reduction factors for road transport calculated in this study during the whole year 2020 (blue) and the initial estimation (green), compared with those of Guevara et al. (2021) (orange) and with the Google mobility transit raw data (red) for Spain.

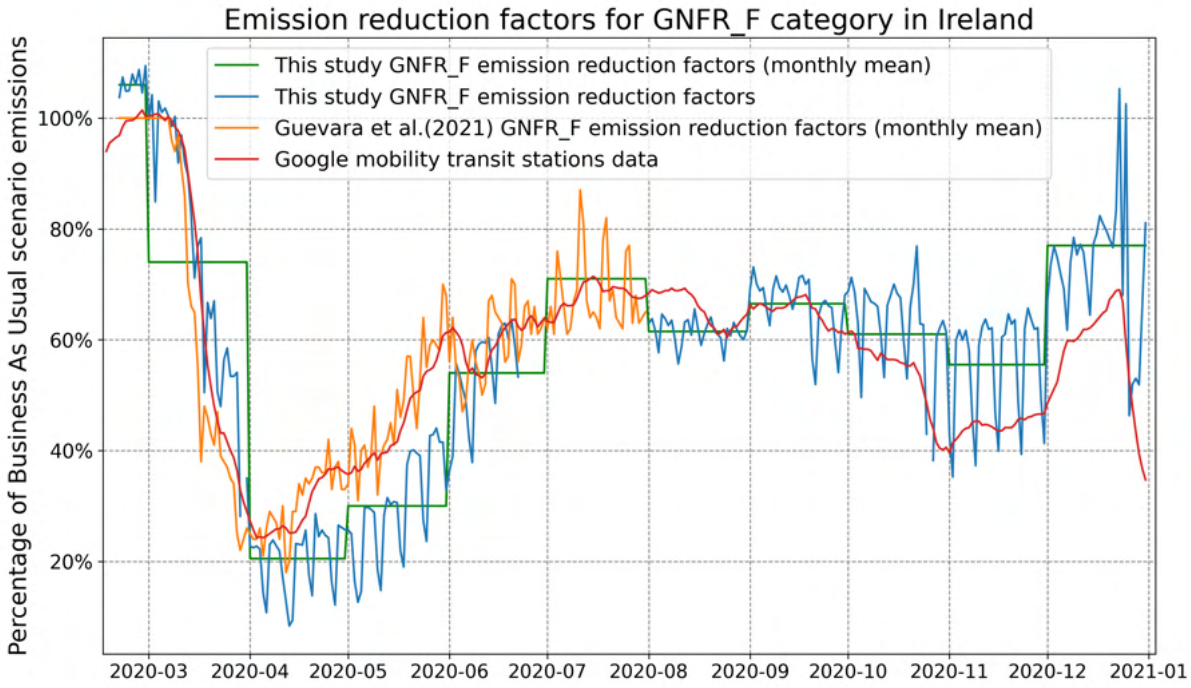

Figure 4.5: Daily emission reduction factors for road transport calculated in this study during the whole year 2020 (blue) and the initial estimation (green), compared with those of Guevara et al. (2021) (orange) and with the Google mobility transit raw data (red) for Ireland.

4.2.5 Aviation

Emission reduction factors for the aviation sector (GNFR_H) were derived from monthly and daily air traffic data published by EUROCONTROL (EUROCONTROL, 2021a,b) classified by country, instead of using individual airport data as in Guevara et al. (2021).

4.2.6 Shipping

For the shipping sector, ERFs were derived from the weekly reports published by the European Maritime Safety Agency. As there are no physical borders in the sea, a weekly ERF for the whole of Europe was estimated using weekly vessel traffic data classivied by type of vessel, as in Guevara et al. (2021):

$$ERF_{GNFR\_G}(w,p,v) = \sum_{v=1}^{n} ERF(w,v) \cdot C(v,p) \tag{4.3}$$

where $ERF_{GNFR\_G}(w,p,v)$ is the resulting emission reduction factor for the shipping sector for the week w, vessel type v and pollutant p; $ERF(w,v)$ is the ERF for vessel type v and week w; and $C(v,p)$ is the contribution of vessel type v to the total emissions of the shipping activities sector for pollutant p. The contribution of each type of vessel to total European

shipping emissions of each pollutant were obtained from Jalkanen et al. (2016).

4.2.7 Other stationary combustion activities

Finally, ERFs for other stationary combustion activities (GNFR_C), which includes commercial and institutional sector activities; residential activities; primary sector (agriculture, fishing, forestry, etc.) activities and other activities, whose contribution is small, were computed. Primary sector activities were considered as essential activities which means that lockdowns and other restrictive measures were not applied to them. Consequently, the ERFs calculated in this work are associated with reductions in residential, institutional and commercial activities. In order to estimate the variations in emissions associated with the aforementioned activities, the "Google COVID-19 Community Mobility Reports" (Google, L.L.C., 2021) database was used. This dataset reports daily variations on mobility by country for different categories of places: public transport stations, grocery stores, parks, residential places, workplaces and recreation sites. Increasing (decreasing) mobility towards the different places is directly associated with increasing (decreasing) activities related to them. These variations are computed by Google for each weekday, using the 5-week period between January 3rd, 2020 and February 6th, 2020 as a baseline.

Again, in order to compare with the study by Guevara et al. (2021), the same criterion was adopted to restrict daily variations of mobility towards places of residence to an upper limit of +10%, according to the data reported by Le Quéré et al. (2020), which are in line with those reported by the thermostat fabricant Tado. This is because the Google mobility database tends to overestimate changes in mobility. Furthermore, mobility changes for journeys to commercial/institutional buildings were limited to a maximum reduction of 66.9%, with respect to the BAU scenario (Guevara et al., 2021).

Depending on the main economic activities of a country, the contribution of each sector to total emissions for the GNFR_C category differs considerably from one country to another in the EU. Taking this into account, the ERFs of residential and commercial/institutional sectors are computed, as in Guevara et al. (2021), as a weighted average of the variations of these sectors from the Google database:

$$ERF_{GNFR\_C}(d,c,p) = RF_{res}(d,c) \cdot S_{res}(c,p) + RF_{comm}(d,c) \cdot S_{comm}(c,p) \tag{4.4}$$

where $ERF_{GNFR\_C}(d,c,p)$ is the resultant ERF for GNFR_C activities for day d, country c and pollutant p; $RF_{res}(d,c)$ is the mobility reducton factor associated with the residential sector for day d and country c; $S_{res}(c,p)$ is the contribution of the residential subcategory to the total emissions of the GNFR_C category for the country c and pollutant p. $RF_{comm}(d,c)$

is the mobility reduction factor related with the commercial/institutional sector for day d and country c; and $S_{comm}(c,p)$ is the contribution of the commercial/institutional subcategory to the total emissions of the GNFR_C category for country c and pollutant p.

The contribution of each subcategory to the total emissions of the GNFR_C category, as well as the total emissions for the GNFR_C category, is obtained from the emission data officially submitted by the Parties to the LRTAP Convention to the EMEP programme for the period 2015-2019. However, these data is highly dependent on how the different Parties submit their emission inventories to the EMEP programme (EMEP/CEIP, 2020). There are cases in which some subcategories have no emissions assigned to them for several reasons, such as that the country does not estimate emissions for that subcategory or the country includes emissions corresponding to one GNFR subcategory in another one. Also it can be that a specific subcategory or process does not exist in a country. These cases in which emissions cannot or have not been estimated for a subcategory are a minority and it has been possible to calculate the contribution of each subcategory (residential and commercial/institutional) to the total emissions corresponding to GNFR_C activities.

4.3 Results and discussion

4.3.1 Energy industry

Figure 4.6 shows a comparison between the daily emission reduction factors calculated for the energy industry in this work and those computed in Guevara et al. (2021) (hereafter as Guevara database) for Spain. It can be seen that the general trends are similar. This study's ERFs have larger variations than those in the Guevara database. This could be due to the fact that in this study a two-year period has been selected as a baseline and so anomalies in one year are not fully compensated. The second reason is that data in this work is not weather normalised for the sake of rapidness and ease of calculation. This can amplify the effect of days of increased consumption occurring on one specific day and year. For example, the peaks observed in Spain during the last days of the year correspond to an unusually cold period that extended until late-January. As Spain is a relatively warm country, electric consumption increased 15% during the first week of 2021 due to the activation of heating systems. However, differences between both databases' ERFs are still small, with an absolute value of 1.08% for the case of Spain -when averaging within the period with data in both databases- and 0.57% when averaging all countries' data.

Figure 4.7 shows the computed ERFs for the GNFR_A category for some European countries (Spain, France, Italy and Germany). In general, those countries behave quite similarly, with Italy having the larger reductions during the first wave of COVID-19-related lockdowns and

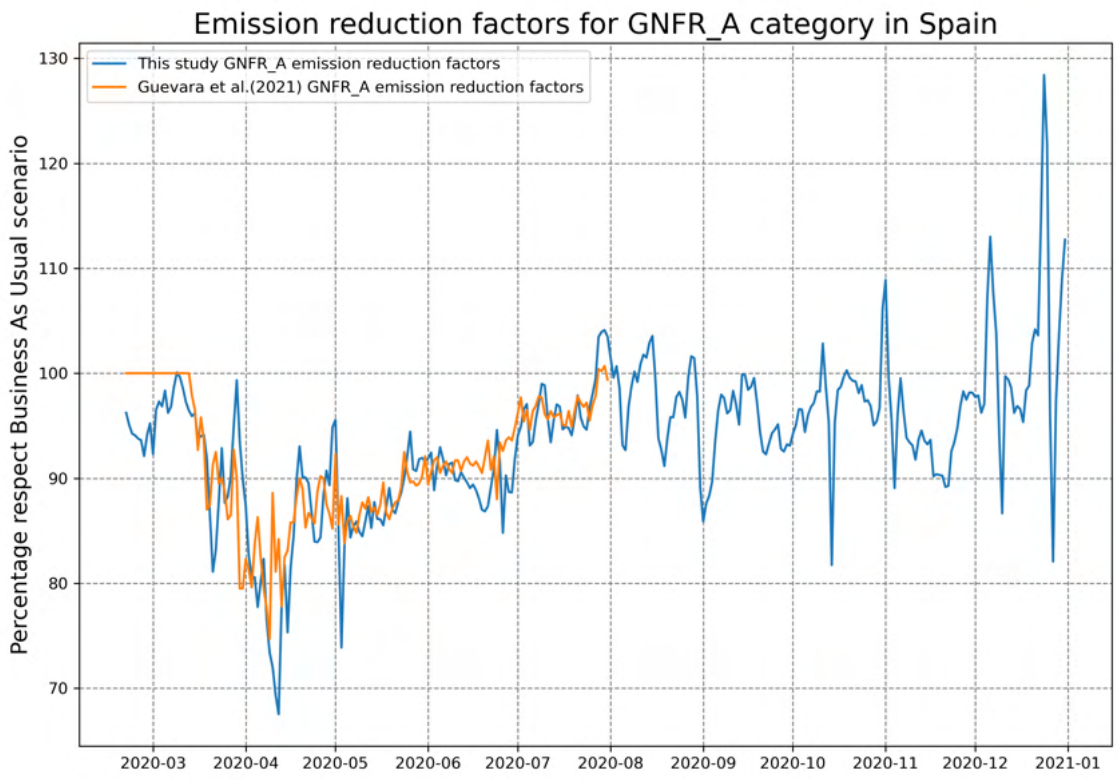

Figure 4.6: Emission reduction factors calculated in this study for the energy industry in Spain for the period February 21st, 2020 to end of year (blue line) and calculated by Guevara et al. (2021) for the period February 21st to July 31st (orange line).

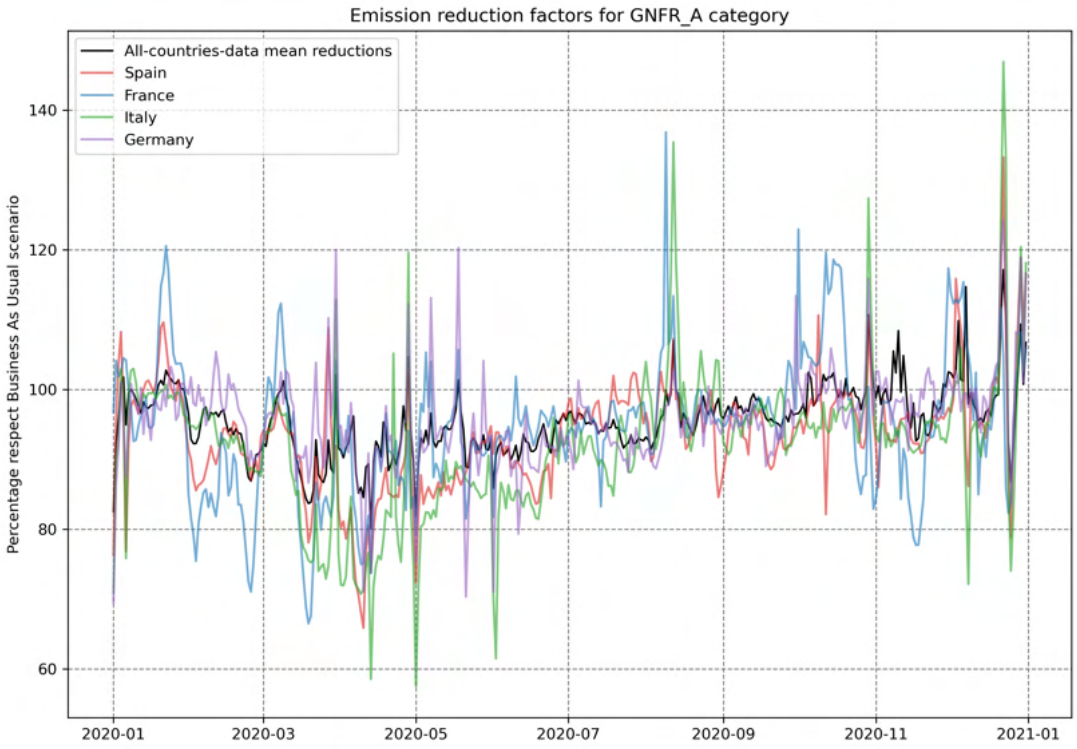

Figure 4.7: Emission reduction factors calculated in this study for the energy industry for the period February 21st, 2020 to end of year for some selected countries (Spain in red; France in blue; Italy in green; and Germany in purple), and the mean of all countries in the study (black line).

France showing a larger variation in emissions during November 2020, which is consistent with an abrupt increas in its stringency index in that month. As for the number of days for the period February 21st, 2020 to December 31st, 2020 below or above BAU emissions for the energy industry, there is a predominance of days with below average emissions, especially in Italy, as shown in Figure 4.8. Small countries such as Cyprus and Luxembourg show the largest number of days with emissions above 125% and below 75% of BAU values. The maximum possible value for the cumulative number of days exceeding these significant variations is 315 (number of days between February 21st and December 31st).

4.3.2 Manufacturing industry

Figure 4.9 illustrate the daily ERFs for the manufacturing sector. Again, data from this work fluctuate more than that obtained using complex methodologies but show the same trend. There is a slight overestimation of ERFs for Spain with respect to the Guevara database. This translates in slightly larger differences than for the energy industry sector between both database: 3.30% in Spain and 2.01% for all countries' data. Very similar trends to those of GNFR_A category are found for the European countries highlighted on the previous sections (Figure 4.10), which the previously mentioned exception of France in October and November 2020.

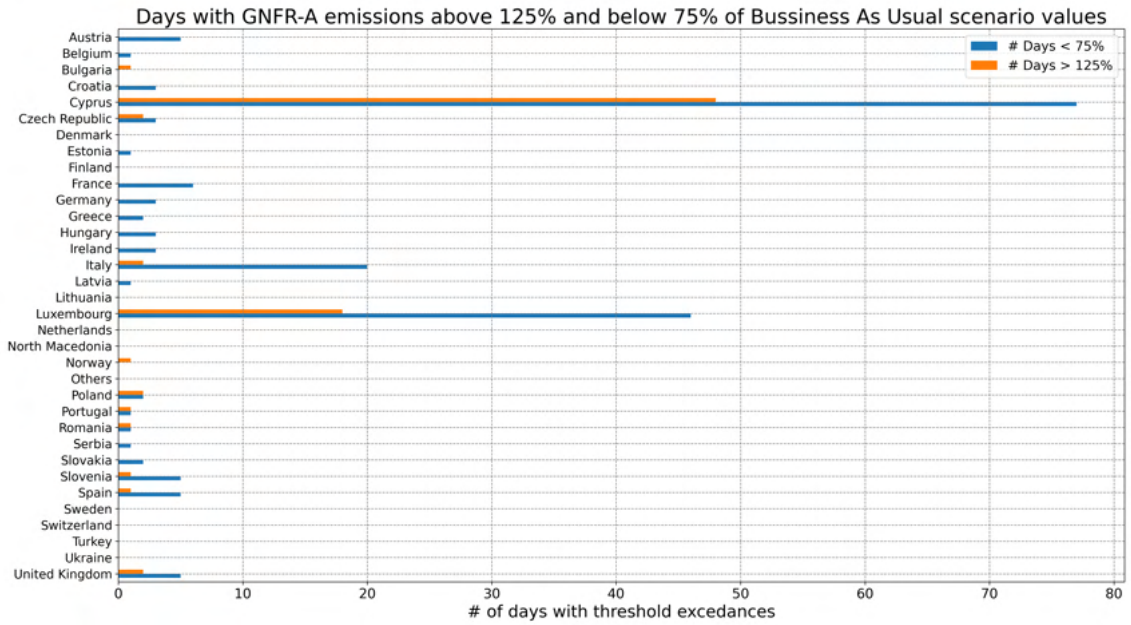

Figure 4.8: Number of days with emissions for the energy industry above 125% of business-as-usual (BAU) values (orange) and below 75% of BAU values (blue).

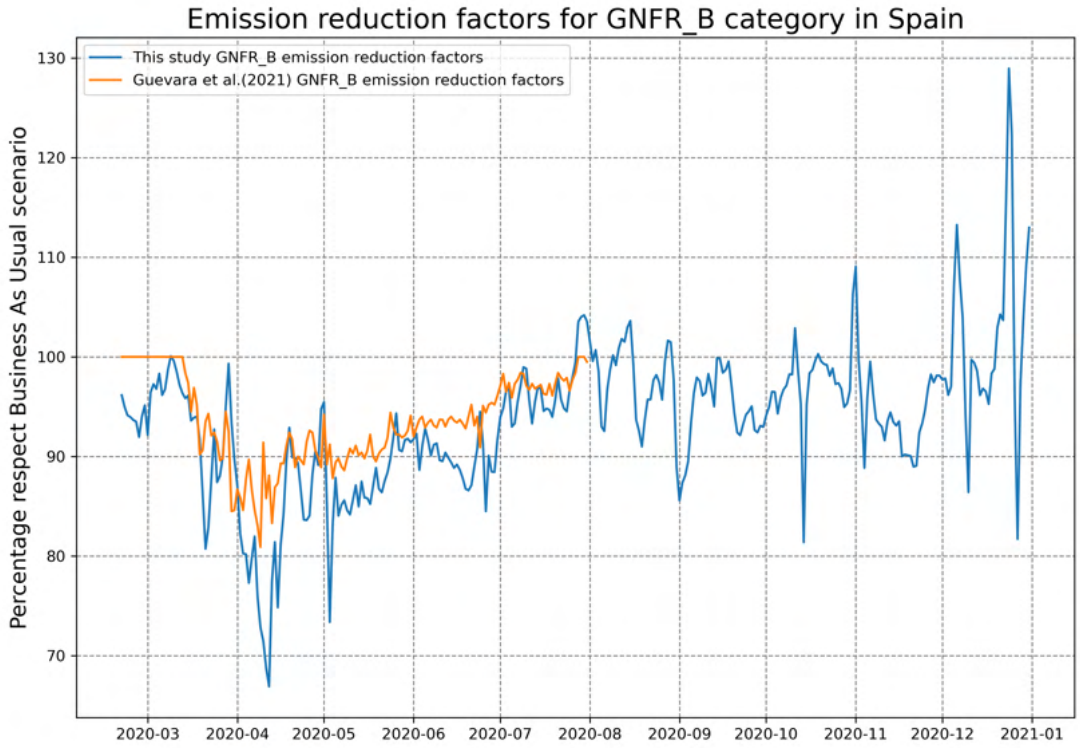

Figure 4.9: ERFs for the manufacturing industry in Spain for the period February 21st, 2020 to end of year (blue line) and calculated by Guevara et al. (2021) for the period February 21st to July 31st (orange line).

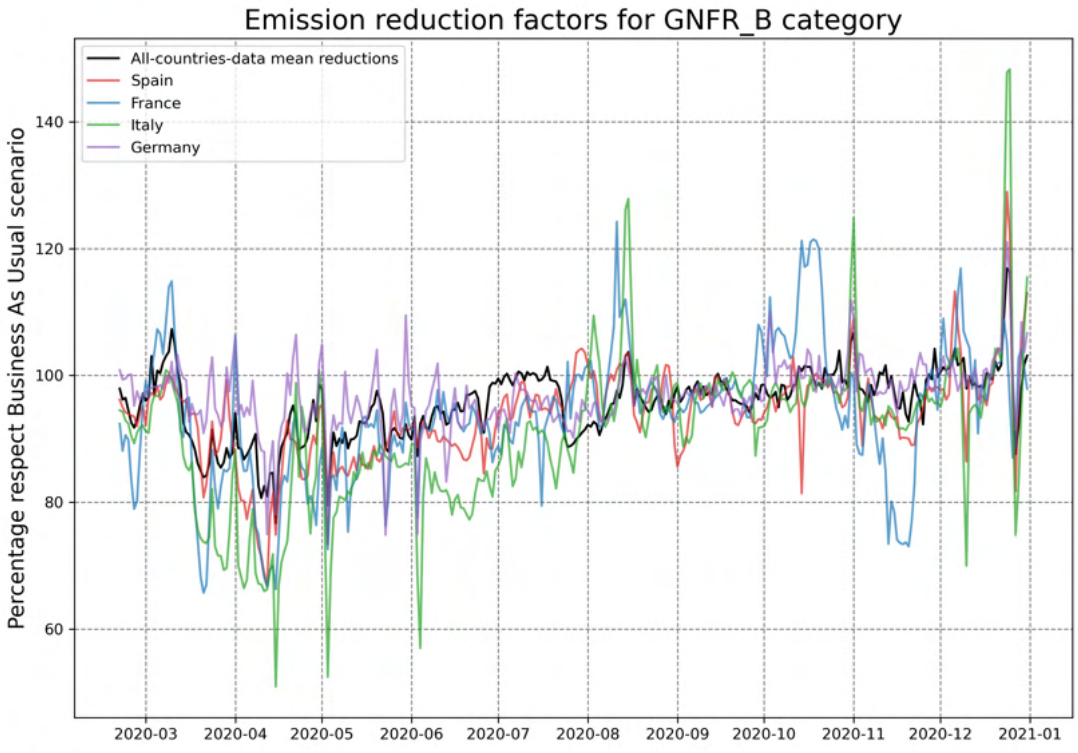

Figure 4.10: Emission reduction factors calculated for manufacturing industry for the period February 21st, 2020 to end of year for some selected countries (Spain in red; France in blue; Italy in green; and Germany in purple), and the mean of all countries in the study (black line).

4.3.3 Road transport

Figure 4.11 shows the initial estimation of monthly ERFs for road transport in Spain. As can be seen, the data for Spain in this work's database (blue line) agrees with the monthly mean of the data from Guevara database (green line), with a more pronounced drop and recovery of road traffic emissions in the Guevara database. The absolute value of the period-average difference between the monthly ERFs of both databases for Spain is of 1.42% and of 3.50% for all the countries. For some countries, such as Spain, the data in this work is more consistent with the Guevara database than with Google mobility data after the first COVID-19 wave, which tend to overestimate the emission reductions (Guevara et al., 2021). The maximum monthly emission reduction in Spain is observed in this work for April, with a 85% reduction (i.e., an ERF of 0.15), an an average reduction for the period February 21st, 2020 - January 1st, 2021 of a 25% (i.e., an ERF of 0.75).

Transforming the monthly emission reduction factors into daily ERFs results in good agreement with the Guevara database for the cases of Spain (Figure 4.12) and Ireland. These results suggest that this method represents a good alternative to estimate national road transport emissions derived from monthly rush hour data and the available traffic counts. In both cases the differences in ERFs between weekdays and weekends grows notably during the

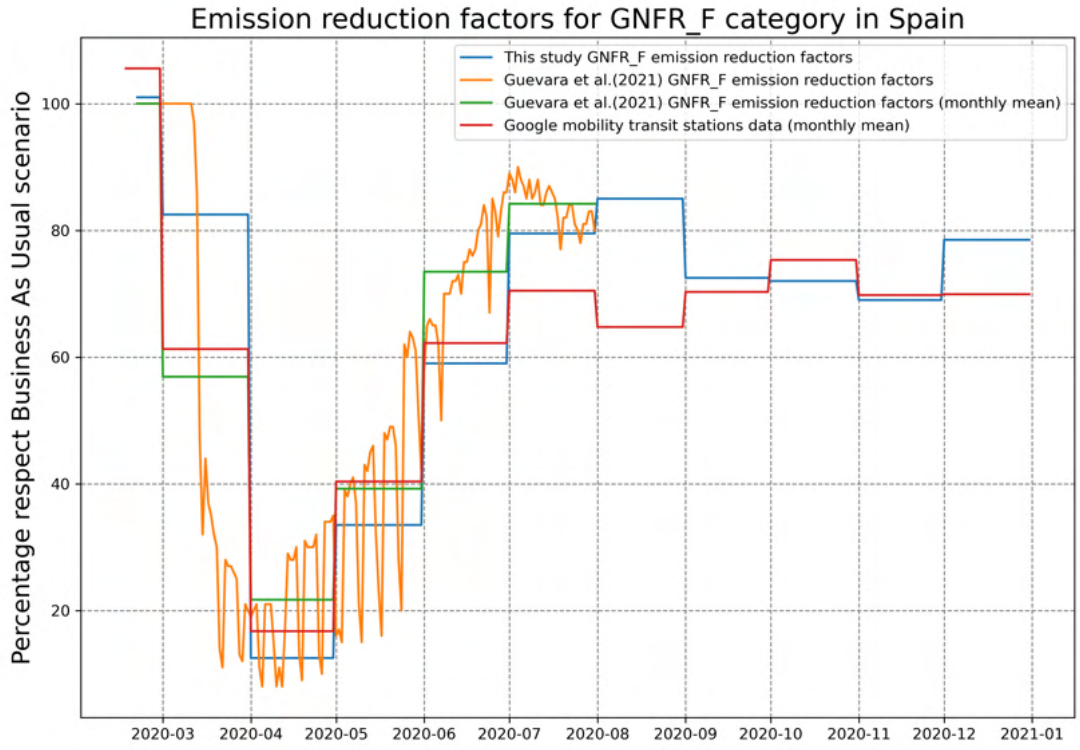

Figure 4.11: Emission reduction factors for road transport in Spain calculated in this study for 2020 (blue) compared with those of Guevara et al. (2021) (orange) and their monthly mean (green) and compared with the Google mobility transit monthly data (red).

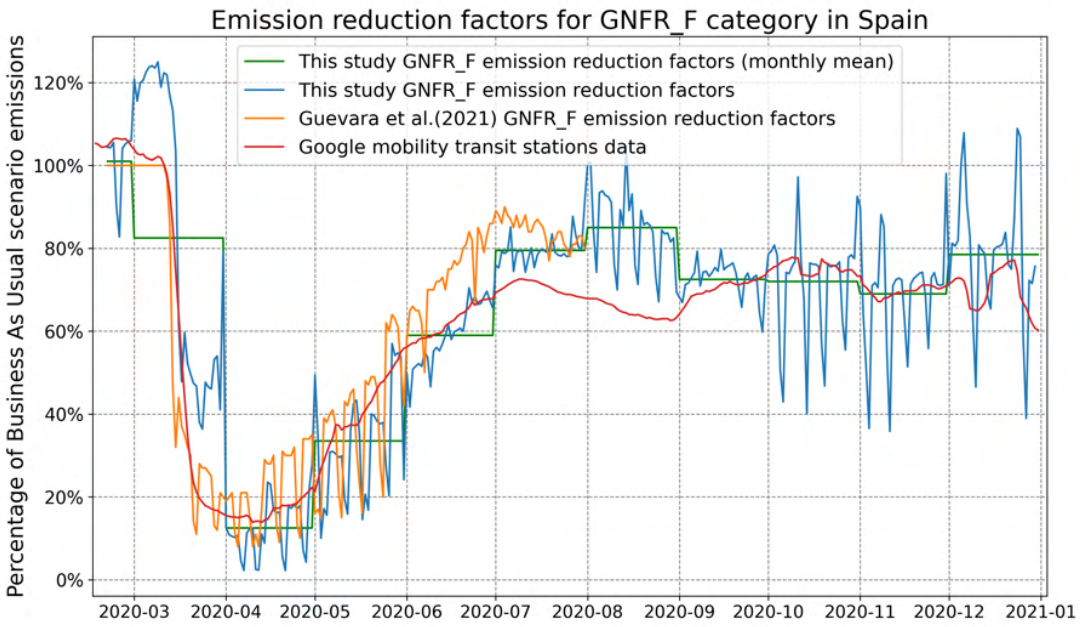

Figure 4.12: Emission reduction factors for road transport in Spain calculated in this study for 2020 (blue) compared with those of Guevara et al. (2021) (orange) and their monthly mean (green) and compared with the Google mobility transit monthly data (red).

second wave of the pandemic. Especially in the case of Spain, differences of up to 60% were seen between consecutive days. This is a limitation of the methodology introduced: the lack of data from more cities gives more weight to the traffic variations in the capital cities -of Madrid and Dublin in these cases- and their local restrictions. In the case of Madrid, during the last months of 2020 and the beginning of 2021, relatively light restrictions were applied to recreational activities: bars opened until curfew at midnight, 50% or more of capacity in bars and other recreational sites, etc.; while teleworking was by the time the predominant form of work. This makes the difference between weekend traffic, which tend to increase, and weekday traffic, which stayed quite low, giving rise to abrupt changes in the ERFs. For several other countries, freely available data of traffic counts was not found. Because of that reason and for the sake of consistency, Figure 4.13 shows the monthly ERFs obtained for all the countries included in this study. It can be identified the second wave of the pandemic affecting road traffic during late autumn after a relatively normal summer.

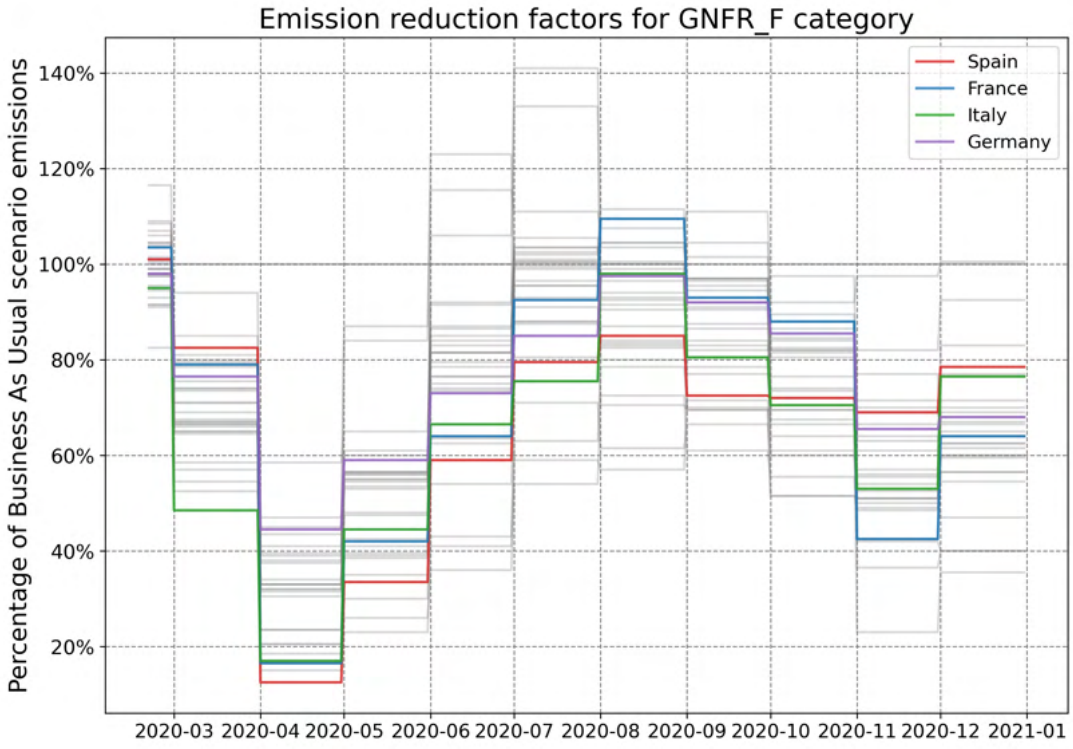

Figure 4.13: Emission reduction factors calculated in this study for road transport sector for the period February 21st, 2020 to end of year and every country considered in this study. Some selected countries highlighted (Spain in red; France in blue; Italy in green; and Germany in purple).

4.3.4 Aviation

Figure 4.14 and shows the ERFs computed for the aviation sector in some European countries. This is the sector most affected by the COVID-19 pandemic. The figure shows how emissions dropped to almost zero in April and did not fully recover during the analysis

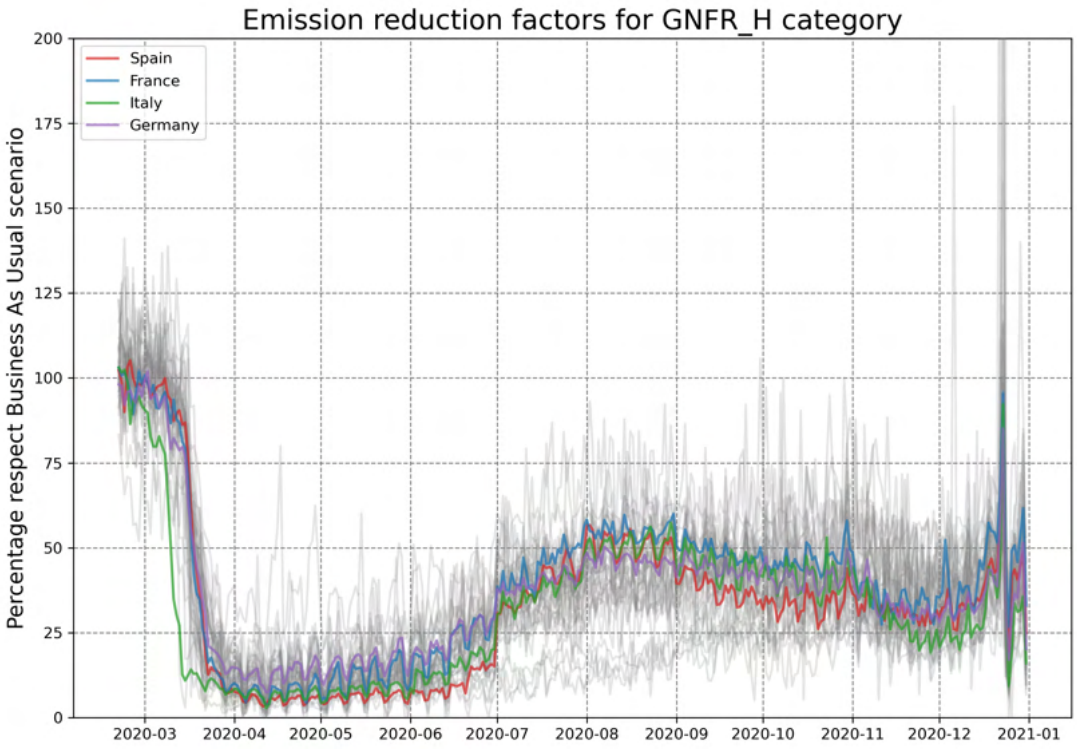

Figure 4.14: Daily emission reduction factors calculated for the aviation sector for the period February 21st, 2020 to end of year for every country considered in this study, with some selected countries highlighted (Spain in red; France in blue; Italy in green; and Germany in purple).

period, with a peak in summer with emissions approaching 50% of business-as-usual values. As in road transport, the effect of the second wave of COVID-19 on the emissions related to the aviation sector is visible, with emissions decreasing during autumn 2020 and recovering slightly by the end of the year for the Christmas holidays. The total emission reduction between February 21st and the end of the year 2020 for the aviation sector is 60%. Almost every day of the analysed period, since mid-March, had emissions below 75% of the BAU values in almost every country.

4.3.5 Shipping

Figure 4.15 shows the ERFs for the shipping sector. In this work, larger emission reductions than in Guevara et al. (2021) are computed, but again differences are quite small (maximum difference is of 5% in the first week of May), which allows to assume that calculations in this work are valid for the rest of the year. Here, the mean difference between both datasets are of 2.05%.

Figure 4.16 shows that there were no substantial differences between the different pollutants emitted by shipping, which indicates that all vessel types followed the same drop and recovery in their activities as each vessel type has a particular contribution from each pollutant to

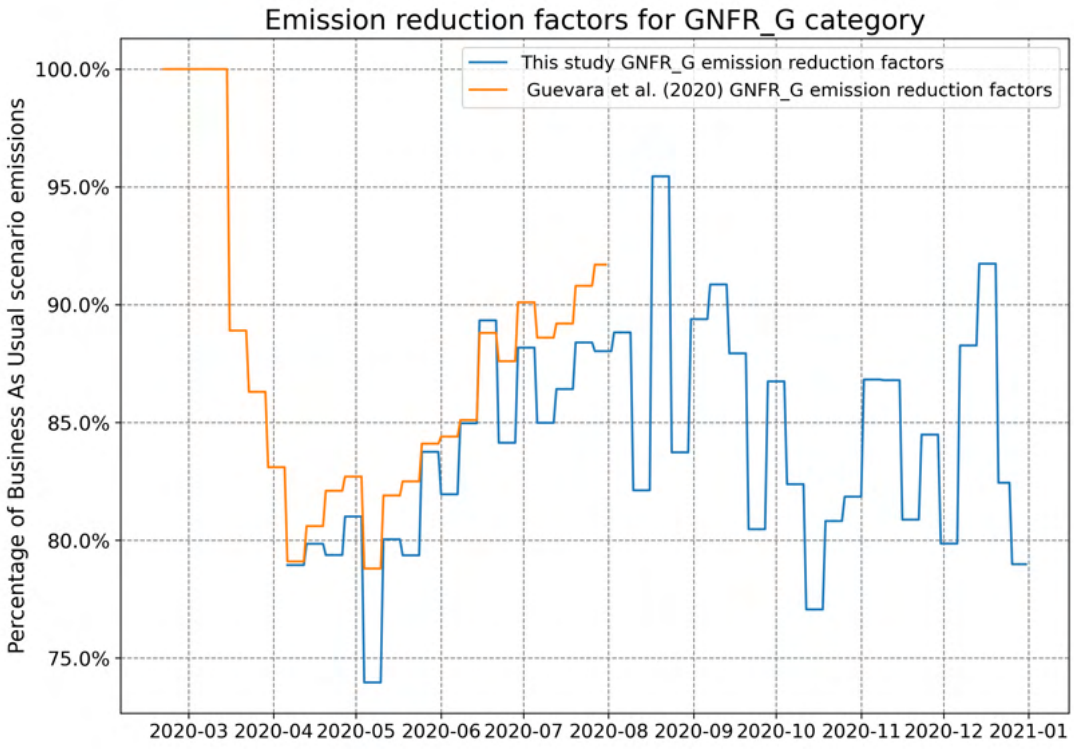

Figure 4.15: Emission reduction factors calculated in this work for shipping during 2020 (blue) compared with emission reduction factors of Guevara et al. (2021) for the period 21 February to 31 July (orange).

total emissions. The only significantly different behaviour is found in the last week of the year, where NO_X emissions increased with respect to the previous week due to an increase of roll on-roll off cargo ship and chemical tanker traffic.

4.3.6 Other stationary combustion activities

Figure 4.17 shows the NO_X ERFs for other stationary combustion activities across Europe. As for the road traffic data, it can be distinguished both the first and the beginning of the second wave of the COVID-10 pandemic in the ERFs, for most countries, particularly in France an Italy, where NO_X emissions dropped in November 2020 and again at the end of December 2020, corresponding to rises in the stringency index (Figure 4.1). Less evident is the emissions variation at the end of 2020 in countries with much more steady stringency index such as Spain, where NO_X emissions corresponding to GNFR_C activities barely drop in November, and drop significantly less than for the countries with higher stringency index in the last week of December 2020.

Although for NO_X emission reductions are observed due to the predominance of commercial/institutional sector -which reduced their activities- with respect to the residential sector, the picture is quite different for pollutants such as non-methane volatile organic

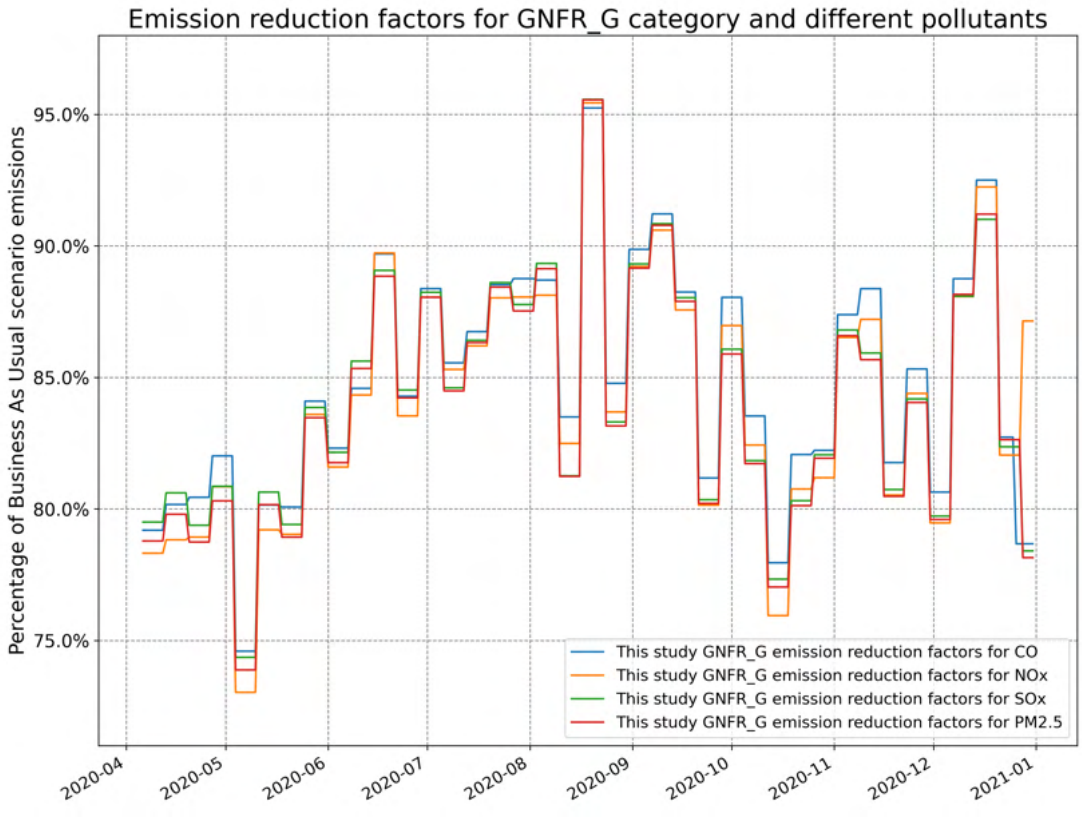

Figure 4.16: Emission reduction factors calculated for shipping during 2020 for the following pollutants: CO (blue), NO_X (orange), SO_X (green) and $PM_{2.5}$ (red).

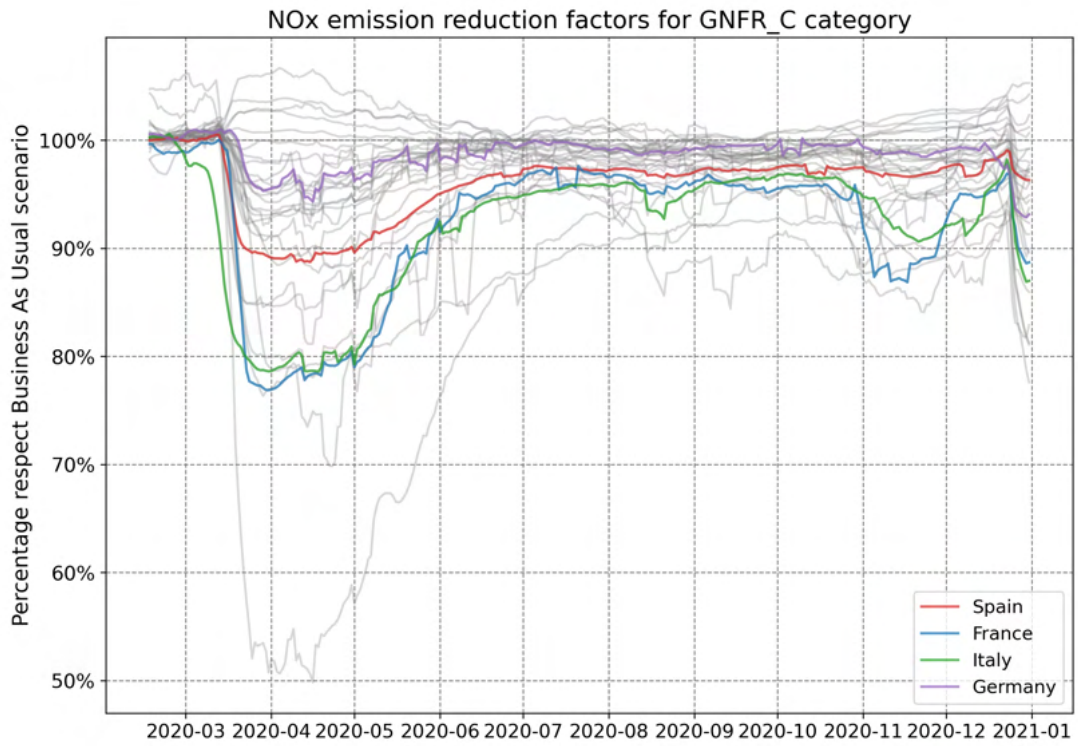

Figure 4.17: Daily ERFs for NO_X emitted by GNFR_C activity sector for the period February 21st, 2020 to end of year for every country considered in this study, with some selected countries highlighted (Spain in red; France in blue; Italy in green; and Germany in purple).

compounds (NMVOC), where the two waves of COVID-19 can be identified as increases in NMVOC emissions (Figure 4.18), with some notable exceptions such as Italy. This increase in NMVOCs emissions is clearly dominated by the contribution of the residential sector, which increases NMVOC emissions (Figure 4.19a)) when at the same time NMVOC emissions from the commercial/institutional activities were reduced (Figure 4.19b)). Italy is the main exception, indicating than the institutional/commercial sector was more affected by restrictive measures than in other countries.

Figure 4.20 shows the obtained NO_X ERFs for GNFR_C activities (blue line) compared with those from Guevara et al. (2021) (in orange). In this work, a slightly larger reduction is obtained, with a difference of about 2% in average. But the trends are consistent between the two databases. This conclusion is the same for every analysed pollutant (CO, $PM_{2.5}$, PM_{10}, NH_3, NMVOC and SO_X).

No days with emissions above 110% of BAU values have been observed in any of the countries for any of the pollutants, while several countries have registered up to more than 100 days with emissions below 90% of BAU values for NH_3, NO_X or SO_X (Figure 4.21). On the other hand, for pollutants dominated by residential activities (i.e. NMVOC, $PM_{2.5}$ and PM_{10}) no reductions were found.

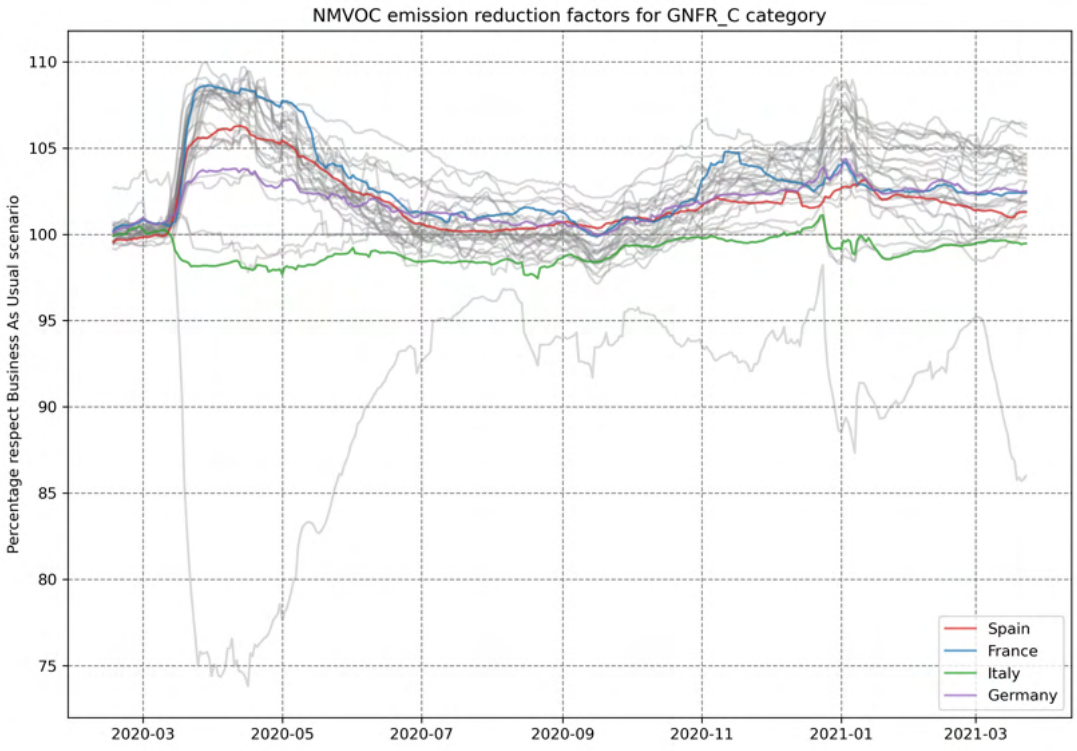

Figure 4.18: Daily ERFs for NMVOC emissions from GNFR_C activities for the period February 21st, 2020 to end of year for every country considered in this study, with some selected countries highlighted (Spain in red; France in blue; Italy in green; and Germany in purple).

4.3.7 Overall trends

Figure 4.22 presents a summary of the emission changes for the periods between February 21st, 2020 and December 31st, 2020 with respect to business-as-usual values for every country considered in the study and for all categories except GNFR_G (shipping), which has a single value representing all countries. For every country, aviation is the sector with the largest average drop in emissions due to mobility restrictions and drop in international tourism. This sector is followed by the road transport activities, which represent the second largest drop in emissions for all countries.

However, differing trends are observed for the industrial and public sectors. While for those sectors the mean reduction averaged over all countries was about 4% (Table 4.2), increases were found for both sectors in Denmark and Switzerland. From the available electricity consumption data from the Danish Government COVID-19 reference page, it can be seen that there were no significant changes between electricity consumption associated with manufacturing and public sectors industries for Denmark during 2020 with respect to the previous year (Figure 4.23). In fact, electricity consumption is greater after summer, which can explain an increase in emissions in this country. This agrees with the Stringency Index for Denmark, which has lower values for the second wave of COVID-19 than for the

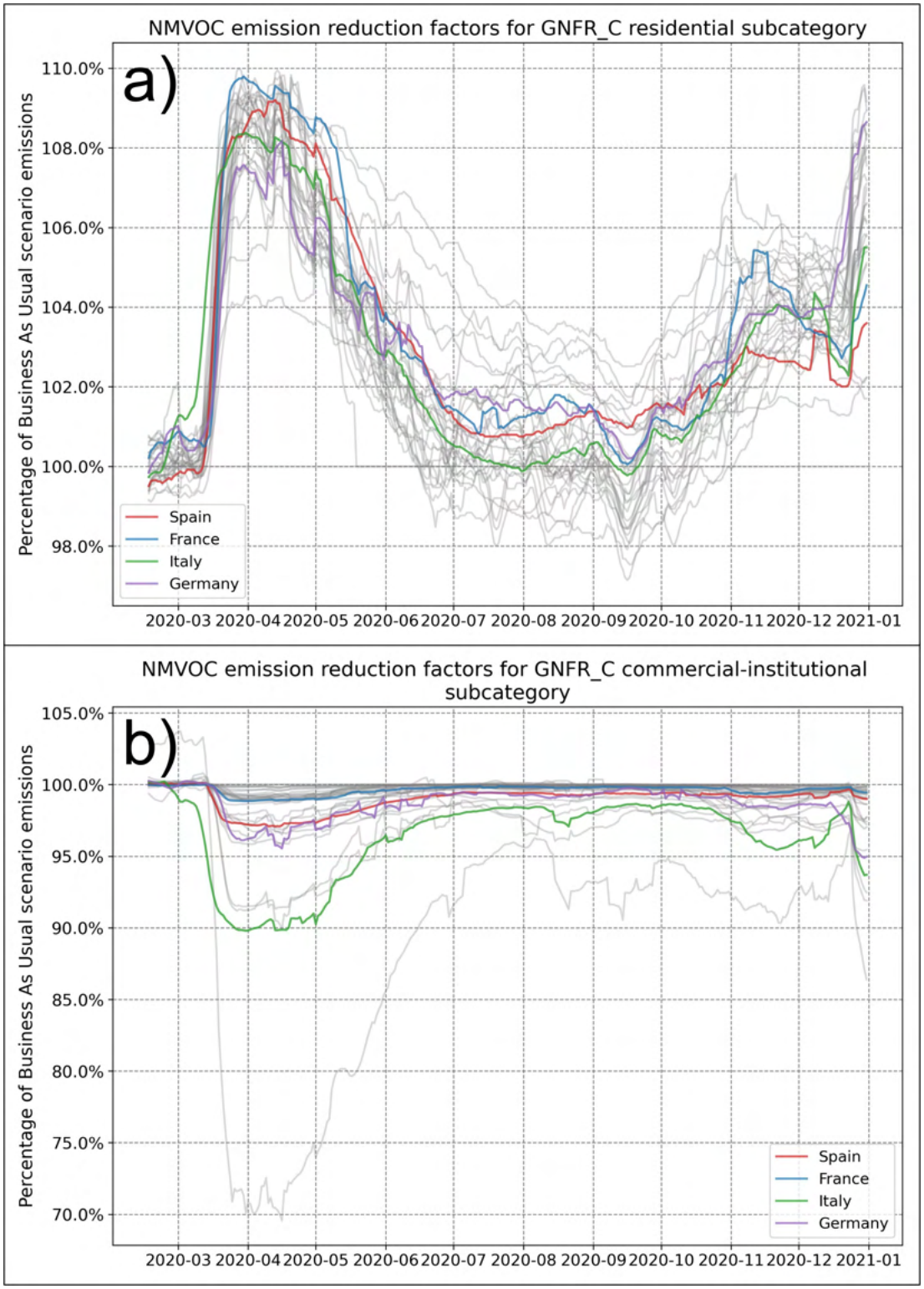

Figure 4.19: Daily ERFs for NMVOC emissions from a) residential and b) commercial/institutional activities for the period February 21st, 2020 to end of year for every country considered in this study, with some selected countries highlighted (Spain in red; France in blue; Italy in green; and Germany in purple).

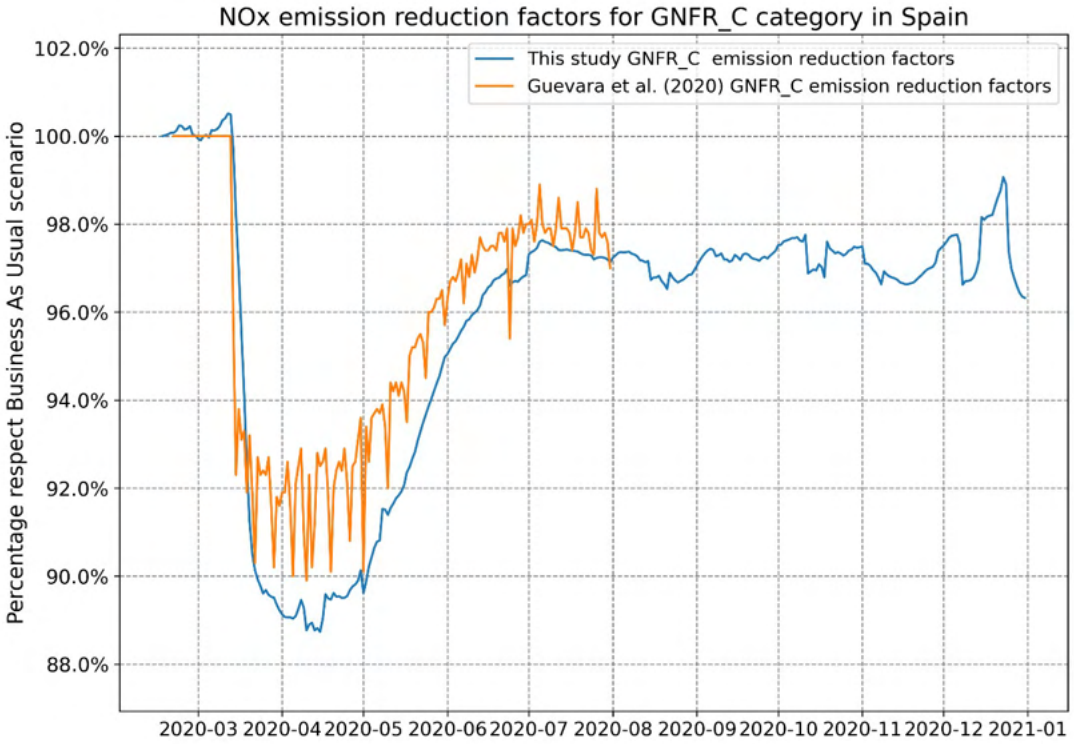

Figure 4.20: Emission reduction factors calculated in this work for GNFR_C activities during 2020 (blue) compared with emission reduction factors of Guevara et al. (2021) for the period 21 February to 31 July (orange).

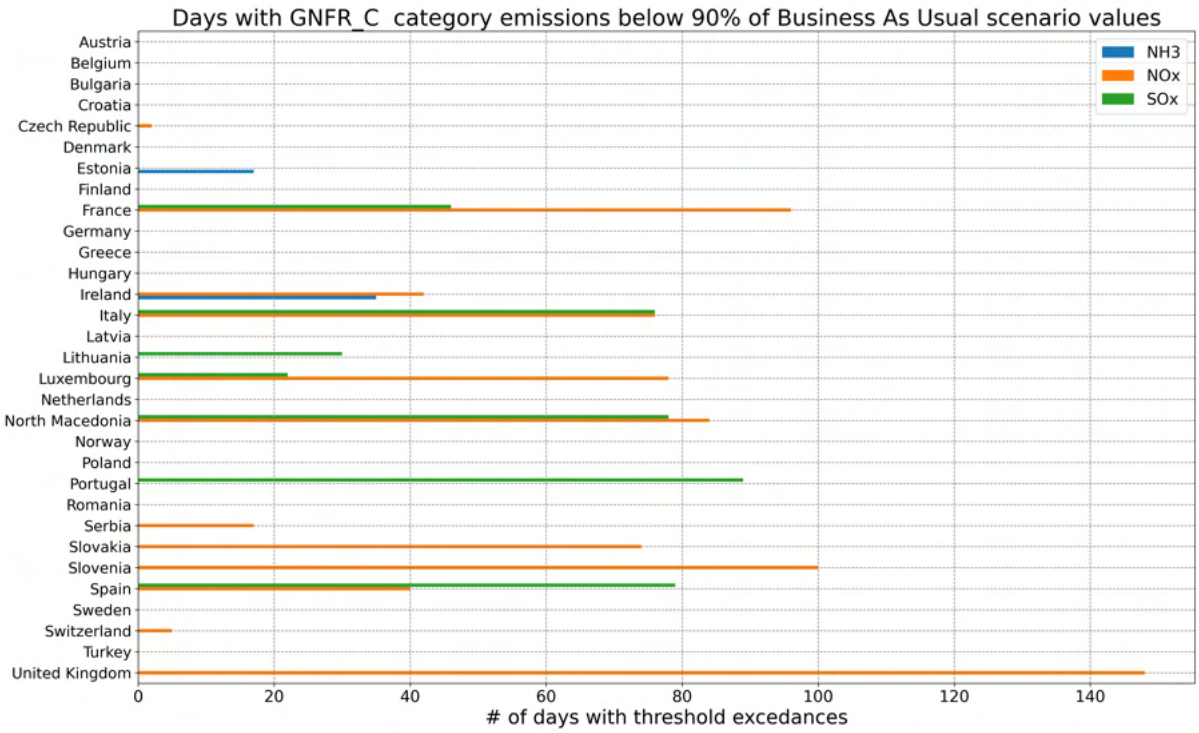

Figure 4.21: Number of days with emissions from other stationary combustion activities below 90% of business-as-usual values for NH_3 (blue), NO_X (orange) and SO_X (green).

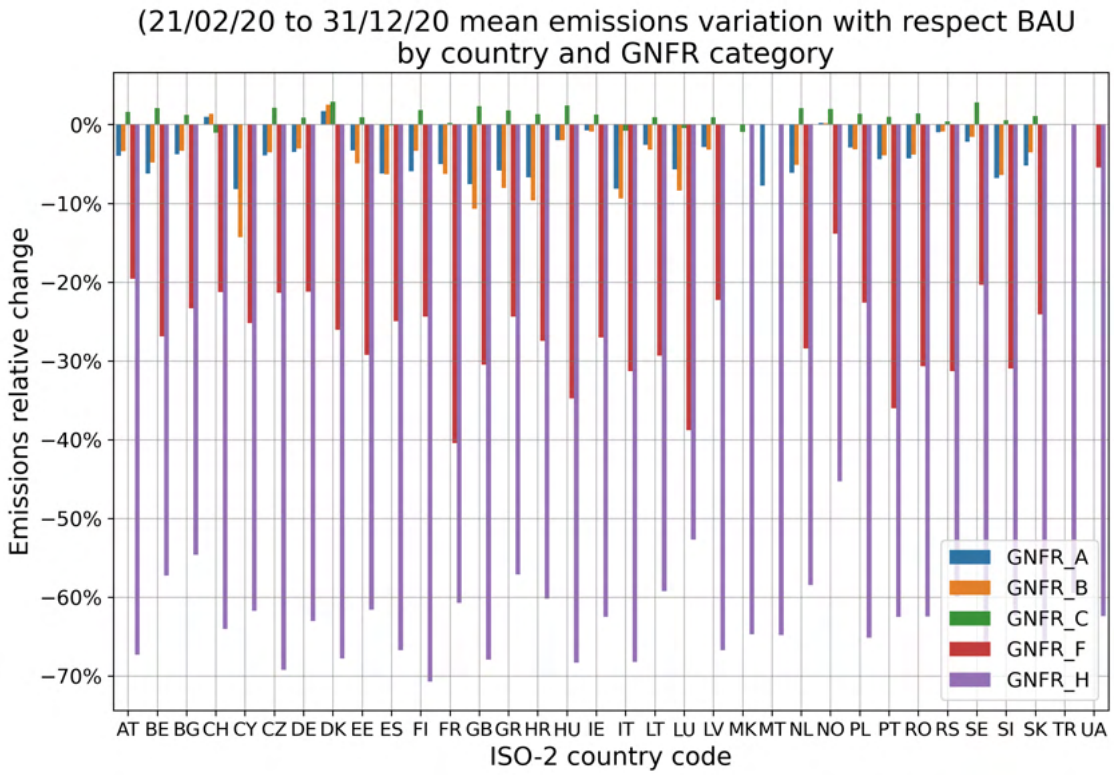

Figure 4.22: Mean emission reduction factors for the period February 21st, 2020 to December 31st, 2020 by sector category for all studied countries. Shipping (GNFR_G) is not included because there is a single value for all countries.

Table 4.2: Time- and spatially-averaged ERFs for each GNFR category.

Category	GNFR_A	GNFR_B	GNFR_C	GNFR_F	GNFR_G	GNFR_H
Variation with respect to BAU (%)	-4.07	-4.44	+1.14	-26.08	-15.81	-62.65

other European countries (Figure 4.1) implying a lower reduction of emissions.

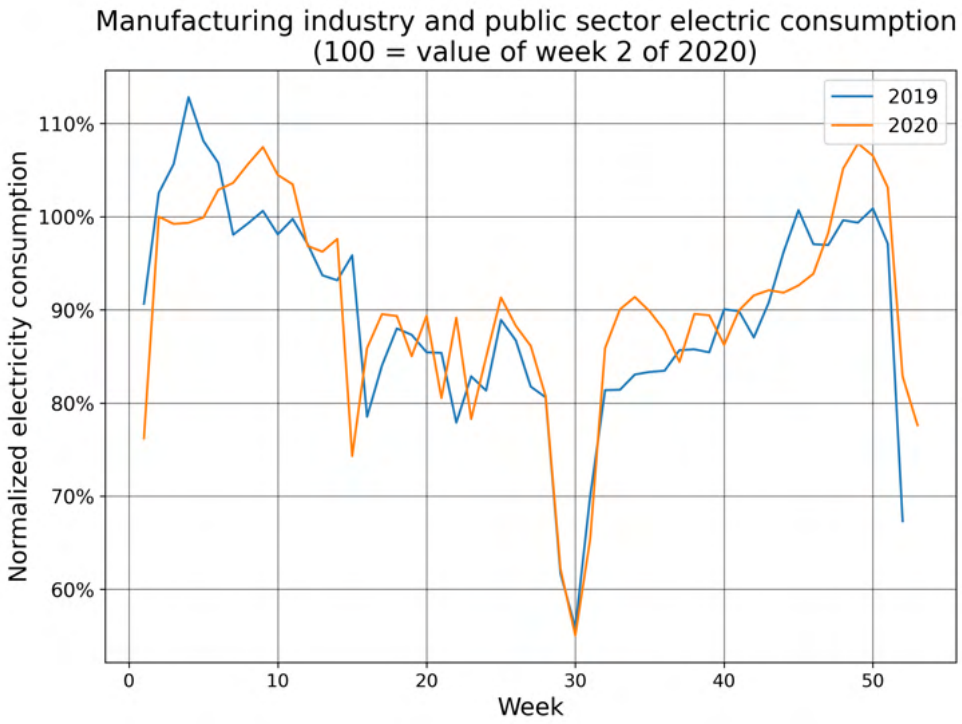

Figure 4.23: Electricity consumption for the manufacturing and energy industries in Denmark for 2019 (blue) and 2020 (orange). No significant reductions are observed, indicating a relatively normal activity in those sectors during the pandemic.

The GNFR_C activities have the lowest emission variations for most of the countries. Emissions in this category actually increased by 1%, on average, probably due to the increase from the residential sector more than compensating the emission reductions in the commercial/institutional sector as people spent more time in their homes in 2020 than on average.

4.4 Conclusions

This paper presents a dataset of day-, sector- and country-dependent emission reduction factors that allow the quantification of the impact of the COVID-19 lockdown on European primary emissions. The reduction factors are provided for a period that covers the whole

period with any restrictions during the year 2020, and for the six emission sectors that presumably contribute the most to emission reductions as a result of mobility restrictions, i.e. road transport, energy industry, manufacturing industry, aviation, shipping and other stationary combustion activities, in particular residential and commercial/institutional ones. ERFs in this work are based on a wide range of open-access information sources and near-real-time measured activity data, proxy indicators and other available information. It has been used a simple methodology that is easy to reproduce and does not require specific expertise nor substantial computational resources, but provides reasonable estimations of ERFs. The main findings and conclusions of this work are as follows:

- A simple methodology without the use of tools requiring specific expertise, such as machine learning, to weather-normalize the results is sufficient to estimate emission reduction factors with little deviations from more complex approaches. Moreover, we extend the estimates to the whole period of 2020 with any restrictions due to pandemic, which, to date of the elaboration of this work, had not been done before (Rodríguez-Sánchez et al., 2022)
- Emission reductions during the pandemic situation are clearly driven by national mobility restrictions
- The largest emission reductions during the period February 21st, 2020 to December 31st, 2020 were in the aviation sector, with an emission reduction of 62.7% on average, for the countries considered in this study
- Countries with the lightest restrictions were estimated to increase emissions in public and manufacturing industry sectors (i.e. Denmark and Switzerland)
- Open-access data availability is key to the scientific community being able to regularly estimate emission variations due to changes in anthropogenic activities (e.g. population increases in urban areas) and to elaborate pollution exposure mitigation strategies. Although great advances have been made recently, further effort is needed to extend open-access policies

Chapter 5

Evaluating air pollution mitigation measures in an urban hot-spot for different meteorological conditions[1]

5.1 Introduction

Despite the fact that emissions and concentration of air pollutants have fallen over the last few years, air pollution remains the largest environmental health risk in Europe (EEA, 2023) and so, air quality management is nowadays an important ongoing challenge. High pollution levels have been often observed in urban areas, where both emissions and population concentrate. Particularly, citizens living in large metropolitan areas are exposed to elevated concentrations of nitrogen dioxide (NO_2) mainly because of traffic emissions (EEA, 2021). Road transport is responsible of most nitrogen oxides (NO_X) emissions in Europe, and also accounts for an important part of the particulate matter (PM) emissions in that region (EEA, 2022; Thunis et al., 2023).

Meteorological conditions are one of the main factors that affect air quality, as they affect how pollutants are transported by or removed from the atmosphere. Precipitation can help dissipating heavier pollutants, whereas wind can disperse lighter ones (Kassomenos et al., 1998, 2014). Other parameters such as solar radiation and temperature can favour the removal or creation of pollutants by triggering chemical transformations of pollutants (Latini et al., 2002). Furthermore, in a city, interactions between the atmosphere and the urban obstacles (buildings, vegetation, etc.) induce complex flow patterns. Inside the urban

[1]The main contents of the chapter are included in the published research article: Rodríguez-Sánchez, A., Santiago, J.-L., Vivanco, M. G., Sanchez, B., Rivas, E., Martilli, A. and Martin, F.: How do meteorological conditions impact the effectiveness of various traffic measures on NO_X concentrations in a real hot-spot?, *Science of The Total Environment*, 954, 176667, DOI:10.1016/j.scitotenv.2024.176667, 2024.

canopy, the wind flow can be channelled and slowed down by urban obstacles depending on the wind speed and direction, which affects the distribution of air pollutants inside the streets (Dejoan et al., 2010; Parra et al., 2010; Santiago et al., 2013). This fact, joined to the irregular spatial distribution of anthropogenic emissions, produces high levels of pollution and strong gradients of pollutant concentrations in streets. Therefore, pollutant concentrations in the streets are affected by both the emissions and the meteorological conditions. Hence, accurate estimates of anthropogenic pollutant emissions to the atmosphere and high-resolution modelling of the wind flow properties (wind speed and direction) and of the dispersion of pollutants through the urban atmosphere is key to estimate the population's exposure to high air pollution levels (Santiago et al., 2021).

To improve the air quality, air pollution mitigation strategies are being developed and implemented around the world, especially in urban areas. Examples of these measures include the promotion of public transportation usage, ring road utilization, traffic flow improvements, speed limit reduction, and the low emission zones (LEZ). LEZs are areas where access for road vehicles is restricted, usually based on their emission classes. In Europe, there are more than 200 LEZs in operation (Holman et al., 2015). As in urban areas traffic is one important source of PM and the major source of NO_2 (Belis et al., 2013; Degraeuwe et al., 2017; Coelho et al., 2022), the implementation of LEZ could be an effective measure to reduce traffic related pollution and to improve urban air quality. Nonetheless, some studies question the efficiency of already existing LEZ in Europe because most of them do not apply to most vehicles (Holman et al., 2015) or their size is not big enough to dissuade people from using private transport (Moral-Carcedo, 2024).

However, despite their wide implementation, estimating the impact of mitigation measures remains a major challenge. Multiple studies have been carried out to assess the effects after a LEZ implementation using monitoring data and comparing the air quality before and after LEZ implementation (Boogaard et al., 2012; Ellison et al., 2013; Panteliadis et al., 2014). However, a simple comparison of concentrations neglects several factors other than LEZs that affect the concentrations of air pollutants such as the meteorology. This is considered by some studies (Ma et al., 2021; Gu et al., 2022), but an estimation of the effects of external factors as meteorology with high-spatial resolution at street level is still needed due to the heterogeneity of air pollutant concentrations in urban areas, which affects the spatial representativeness of air quality monitoring stations (Santiago et al., 2013; Martín et al., 2015).

The main goal of this work is to compare the impact of several air pollution mitigation strategies on a real hot-spot and explore their sensitivity to meteorological conditions. With that purpose, this chapter is addressed to achieve the following specific objectives:

- The estimation of high-resolution emissions, and their uncertainty due to the incertitude in vehicle's routes, for different traffic configurations.

- The estimation of the impact of several measures on NO_X emissions.

- The estimation of the impact of several traffic measures on air quality.

- The evaluation of the impact of meteorological conditions on air quality and on the effectiveness of air pollution mitigation strategies.

With that purpose, this Chapter first presents an estimation of the traffic patterns taking place in an urban area, their derived emissions and their correspondent uncertainty ranges using open data from the Madrid City Council (Madrid City-Council, 2025). Then, using the computed emissions, NO_X concentrations are estimated for various meteorological conditions and emissions cases, with special focus on a winter month, where air pollution quality problems are more likely to arise in Spain. Finally, annual values of NO_X and NO_2 are computed along the same domain area to assess the potential impact of meteorological conditions on regulated parameters (i.e., annual mean NO_2 concentrations) and on the spatial representativeness of an AQMS and on the fraction area of the domain study exceeding different thresholds.

5.2 Modelling domain

A hot-spot area where systematic exceedances of limit values of annual NO_2 have occurred has been selected for the study. This hot-spot, which has been exhaustively studied (Borge et al., 2016; Quaassdorff et al., 2016;Sanchez et al., 2017; Santiago et al., 2021), has recorded the highest NO_2 concentrations values in Madrid since 2010. Therefore, several traffic-related measures have been implemented in this area in order to reduce NO_2 levels.

Plaza Elíptica (PE) square is located in the southern part of Madrid, between the districts of Carabanchel and Usera (Figure 5.1). This is a heavily trafficked area, characterized by a complex interaction between emission sources and urban geometry. The area consists of a roundabout with five accesses and a motorway that crosses the square through a tunnel. Furthermore, the presence of several specific services (a private school, a public transport interchange hub, a park, a petrol station, a taxi stop, and five metro station exits) makes the Plaza Elíptica square also a pedestrian-busy area, including sensitive population such as schoolchildren.

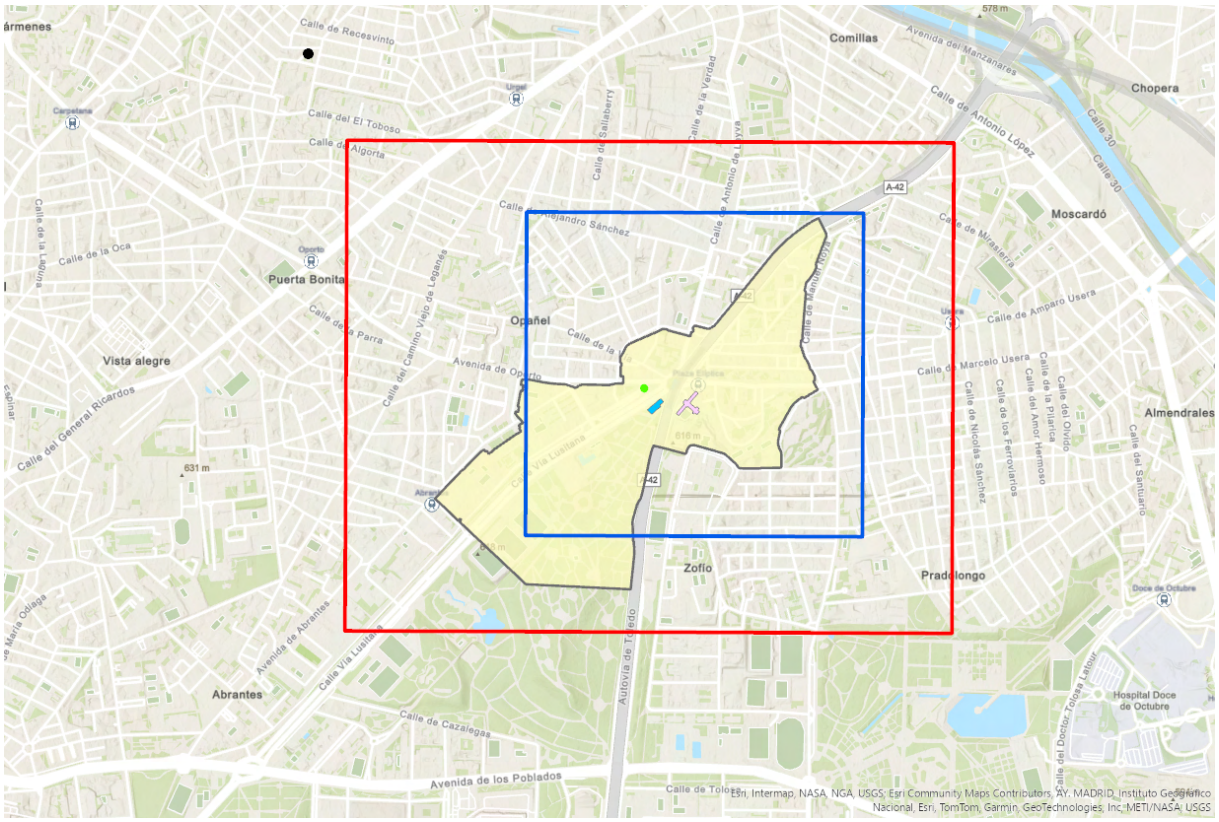

Figure 5.1: Location of Plaza Elíptica square, Madrid (Spain) and selected modelling domains. Red (blue) rectangle represents the traffic domain (CFD domain) limits. The green point represents the Plaza Elíptica AQMS; the pink building is the San Viator private-concerted school; and the blue building represents a public transport interchange hub. The black point represents the location of the Farolillo AQMS, used to obtain the background concentrations. Yellow area is the LEZ implemented since 2022.

In contrast to previous works, which were focused on a domain of 300 m x 300 m around the PE roundabout, the traffic domain covers an area of about 1.85 x 1.7 km^2 (the red in Figure 5.1 marks its limits), whereas the CFD model domain covers an area of about 1.3 x 1.3 km^2 (blue line in Figure 5.1). The larger domains compared to previous works allow for a more extensive analysis of the air pollutants concentrations patterns within the urban geometry.

In order to evaluate the results, hourly data from the PE AQMS, located west to PE square, is used. Also data from the AQMS in Farolillo, located 1.5 km NW to the square has been used to provide the background concentrations (Figure 5.1). Those concentrations are given from an AQMS instead of a mesoscale transport-chemistry model for more accurate results.

5.3 Traffic emissions estimation

The traffic emissions have been computed using the SUMO traffic simulator with an on-line coupling with the emissions model PHEMLight v5. At each timestep, SUMO provides

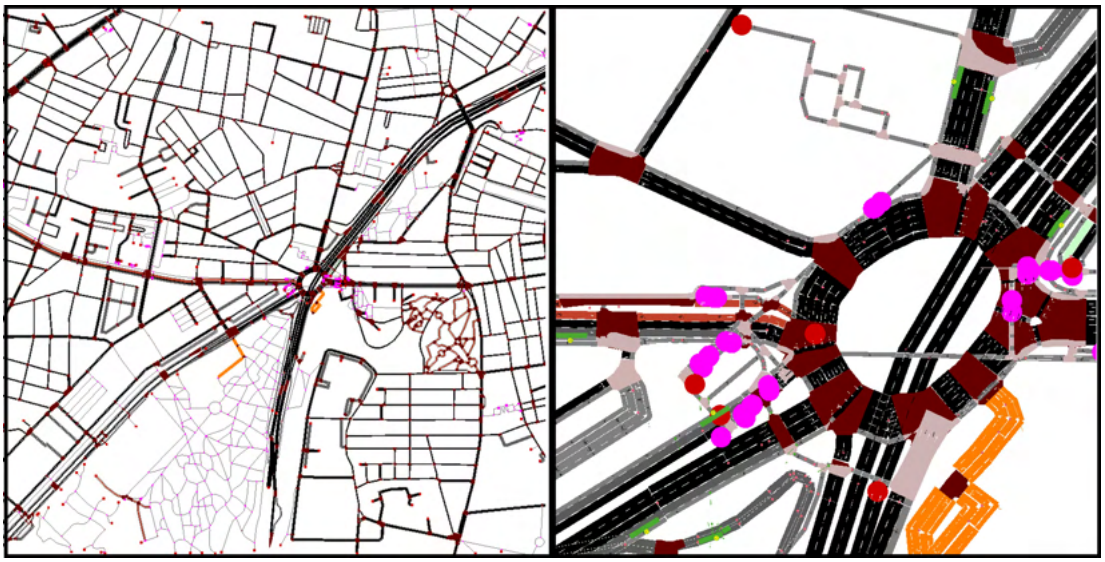

Figure 5.2: SUMO road network of the traffic domain (left) and detail of the Plaza Elíptica roundabout (right). Junctions are represented with brown patches, red and pink points; bus stops in green rectangles. Yellow area indicates the extension of the Plaza Elíptica LEZ, implemented in 2022. The green point indicates the location of the Plaza Elíptica AQMS.

PHEMLight the necessary variables to compute the engine power of each vehicle present in the simulation. With that information, PHEMLight returns the instantaneous emissions of every vehicle in the simulation.

5.3.1 Data sources

In order to perform the traffic simulations, information about the traffic flows and vehicle types in the area were obtained from the OpenData dataset available in the Madrid city council website (Madrid City-Council, 2025). The road network configuration was obtained from OpenStreetsMaps and converted to a SUMO readable format using a Python script. The public transport lines, bus stops and routes have been obtained from EMT Madrid information.

The traffic network configuration consists on 2644 edges, 1475 junctions and 96 bus stops (Figure 5.2). 66 traffic light systems regulate the main intersections of the network.

5.3.2 Scenarios

5.3.2.1 Weekly traffic simulation

The study area is one of the main communication points between Madrid and the southern metropolitan area. This makes it a heavily transited area throughout the day. It was found that for all years studied, and as explained in Quaassdorff (2018) and Quaassdorff et al. (2016), the traffic pattern around PE differs from the traditional two-humped urban

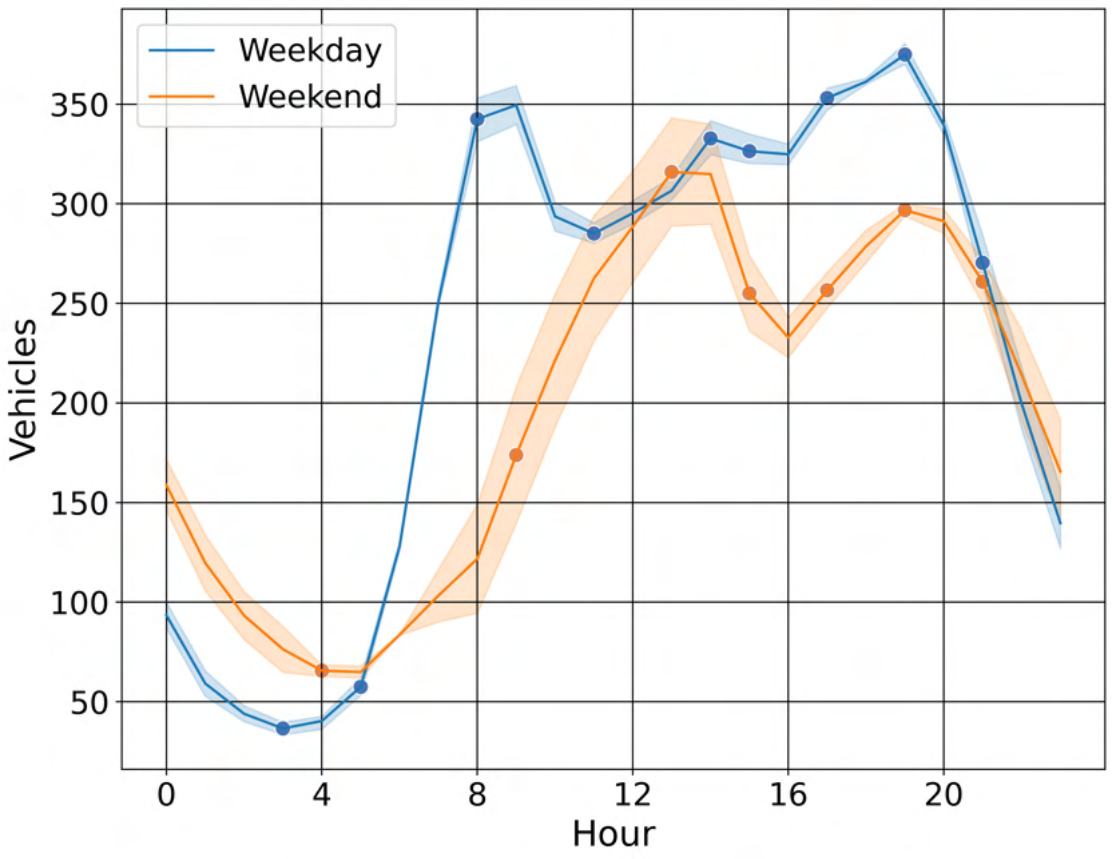

Figure 5.3: 2016 daily traffic profiles inside the modelling domain and selected traffic scenarios (dots).

commute pattern, as it presents a third relative maximum of traffic flow around 13:00 to 14:00 h (local time of Madrid) during working days, besides the typical two rush hours occurring in the morning (present in PE between 8:00 and 9:00 h) and in the evening (from 19:00 and 20:00 h). The findings of the previous works apply to the traffic flows corresponding to a regular working week of 2013, but in this work it has been found that those still apply to the traffic flows of more recent years. To accurately describe emissions under different vehicle flow conditions, typical weekly and daily patterns in the area were analysed using traffic profiles generated from the traffic detectors. Sixteen representative scenarios of 1-h length were defined to simulate the weekly traffic pattern (Figure 5.3).

5.3.2.2 Emission cases

Four different periods corresponding to four different traffic-related situations have been considered. A representative weekly traffic pattern for each of them has been simulated.

1. Year 2016: The traffic flows and the road network existent by this date are considered the base case. This emission case is labelled as Em16.

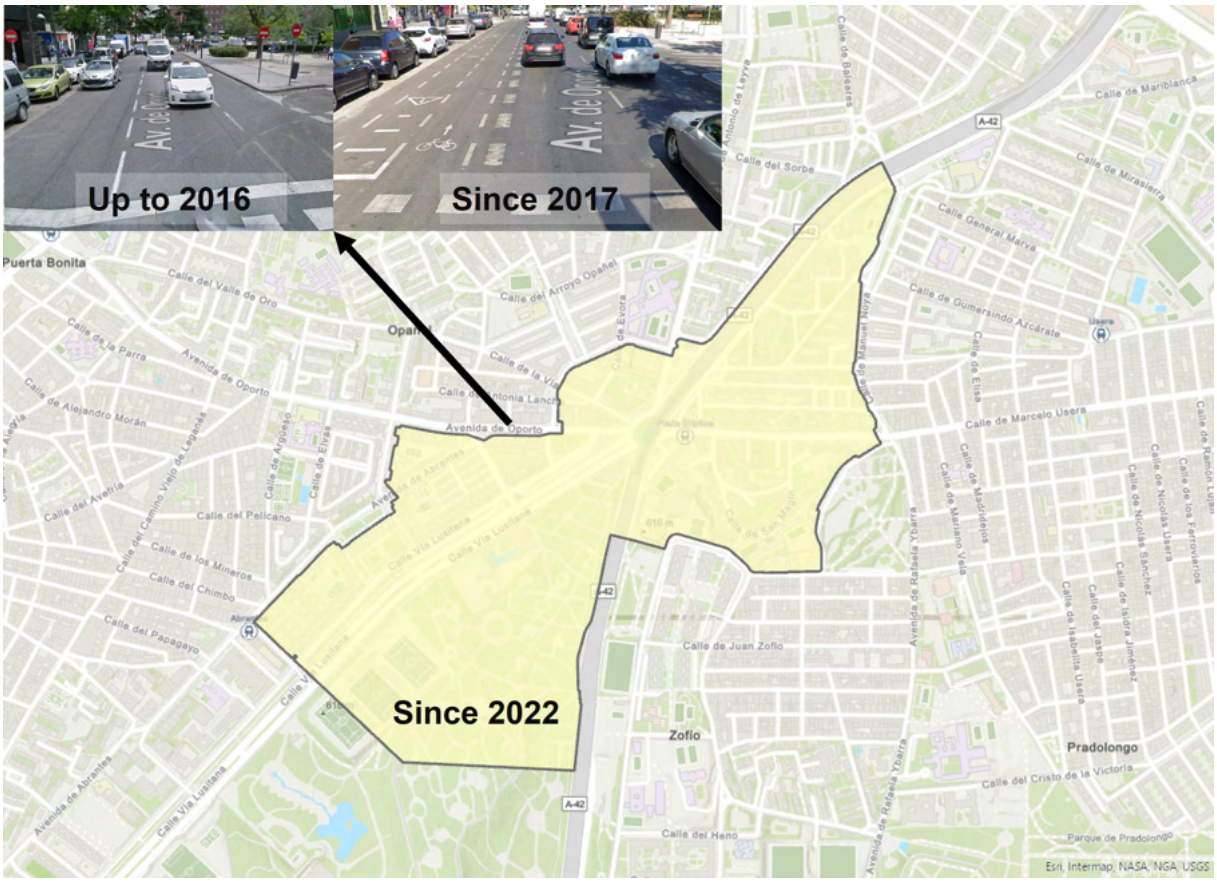

Figure 5.4: Changes in the PE road network between 2016 and 2023.

2. Year 2019: In this scenario, the number of lanes of one main street inside the area was reduced from 3 to one, and its direction reversed. In addition, a bikelane was added replacing the rightmost lane (Figure 5.4). This emission case is labelled as Em19. Moreover, a significant change in the vehicle fleet happened between the 2016 and 2019.

3. Year 2022: Since December 2021, a LEZ was implemented affecting the area surrounding Plaza Elíptica roundabout (Figure 5.1). At this time, the LEZ restricted access to gasoline vehicles previous to EURO2 emissions standard and diesel vehicles prior to EURO3 to vehicles registered outside the affected neighbourhoods. This emission case is labelled as Em22. In addition, in early 2022 some mobility restrictions were still prevailing due to the COVID-19 pandemic.

4. Year 2023: The network configuration remains the same as in 2022 but traffic flows recovered fully after the pandemic. This emission case is labelled as Em23.

For each year, sixteen 1-h length scenarios have been simulated to represent the weekly traffic pattern, as previously mentioned. In all cases, those scenarios correspond to sixteen hours of the weekly traffic flows during the month of February. Thus, the simulated weekly traffic

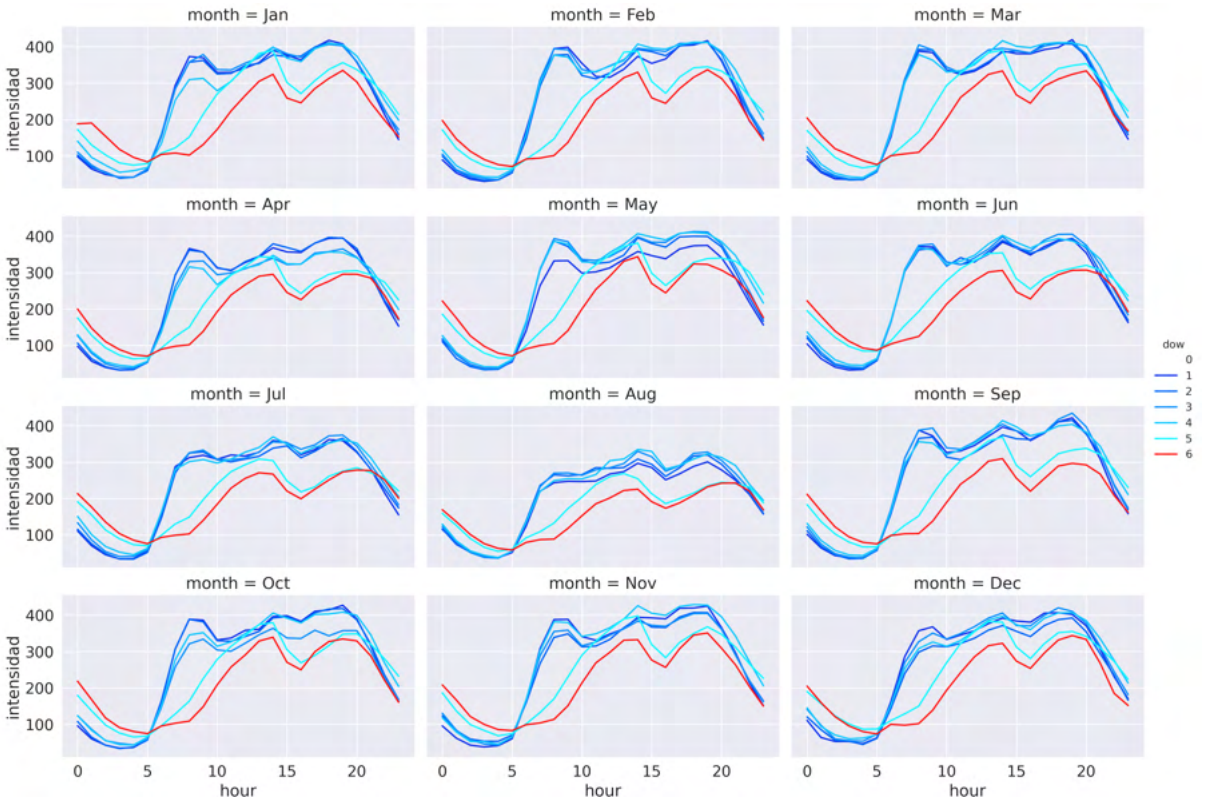

Figure 5.5: Mean observed traffic flows during each month of the year 2023 within the simulated domain.

pattern corresponds to the typical pattern observed in February in Plaza Elíptica, assuming that the traffic is constant throughout the year. Observations support this assumption -as shown in Figure 5.5, the daily cycles of traffic are fairly constant along the year- which allows to avoid simulating very long periods of time, which saves large amounts of computational resources, without compromising the reliability of the results.

5.3.3 Traffic simulation specifications

Figure 5.6 shows the location of every traffic count available within the traffic study domain for each simulated year. The number of traffic counts is not constant in time as they are installed or removed by the Madrid City Council due to several reasons. For the 2016 simulations, data from 77 traffic counts locations where available. This number increased to 93 in 2019 and to 119 in 2022. In 2023, the number of traffic counts in operation within the domain decreased to 113. To elaborate each emissions case, vehicle routes were constructed using as input data the traffic counts at the traffic detectors locations. 80% of the data was used to construct the routes, and the remaining 20% was reserved to evaluate the results of the traffic simulations. As no data from traffic lights were available, some test simulations were performed to adjust the traffic light cycles to avoid unrealistic traffic jams but matching the cycles as much as possible with those in reality. Real traffic cycles were obtained by in

situ observations.

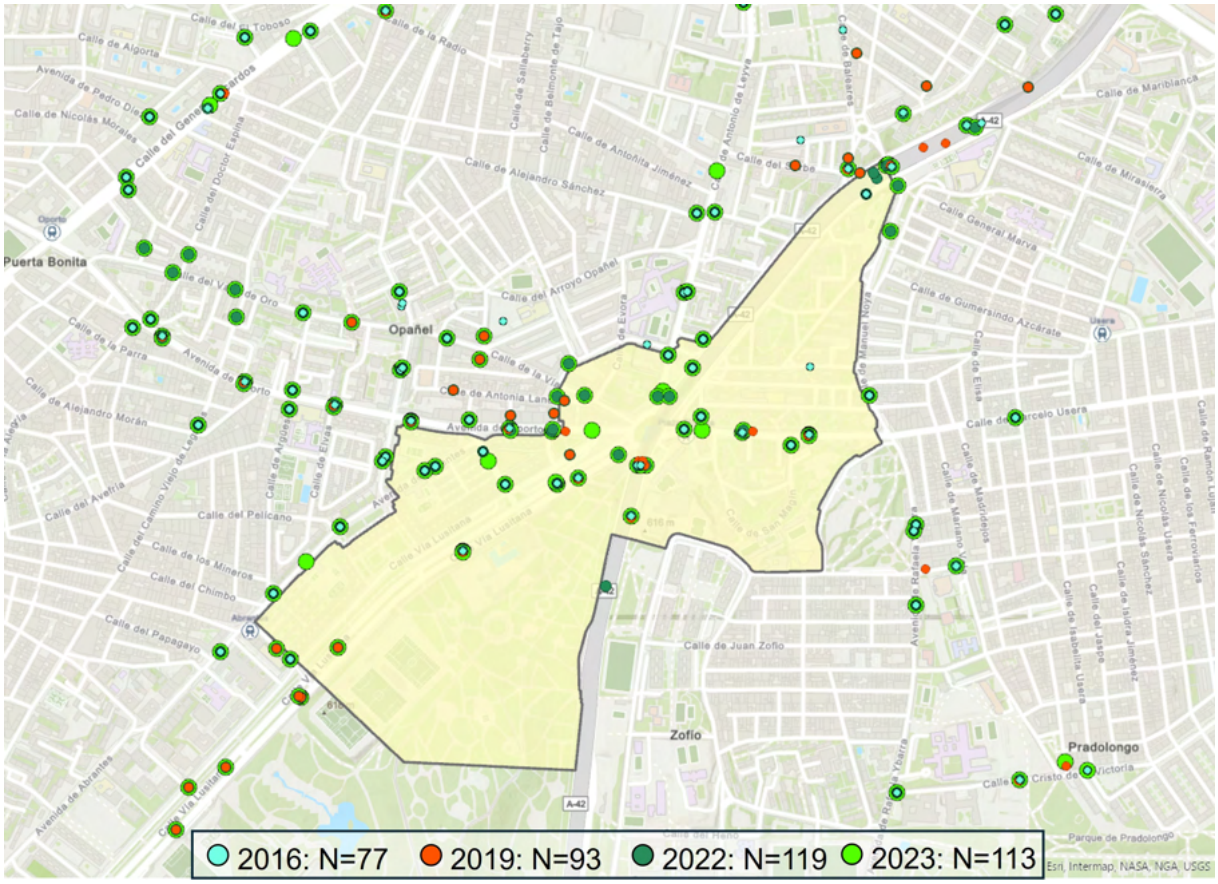

Figure 5.6: Location of traffic counts for each simulated year.

In addition, driving behaviour has been adjusted to match local urban traffic conditions in the area minimizing changes for the default data included in the model. The main changes are the reduction of the default safety distance for each vehicle type , the increase on driving imperfection, the reduction of the probability of a driver returning to the right lane after an overtaking manoeuvre inside the city and the increase in cooperation between drivers in a roundabout (Appendix A). The same values were applied to every simulated case.

To appropriately describe emissions under different vehicle flow conditions with a compromise with the amount of computational resources employed, sixteen 1-h length scenarios (Table 5.1) were simulated to represent the weekly traffic pattern, as it was done in Quaassdorff et al. (2016). From the sixteen scenarios, the weekly traffic pattern is constructed as illustrated in Table 5.2.

In all cases, simulations where performed using traffic count data from the month of February, as it is a normal, representative time period, with no bank holidays neither significant incidents. It was also assumed that traffic was approximately constant throughout the year, so the simulated scenarios and their associated emissions where applied to reconstruct the whole year patterns.

Table 5.1: Simulated scenarios.

Simulated traffic scenarios			
Weekday	**Hour**	**Scenario**	**Hourly emissions [kg]**
Monday to Friday	3:00-4:00	S1	2.39
	5:00-6:00	S2	4.74
	8:00-9:00	S3	44.3
	11:00-12:00	S4	38.8
	14:00-15:00	S5	44.0
	15:00-16:00	S6	43.7
	17:00-18:00	S7	45.9
	19:00-20:00	S8	46.9
	21:00-22:00	S9	36.5
Saturday and Sunday	4:00-5:00	S10	8.12
	9:00-10:00	S11	6.78
	13:00-14:00	S12	19.5
	15:00-16:00	S13	39.6
	17:00-18:00	S14	33.4
	19:00-20:00	S15	39.4
	21:00-22:00	S16	33.9

Table 5.2: Correspondence between hours of each weekday and simulated scenarios.

Weekday	**Hour**	**Scenario**	**Weekday**	**Hour**	**Scenario**
Monday to Friday	0:00-1:00	S1	Saturday and Sunday	0:00-1:00	S10
	1:00-2:00	S1		1:00-2:00	S10
	2:00-3:00	S1		2:00-3:00	S10
	3:00-4:00	S1		3:00-4:00	S10
	4:00-5:00	S2		4:00-5:00	S10
	5:00-6:00	S2		5:00-6:00	S10
	6:00-7:00	S2		6:00-7:00	S10
	7:00-8:00	S2		7:00-8:00	S10
	8:00-9:00	S3		8:00-9:00	S10
	9:00-10:00	S3		9:00-10:00	S11
	10:00-11:00	S3		10:00-11:00	S11
	11:00-12:00	S4		11:00-12:00	S11
	12:00-13:00	S4		12:00-13:00	S11
	13:00-14:00	S4		13:00-14:00	S12
	14:00-15:00	S5		14:00-15:00	S12
	15:00-16:00	S6		15:00-16:00	S13
	16:00-17:00	S6		16:00-17:00	S13
	17:00-18:00	S7		17:00-18:00	S14
	18:00-19:00	S7		18:00-19:00	S14
	19:00-20:00	S8		19:00-20:00	S15
	20:00-21:00	S8		20:00-21:00	S15
	21:00-22:00	S9		21:00-22:00	S16
	22:00-23:00	S9		22:00-23:00	S16
	23:00-24:00	S9		23:00-24:00	S16

Mean traffic volumes simulated across the modelling domain for each simulated year are shown in Figure 5.7. Working days present higher traffic intensities during daytime, and the characteristic three-peak traffic pattern is observed. The maximum traffic flow occurs in the evening peak hour in all scenarios. The minimum flux occurs during weekday nocturnal time between 3:00 and 4:00 h. During the weekends, intra-day traffic fluctuations are smaller, the morning rush-hour is delayed, and the third maximum in traffic flow disappears. When comparing the mean simulated traffic flows with the also spatially-averaged data from the traffic counts, some underestimation of traffic flows is observed in 2016, specially at weekends, and 2019, but their temporal correlation is good.

Before discussing the traffic simulation evaluation, a brief description of the anaylsed statistical parameters must be presented. The correlation coefficient (R) is a numerical measure reflecting the statistical relationship between two variables. It ranges from -1 to 1, being ± 1 the strongest correlation and 0 representing no correlation between the two variables. The Fractional Bias (FB) indicates the tendency of a model to overestimate ($FB > 0$) or underestimate ($FB < 0$) observed values. The Normalised Mean Squared Error ($NMSE$) is an estimation of the deviation between two sets of variables. Finally, the Fraction within a factor of two ($FAC2$) statistic is the fraction of the predicted values between 0.5 and 2 times the observed values. Equations 5.1 to 5.4 illustrate the mathematical representation of the R, FB, $NMSE$ and $FAC2$ statistics respectively.

$$R = \frac{\sum_{i=1}^{n} \left[\left(O_i - \overline{O} \right) \left(P_i - \overline{P} \right) \right]}{\left[\sum_{i=1}^{n} \left(O_i - \overline{O} \right)^2 \right]^{1/2} \left[\sum_{i=1}^{n} \left(P_i - \overline{P} \right)^2 \right]^{1/2}} \tag{5.1}$$

$$FB = \frac{\overline{P} - \overline{O}}{0.5 \left(\overline{P} + \overline{O} \right)} \tag{5.2}$$

$$NMSE = \frac{\sum_{i=1}^{n} \left(O_i - P_i \right)^2}{\sum_{i=1}^{n} \left(O_i P_i \right)} \tag{5.3}$$

$$FAC2 = fraction\ of\ data\ satisfying\ 0.5 \leq P_i / O_i \leq 2 \tag{5.4}$$

Chang and Hanna (2005) provides a guidance for acceptance criteria for a simulation. Following their criteria, a good simulation should have an $NMSE$ value lower than 1.5; a FB greater than -0.3 and lower than 0.3; the correlation coefficient R should be greater than 0.8 (in absolute value); and the $FAC2$ parameter should be greater than 0.5.

Table 5.3 summarizes some statistical parameters derived from the evaluation of the simulated traffic flows. The correlation coefficient R shows a very good correlation between the simulated and observed traffic flows for every year in the study. The $NMSE$ values

Table 5.3: Statistical parameters R, FB, NMSE and FAC2 for the modelled weekly traffic cycles.

Statistical parameters for the modelled weekly traffic cycles.				
	Em16	Em19	Em22	Em23
R	0.98	0.99	0.98	0.98
FB	-0.02	-0.08	0.02	0.04
NMSE	0.01	0.02	0.01	0.01
FAC2	1	1	1	1

show small errors for the simulated traffic flows. Regarding the FB, some systematic underestimations are found in the Em16 and Em19 cases, but with every value within the factor of two ($FAC2$).

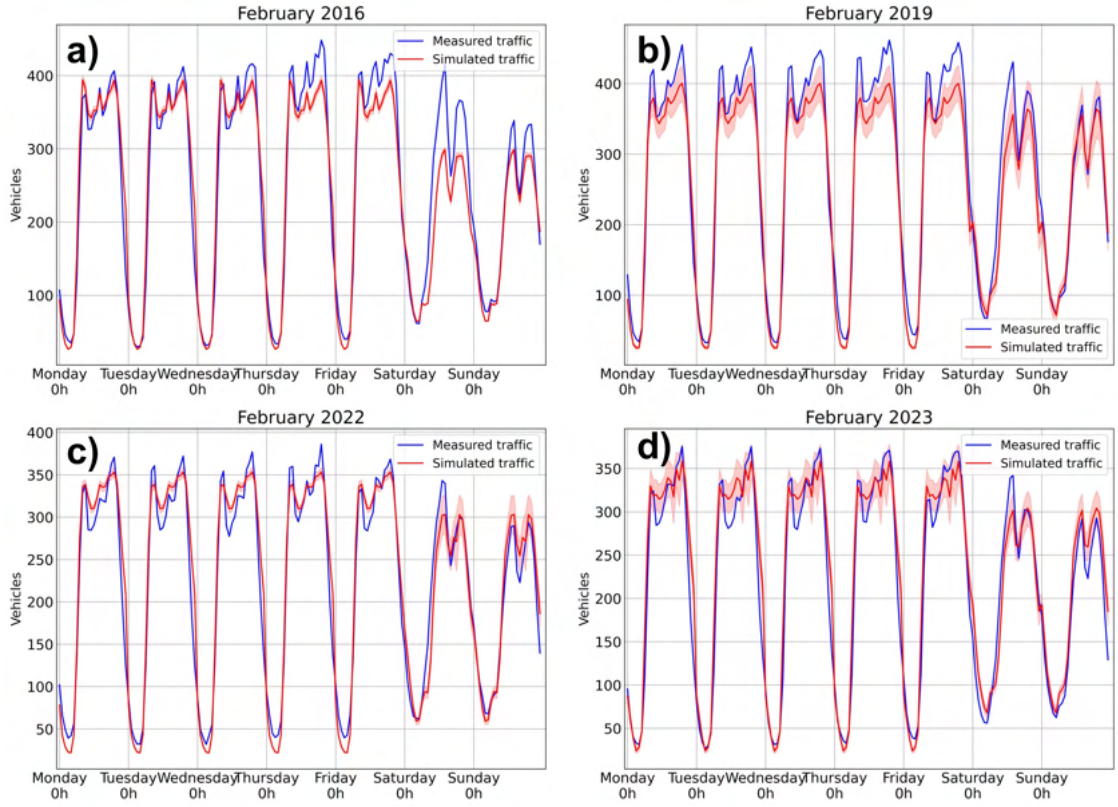

Figure 5.7: Modelled (red) and observed (blue) traffic profiles inside the modelling domain for each emissions case. a) Em16 case; b) Em19 case; c) Em22 case; and d) Em23 case.

For the emissions computation is fundamental to have precise knowledge about the vehicle fleet composition (Quaassdorff, 2018). Figure 5.8 shows the composition of the vehicle fleet within the simulation area (Madrid City-Council, 2025). The predominant vehicle type in Plaza Elíptica is passenger car, with approximately a 90% share of the total fleet. Motorbikes is the second most common vehicle type, although is has declined from a 10.5% share to an 8.5% in average between 2016 and 2023. Regarding the fuel type, there is a trend to replace diesel-powered vehicles with gasoline ones. In 2016, 61.9% of the total simulated vehicles were diesel, and 38.1% gasoline, whereas in 2023 the proportion was 56.2% diesel-powered

vehicles to 43.8% gasoline. In addition, there is a substantial decrease of Euro 1 and Euro 2 compliant vehicles in time. Euro 1 compliant vehicles represented the 15.3% of the total vehicle fleet in 2016, reducing it to a 9.4% in 2019 and to a 6.3% by 2023. For the Euro 2 compliant vehicles, the decrease in vehicle share has been from a 15.5% in 2016 to a 7.2% in 2023. On the other hand, a significant increase on Euro 5 compliant vehicles has been observed, from representing a 24.4% of the total fleet in 2016 to a 37.1% in 2023. The second largest increase correspond to the Euro 4 compliant vehicles (from 16.3% to 24.1%) followed by the Euro 6 compliant vehicles, which in the 2023 simulations represented a 13.4% of the total vehicle fleet, almost 4% more than in 2016.

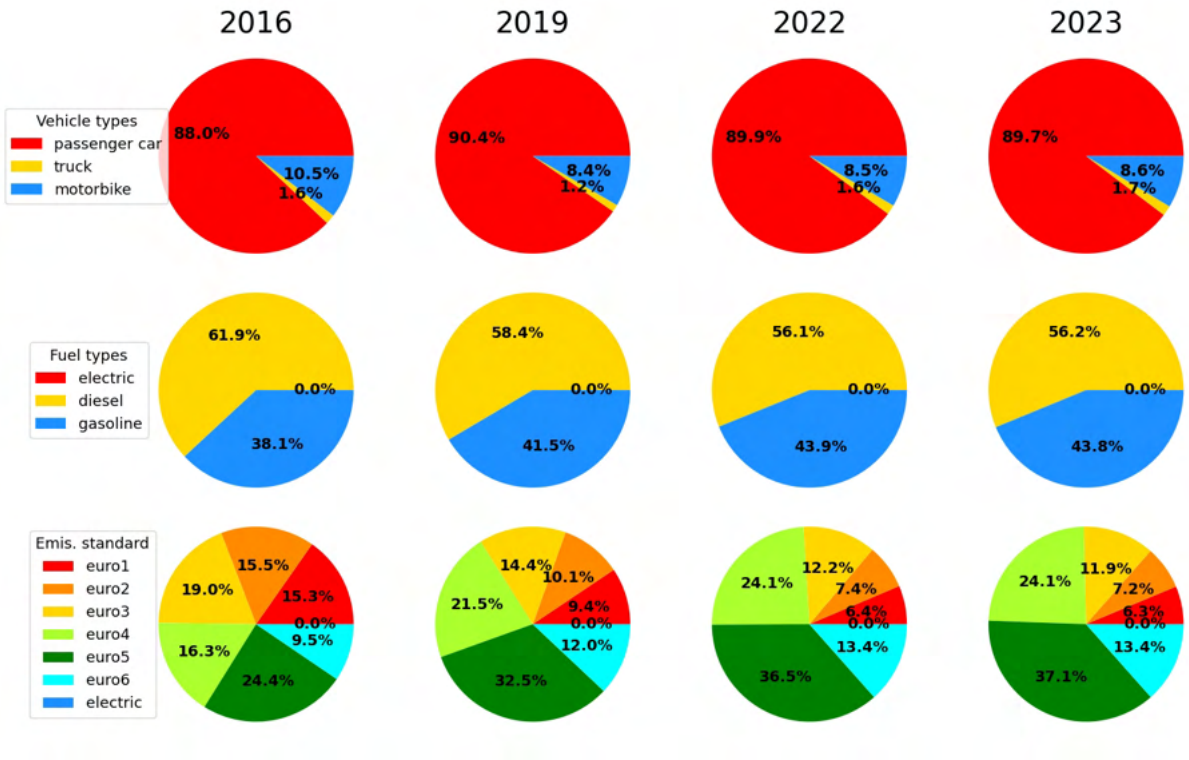

Figure 5.8: Modelled vehicle fleet composition for each traffic scenario classified by the vehicle type (top row), the fuel type (middle row) and the emission standard (bottom row). Data from Madrid City-Council (2025)

The spatial distribution of emissions for a saturated traffic scenario (S9) and a fluid traffic scenario (S1) is shown in Figure 5.9. The saturated traffic scenario has higher emissions than the fluid one. This is due to the smaller number of vehicles in scenario S1. The areas with the largest emissions in both scenarios are the PE square and the motorway. However, some relative maxima of NO_X emissions are found in several intersections along the domain. This highlights the importance of stop & go situations in traffic-related emissions (Smit et al., 2008; Abou-Senna et al., 2013). These results are similar to those obtained in Quaassdorff (2018), for the common areas of the domain between both works. The main difference is that, whereas in this work in both fluid and saturated scenarios exists two maxima of emissions

in the northern and southern sides of the PE roundabout -coinciding with the presence of traffic lights-, in Quaassdorff (2018) for the saturated scenario the maxima is located in the eastern part of the roundabout.

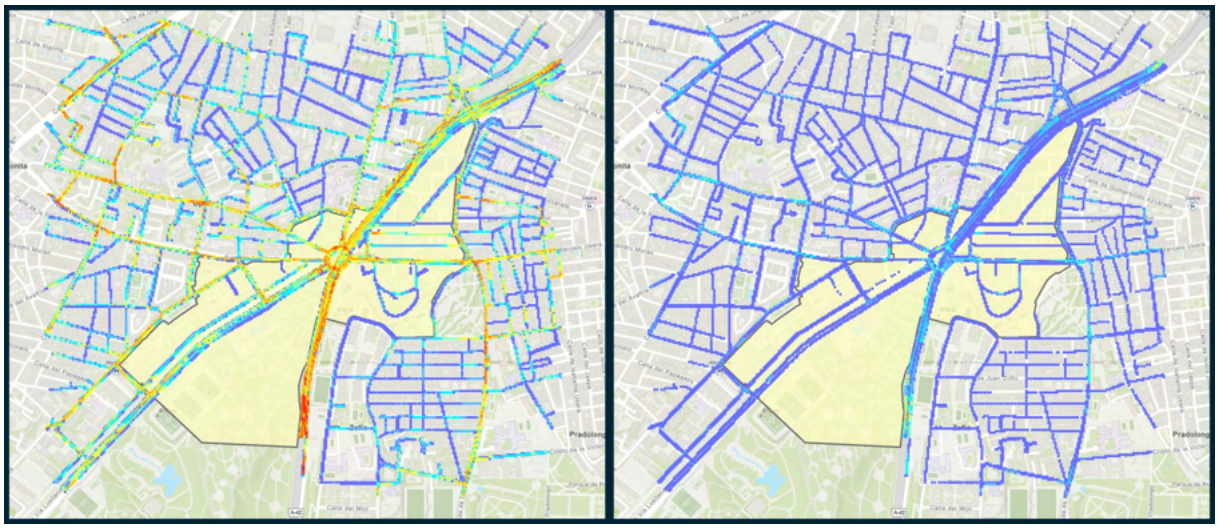

Figure 5.9: NO_X emitted along the modelling domain for saturated traffic scenario (S9, left) and a fluid traffic scenario (S1, right).

Figure 5.10 shows the total emissions modelled inside the traffic domain for each simulated scenario and year. It is observed that the Em16 emissions scenario has the largest emissions on all scenarios. It is followed by the Em19 scenario. Between the Em22 and Em23, small differences arise with the Em23 scenario showing slightly larger emissions for the weekend scenarios (S10 to S16, Table 5.1).

These differences in hourly scenarios translate to a decrease in total annual emissions between Em16 and Em22 scenarios (Figure 5.11), with Em19 almost halving the emissions of Em16 scenario and Em22 more than halving the initial value of Em16. Emissions in the Em22 case where a 18% lower than those of the Em19 case. This reduction is smaller than the annual reduction in emissions observed by Rodríguez-Sánchez et al. (2022) for the road transport sector in Spain in 2020 due to the COVID-19 lockdown, which was in average a 25% in Spain. On the other hand, a slight increase in emissions is modelled between Em22 and Em23, as traffic volumes increased. The uncertainty in emissions also decreases in time, partially due to the increase in available data from traffic counts, which reduces the uncertainty on the number of vehicles circulating by streets without observations. In 2016, the uncertainty in emissions was near a 50% of the total emissions, with this value decreasing to a 25% in 2022 and 2023.

Figure 5.12 shows the total annual emissions for all the simulated emission cases. A significant decrease in emissions is modelled from the emissions case Em16 to Em19. From Em19 to Em22, some decreases in annual emissions are observed inside the LEZ-affected area. On the other hand, increases are observed outside that area. No significant changes in the

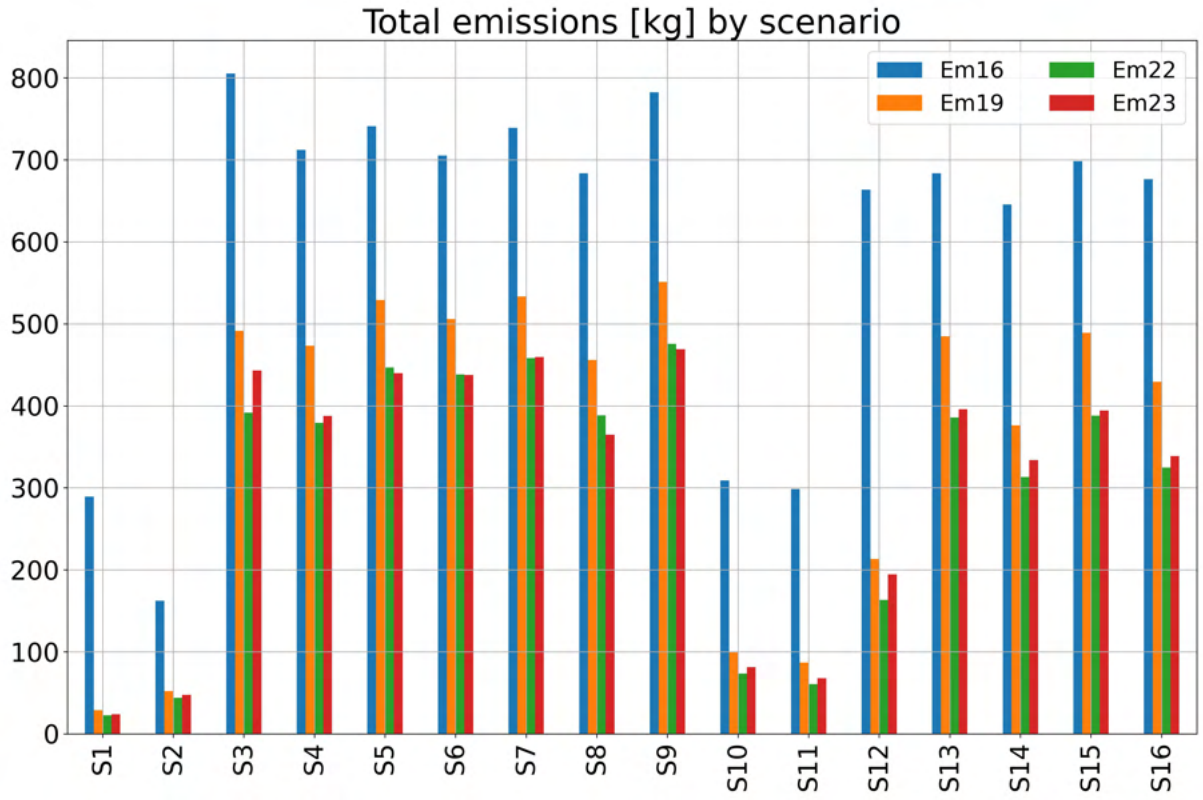

Figure 5.10: Spatially aggregated emissions inside the study domain for each simulated scenario and year in kg.

spatial distributions of emitted NO_X are observed between Em22 and Em23 emissions cases. The computed emissions are then transformed to the CFD model cells and to volumetric fluxes in order to compute the NO_X concentrations resulting from those emissions. After the conversion, the differences between the original computed emissions and the emissions interpolated to the CFD mesh were lower than 0.5% in every scenario.

5.4 Impacts of meteorological conditions on NO_X and NO_2 concentrations

5.4.1 High-resolution estimation of NO_X and NO_2 concentrations.

In order to assess the temporal and spatial evolution of NO_X concentrations (hereafter as $[NO_X]$) and NO_2 concentrations (hereafter as $[NO_2]$) along the domain and for several meteorological conditions, NO_X emissions from traffic simulations and hourly data from an AQMS were used.

Numerical simulations are based on a steady state RANS approach with the Realizable $k-\varepsilon$ model. The traffic-related pollutants are included in the simulation through passive scalars, for which transport equations have been included (i.e., no chemical reactions of the pollutants

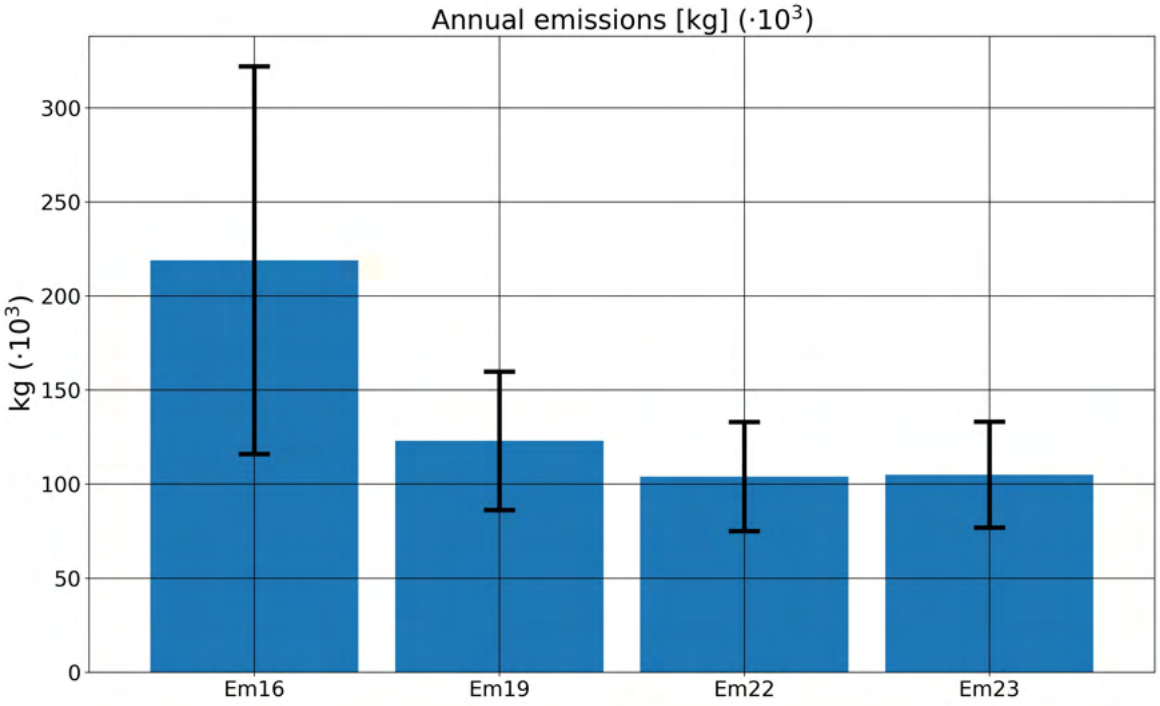

Figure 5.11: Spatial and temporal aggregated emissions inside the study domain for each simulated year in kg.

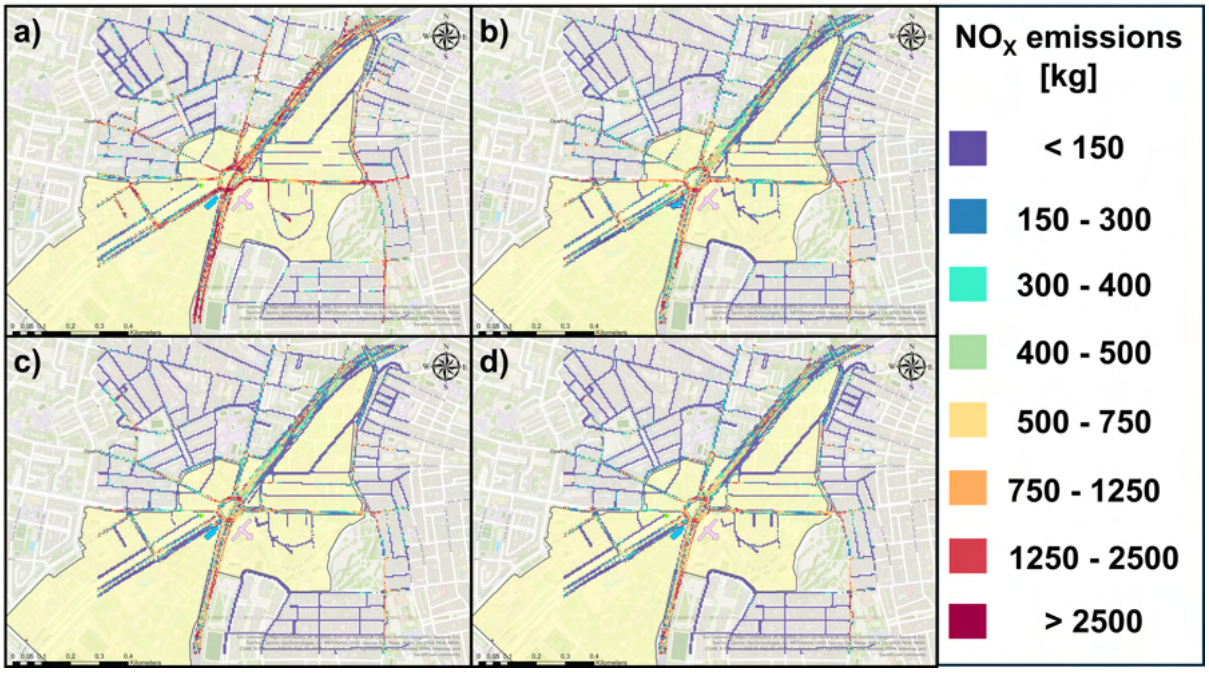

Figure 5.12: Total annual NO_X emissions, restricted to the CFD domain, for each simulated emissions case: a) Em16; b) Em19; c) Em22; and d) Em23. Yellow area represents the LEZ-affected area; the pink building represents the San Viator school; and the blue building, the public transport interexchange hub. Green point indicates the location of the PE AQMS.

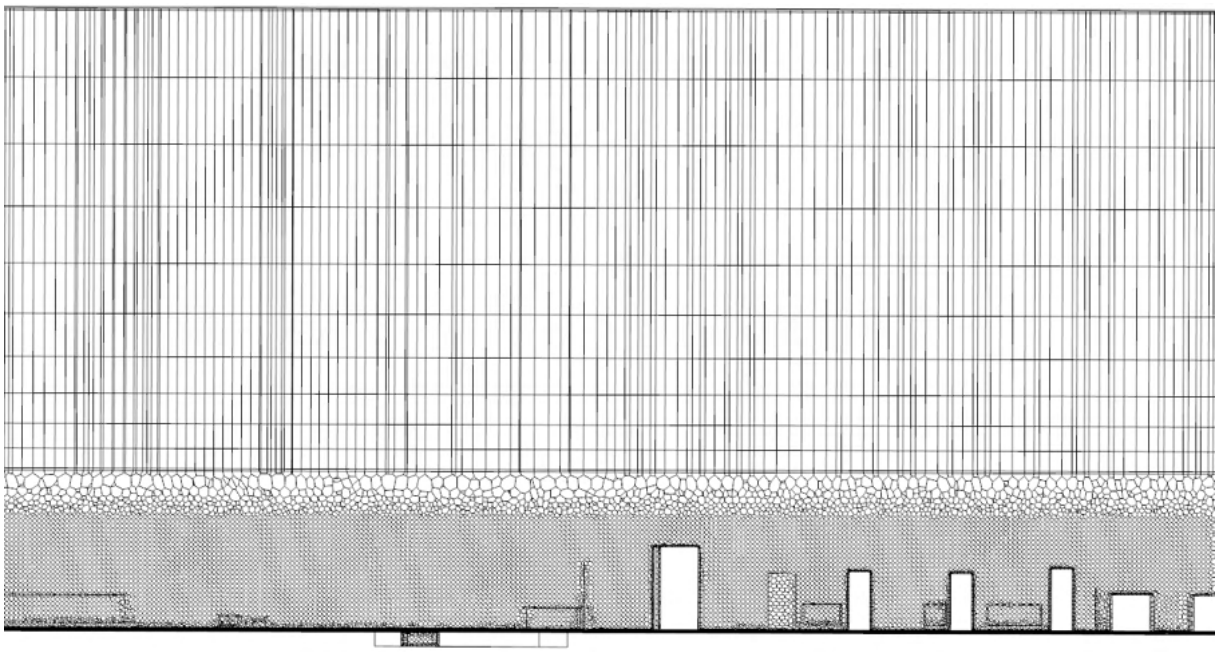

Figure 5.13: Cross section of the computational grid. The rectangle area below the ground level corresponds to the tunnel traversing PE square.

are assumed). The diffusivity is proportional to the turbulent viscosity, computed by the Realizable $k-\varepsilon$ model, and inversely proportional to the turbulent Schmidt number. This approach has been employed in other studies, such as (Santiago et al., 2013, 2017a,b; Rivas et al., 2019).

For this purpose, the methodology explained in 3.3.2 is used to compute the local traffic-related NO_X concentrations. This methodology has been proved to provide good results without the high computational resources that a long period of unsteady simulations would require, which at the time being are unreachable.
The computational grid is a combination of polyhedral cells between $z_H = [0, 1.5Z_{max}]$ (Figure 5.13) and tetrahedral cells (between $z_H = [1.5Z_{max}, 7Z_{max}]$). The base cell size is 5 m, but finer resolutions are set in different areas: Inside a 400 m x 400 m area the cell size is 2 m, but even in this area cells smaller than 1 m are defined near the ground, buildings and vegetation in order to improve the representation of exchanges occurring between those urban surfaces and the air (Figure 5.14). The vertical and horizontal dimensions of the numerical domain have been set following the recommendations given by Franke (2007) and Di Sabatino et al. (2011). A grid independence test was performed in Sanchez et al. (2016). Boundary conditions at buildings and ground surfaces are modelled by means of standard wall functions. Ground is considered a roughness wall with $z_0 = 0.05$ m. 16 different wind directions are simulated. Inlet profiles for wind speed are logarithmic and follows Equation 5.5. Vertical profiles for turbulent kinetic energy (k) and turbulence dissipation rate (ε) are computed by Equations 5.6 and 5.7 (Richards and Hoxey, 1993).

Figure 5.14: Air view of the computational grid. Green cells indicate cells within a vegetation area; pink cells correspond to buildings; and black cells are cells within the air.

$$u(z) = \frac{u_*}{\kappa} ln\left(\frac{z + z_0}{z_0}\right) \tag{5.5}$$

$$k = \frac{u_*^2}{\sqrt{C_\mu}} \tag{5.6}$$

$$\varepsilon = \frac{u_*^3}{\kappa(z + z_0)} \tag{5.7}$$

where u_* is the friction velocity, z_0 is the roughness length, $C_\mu = 0.09$ is a model constant and κ is the von Karman's constant ($\kappa = 0.4$).

These vertical profiles correspond to neutral atmospheric conditions and are usually employed in CFD simulations (Rivas et al., 2019). In these conditions, simulated pollutant concentrations are inversely proportional to wind speed, which allows to employ the WA CFD-RANS methodology explained in Section 3.3.2.

Once the traffic-related concentrations are computed, it is essential -when aiming to compute the total NO_X concentrations- to add to the result the background concentrations since the CFD results only represent the local traffic contribution. They are considered by adding a term to Equation 3.33:

$$C_{comp}(t) = \frac{u_{*,CFD}(t)}{u_{*,WRF}(t)} \cdot C_{sim}(t) + C_{back}(t) \tag{5.8}$$

where $C_{back}(t)$ are the background concentrations at time t. And equally, when considering the background concentrations Equation 3.37 becomes

$$C_{comp}(t) = \frac{u_{*,CFD}(t)}{0.07} \cdot \overline{C_{sim}^{16WD}}(t) + C_{back}(t) \tag{5.9}$$

In this work, the background concentrations are obtained from an urban background AQMS located 1.5 km NW the study domain, which allows for a precise estimation of the hourly values of background concentrations.

The hourly values of NO_2 have been computed from those of the NO_X using the methodology described in Section 3.3.3. To that end, historical data (2010-2024) from the PE AQMS has been adjusted to the Romberg equation (Equation 3.38) in order to obtain the regression parameters. The obtained parameters are presented in Table 5.4.

Table 5.4: Values of the regression parameters of Eq.3.38.

Optimised regression parameters of Eq. 3.38		
A	B	C
81.8200	131.6479	0.2170

5.4.1.1 Meteorological conditions analysis

Some meteorological variables that influence air pollutant concentrations are wind speed, wind direction and precipitation (Kassomenos et al., 1998; Latini et al., 2002; Kassomenos et al., 2014). Therefore, a good estimation of these variables is important to properly estimate their effect on air quality.

The meteorological parameters used in the methodology have been derived from mesoscale simulations performed with the meteorological mesoscale model WRF (Chen et al., 2011). This model has been run for four different years (2016, 2019, 2022 and 2023). For each one, the simulation starts at 0000 UTC of the December 21st of the previous year and ends at midnight of the January 1st of the following year. The domain configuration consists of four nested domains, with horizontal resolutions of 27, 9, 3 and 1 km, with the finest domain encompassing a region with dimensions of 112 km (E-W) and 124 km (N-S), that includes the whole urban area of Madrid and surrounding satellite cities. The first domain was fed with input boundary data from ERA5 (Hersbach et al., 2020). The vertical resolution is 5 m in the lowest 50 m of the atmosphere. Above, the grid spacing gradually increases up to the top of the domain, located at 20 km. The higher resolution in the lowest 50 m is chosen to resolve the strong vertical gradients of mean variables and turbulent fluxes that are present in the Urban Roughness Sublayer and to take maximum advantage of the multilayer urban scheme used to represent the urban areas (BEP-BEM, Martilli et al., 2002; Salamanca et al., 2010). This scheme solves a separate energy budget for roof, walls and street, and computes the generation of heat in the buildings due to equipment, occupants and cooling/heating systems, and its exchange with the exterior. Detailed configurations can be found in Sanchez et al. (2017).

When comparing the modelled wind speed with observations, although the instrumentation appears to have a lower limit at 0.5 $m \cdot s^{-1}$ for most of the simulated periods -which is suddenly dropped to zero between January and February of 2022 (Figure 5.16), the model is able to represent the daily variations in wind, as well as the episodes of high wind speeds when observations are available (Figures 5.15 to 5.17), as also the statistical parameters in Table 5.5 show. Despite the fact that the apparent lower limit of the observations can affect the statistical parameters, the correlation coefficient R is above 0.50 in all cases, and fractional biases, $NMSE$ and $FAC2$ values comply the acceptance value for a "good" simulation given by Chang and Hanna (2005). No observed data was available for 2016.

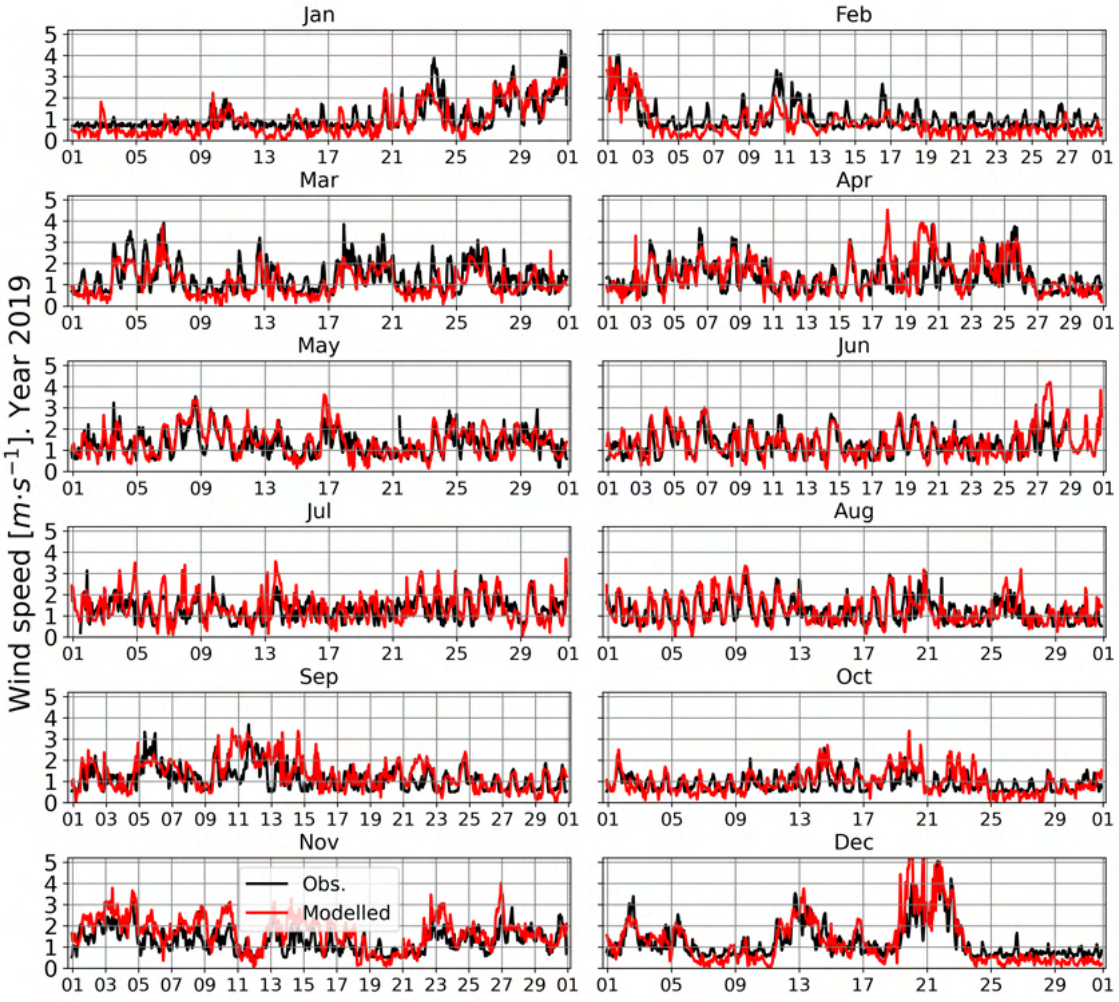

Figure 5.15: Modelled (red) and observed (black) wind speed at PE AQMS location during the 2019.

Table 5.5: Statistical parameters R, FB, NMSE and FAC2 for the modelled wind speed.

Statistical parameters for the modelled wind speed.				
	2016_Em16	2019_Em19	2022_Em22	2023_Em23
R	NA	0.64	0.50	0.53
FB	NA	0.02	0.17	0.13
NMSE	NA	0.24	0.33	0.34
FAC2	NA	0.80	0.76	0.76

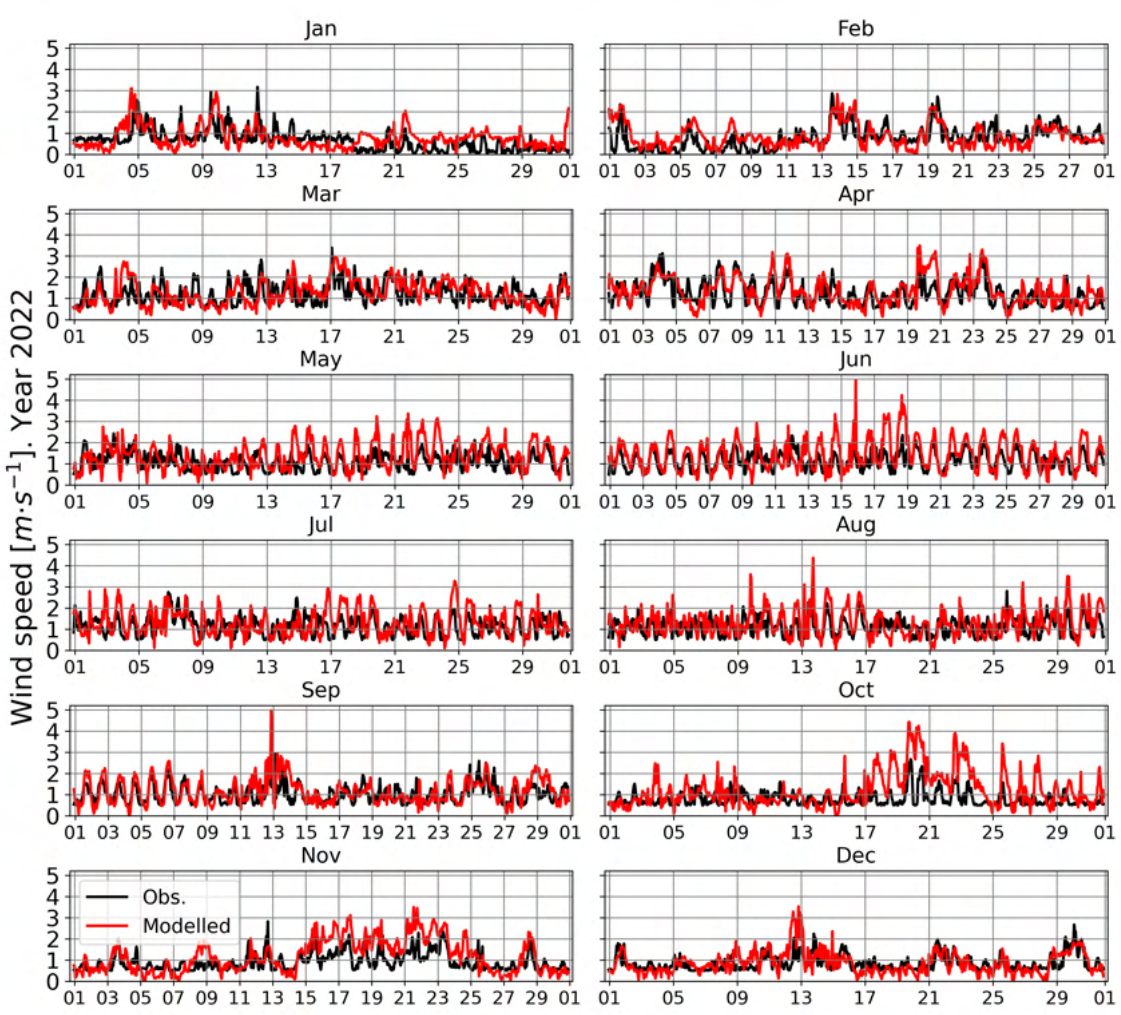

Figure 5.16: Modelled (red) and observed (black) wind speed at PE AQMS location during the 2022.

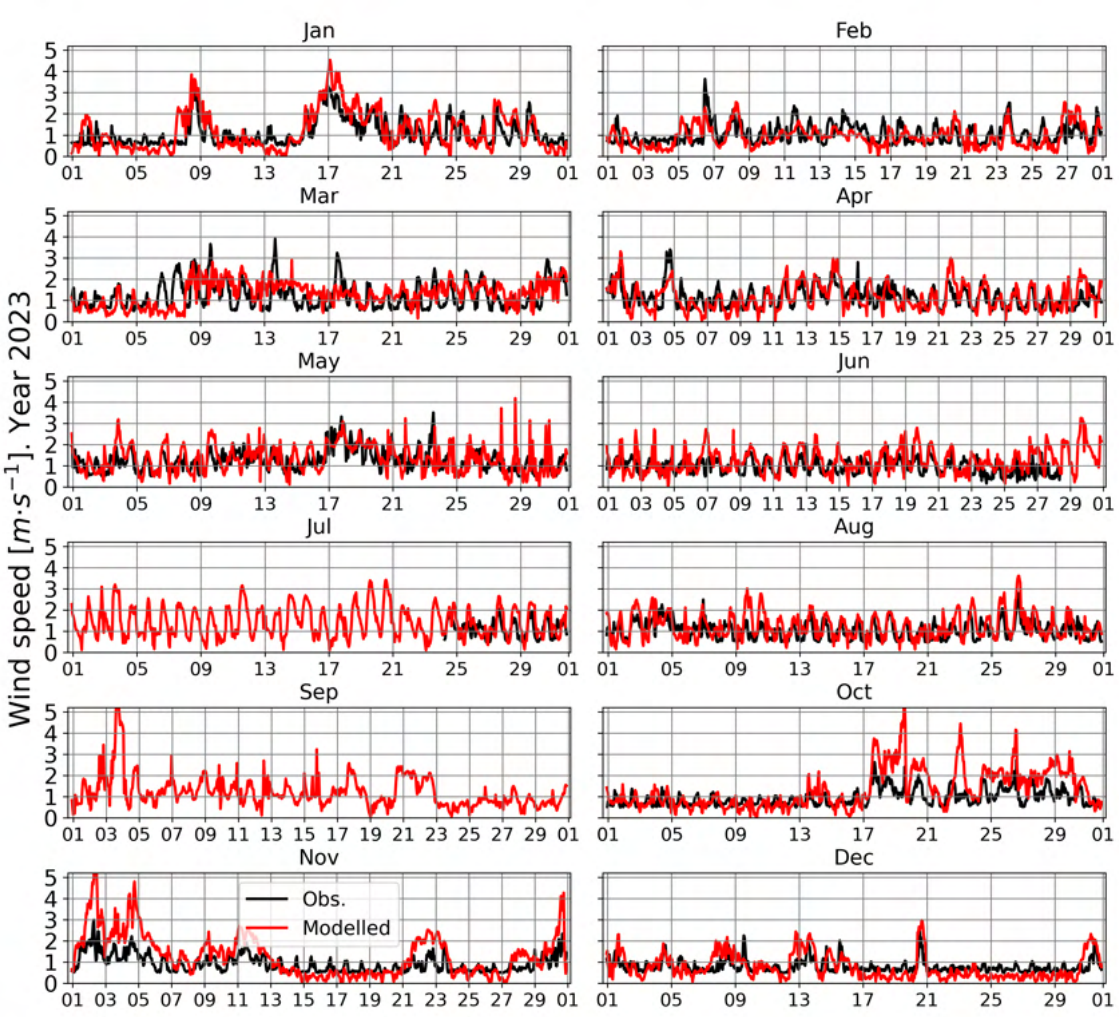

Figure 5.17: Modelled (red) and observed (black) wind speed at PE AQMS location during the 2023.

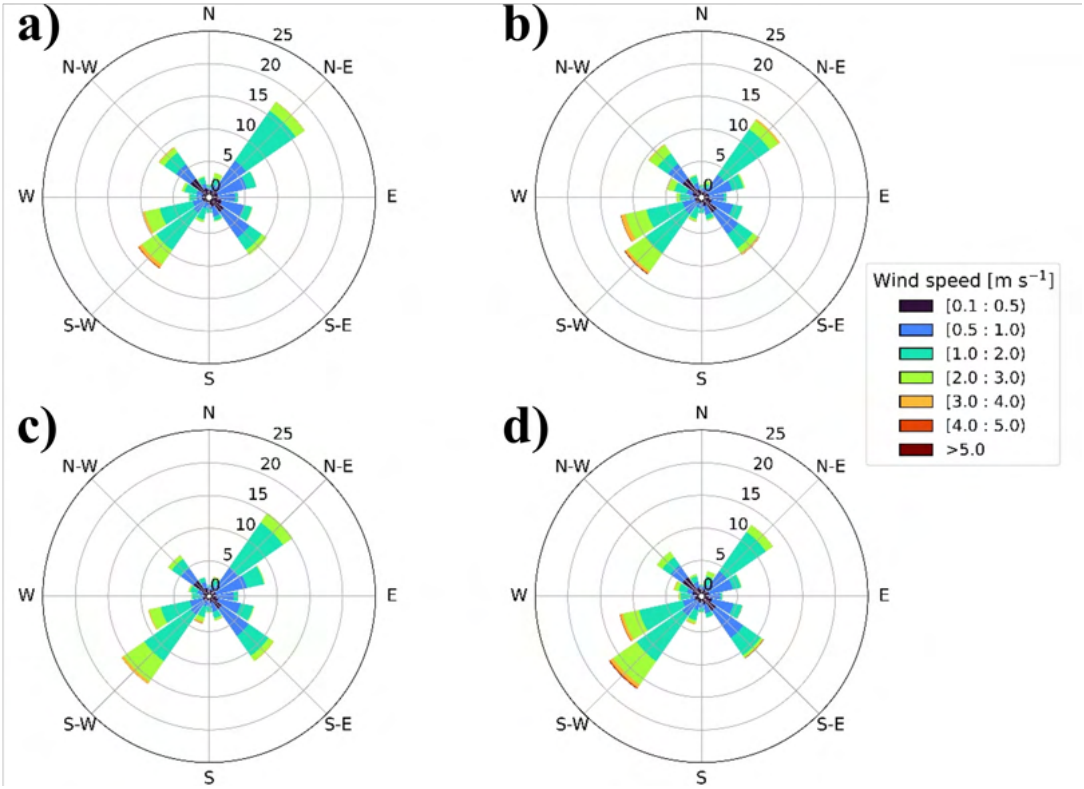

Figure 5.18: Modelled annual windroses for each simulated year: a) 2016; b) 2019; c) 2022; and d) 2023.

The modelled annual windroses show little differences between them (Figure 5.18). In all cases, the typical bidirectional thermally-driven wind flow pattern of the city of Madrid is properly modelled (Román-Cascón et al., 2023). Figures 5.19 to 5.22 show the hourly wind speed and rainfall values for the years 2016, 2019, 2022 and 2023 respectively. Despite the similarity of annual values, it can be observed that at finer time resolutions the meteorological conditions of the four years differ significantly. When analysing the monthly-averaged values of wind speed, some significant differences between each simulated year arise (Figure 5.23). For example, in February and December the mean wind speed varies up to a factor 2 between different years. Nonetheless, the differences tend to compensate each other along the year after a maximum spread in February, only increasing slightly in December. At the end of the year, 2019 has the largest annual mean wind speed value and 2016 the lowest. Between those scenarios the annual mean wind speed difference is smaller than 0.1 $m \cdot s^{-1}$.

The similarities between the annual values of meteorological parameters will mean that a limited impact of them on annually-averaged air pollutant concentrations is expected to be modelled.

With all of the above in mind, two additional subsets of meteorological conditions were created to increase the range of meteorological conditions and further analyse their impact

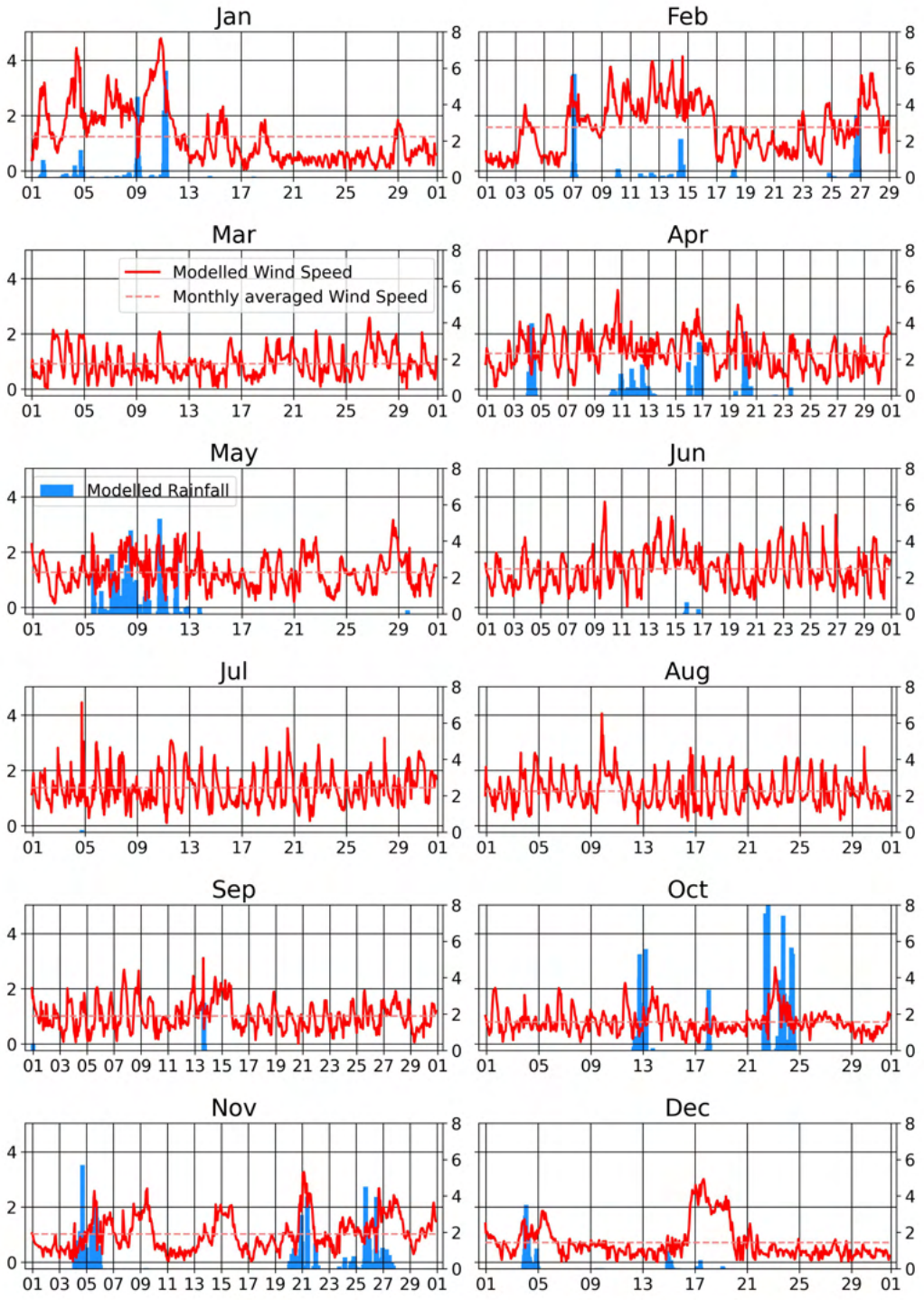

Figure 5.19: Hourly modelled values of wind speed (red lines) and rainfall (blue bars) for the year 2016 at Plaza Elíptica. Dashed red line indicates the monthly averaged wind speed.

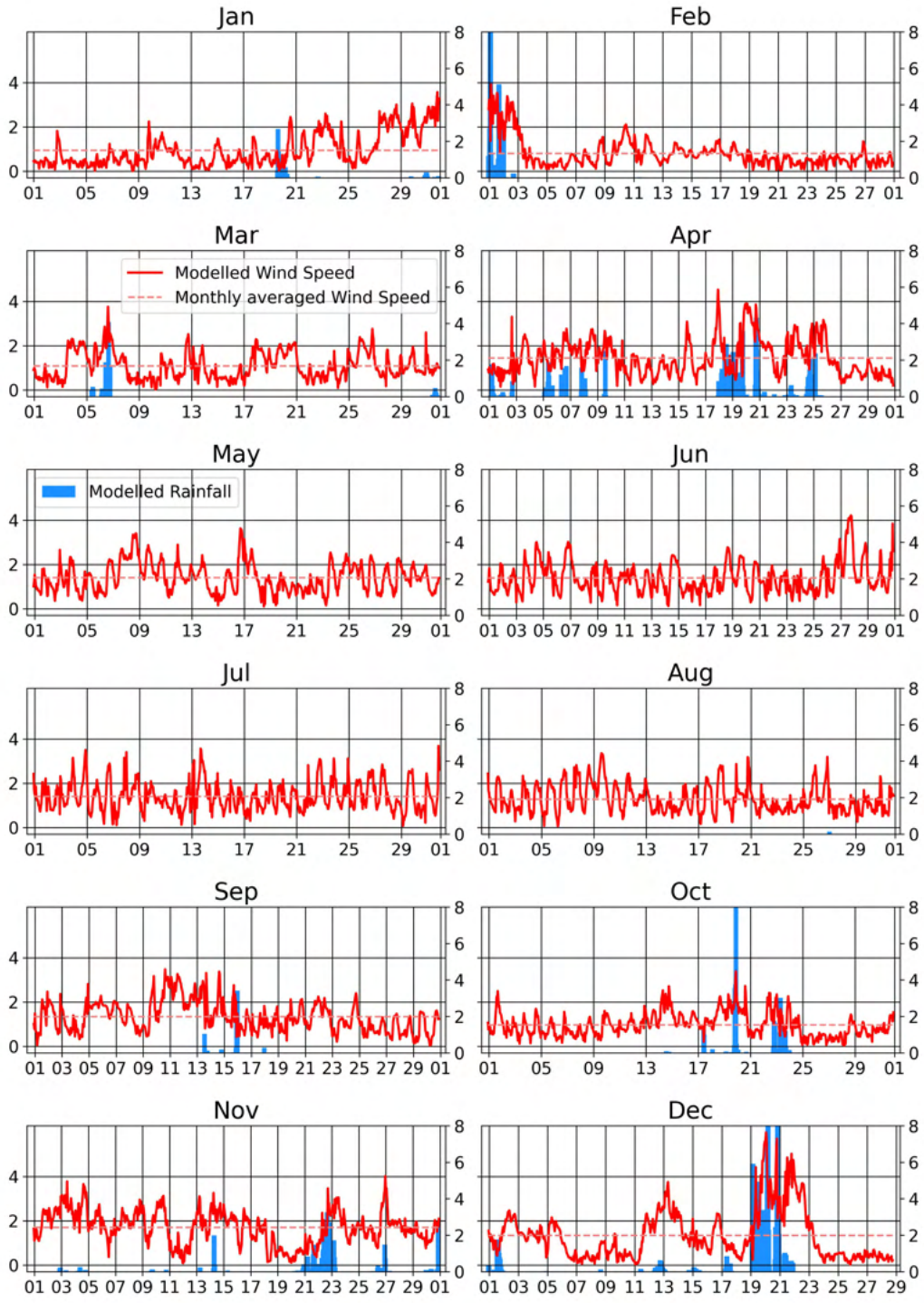

Figure 5.20: Hourly modelled values of wind speed (red lines) and rainfall (blue bars) for the year 2019 at Plaza Elíptica. Dashed red line indicates the monthly averaged wind speed.

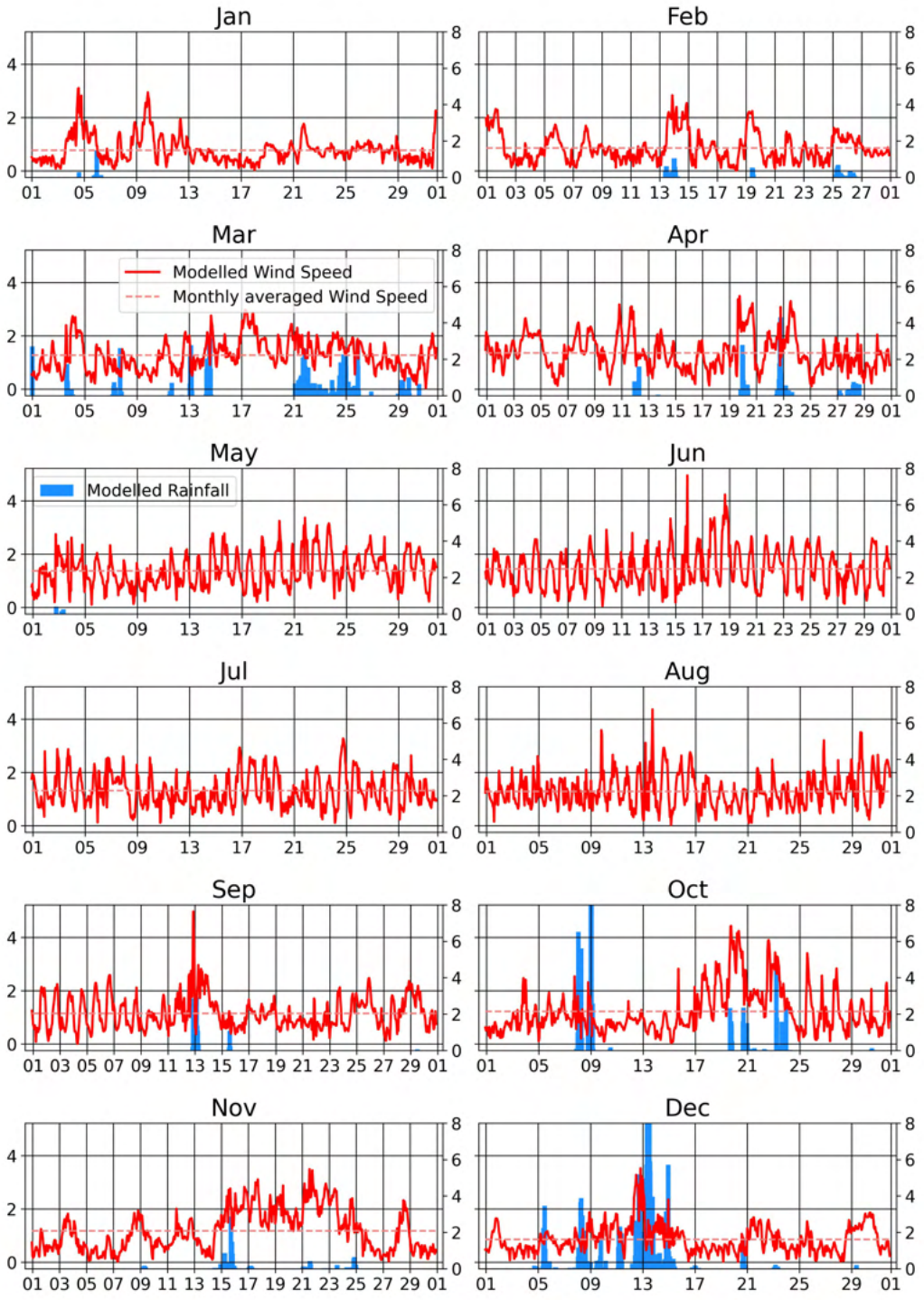

Figure 5.21: Hourly modelled values of wind speed (red lines) and rainfall (blue bars) for the year 2022 at Plaza Elíptica. Dashed red line indicates the monthly averaged wind speed.

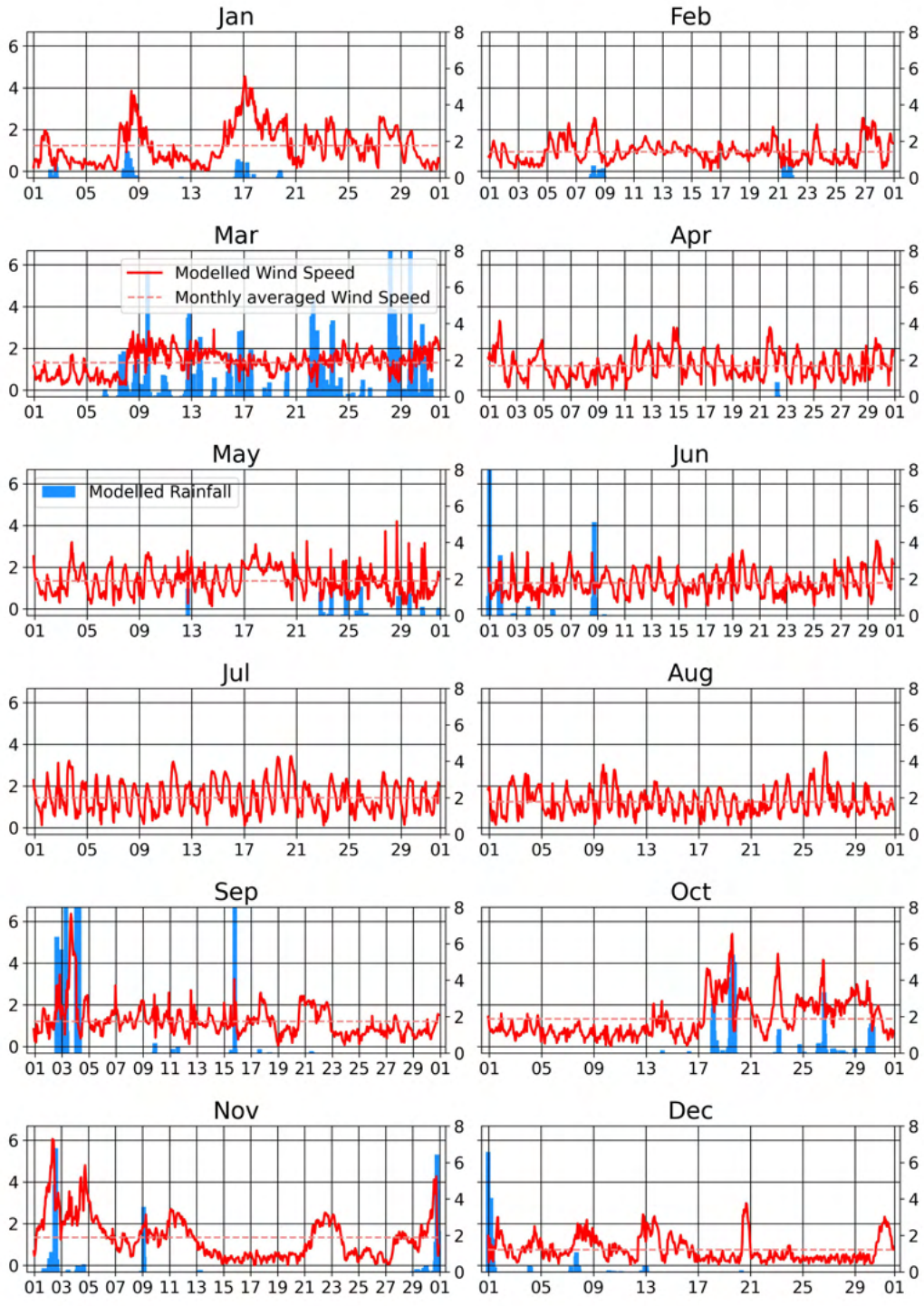

Figure 5.22: Hourly modelled values of wind speed (red lines) and rainfall (blue bars) for the year 2023 at Plaza Elíptica. Dashed red line indicates the monthly averaged wind speed.

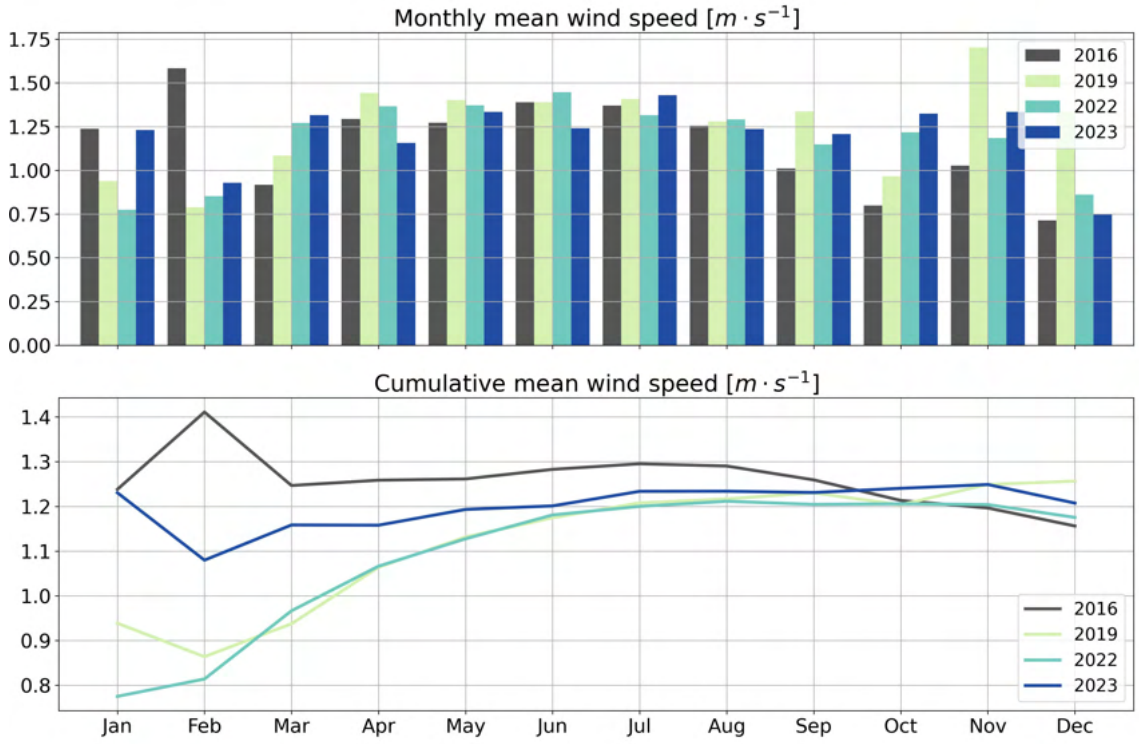

Figure 5.23: Above: Monthly average of wind speed for each simulated year, in $m \cdot s^{-1}$. Below: Cumulative mean of wind speed along each simulated year, in $m \cdot s^{-1}$

on air quality. Those two subsets, called "calmest" and "windiest" are composed of the hourly values of the simulated years. For each month, the hourly values are those of the simulated year with the lowest or the highest monthly mean wind speed, for the "calmest" and "windiest" subset respectively. Only wind speed was considered in order to create these additional subsets, wind direction was not considered.. Table 5.6 shows the resulting monthly mean wind speed values for the two new subsets, whereas Figure 5.24 illustrate the wind roses of all the six meteorological subsets: the four corresponding to the simulated years plus the "calmest" and "windiest" configurations. The variations in rainfall monthly accumulations is neglected in the computation of the new meteorological conditions as the rainfall is not considered in the WA CFD-RANS methodology when computing the air pollutants' concentrations.

5.4.1.2 Model evaluation

The modelled timeseries of $[NO_X]$ at the AQMS location and the statistical parameters derived from its evaluation with observational data show a good performance of the methodology. Figures 5.25 to 5.28 show the modelled (red) and the observed (black) timeseries of $[NO_X]$ for every simulated year. Some very high values ($> 500 \mu g \cdot m^{-3}$) are observed in every year. Episodes with high NO_X levels are well captured by the methodology. Table 5.7 shows some statistical parameters derived from the evaluation of the modelled NO_X

Table 5.6: Monthly and annual averaged modelled wind speed $[m \cdot s^{-1}]$ at PE AQMS location.

Monthly averages of modelled wind speed $[m \cdot s^{-1}]$						
	2016	**2019**	**2022**	**2023**	**calmest**	**windiest**
Jan	1.26	0.94	0.78	1.19	0.78	1.26
Feb	1.59	0.79	0.85	0.93	0.79	1.59
Mar	0.92	1.09	1.27	1.32	0.92	1.32
Apr	1.29	1.44	1.37	1.16	1.16	1.44
May	1.27	1.40	1.37	1.33	1.27	1.40
Jun	1.39	1.39	1.45	1.24	1.24	1.45
Jul	1.37	1.41	1.32	1.43	1.32	1.43
Aug	1.26	1.28	1.29	1.24	1.24	1.29
Sep	1.01	1.34	1.15	1.21	1.01	1.34
Oct	0.80	0.97	1.22	1.33	0.80	1.33
Nov	1.03	1.70	1.19	1.33	1.03	1.70
Dec	0.71	1.23	0.86	0.75	0.71	1.23
Annual	1.16	1.25	1.18	1.20	1.02	1.40

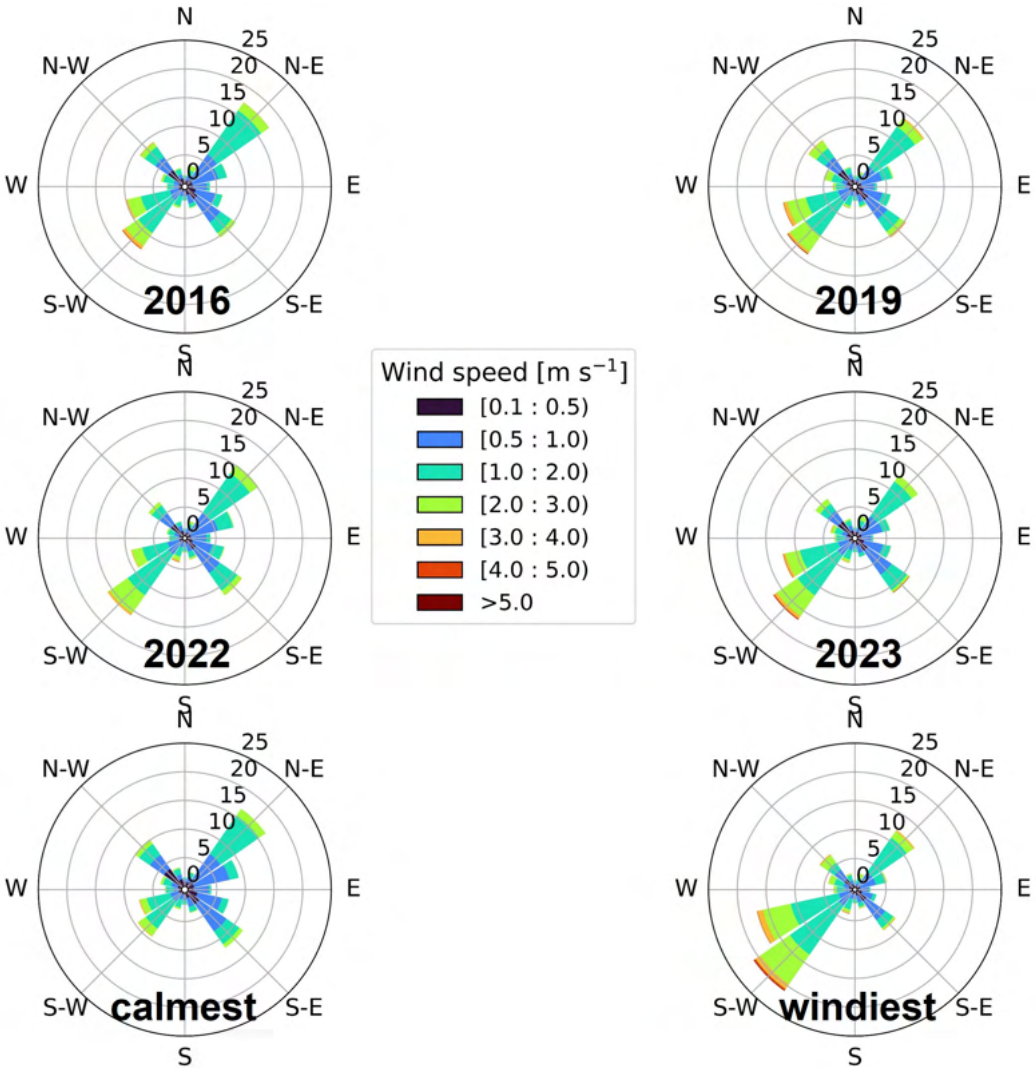

Figure 5.24: Annual windroses at PE AQMS location obtained from the WRF simulations.

concentrations of the real scenarios. Good correlations are found between the modelled and observed values. Only the correlation coefficient (R) for the 2019_Em19 scenario does not meet the highest level of acceptance criteria of $|R| > 0.8$ given in Goricsán et al. (2011). That same scenario has the largest underestimation of NO_X ($FB = -0.29$), partly due to the underestimation of the traffic flows in the corresponding emissions case (as discussed in Section 5.3.3). On the other hand, all the other parameters meet the acceptance criteria.

Table 5.7: Statistical parameters R, FB, NMSE and FAC2 for the modelled NO_X concentrations.

Statistical parameters for the modelled [NO_X].				
	2016_Em16	2019_Em19	2022_Em22	2023_Em23
R	0.80	0.78	0.81	0.82
FB	-0.05	-0.29	-0.15	-0.08
NMSE	0.43	0.66	0.39	0.44
FAC2	0.83	0.70	0.84	0.84

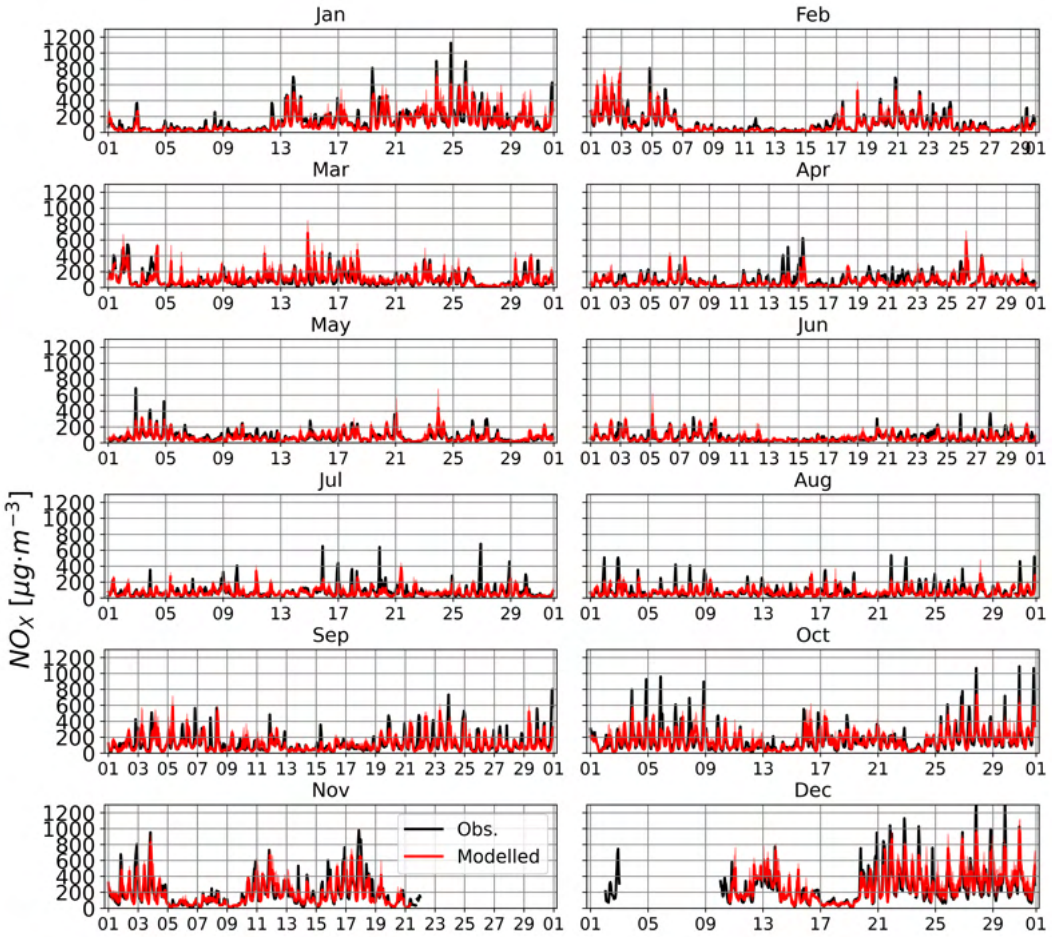

Figure 5.25: Timeseries of the modelled NO_X concentration values (red) and observed values (black) at the PE AQMS location for the year 2016. Red bands indicate the standard deviation (σ) of the modelled values.

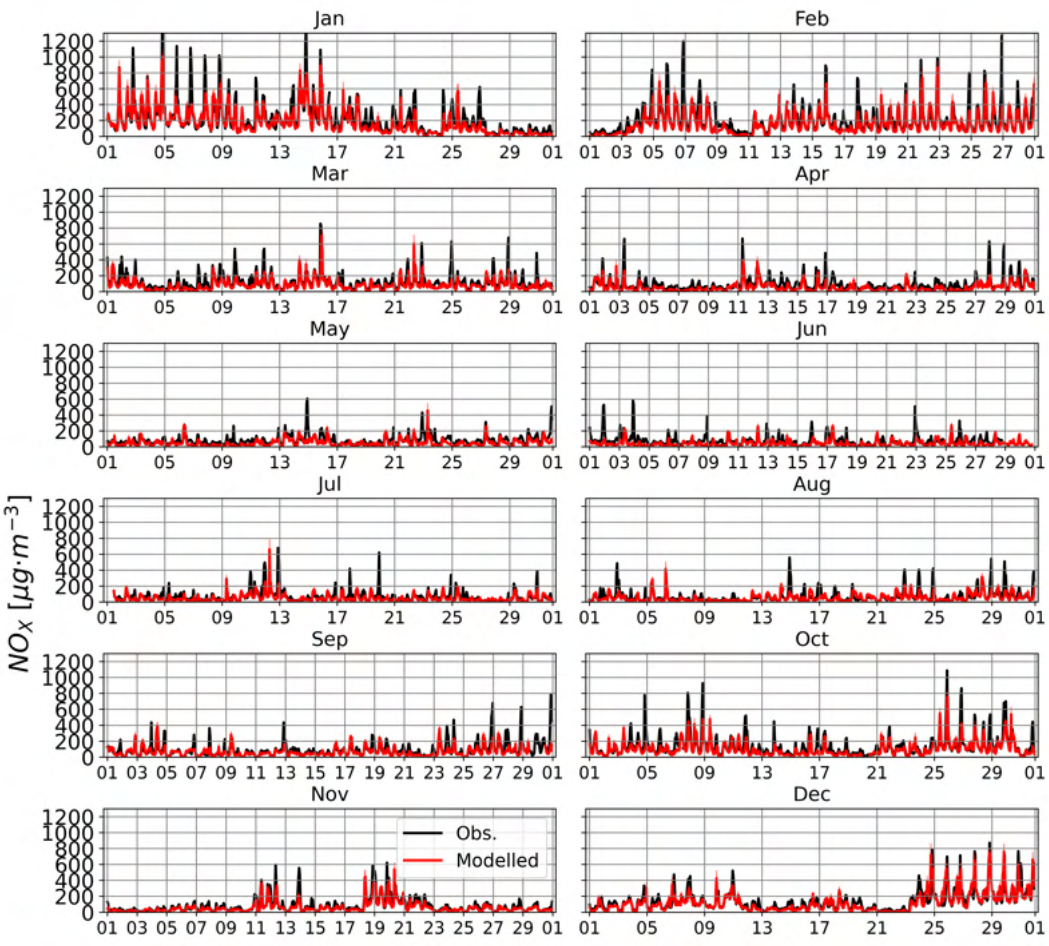

Figure 5.26: Timeseries of the modelled NO_X concentration values (red) and observed values (black) at the PE AQMS location for the year 2019. Red bands indicate the standard deviation (σ) of the modelled values.

Table 5.8: Statistical parameters R, FB, NMSE and FAC2 of the modelled [NO_2] validation.

Statistical parameters of the modelled [NO_2] validation.				
	R	FB	NMSE	FAC2
2016_Em16	0.70	0.02	0.27	0.88
2019_Em19	0.74	-0.18	0.32	0.82
2022_Em22	0.72	-0.11	0.27	0.85
2023_Em23	0.69	-0.04	0.35	0.85

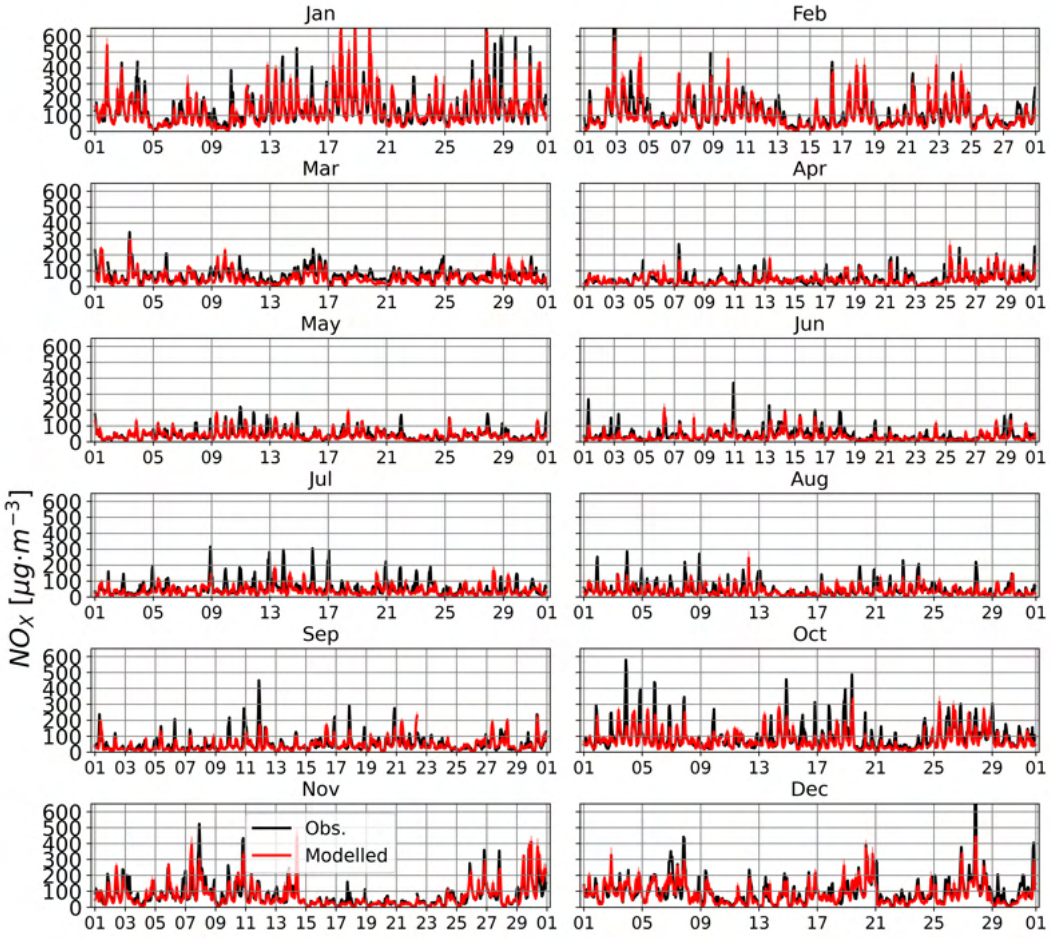

Figure 5.27: Timeseries of the modelled NO_X concentration values (red) and observed values (black) at the PE AQMS location for the year 2022. Red bands indicate the standard deviation (σ) of the modelled values.

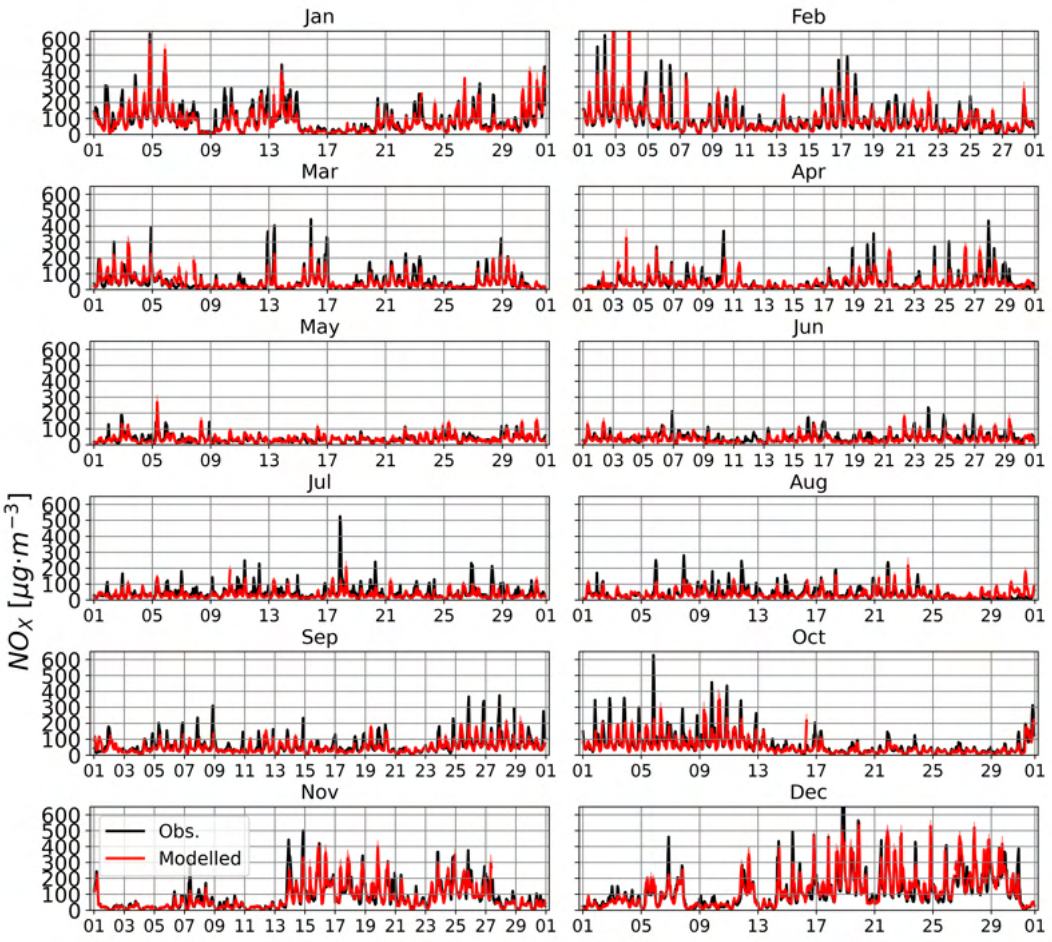

Figure 5.28: Timeseries of the modelled NO_X concentration values (red) and observed values (black) at the PE AQMS location for the year 2023. Red bands indicate the standard deviation (σ) of the modelled values.

The evaluation of [NO_2] also shows a good agreement between modelled and observed values. The correlation coefficient R of all four scenarios is relatively high, meeting the criteria for a "fair" simulation established by Goricsán et al. (2011). All of the other statistical parameters for the four real cases meet the highest level of the acceptance range proposed by Chang and Hanna (2005) and Goricsán et al. (2011) (Table 5.8).

Figures 5.29 to 5.32 show the timeseries of the modelled (red) and observed (black) values of NO_2 at the PE AQMS location. Also good agreement are observed between modelled and observed values. The employed methodology is able to capture most of the observed exceedances for the NO_2 hourly threshold level set by Directives 2008/EC/50 and 2024/2881.

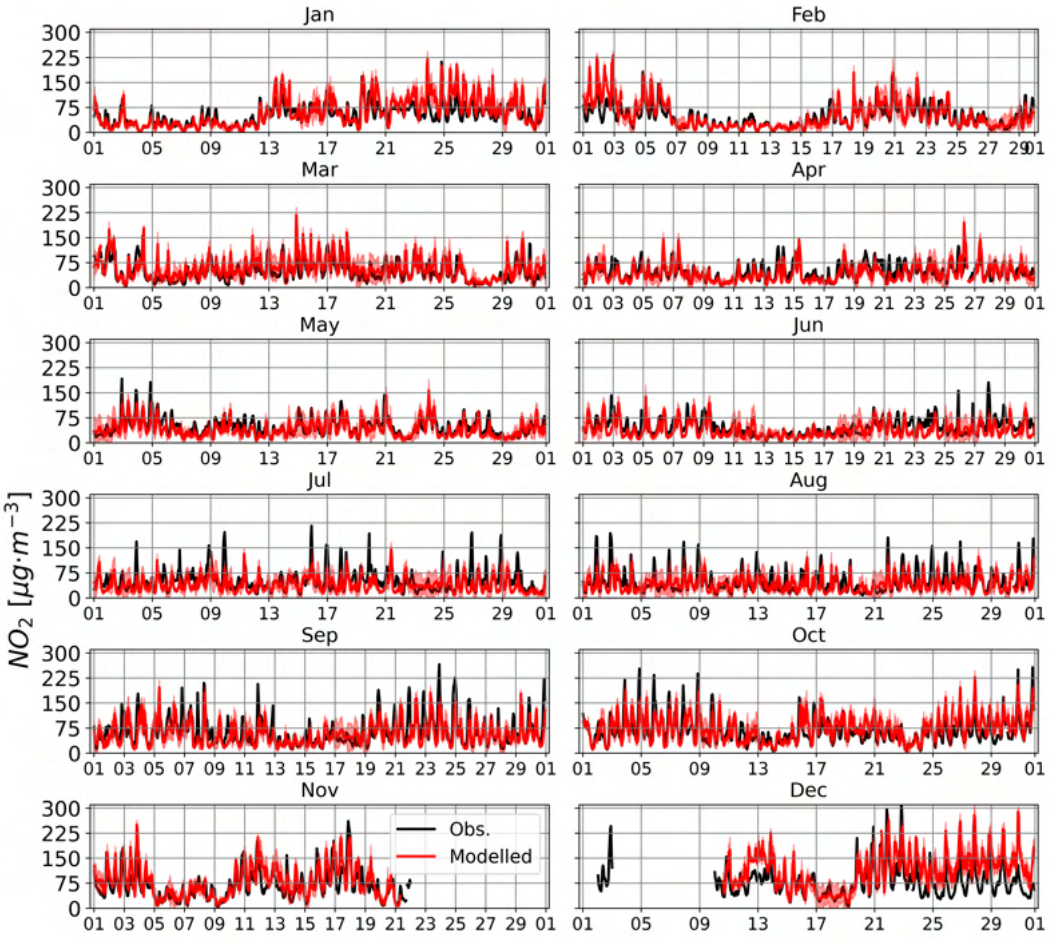

Figure 5.29: Timeseries of the modelled NO_2 concentration values (red) and observed values (black) at the PE AQMS location for the year 2016. Red bands indicate the standard deviation (σ) of the modelled values. As the methodology uses the background NO_X measured at Farolillo AQMS, which did not report data from November 22nd to December 11th, that period has not modelled data, even if observations at PE AQMS are available.

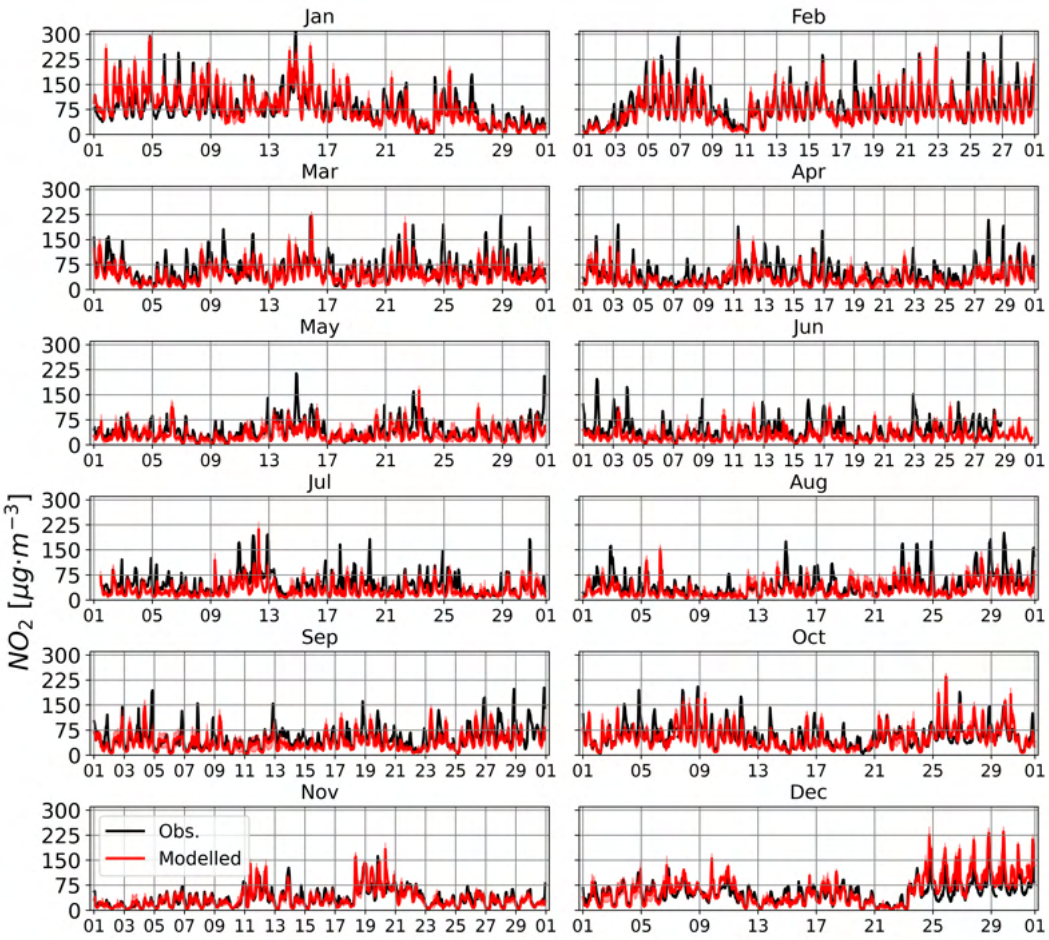

Figure 5.30: Timeseries of the modelled NO_2 concentration values (red) and observed values (black) at the PE AQMS location for the year 2019. Red bands indicate the standard deviation (σ) of the modelled values.

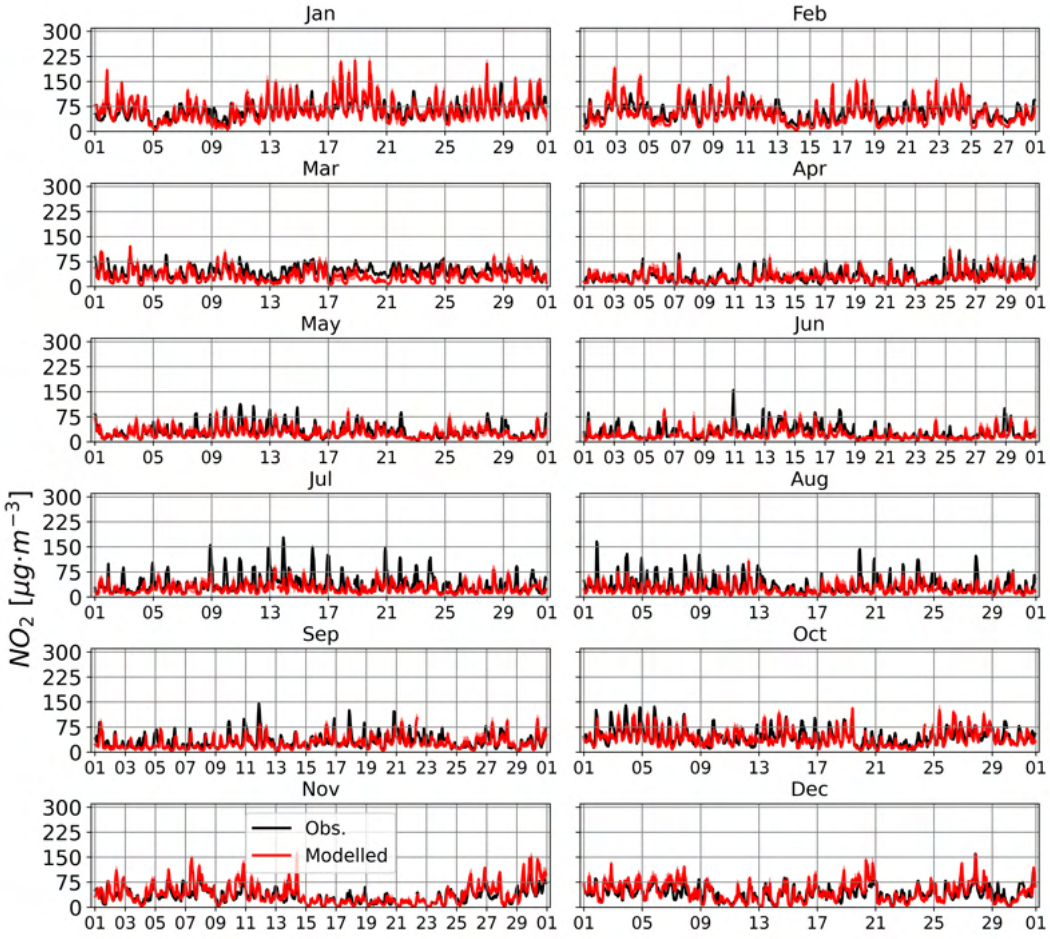

Figure 5.31: Timeseries of the modelled NO_2 concentration values (red) and observed values (black) at the PE AQMS location for the year 2022. Red bands indicate the standard deviation (σ) of the modelled values.

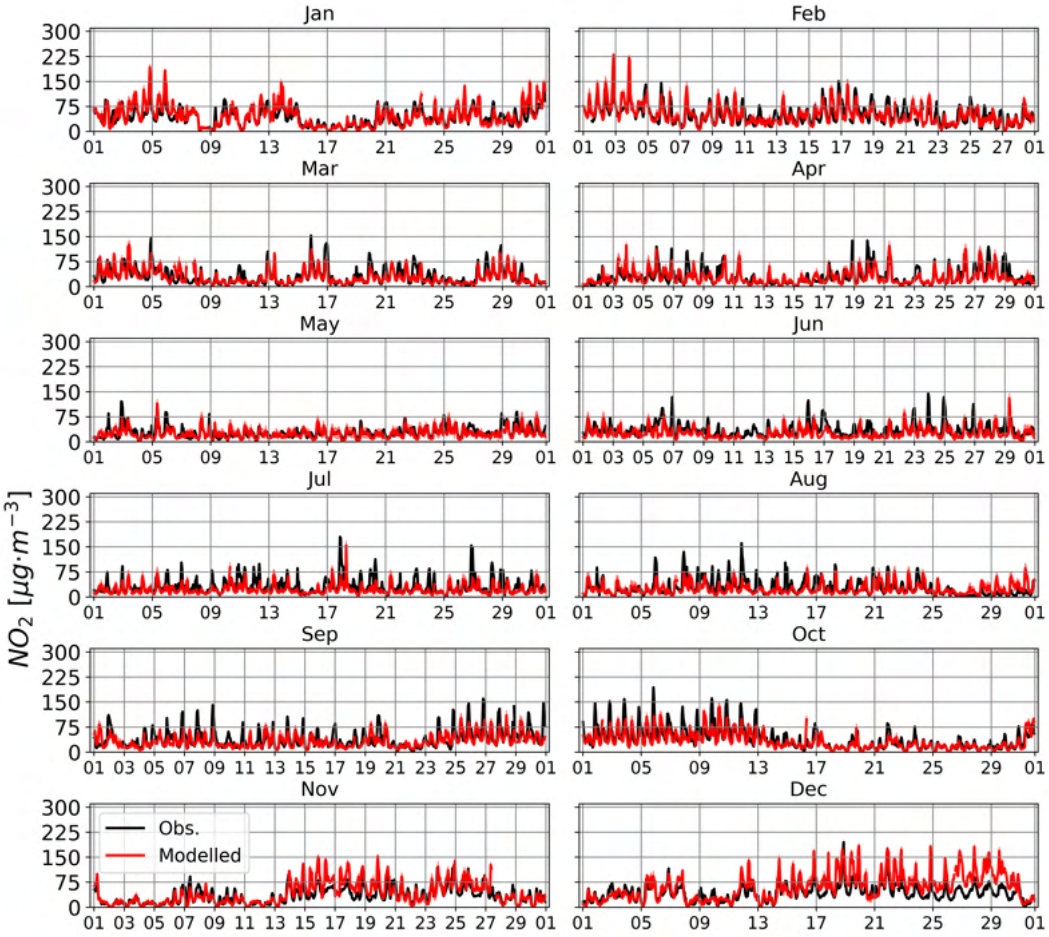

Figure 5.32: Timeseries of the modelled NO_2 concentration values (red) and observed values (black) at the PE AQMS location for the year 2023. Red bands indicate the standard deviation (σ) of the modelled values.

5.4.2 The impact of meteorological conditions on annual NO_X concentrations

To assess the effects of local traffic measures and meteorology on [NO_X] at pedestrian level, concentrations due to each local mitigation strategy and meteorological conditions are estimated. Although meteorological conditions also affects background concentrations, a mesoscale transport-chemistry model should be used to compute this impact, which increases the computational cost of the methodology. In this work, it is assumed the background concentrations are constant with the changes in meteorological conditions, focusing on the impact of meteorological conditions on the local component of [NO_X].

Each emission case has associated a set of meteorological conditions (those of the year of the emissions). However, to assess the impact of meteorological conditions on air pollutant concentrations, for each emission case, six scenarios are possible (one for each set of meteorological conditions). Each scenario will be labelled hereafter as X_EmY, where X represents the label of the meteorological conditions and Y the year of the emissions case.

Therefore, the set of all possible scenarios can be classified by:

1. Real scenarios: Those which use the meteorological conditions and emissions of the same year. Therefore, these are scenarios for which observational data exists.
2. Virtual scenarios: Those scenarios that combine the emissions of a certain year with the meteorological conditions of another.

Figure 5.33 shows the CFD with some streets relevant for the upcoming discussions labelled with numbers. Figure 5.34 shows the spatial distribution of annual NO_X for the real scenarios 2016_Em16, 2019_Em19, 2022_Em22 and 2023_Em23. The spatial distribution of NO_X is broadly the same in all of them: strong spatial gradients are present, with maxima in the PE roundabout and their entries. This is similar to the spatial distribution modelled in Sanchez et al. (2017) for a winter week. In addition, several relative maxima are found in the entry and exit of the tunnel traversing it; and several intersections across the domain, such as the intersection inside Street 5 in Figure 5.33 . On the contrary, the minimum concentrations are found within inner blocks and green zones. Only the 2016_Em16 scenario shows points with annual [NO_X] near or exceeding 200 $\mu g \cdot m^{-3}$. The 2016_Em16 shows the broader concentrations of large NO_X values, being more restricted to the most emitting streets in the rest of scenarios.

The annual mean value of [NO_X] for each emissions case and meteorological conditions, averaged across the CFD domain, is shown in Table 5.9. Considering the emissions case "i" as reference, the maximum potential meteorological impact ($max(\Delta[NO_X]_{meteo})$) can be defined as the difference in NO_X concentrations between the most polluted meteorological

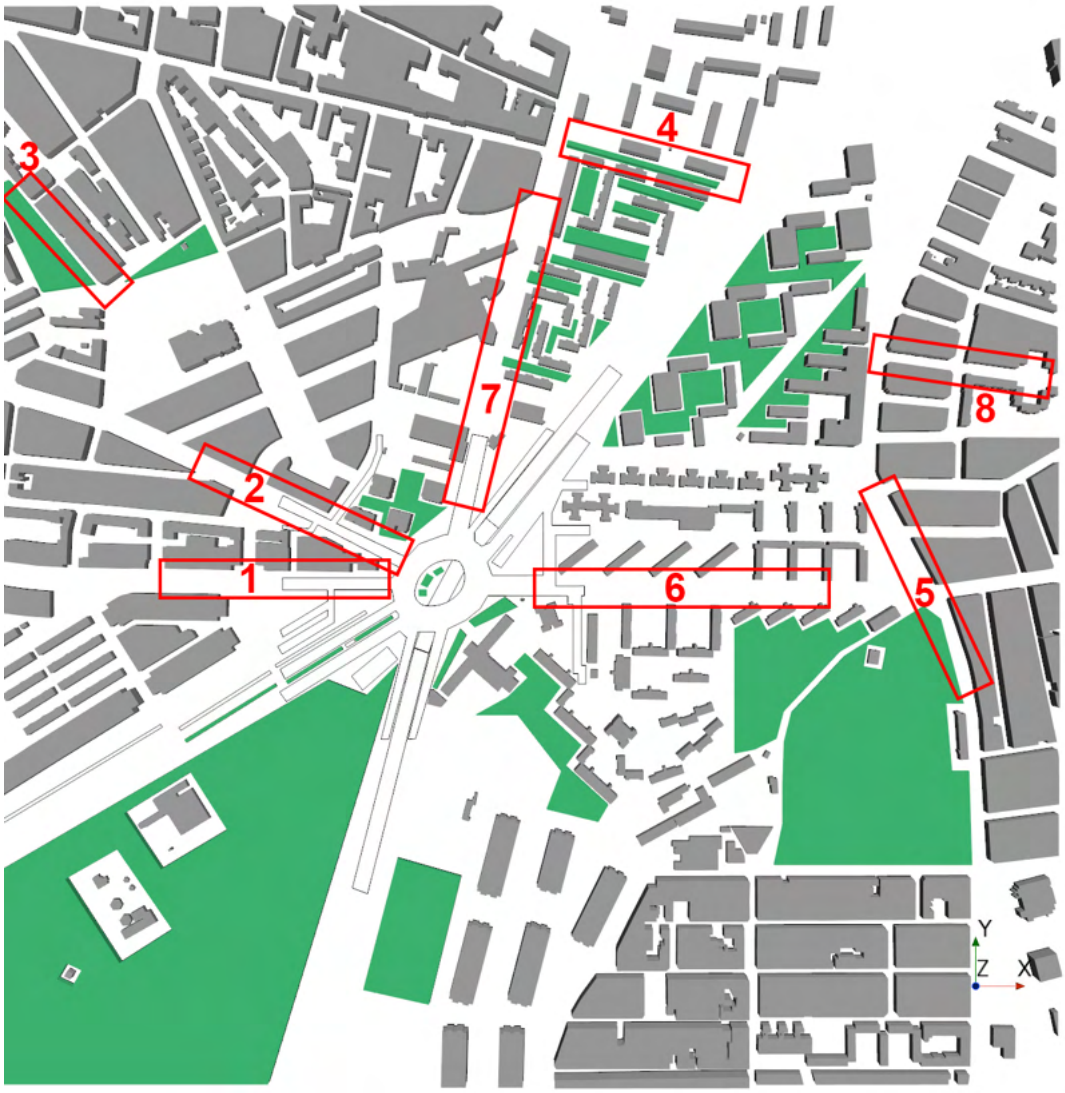

Figure 5.33: CFD domain with some relevant streets labelled. Green areas indicate vegetated areas.

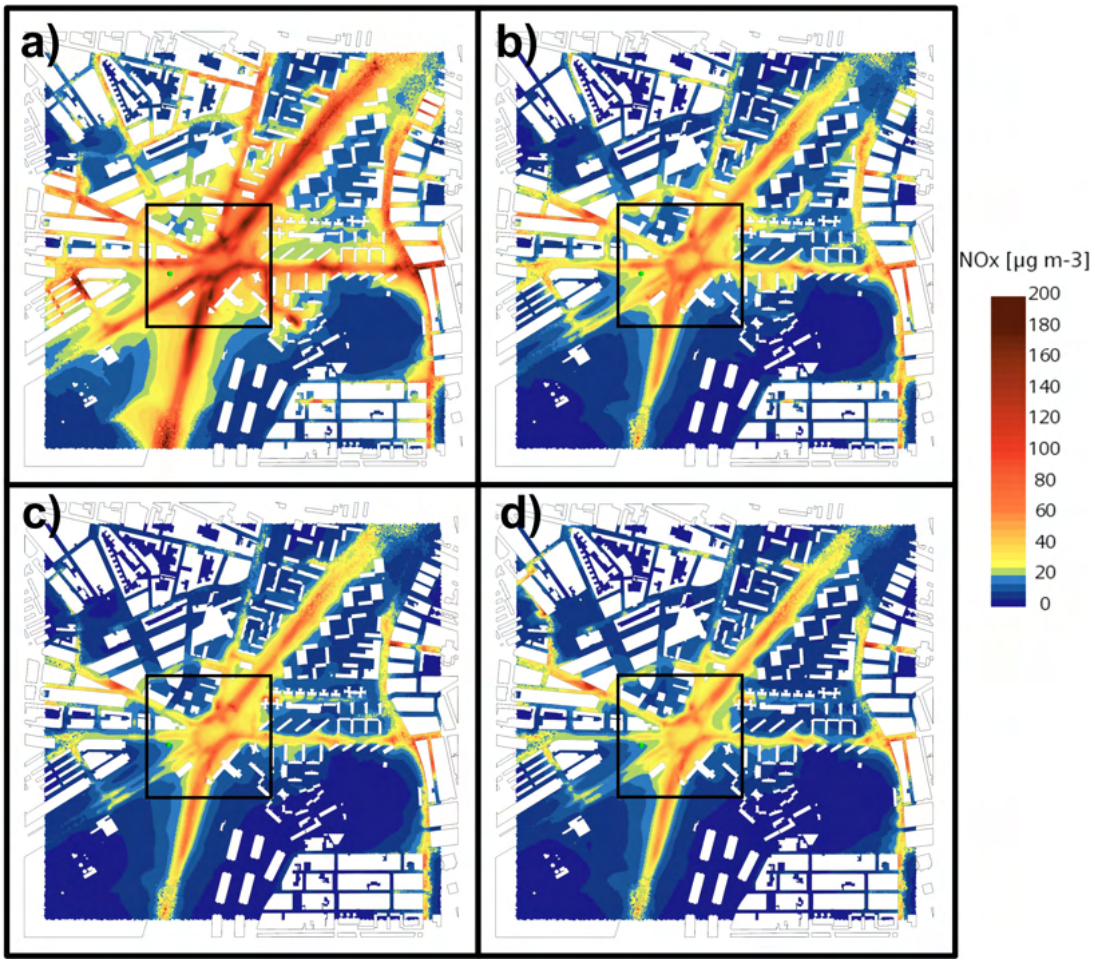

Figure 5.34: Maps of the modelled NO_X concentration values along the CFD model domain for scenarios: a) 2016_Em16; b) 2019_Em19; c) 2022_Em22; and d) 2023_Em23. Inner black square indicates a study area of 300 m x 300 m used in previous works.

conditions and the less polluted one, as Equation 5.11 shows.

$$max(\Delta[NO_X]_{meteo}) = [NO_X]^i_{max} - [NO_X]^i_{min} \tag{5.10}$$

where $[NO_X]^i_{max}$ represents the largest [NO_X] among every meteorological conditions for the emissions case i, and $[NO_X]^i_{min}$ the lowest one.

Considering this, the simulated meteorological conditions have little impact on the annual concentrations of NO_X (no longer than 5%). However, when including the "calmest" and "windiest" conditions, the maximum potential impact of the meteorological conditions raises notably to approximately a 25%. Nonetheless, these impacts are still lower than the uncertainty in annual [NO_X] due to the uncertainty in traffic-related emissions (Figure 5.35). The same impacts are observed within the 300 m x 300 m subdomain (Table 5.10). In both the whole domain and the 300 m x 300 m subdomain, and for all emission cases, the highest annual mean values of [NO_X] correspond to the "calmest" meteorological conditions, and the lowest to the "windiest" meteorological conditions.

Table 5.9: Annually-averaged [NO_X] for each meteorological conditions and each emissions case. Each row represents an emissions case, whereas the columns represents meteorological conditions.

Spatially averaged annual mean of NO_X concentrations [$\mu g \cdot m^{-3}$]						
	2016	2019	2022	2023	"calmest"	"windiest"
Em16	33.78	33.54	32.48	33.90	39.35	30.41
Em19	18.80	18.10	17.87	18.50	21.86	17.15
Em22	14.64	14.24	13.84	14.38	16.77	13.15
Em23	15.49	14.95	14.67	14.99	17.22	13.44

Table 5.10: Annually-averaged [NO_X] for each meteorological conditions and each emissions case inside the 300 m x 300 m subdomain. . Each row represents an emissions case, whereas the columns represents meteorological conditions.

Spatially averaged annual mean of NO_X concentrations [$\mu g \cdot m^{-3}$]						
	2016	2019	2022	2023	"calmest"	"windiest"
Em16	65.20	64.68	62.73	65.31	75.35	58.19
Em19	36.52	35.18	34.62	35.79	43.29	33.96
Em22	28.20	27.39	26.62	27.61	31.93	25.23
Em23	30.08	28.97	28.44	29.00	33.13	25.92

Figure 5.36 shows the spatial distribution of annually-averaged [NO_X] for each real scenario -leftmost column- and for the "calmest" and "windiest" configurations. In all cases, as aforementioned, the "calmest" configuration leads to largest values of NO_X, specially in the most emitter roads; and the windiest to the lowest concentrations. Furthermore, it can be observe an impact of the meteorological conditions in the spatial distribution of

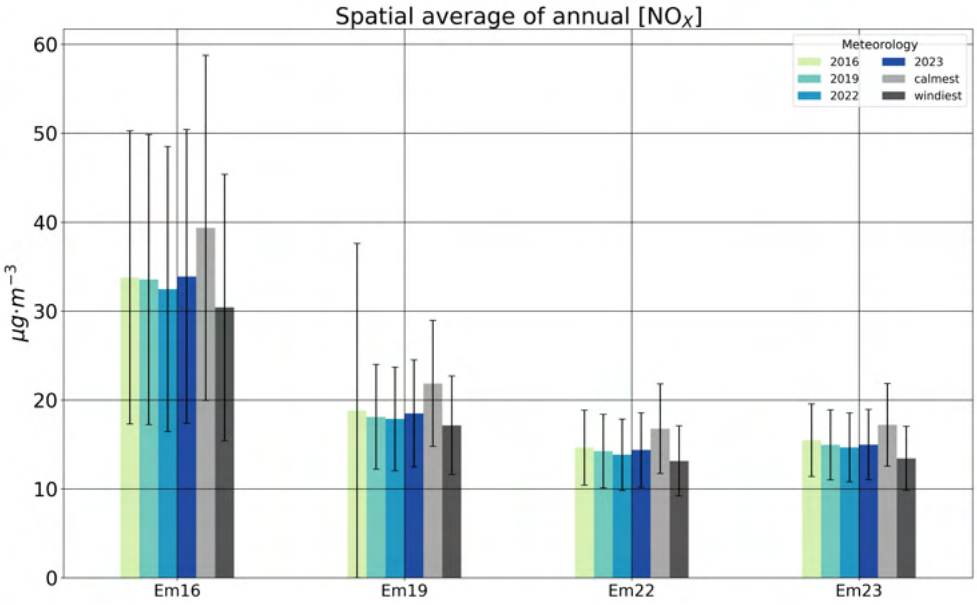

Figure 5.35: Modelled spatially-averaged annual [NO_X] concentration along the CFD model domain for each emissions case and meteorological conditions. Black spines indicate the STD of [NO_X] due to uncertainty in the computation of traffic-related emissions

the pollutants: in the "calmest" configuration exists a clear tendency to disperse the concentrations to the eastern part of the domain, also visible for the "windiest" configuration although to less extent. This has a notable impact on the [NO_X] around buildings. For example, it can be observed a large channelling of the NO_X between several buildings located at the right of the PE roundabout increasing their concentrations with respect the real scenario even in the "windiest" configuration. This also affects the San Viator school (pink building in Figure 5.1), which sees its NO_X concentration increased with respect the base scenarios -specially in its eastern wing.

In order to investigate the impact of changing emissions and meteorological conditions in specific points of the domain, Figure 5.37 illustrate the positions of three relevant points within the CFD domain. The green point represents the location of the Plaza Elíptica AQMS; the red point represents the most polluted point in the most recent simulated scenario (2023_Em23); and the grey point represents the playground of the San Viator school, which is frequented by schoolboys every working day.

When analysing the annual [NO_X] at these points (Figure 5.38), different behaviours are modelled: In the PE AQMS, [NO_X] decreases from Em16 to Em22, and remains almost steady between Em22 and Em23 scenarios. This agrees with the trend of the mean value of the CFD domain (Table 5.9). Also, little variation due to the meteorological conditions is modelled, being lower their impact than the uncertainty in [NO_X] (Figure 5.38). In this point, the calmest scenario results in the largest concentrations, and the windiest in the lowest. However, when analysing the [NO_X] in the location of a playground belonging to the

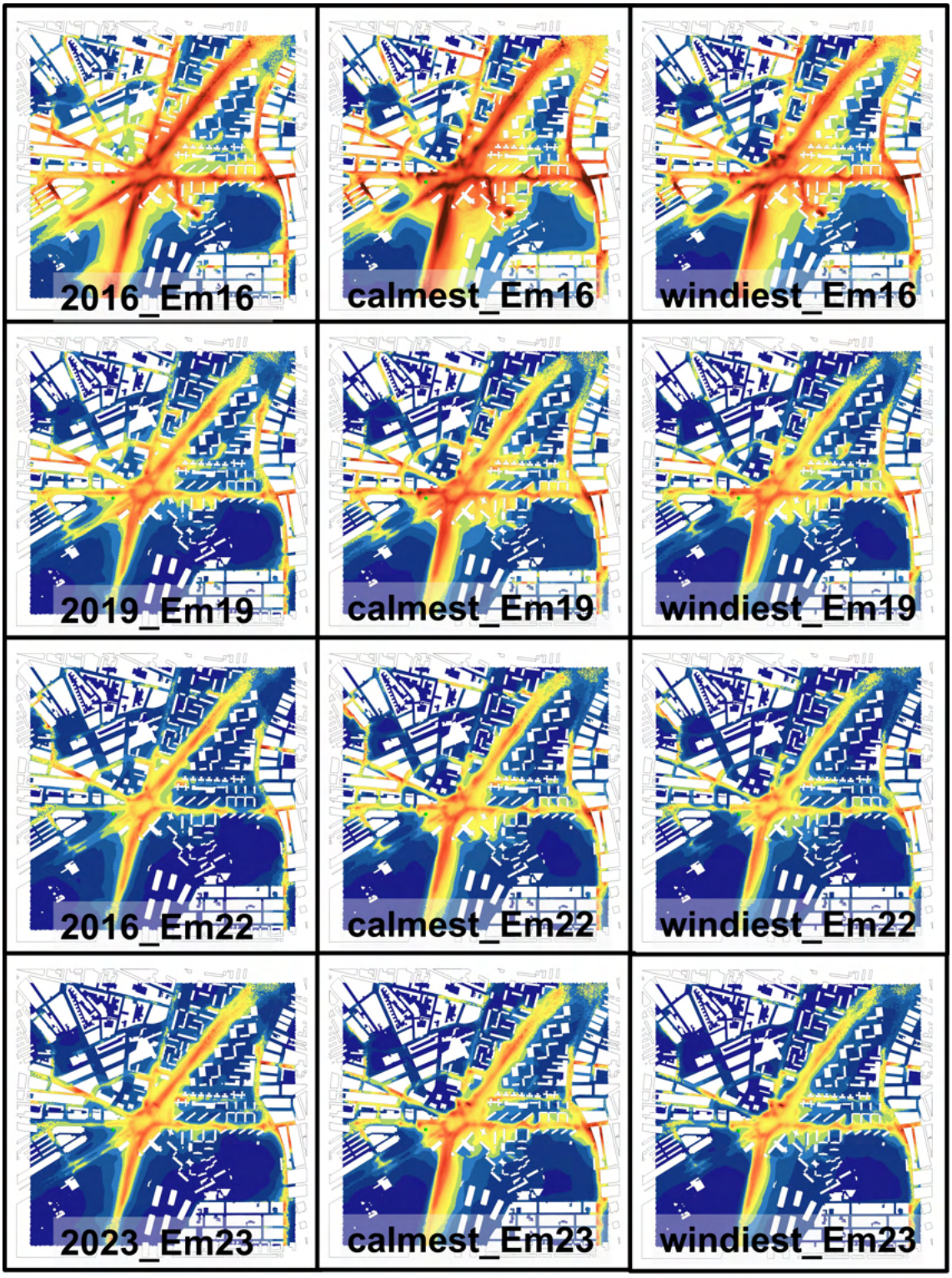

Figure 5.36: Maps of the modelled NO_X concentration values along the CFD model domain for scenarios (from left to right and from up to down): 2016_Em16, calmest_Em16, windiest_Em16, 2019_Em19, calmest_Em19, windiest_Em19, 2022_Em22, calmest_Em22, windiest_Em22, 2023_Em23, calmest_Em23 and windiest_Em23.

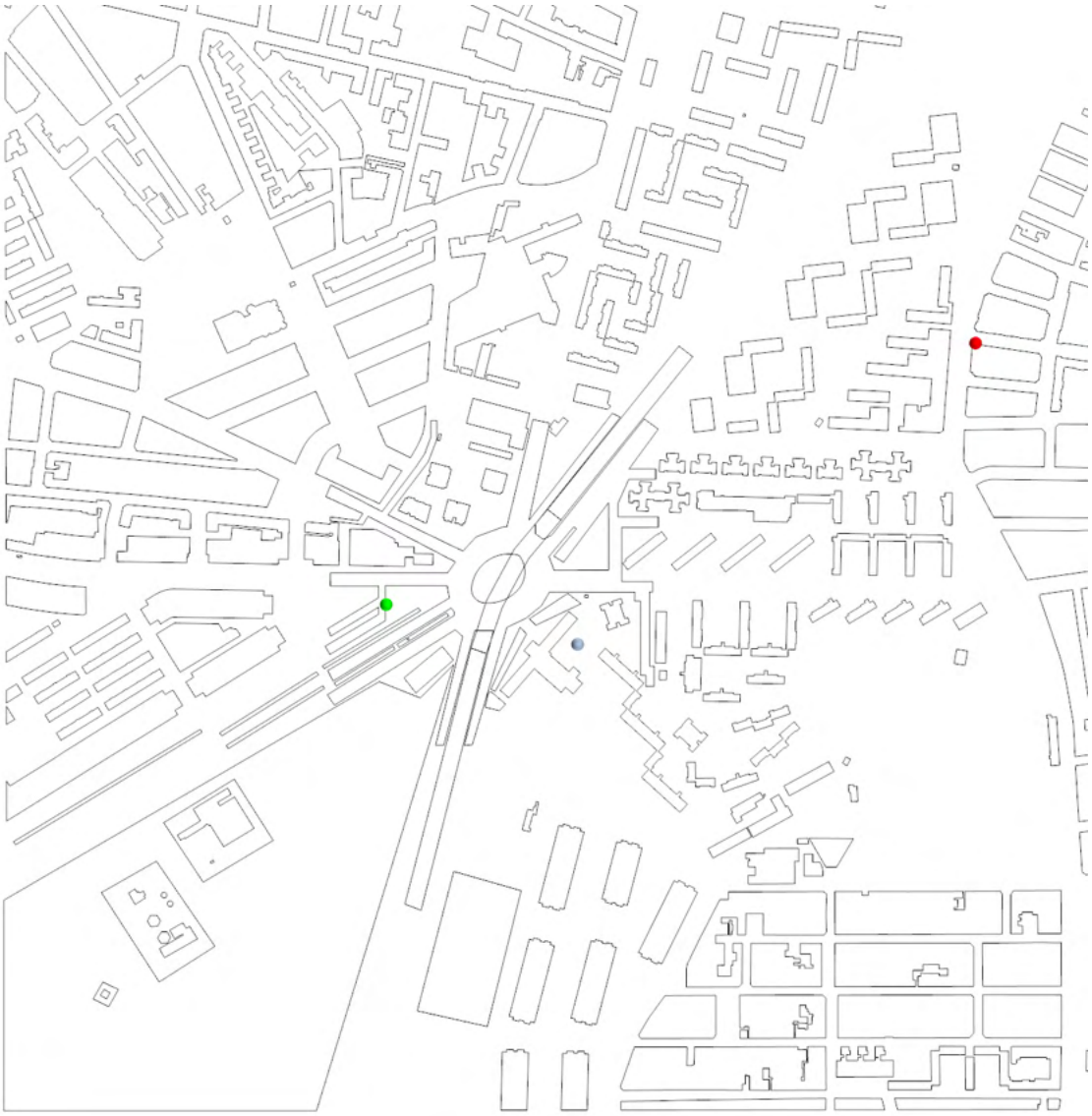

Figure 5.37: Location of three analysed points within the CFD domain. Green point represents the location of AQMS; grey point represents the SVP point; and the red point is the MP23 point.

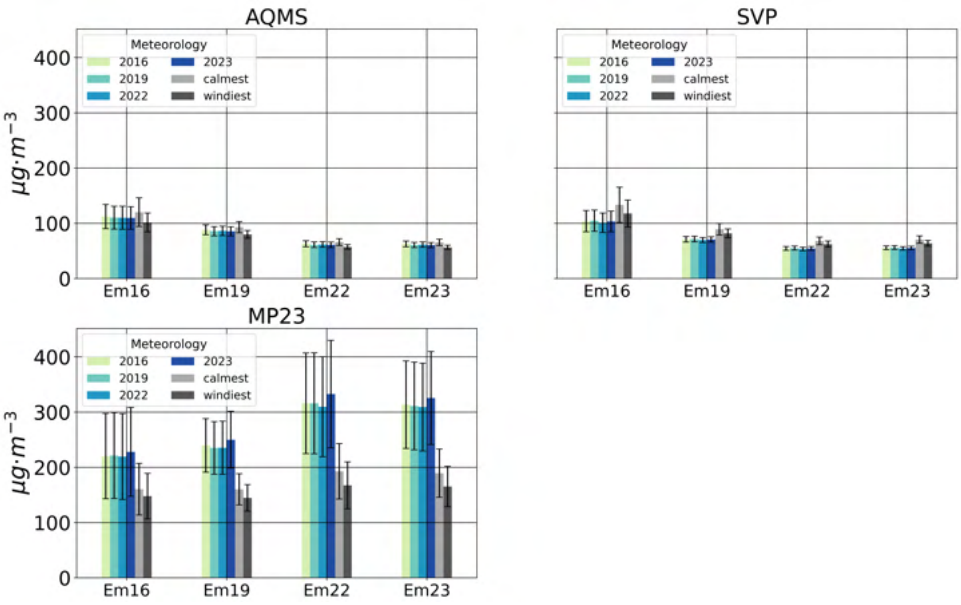

Figure 5.38: Annual averaged [NO_X] in three points of the CFD domain for each meteorological conditions and emissions case. Spines indicate the standard deviation of [NO_X].

San Viator school -the point labelled as SVP- both the calmest and windiest meteorological conditions result in higher concentrations than any other meteorological conditions. In the calmest scenario, the predominant wind direction is the NE, followed by the SE and NW directions respectively. In this point, when the main flow is from NE, it is channelized from Street 6 (refer to Figure 5.33 for street labelling), reaching the SVP location and transporting pollutants until that point (Figure 5.39). This, together with lower wind speeds that favours the accumulation of pollutants in that area, explains why in the calmest scenario it is modelled such an increase of [NO_X] (between 25% and 33% more) within the San Viator playground. In the windiest case, however, higher wind speeds should favour the ventilation of the domain and, therefore, lower concentrations of NO_X. This is not the case here because the predominant wind directions, SW and WSW -which together represent almost a 40% of the total wind direction distribution (Figure 5.24), tend to accumulate air pollutants in this playground due to the interaction of the mean flow with the urban morphology. The range of variability in [NO_X] in this point due to changing meteorological conditions is comparable to the range due to the uncertainty in emissions.

Finally, in the MP23 point location [NO_X] increases from Em16 and Em23, which differs with the general trend in the domain. This is due to an increase of emissions upwind this point (Figure 5.12). In addition, the calmest meteorological conditions results in much lower concentrations than the 2016, 2019, 2022 and 2023 meteorological conditions, with the variation comparable to or exceeding the standard deviation on [NO_X] in some cases. Furthermore, the 2023 meteorological conditions stand outs for higher NO_X concentrations than the others. This is another case in which the interaction between the predominant flow

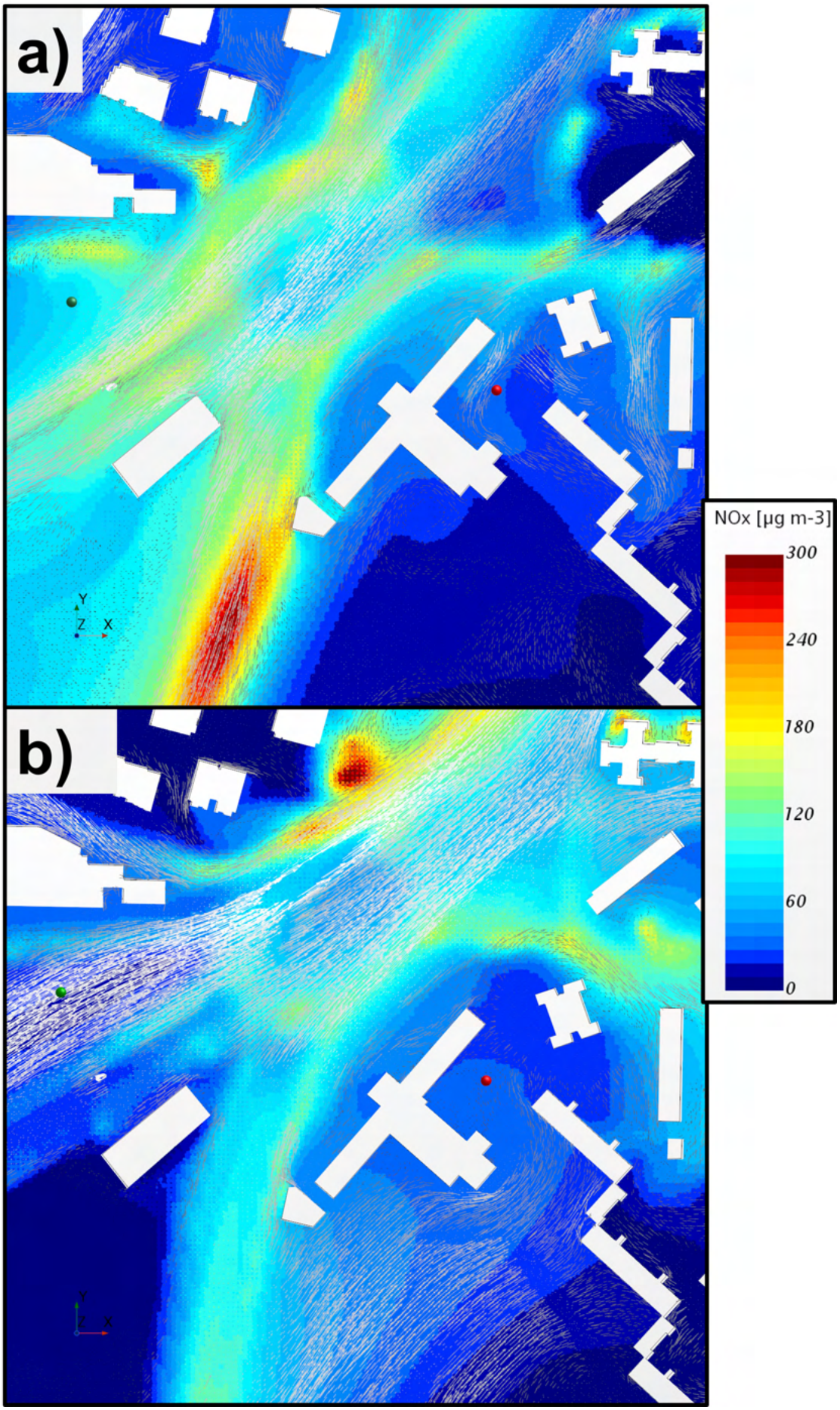

Figure 5.39: Zoomed maps around the PE roundabout location of NO_X distribution and windspeed for two scenarios: a) Predominant wind flow from NE; b) Predominant wind flow from SW. Green point indicates the AQMS location, the red one indicates the SVP point location.

and the urban morphology can be observed. When the mesoscale wind direction enters the CFD simulation from the SW (the most common case for the year 2023) the wind flow is channelled inside Street 5 from south to north, reducing its intensity along it (Figure 5.40). In addition, a small clockwise vortex is produced at the northwestern part of Street 8, which is the street where the MP23 point is located at, inducing a light eastern flow across the southern part of the street. This flow encounters the main flow from the Street 5 and its blocked, trapping the air pollutants at the MP23 location. In cases when the main wind flow comes from the NE (the predominant case in the calmest configuration), the main flow is again channelized inside Street 5, but now from north to south and with a higher intensity. Nonetheless, in this case the main flow is also channelized upwind the MP23 point, with enough intensity to produce a light ventilation that removes the pollutants to the eastern part of Street 5. The different impacts of the urban morphology on street ventilations for different wind directions illustrates the complexity of air quality distribution inside urban areas and the necessity of the use of high-resolution techniques to predict it. In addition, it explains why a configuration with lower mean wind speed leads to lower NO_X concentrations than a windier one, indicating the importance not only of wind speed but wind direction on air pollution dispersion.

Impact of meteorological conditions on the effectiveness of a mitigation strategy

Figure 5.41 shows the spatial distribution of the differences in annual mean local contribution to [NO_X] associated to the implementation of each mitigation strategy. Significant differences are modelled between the 2016_Em16 and 2019_Em19 scenarios. Large reductions (even larger than 100 $\mu g \cdot m^{-3}$) are observed in the most emitter streets and inside the PE roundabout. When comparing the 2022_Em22 and the 2019_Em19 scenario, decreases in annual values of [NO_X] are found mostly in roads inside the LEZ-affected area, with the largest decreases found near the PE roundabout. On the other hand, some increases are found in the northwestern area of the domain and near the MP23 point. Finally, little significant differences are found between the 2023_Em23 and the 2022_Em22 scenario, with some increases inside the LEZ-affected area and decreases in the western part of the domain.

Table 5.11 illustrates the impact on spatially-averaged local concentrations of the different mitigation measures for all the possible meteorological conditions within the studied period. The largest impact is observed between the Em19 and Em16 emissions cases, as it was expected due to its larger variation in emissions. In all the studied cases, the net effect of the meteorological conditions is smaller than the net effect of the mitigation strategy, but not negligible. The maximum computed meteorological effect, defined as the difference between the meteorological conditions with largest and lowest net impact on [NO_X], represents a 27.8 %, a 53.1% and a 63.7% of the mean impact of each mitigation strategy respectively.

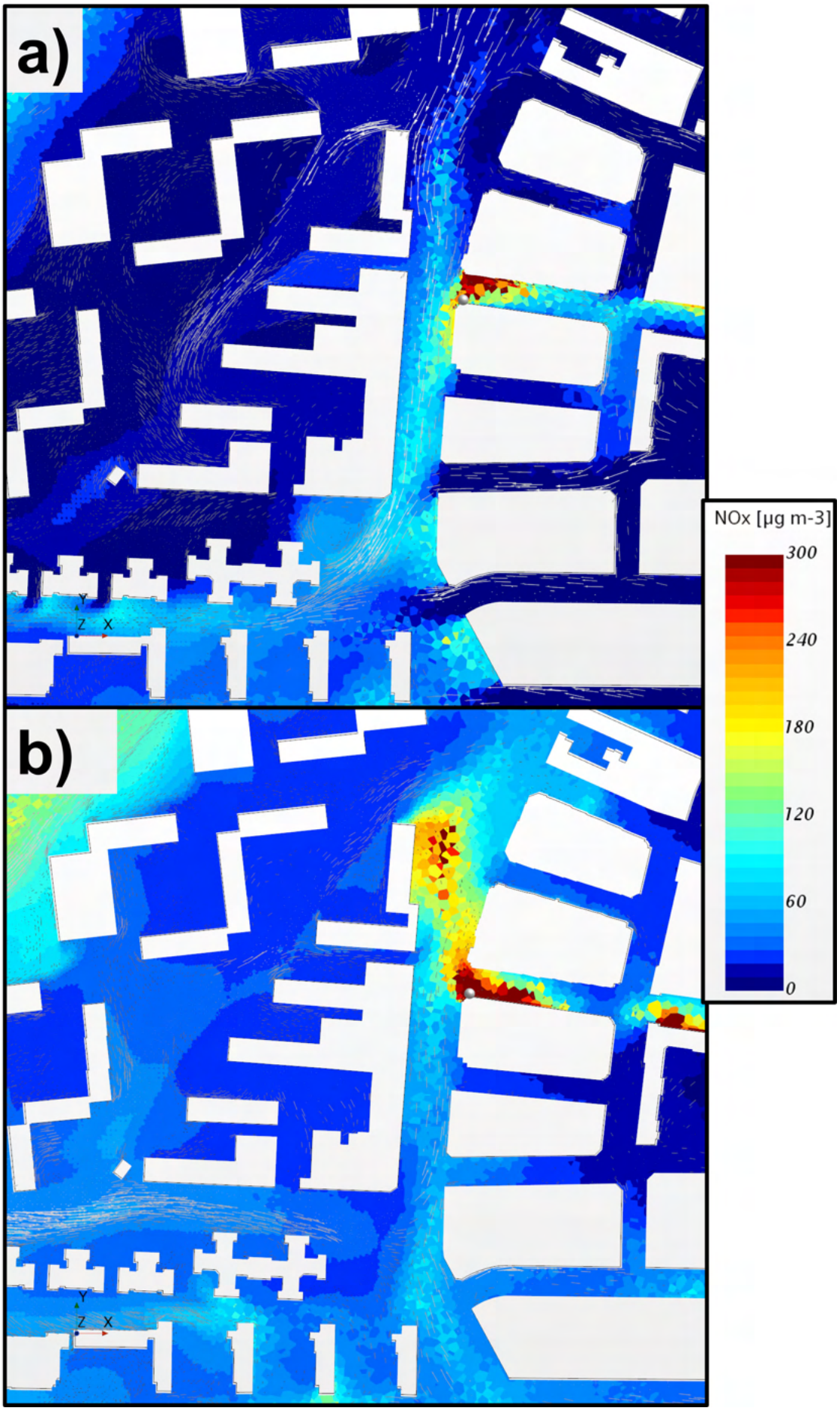

Figure 5.40: Zoomed maps around the MP23 location of NO_X distribution and windspeed for two scenarios: a) Predominant wind flow from NE; b) Predominant wind flow from SW. The grey point indicates the MP23 location

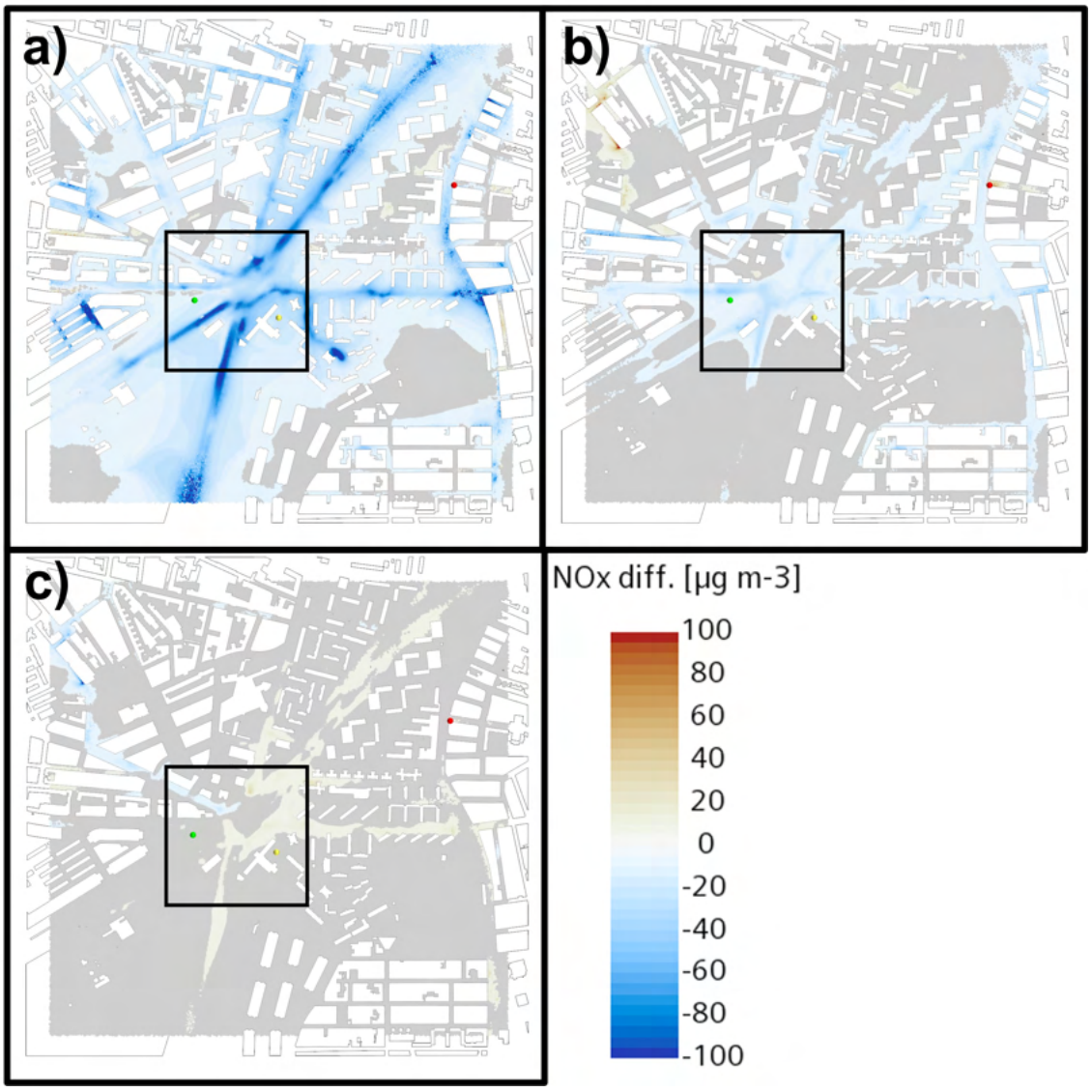

Figure 5.41: Differences of annual mean local contribution to [NO_X] between: a) 2019_Em19 and 2016_Em16; b) 2022_Em22 and 2019_Em19; c) 2023_Em23 and 2022_Em22. Areas with differences lower than 5 $\mu g \cdot m^{-3}$ in absolute value are shaded in grey. AQMS, SVP and MP23 points marked with green, yellow and red points respectively. Black rectangle shows the limits of the 300 m x 300 m study area.

$$max(\Delta[NO_X]_{meteo}) = [NO_X]^i_{max} - [NO_X]^i_{min} \tag{5.11}$$

In addition, its is noteworthy that the maximum impact of the meteorological conditions not always is observed when comparing the "calmest" and the "windiest" conditions. This suggests the influence of other parameter but the wind speed in the impact of meteorological conditions on the effectiveness of a mitigation strategy. The impacts of each mitigation strategy on the 300 m x 300 m study area are larger in absolute values -but not in percentage- (Table 5.12). Similarly, the maximum computed impact of changing meteorological conditions in this subdomain are not negligible representing a 27.2 %, a 41.0% and a 79.2% of the mean impact of each mitigation strategy respectively. As in the case of the whole CFD domain, those are smaller than the net impacts of the strategies but not negligible.

Table 5.11: Spatial average across the CFD domain of changes in annually-averaged [NO_X] when comparing different emissions scenarios for each meteorological condition.

Variation in the local contribution to annual mean NO_X concentrations $[\mu g \cdot m^{-3}]$ (% of local values)			
	Em19 vs Em16	Em22 vs Em19	Em23 vs Em22
Meteo 2016	-14.98 (-44.3)	-4.17 (-22.2)	+0.85 (+5.8)
Meteo 2019	-15.44 (-46.0)	-3.86 (-21.3)	+0.71 (+5.0)
Meteo 2022	-14.61 (-45.0)	-4.02 (-22.5)	+0.82 (+6.0)
Meteo 2023	-15.40 (-45.4)	-4.11 (-22.2)	+0.61 (+4.2)
Meteo "calmest"	-17.49 (-44.4)	-5.09 (-23.2)	+0.45 (+2.7)
Meteo "windiest"	-13.26 (-43.6)	-3.99 (-23.3)	+0.29 (+2.2)
Meteo effect	-13.26 (-43.6)	-3.99 (-23.3)	+0.29 (+2.2)

Table 5.12: Spatial average across the the 300 m x 300 m study area of changes in annually-averaged [NO_X] when comparing different emissions scenarios for each meteorological condition.

Variation in local contribution to annual mean NO_X concentrations $[\mu g \cdot m^{-3}]$. 300 m x 300 m subdomain. (% of local values)			
	Em19 vs Em16	Em22 vs Em19	Em23 vs Em22
Meteo 2016	-28.67 (-44.0)	-8.33 (-22.8)	+1.88 (+6.7)
Meteo 2019	-29.50 (-45.6)	-7.79 (-22.1)	+1.58 (+5.76)
Meteo 2022	-28.11 (-44.8)	-8.00 (-23.1)	+1.82 (+6.8)
Meteo 2023	-29.51 (-45.2)	-8.18 (-22.9)	+1.3 (+5.0)
Meteo "calmest"	-32.06 (-42.5)	-11.37 (-26.3)	+1.20 (+3.8)
Meteo "windiest"	-24.24(-41.7)	-8.73 (-25.7)	+0.69 (+2.7)

Figure 5.42 shows the impact of each strategy mitigation for each meteorological conditions in the points AQMS, SVP and MP23. It can be observed that the impacts of each strategy is

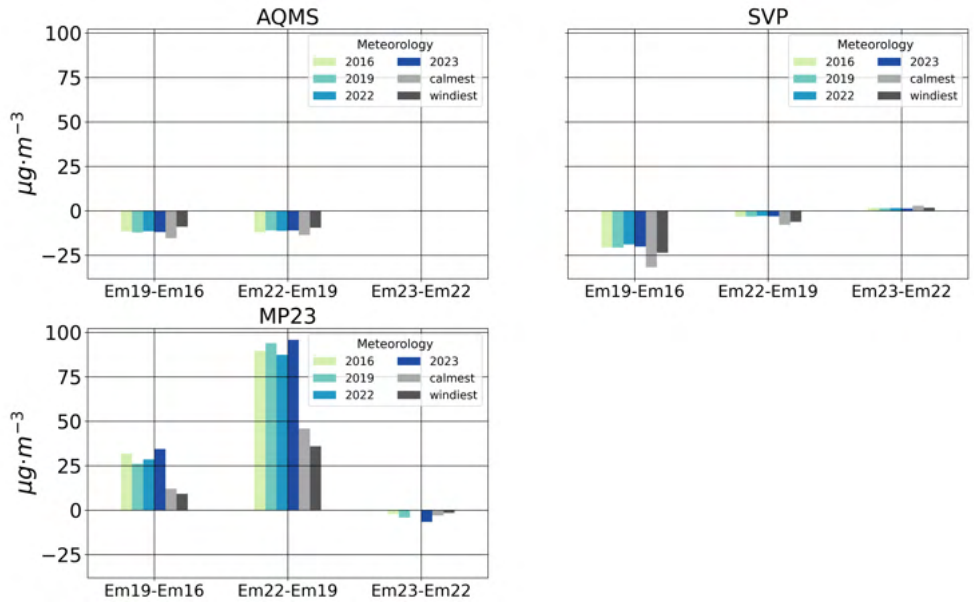

Figure 5.42: Impact of different air mitigation strategies on annual averaged [NO_X] in three points of the CFD domain for each meteorological conditions and emissions case.

highly dependent of the location of each point. In the AQMS location, both the introduction of changes in the road network (Em19 vs Em16) and the implementation of a LEZ (Em22 vs Em19) reduce the annual [NO_X] about 12 $\mu g \cdot m^{-3}$ in average. In both cases, the largest impact is modelled with the "calmest" conditions and the lowest, with the "windiest" conditions, which also had the highest and lowest concentrations for each emissions case. No significant change in air quality is seen when comparing the Em23 scenario with the Em22 scenario. The differences in the effectiveness of the each strategy are lower than the net effect of both strategies, representing a 54% of the average net effect of the strategy for the road management strategy, and a 36% of the average net effect for the LEZ implementation strategy.

In the SVP point, the two first strategies imply a reduction in [NO_X] concentrations, of about 22 and 4 $\mu g \cdot m^{-3}$ in average respectively, whereas the removal of pandemic-related mobility restrictions (Em23 vs Em22) leads to slightly larger concentrations (about 1 $\mu g \cdot m^{-3}$). Again, the largest impacts are observed with the meteorological conditions with largest concentrations, and vice-versa. As it was modelled for the AQMS location, the impact of the effectiveness of the mitigation strategy consisting on actuations on the traffic network with a change in vehicle fleet (i.e., when comparing Em19 with Em16) varies 12 $\mu g \cdot m^{-3}$ due to the change in meteorological conditions, which is a 43% lower than the average net impact of the mitigation strategy. However, for the LEZ implementation and the removal of mobility restrictions, the impacts that changing the meteorological conditions induce in air quality is comparable to -or even larger than- the impacts of those strategies. In particular, changing meteorological conditions affect the impact of the LEZ strategy in this point by 5

$\mu g \cdot m^{-3}$, which is a 12% larger than the net average impact of this strategy (4.43 $\mu g \cdot m^{-3}$). For the COVID-19-related strategy, the impact of meteorological conditions represents a 90% of the average variation due to that strategy.

Finally, for the MP23 point, a notable increase of annual [NO_X] is observed when implemented the LEZ. This large increase is associated to an increase in traffic emissions in that area (Figure 5.12). In this case, the variability in the effectiveness of the measure is comparable to the average net impact of the measure for the first two first strategies (a 94% and a 80% of their average net impact) and twice larger than the impact of the end of the mobility restrictions.

5.4.3 The impact of meteorological conditions on monthly NO_X concentrations

As mentioned before, albeit the annually-averaged meteorological conditions are quite similar between each simulated year, there are substantial differences in monthly values. The month with the largest variability in meteorological conditions is February (Figure 5.23). In addition, February is a winter month, when air pollution problems are more likely to arise in Spain. Therefore this month will be use to describe the potential impacts of meteorological conditions on monthly NO_X concentrations.

The monthly-averaged modelled wind roses for each simulated month are illustrated in Figure 5.43. It can be seen how February 2016 had the largest frequency of winds above 2 $m \cdot s^{-1}$ of all the simulated months. On the other hand, February 2019 show a large frequency of low speed winds. In addition, the wind directions are highly variable. Meanwhile February 2016 shows a predominance of westerly winds (specially SW, WSW and NW), 2022 and 2023 show a predominance of easterly winds, with the NE being the most common wind direction. On the other hand, 2019 shows a bidirectional pattern, with predominance of NW and SE winds.

Figure 5.44 shows the spatial distribution of the monthly-averaged [NO_X] for the month of February corresponding to the real scenarios 2016_Em16, 2019_Em19, 2022_Em22 and 2023_Em23. The scenario which presents larger concentrations is the 2019_Em19 -despite the emissions of the Em19 case being 50% those of the Em16 case-, with large areas approaching or exceeding a monthly mean value of 200 $\mu g \cdot m^{-3}$. This is in part due to a larger contribution of background concentrations, but also the local contribution to the monthly average of [NO_X] is the largest in the 2019_Em19 scenario (Table 5.13), which indicates a larger impact of meteorological conditions on [NO_X] than the change in emissions between 2016_Em16 and 2019_Em19 scenarios.

The implementation of the LEZ (Em22 vs Em19) had an impact of -11.64 $\mu g \cdot m^{-3}$ on

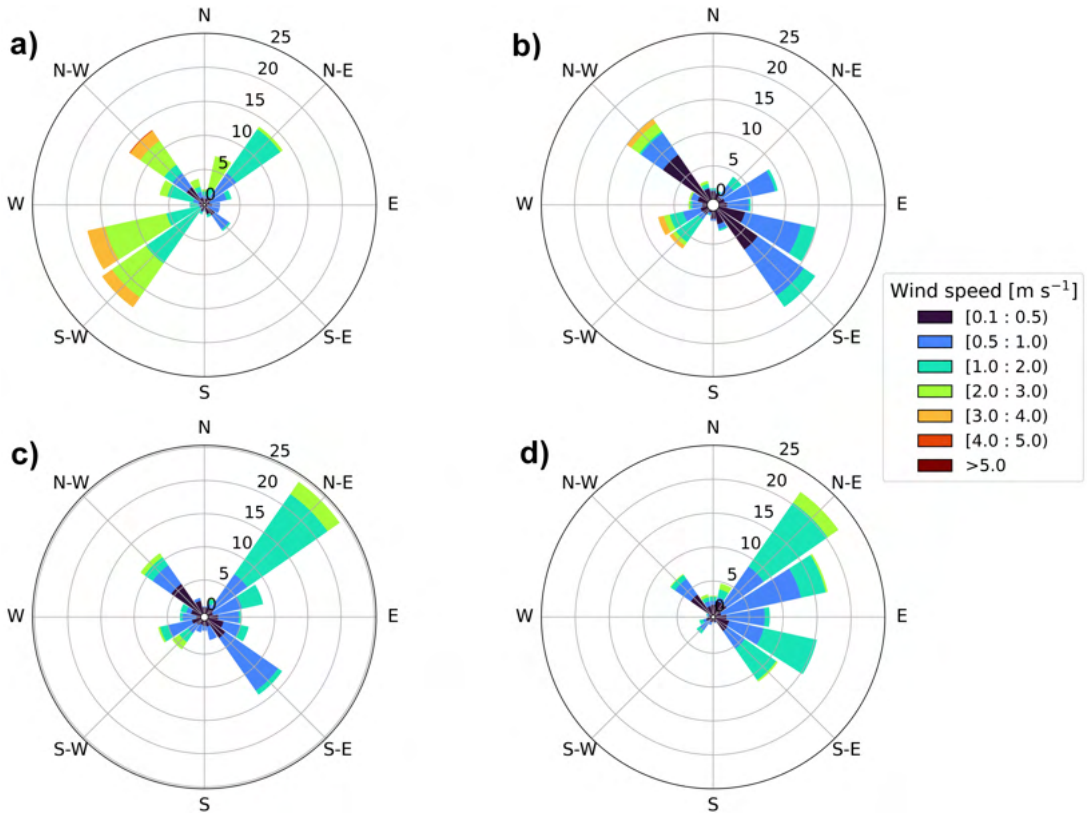

Figure 5.43: February-averaged modelled wind roses. a) February 2016; b) February 2019; c) February 2022; and d) February 2023.

Table 5.13: Spatial average across the CFD domain of monthly-averaged [NO_X] contributions.

Monthly-averaged [NO_X] [$\mu g \cdot m^{-3}$]					
Scenario	Background	Local	Total	Local STD	Local contribution to [NO_X] (%)
2016_Em16	65.90	34.70	100.61	15.51	34.49
2019_Em19	109.00	39.26	148.26	12.51	26.48
2022_Em22	71.01	27.62	98.64	7.84	28.00
2023_Em23	63.56	23.28	86.84	6.10	26.81

Table 5.14: Spatial average across the CFD domain of changes in monthly-averaged [NO_X] when comparing different emissions scenarios for each meteorological condition.

Variation in spatially averaged monthly mean NO_X concentrations [$\mu g \cdot m^{-3}$] (% of local values)			
	Em19 vs Em16	Em22 vs Em19	Em23 vs Em22
Meteo 2016	-12.43 (-35.8)	-6.14 (-27.6)	0.55 (+3.4)
Meteo 2019	-27.43 (-41.1)	-8.28 (-21.1)	1.13 (+3.6)
Meteo 2022	-21.94 (-36.6)	-10.41 (-24.2)	1.20 (+4.4)
Meteo 2023	-16.73 (-35.4)	-8.37 (-27.4)	1.09 (+4.9)

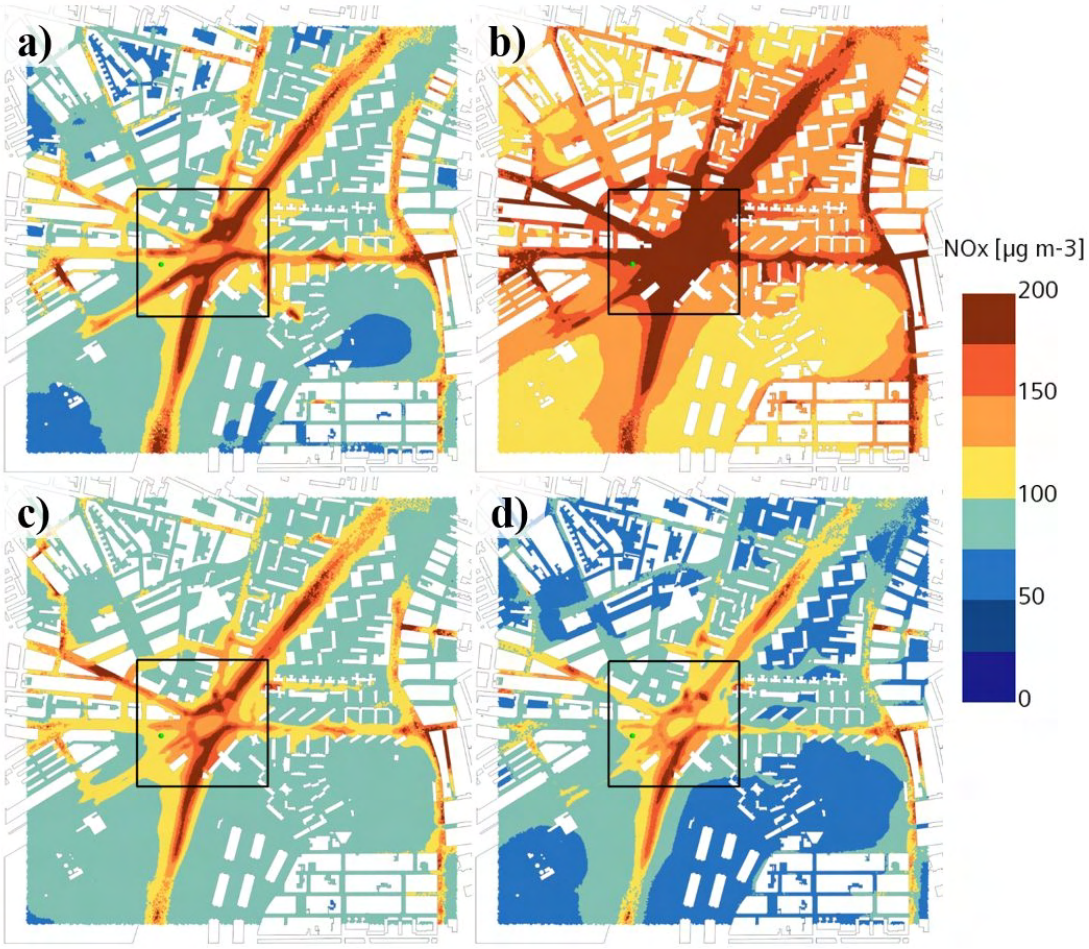

Figure 5.44: Maps of the modelled February-averaged NO_X concentration values along the CFD model domain for scenarios: a) 2016_Em16; b) 2019_Em19; c) 2022_Em22; and d) 2023_Em23. Inner black square indicates a study area of 300 m x 300 m used in previous works.

monthly-averaged local concentrations when evaluating it using different meteorological conditions (2022_Em22 vs 2019_Em19 in Table 5.13). However, when comparing using the same meteorological conditions, its impact ranges between -6.14 and -10.41 $\mu g \cdot m^{-3}$. That is a range of potential impacts of ±70% depending on the choice of the meteorological conditions (Table 5.14). In addition, this range of values is near the standard deviation of the emissions for those scenarios (Table 5.13). The impact of changing the meteorological conditions in the spatial averaged [NO_X] due to the full recovery of traffic flows after the pandemic ranges between 0.04 and 0.65 $\mu g \cdot m^{-3}$. The largest change in NO_X occurs, for every meteorological conditions, when comparing the emissions of 2016 with those of 2019, which is are the windiest and the calmest February months respectively. For the 300 m × 300 m study area, the impacts of the mitigation strategies are significantly larger in absolute values due to the removal of significant areas with no emissions (e.g., parks and pedestrian areas) (Table 5.15).

Table 5.15: Spatial average across the the 300 m x 300 m study area of changes in monthly-averaged [NO_X] when comparing different emissions scenarios for each meteorological condition.

Variation in monthly mean NO_X concentrations [$\mu g \cdot m^{-3}$]. 300 m x 300 m subdomain. (% of local values)			
	Em19 vs Em16	Em22 vs Em19	Em23 vs Em22
Meteo 2016	-21.94 (-40.0)	-7.26 (-22.1)	0.85 (+3.3)
Meteo 2019	-44.80 (-42.7)	-12.91 (-21.5)	1.19 (+2.5)
Meteo 2022	-40.78 (-42.7)	-12.00 (-21.9)	2.01 (+4.7)
Meteo 2023	-31.36 (-41.8)	-9.66 (-22.2)	2.04 (+6.0)

Figure 5.45 illustrates the sensitivity of the spatial distribution of February-averaged [NO_X] to meteorological conditions. It can be seen how different meteorological conditions induce large differences in the monthly averages of [NO_X]. The meteorological conditions of 2019 lead to the most polluted scenarios in every emissions case. For the Em16 emissions case, those meteorological conditions increase the [NO_X] in more than 75 $\mu g \cdot m^{-3}$ inside the most emitter roads, (including the roundabout, the motorway, and Streets 1, 2 and 5 (Figure 5.33)) and in the order of 25-50 $\mu g \cdot m^{-3}$ in the rest of the domain, when comparing with the 2016 meteorological conditions. The meteorological conditions of 2022 also induce notable increments of NO_X with respect to those of 2016, but the increments are limited to the main emitter roads. On the other hand, the 2023 meteorological conditions increase the concentrations on the western part of the domain, and Street 5, but induces some reductions in the eastern part of the domain. This polarized pattern can be explained by the changes in the predominant wind directions between 2016 and 2023. February 2023 has a predominance of NE winds that, together with the interaction of the mean flow with the urban morphology, favours the ventilation of the NE cuadrant of the domain and the accumulation of pollutants

into the SW cuadrant. On the other hand, February 2016 has a predominance of SW winds, which favours the dispersion of pollutants into the NE cuadrant of the study domain (Figure 5.46). That is why some reductions are observed in the 2023_Em16 case with respect to the 2016_Em16 case, despite having lower wind speeds than the 2016 meteorological conditions.

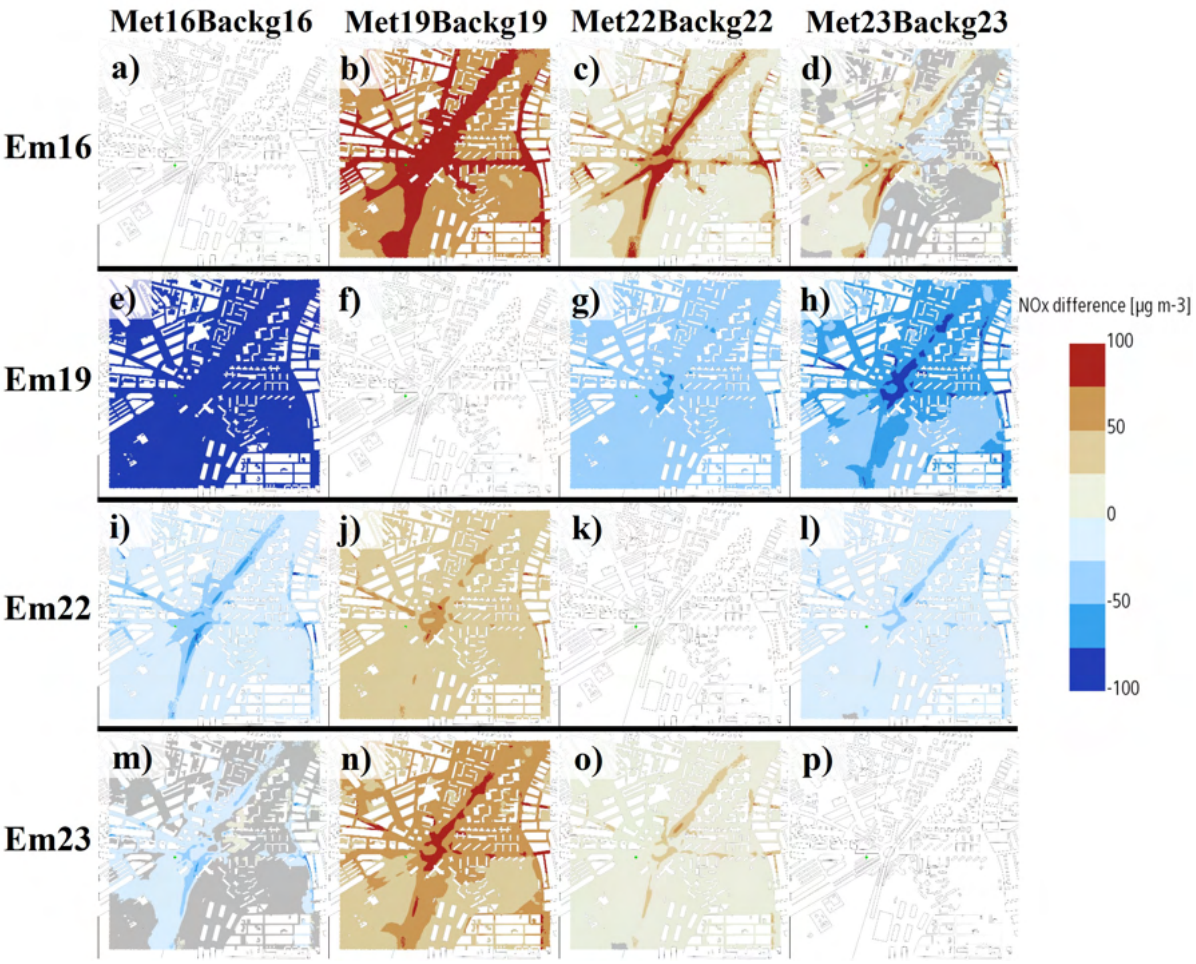

Figure 5.45: Maps of the modelled differences between the base case and different meteorological conditions for February-averaged NO_X concentration values along the CFD model domain for scenarios: a) 2016_Em16; b) 2019_Em19; c) 2022_Em22; and d) 2023_Em23.

The spatially-averaged impact of the meteorological conditions monthly-averaged local $[NO_X]$ for each emissions case is illustrated in Table 5.16. Albeit the impact is emission-dependent, the impact of meteorological conditions be comparable or even overcome the impacts of changes in emissions (Table 5.14). This contrasts with the findings in annual values, where the meteorological impacts in $[NO_X]$ were lower than those of the mitigation strategies. When analysing the impacts of the meteorological conditions within three points in the domain, it can be observed that in the AQMS and SVP points the impact of the change of meteorological conditions has a lower impact on the monthly $[NO_X]$ than the uncertainty of the emissions. However, there are cases for the MP23 point where the opposite occurs. For example, the variation in $[NO_X]$ due to the change of meteorological conditions from

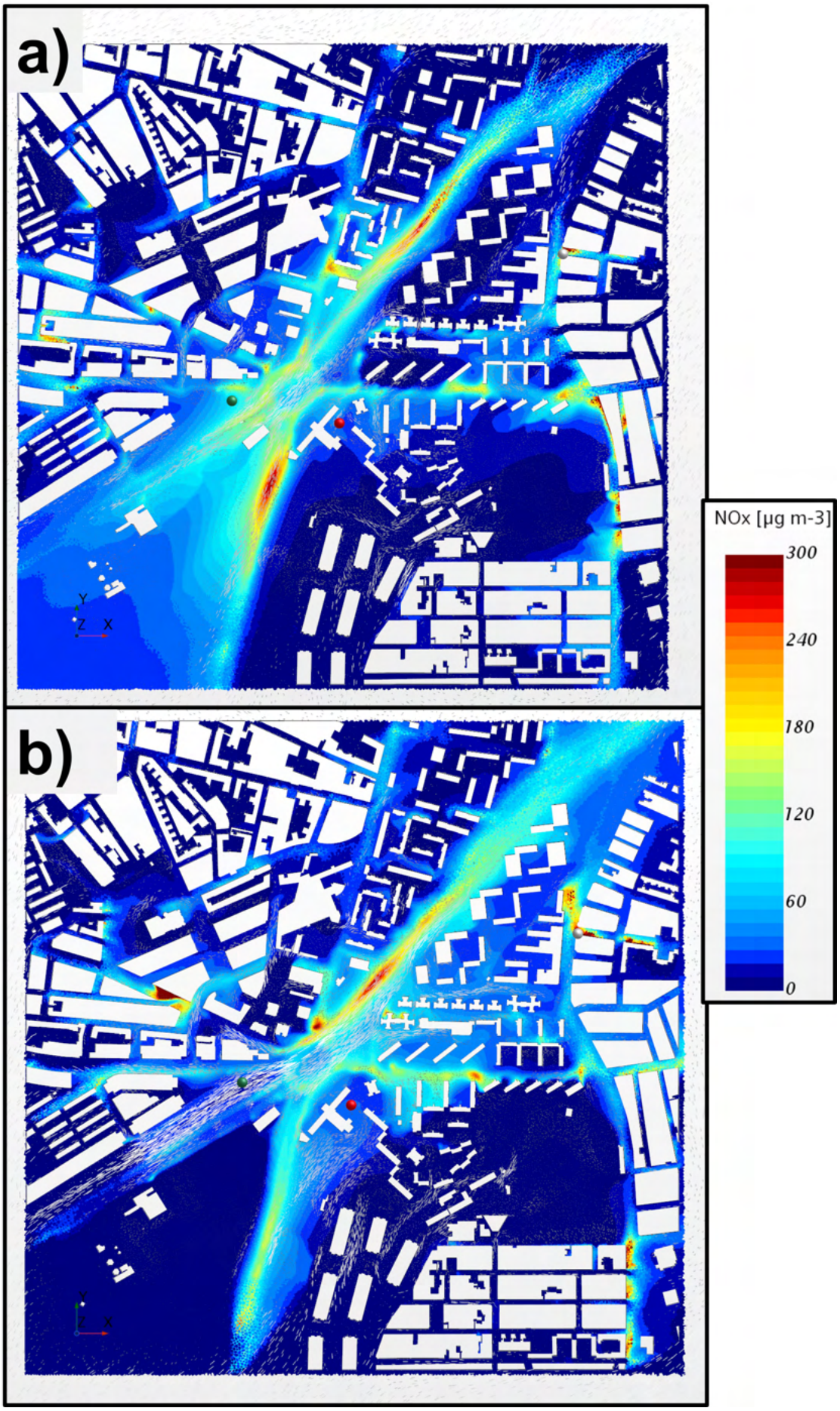

Figure 5.46: Maps of NO_X distribution and windspeed for two scenarios: a) Predominant wind flow from NE; b) Predominant wind flow from SW.

2016 to 2019 for the Em19 and Em23 emission cases is greater than the standard deviation in $[NO_X]$.

Table 5.16: Spatial average of changes in monthly-averaged $[NO_X]$ when comparing different meteorological conditions for each emissions case.

	Variation in spatially averaged monthly mean NO_X concentrations $[\mu g \cdot m^{-3}]$ (% of local values)					
	2016 vs 2019	2016 vs 2022	2016 vs 2023	2019 vs 2022	2019 vs 2023	2022 vs 2023
Em16	-25.3 (-46.8)	-20.71 (-41.9)	-9.55 (-26.8)	+4.60 (+9.3)	+15.77 (+41.1)	+11.17 (+29.1)
Em19	-13.73 (-44.6)	-11.16 (-39.6)	-5.21 (-24.2)	+2.57 (+9.1)	+8.52 (+38.3)	+5.95 (+26.7)
Em22	-10.89 (-44.8)	-8.77 (-39.6)	-3.97 (-22.1)	+2.12 (+9.6)	+6.92 (+39.8)	+4.79 (+27.6)
Em23	-11.01 (-44.3)	-9.31 (-40.2)	-4.44 (-24.7)	+1.70 (+7.3)	+6.57 (+36.0)	+4.87 (+26.7)

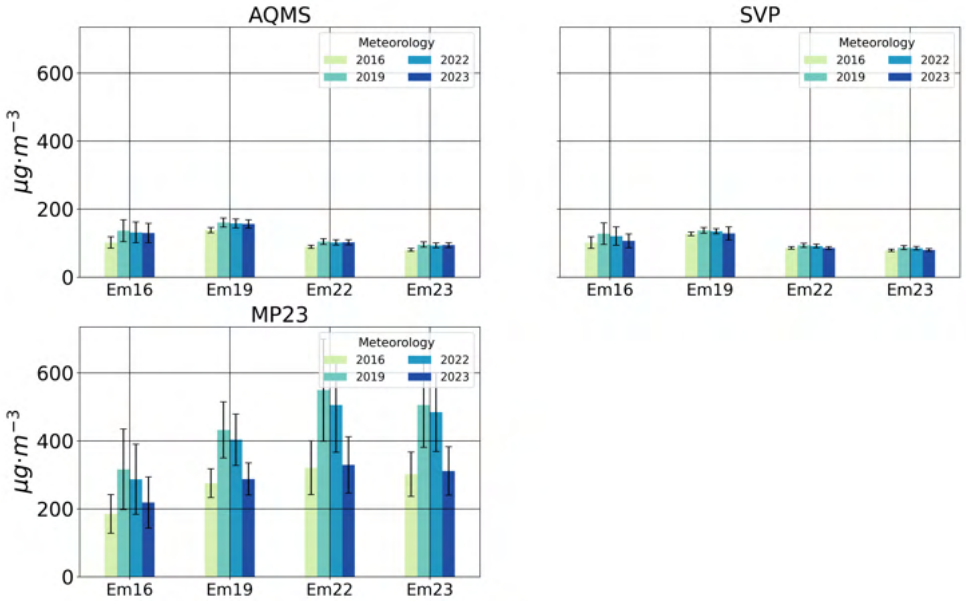

Figure 5.47: February average of $[NO_X]$ in three points of the CFD domain for each meteorological conditions and emissions case. Spines indicate the standard deviation of $[NO_X]$.

5.4.4 The impact of meteorological conditions on exceedances of NO_2 annual limit values and annual SRA

To compute NO_2 concentrations, the methodology described in Section 3.3.3 has been followed to transform the previously analysed NO_X concentrations into NO_2 concentrations.

Figure 5.48 illustrates the spatial distribution of the annual mean value of NO_2 for the real scenarios. The spatial distributions are quite similar to those of the annual $[NO_X]$ with the highest values inside the most emitter roads. Modelled annual concentrations of NO_2 have been decreasing with time from the scenario 2016_Em16 to the 2022_Em22. Then, in 2023 they remained almost the same as in 2022. In the scenario 2016_Em16 every point inside the

CFD domain exceeded the 40 $\mu g \cdot m^{-3}$ established by Directive 2008/EC/50. In 2019, the exceedances area reduced almost a 40% as green zones and some inner blocks were no longer exceeding that limit value. In the scenarios 2022_Em22 and 2023_Em23 the exceedances were limited to the streets with the highest emissions. In all of the four scenarios, the limit of 20 $\mu g \cdot m^{-3}$ for annual [NO_2] proposed by Directive 2024/2881 was exceeded in the whole domain. On the other hand, the maximum value of annual [NO_2] inside the domain increases since 2019. The reason is the deviation of traffic due to the implementation of the LEZ, which increases traffic flows -and therefore pollutants emissions- in the area of the domain where the maximum value occurs.

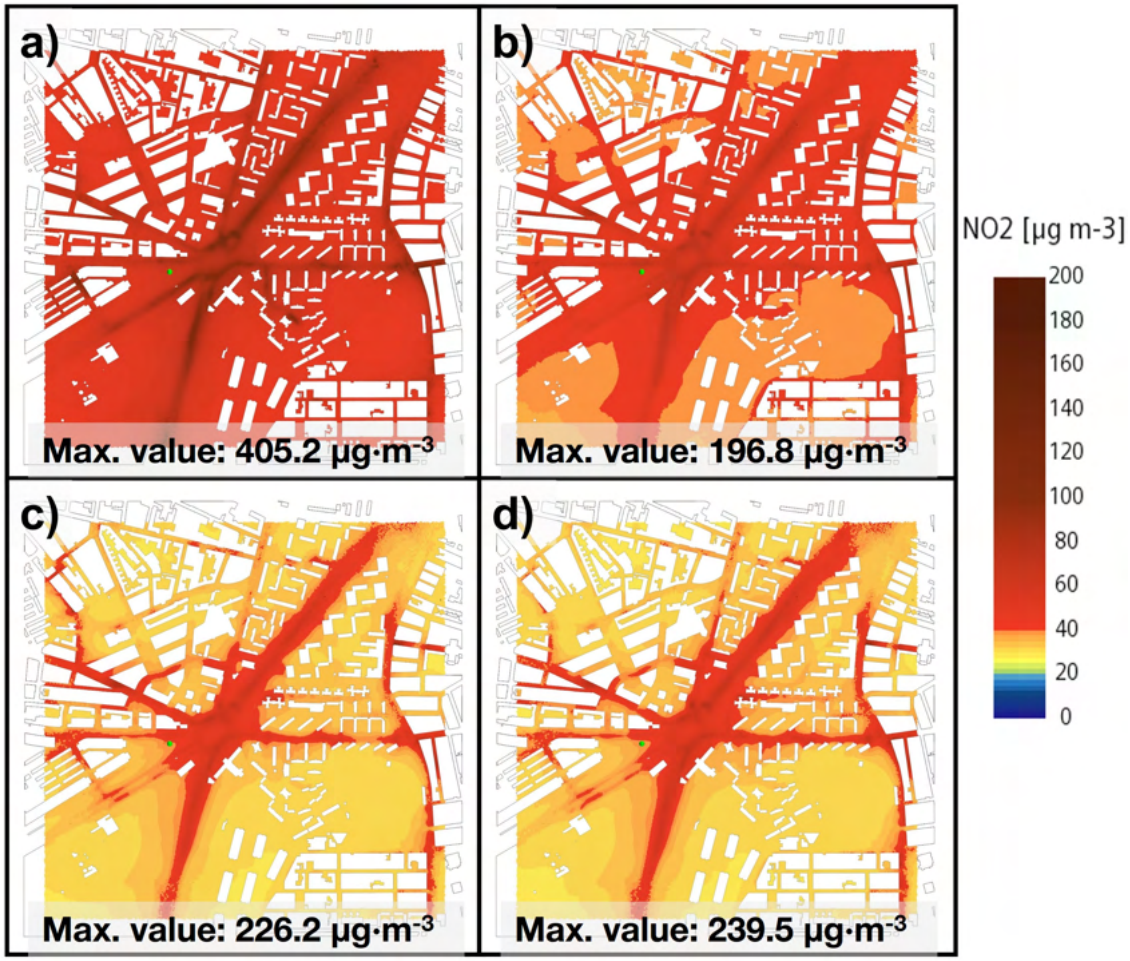

Figure 5.48: Maps of the modelled annually-averaged [NO_2] along the CFD model domain for scenarios: a) 2016_Em16; b) 2019_Em19; c) 2022_Em22; and d) 2023_Em23. Green point indicates the location of the AQMS station. Maximum value indicated at the lower part of each subfigure.

In order to analyse the sensitivity of NO_2 concentrations to the meteorological conditions, it is important to estimate the impact of the changes in meteorological conditions on the background NO_X concentrations, as they will affect the computation of NO_2. To estimate the impact of the changes in meteorological conditions on the background concentrations, a simple methodology has been developed. Assuming that local and

background concentrations are equally affected by the meteorology and neglecting external effects such as intra-annual changes in emissions, a month is set as reference and a linear relation between the monthly-averaged annual change of background ($\Delta[NO_X]_{back}$) and spatial-averaged local ($\Delta[NO_X]_{local}$) concentrations for a certain year is aimed for:

$$\Delta[NO_X]_{back} = A \cdot \Delta[NO_X]_{local} + B \tag{5.12}$$

Then, this relation is applied to compute the background concentrations for the same set of local emissions but different meteorological conditions. The computation of the meteorology-modified background concentrations for each month of the year j can be expressed as in Equation 5.13.

$$Adjusted\ [NO_X]^j_{back} = [NO_X]^j_{back} + A \cdot \Delta[NO_X]^j_{local} + B \tag{5.13}$$

$\Delta[NO_X]^j_{back}$ is the variation of the background [NO_X] between the reference month and the month of the computation; A and B are the slope and the intercept, respectively, of the linear regression described by Equation 5.12. Figure 5.49 summarizes this procedure. In this example, the month of January is set as reference month to compute $\Delta[NO_x]_{local}$ and $\Delta[NO_x]_{back}$. The same linear regression parameters would have been obtained if using another different month of the year as reference. When comparing with the observations, this methodology provides satisfactory results for the annual averaged values of background NO_2 concentrations (Table 5.17).

Annual-averaged [NO_2] background concentrations.			
	Observed	**Computed**	**Relative error (%)**
2016	63.85	64.32	0.73
2019	54.61	54.57	-0.08
2022	41.50	41.39	-0.27
2023	40.93	40.95	0.06

Table 5.17: Annual-averaged NO_2 background concentrations [$\mu g \cdot m^{-3}$] (in this work, background concentrations are considered those observed in Farolillo urban background AQMS) and computed using the aforementioned methodology.

The annual mean [NO_2] averaged along the whole CFD domain for each scenario is shown in Figure 5.50. In the upper figure, no impact of meteorological conditions are considered in the background concentrations (i.e., background concentrations are constant for each emissions case), whereas in the lower figure the impacts of meteorological conditions on the background concentrations are considered as explained in the previous paragraph. It can be seen that the impact of meteorological conditions is larger when considering their impact on the background concentrations. Their impact on the annual value of NO_2 exceed

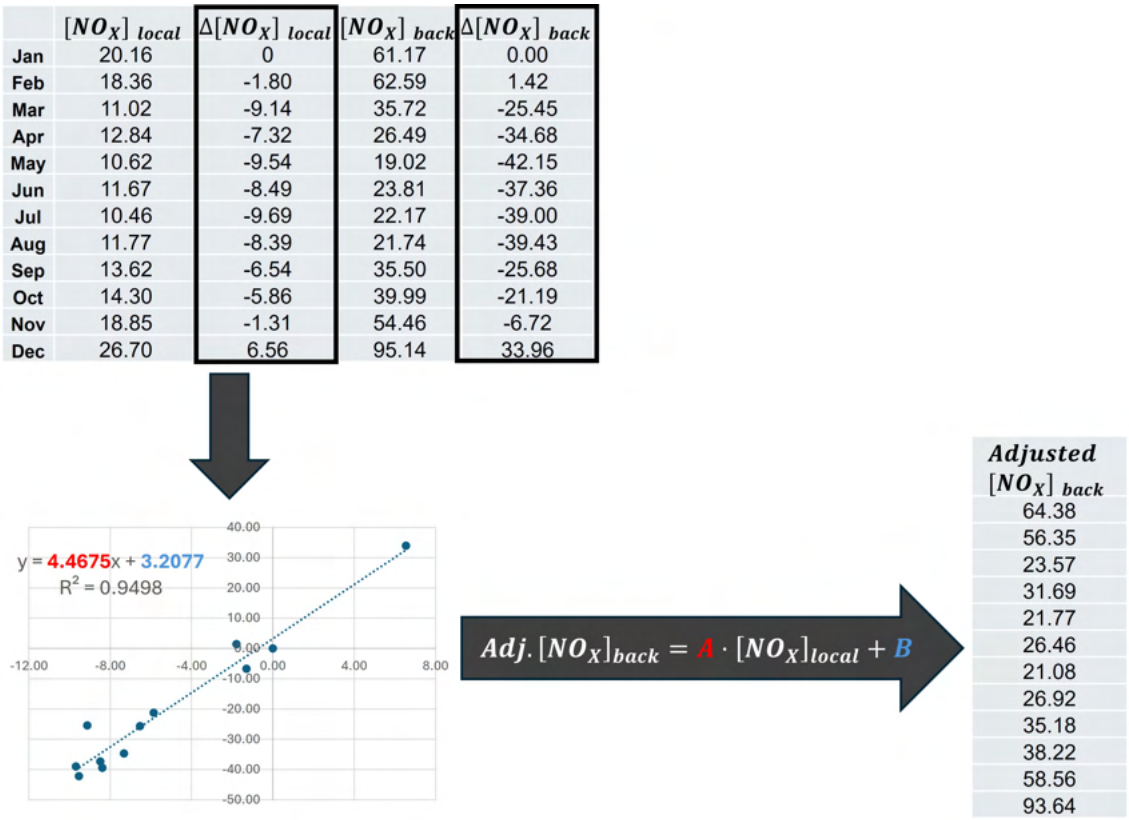

	$[NO_X]$ local	$\Delta[NO_X]$ local	$[NO_X]$ back	$\Delta[NO_X]$ back	Adjusted $[NO_X]$ back
Jan	20.16	0	61.17	0.00	64.38
Feb	18.36	-1.80	62.59	1.42	56.35
Mar	11.02	-9.14	35.72	-25.45	23.57
Apr	12.84	-7.32	26.49	-34.68	31.69
May	10.62	-9.54	19.02	-42.15	21.77
Jun	11.67	-8.49	23.81	-37.36	26.46
Jul	10.46	-9.69	22.17	-39.00	21.08
Aug	11.77	-8.39	21.74	-39.43	26.92
Sep	13.62	-6.54	35.50	-25.68	35.18
Oct	14.30	-5.86	39.99	-21.19	38.22
Nov	18.85	-1.31	54.46	-6.72	58.56
Dec	26.70	6.56	95.14	33.96	93.64

Figure 5.49: Schematic representation of the procedure to compute the impact of changing meteorological conditions in background $[NO_X]$.

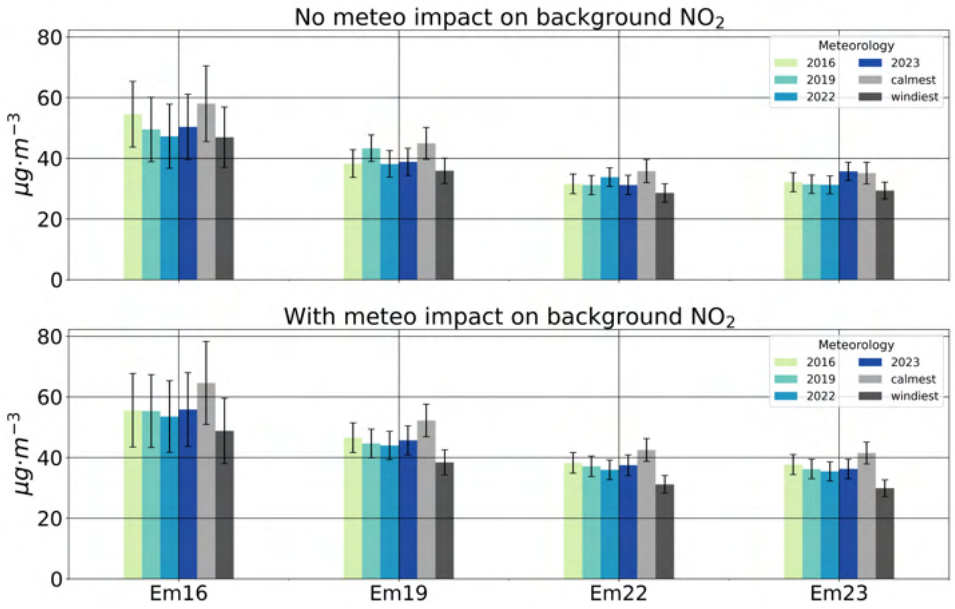

Figure 5.50: Annual average of $[NO_2]$ along the CFD domain for each scenario. Above: With no impact of meteorological conditions in background NO_2 concentrations. Below: With impact of meteorological conditions in background NO_2 concentrations.

the uncertainty range due to the emissions computation when considering the impact of meteorological conditions on background concentrations.

Figure 5.51 shows the change in the fraction area exceeding the 40 and 20 $\mu g{\cdot}m^{-3}$ limit values for annual NO_2 due to the uncertainty in emissions, for each real scenario and considering the impact of meteorological conditions on the NO_2 background concentrations. When taking into account the standard deviation of the emissions, no impact its observed in the area with exceedances of the 20 $\mu g \cdot m^{-3}$ limit. However, the uncertainty on emissions has a significant impact on the fraction area with exceedances of the 40 $\mu g \cdot m^{-3}$ limit in all scenarios but the 2016_Em16. In the 2019_Em scenario the area of exceedances can vary from 80% to 30% when considering the standard deviation of the emissions. The range of areas decreases with time, but still the standard deviation of emissions induce large uncertainty in the fraction area exceeding the annual limit of 40 $\mu g \cdot m^{-3}$ for NO_2.

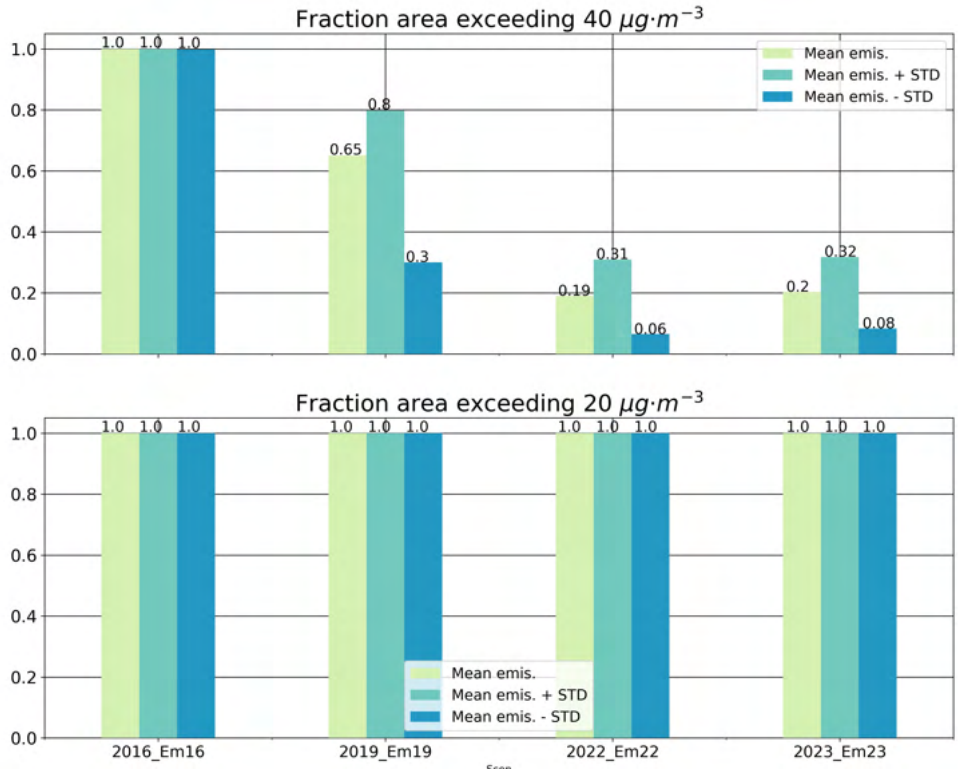

Figure 5.51: Fraction area exceeding annual limit values for NO_2 for each real scenario, considering the standard deviation in emissions. Above: Fraction area exceeding annual limit value of 40 $\mu g \cdot m^{-3}$. Below: Fraction area exceeding annual limit value of 20 $\mu g \cdot m^{-3}$.

Figure 5.52 shows the spatial distribution of the fraction area exceeding 40 $\mu g \cdot m^{-3}$ for the Em19 scenarios for several cases. The upper left map corresponds to the 2019_Em19+STD scenario, whereas the upper right map corresponds to the 2019_Em19-STD scenario. The lower left map corresponds to the calmest_Em19 scenario and the lower right map to the windiest_Em19. It can be seen that the changing in meteorological conditions has a larger

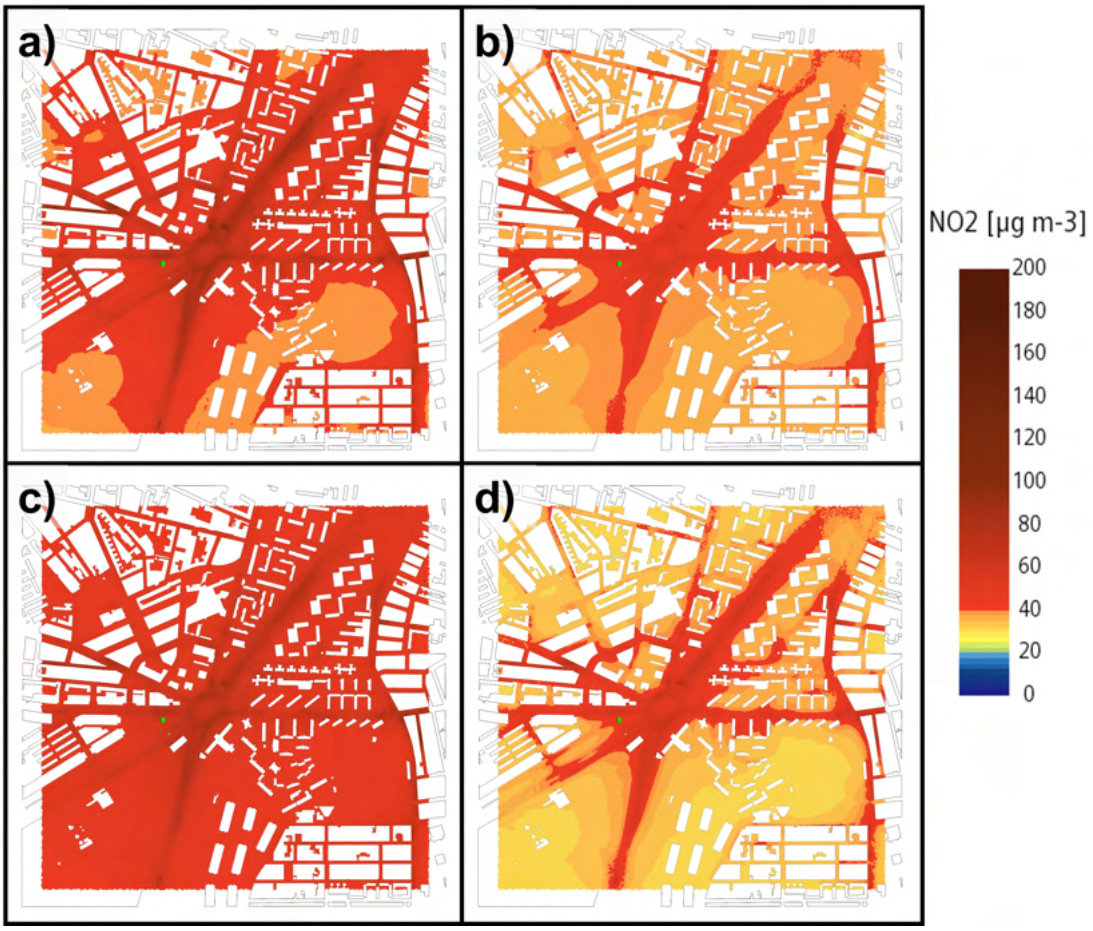

Figure 5.52: Maps of modelled annually-averaged [NO_2] along the CFD model domain for scenarios: a) 2019_Em19+STD; b) 2019_Em19-STD; c) calmest_Em19; and d) windiest_Em19. Green point represents the location of the PE AQMS.

impact on the spatial distribution of annual [NO_2] -and, therefore, on the fraction area exceeding 40 $\mu g \cdot m^{-3}$- than the uncertainty on emissions computation.

Figure 5.53 shows the fraction area exceeding the annual mean value of 40 $\mu g \cdot m^{-3}$ for NO_2 for different meteorological conditions, and for different emissions configurations. In all cases, changing the meteorological conditions results in significant changes in the exceedances area. Even a small change in those conditions (as it is the case of the 2016, 2019, 2022 and 2023 meteorological conditions) can alter the fraction area exceeding an annual mean of 40 $\mu g \cdot m^{-3}$ by up to a 25%. When considering the windiest and the calmest conditions, the reductions are much larger. The most extreme case is modelled for the Em19 scenario, where the fraction area exceeding 40 $\mu g \cdot m^{-3}$ can change from 100% to less than 10% if considering the lowest emissions within their uncertainty range. The impact of the meteorological conditions is in all cases at least comparable to the impact of the uncertainty in emissions, even larger in some cases.

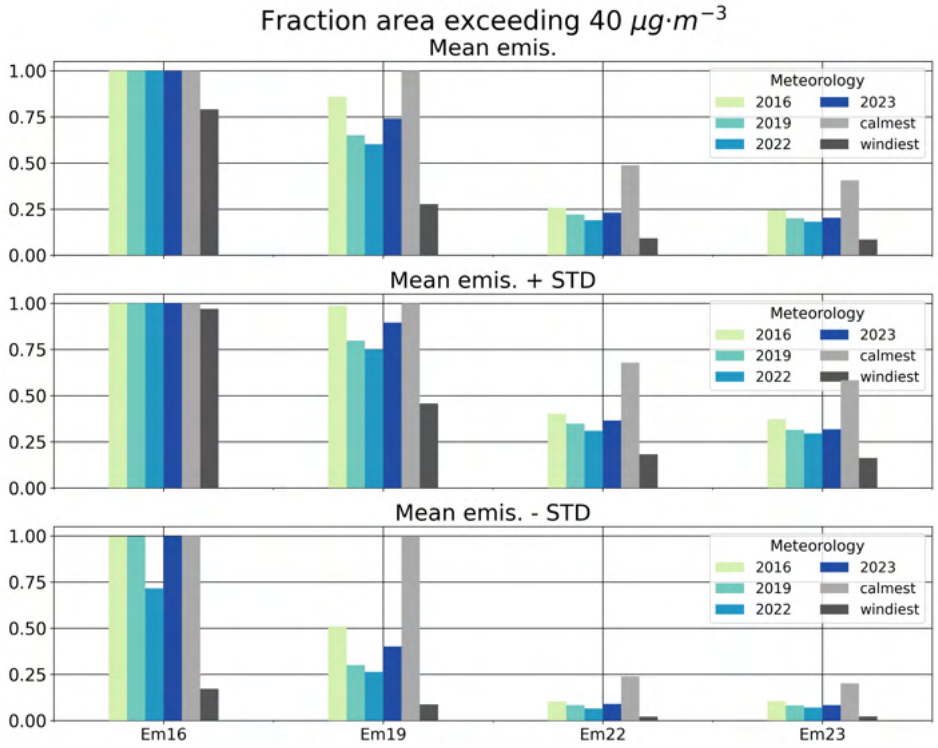

Figure 5.53: Fraction area exceeding annual limit value of 40 $\mu g \cdot m^{-3}$ for NO_2 for each scenario and meteorological conditions using different emissions configuration. Above: Mean emissions. Centre: Mean emissions + STD. Below: Mean emissions - STD

On the other hand, when the impact of the change of meteorological conditions in background concentrations the impacts of the meteorological conditions are notably reduced, remaining the areas of exceedances nearly constant across every the meteorological conditions 5.54). This contrasts with the high variability found when considering the impacts on the background concentrations (Figure 5.53).

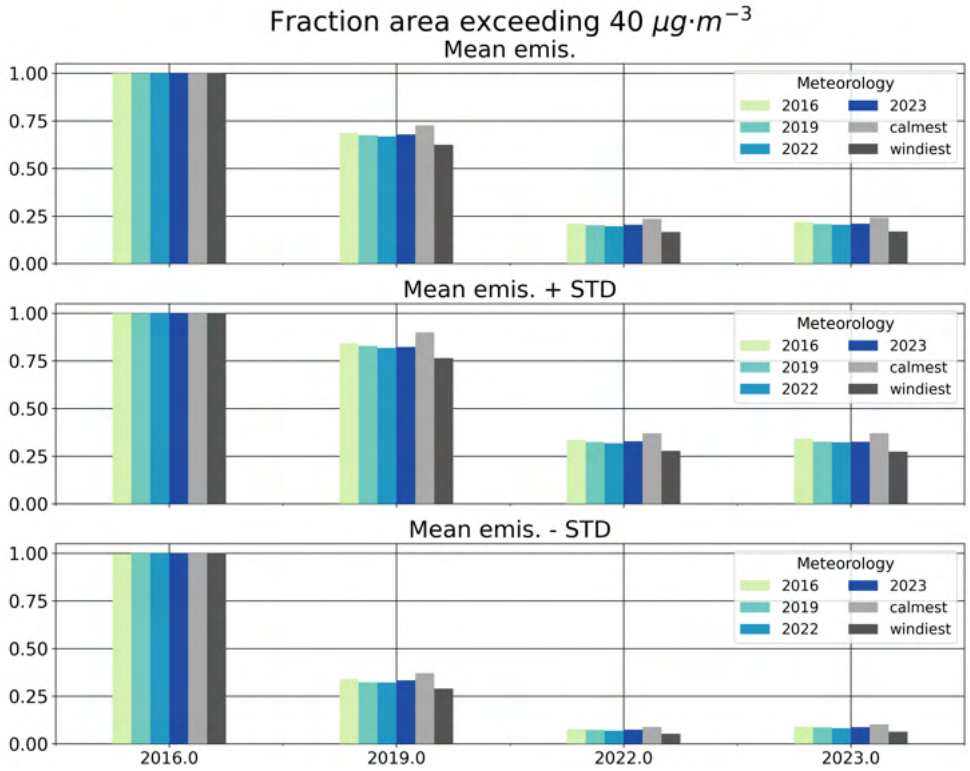

Figure 5.54: Fraction area exceeding annual limit value of 40 $\mu g \cdot m^{-3}$ for NO_2 for each scenario and meteorological conditions using different emissions configuration. Above: Mean emissions. Centre: Mean emissions + STD. Below: Mean emissions - STD

Regarding the station representativeness area (SRA), Figure 5.56 shows the SRA of the PE AQMS superposed in grey to the mean annual NO_2 concentrations, for each real scenario. The SRA is supposed to be the area where the mean annual [NO_2] is within a certain range of concentrations around the concentrations measured by an AQMS. In this work, a range of $\pm$20% the concentrations of the PE AQMS (hereafter as SRA20), and a range of $\pm$15% the concentrations of the PE AQMS (hereafter as SRA20) are used to analyse the SRA. These ranges are also used in previous works, such as Martín et al. (2025). In the case of SRA20, no significant changes are modelled between each real scenario, with the SRA covering most streets within the modelling domain with the main exceptions of the PE roundabout, the motorway, the green zones and some inner blocks. On the other hand, the SRA20 is limited to the most polluted streets (besides the motorway and the roundabout) and their adjacent areas (Figure 5.56).

Figure 5.57 shows the SRA for each real scenario considering their mean emissions, and their uncertainty ranges. For both cases -the SRA20 and SRA20- SRA increases with time. This is because SRA tends to increase with lower concentration values, as the ranges in [NO_2] narrow. This is also the case of when considering the uncertainty in emissions. For the cases with the lowest emissions (mean emissions minus their STD), the SRA is significantly larger than for the cases with larger emissions. When using the mean emissions in each scenario,

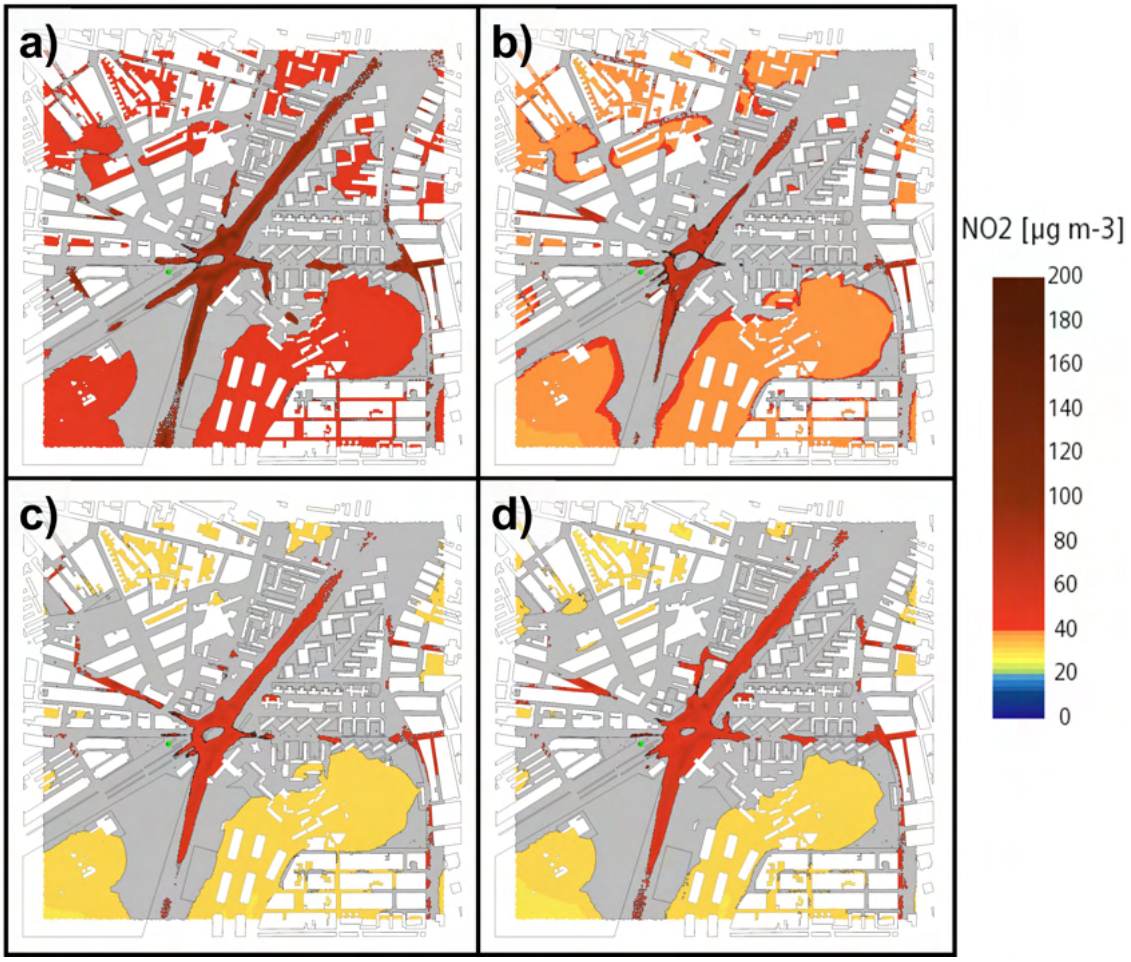

Figure 5.55: Modelled annually-averaged [NO_2] along the CFD model domain for each real scenario. Maps correspond to the following scenarios: a) 2016_Em16; b) 2019_Em19; c) 2022_Em22; and d) 2023_Em23. Grey area indicates the SRA20. Green point indicates the location of PE AQMS.

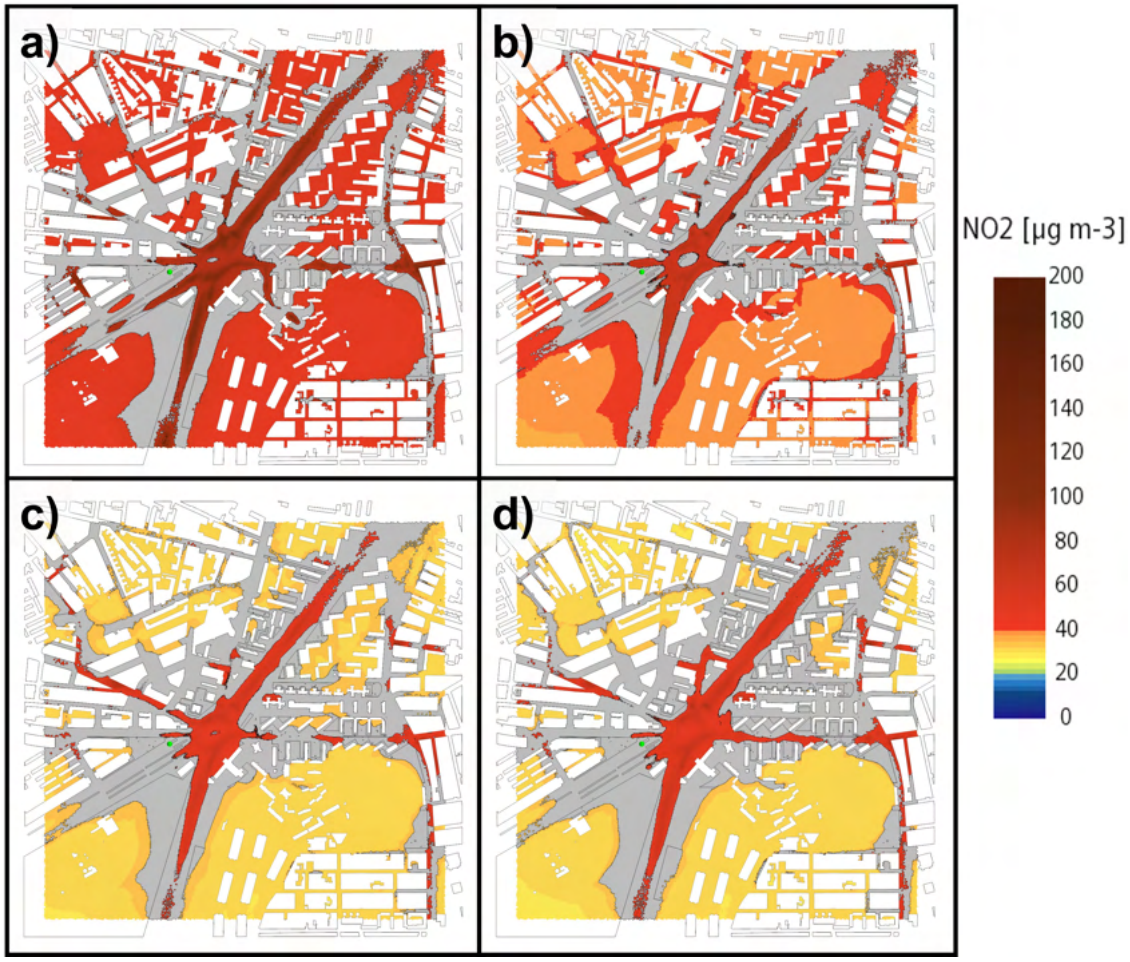

Figure 5.56: Modelled annually-averaged [NO_2] along the CFD model domain for each real scenario. Maps correspond to the following scenarios: a) 2016_Em16; b) 2019_Em19; c) 2022_Em22; and d) 2023_Em23. Grey area indicates the SRA15. Green point indicates the location of PE AQMS.

the SRA20 ranges between 55% and 67% , whereas the SRA20 ranges between 37% and 45%. However, for the case using the mean emissions minus their STD, the SRA increases to a range between 89% and 97%, and between 79% and 94% respectively. The cases with the largest emissions (i.e., the mean emissions plus their STD) has the lowest SRA, ranging between 28% and 48% for the SRA20 case, and the SRA20 between 20% and 31%.

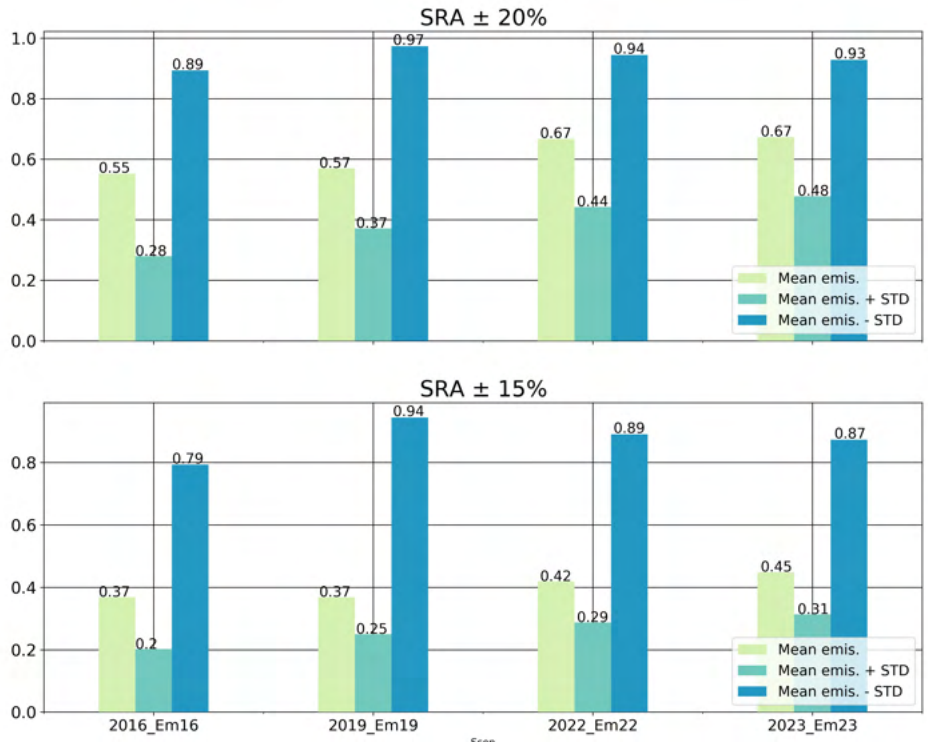

Figure 5.57: SRA of PE AQMS for annual NO_2 for each real scenario, considering the standard deviation in emissions. Above: SRA for ±20% the value of the AQMS. Below: SRA for ±15% the value of the AQMS.

When comparing the SRA for different meteorological conditions, no significant differences are observed. The changes in meteorological conditions affect in no more than a 7% the SRA20 (Figure 5.59) and the SRA20 (Figure 5.59), which is notably lower than the impact of the uncertainty in emissions. These findings are similar to those when no considering the impact of meteorological conditions on background concentrations.

5.5 Concluding remarks

This chapter is addressed to estimate the emissions related to the traffic patterns taking place in an urban area for several road network conditions, and to estimate the role that meteorological conditions play in their distribution and on the effectiveness of mitigation strategies. To that end, traffic-related emissions were computed by performing microscopic traffic simulations coupled to an instantaneous emissions model, and different meteorological

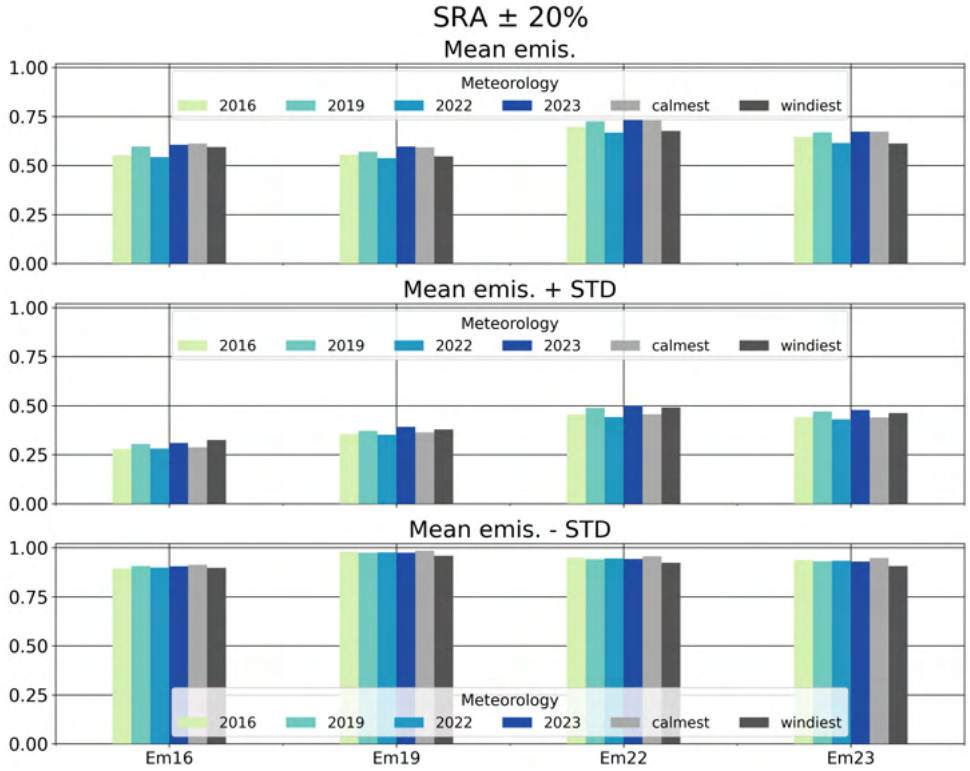

Figure 5.58: SRA20 of PE AQMS for annual NO_2 for each scenario and meteorological conditions using different emissions configuration. Above: Mean emissions. Centre: Mean emissions + STD. Below: Mean emissions - STD.

conditions were computed using the mesoscale meteorological model WRF.

In first place, the simulated weekly traffic pattern is compared with observational data along the simulation domain. The evaluation of the modelled data showed a good agreement with the observed traffic flows. Only some underestimation of the traffic flows are found for 2019, and the weekend days of 2016. Using these simulations the spatial distribution of traffic-related emissions could be obtained. In all simulations and scenarios, the most polluted areas are the PE roundabout and the motorway traversing it. In addition, emissions have progressively declined between 2016 and 2022. Then, after the total recovery of traffic flows post the pandemic, emissions of 2023 were slightly larger than those of 2022 during the weekend scenarios. The uncertainty in emissions due to their computation procedure was also computed, which is also reduced when the number of traffic count stations increased. After that, the time series of NO_X were obtained with the help of the computed emissions, and compared against the experimental data at the PE AQMS. Despite the assumption of neutral atmospheric conditions -without including thermal effects-, and of constant traffic flows throughout the year, the NO_X validation shows that the dispersion of pollutants is properly reproduced by the methodology. In addition, an empirical formula was employed to compute NO_2 from the modelled values of NO_X without chemical reactions within the CFD model, which increases its computational load. When compared against the observations,

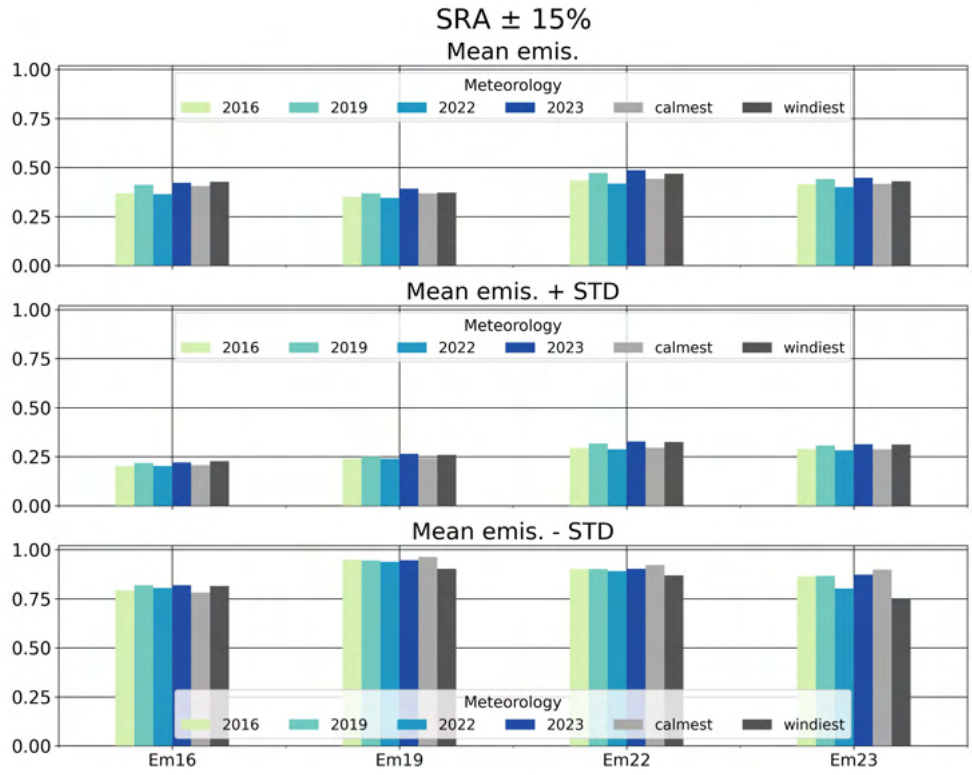

Figure 5.59: SRA20 of PE AQMS for annual NO_2 for each scenario and meteorological conditions using different emissions configuration. Above: Mean emissions. Centre: Mean emissions + STD. Below: Mean emissions - STD.

NO_2 values also showed a good agreement with them.

Once the air pollutants concentrations are evaluated, their behaviour across several meteorological conditions is analysed. Although at a monthly time-scale significant differences were found, the annual values of wind speed and wind direction of the simulated years were particularly similar, which can mask the impact of the meteorological conditions on annual values of air pollutants concentrations. To overcome this issue, two additional sets of meteorological conditions were constructed to consider the windiest and calmest possible conditions within the 4 simulated years.

The annual mean concentrations of NO_X are affected up to a 25% by the meteorological conditions, with independence of the size of the domain analysed. Although this variation is smaller than the variation in annual $[NO_X]$ due to the uncertainty in the emissions, it is not negligible. The spatial distribution of NO_X is also affected by the meteorological conditions. More westerly flows induce larger downwind concentrations, affecting the channelling of air pollutants through some streets. Furthermore, the impacts of the meteorological conditions is irregular through the domain due to the interactions of the mean flow with the urban morphology. These interactions depend on the orientation of each obstacle with respect the mean flow, observing that the impacts of the meteorological condition in one point of the

domain are the opposite to another point with a different urban morphology configuration. The interaction between the mean flow and urban morphology can also affect the net impact of meteorological conditions on annual [NO_X], which -in contrast to the observed with the spatially-averaged values- in some points can exceed the uncertainty due to the emissions computation.

The effectiveness of air pollutant mitigation strategies for different meteorological conditions is also analysed. Their spatially-averaged effectiveness is modified by the meteorological conditions, but not exceeding the net impact of the strategy. However, different impacts are observed for different points of the domain due both to the heterogeneity of the changes in emissions along the domain and to the interactions of the meteorological conditions with the urban morphology. In some points of the domain, the impacts of the meteorological conditions are comparable to the impact of the mitigation strategies, even exceeding them for mitigation strategies with low impact in NO_X concentrations.

When analysing the impact of meteorological conditions on the monthly-averaged values of NO_X for a winter month, it has been found than the change in NO_X concentrations due to changes in meteorological conditions can exceed the impact of changes in emissions. This is particularly clear between the 2016_Em16 and 2019_Em19 scenarios, when the spatially-averaged local contribution to [NO_X] increases despite a 50% reduction in emissions. In addition, different impacts are observed for different points of the domain -as observed for annual values- with some cases in which meteorological conditions caused larger impact on [NO_X] than the uncertainty in [NO_X].

Finally, the impact of meteorological concentrations in NO_2 concentrations, SRA and exceedances areas has been thoroughly studied. When considering the impact of meteorological conditions on background concentrations, the modelled NO_2 concentrations are lightly larger for every emissions case. In addition, considering the impacts of meteorological conditions on background concentrations accentuates the variability in the fraction area exceeding the annual limit of 40 $\mu g \cdot m^{-3}$ for NO_2, making it even larger than the variability induced by the uncertainty in [NO_2] associated to the emissions computation. No changes are observed in the exceedances are of the annual limit of 20 $\mu g \cdot m^{-3}$ as in every case it is exceeded along all the domain. On the other hand, not significant impact of the meteorological conditions has on the SRA has been observed. In every case, the variability of SRA due to the changes in meteorological conditions is significantly smaller than that due to the uncertainty in emissions.

Chapter 6

Modelling the impact of a potential mitigation strategy.

In this chapter the impact of a future mitigation strategy in an urban area is estimated using a methodology similar to that employed in the previous chapter. It starts with a description of the analysed mitigation strategy followed by a description of the emission cases. After that, a detailed analysis of the changes on traffic-related emissions in the study area due to the implementation of the mitigation strategy is presented, followed by an analysis of the impact on air quality of those changes and their comparison with an already-implemented mitigation strategy. The chapter ends with a summary and some concluding remarks.

6.1 Mitigation strategy description

The Directive 2001/81/EC established national emission ceilings to limit emissions of acidifying and eutrophicating pollutants and ozone precursors in order to improve the protection in the Community of the environment and human health against risks of adverse effects from acidification, soil eutrophication and ground-level ozone and to move towards the long-term objectives of not exceeding critical levels and loads and of effective protection of all people against recognised health risks from air pollution (Directive 2001/81/EC, 2001). This Directive was revised by the Directive 2016/2284 (Directive 2016/2284, 2016) in order to move towards achieving levels of air quality compromised through Directive 2008/50/EC. The article 6 of the Directive 2016/2284 establishes that every State Member of the European Union shall draw up, adopt and implement their respective national air pollution control programmes (NAPCP) in order to limit their annual anthropogenic emissions.

The Spanish NAPCP (Ministerio Para la Transición Ecológica y Reto Demográfico, 2019) and its update for the period 2023-2030 (Ministerio Para la Transición Ecológica y Reto

Demográfico, 2024) establishes a series of 57 strategies grouped in 12 packages, oriented to the compliance of the emission reduction objectives assigned to Spain. One of those strategies is the introduction of electric vehicles (EV) in the Spanish vehicle fleet. The Spanish NAPCP does not specify a goal for the degree of implementation of electric vehicles in the market share. However, in the TRANSAIRE project (TRANSAIRE: Transition to cleaner air in Spain, TED2021-132431B-I00) three possible scenarios were proposed and studied for the impact of the implementation of electric vehicles in the air quality at a national scale:

- Scenario T7: This scenario considers that by the year 2030, 5.5 million passenger cars from the Spanish vehicle fleet will be EV. This means a 22% of the total Spanish vehicle fleet of passenger cars.
- Scenario T8: In this scenario, 11 million vehicles (42% of the fleet) will be EV by 2030.
- Scenario T9: This scenario considers an implementation quota of EV of 22 million vehicles (85% of the fleet) by 2030.

This chapter aims to analyse the impact of two scenarios (T7 and T9) on the air quality of an urban area at high resolution using CFD modelling. In addition, it addresses the question of how changing meteorological conditions could impact the effectiveness of this mitigation strategy. To that end, the simulations from Chapter 5 were employed as base cases. The T7 and T9 scenarios were created by randomly removing the emissions of the correspondent percentage of vehicles in the simulation in order to simulate the electrification of the vehicle fleet for each scenario.

6.2 Emission cases

The base cases correspond to the same traffic simulations described in Section 5.3.2.2:

1. Year 2016: The traffic flows and the road network existent by this date are considered the reference case. This emission case is labelled as Em16.
2. Year 2019: In this scenario, the number of lanes of one main street inside the area was reduced from 3 to one, and its direction reversed. In addition, a bikelane was added replacing the rightmost lane. This emission case is labelled as Em19. Also, a significant change in vehicle fleet took place between 2016 and 2019.
3. Year 2022: Since December 2021, a LEZ was implemented affecting the area surrounding Plaza Elíptica roundabout (Figure 5.1). At this time, the LEZ restricted access to gasoline vehicles previous to EURO2 emissions standard and diesel vehicles prior to EURO3. This emission case is labelled as Em22. In addition, in early 2022 some mobility restrictions were still prevailing due to the COVID-19 pandemic.

4. Year 2023: The network configuration remains the same as in 2022 but traffic flows recovered fully after the pandemic. This emission case is labelled as Em23.

Both the domain of the traffic simulations and of the CFD simulations are the same as those described in Figure 5.1.

Strategies T7 and T9 can be applied to each emission case resulting in a total of 12 emission cases (three for each year, the base case plus the T7 and T9 scenarios). Each emission case that incorporates the strategies T7 and T9 will be labelled with the suffix "_T7" and "_T9" respectively (for example: Em16_T7). For develop these strategies, emissions were replaced to the correspondent fraction of vehicles described in the aforementioned strategies. There are numerous variables to consider when a person decides replacing a fuel-powered vehicle by an EV, including enviromental factors, but also others such as economic factors (Pamidimukkala et al., 2024). Developing a study to consider the order in which vehicles in the study area should be replaced by electric vehicles would require an enormous amount of effort and knowledge that is out of the scope of this work. For this reason, the replacement of fuel-powered vehicles by electric vehicles is done by random sampling for each one of the emissions scenarios.

To assess the impact of meteorological conditions on air pollutant concentrations six scenarios are possible for each emissions case, one for each set of meteorological conditions, including the two additional subsets of meteorological conditions -"windiest" and "calmest"- created in Chapter 5. Each resulting scenario will be labelled hereafter as X_Y, where X represents the year of the meteorological conditions and Y is the label of the emissions case. Table 6.1 summarizes all the possible scenarios resulting of combining all the meteorological conditions with every emissions case.

To appropriately describe emissions under different vehicle flow conditions with a compromise with the amount of computational resources employed, the same sixteen 1-h length scenarios described in Chapter 5 were simulated to represent the weekly traffic pattern (Table 5.1).

Therefore, the set of all possible scenarios can be classified by:

1. Real scenarios: Those which use the meteorological conditions and emissions of the same year, and that have occurred in reality. Therefore, these are scenarios for which observational data exists.

2. Virtual scenarios: Those scenarios that combine the emissions of a certain year with the meteorological conditions of another (i.e. 2016_Em22), or have not occurred (i.e.: 2016_Em16_T7).

Table 6.1: All possible scenarios resulting of combining every emission case with every simulated meteorological conditions.

		Em16	
Meteo	base	T7	T9
2016	2016_Em16	2016_Em16_T7	2016_Em16_T9
2019	2019_Em16	2019_Em16_T7	2019_Em16_T9
2022	2022_Em16	2022_Em16_T7	2022_Em16_T9
2023	2023_Em16	2023_Em16_T7	2023_Em16_T9
calmest	calmest_Em16	calmest_Em16_T7	calmest_Em16_T9
windiest	windiest_Em16	windiest_Em16_T7	windiest_Em16_T9
		Em19	
Meteo	base	T7	T9
2016	2016_Em19	2016_Em19_T7	2016_Em19_T9
2019	2019_Em19	2019_Em19_T7	2019_Em19_T9
2022	2022_Em19	2022_Em19_T7	2022_Em19_T9
2023	2023_Em19	2023_Em19_T7	2023_Em19_T9
calmest	calmest_Em19	calmest_Em19_T7	calmest_Em19_T9
windiest	windiest_Em19	windiest_Em19_T7	windiest_Em19_T9
		Em22	
Meteo	base	T7	T9
2016	2016_Em22	2016_Em22_T7	2016_Em22_T9
2019	2019_Em22	2019_Em22_T7	2019_Em22_T9
2022	2022_Em22	2022_Em22_T7	2022_Em22_T9
2023	2023_Em22	2023_Em22_T7	2023_Em22_T9
calmest	calmest_Em22	calmest_Em22_T7	calmest_Em22_T9
windiest	windiest_Em22	windiest_Em22_T7	windiest_Em22_T9
		Em23	
Meteo	base	T7	T9
2016	2016_Em23	2016_Em23_T7	2016_Em23_T9
2019	2019_Em23	2019_Em23_T7	2019_Em23_T9
2022	2022_Em23	2022_Em23_T7	2022_Em23_T9
2023	2023_Em23	2023_Em23_T7	2023_Em23_T9
calmest	calmest_Em23	calmest_Em23_T7	calmest_Em23_T9
windiest	windiest_Em23	windiest_Em23_T7	windiest_Em23_T9

6.3 Impact on NO_X emissions

In order to estimate the emissions' reduction of these strategies applied to each base case, the first step is to identify all the vehicle cars in the simulations. This is possible as each vehicle in the simulation is labelled depending on its vehicle class, fuel type and EURO standard (Section 2.2.2.2). Then, a random sample of vehicles comprising the 22% and 85% respectively of the total passenger cars entering the simulation were selected and their NO_X emissions removed.

Figure 6.1 shows the relative emission reductions for all the emission cases and by hourly scenario. In all cases, the reductions are the largest for the Em16 emission case, and the others are similar among them. This is because Em16 is the scenario with the oldest and most pollutant vehicle fleet (Table 5.8) and the substitution of the original vehicles by electric ones has a larger impact on NO_X emissions. On the other hand, the vehicle fleet for the Em19, Em22 and Em23 are more similar between each other, leading to smaller differences among them. The T7 scenario has already a significant impact on NO_X emissions, with reductions greater than 60% during the weekday morning peak hour (scenario S3) and the weekend rush hour (scenario S13). For fluid traffic scenarios, emission reductions are usually smaller. On the other hand, the T9 scenario has a large impact on emissions in every traffic scenario, with reductions ranging between 65 and 84%. These levels of reductions are comparable to the reductions in road transport emissions observed during the most stringent period of the COVID-19 in Spain, results obtained in the previous work related to macroscopic emissions reductions (Rodríguez-Sánchez et al., 2022). Moreover, in the T7 scenario the emissions reduction is not constant in time. This is because the number of substituted vehicles is not large enough to be equally distributed throughout the day. Instead, the replacing of vehicles will occur with greater probability in scenarios with larger number of vehicles. In other cases, such as the Em16 emissions case, a larger proportion of the replaced vehicles circulate by night, which accentuates the emissions reductions in nightly scenarios. On the other hand, in the T9 strategy the number of replaced vehicles is large enough to be equally distributed in time.

Figure 6.2 shows the total annual emissions, within the CFD model domain, of each simulated emissions base case and their corresponding T7 and T9 scenarios (from left to right). Both the T7 and T9 has associated important decreases in NO_X emissions with respect to the base case. This is specially notable for the Em16 emissions case. The Em16 emissions scenario showed large areas exceeding total emissions of 1250 kg, but those areas are reduced to a few points within the PE roundabout and the motorway in the Em16_T7 scenario and practically disappear for the Em16_T9 scenario. In the latter, most of the domain has emissions lower than 150 kg. Nonetheless, the spatial distribution of maximum and minimum values are the

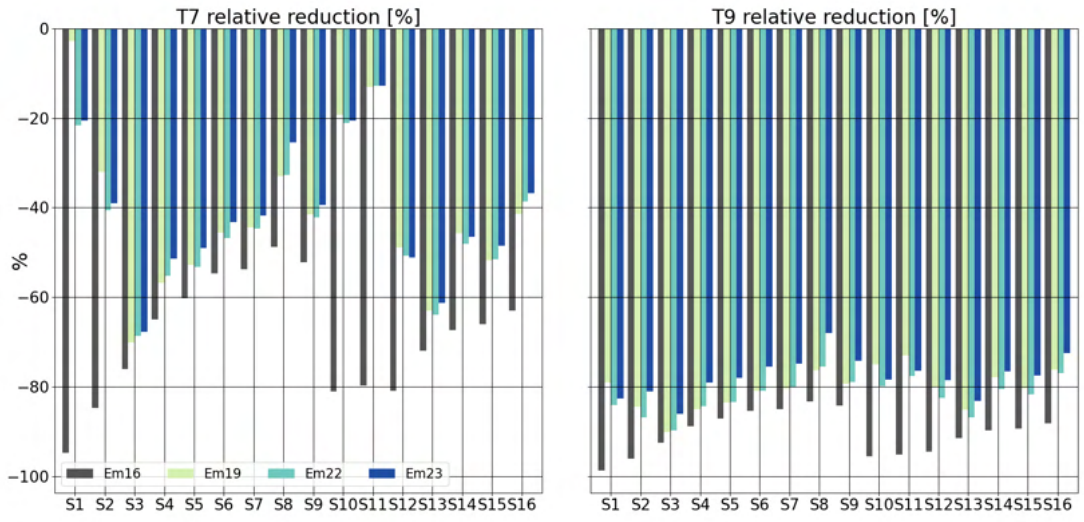

Figure 6.1: Relative emission reductions by traffic scenario for every emissions case due to the implementation of the T7 (left) and the T9 (right) strategies.

same for all scenarios: maximum values of NO_X emissions are located within the roundabout, the motorway and some intersections. Despite the base cases having large differences in the total value of emitted NO_X, the scenarios corresponding to the T7 and T9 strategies tend to reduce the differences between different emissions cases. This can also be observed when analysing the spatially-averaged annual NO_X emissions (Figure 6.3). As mentioned in Chapter 5, for the base case the emissions of Em16 case where at least a factor 2 larger than the others'. However, for the scenarios T7 and T9, the differences are minimal. This is because a combination of two factors. First, the Em16 emissions case was the simulation with the largest volume of traffic, therefore a larger number of vehicles will be replaced than in other simulations. The other factor is that its vehicle fleet is the oldest, and the probability of replacing a largely-pollutant vehicle by an electric one is larger than in other simulations, having a larger impact on emissions.

The randomness of the procedure of replacing vehicles, however, introduces another source of uncertainty to the computed emissions. This is why the standard deviations of the T7 and T9 scenarios are even larger than those of the base case. Nonetheless, the emissions reductions due to the implementation of the T7 and T9 strategies are larger than the uncertainty of the base cases' emissions.

6.4 Impact on local NO_X concentrations

To assess the impact of the T7 and T9 strategies in the NO_X concentrations on the modelling domain, the local concentrations of NO_X (hereafter as $[NO_X]_{local}$) were computed for each

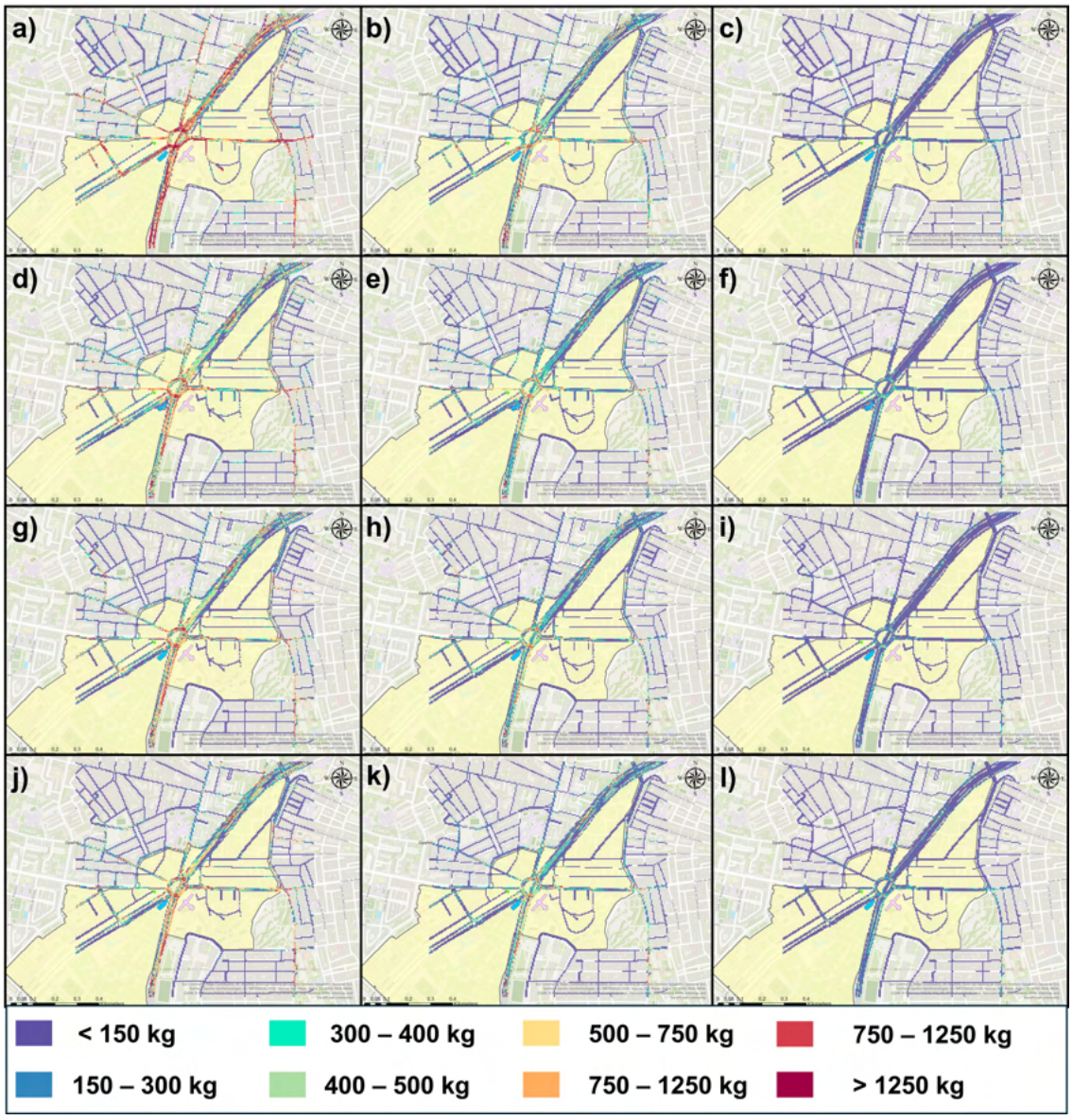

Figure 6.2: Panel of figures showing the spatial distribution of the annual total emissions of different emissions scenarios: a) Em16; b) Em16_T7; c) Em16_T9; d) Em19; e) Em19_T7; f) Em19_T9; g) Em22; h) Em22_T7; i) Em22_T9; j) Em23; k) Em23_T7; l) Em23_T9.

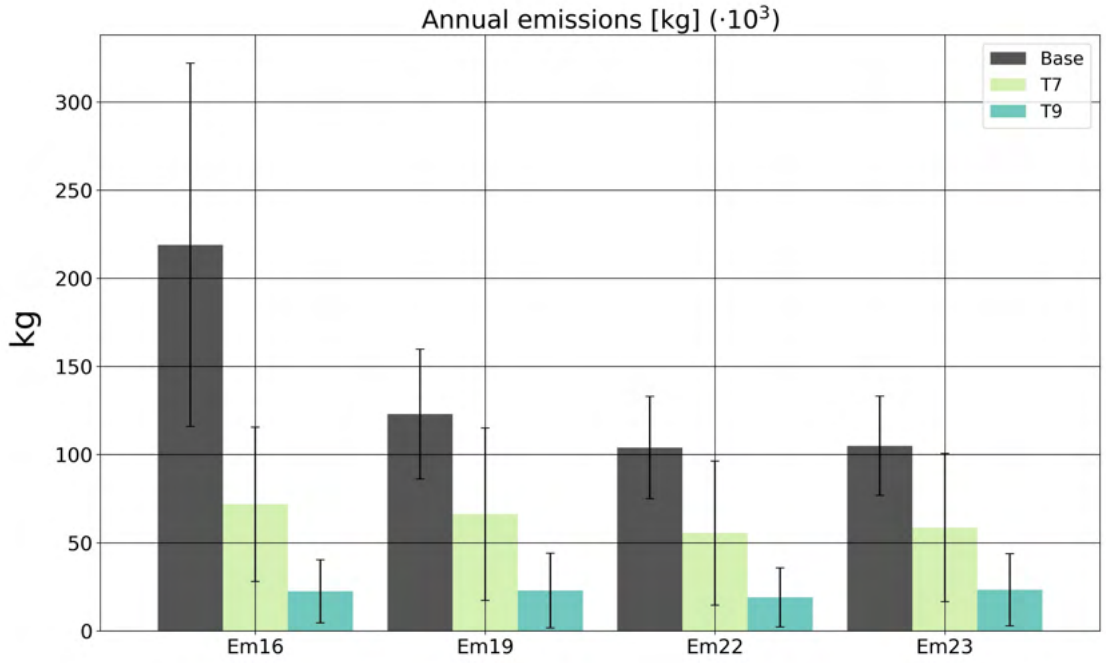

Figure 6.3: Total annual NO_X emissions (in kg) for each emissions scenario. Standard deviations are indicated by spines.

emission scenario and different meteorological conditions using the numerical methodology explained in Section 3.3.2. The original methodology for computing NO_X concentrations from traffic emissions was based on 16 wind directions to reconstruct the temporal evolution of NO_X concentrations along the domain. However, in order to save resources, a test using 8 wind directions was performed.

Table 6.2: Statistical parameters of the evaluation of [NO_X] when using the methodology with 8 and 16 wind directions.

	2016_Em16		2019_Em19		2022_Em22		2023_Em23	
	8WD	16WD	8WD	16WD	8WD	16WD	8WD	16WD
R	0.813	0.803	0.797	0.785	0.827	0.815	0.833	0.817
FB	-0.076	-0.051	-0.317	-0.289	-0.177	-0.152	-0.112	-0.083
NMSE	0.425	0.434	0.662	0.659	0.376	0.387	0.414	0.442
FAC2	0.857	0.831	0.715	0.705	0.847	0.836	0.854	0.840

When comparing the results for the base case using 16 and 8 wind directions, no significant differences were observed. Table 6.2 summarizes the variations between the NO_X computation using 16 and 8 wind directions. When reducing to 8 wind directions, the fractional bias decreases slightly further. On the other hand, correlation and FAC2 increase slightly. The small variations in the results justify the change to 8 wind directions in the

methodology. Other works, such as Martín et al. (2024), also have found good results using this methodology with 8 wind directions.

Figure 6.4 shows the spatial distribution of $[NO_X]_{local}$ for every simulated real scenario. In the left column the $[NO_X]_{local}$ of the real scenarios 2016_Em16, 2019_Em19, 2022_Em22 and 2023_Em23 (from top to bottom) is shown, and in the middle and left columns the concentrations for their corresponding T7 and T9 strategies are shown. It can be observed that the spatial distribution (with lower concentrations than in the base cases) does not change when replacing some vehicles with electric vehicles: the maximum concentrations are in every case located in the roundabout; the motorway traversing the domain; Streets 5 and 6 (Figure 5.33); and some other intersections along the domain. In addition, the T7 strategy reduces the annual $[NO_X]_{local}$ along the domain, with different impacts depending on the base case considered. For the 2016_Em16 base case, the reductions are larger than 100 $\mu g \cdot m^{-3}$ in the most emitter roads of the domain. As the concentrations in the base case decrease, so it does the impact of the T7 strategy both in concentration values and in its spatial extension. However, the impact of the T9 strategy with respect the T7 strategy is nearly constant for each scenario, providing additional reductions of up to 40 $\mu g \cdot m^{-3}$ inside the main emitter roads. Outside them, the T9 strategy provides no significant change in air quality with respect the T7 strategy.

Table 6.3 summarizes the annual $[NO_X]_{local}$, averaged along the CFD domain, for every scenario using the same meteorological conditions and considering two cases of different ages of vehicle fleet. As vehicle fleet compositions of Em19, Em22 and Em23 were fairly similar (as explained in Section 5.3.3). Em23 is used as the reference case of a newer vehicle fleet. From the table can be seen that the impacts on $[NO_X]_{local}$ are larger for an older vehicle fleet (Em16), as the strategies had a larger impact on the NO_X emissions of an older fleet . In addition, the differences in spatial-averaged $[NO_X]$ for both emission cases decreases substantially in the T7 strategy, even equaling each other in the T9 strategy. These results suggest that for the T9 strategy, the reduction in NO_X emissions is large enough to make the contribution of the non-passenger vehicles to the $[NO_X]_{local}$ the predominant one. For the Em16 emissions case, the T7 strategy has an impact on $[NO_X]_{local}$ of between 21.3 and 27.3 $\mu g \cdot m^{-3}$, whereas the T9 scenario has an impact of between 27.5 and 35.5 $\mu g \cdot m^{-3}$. For the Em23 case, the impacts range between 6.27 and 7.68 $\mu g \cdot m^{-3}$ (44.5-46% reduction) and 10.48 and 13.25 $\mu g \cdot m^{-3}$ (77-78% reduction) for the T7 and T9 strategies respectively. In average, the T7 strategy reduces $[NO_X]_{local}$ by a 68% for the Em16 scenarios and a 43% for the Em23 ones. On the other hand, the T9 strategy reduces the concentations by a 90% and by a 76% for the Em16 and Em23 scenarios respectively.

Furthermore, the impacts of the strategies T7 and T9 are notably larger than the variation on local $[NO_X]$ due to a change in meteorological conditions. The meteorological conditions

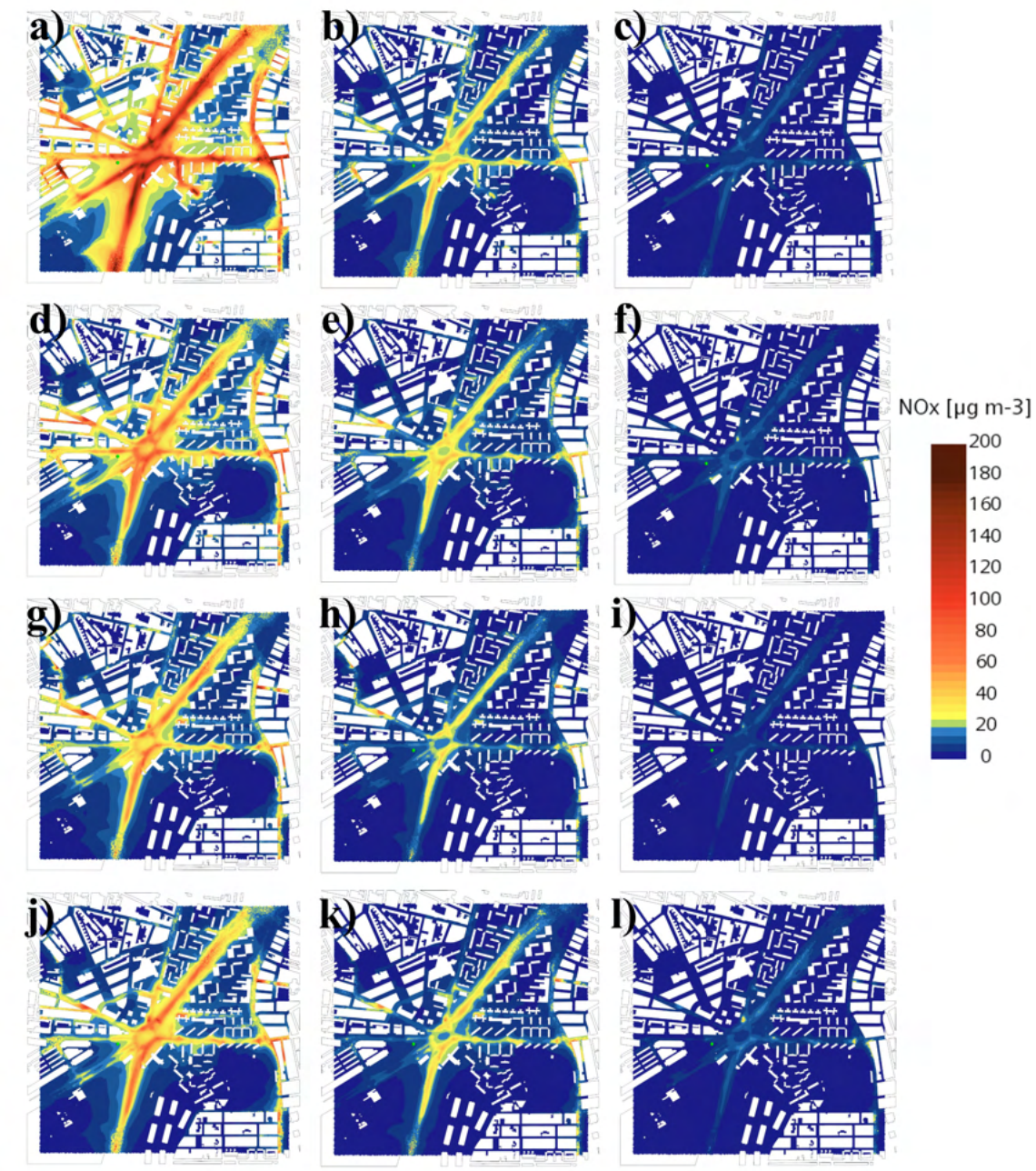

Figure 6.4: Annual average of $[NO_X]_{local}$ for the scenarios: a) 2016_Em16; b) 2016_Em16_T7; c) 2016_Em16_T9; d) 2019_Em19; e) 2019_Em19_T7; f) 2019_Em19_T9; g) 2022_Em22; h) 2022_Em22_T7; i) 2022_Em22_T9; j) 2023_Em23; k) 2023_Em23_T7 and i) 2023_Em23_T9.

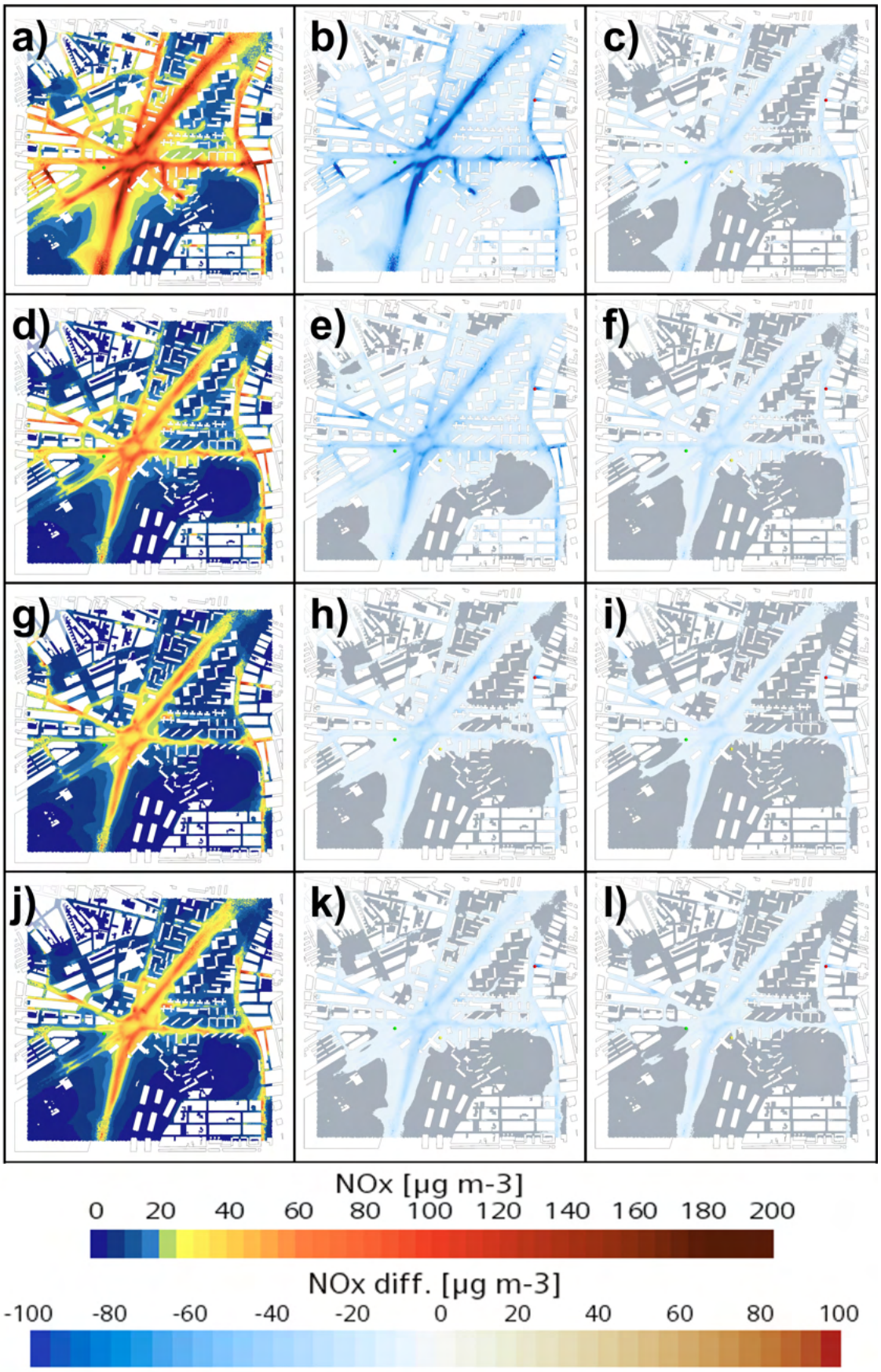

Figure 6.5: Left column: Annual average of $[NO_X]_{local}$ for the real scenarios a) 2016_Em16; d) 2019_Em19; g) 2022_Em22; j) 2023_Em23. Center and right columns: Reductions in annual average local NO_X, non-significant changes (between -5 and 5 $\mu g \cdot m^{-3}$) are shaded in grey: b) 2016_Em16_T7 - 2016_Em16; c) 2016_Em16_T9 - 2016_Em16_T7; e) 2019_Em19_T7 - 2019_Em19; f) 2019_Em19_T9 - 2019_Em19_T7; h) 2022_Em22_T7 - 2022_Em22; i) 2022_Em22_T9 - 2022_Em22_T7; k) 2023_Em23_T7 - 2023_Em23; l) 2023_Em23_T9 - 2023_Em23_T9. Green, yellow and red points indicates the location of the AQMS, SVP and MP23 points respectively.

affects the Em16 scenario spatially-averaged $[NO_X]$ up to 9 $\mu g \cdot m^{-3}$, just a third of the net impact of the T7 strategy and a fourth of those of the T9. For the Em23 strategy, the meteorological conditions changes $[NO_X]_{local}$ no more than 4 $\mu g \cdot m^{-3}$, which is a 52% and a 30% of the largest reductions modelled for the T7 and T9 strategies respectively, and a 60% and a 36% of the lowest ones. The impact of the meteorological conditions on the effectiveness of the strategies ranges between 1 and 6 $\mu g \cdot m^{-3}$ and between 2.8 and 8 $\mu g \cdot m^{-3}$ for the strategies T7 and T9 respectively, also significantly lower than the net impact of the T7 and T9 strategies. This is in line with the findings for other strategies presented in Chapter 5.

Table 6.3: Impacts of T7 and T9 strategies on annual- and spatially-averaged $[NO_X]_{local}$ $[\mu g \cdot m^{-3}]$ for different meteorological conditions.

Spatially-averaged annual mean $[NO_X]_{local}$ (Variation from base case) $[\mu g \cdot m^{-3}]$						
Meteo	Em16	Em16_T7	Em16_T9	Em23	Em23_T7	Em23_T9
2016	33.78	10.70 (-23.08)	3.41 (-30.37)	15.49	8.75 (-6.73)	3.65 (-11.83)
2019	33.54	10.69 (-22.85)	3.41 (-30.13)	14.95	8.47 (-6.48)	3.52 (-11.43)
2022	32.48	10.13 (-22.35)	3.22 (-29.26)	14.67	8.26 (-6.41)	3.42 (-11.25)
2023	33.90	10.84 (-23.05)	3.46 (-30.43)	14.99	8.54 (-6.45)	3.53 (-11.45)
calmest	39.35	12.02 (-27.34)	3.82 (-35.54)	17.22	9.54 (-7.68)	3.97 (-13.25)
windiest	30.41	9.11 (-21.3)	2.89 (-27.52)	13.44	7.17 (-6.27)	2.96 (-10.48)

When limiting the area of study to the 300 m x 300 m subdomain centered on the PE roundabout, it is found that the base concentrations are larger, but also the $[NO_X]_{local}$ reductions due to the implementation of the T7 and T9 strategies. Although the absolute reductions are larger, the relative reductions are the same as those for the CFD domain. Also, as it happened when considering the spatially-averaged values along all the CFD domain, the meteorological impacts on $[NO_X]_{local}$ is lower than the net impacts of the T7 and T9 strategies. When considering the Em16 base case, the meteorological conditions can alter the $[NO_X]_{local}$ by 17 $\mu g \cdot m^{-3}$, when the ranges of the reductions of $[NO_X]_{local}$ due to the T7 and T9 strategies are [-52, -40] and [-68, -52] respectively. The same applies when considering the emissions of the Em23 base case. In this case, the variation in $[NO_X]_{local}$ due to changes in meteorological conditions is between 27% and 35% the reductions due to the implementation of the T7 strategy and between 16% and 21% the net impact of the T9 strategy (Table 6.4).

In addition, as Figure 6.6 shows, the air pollutant concentrations reductions due to the T9 strategy are larger than the standard deviation of $[NO_X]_{local}$ for both the whole domain and the 300 m x 300 m area, even after considering the large uncertainty in $[NO_X]_{local}$ for the strategies T7 and T9. In those cases, the random nature of the substitution of vehicles by electric vehicles significantly increases the uncertainty in $[NO_X]_{local}$, making it comparable to the net concentrations.

Table 6.4: Impacts of T7 and T9 strategies on annual- and spatially-averaged $[NO_X]_{local}$ $[\mu g \cdot m^{-3}]$ along the 300 m x 300 m subdomain for different meteorological conditions.

Annual- and spatially-averaged $[NO_X]_{local}$ (Variation from base case) $[\mu g \cdot m^{-3}]$						
Meteo	Em16	Em16_T7	Em16_T9	Em23	Em23_T7	Em23_T9
2016	65.20	19.99 (-45.21)	6.32 (-58.88)	30.08	16.42 (-13.66)	7.17 (-22.91)
2019	64.68	19.93 (-44.75)	6.31 (-58.37)	28.97	15.85 (-13.12)	6.89 (-22.08)
2022	62.73	18.91 (-43.82)	5.97 (-56.76)	28.44	15.48 (-12.96)	6.71 (-21.73)
2023	65.31	20.22 (-45.09)	6.41 (-58.90)	29.00	15.96 (-13.04)	6.91 (-22.09)
calmest	75.35	23.34 (-52.01)	7.47 (-67.88)	33.13	18.27 (-14.86)	8.13 (-25.00)
windiest	58.19	18.08 (-40.11)	5.79 (-52.4)	25.92	14.16 (-11.76)	6.26 (-19.66)

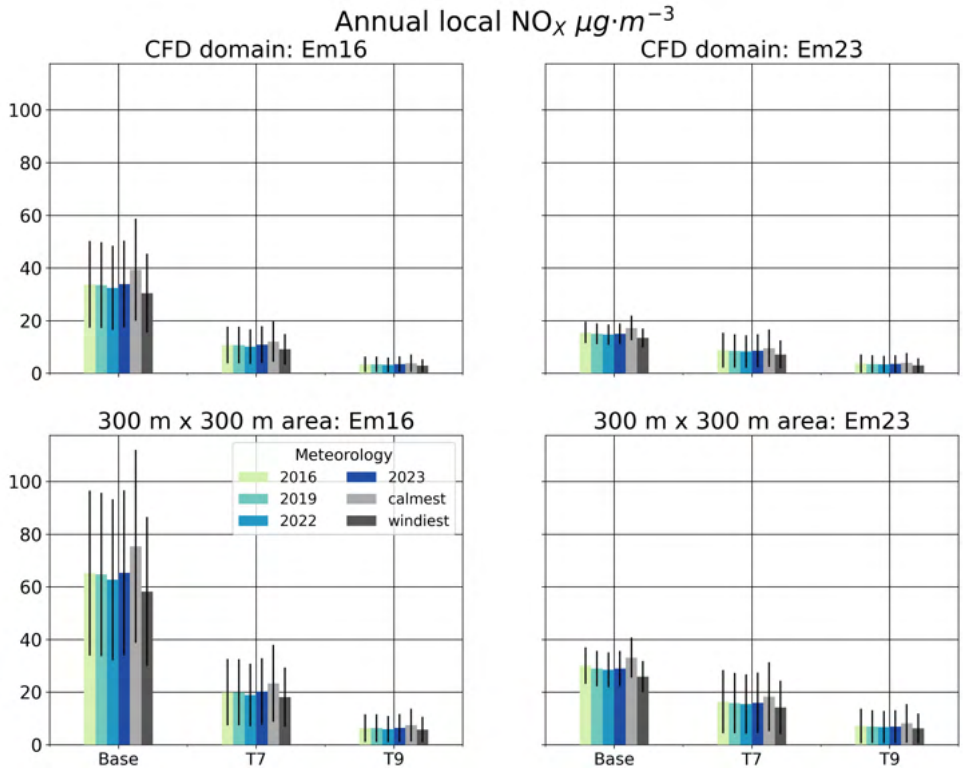

Figure 6.6: Annual $[NO_X]_{local}$ for the CFD domain and the 300 m x 300 m selected area for every possible meteorological conditions and emissions scenarios Em16 and Em23. The spines indicate the standard deviation of $[NO_X]_{local}$.

A further analysis of the impacts of the implementation of EV can be done by considering different points inside the domain. The three points chosen for this analysis where the location of the same points described in Chapter 5: the AQMS station; the most polluted point in the 2023_Em23 scenario (hereafter as MP23); and a point belonging to the playground of the San Viator school (referred to as SVP).

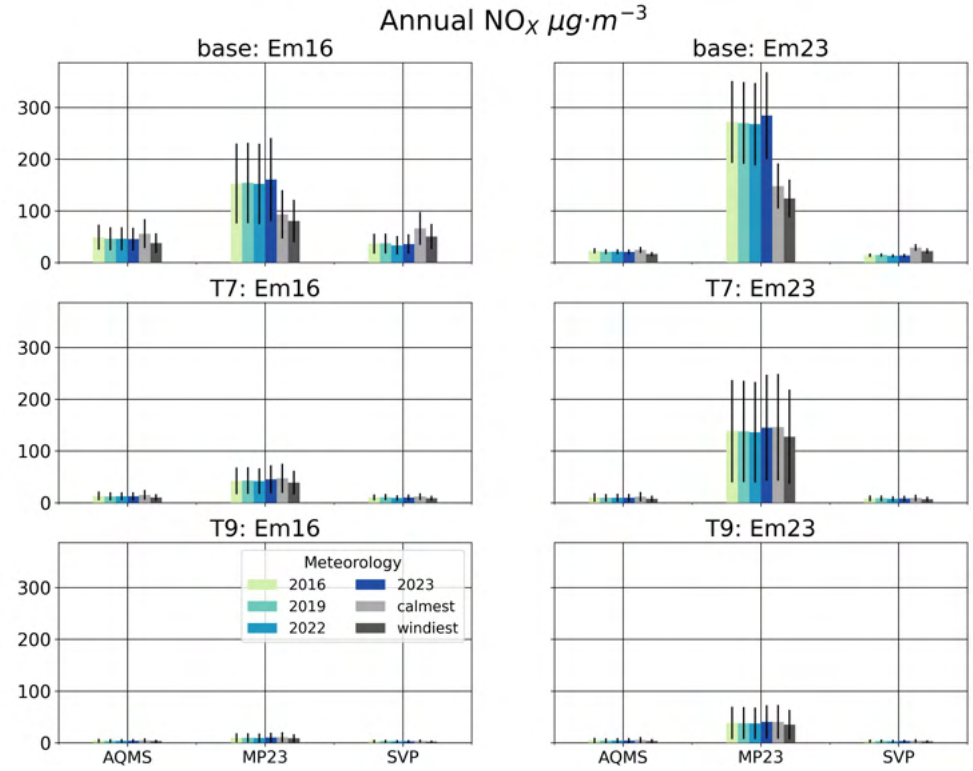

Figure 6.7: Annual $[NO_X]_{local}$ for three selected points within the domain for every possible meteorological conditions and emissions scenarios Em16 and Em23.

Figure 6.7 shows the annual concentrations of the local contribution to NO_X for the three selected points and for two different emissions cases representing two different vehicle fleets. The base cases were already discussed in Chapter 5. For the T7 and T9 strategies, large impacts can be seen for the three points. When considering the Em16 emissions as base case, T7 strategy reduces annual $[NO_X]_{local}$, in average across every meteorological condition, in 34.2 $\mu g \cdot m^{-3}$ (73% reduction) for the AQMS, in 89 $\mu g \cdot m^{-3}$ (65 %) in the MP23 location and in 33 $\mu g \cdot m^{-3}$ (75%) in the SVP location. The T9 reductions for the same points are, respectively, of 42.7 $\mu g \cdot m^{-3}$ (91% reduction), 122.4 $\mu g \cdot m^{-3}$ (92%) and 40.1 $\mu g \cdot m^{-3}$ (92%). Those reductions are consistent with a 68% and a 90% emission reduction inside the study domain for the T7 and T9 scenarios respectively. On the other hand, when considering the Em23 emissions as base case, the average reductions due to the T7 strategy are 11.5 $\mu g \cdot m^{-3}$ (54% reduction), 89 $\mu g \cdot m^{-3}$ (32% reduction) and 9.9 $\mu g \cdot m^{-3}$ (52%) in AQMS, MP23 and SVP locations respectively. For the T9 scenario, the reductions increase to 16.5 $\mu g \cdot m^{-3}$ (78% reduction), 189 $\mu g \cdot m^{-3}$ (81%) and 14.6 $\mu g \cdot m^{-3}$ (80% reduction). Again,

those reductions in annual [NO_X] are consistent with the modelled average reduction of 45% and 78% in NO_X emissions within the T7 and T9 scenarios respectively. Reductions are larger when considering the emissions from the Em16 than from those of Em23. This is due to the larger impact in NO_X emissions of replacing older vehicles. In addition, annual values of $[NO_X]_{local}$ are much more homogeneous for the T9 scenario than for the base case. In the base cases, the maximum difference was observed between the MP23 and SVP points and these differences exceeded an average value of 88 $\mu g \cdot m^{-3}$ for the Em16 reference case. This difference increased to 210 $\mu g \cdot m^{-3}$ for the Em23 reference case. However, when applying the emissions reductions of the T9 strategy, those differences declined to 6 and 35 $\mu g \cdot m^{-3}$ respectively.

Another interesting result is that the implementation of the T7 and T9 strategies affects how the meteorological conditions impact the concentrations in an specific points. In the location of the MP23 point, the calmest and windiest conditions lead to lower concentrations than the rest of the meteorological conditions for the reasons explained in Chapter 5. However, this is not the case for the T7 and T9 strategies. In those cases, every meteorological conditions results in similar absolute concentrations, with the calmest conditions resulting in slightly larger concentrations than the rest, and the windiest concentrations in the lowest. In addition, for both the T7 and T9 strategies the uncertainty on $[NO_X]_{local}$ is significantly larger than the impact of the meteorological conditions, although in particular for th T7 scenario the impacts of changing meteorological conditions are not neglegible. In general, the impacts of meteorological conditions are reduced with lower air pollutant concentrations.

On a monthly time scale, the T7 and T9 strategies also have a notable impact on $[NO_X]_{local}$. For the analysis of the monthly variations the month of February has been selected as it presents one of the largest variabilities in meteorological variables, as discussed in Chapter 5. Figure 6.8 shows the variation in the February-averaged $[NO_X]_{local}$ due to different meteorological conditions and emissions configurations for the CFD domain and the 300 m x 300 m study area. The impacts of the T7 and T9 strategies are larger for the Em16 base case, which is consistent with the observed at an annual timescale. Also, the relative reductions of $[NO_X]_{local}$ are virtually the same than for the annual values in both study areas. Furthermore, the reductions in $[NO_X]_{local}$ due to the T9 strategy are larger than the uncertainty in $[NO_X]_{local}$. However, the impacts of changing meteorological conditions in absolute values of $[NO_X]_{local}$ decrease with lower emissions. For the base case they can be larger than the uncertainty in local NO_X concentrations, but for the T7 and T9 strategies that is not the case.

For the three selected points within the CFD domain the findings on a monthly timescale are also similar to the findings at an annual timescale. $[NO_X]_{local}$ differences between them tend to reduce with the implementation of the T7 and T9 strategies. In absolute values, the

point MP23 is the most benefited from these measures, reducing its $[NO_X]_{local}$ concentrations from 338 $\mu g \cdot m^{-3}$ to 47 $\mu g \cdot m^{-3}$, considering an averaged value across every meteorological condition (Table 6.5). In relative values, there are significant differences between the Em16 and Em23 reference cases. For the Em16, the relative reductions of February-averaged local NO_X are about 68% and 90% for the AQMS point in both the T7 and T9 strategies respectively (Table 6.6). For the MP23, the T7 strategy induces a reduction in local NO_X of 71%, which increases to a 93% for the T9 strategy. And for the SVP, reductions are of 71% and 91% respectively (Table 6.7). However, when considering the Em23 emissions as reference case, the relative reductions are quite different, as it happened with annual values. In this case, the T7 strategy reduces $[NO_X]_{local}$ in a 47%, 49% and 44% for the AQMS, MP23 and SVP points respectively, whereas the T9 strategy does so in a 74%, 86% and 76% respectively. In all cases, the most polluted point (MP23) is more benefited one from the implementation of the T7 and T9 strategies.

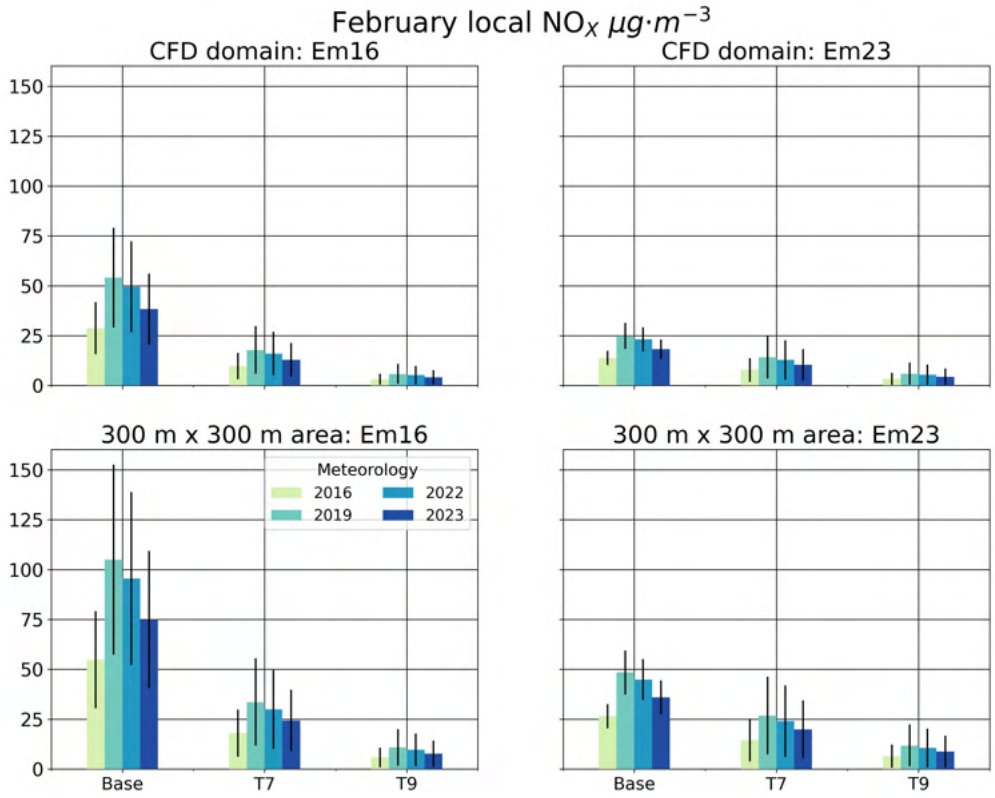

Figure 6.8: February-averaged $[NO_X]_{local}$ for the CFD domain and the 300 m x 300 m selected area for every possible meteorological conditions and emissions scenarios Em16 and Em23. The spines indicate the standard deviation of $[NO_X]_{local}$.

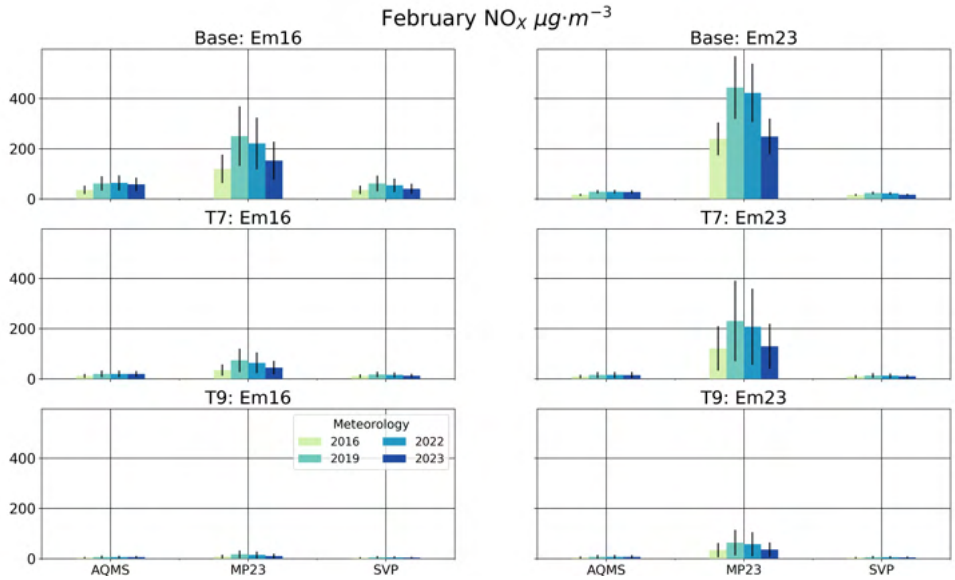

Figure 6.9: February-averaged $[NO_X]_{local}$ for three selected points within the domain for every possible meteorological conditions and emissions scenarios Em16 and Em23. The spines indicate the standard deviation of $[NO_X]_{local}$.

Table 6.5: Absolute $[\mu g \cdot m^{-3}]$ and relative reductions of $[NO_X]_{local}$ due to the implementation of T7 and T9 strategies for 2 reference emissions cases in MP23.

Meteo	T7 (Em16)	T9 (Em16)	T7 (Em23)	T7 (Em23)
2016	-85.13 (-71.1)	-111.80 (-93.3)	-118.23 (-49.4)	-205.70 (-85.9)
2019	-177.13 (-70.7)	-233.36 (-93.2)	-213.16 (-48.1)	-379.75 (-85.7)
2022	-157.67 (-71.3)	-206.51 (-93.4)	-215.00 (-50.9)	-364.69 (-86.4)
2023	-108.48 (-71.0)	-142.62 (-93.3)	-119.29 (-47.9)	-212.97 (-85.6)

Table 6.6: Absolute $[\mu g \cdot m^{-3}]$ and relative reductions of $[NO_X]_{local}$ due to the implementation of T7 and T9 strategies for 2 reference emissions cases in AQMS.

Meteo	T7 (Em16)	T9 (Em16)	T7 (Em23)	T7 (Em23)
2016	-24.25 (-67.4)	-32.07 (-89.1)	-7.69 (-45.73)	-12.35 (-73.4)
2019	-42.39 (-68.5)	-55.45 (-89.5)	-13.21 (-46.6)	-20.97 (-73.9)
2022	-44.12 (-69.4)	-57.23 (-90.0)	-13.77 (-47.6)	-21.56 (-74.6)
2023	-39.38 (-67.3)	-52.35 (-89.5)	-13.13 (-46.7)	-20.87 (-74.1)

Table 6.7: Absolute $[\mu g \cdot m^{-3}]$ and relative reductions of $[NO_X]_{local}$ due to the implementation of T7 and T9 strategies for 2 reference emissions cases in SVP.

Meteo	T7 (Em16)	T9 (Em16)	T7 (Em23)	T7 (Em23)
2016	-25.06 (-69.6)	-32.51 (-90.3)	-7.02 (-44.0)	-12.12 (-76.0)
2019	-44.41 (-72.1)	-56.21 (-91.3)	-10.79 (-44.9)	-18.46 (-76.8)
2022	-38.84 (-71.4)	-49.44 (-90.9)	-10.21 (-45.6)	-17.15 (-76.6)
2023	-27.97 (-69.2)	-36.4 (-90.0)	-7.29 (-43.1)	-12.57 (-74.2)

6.5 Comparison with already-implemented measures

In Chapter 5 the developed methodology was evaluated using already-implemented mitigation strategies. After being evaluated, in this Chapter the methodology has been applied to estimate the impacts on air quality of planned mitigation strategies. Now, a comparison between already-implemented and planned mitigation strategies can be done. In particular, the study is focused in the comparison between the implementation of electric vehicles and the implementation of a LEZ. The Plaza Elíptica LEZ prohibited the entrance to the highlighted area shown in Figure 5.1 to gasoline vehicles previous to EURO2 emissions standard and diesel vehicles prior to EURO3 to vehicles non-resident inside the neighbours affected by the LEZ area since its implementation in 2022. The average modelled impact of this measure on annual NO_X emissions is of about 20 Mg. This impact is lower than the impacts of the T7 and T9 strategies, whose modelled impact on annual emissions is of 56 and 100 Mg respectively (Figure 6.10).

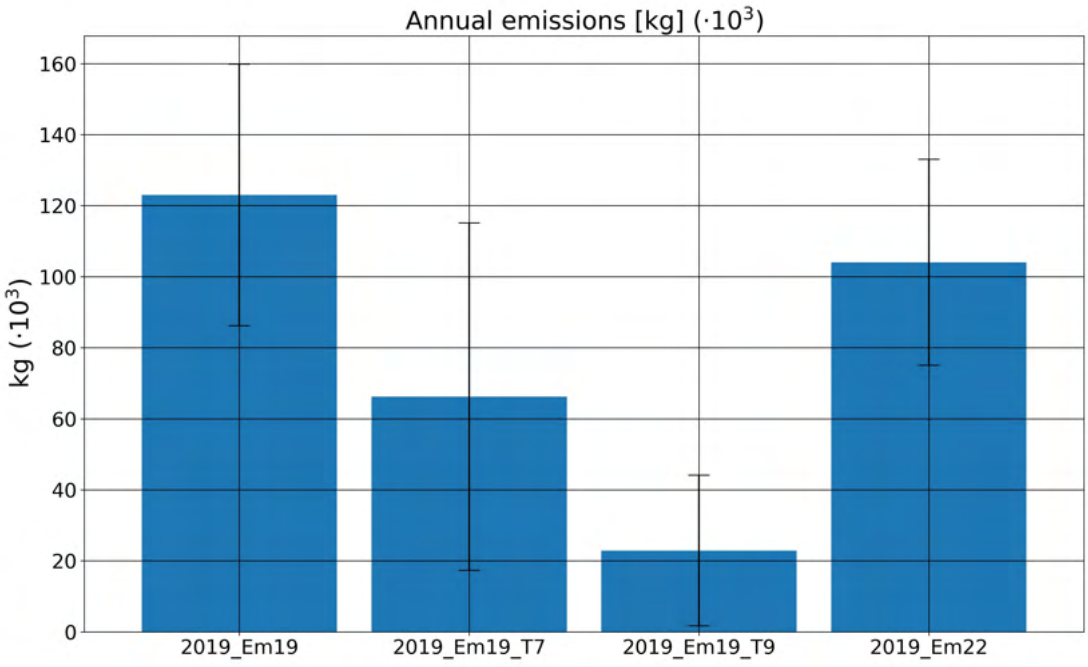

Figure 6.10: Annual total NO_X emissions for several of the simulated scenarios.

Figure 6.11 illustrates this comparison for $[NO_X]_{local}$. The base case corresponds to the 2019_Em19 scenario, the LEZ case to the 2019_Em22 and the T7 and T9 cases to the 2019_Em19_T7 and 2019_Em19_T9 scenarios, respectively. The 2019_Em19 scenario corresponds to the real case previous to the implementation of the LEZ. 2019_Em22 corresponds to the emissions after the LEZ implementation but the same meteorological

conditions than in the base case. The latter is important in order to compare only the impact of changing emissions in NO_X concentrations. The 2019_Em19_T7 and 2019_Em19_T9 scenarios corresponds to the situation that would be happen if the T7 and T9 strategies would have been implemented in 2019. It can be observed that, as it was modelled for the emissions, the impacts in $[NO_X]_{local}$ of the T7 and T9 strategies are larger than that from the LEZ implementation.

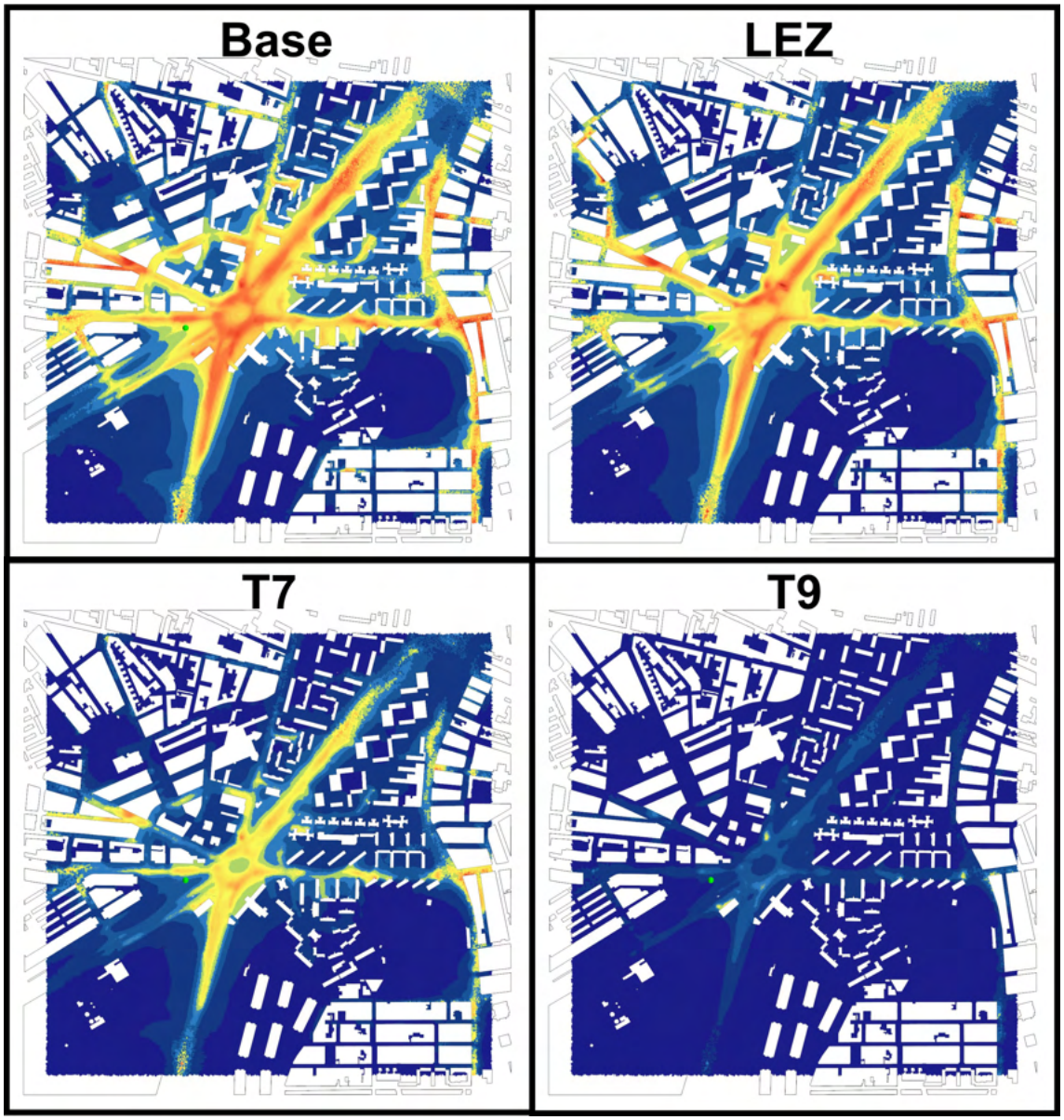

Figure 6.11: Annually-averaged local NO_X concentrations for scenarios: a) 2019_Em19; b) 2019_Em22; c) 2019_Em19_T7; and d) 2019_Em19_T9

In order to analyse the potential role of changing meteorological conditions on the effectiveness of each measure, Table 6.8 shows the absolute impact on the annual mean (averaged along the CFD domain) of local $[NO_X]$ of those measures. For every meteorological conditions the effect of the LEZ implementation on local $[NO_X]$ considering the Em19

emissions is between 4.2 and 5.5 $\mu g \cdot m^{-3}$ (51 to 53%) lower than the impact of the T7 strategy, and about 10.2 to 12.9 $\mu g \cdot m^{-3}$ (71 to 73 %) lower than the impact of the T9 strategy. The differences annual total NO_X emissions of the LEZ with respect the T7 and T9 EV-based strategies were about an 67% and a 81% respectively, a bit larger than the impact on annual [NO_X]. However, the LEZ strategy is the less sensitive to changing meteorological conditions, with an uncertainty range of 1.1 $\mu g \cdot m^{-3}$. This is in line with previous findings in this work in which the impacts of meteorological conditions were lower for lower emissions. The relative reductions are fairly constant for every meteorological conditions in all cases. For the T7 and T9 strategies, the largest relative impact is modelled for the windiest conditions, by a narrow margin. The reductions in the aforementioned 300 m x 300 m study area are larger in absolute values, but quite similar in relative values than those for the whole CFD domain (Table 6.9).

Table 6.8: NO_X local concentrations [$\mu g \cdot m^{-3}$] variations due to the implementation of LEZ, T7 and T9 strategies on for different meteorological conditions. Values represent average variations along the CFD domain

Impacts of different strategies on annual-averaged $[NO_X]_{local}$ [$\mu g \cdot m^{-3}$] (%)			
	LEZ	T7 (Em19)	T9 (Em19)
2016	-4.17 (-22.2)	-8.63 (-45.9)	-15.25 (-81.1)
2019	-3.86 (-21.3)	-8.27 (-45.7)	-14.66 (-81.0)
2022	-4.02 (-22.5)	-8.21 (-45.9)	-14.49 (-81.1)
2023	-4.11 (-22.2)	-8.43 (-45.6)	-14.99 (-81.1)
calmest	-5.09 (-23.3)	-10.62 (-48.6)	-17.94 (-82.1)
windiest	-3.99 (-23.3)	-8.55 (-49.8)	-14.14 (-82.5)

Table 6.9: NO_X local concentrations [$\mu g \cdot m^{-3}$] variations due to the implementation of LEZ, T7 and T9 strategies on for different meteorological conditions. Values represent average variations along the 300 m x 300 m studied area.

Impacts of different strategies on annual-averaged $[NO_X]_{local}$ [$\mu g \cdot m^{-3}$] (%)			
	LEZ	T7 (Em19)	T9 (Em19)
2016	-4.17 (-22.2)	-8.63 (-45.9)	-15.25 (-81.1)
2019	-3.86 (-21.3)	-8.27 (-45.7)	-14.66 (-81.0)
2022	-4.02 (-22.5)	-8.21 (-45.9)	-14.49 (-81.1)
2023	-4.11 (-22.2)	-8.43 (-45.6)	-14.99 (-81.1)
calmest	-5.09 (-23.3)	-10.62 (-48.6)	-17.94 (-82.1)
windiest	-3.99 (-23.3)	-8.55 (-49.8)	-14.14 (-82.5)

Another way to assess the effectiveness of an abatement measure is to analyse the changes in the areas exceeding a certain threshold value, generally established following health-related criteria. For NO_X no official threshold is established, therefore three different values have been analysed in this work: 100, 75 and 50 $\mu g \cdot m^{-3}$. Figure 6.12 shows the impact of each strategy on the exceedances of these threshold values for $[NO_X]_{local}$. In all cases, the impact

of the T7 and T9 strategies is larger than the impact due to the LEZ implementation, and they also overcome the impacts of meteorological conditions. When considering a limit value of 50 $\mu g \cdot m^{-3}$, the meteorological conditions can induce a maximum change of 4% in the fraction area exceeding that limit value when no strategy is applied. However, the T7 and T9 strategy reduce this area to practically zero. The LEZ strategy reduces this area, in average, by a 3%.

Both EV-based strategies reduce the fraction of the domain area exceeding several threshold values to zero or almost zero, even in the most restrictive case which considers a threshold value of 50 $\mu g \cdot m^{-3}$ for the annual value of $[NO_X]_{local}$. The LEZ, on the other hand, reduces the area of exceedances on about a 50% in average when considering threshold values of 100, 75 and 50 $\mu g \cdot m^{-3}$. In addition, the variability of the exceedances areas in the base case induced by the change in the meteorological conditions always exceeds the impact of the LEZ, and exceeds the impacts of the T7 and T9 strategies for lower threshold values.

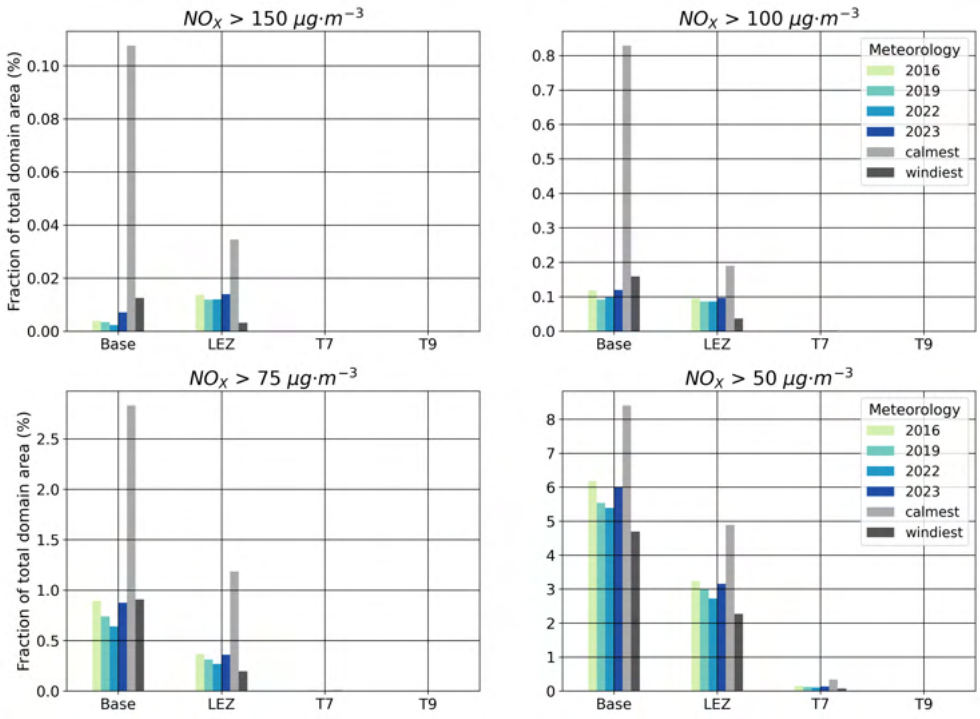

Figure 6.12: Fraction of the total domain area exceeding several annual $[NO_X]_{local}$ values for different scenarios and meteorological conditions. a) Limit value of 100 $\mu g \cdot m^{-3}$; b) 75 $\mu g \cdot m^{-3}$; and c) 50 $\mu g \cdot m^{-3}$.

6.6 Summary and concluding remarks

In this chapter, the impacts of two planned strategies regarding the implementation of electric vehicles in the vehicle fleet have been analysed and compared with an already-implemented strategy. The two strategies consist on a replacement of fuel-powered vehicles by electric

vehicles to a different level. The first strategy, named T7, replaces 22% of the vehicles by electric vehicles. The second, T9, replaces a 85% of them. First, the impacts on NO_X emissions have been estimated using the outputs of previously-evaluated microscopic traffic simulations. Both strategies have significant impacts on NO_X emissions and their impact accentuates when using an older vehicle fleet as reference. For the T7 strategy, those reductions depend on the time of the day and day type of the simulated scenario, whereas for the T9 strategy the emissions reductions are constant in time. For all emissions cases the T7 and T9 significantly reduce annual NO_X emissions, and also diminish the differences in emissions between different vehicle compositions.

To compute the impact on NO_X concentrations the WA CFD-RANS methodology has been applied, but with 8 wind directions sectors instead of 16, to save resources. An evaluation shows that this change does not affect the results in a significant manner. The results show that the implementation of the T7 and T9 strategies does not have a significant impact on the spatial distribution of the local contribution to NO_X, but their impact -specially of the T7 strategy- is greater for areas with larger initial concentrations of NO_X. This translates to spatially-averaged reductions In particular, the changes induced in spatially-averaged - both along all the CFD domain and the 300 m x 300 m study area- local NO_X concentrations are about a 43% for the case of the T7 strategy, and up to a 77% for the T9. Those reductions increase to up to a 68% and 90% $\mu g \cdot m^{-3}$ respectively when considering an older vehicle fleet as reference. The impacts of the strategies on the annual values of spatially-averaged NO_X concentrations overcome the potential impacts of changing meteorological conditions. Changing the meteorological conditions can affect the spatial average of local NO_X concentrations up to a 25%. Furthermore, those changes in meteorological conditions can affect the efficacy of the T7 and T9 strategies up to 6 and 8 $\mu g \cdot m^{-3}$ respectively, which is significantly lower than the net impact of the strategies, but not negligible. However, meteorological conditions impacts are not homogeneous along all the domain due to the interactions of the urban morphology with the wind flow, which induces vortices that affect the ventilation in streets, which at the same time affects the dispersion of air pollutants. In particular, it has been observed that wind direction plays an important role on this interaction, even overcoming -very locally- the impacts of wind speed in air pollutant dispersion. The impacts of the T7 and T9 strategies are fairly similar to those aforementioned when considering a one-month-length period instead of annual values.

When comparing the impacts of the planned strategies with those of the implementation of a LEZ in Plaza Elíptica, it is seen that the planned strategies provide greater NO_X emissions reductions than the LEZ. This translates in a greater impact on the local component of NO_X. When assessing the fraction of the domain with areas exceeding certain threshold values for the local contribution to annual NO_X, it was seen that the T7 and T9 scenarios

could reduce significantly the areas exceeding an annual value of 50 $\mu g \cdot m^{-3}$, and virtually to zero those exceedin an annual value of local NO_X of 75 and 100 $\mu g \cdot m^{-3}$. In this sense, their impacts are larger than the changes in the areas with exceedances induced by changing meteorological conditions, while the LEZ was not able to lower the fraction of areas with exceedances to a larger extent than meteorological conditions.

Chapter 7

Using high-resolution emission data for mesoscale air quality modelling

7.1 Introduction

Despite overall improvements in recent years, air pollution remains as the main environmental problem in Europe (EEA, 2023). In order to address this problem, the Directive 2008/50/EC (Directive 2008/50/EC, 2008) and Directive (EU) 2024/2881 (Directive (EU) 2024/2881, 2024) establishes limit values for the concentrations of different pollutants considered harmful to the human health. The compliances of the limit values are usually evaluated with air quality monitoring stations (AQMS) located strategically to be representative of their area of emplacement. Although many locations in the European Union already meet the new EU 2023 standards, additional measures are needed to improve air quality in those places not yet meeting the standards (EEA, 2025). Particularly, citizens living in large metropolitan areas are exposed to elevated concentrations of nitrogen dioxide (NO_2) mainly because of traffic emissions (EEA, 2021). Road transport is responsible of most nitrogen oxides (NO_X) emissions in Europe, and also accounts for an important part of the particulate matter (PM) emissions in that region (EEA, 2022; Thunis et al., 2023).

Modelling techniques can provide, in advance to their implementation, the impact on air quality of mitigation strategies. In addition, Directive 2024/2881 requires the use of modelling techniques to inform air quality plans, roadmaps and to estimate the impacts of short-term measures. Thus, reliable and detailed input data of emissions is an important necessity for those purposes.

The main goal of this chapter is to develop a methodology to use a new dataset of emissions calculated at street level resolution in CHIMERE, instead of the spatial disaggregation of national inventory data. To that end, this chapter is intended to fulfil the following specific

objectives:

- The development of an interface to adapt high-resolution emissions to a mesoscale model.
- The evaluation of the impact of implementing detailed emissions on a mesoscale air quality model's performance.

With that purpose, emissions from the road transport sector are computed using a microscopic traffic simulator coupled with an instantaneous modal emissions model for the entire city of Zaragoza, which is the fifth largest population in Spain. The computed emissions, once translated into the spatial resolution of the most commonly used inventories, are compared with those from these inventories. The emissions are then incorporated as input data in a mesoscale chemistry-transport model through the use of an interface developed in this research to estimate the air quality throughout a year in Zaragoza. Two estimations of air quality are compared: one performed with the computed emissions, and another with the original emissions from an official inventory. The results were then evaluated with observations from eight AQMS located along Zaragoza.

The advances in the estimates of traffic emissions presented in this chapter, coming from detailed street description, real traffic count data and detailed vehicle fleet composition and driving styles, open the door to the application of the model to the assessment of different traffic measures, also in a prediction mode, as required in the Directive 2024/2881 (Directive (EU) 2024/2881, 2024).

7.2 Traffic-related emissions computation

The traffic simulations have been performed using the SUMO traffic simulator. A time step of 0.5 s has been used to compute vehicles variables such as position, velocity and acceleration. Emissions have been computed with an on-line coupling with the emissions model PHEMLight v5. At each timestep, SUMO provides PHEMLight the necessary variables to compute the engine power of each vehicle present in the simulation. With that information, PHEMLight returns the emissions of every vehicle in the simulation at each timestep.

7.2.1 Modelling domain

The traffic network covers an area of 16.5 km x 11 km, approximately. It covers the whole city of Zaragoza and its ring roads. The network configuration consists on 58959 edges, 30570 junctions and 1347 bus stops (Figure 7.1). 1016 traffic light systems regulate the main intersections of the network.

Figure 7.1: SUMO road network of the traffic domain of Zaragoza. Green colors represent arterial roads; blue represents distributors; and black represent other smaller local roads.

7.2.2 Data sources

In order to perform the traffic simulations, information about the traffic flows and vehicle types in the area during the year 2022 were provided by the Zaragoza City Council. The road network configuration was obtained from OpenStreetMap and converted to a SUMO readable format using a Python script. The public transport lines, bus stops and routes were also provided by the Zaragoza City Council.

7.2.3 Traffic simulation specifications

7.2.3.1 Scenarios

Zaragoza is the fifth largest populated city of Spain, located in the Aragon region, in the north-east of Spain. Its traffic temporal pattern is represented in Figure 7.2. It is fairly constant along the year, excepting August. For all months but August, during working days (in blue) three peaks of maximum traffic flows can be observed. Two of those maxima correspond to the typical morning and evening rush hours, that in Zaragoza occurs from 8:00 to 9:00 h and between 18:00 and 19:00 h respectively. The third maxima appears from 14:00 to 15:00 h. However, during the weekends the pattern is characterised by a two-humped

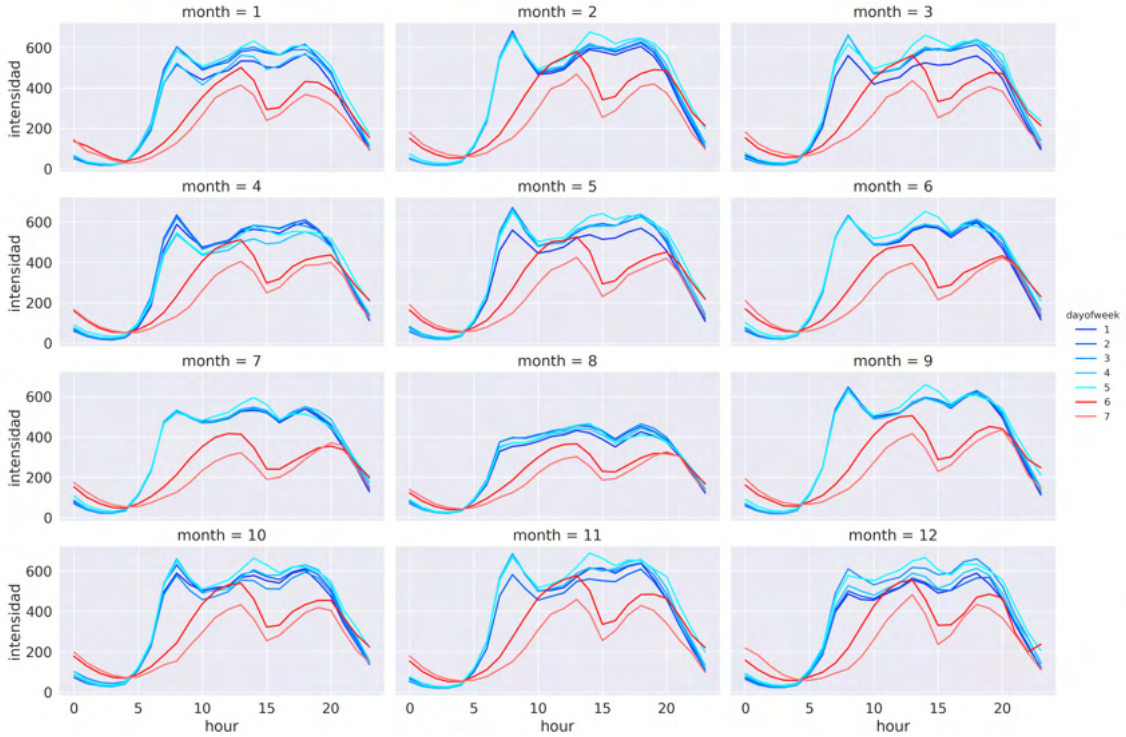

Figure 7.2: Weekly traffic pattern of Zaragoza, for each month and averaged across every permanent detector in the city. Blue colors represent working days, whereas red ones represent weekend days.

pattern with maxima occurring from 13:00 to 14:00 h and from 19:00 to 20:00 h (Figure 7.2). In August, the morning rush hour is diluted along the morning, with traffic progressively increasing from 8:00 h to 14:00 h.

To accurately estimate the weekly pattern of traffic-related emissions the typical weekly and daily patterns in the city were analysed using traffic profiles generated from the available traffic detectors provided by the Zaragoza City Council (Figure 7.3). For the simulated year, 2022, 772 detectors with available data were installed across the city. However, only 127 of them are permanently recording data, whereas the remaining 645 were installed temporarily during campaign measurements.

Seventy two representative scenarios of 1-h length were defined to simulate the weekly traffic pattern. Those scenarios correspond to one working day -Thursday-, a typical Saturday and a typical Sunday. All scenarios are described in Table 7.1. As aforementioned, traffic in Zaragoza along the year is fairly constant, with the main exception of August. This allows to assume a fairly constant weekly traffic pattern along the year so these 72 scenarios will represent the traffic throughout the whole year. This allows to reduce time and resources in a significant way without compromising the accuracy of the results.

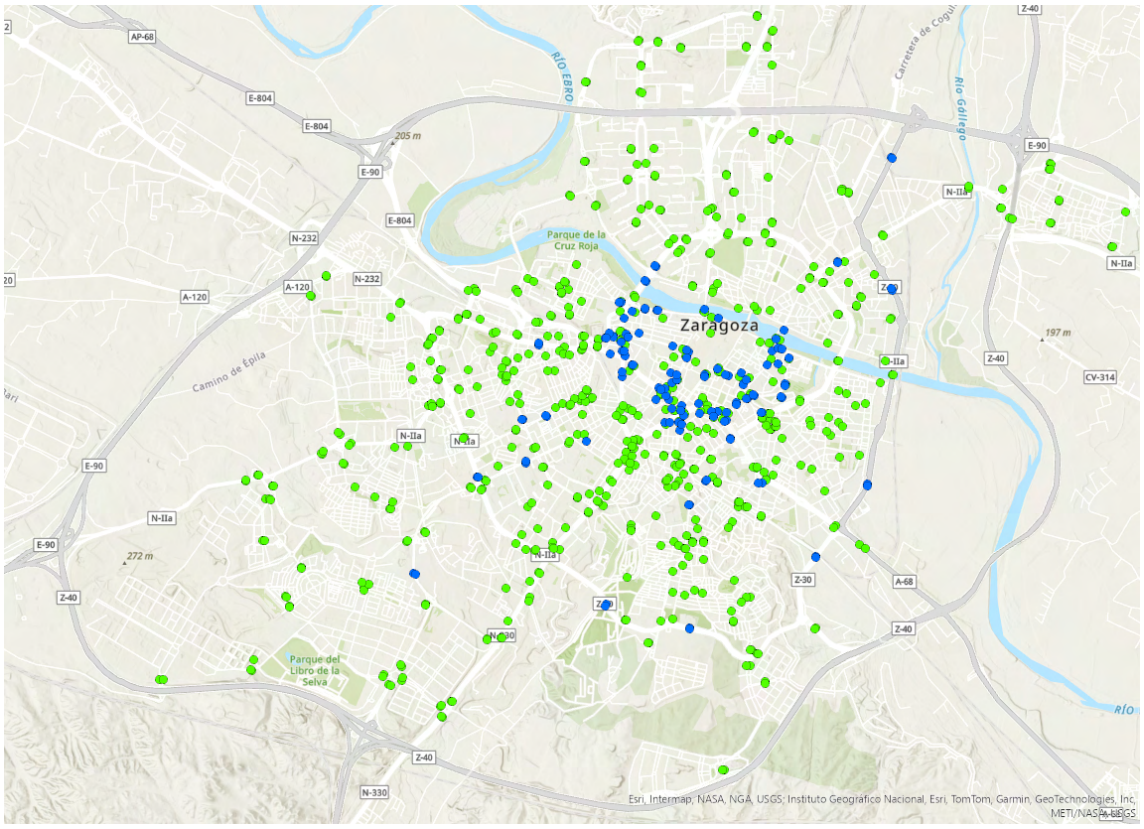

Figure 7.3: Traffic counts with available data within the traffic simulation domain. Blue points represent permanent detectors; green points are non-permanent detectors.

Table 7.1: Simulated 1-h length scenarios to represent the weekly traffic pattern.

Simulated traffic scenarios					
Weekday	Hour	Scenario	Weekday	Hour	Scenario
Thursday	0:00-1:00	L1	Sunday	0:00-1:00	F25
	1:00-2:00	L2		1:00-2:00	F26
	2:00-3:00	L3		2:00-3:00	F27
	3:00-4:00	L4		3:00-4:00	F28
	4:00-5:00	L5		4:00-5:00	F29
	5:00-6:00	L6		5:00-6:00	F30
	6:00-7:00	L7		6:00-7:00	F31
	7:00-8:00	L8		7:00-8:00	F32
	8:00-9:00	L9		8:00-9:00	F33
	9:00-10:00	L10		9:00-10:00	F34
	10:00-11:00	L11		10:00-11:00	F35
	11:00-12:00	L12		11:00-12:00	F36
	12:00-13:00	L13		12:00-13:00	F37
	13:00-14:00	L14		13:00-14:00	F38
	14:00-15:00	L15		14:00-15:00	F39
	15:00-16:00	L16		15:00-16:00	F40
	16:00-17:00	L17		16:00-17:00	F41
	17:00-18:00	L18		17:00-18:00	F42
	18:00-19:00	L19		18:00-19:00	F43
	19:00-20:00	L20		19:00-20:00	F44
	20:00-21:00	L21		20:00-21:00	F45
	21:00-22:00	L22		21:00-22:00	F46
	22:00-23:00	L23		22:00-23:00	F47
	23:00-24:00	L24		23:00-24:00	F48
Saturday	0:00-1:00	F1			
	1:00-2:00	F2			
	2:00-3:00	F3			
	3:00-4:00	F4			
	4:00-5:00	F5			
	5:00-6:00	F6			
	6:00-7:00	F7			
	7:00-8:00	F8			
	8:00-9:00	F9			
	9:00-10:00	F10			
	10:00-11:00	F11			
	11:00-12:00	F12			
	12:00-13:00	F13			
	13:00-14:00	F14			
	14:00-15:00	F15			
	15:00-16:00	F16			
	16:00-17:00	F17			
	17:00-18:00	F18			
	18:00-19:00	F19			
	19:00-20:00	F20			
	20:00-21:00	F21			
	21:00-22:00	F22			
	22:00-23:00	F23			
	23:00-24:00	F24			

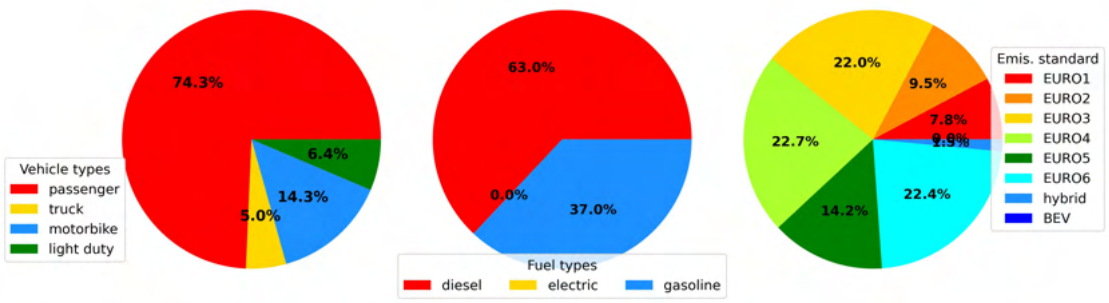

Figure 7.4: Vehicle fleet classified by vehicle type, fuel type and emission standard. Data provided by Zaragoza City Council.

7.2.3.2 Fleet composition

The fleet composition of the simulations is illustrated in Figure 7.4. There is a predominance of passenger vehicles, representing almost a 75% of the total fleet. It is followed by motorbikes (14.3%) and light duty vehicles (6.4%). The less represented is the vehicle type "truck", with a 5% share of the total fleet. Regarding the fuel types, the most abundant is diesel (63% to 37% gasoline). Electric vehicles representation is residual. By emission standard, there is a predominance of Euro6, Euro4 and Euro3 vehicles, each of them representing a 22% of the vehicle fleet. Hybrid vehicles represent a 1.5% of the total fleet, whereas most pollutant vehicles Euro1 and Euro2 still represent a 17.3% of the total vehicle fleet.

7.2.3.3 Emissions

Figure 7.5 shows the total emissions for each simulated scenario. For the working-day scenarios (upper plot of the figure), there is a rapid increase of emissions between 4:00 and 9:00 h, with the maximum of emissions reached between 8:00 and 9:00 h (scenario L9), coinciding with the most trafficked hour. After that hour, emissions decrease until reaching a minimum between 11:00 and 12:00 h, and then starts to grow again as traffic flow increases. During the afternoon, two maxima of emissions are slightly appreciable between 15:00 and 16:00 h and between 18:00 and 19:00 h. Then, emissions rapidly decrease. On the other hand,

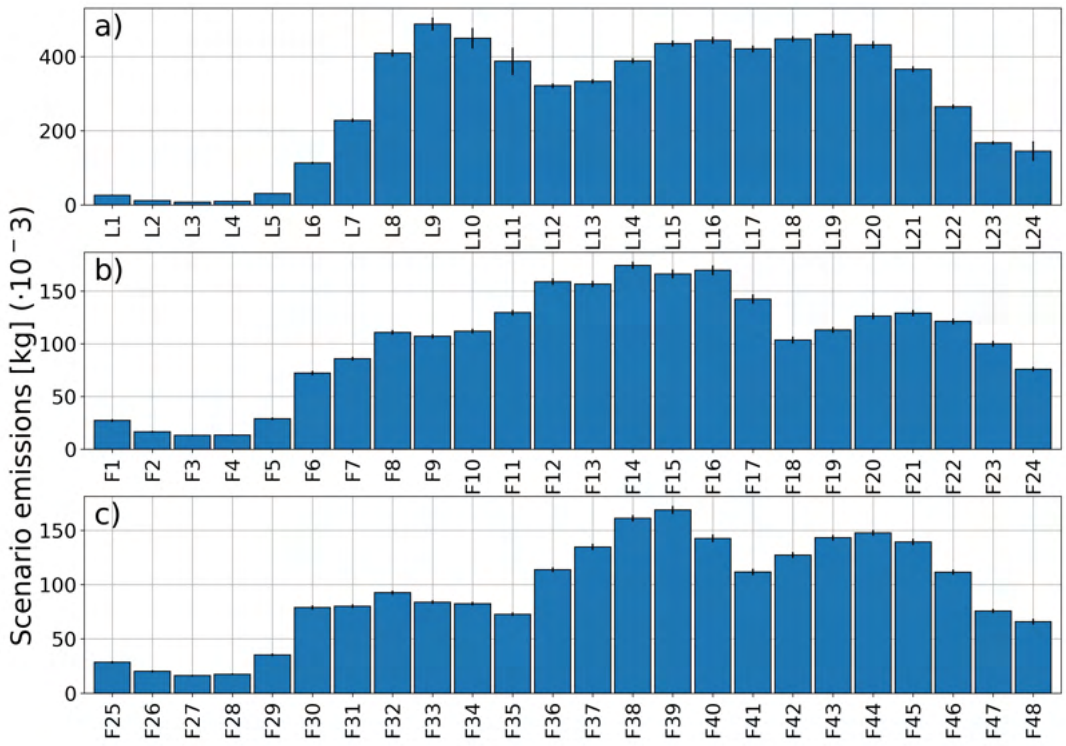

Figure 7.5: Traffic-related emissions for each scenario across the simulation domain during a) Working days; b) Saturdays; c) Sundays. Black spines indicate the emissions' standard deviation.

during Saturdays (scenarios F1 to F24) there is a more progressive ascend of emissions during the morning, starting to rise at 4:00 -such as in weekdays- but the maximum of emissions is shifted to 14:00 h. Then, emissions decrease to reach another maximum between 20:00 and 21:00 h. This behaviour is similarly -but not identically- reproduced during the Sundays. In Sundays, the morning emissions follow a different pattern than during Saturdays: between 3:00 and 6:00 h (scenarios F28 to F30) there is a rapid increase in emissions, such as in the Saturday, but then between 6:00 and 11:00 h (scenarios F30 to F35) emissions are stagnated, even slightly decreasing, and then rise again rapidly from 11:00 h to 14:00 h, in contrast to Saturdays when emissions gradually increased from 6:00 h to 14:00 h. The afternoon maxima is also observed during the Sundays, with higher emissions that those in Saturday and a quicker descend in emissions during the lasts hours of the day.

Figure 7.6 shows the spatial distribution of NO_X emissions in Zaragoza for the L9 scenario, which corresponds to the working-day morning rush hour. In can be observed how the arterial roads and the distributors present the largest values of NO_X emissions. In contrast, smaller local streets present low values of emissions.

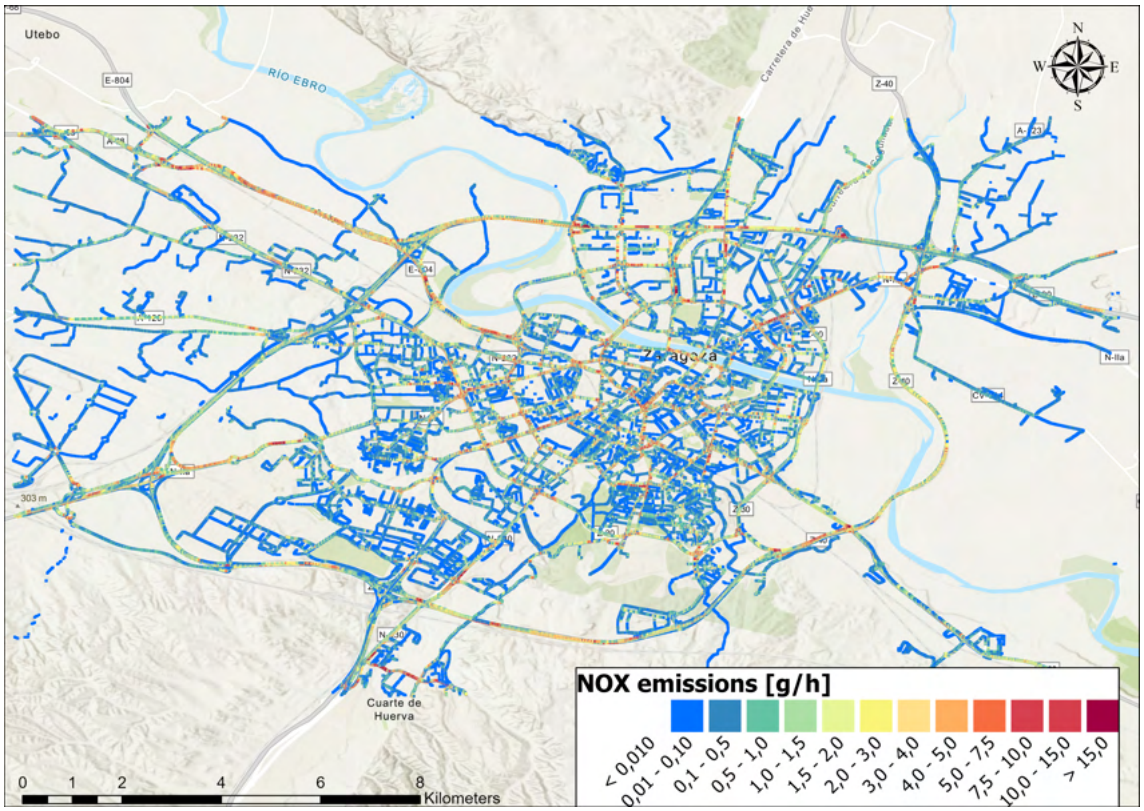

Figure 7.6: Spatial distribution of traffic-related emissions for the L9 scenario across the simulation domain.

Comparing emissions with inventories

The emissions computed in this work have been compared with the emissions from other existent inventories. These inventories and their sources are detailed in Table 7.2. Due to their different resolutions, all datasets were compared to the coarser grid. To that end, a process of upscaling was applied to all the datasets with resolutions finer than 0.1^{o} x 0.1^{o}.

Table 7.2: Reference inventories to compare the traffic-related NO_X emissions with.

Inventory	Horizontal resolution	Source
SUMO	Punctual	This PhD thesis
CAMS-REG-ANT	0.05^{o} x 0.1^{o}	Kuenen et al. (2022)
AytoZgz	100 m x 100 m	Zaragoza City Council
NEI	0.1^{o} x 0.1^{o}	MITERD

From the upscaling process, the Zaragoza city is covered by two 0.1^{o} x 0.1^{o} cells of those inventories (Figure 7.7), one with its centroid at coordinates (-0.95^{o},41.65^{o}) and the other at (-0.85^{o}, 41.65^{o}). The comparison between the total annual NO_X emissions at these cells is shown in Table 7.3. The novel emissions estimated in this research from microscopic input data are significantly larger than those in the current public inventories. Particularly, the emissions from this work are 74% larger than those from the EMEP inventories in both

Figure 7.7: Map of the city of Zaragoza with cell grids of 0.1º x 0.1º superposed.

cells; 319% and 290% larger than those of the CAMS-REG-ANT inventory; and 327% and 311% larger than the emissions from the Zaragoza City Council. The uncertainty of the emissions estimated in this work were also computed in terms of the standard deviation. This uncertainty arises from the incertitude of the traffic fluxes inside the streets without any traffic count data. The standard deviation of the novel emissions estimated in this work are of about 1% of total emissions, much lower than the differences with the current public inventories' emissions.

Table 7.3: Total 2022 NO_X emissions in Mg.

Inventory	Cell (-0.85º, 41.65º)	Cell (-0.95º, 41.65º)
SUMO	996.99	817.71
SUMO STD	10.76	11.15
CAMS-REG-ANT	230.81	209.90
AytoZgz	226.55	198.83
EMEP	553.45	469.32

7.2.4 Preparation of traffic emissions for a regional model

The versatility of the emissions outputs files provide by SUMO allows for specific treatment of those emissions depending on the study case. In order to use the emissions provided by

SUMO within the CHIMERE model, a Python module has been developed in this PhD thesis that allows any user to easily modify the original EMI files from CHIMERE to run specific scenarios. The rest of the subsection will be devoted to detail the functionalities of this Python module, which has been called **SUMO2CHIMERE**.

7.2.4.1 The SUMO2CHIMERE Python module

The **SUMO2CHIMERE** Python module has been developed in the scope of this PhD thesis in order to easily include SUMO emission in CHIMERE's EMI files. It consists on two functions that:

- Aggregate the punctual emissions into user-specified cells.
- Modifies an existent EMI file by substituting the original emissions by the user-provided SUMO emissions.

The version described in this document is a first version of the module focused on the needs of this research. In the future, this module will be improved to generalize its use. For example, a future development will be the aggregation of linear data into cells, not only punctual emissions.

It provides several advantages over the original standard emissions preprocessing system incorporated in CHIMERE:

- **Flexibility**: It doesn't require a gridded input file. SUMO2CHIMERE also admits punctual data, and it is planned to admit linear data as well in the future.
- **Independence**: Due to the high- temporal and spatial resolution characteristic of the SUMO emissions outputs, the SUMO2CHIMERE module does not need spatial proxies nor temporal profiles to perform the emissions assignment.
- **Portability**: The user can easily define their own species speciation and vertical distributions of emissions by just modifying a text file. No code compilations are needed to run the module.

The SUMO2CHIMERE module is structured in two functions. The first function, called *aggregate_to_cells*, is devoted to perform an aggregation or averaging of data within the cells of a given grid. It takes four parameters:

1. A file containing the initial data to be aggregated. This file must include the values to be aggregated, and the coordinates of the values.
2. A file containing the objective grid to which the initial data is going to be aggregated. It must also be georeferenced.

3. The Coordinate Reference Systems (CRS) of both the data to be aggregated and the objective grid.

4. A parameter indicating the type of operation to perform. At the moment, only "agg" (from "aggregate") and "avg" (from "averaging") are possible values for this parameter.

The data to be aggregated can be punctual data -as in the case of SUMO emissions- or gridded data. There are no restrictions, further than to be georeferenced, to objective grid. It can be a regular grid or an irregular one. The *aggregate_to_cells* function takes the data to be aggregated and performs the desired operation to the data, returning gridded data with the resolution and extension of the objective grid, and georeferenced in the desired CRS.

The second part of the module is the *modify_EMI* function. This function takes as input the aggregated emissions file generated by the *aggregate_to_cells* function and uses this data to replace values in the original EMI file(s) from CHIMERE. This function replaces some functionalities of CHIMERE's standard emission preprocessing system (Section 3.2.1). The *modify_EMI* function, in its actual version, makes some assumptions that one must consider in order to get the desired results. The first assumption is that the emission files must end with the following chain of strings: "_<hour><dtlabel>.csv". <hour> represents the hour of the emission scenario to be considered, whereas <dtlabel> must be the label assigned by the user to the day type corresponding to that emissions. Other important assumption is that *modify_EMI* assumes that the emissions values are given in kg.

The **modify_EMI** function starts with the definition of some parameters that may be needed afterwards in the code. *N_av* represents the Avogadro constant. *MM_pol* defines the molar mass of the pollutant considered, using an external module for its computation. If *convert_to_molec* is set to True, the Avogadro constant and the molar mass of the considered pollutant are needed, as well as the areas of each cell, to convert from kg to molecules/cm^2/s. Otherwise, the function will assume that the final units to be g/km^2/s. Both molecules/cm^2/s and g/km^2/s are the units of the variables within CHIMERE's EMI files, which is the reason to convert the input data to these units. In addition, the data necessary for the vertical distribution and the speciation are also read at the beginning of the function, if a file is specified for each purpose.

The absolute path of the file containing the data for the vertical distribution is given by the user with the parameter *vdist_file*. This file must include two columns: One column named "MODEL_VLEVEL"containing the EMI file vertical levels indices; and other column named "FRAC" containing the fraction of the total emissions (in %) to be assigned to each vertical level. In the example given by Figure 7.8, all emissions will be assigned to the first vertical level when the vertical distribution is done later in the code.
Regarding the speciation process, an speciation factor is defined within the code in order

	A	B
1	MODEL_VLEVEL	FRAC
2	0	100
3	1	0
4	2	0
5	3	0
6	4	0
7	5	0
8	6	0

Figure 7.8: Example of the contents of the vertical distribution file.

to multiply the emissions by that factor. If a filename is passed through the *speciation_file* parameter, the speciation factor is read from the given file; otherwise, it is set to 1. The speciation file must include four columns. One column must include the name(s) of the original specie(s). This column must be named "SPECIE". Other column, named as "MODEL_SPECIE" must include the names of the model species into which the original species must be speciated. The third column ("FRAC") should define the fraction of the original species to be converted into each model species (in %). Finally, a fourth column, named as "ACTIVITY_SECTOR", sets the activity sector of the speciation. Each conversion from original to model species can have a different "FRAC" value for each activity sector. The *activity_sector* parameter is used to select the speciation sector within the speciation file. It can be better illustrated with a small example. Suppose that the speciation file is that of Figure 7.9. In this case, if the user sets *activity_sector* to "SNAP7", *pol* is set to "NO2" and *emis_pol* is "NOx" , the modify_EMI function will search define the speciation factor as 0.9 ($90 \cdot 0.01$).

	A	B	C	D
1	SPECIE	MODEL_SPECIE	FRAC	ACTIVITY_SECTOR
2	NOx	NO2	90	SNAP7
3	NOx	NO	9.2	SNAP7
4	NOx	HONO	0.8	SNAP7
5	NOx	NO2	95	SNAP2
6	NOx	NO	4.5	SNAP2
7	NOx	HONO	0.5	SNAP2

Figure 7.9: Example of the contents of the speciation file.

The script also allows to perform a correction of the hourly emission values when *hourly_corr* is set to True. In this case, the hourly correction factors are read from a file, which is read in

this first section of the function. After reading the different parameters and optional files, the first step consists on reading all the emission data and merging them into one unique pandas DataFrame. To do so, the emission files are grouped in day types (from 1 to 7) depending on its filename ending. Then, for each day type the scripts checks that the number of hourly data does not exceed 24. If it happens, the function raises an error. For example, if the user has defined a day type as "weekend" with 48 hourly values corresponding to Saturday and Sunday, the user must disaggregate the day types as "Saturday" and "Sunday". This is done to simplify the process of matching each emissions file with the corresponding dimension of the EMI file.

The second step consists on identify the cells of the original EMI file to be modified. This is done by reading the edge's coordinates of the emissions file and finding the nearest EMI's cell to them. The third step is the modification of the EMI file values. This is done iteratively for each vertical level specified in the *vdist_file* (if not value given, all emission will be assigned to the first vertical model level. To do this assigment, several processes are done for each vertical level:

- Firstly, a numerical factor is read from the *vdist_file* to perform the vertical distribution of the emissions.
- Then, the data from the emissions DataFrame corresponding to the current hourly scenario is read and transformed into a matrix matching the EMIs format.
- The next process, if needed, is the speciation of the pollutant into model species. This is done by reading the *speciation_file*. This file contains three columns: the first column contains the original species (given to the function as *emis_pol*, the second contains the model species (*pol*) and the third column contains the fraction of the original species to be converted to the model species. The speciation factor to be applied, which was defined at the preamble of the function, is that which contains the *pol* parameter in the second column and the *emis_pol* in the first one. If no speciation file is given, the speciation factor is set to 1 and no changes are done to the matrix from the previous step.
- Then a unit conversion from total mass to mass fluxes is done. The conversion can be done from kg to molecules/cm^2/s (if *convert_to_molec* is set to True) or from kg to g/cm^2/s. After the conversion, the result is multiplied by the vertical distribution factor.
- If needed, correction factors are applied.
- Finally, the transformed emission data is added into the corresponding cells of the EMI date.

At the end of the function, a new netcdf is returned with the modified values. The path of the new netcdf is given by the user in the parameter *outfile*.

SUMO2CHIMERE can be an useful tool for air quality modellers working with punctual emissions of any activity sector. Figure 7.10 compares the working flows of the CHIMERE's standard preprocessing system and SUMO2CHIMERE. The module developed in this work uses less input data than CHIMERE's standard preprocessing system, and allows for more flexibility on the inventory input data to reach the same output file. This make this module useful, for example, for mesoscale studies of mitigation strategies.

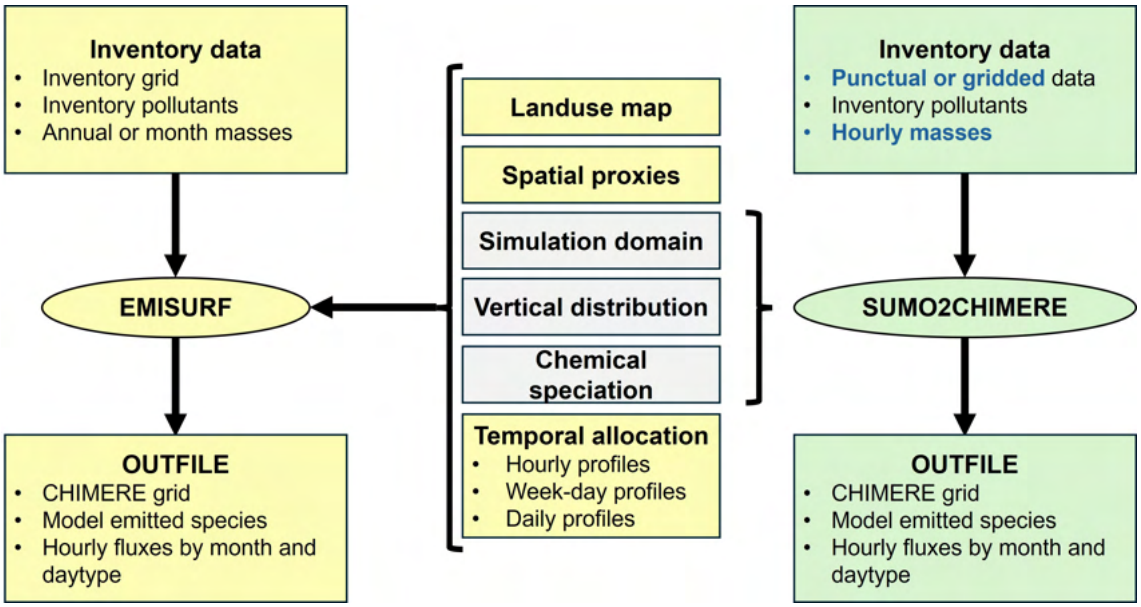

Figure 7.10: Working flow of CHIMERE's standard preprocessing system program and SUMO2CHIMERE Python module. Grey boxes indicate common inputs for both tools. Blue labels indicates differences with respect to the standard preprocessing method.

7.3 Mesoscale air quality modelling

The main goal of this chapter is to develop a methodology to use a new dataset of emissions calculated at street level resolution in CHIMERE, instead of the spatial disaggregation of national inventory data. This will allow to study the model's sensitivity to a high-resolution set of emissions computed with SUMO, comparing the resultant air pollutants estimations with simulations performed with emissions from official inventories.

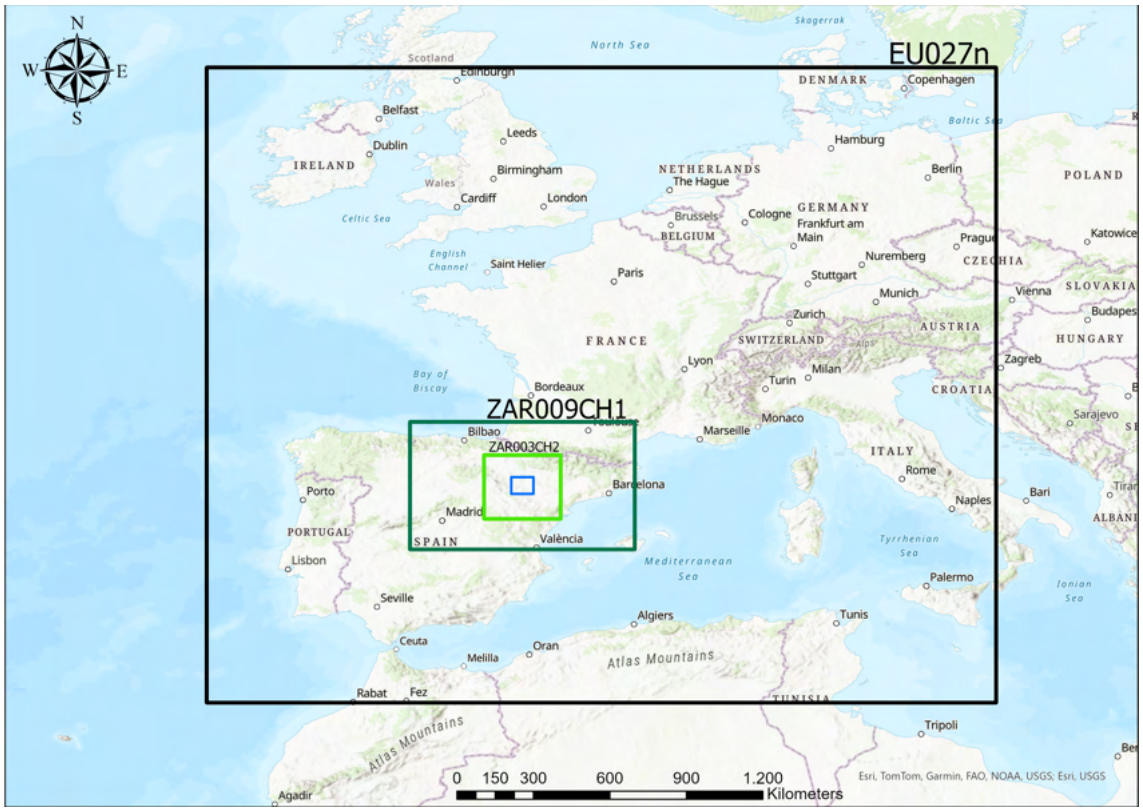

Figure 7.11: Modelling domains employed within CHIMERE. The unlabelled blue polygon represents the limits of the ZAR001CH2 domain.

7.3.1 Modelling setup

7.3.1.1 Modelling domains

CHIMERE simulations were performed over four nested domains. Figure 7.11 illustrates the domains used in this work. The coarser domain, the EU027n, has a spatial resolution of 0.27^{o} x 0.27^{o}. The ZAR009CH1 is nested within the EU027n and has an horizontal resolution of 0.09^{o} x 0.09^{o} and covers the whole region of Aragón, as well as another adjacent regions and the entire Pyrenees mountain range. The ZAR003CH2 domain has a resolution of 0.03^{o} x 0.03^{o} and covers the most of the Aragón region. Finally, the ZAR001CH2 is centred in the city of Zaragoza and covers the whole city and its adjacents areas with an horizontal resolution of 0.01^{o} x 0.01^{o}.

7.3.1.2 Meteorological data

The CHIMERE model uses hourly meteorological variables from a meteorological model as input data to compute the spatial and temporal distribution of pollutants concentrations. In this work, simulations of the WRF mesoscale model have been performed to feed the CHIMERE model. The WRF model has been run using four nested domains, with an horizontal resolution of 27, 9, 3 and 1 km respectively. The BEP-BEM parametrization has

been used in order to properly represent the energy and momentum balances within urban areas. The NOAH-MP vegetation model has been used for the non-urban grid points. The Bougeault and Lacarrere PBL scheme (Bougeault and Lacarrere, 1989) has been used for turbulence parametrization. The simulations were performed in one-month-length periods with nine days of spin-up. To construct the annual timeseries, the one-month-length periods were concatenated excluding the spin-up periods.

7.3.1.3 Boundary conditions

In addition to meteorological data, CHIMERE needs hourly information about the emission fluxes for each model species. Current public inventories usually provide this information in annual basis, which makes necessary a previous work to transform this information into hourly data. In addition, these inventories are elaborated for domains and resolutions that can differ from the model application. The same happens with the novel emissions estimated in this work. Thus, a preprocessing of those emissions is needed to re-grid them into the model simulation domains. Finally, the information provided by the public inventories refer to certain compounds, that may not coincide with the species included in the model chemical mechanism. For example, NMVOCs emission in the inventories refer to the whole set of these compounds, while the model needs information about each one of the species comprising the NMVOCs group defined in the model chemical mechanism. This makes necessary a preprocessing that disaggregates NMVOCs emissions into the model species.

For the EU027n domain, NO, NO_2, NMVOCs, SO_2, CO, PM_10, $PM_2.5$, Pb, Cd and BaP emissions were taken from the EMEP inventory (EMEP, 2025), for the year 2022 (2024 edition) and with a spatial resolution of 0.1^{o} x 0.1^{o}. These emissions were only used outside the Spain frontiers. Inside Spain, the emissions from the National Emissions Inventory (NEI) provided by Ministerio para la Transición Ecológica y el Reto Demográfico (MITERD), also for the year 2022. In addition, information about the emissions from shipping is based on the information provided by the Finish Meteorological Institute (FMI) (Jalkanen et al., 2012; Johansson et al., 2013; Jalkanen et al., 2016; Johansson et al., 2017; Granier et al., 2019). On the other hand, Arsenic (As) and Nickel (Ni) are not included in the georeferenced database from EMEP, and only information from TNO has been found for the year 2000 at a 50 km x 50 km horizontal resolution. Therefore, those pollutants have been only modelled at a national scale, using the information from the NEI.

For the ZAR009CH1, ZAR003CH2 and ZAR001CH2 domains, emission data corresponding to 2022 (2024 edition) for every pollutant were provided by MITERD, at a resolution of 0.1^{o} x 0.1^{o}.

7.3.1.4 Biogenic emissions

Biogenic emissions of six CHIMERE species – isoprene, α-pinene, β-pinene, limonene, ocimene, and NO, for every simulation domain, were computed using the MEGAN model data and parametrizations. The MEGAN model (Guenther et al., 2006b) exploits most recent measurements in a gridded and canopy scale approach, which is more appropriate for use in CTMs since it estimates the effective burden of gases that mix and react in the boundary layer (Menut et al., 2013).

7.3.2 Preparation of the emissions files

In order to estimate the air quality with the CHIMERE model, a preparation of the files containing the emission fluxes must be done. To compute the biogenic and all the anthropogenic emission fluxes sector within each of the four domains, the CHIMERE's standard emission preprocessing system has been used. As described in Section 3.2.1, this system regrids the original emissions data to each simulation domain in CHIMERE, distributes them vertically and temporally using different proxies. In this work, the biogenic emissions have been obtained from the MEGAN dataset, and the anthropogenic emissions are from the EMEP inventory. For the road-transport sector, the EMI files obtained from CHIMERE's standard emission preprocessing system where modified to include the SUMO emissions in each domain. To that end, the *SUMO2CHIMERE* module was used to transform the output emissions from SUMO into gridded emissions within the cells of each simulation domain. As the SUMO domain is smaller than any simulation domain in CHIMERE, the emissions of SUMO where only implemented in those cells of the CHIMERE domain with emissions from SUMO. Otherwise, the original emissions from the CHIMERE EMI file were considered.

7.3.3 Study cases

Several study cases have been performed in order to analyse the impacts on the model performance of the implementation of a newly created set of emissions, and their spatial distribution, in CHIMERE:

1. **Base case**: In this case the CHIMERE model has been executed using the emissions of the national inventory (2024 edition) for the cells in Spain and for every activity sector, including the SNAP7 activity sector.

2. **SUMO_proxychim case**: This case uses the emissions from SUMO as emissions for the SNAP7 activity sector. But for their spatial distribution, the road proxy of CHIMERE has been applied. To that end, the emissions from SUMO have been aggregated to the national inventory cell grid resolution, and then the CHIMERE's

standard emission preprocessing system has been applied to distribute the emissions spatially and temporally. Therefore, the spatial and temporal distribution of SNAP7 emissions is the same than in the Base case, but not the absolute value within each cell.

3. **SUMO case**: In this case, the emissions for the SNAP7 are those from SUMO, introduced within CHIMERE using the SUMO2CHIMERE module. In this case, neither the spatial or temporal distribution of the emissions match those of the Base case.

Figure 7.12 shows the differences in the inserted NO_2 emission fluxes for the different cases, for the ninth hour of the day type 1 (which represents Mondays) inside the ZAR001CH2 domain. In all cases, the NO_2 emission fluxes have been computed using the NO_X speciation from the GENEMIS recommendations (Friedrich, 2000; Kurtenbach et al., 2001; Aumont et al., 2003). The spatial distribution of those fluxes for the Base and the SUMO_proxychim are almost identical, although the values within each cell are not the same. In those cases, the maximum NO_2 emission fluxes for this specific hour are located at the north of the city of Zaragoza, and in some cells in the city center. The largest differences are found in the SUMO case, where the NO_X fluxes are notably larger in general across the city, with large values in an extense region near the city center. Those differences are consistent in time, as Figure 7.13 shows for a weekend rush hour scenario. In this case, the emission fluxes are smaller but their spatial distribution are similar to those of a weekday scenario for all cases, with the main difference being a slight shift to the SW of the maxima of emission fluxes.

The use of the SUMO2CHIMERE module to implement the emissions within CHIMERE allows to maintain the original temporal distribution of emissions, instead of applying the default profiles in CHIMERE which are country-specific and may not be able to represent the temporal evolution of emissions of a certain study area. Figure 7.14 illustrates the difference in the temporal profiles inserted using the SUMO2CHIMERE module, which is the same that the temporal evolution of the original emissions originally computed with SUMO and PHEM-light, and the original profile defined within the CHIMERE model, which has been used for the base and SUMO_proxychim cases. The modified profile differs significantly from the original one. Both of them are normalized by the weekly mean value of emissions. During the week, the modified profile presents the three-humped profile observed when analysing the traffic flows in Zaragoza, whereas the original profile only models two maxima, with the second one delayed until 22:00 h, which differs from both the modelled and observed traffic. During the weekend, the differences are even more significant. The original profile shows three maxima, one at 0:00 h, other at 9:00 h and the last one at 23:00 h (hours in local time) on Saturdays and 22:00 h on Sundays. On the other hand, the modified profile shows its maximum values at around 15:00 h and 20:00 h, which is more in line with the

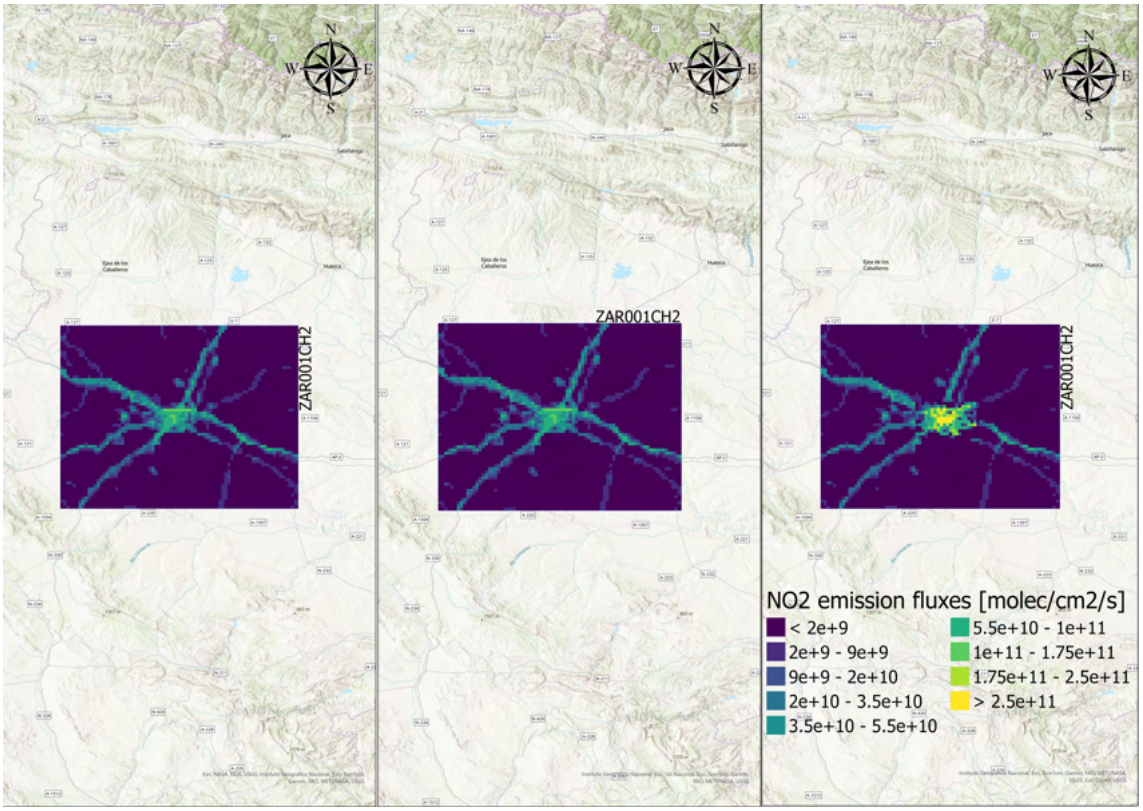

Figure 7.12: Emission fluxes for NO_2, at the lowest vertical level of CHIMERE, for the day type 1 (which is Monday) at 9 h local time for: a) Base case; b) SUMO_proxychim case; and c) SUMO case.

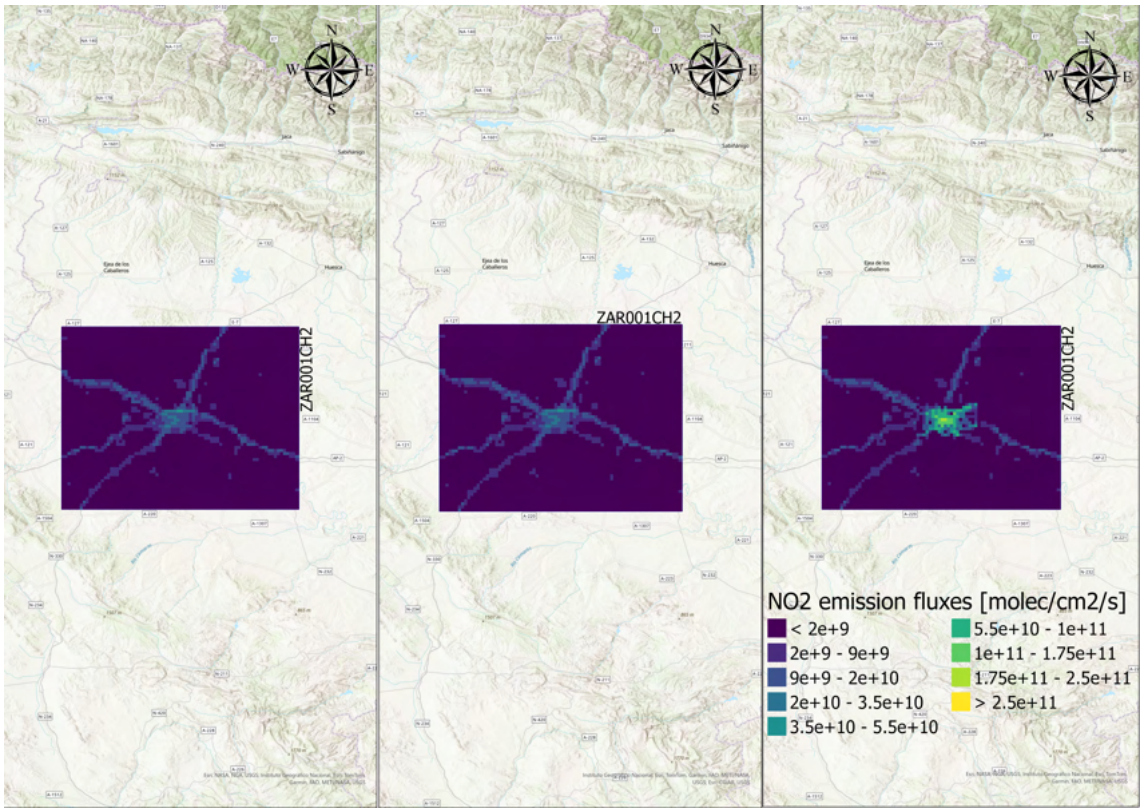

Figure 7.13: Emission fluxes for NO_2, at the lowest vertical level of CHIMERE, for the day type 6 (which is Saturday) at 14 h for: a) Base case; b) SUMO_proxychim case; and c) SUMO case.

observed traffic fluxes in Zaragoza (Figure 7.2). In addition, the original profiles showed for the weekend nighttime, emission values up to twice the weekly mean value -similar to the weekdays' maxima-, whereas the modified profiles for the weekends shows it maxima value at the mean week value, which is three times lower the morning rush hour value during weekends.

7.3.4 Evaluation of meteorological variables

The WRF simulations used to feed CHIMERE with meteorological data were evaluated at the two AEMET stations located in the periphery of the city of Zaragoza: Zaragoza-aeropuerto and Zaragoza-Valdespartera (Figure 7.15). Zaragoza-aeropuerto station is located 12.5 km west to the city center, whereas Zaragoza-Valdespartera is located 6 km SW to the city center.

Figures 7.16 and 7.17 show the observed and modelled wind speed values for the Zaragoza-Valdespartera and Zaragoza-aeropuerto stations respectively. The wind regime in the Zaragoza-Valdespartera station is strongly characterised by the "cierzo" wind (gren areas), which is a NW wind typical of Zaragoza, and its SE counterpart, the "bochorno" wind (red areas). In this station the WRF model is able to represent the variable wind

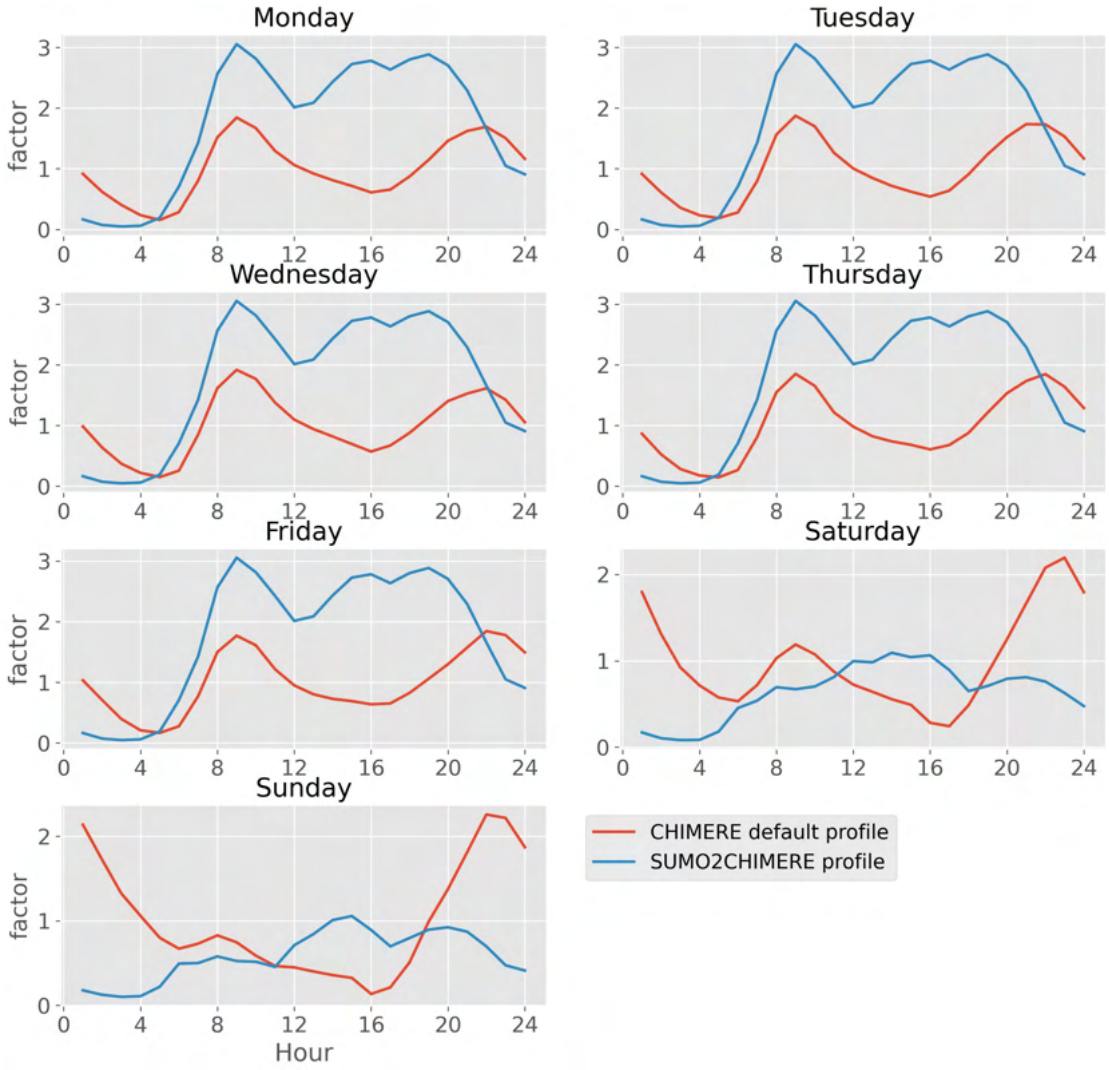

Figure 7.14: Daily evolution of inserted emissions in CHIMERE model, corresponding to SNAP7 emissions. Red line indicates the default profiles in CHIMERE model, whereas the blue lines indicates the temporal profile inserted within the SUMO case. Factor is an adimensional number.

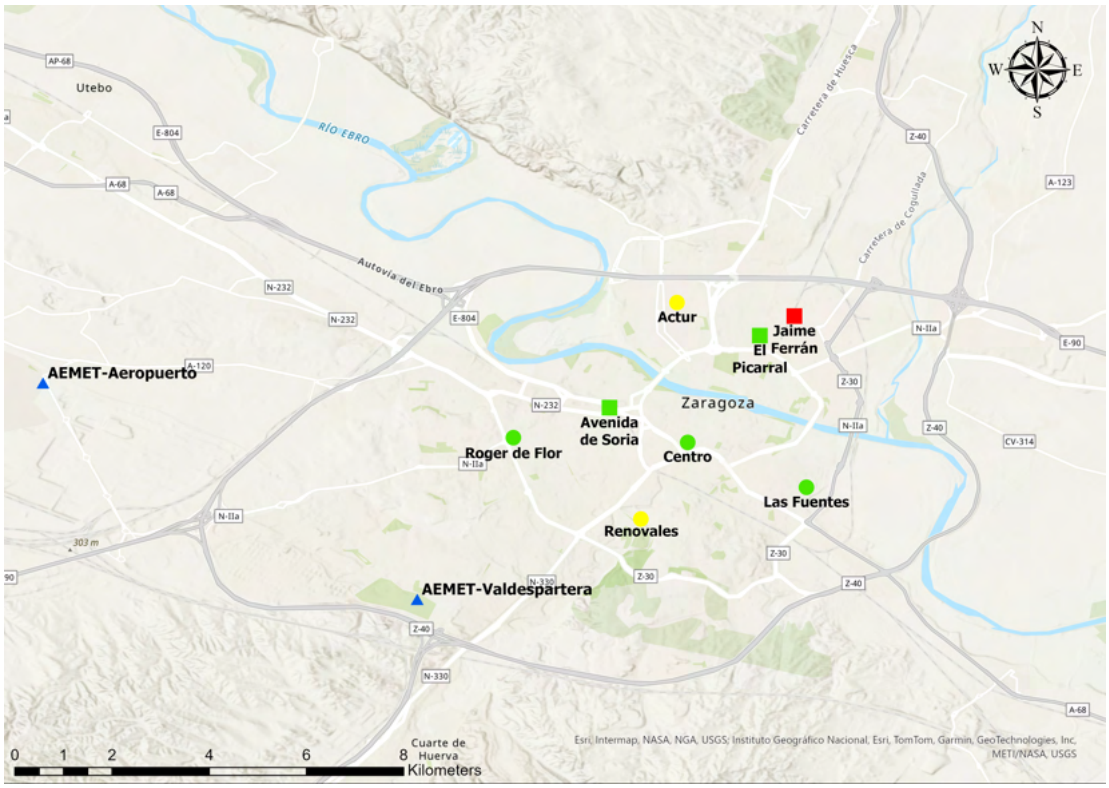

Figure 7.15: Location of the eight AQMS in the city of Zaragoza employed to evaluate the CHIMERE simulations. Circles represent air quality urban stations, whereas squares represent suburban stations and triangles represent meteorological stations. Red colors represent industrial stations; green represent traffic stations; and yellow colors represent background stations. Blue triangles represent meteorological stations used to evaluate the data from WRF.

intensity, even the step temporal gradients of wind speed when a change to cierzo regime is observed. Nonetheless, some overestimation of the wind intensity is modelled, specially during the month of November. In the Zaragoza-aeropuerto station, the bochorno wind is much less frequent than the cierzo regime, probably due to the impact of the Zaragoza city in the upwind wind direction due to its increased surface roughness. In this station the model is also able to predict the temporal evolution of wind speed and its abrupt changes, and, at the contrary that in Zaragoza-Valdesperatera, no significant overestimations are observed. This is also confirmed by the statistical parameters presented in Table 7.4. For both stations, a good correlation coefficient is obtained, of 0.74 and 0.70 for Zaragoza-aeropuerto and Zaragoza-Valdespartera stations respectively. For the former, the FB is zero, the $NMSE$ is 0.21 and the $FAC2$ parameter is equal to 0.79. For the latter, a larger FB (0.29) is obtained, with an $NMSE$ of 0.32 and $FAC2$ of 0.72.

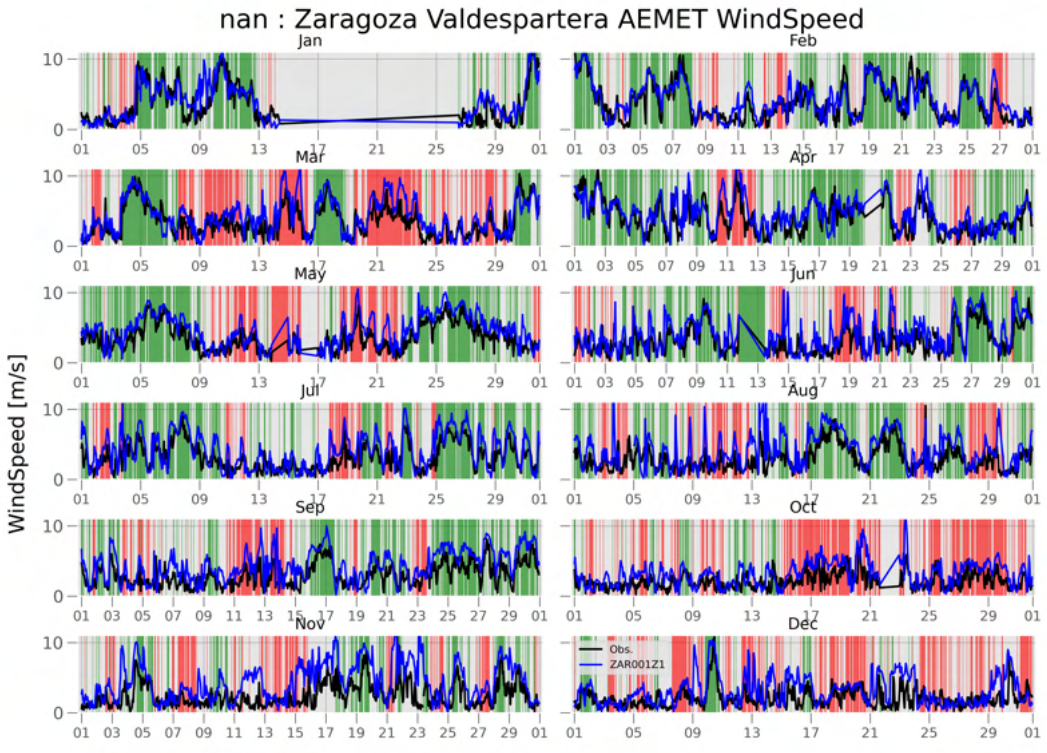

Figure 7.16: Observed (black) and modelled (blue) wind speed at Zaragoza Valdespartera AEMET station. Modelled values correspond to the finest domain ZAR001Z1. Green areas represent periods with observed cierzo wind, whereas red areas represent periods with its SE counterpart, called "bochorno wind"

7.3.5 Estimating air quality

The CHIMERE model has been run for the whole year 2022, with a spin up period of 10 days for the three aforementioned cases: Base case, SUMO_proxychim case and SUMO case. The modelled values are evaluated with observational data from eight different AQMS situated

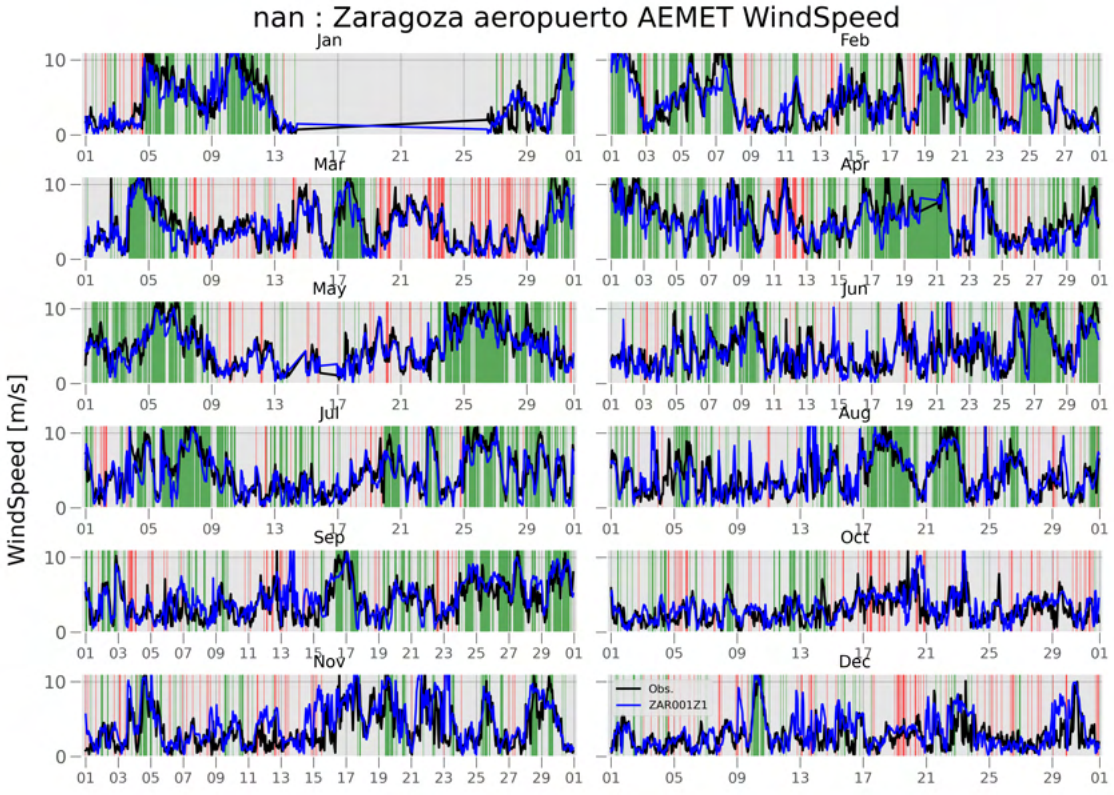

Figure 7.17: Observed (black) and modelled (blue) wind speed at Zaragoza aeropuerto AEMET station. Modelled values correspond to the finest domain ZAR001Z1. Green areas represent periods with observed cierzo wind, whereas red areas represent periods with its SE counterpart, called "bochorno wind".

Table 7.4: Statistical parameters R, FB, NMSE and FAC2 for the modelled wind speed.

Statistical parameters for the modelled wind speed.		
	Zaragoza-aeropuerto	Zaragoza-Valdespartera
R	0.74	0.70
FB	0.00	0.29
NMSE	0.21	0.32
FAC2	0.79	0.72

in different points of the city of Zaragoza, which are represented in 7.15. The stations are classified as follows: One industrial suburban station (Jaime Ferrán), two traffic suburban stations (El Picarral and Avenida de Soria), three traffic urban stations (Roger de Flor, Centro and Las Fuentes) and two background urban stations (Actur and Renovales).

Figure 7.18 shows the modelled annual mean of NO_2 inside the ZAR001CH2 domain. It can be observed that the SUMO case results in significantly larger NO_2 concentrations than the base and the SUMO_proxychim cases. The SUMO case models an annual mean value of NO_2 larger than 20 $\mu g \cdot m^{-3}$ (the threshold limit established by Directive 2024/2881) in most of the eastern part of Zaragoza, with a total area of 0.17^{o} x 0.17^{o} exceeding that limit value. Most of the population in the Zaragoza city is predicted to have been exposed to annual NO_2 values larger than 10 $\mu g \cdot m^{-3}$. On the other hand, the base case only predicts values exceeding 10 $\mu g \cdot m^{-3}$ in the city centre, with most of the domain under 5 $\mu g \cdot m^{-3}$. In addition, in the SUMO case there is a large area in the axis of the predominant winds with values higher than 5 $\mu g \cdot m^{-3}$ that is not present in the base case. This is also present in the SUMO_proxychim cases, but not in the base case. In addition, the SUMO_proxychim case shows two cells with annual mean NO_2 concentration larger than 15 $\mu g \cdot m^{-3}$ at the northern part of the city of Zaragoza, and one cell at the SW of the city.

Inside cities, strong gradients of air pollutant concentrations can be observed due to the heterogeneity of pollutants sources (i.e., road traffic) and the interaction between the mean flow and the urban morphology. For that reason, when evaluating mesoscale air quality models it is advised to use background stations. There are two of them in Zaragoza: Actur and Renovales. The latter one presents a lack of observations since mid July. Figure 7.19 shows the temporal evolution of observed (black line) and modelled NO_X concentrations (hereafter as $[NO_X]$) for the Actur AQMS station. Modelled values correspond to the ZAR001CH2 domain. It can be observed that the SUMO_proxychim case has little impact with respect to the base case along all the year, with both cases far below the observed values during most of the year. However, the SUMO case has a notable impact on $[NO_X]$. Some overestimations are produced, but in general the SUMO case has a better correlation with observations than the base and SUMO_proxychim cases. Specially during the months of February to June, the SUMO case achieves a good representation of the diurnal variations of $[NO_X]$ and captures well the high-concentration episodes. Two periods of significant underestimation in NO_X concentrations can be observed in mid-November and mid-December. Those two periods coincide with the periods with largest overestimations of wind speed at Zaragoza-Valdespartera station, which is the nearest available station from the city center.

NO_2 is also well predicted by the model (Figure 7.20). All three scenarios are able to reproduce the episodes of high NO_2 levels that take place in Actur in January and February,

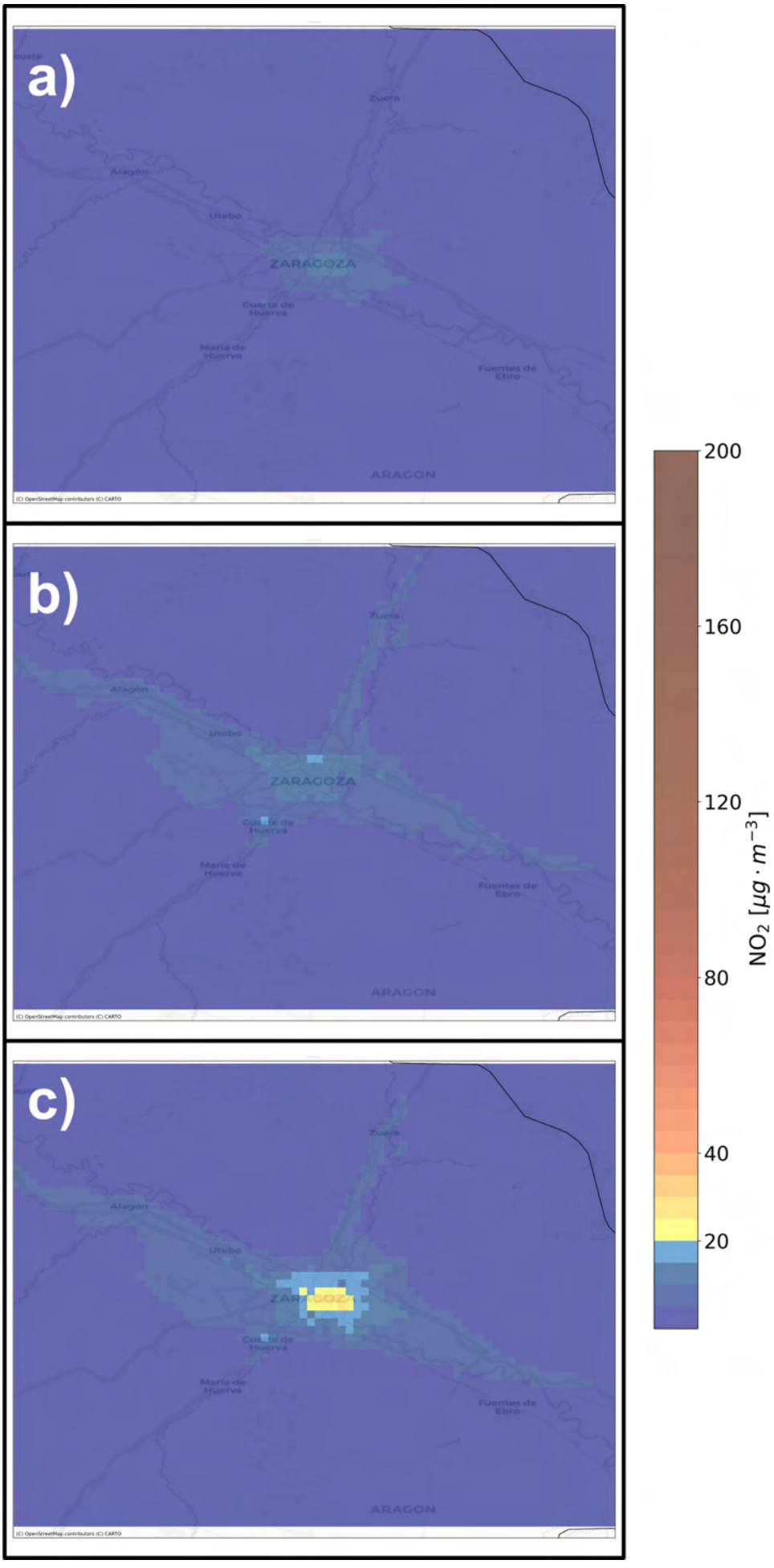

Figure 7.18: Maps of annual mean NO_2 values inside the ZAR001CH2 domain for: a) Base case; b) SUMO_proxychim case; c) SUMO case.

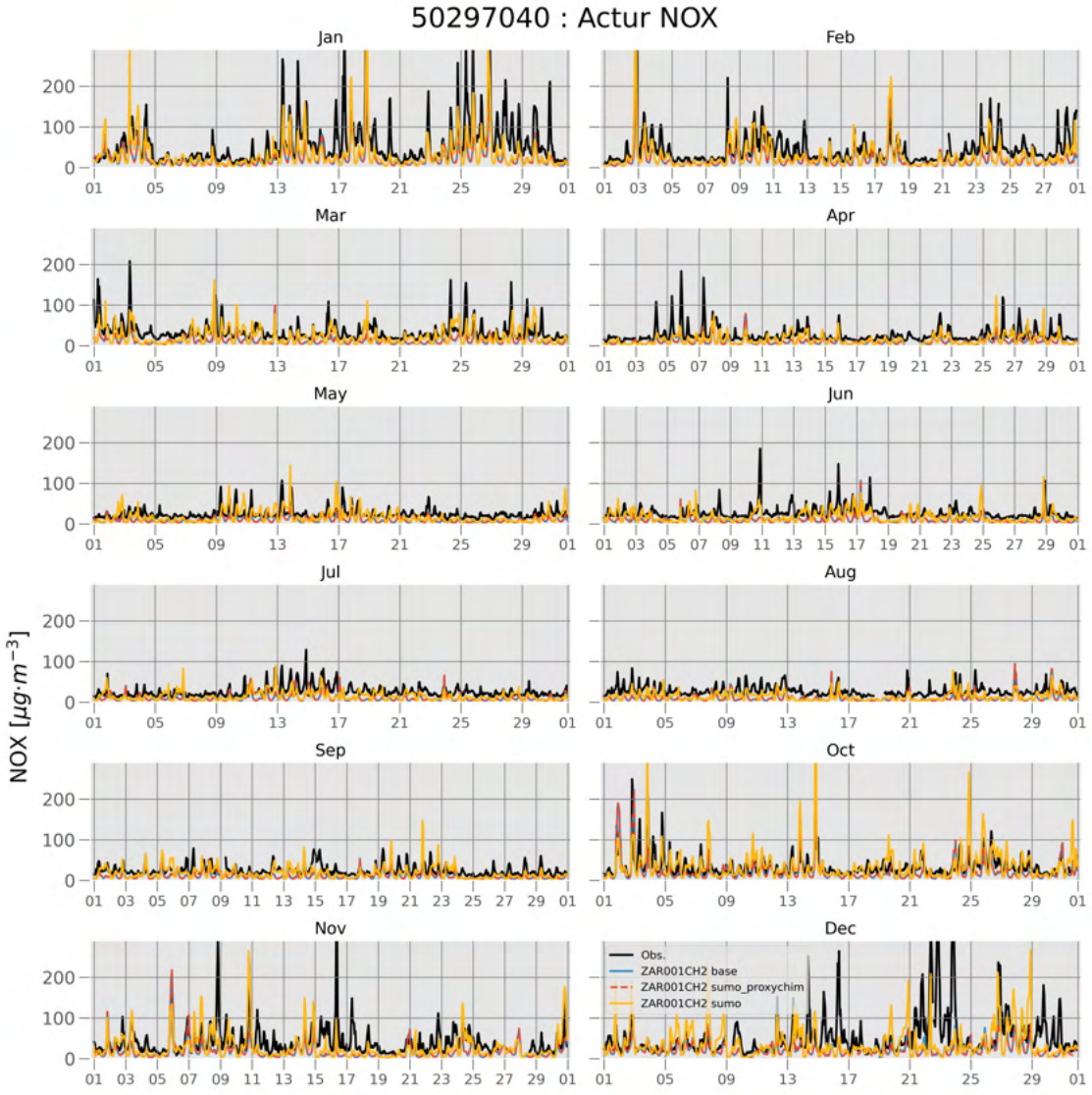

Figure 7.19: NO_X timeseries for the year 2022 in the Actur AQMS station. Black line indicates observed values, whereas the coloured ones correspond to different modelled values. The blue continuous line represents the base case; the red dashed one represents the SUMO_proxychim case; and the yellow line, the SUMO case. Modelled values correspond to the ZAR001CH2 domain.

but it is the SUMO case which most approximates to these peaks of NO_2. For example, during the episode of late January, SUMO almost reaches the observed values during five consecutive days (January 22^{nd} to 26^{th}). In the following two days, every case underestimates the concentrations but the SUMO case is still able to predict concentrations twice as large as the other two cases. In general, the SUMO case notably improves the representation of peaks of NO_2 during the year.

Table 7.5 shows the correlation coefficient R, the fractional bias (FB), the normalised mean squared error ($NMSE$) and the number of data within a factor 2 -with respect to the observations- ($FAC2$) of the evaluation of the timeseries of [NO_X] for each simulation case at every AQMS location, using the values of the finest domain -ZAROO1CH2. In general, the SUMO simulation provides the best performance in terms of the statistical parameters. The correlation coefficient R is relatively low for all simulations and small variations are observed between them for most locations. However, the SUMO provides large improvements in terms of FB, NMSE and FAC2. When compared with the base case, the SUMO simulation reduces the absolute error of the average FB by more than a factor 2, the NMSE is reduced a 42% and the average FAC2 is increased a factor 2. The lower impact of the SUMO simulation is observed for the Roger de Flor AQMS. On the other hand, the SUMO simulation has a large impact on Las Fuentes. Although the R value is reduced from 0.55 to 0.46, the FB is reduced from -1.04 to -0.11, the NMSE almost halved, and the FAC2 in this station is increased from 0.12 to 0.59. The SUMO_proxychim performance is in general terms similar to the base case, as it was discussed for the NO_X timeseries at the Actur AQMS. In addition, the SUMO case is the only one with at least one station with one or more parameters meeting the acceptance criteria of Chang and Hanna (2005). In particular for the Actur background station, the SUMO case provides a similar R value than the base case, but significantly reduces the negative bias from $FB = -0.83$ to $FB = -0.38$ (an improvement over a factor of 2); reduces the $NMSE$ almost to the half value of the base case; and doubles the number of data within a factor of 2 ($FAC2$). In this case, both the $NMSE$ and the $FAC2$ values comply the acceptance criteria given by Chang and Hanna (2005), being the only simulation able to achieve that.

The NO_2 estimations are also notably improved by the SUMO case (Table 7.6). In this case, the FB is reduced by a factor 4 in average, the NMSE by a 30% and the FAC2 is increased by a 44% in average. In addition, for the simulated NO_2 in the SUMO case, most stations meet the acceptance criteria for FB, NMSE and FAC2 simultaneously proposed by Chang and Hanna (2005) for a good simulation. In the base case, none station met the criteria of $|FB| < 0.3$ and only two of them met the criteria of $FAC2 > 0.5$, whereas in the SUMO simulation the Actur station meets the criteria for FB, $NMSE$ and $FAC2$.

The NO is the most problematic pollutant in all the three simulation cases. The R values are

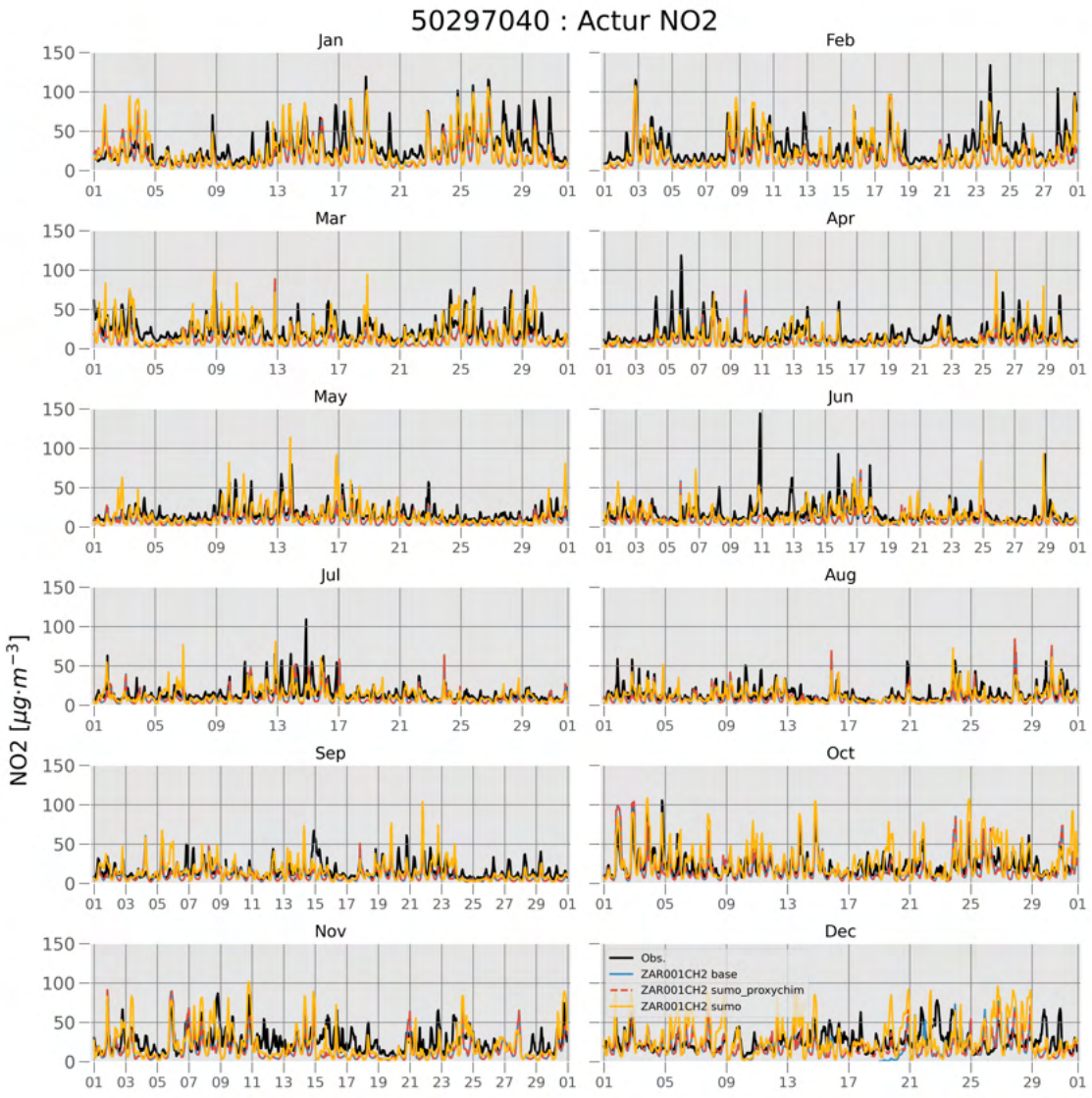

Figure 7.20: NO_2 timeseries for the year 2022 in the Actur AQMS station. Black line indicates observed values. The blue continuous line represents the base case; the red dashed one represents the SUMO_proxychim case; and the yellow line, the SUMO case. Modelled values correspond to the ZAR001CH2 domain.

Table 7.5: Statistical parameters R, FB, NMSE and FAC2 for the modelled [NO_X] at the AQMS locations. Highlighted values are the best value of the parameter across the three simulations.

		Actur	Avenida de Soria	Centro	El Picarral	Jaime Ferrán	Las Fuentes	Renovales	Roger de Flor
R	Base	**0.58**	**0.56**	0.47	0.50	**0.44**	**0.55**	0.42	**0.50**
	SUMO_proxychim	0.54	0.51	0.42	0.46	0.39	0.51	0.38	0.42
	SUMO	0.56	0.54	**0.49**	**0.58**	0.43	0.46	**0.44**	0.42
FB	Base	-0.83	-1.06	-0.93	-0.95	-0.82	-1.04	-0.84	-1.07
	SUMO_proxychim	-0.81	-1.05	-0.94	-0.94	-0.76	-1.05	-0.88	-1.02
	SUMO	**-0.38**	**-0.89**	**-0.24**	**-0.46**	**-0.21**	**-0.11**	**-0.38**	**-0.94**
NMSE	Base	2.12	3.65	2.35	3.16	2.23	3.01	2.39	4.44
	SUMO_proxychim	2.12	3.63	2.52	3.11	2.06	3.05	2.44	4.06
	SUMO	**1.09**	**2.61**	**1.24**	**1.23**	**1.10**	**1.52**	**1.34**	**3.57**
FAC2	Base	0.26	0.18	0.23	0.28	0.31	0.12	0.32	0.16
	SUMO_proxychim	0.28	0.18	0.22	0.29	0.33	0.12	0.29	0.19
	SUMO	**0.52**	**0.21**	**0.58**	**0.54**	**0.55**	**0.59**	**0.53**	**0.19**

Table 7.6: Statistical parameters R, FB, NMSE and FAC2 for the modelled [NO_2] at the AQMS locations. Highlighted values are the best value of the parameter across the three simulations.

		Actur	Avenida de Soria	Centro	El Picarral	Jaime Ferrán	Las Fuentes	Renovales	Roger de Flor
R	Base	**0.60**	**0.54**	0.47	0.51	**0.48**	**0.54**	0.49	**0.41**
	SUMO_proxychim	0.58	0.50	0.45	0.48	0.43	0.52	0.45	0.41
	SUMO	0.58	0.54	**0.56**	**0.58**	0.44	0.54	**0.55**	0.33
FB	Base	-0.53	-0.73	-0.76	-0.54	-0.38	-0.79	-0.47	-0.73
	SUMO_proxychim	-0.49	-0.70	-0.75	-0.49	-0.30	-0.77	-0.49	-0.65
	SUMO	**-0.11**	**-0.53**	**-0.18**	**-0.05**	**0.18**	**0.02**	**-0.06**	**-0.56**
NMSE	Base	0.89	1.34	1.27	0.99	0.85	1.32	0.95	1.63
	SUMO_proxychim	0.85	1.29	1.27	0.97	0.88	1.30	0.99	1.64
	SUMO	**0.60**	**1.00**	**0.55**	**0.59**	**0.89**	**0.61**	**0.73**	**1.54**
FAC2	Base	0.46	0.33	0.30	0.48	0.52	0.25	0.52	0.29
	SUMO_proxychim	0.48	0.35	0.30	0.50	0.53	0.26	0.50	**0.34**
	SUMO	**0.62**	**0.37**	**0.58**	**0.66**	**0.64**	**0.64**	**0.68**	0.19

low in all of them. In addition, all of the simulations underestimates the NO concentrations ([NO] hereafter) at the AQMS locations. Nonetheless, the SUMO simulation is still able to make some notable improvements. For example, it largely reduces the NMSE at all stations but Roger de Flor. The NMSE are very large in the base and SUMO_proxychim cases, exceeding a value of 15 at all stations. Furthermore, the SUMO_proxychim even is slightly worse than the base case. On the other hand, the SUMO case reduces the NMSE to values lower than 10 in all stations but 2, with reductions even larger than a factor 4 in Jaime Ferrán and Las Fuentes. Regarding the FAC2 parameter, it is also low for all stations within the base and SUMO_proxychim simulations. However, the SUMO simulation is able to improve this value significantly for more of the stations. In the Actur station, NO is systematically underestimated along the year in all simulations. Nonetheless, the SUMO case provides some improvements in winter months where NO shows some peaks and some periods with appreciable concentrations. On the other hand, NO is almost a flatline for all the year in the base and SUMO_proxychim cases.

Focusing the evaluation in the Actur background station, the SUMO simulation is able to improve every statistical parameter, even the R value, for NO in this station. In particular, reduces the $NMSE$ by almost a factor of 3 and increases the $FAC2$ by a factor of 4, with respect to the base case. Figure 7.21 shows the time series of NO in Actur AQMS station, for every simulated case. Although systematic underestimations of this pollutants are modelled in every simulation, the SUMO case is able to capture some episodes of high NO concentrations, specially during the wintertime.

Figure 7.22 displays the statistical parameters R, FB, $NMSE$ and $FAC2$ resulting from the evaluation of the NO_X for each simulation and domain. The correlation coefficient is in general better for the finer domains, but with some exceptions (i.e. Las Fuentes). In addition, similar values are modelled for each simulation. However, significant differences are found for the FB, $NMSE$ and $FAC2$ statistics. In those case, the finer simulation domains ZAR003CH2 and ZAR001CH2 provide significantly better results than the other two, specially for the $FAC2$ statistic. In general, the values from the ZAR001CH2 domain provide the better results. In adition, the SUMO simulation provides the lowest absolute values of FB and $NMSE$ and the largest for the $FAC2$. The same occurs for NO_2 and NO (Figures 7.23 and 7.24).

An important requirement for an air quality model is to be able to properly represent the daily cycle of pollutants concentrations. In this sense, the SUMO simulation improves significantly the representation of the diurnal cycle of NO_X, NO and NO_2. Figure 7.25 shows the diurnal cycle of NO_X for each month of the year, modelled for the ZAR001CH2 domain. The SUMO_proxychim case is practically identical to the base case for every month, making them undistinguishable in the figure. On the other hand, although in every month

Table 7.7: Statistical parameters R, FB, NMSE and FAC2 for the modelled [NO] at the AQMS locations. Highlighted values are the best value of the parameter across the three simulations.

		Actur	Avenida de Soria	Centro	El Picarral	Jaime Ferrán	Las Fuentes	Renovales	Roger de Flor
R	Base	0.38	0.33	0.24	0.31	0.25	0.28	0.22	**0.37**
	SUMO_proxychim	0.33	0.29	0.19	0.27	0.20	0.24	0.19	0.31
	SUMO	**0.42**	**0.36**	**0.33**	**0.43**	**0.30**	**0.30**	**0.24**	0.33
FB	Base	-1.48	-1.63	-1.39	-1.65	-1.66	-1.64	-1.61	-1.65
	SUMO_proxychim	-1.49	-1.64	-1.44	-1.67	-1.65	-1.67	-1.65	-1.64
	SUMO	**-0.94**	**-1.51**	**-0.39**	**-1.15**	**-0.99**	**-0.36**	**-1.01**	**-1.59**
NMSE	Base	18.94	28.15	16.82	30.78	26.00	35.13	24.15	36.61
	SUMO_proxychim	20.14	28.38	18.31	31.23	23.98	36.34	24.74	32.33
	SUMO	**6.96**	**19.00**	**6.56**	**8.38**	**6.12**	**8.72**	**7.47**	**28.10**
FAC2	Base	0.06	0.03	0.12	0.04	0.06	0.02	0.02	**0.02**
	SUMO_proxychim	0.06	0.03	0.10	0.04	0.05	0.02	0.02	0.02
	SUMO	**0.24**	**0.03**	**0.47**	**0.20**	**0.24**	**0.38**	**0.19**	0.02

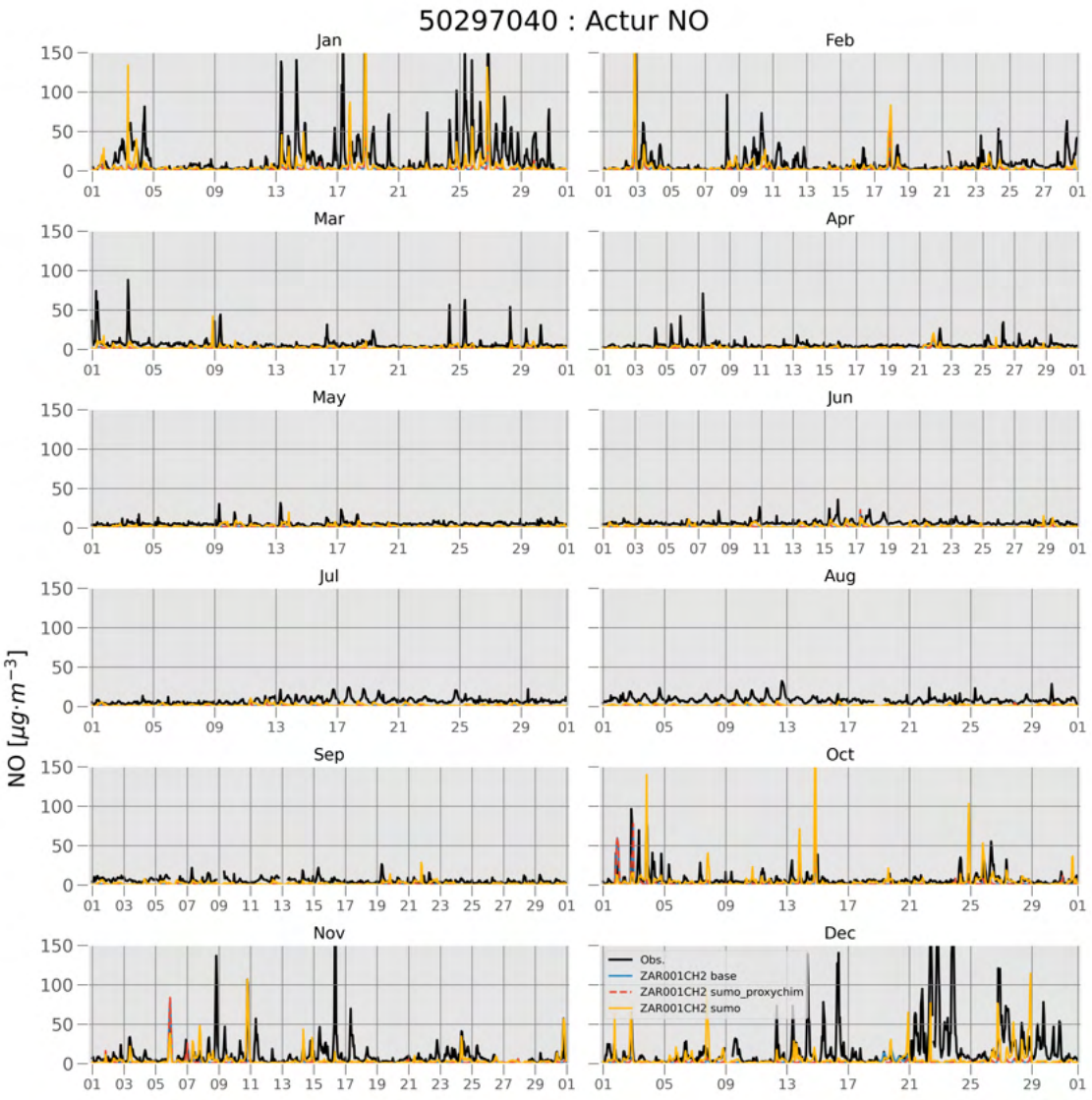

Figure 7.21: NO timeseries for the year 2022 in the Actur AQMS station. Black line indicates observed values. The blue continuous line represents the base case; the red dashed one represents the SUMO_proxychim case; and the yellow line, the SUMO case. Modelled values correspond to the ZAR001CH2 domain.

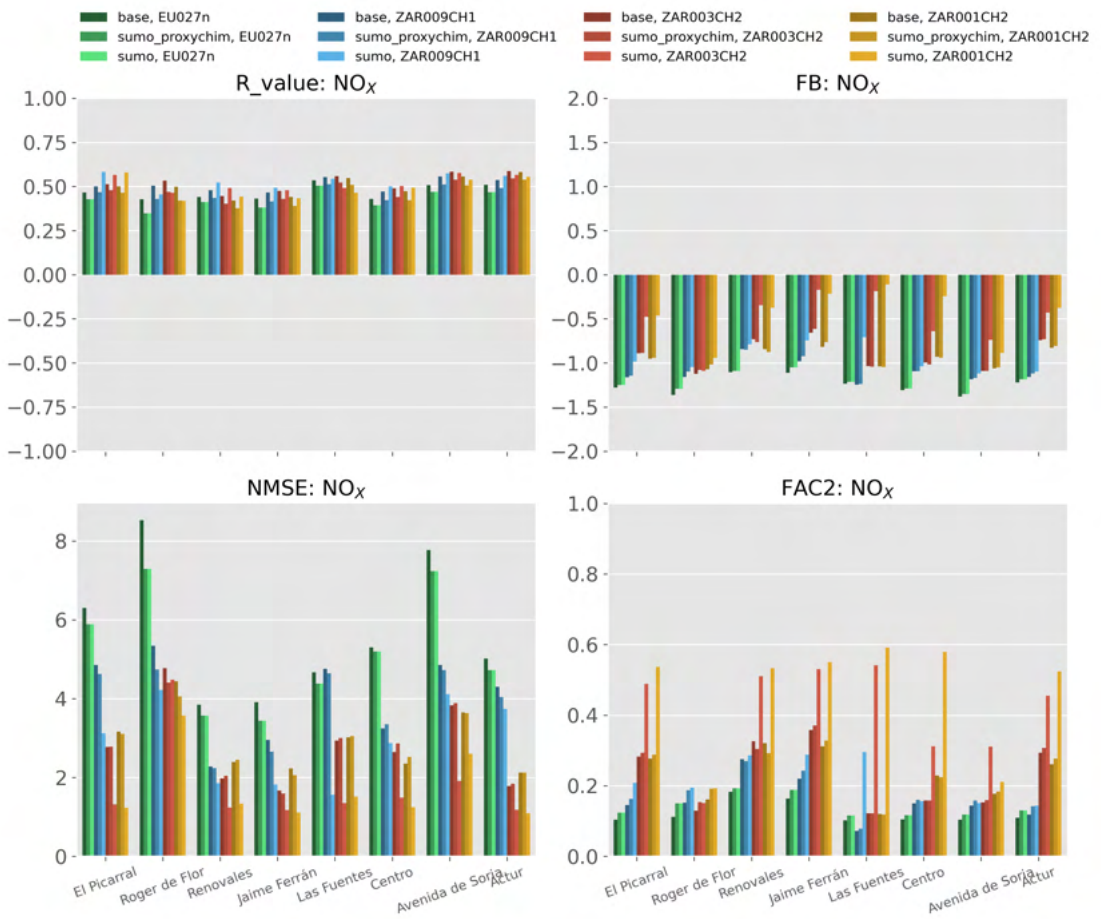

Figure 7.22: Statistical parameters for the evaluation of NO_X. Each domain is represented with a color: green for EU027n, blue for ZAR009CH1, red for ZAR003CH2 and yellow for ZAR001CH2. Each simulation is represented with a different hue of the color.

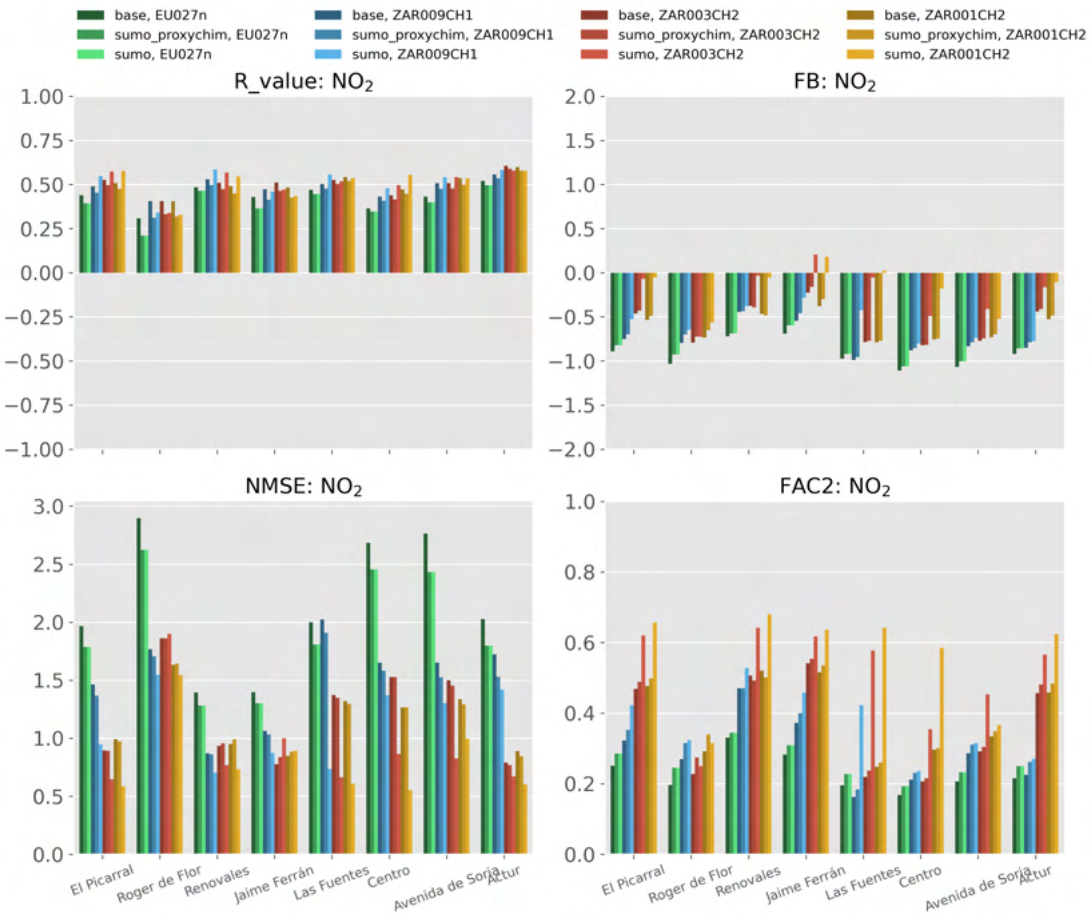

Figure 7.23: Statistical parameters for the evaluation of NO_2. Each domain is represented with a color: green for EU027n, blue for ZAR009CH1, red for ZAR003CH2 and yellow for ZAR001CH2. Each simulation is represented with a different hue of the color.

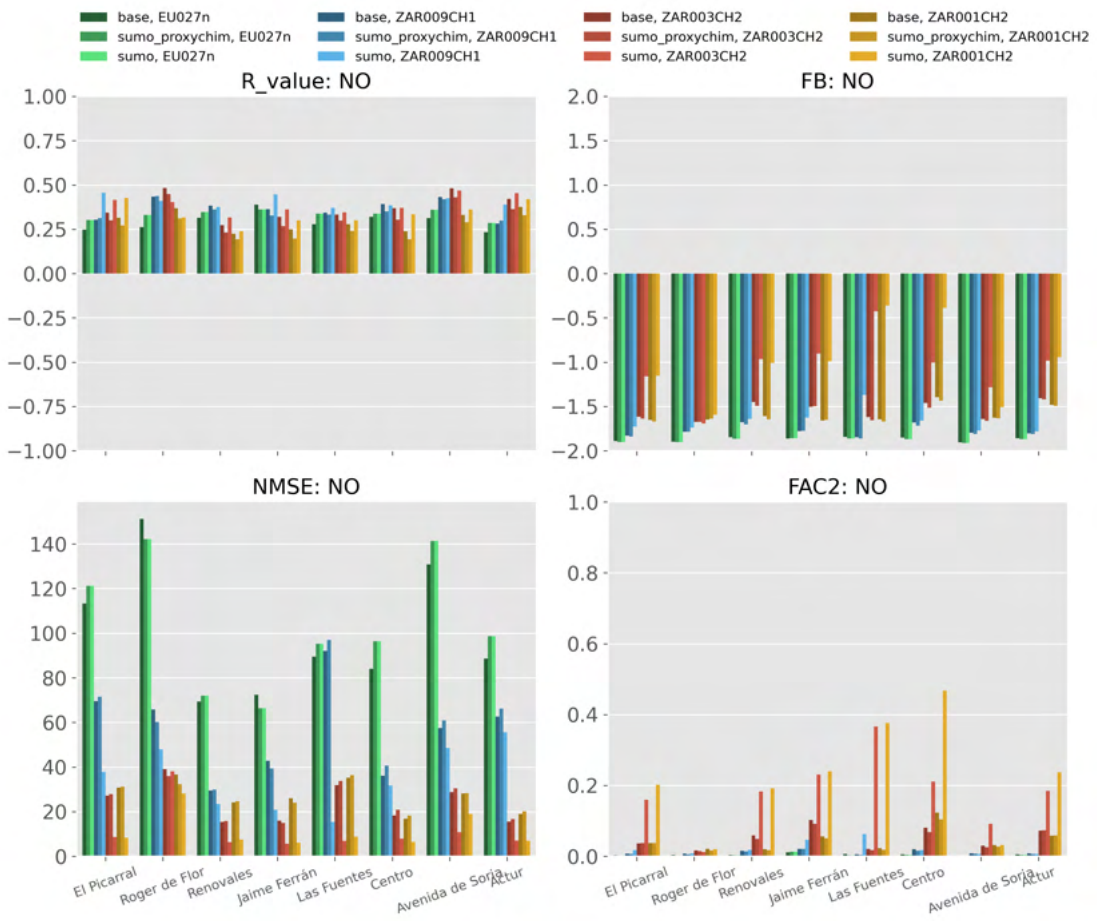

Figure 7.24: Statistical parameters for the evaluation of NO. Each domain is represented with a color: green for EU027n, blue for ZAR009CH1, red for ZAR003CH2 and yellow for ZAR001CH2. Each simulation is represented with a different hue of the color.

of the year the hourly values of the SUMO case are closer to the observations than those of the other two simulations, different behaviours are found along the year. During the winter months, the SUMO case improves the correlation coefficient, as well as in summer. However, in spring and autumn the R value decreases, as the SUMO case predicts the morning peak hour later than the observed values and the previous simulations.

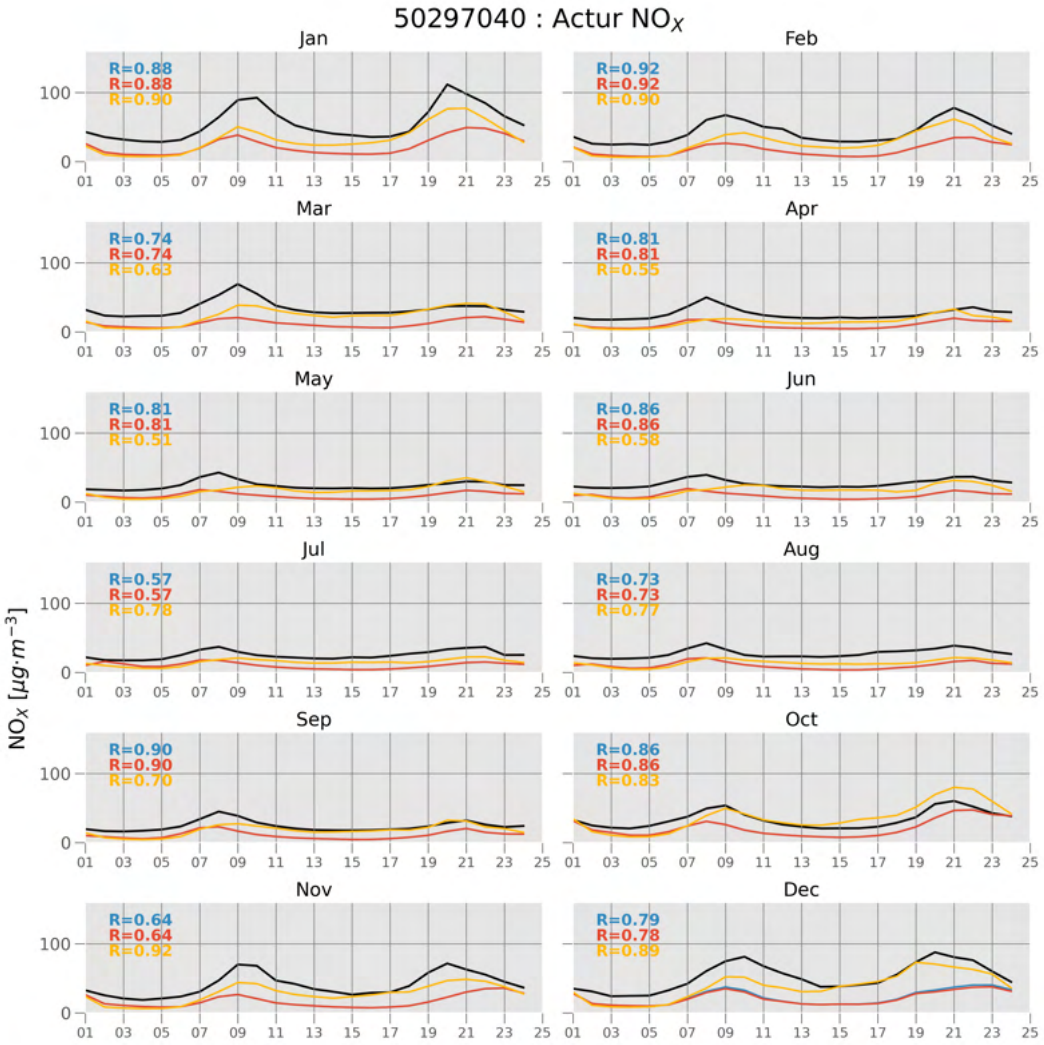

Figure 7.25: Average across all the AQMS locations of the diurnal cycle of NO_X. Black line represents the observed data; the blue line represents the base case; the red line the SUMO_proxychim case; and the yellow line represents the SUMO case.

This behaviour is again reproduced when analysing the mean diurnal cycle of NO_X for every AQMS in Zaragoza (Figure 7.26) but in this case the correlation coefficient is also increased in all months but April and September. A better estimation of traffic fluxes could solve this problem, as in this work it has been used traffic simulations of February to compute the air quality throughout the year, which reduces the amount of resources needed

to perform long-period simulations but can have a small impact on accuracy in some cases. Table 7.8 shows the correlation coefficients of the monthly diurnal cycles of NO_X for every simulation domain and case. The SUMO case improves the correlation coefficient for all of the domains, except for the aforementioned months. For the ZAR009CH1, even in April and September better correlation is found for the SUMO case. This domain also presents high correlation values, near to those of the finer domains ZAR003CH1 and ZAR001CH2. In fact, the ZAR009CH1 domain presents the best correlation values for the months of January and October. This suggests an influence of the redistribution of emissions in the correlation values not only for the finest domains but also at neighbour scale, which in this case improves.

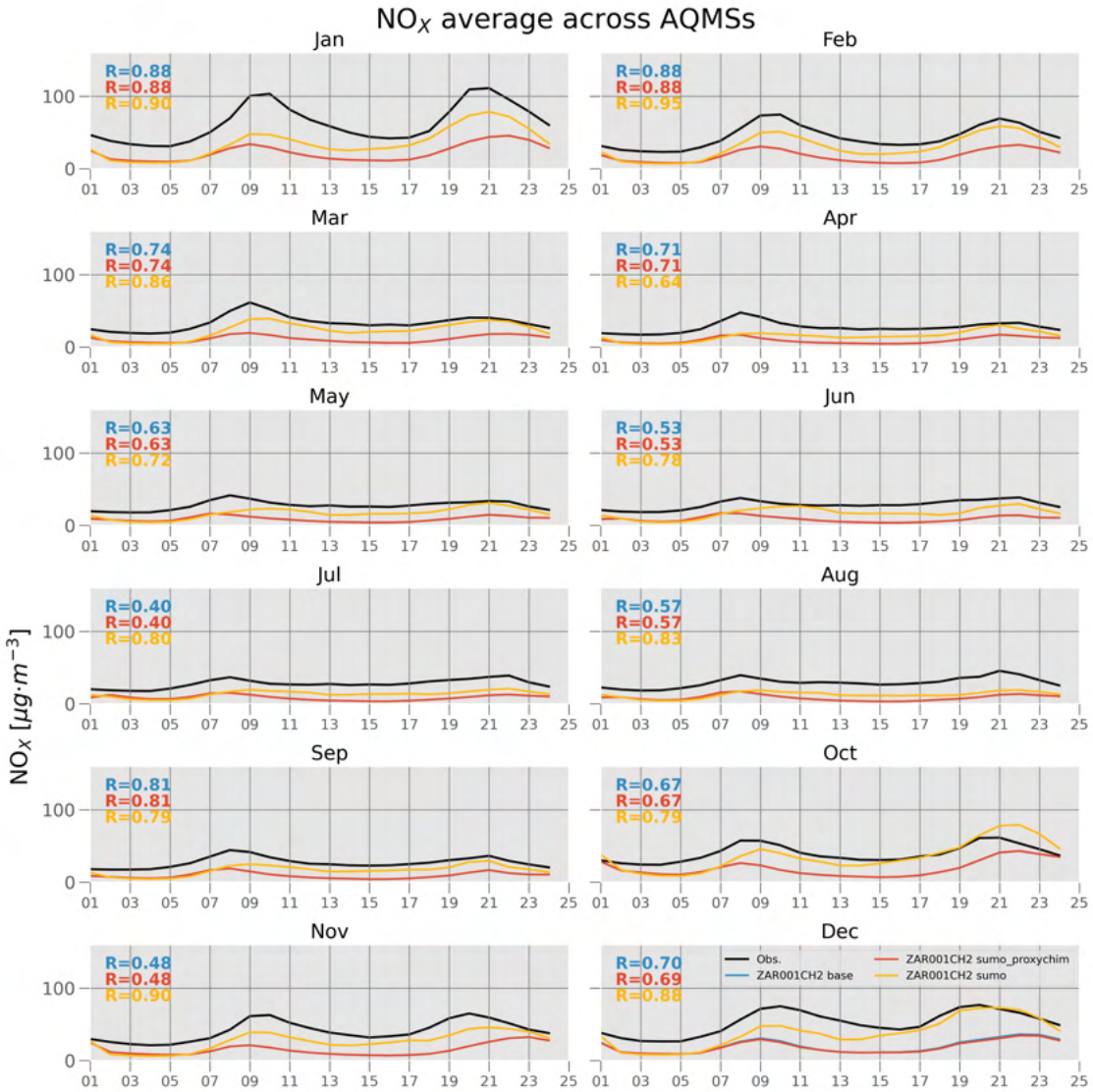

Figure 7.26: Average across all the AQMS locations of the diurnal cycle of NO_X. Black line represents the observed data; the blue line represents the base case; the red line the SUMO_proxychim case; and the yellow line represents the SUMO case.

Table 7.8: Correlation coefficient for the averaged monthly diurnal cycle of NO_X.

		Jan	Feb	Mar	Apr	May	Jun	Jul	Aug	Sep	Oct	Nov	Dec
base	EU027n	0.57	0.61	0.34	0.5	0.13	0.06	-0.01	0.13	0.40	0.45	0.18	0.36
	ZAR009CH1	0.8	0.79	0.61	0.58	0.41	0.40	0.25	0.42	0.63	0.62	0.42	0.61
	ZAR003CH2	0.89	0.89	0.71	0.72	0.62	0.51	0.42	0.56	0.81	0.66	0.46	0.68
	ZAR001CH2	0.88	0.88	0.74	0.71	0.63	0.53	0.50	0.57	0.81	0.67	0.48	0.70
SUMO proxychim	EU027n	0.57	0.61	0.34	0.5	0.13	0.06	-0.01	0.13	0.40	0.45	0.18	0.36
	ZAR009CH1	0.8	0.79	0.61	0.58	0.41	0.40	0.25	0.42	0.63	0.62	0.42	0.6
	ZAR003CH2	0.89	0.89	0.71	0.72	0.62	0.51	0.42	0.56	0.81	0.66	0.46	0.68
	ZAR001CH2	0.88	0.88	0.74	0.71	0.63	0.53	0.40	0.57	0.81	0.67	0.48	0.69
SUMO	EU027n	0.57	0.61	0.34	0.5	0.13	0.06	-0.01	0.13	0.40	0.45	0.18	0.36
	ZAR009CH1	0.95	0.96	0.88	0.61	0.64	0.65	0.55	0.65	0.70	0.82	0.89	0.87
	ZAR003CH2	0.94	0.99	0.90	0.68	0.73	0.76	0.78	0.80	0.79	0.80	0.90	0.88
	ZAR001CH2	0.90	0.95	0.86	0.64	0.72	0.78	0.80	0.83	0.79	0.79	0.90	0.88

However, the NO presents a different behaviour. In this case, the correlation is not clearly improved by the SUMO simulation, with the notable exceptions of October and November, when the improvement is large. In addition, the ZAR009CH1 presents the highest correlation values. This also is observed in the base and SUMO_proxychim simulations. In this domain as well as in the ZAR003CH2, the correlation values for the winter months are higher with respect to the rest of the year. NO_2 shows a similar behaviour to NO_X. In this case, the SUMO simulation clearly improves the other two, specially in the ZAR003CH2 and ZAR009CH1 domains, suggesting again an influence of the redistribution of emissions at neighbour scale.

For all pollutants, the standard deviation of their concentrations due to the uncertainty in the emission fluxes associated with the route computation has been computed. However, that uncertainty is not large enough to have an appreciable influence on their concentrations.

The Directives 2024/2881 and 2008/EC/50 establish limit values for several pollutants in order to preserve the human health and vegetation within the Member States. Those limits were summarized in Table 1.1. Among the regulated pollutants is the NO_2 because its hazardousness for the human health (Spirić et al., 2012). The Directive 2008/EC/50 established an annual limit value for NO_2 of 40 $\mu g \cdot m^{-3}$, and a hourly limit of 200 $\mu g \cdot m^{-3}$, to be reached no more than eighteen times in a year. The Directive 2024/2881 reduces the annual limit value to 20 $\mu g \cdot m^{-3}$ and the exceedances of the hourly limit to no more than three times. In addition, it adds a 24-hour limit value of 50 $\mu g \cdot m^{-3}$, which must not be exceeded more than eighteen times in a year. That means that if in one AQMS the nineteenth maximum value of the 24-hour rolling mean of NO_2 is higher than 50 $\mu g \cdot m^{-3}$, that AQMS would be failing in complying with the Directive 2024/2881 limit for the 24-hour value. The limits provided by Directive 2024/2881 will come into force in 2030. Figure 7.27 shows the regulated indicators for NO_2 by both directives and the modelled values by each

simulation inside each simulation domain, for the year 2022.

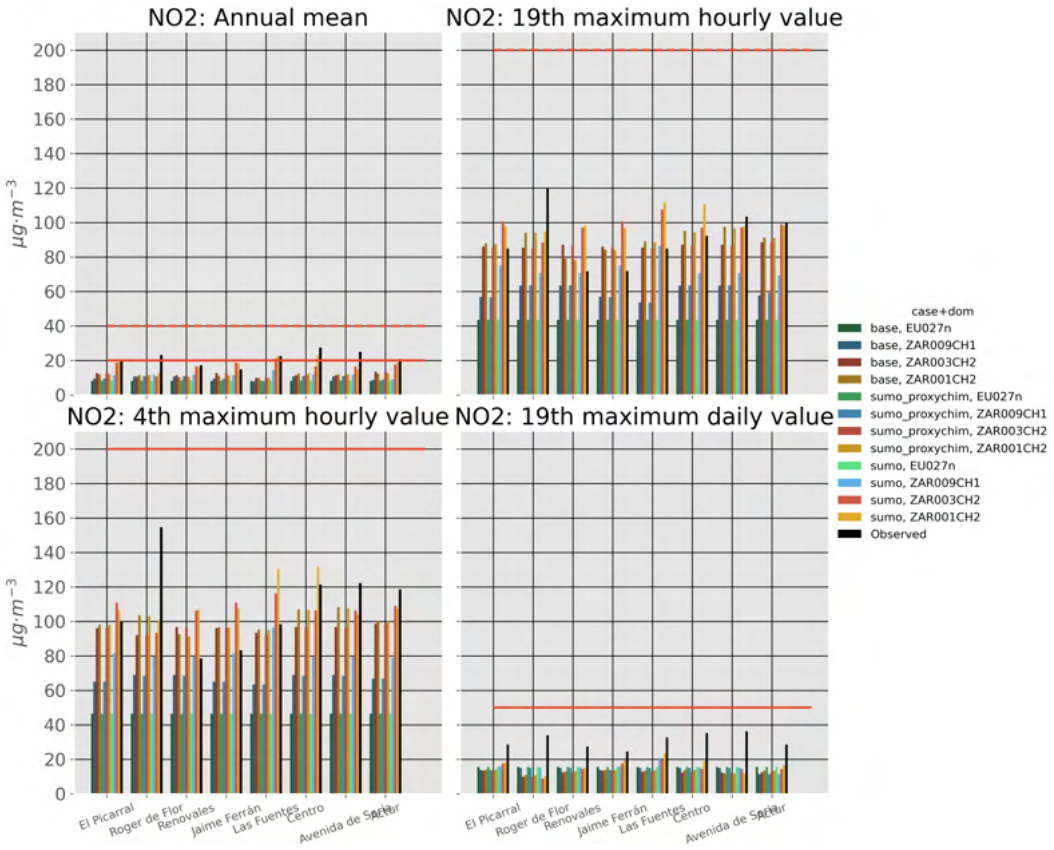

Figure 7.27: NO_2 limit values established by Directive 2024/2881 (continuous lines) and 2008/EC/50 (dashed lines), and corresponding modelled values for the year 2022 by each simulation and for every simulation domain. Black bars represent the statistics obtained from the observed values at the AQMS's locations.

For the Actur background station, the SUMO case significanty improves the representation of several indicators. The annual mean value of NO_2 is almost at the observed levels for both the ZAR001CH2 and ZAR003CH2 model domains. In particular, the base case modelled -in its finest domain- an annual value of 12.35 $\mu g \cdot m^{-3}$ for this pollutant in Actur, by the 12.44 $\mu g \cdot m^{-3}$ and 18.59 $\mu g \cdot m^{-3}$ respectively of the SUMO_proxychim and SUMO cases. The observed annual mean of NO_2 is of 20.74 $\mu g \cdot m^{-3}$. That is, the base and SUMO_proxychim case underestimated the annual NO_2 values by more than the 40% by the 10% underestimation of the SUMO case. The 19th maximum hourly value, which was regulated under previous Directives, is also improved in Actur with respect the base case. While the observed value for this parameter in this background station is of 100.05 $\mu g \cdot m^{-3}$, the base case ZAR001CH2 domain modelled a value of 91.15 $\mu g \cdot m^{-3}$ (8.9% lower than the observed value). In the SUMO_proxychim case this value is decreased to 90.98 $\mu g \cdot m^{-3}$ (a 9.9% underestimation), whereas in the SUMO case the underestimation is reduced to a 2.2% as it models a 19th maximum hourly value of 97.92 $\mu g \cdot m^{-3}$.

Similarly the NO_2 4th maximum hourly value, legislated by the Directive 2024/2881 is improved in this station, reducing its error from a -16% in the base case, to a 15.6% and a 9.3% in the SUMO_proxychim and SUMO cases, respectively. In all cases, modelled and observed, the 19th maximum hourly value is far from the limits established by Directive 2024/2881. Finally, the NO_2 19th maximum daily value representation is also improved, from a 53% underestimation in the base and SUMO_proxychim cases to a 42% underestimation in the SUMO case. For every parameter, values are improved for every simulation domain in where the novel set of emissions had been introduced, even in the ZAR009CH1, whose resolution is much coarser than the original set of emissions. This reflects, again, the usefulness of high-resolution emissions in a mesoscale model, not only for applications with finer domains but also for coarser resolutions. For the other background station, Renovales, apparent improvements using the novel set of emissions are modelled. However, careful must be taken when evaluating this station due to its lack of data for July.

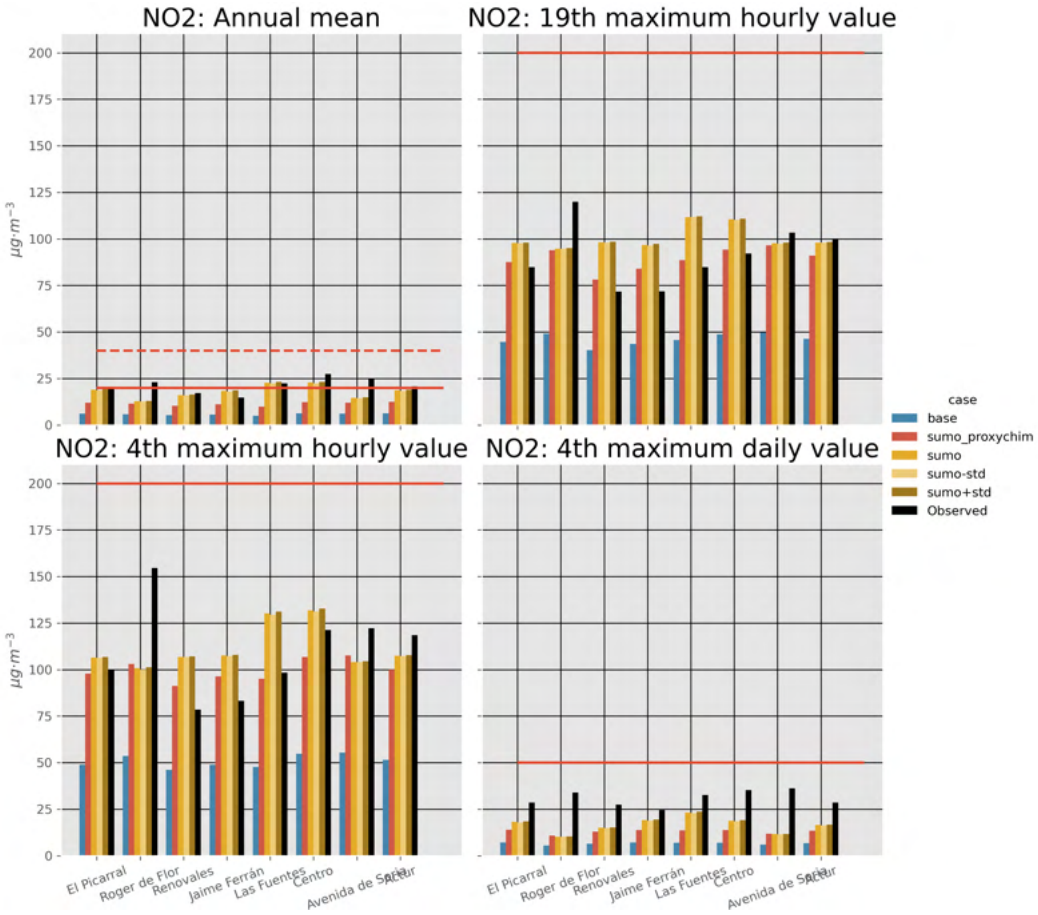

Figure 7.28: NO_2 limit values established by Directive 2024/2881 (continuous lines) and 2008/EC/50 (dashed lines), and corresponding modelled values for the year 2022 by each simulation. Modelled values correspond to those of the ZAR001CH2 domain. Black bars represent the statistics obtained from the observed values at the AQMS's locations.

For the other stations, the evaluation should be done always taking into account the

limitations of mesoscale models in representing air quality in areas with strong gradients, as previously mentioned. Nonetheless, an improvement is also seen in those stations when implementing the novel set of emissions. In particular, with these emissions the model is able to capture the exceedances for the NO_2 annual mean limit of 20 $\mu g \cdot m^{-3}$ for two stations: Centro and Las Fuentes. Also improvements have been seen for other parameters, sometimes overestimating their values but in none case leading to false alarms.

Figure 7.28 shows the estimated values of those indicators inside the ZAR001CH2 domain. The novel set of emissions improves the values of the indicators, as aforementioned. In addition, the standard deviation on the air pollutants concentrations has not appreciable impact.

7.4 Summary and concluding remarks

This chapter is addressed to provide an example of the potential of the methodology employed in this PhD. thesis to feed a mesoscale air quality model with high-resolution emissions, and to evaluate the impacts of incorporating such emissions in the performance of a model. The high-resolution emissions have been computed using the SUMO traffic simulator coupled with the PHEM-light instantaneous emission model for Zaragoza, which is the fifth city in Spain by population. To assess the impact of the implementation of these emissions into the CHIMERE model, three cases were simulated. The base case represents the case with the original emissions, and no changes were made for this simulations. The SUMO_proxychim is the case in which the new emissions -those computed with SUMO and PHEM-light- were implemented into the CHIMERE model but maintaining the spatial distribution of the original emissions. To that end, the emissions were included into the CHIMERE model using the CHIMERE's standard emission preprocessing system program. Finally, the SUMO case represents the case in which the raw emissions from SUMO were directly regridded to the CHIMERE domains' resolutions and introduced into the model by using the interface developed in this research, SUMO2CHIMERE.

An analysis of the emissions showed that the emissions computed in this research were larger than those of several official inventories, by a significant margin. In addition, the standard deviation of the emissions computed in this work, which are related only to the uncertainties in the choice of routes of the simulated vehicles, is lower than the differences with other inventories. Once introduced into the model, the emissions of the SUMO_proxychim case were similar to the base case, which indicates that the preprocessing of emissions performed by CHIMERE significantly reduces the original differences between emission inventories. On the other hand, the emissions introduced with the SUMO2CHIMERE interface were notably different to those of the aforementioned cases. In this case, larger values were found in almost

every domain cell corresponding to the Zaragoza urban area, with the maxima displaced to the city center.

To compute the air pollutants concentrations, CHIMERE needs of external meteorological forcing. The model WRF was employed to that end. The evaluation of the WRF meteorological variables in two meteorological stations from AEMET shows a good performance of the model with respect the observations. In particular for the Zaragoza aeropuerto station, the wind speed is well predicted, even when sudden variations occur due to the change of regimen.

A detailed analysis of the impacts of the new emissions on the model performance has been performed by comparing the three simulations. In general, the SUMO_proxychim simulation does not result in significant differences, as the emissions resulted similar to those of the base case. On the other hand, the SUMO case leads to significant differences with the base case. When analysing the timeseries of NO_X, NO and NO_2, the SUMO case was able to detect the episodes of high pollution. Only two episodes were missed, which coincide with errors in the predictions of the wind speed by the WRF model. In general, the SUMO simulation largely improves the model performance in terms of the statistical parameters. Only the correlation coefficient (R) does not present large variations. For the rest of the analysed parameters (FB, $NMSE$ and $FAC2$) only the SUMO case achieves to comply the acceptance criteria from Chang and Hanna (2005) in at least one AQMS. Then, the monthly daily cycles are studied. Again, the simulation with the emissions values and distribution from SUMO presents the best results, improving the correlation of the daily cycles for NO_X and NO_2. For NO, however, no significant improvement is modelled. The winter months present higher correlation values.

Finally, an assessment of the compliance with Directives 2008/EC/50 and 2024/2881 for NO_2 has been performed using the modelled data at the AQMSs' locations. The novel set of emissions is able to better estimate the legislated values of annual NO_2 mean value, its 19th and 4th maximum hourly value, and its 19th maximum daily value. Moreover, during the whole evaluation it has been seen that the improvements are not limited to the finest domains -ZAR001CH2 and ZAR003CH2-, but also the ZAR009CH2 domain has improved its performance with the new set of emissions. This indicates that even the coarser domains can benefit from the effort of providing high-resolution emissions to mesoscale air quality models.

The case presented in this Chapter is only one among many other possibilities that allows the developed module SUMO2CHIMERE for air quality modelling, as it facilitates the possibility of studying the impacts of emission changes at mesoscale because of its simplicity and its approach that maintains the spatial and temporal distribution of an original set of emissions,

in contrast with the standard emission preprocesing of CHIMERE which required annual emission masses and the use of proxies for their temporal and spatial distribution.

Chapter 8

Conclusions and future research needs

8.1 Summary and conclusions

Estimations of high-resolution traffic emissions have a great utility for air quality model applications at different scales. As they are such an important component of the air quality modelling system, their estimation must rely in a suitable combination of traffic and emission model for the desired applications. In this thesis, a combination of a microscopic traffic simulation model with an instantaneous emission model has been applied for different urban areas. This system allows for emissions estimations at very high resolution (of the order of 1 meter or less). However, in air quality modelling, as important as their estimations is their implementation within air quality models. The implementation of high-resolution emissions within air quality models promotes studies of traffic measures impacts on air quality.

As a first step, a previous work estimating the emission changes for a macroscale emission scenario was performed considering the COVID-19 lockdown. This work allowed the provision of emission data for the COVID-19 scenario for regional CTM, which could be applied to other type of measures. It also serves as reference for microscale studies, to compare the impacts of local traffic measures with large scale scenarios.

The work presented in previous chapters encompasses a comprehensive study of the possibilities offering the use of high-resolution emissions in air quality modelling at different scales. Among them, a detailed study of the impacts of several traffic measures for air pollution mitigation is presented. Not only that, but this study also addresses the potential impacts of meteorological conditions on air quality and on the effectiveness of mitigation strategies. From this comprehensive study, the following conclusions are drawn:

- *The estimation of a global-scale lockdown in emissions*: The emergence of the COVID-19 pandemic required the development of a methodology to estimate its impact

on air pollutant emissions. With that aim, a simple, easily reproducible methodology has been developed in this work which leads to coherent results with more complicated methodologies. In Spain, the COVID-19 pandemic lead to a mean reduction of 25% of the road transport emissions, with monthly reductions of up to 85% in the most stringent periods. The results from this work serve as reference values for future mitigation strategies.

- *The estimation of high-resolution emissions, and their uncertainty due to incertitude in vehicle's routes, for different traffic configurations.*

  A traffic simulation has been properly calibrated for different traffic configurations and study areas, allowing for the estimation of detailed emissions and their uncertainties for several traffic configurations and study areas. Those emissions have been compared, when possible, with previous works or with other inventories. This analysis concludes that important differences can be found between traffic configurations, and with other methodologies, which remarks the potential of high-resolution emissions estimations for a range of uses.

- *The estimation of the impact of several measures on NO_X emissions*

  The emissions obtained by the coupling between a traffic simulation model and an instantaneous emissions model have been analysed for each traffic configuration. Both their spatial and temporal evolution have been estimated. It has been concluded that the impact of different studied strategies can be diverse. Meanwhile the change in traffic emissions due to the implementation of a LEZ has been estimated to be small, other measures such as the implementation of electric vehicles can have significant impacts on NO_X emissions, that can be comparable to the large-scale impacts on those emissions related to the most stringent periods of the COVID-19 lockdown.

- *The estimation of the impact of several traffic measures on air quality*

  The modelling of traffic-related emissions for different traffic configurations allow to estimate the impact on air quality of traffic measures. In the Plaza Elíptica study domain, the changes in emissions between 2016 and 2019 had a large impact on air quality, larger than the impact of the LEZ implementation in 2022. The full recovery of traffic fluxes after the pandemic had little impact on air quality (as in 2022 restrictions were already scarce), although not negligible. However, those impacts were unequally distributed along the study domain. Depending on the location of each studied point, and their surrounding urban morphology, the impacts of a mitigation strategy can largely vary, even being of different sign. In general, changes in annual NO_X concentrations due to the implementation of strategies are smaller than their uncertainty associated to the emissions computation, but under certain circumstances

they can be comparable. In addition, for shorter periods, the changes in air quality due to the change in emissions, mainly due to the change of vehicle fleet, can overcome that uncertainty in the NO_X values. Furthermore, planned strategies such as the implementation of electric vehicles can have an impact on NO_X concentrations large enough to overcome their uncertainty.

The mitigation strategies also help to reduce the size of areas exceeding limit values established by several Directives. Nonetheless, it is concluded that accurate emissions estimations are necessary in order to properly estimate the effectiveness of a mitigation measure in reducing exceedances areas. Finally, the mitigation strategies can affect the spatial representativeness of an AQMS.

- *The evaluation of the impact of meteorological conditions on air quality and the effectiveness of air pollution mitigation strategies*

  The air quality conditions for each emission configuration have been analysed using different meteorological conditions in order to investigate the influence of meteorological conditions on air quality and their impact on the effectiveness of air pollution mitigation strategies.

  It has been modelled that the meteorological conditions can affect annual NO_X concentrations. They affect not only the annual values but the spatial distribution of air pollutants. In addition, the interaction of meteorological conditions with urban morphology induces different impacts along the study domain. The impacts of the meteorological conditions can exceed the uncertainty range of NO_X concentrations under specific scenarios. Moreover, the meteorological conditions affect the degree of effectiveness of a mitigation strategy, even exceeding the net impact of the traffic measure for specific locations.

  Meteorological conditions should also be considered when assessing the areas exceeding certain limit values, as they can impact those areas in a very significant way. However, they seem to have less impact on the spatial representativeness of the Plaza Elíptica AQMS. However, for low polluted scenarios, the impacts of meteorological conditions lose relevance when emissions have been reduced enough, as it has been modelled for planned strategies.

- *The development of an interface to adapt high-resolution emissions to a mesoscale model*

  High-resolution emissions are a useful information that should be exploited by as much tools as possible. In this sense, a Python module has been developed in the scope of this research in order to easily provide high-resolution emissions to a mesoscale air quality

model. The preparation and implementation of these emissions within the CHIMERE model has been successfully achieved using the SUMO2CHIMERE module.

- *The impact of detailed emissions on the performance of a mesoscale air quality model*

  The CHIMERE model sensitivity to traffic emissions is analysed through the implementation of previously adapted high-resolution traffic emissions into the model. Those emissions have been implemented in two different ways: using the CHIMERE preprocessor system, and using the SUMO2CHIMERE module developed in this work.

  The resulting emission fluxes present significant differences between each other. When using the CHIMERE preprocessor, most of the differences between the original set of emissions and the new ones are diluted. On the other hand, when implementing the emissions using the SUMO2CHIMERE module, large differences are obtained in the emission fluxes with respect to the original emission fluxes. The difference between the two cases arises in the temporal and spatial disaggregation of the original emissions. The CHIMERE pre-processor has pre-defined spatial and temporal proxies to distribute the emissions in time in space, whereas the SUMO2CHIMERE module is confined to aggregate the emissions within the simulation domains, maintaining the advantages of the original set of emissions which were its temporal and spatial resolutions. In the end, this leads to significant differences in the predicted NO_X, NO and NO_2 concentrations.

  After implementing the emissions with the SUMO2CHIMERE module, the model is able to reproduce episodes with high levels of pollution, significantly reducing the negative bias that the base case presented. This greatly differs from the case in which the high-resolution computed emissions were implemented using the CHIMERE preprocessor. The evaluation with observational data also shows that the new method for implementing emissions, together with the new set of emissions, also translates into an improvement of the estimation of several indicators regulated by several Directives. In addition, it has been proved that the coarser domains can also benefit from the new set of emissions.

The main contributions of this work are:

- *The computation of high-resolution emissions for urban areas as big as a city.* In this work, high-resolution traffic emissions for two urban areas have been computed. In one case, emissions for the whole city of Zaragoza (an area of 16.5 km x 11 km) have been estimated, which has been used to provide reliable and detailed input data for air quality estimations within a mesoscale CTM. These emissions also provides a new reference value to compare with data from publicly available inventories. On the other studied case, emissions have been estimated for different traffic scenarios inside an urban air pollution hot-spot. It has been found a decrease of 50% in NO_X emissions

between 2016 and 2019 due to both a rearrangement of traffic directions and vehicle fleet renewal, and a decrease of about a 18% due to the implementation of a LEZ. Again, these emissions have been useful for air quality studies.

- *The use of computed high-resolution emissions for an extensive study of the impacts of traffic measures in both traffic emissions and air quality, as well as a comprehensive study of the impacts of meteorological conditions on air quality and on the effectiveness of traffic measures.* When studying the impacts of already implemented mitigation strategies inside an urban air pollution hot-spot it has been found that a decrease in emissions has helped to reduce NO_X concentrations within the area. However, different evolutions in the spatial distributions of emissions -due to the redistribution of traffic after a LEZ was implemented- lead to different NO_X concentration trends in different points of the domain. In addition, meteorological conditions can have an important influence on how air pollutants are distributed within an urban area and even can reverse a trend in emissions due to increased or decreased stability. However, their influence decreases with lower air pollutant concentrations as it has been shown when analysing planned, effective, mitigation strategies.

- *The estimation of the uncertainty of those emissions, and their impact on air quality estimations.* In this thesis not only the traffic-related emissions have been estimated with a high-resolution, but also their uncertainty due to the limited data availability has been computed. Results show that the uncertainty can be comparable to the mean emissions, although they decrease with larger availability of input data. This work also shows that this uncertainty should carefully considered in air quality studies, as several metrics can be very sensitive to the emissions, as it is the case of the fraction area of a domain exceeding a threshold value for an air pollutant.

- *The development of an interface to exploit the benefit of high-resolution -spatial and temporal- emissions into a mesoscale air quality model.* A bottom-up method has been developed in this thesis to avoid the use of proxies in a mesoscale CTM and, therefore, maintain the benefits that high-resolution emissions provide (accurate spatial and temporal distribution) when used as input data into a mesoscale model. An analysis of the usefulness of this interface shows its great relevance as it demonstrates the importance of spatial and temporal distribution of emissions in air quality estimations. Whereas the implementation of high-resolution emissions without this interface (i.e., using proxies) lead to similar results in air quality estimations than the reference case, the use of the developed interface provided notable improvements in those estimations.

8.2 Future research needs

This work covers the development of a high-resolution emissions database and some of their most important applications in air quality modelling. However, there are further interesting aspects to be considered:

- The use of high-resolution traffic emissions in a fully coupled multi-scalar air quality modelling system. In this work the computed emissions have been used separately in microscale and mesoscale models, but they can be used to feed a multi-scalar modelling system in which the mesoscale model provides the background concentrations to a microscale model. In this system, the high-resolution traffic emissions is used in both components, providing potential benefits to the estimation of both the background concentrations and the high-resolution local concentrations.
- The implementation of traffic measures in a mesoscale air quality model. The creation of an interface to implement emissions from a microscopic traffic simulation facilitates the study of impacts of traffic-related mitigation strategies at the mesoscale.
- Machine-learning and artificial intelligence techniques could be applied as a complement to the emissions and air quality modelling. They can be specially useful for the kind of modelling used in this work, which requires large amount of computational resources. In this sense, these tools could help reducing computing times and/or implementing large amounts of data on each step of the methodology (i.e., processing traffic counts data in traffic simulations; or meteorological data in the air pollution dispersion computation).
- The traffic simulation system could be improved by testing it in other urban configurations, strengthening the generalization of the results obtained in this work as well as analysing the impacts of other vehicle fleets.
- The development of an interface for implementing high-resolution emissions into a regional CTM constitutes a crucial start point for inter-model data sharing, which is essential for air quality applications. Future work should further explore this area, developing more automatized interfaces to facilitate the applicability of multimodel methodologies.

PUBLICATIONS

The main contributions of this research have been published in the following articles:

- Rodríguez-Sánchez, A., Vivanco, M. G., Theobald, M. R., and Martín, F., 2022. Estimating the effect of the COVID-19 pandemic on pollutant emissions in Europe. *Atmospheric Pollution Research* 101388. URL: `https://www.sciencedirect.com/science/article/pii/S1309104222000745`

- Rodríguez-Sánchez, A., Santiago, J.-L., Vivanco, M.G., Sanchez, B., Rivas, E., Martilli, A., and Martín, F., 2024. How do meteorological conditions impact the effectiveness of various traffic measures on NO_X concentrations in a real hot-spot?. *Science of The Total Environment* 954 176667. URL https://doi.org/10.1016/j.scitotenv.2024.176667

- Rodríguez-Sánchez, A. et al., 2025. *High-resolution modelling of the impacts of the deployment of electric vehicles on air quality in a urban hot-spot and its sensitivity to meteorological conditions.* (In preparation)

Other contributions related to this work:

- Gamarra, A. R., Lechón, Y., Vivanco, M. G., Theobald, M. R., Lago, C., Sánchez, E., Santiago, J.-L., Garrido, J. L., Martín, F., Gil, V., and Rodríguez-Sánchez, A., 2021. Avoided Mortality Associated with Improved Air Quality from an Increase in Renewable Energy in the Spanish Transport Sector: Use of Biofuels and the Adoption of the Electric Car. *Atmosphere*, 12(12), 1603. URL: `https://doi.org/10.3390/atmos12121603`

- Santiago, J.-L., Sanchez, B., Rivas, E., Vivanco, M. G., Theobald, M. R., Garrido, J. L., Gil, V., Martilli, A., Rodríguez-Sánchez, A., Buccolieri, R., and Martín, F. (2022). High Spatial Resolution Assessment of the Effect of the Spanish National Air Pollution Control Programme on Street-Level NO2 Concentrations in Three Neighborhoods of Madrid (Spain) Using Mesoscale and CFD Modelling. *Atmosphere*, 13(2), 248. URL: `https://doi.org/10.3390/atmos13020248`

- Barragán, R., Molero, F., Salvador, P., Theobald, M. R., Vivanco, M. G., Rodríguez-Sánchez, A., Gil, V., Garrido, J. L., Pujadas, M., and Artíñano, B., 2023.

Study of the Effect of Different Atmospheric Conditions on the Temporal Evolution of the Mixing Layer over Madrid during the Year 2020 by Means of Two Different Methods: Ceilometer Signals and the ECMWF-IFS Meteorological Model. *Remote Sensing*, 15(23), 5583. URL: https://doi.org/10.3390/rs15235583

- Santiago, J.-L., Rivas, E., Sanchez, B., Vivanco, M. G., Theobald, M. R., Garrido, J.-L., Gil, V., Buccolieri, R., Martilli, A., Rodríguez-Sánchez, A., and Martín, F., 2023. How do emission reductions of individual national and local measures impact street-level air quality in a neighbourhood of Madrid, Spain? *Air Quality, Atmosphere & Health*, 17 813-826. URL: https://link.springer.com/article/10.1007/s11869-023-01482-2

- Martilli, A., Nazarian, N., Krayenhoff, E. S., Lachapelle, J., Lu, J., Rivas, E., Rodriguez-Sanchez, A., Sanchez, B., and Santiago, J.-L., 2024: WRF-Comfort: simulating microscale variability in outdoor heat stress at the city scale with a mesoscale model, *Geosci. Model Dev.*, 17, 5023–5039, URL: https://doi.org/10.5194/gmd-17-5023-2024

Appendix A

SUMO's parameters tables

Table 8.1: SUMO's default car-following model parameters

Attribute	**Default value**	**Range**	**Description**
minGap	vClass specific	≥ 0	Minimum Gap when standing (m)
accel	vClass specific	≥ 0	The acceleration ability of vehicles of this type in $m \cdot s^{-2}$
decel	vClass specific	≥ 0	The deceleration ability of vehicles of this type in $m \cdot s^{-2}$
emergencyDecel	vClass specific	$\geq$ *decel*	The maximum deceleration ability of vehicles of this type in case of emergency in $m \cdot s^{-2}$
speedTable	-	list of float ≥ 0	list of speed values to be used for each vehicle type
maxAccelProfile	-	list of float ≥ 0	The maximal physically possible acceleration for the vehicle corresponding to the same index in *speedTable* in $m \cdot s^{-1}$ $m \cdot s^{-2}$
desAccelProfile	-	list of float ≥ 0	The maximal desired acceleration for the vehicle corresponding to the same index in *speedTable* in $m \cdot s^{-1}$ $m \cdot s^{-2}$
startupDelay	0	≥ 0	The extra delay time before starting to drive after having had to stop. Not applied after a scheduled stop
tau	1	≥ 0	The driver's desired (minimum) time headway. For the default model (Krauss) this is based on the net space between leader back and follower front.

Table 8.2: SUMO's default lane-changing model parameters

Attribute	Default value	Range	Description
lcStrategic	1.0	[0,inf) and -1	The eagerness for performing strategic lane changing. Higher values result in earlier lane-changing. A value of 0 sets the lookahead-distance to 0 (vehicles can still change at the end of their lane) where as -1 disables strategic changing completely
lcCooperative	1.0	[0,1] and -1	The willingness for performing cooperative lane changing. Lower values result in reduced cooperation. A value of 0 would still permit changing if the target lane affords higher speeds whereas -1 disables cooperative changing completely
lcSpeedGain	1.0	[0,inf)	The eagerness for performing lane changing to gain speed. Higher values result in more lane-changing. A value of 0 disables lane changing for speed gain
lcKeepRight	1.0	[0,inf)	The eagerness for following the obligation to keep right. Higher values result in earlier lane-changing. A value of 0 disables this type of changing

Continued on next page

lcContRight	1.0	[0,1]	The probability for selecting the rightmost lane whenever the number of lanes increases
lcOvertakeRight	0	[0,1]	The probability for violating rules against overtaking on the right
lcOpposite	1.0	[0,inf)	The eagerness for overtaking through the opposite-direction lane. Higher values result in more overtaking
lcStrategicLookahead	3000.0	[0, inf)	Lookahead distance when computing strategic best lanes (best lanes are recomputed on entering a new lane)
lcLookaheadLeft	2.0	[0,inf)	Factor for configuring the strategic lookahead distance when a change to the left is necessary
lcSpeedGainRight	0.1	[0,inf)	Factor for configuring the threshold asymmetry when changing to the left or to the right for speed gain. By default the decision for changing to the right takes more deliberation. Symmetry is achieved when set to 1.0
lcSpeedGainLookahead	0	[0,inf)	Lookahead time in seconds for anticipating slow down
lcSpeedGainRemainTime	20	[0,inf)	Minimum duration in seconds that can be driven on the new lane after changing for speed gain

Continued on next page

lcSpeedGainUrgency	50	[0,inf)	A threshold value for the internal speedGain-motivation that classifies the lane change as urgent and triggers speed adaptation in neighbouring (obstructing) vehicles
lcOvertakeDeltaSpeedFactor	0	[-1,1]	Speed difference factor for the eagerness of overtaking a neighbour vehicle before changing lanes. If the actual speed difference between ego and neighbour is higher than factor*speedlimit, this vehicle will try to overtake the leading vehicle on the neighboring lane before performing the lane change
lcKeepRightAcceptanceTime	-1	[0,inf)	Time threshold for changing the willingness to change right. The value is compared against the anticipated time of unobstructed driving on the right. Lower values will encourage keepRight changes. If the value is changed from its default, fast approaching follower vehicles will also impact willingness to move to the right lane
lcCooperativeRoundabout	lcCooperative	[0-1]	Factor that increases willingness to move to the inside lane in a multi-lane roundabout

Continued on next page

lcCooperativeSpeed	lcCooperative	[0,1]	Factor for cooperative speed adjustments
lcAssertive	1	positive reals	Willingness to accept lower front and rear gaps on the target lane. The required gap is divided by this value
lcMaxSpeedLatStanding	maxSpeedLat (i.e., disabled)		Constant term for lateral speed when standing. Set to 0 to avoid orthogonal sliding
lcMaxSpeedLatFactor	1		Bound on lateral speed while moving computed as lcMaxSpeedLatStanding + lcMaxSpeedLatFactor * getSpeed(). If > 0, this is an upper bound (vehicles change slower at low speed), if < 0 this is a lower bound on speed and should be combined with lcMaxSpeedLatStanding $>$ maxSpeedLat (vehicles change faster at low speed)
lcSigma	0		Lateral positioning-imperfection

Table 8.3: SUMO's main parameters describing a vehicle type

Attribute	**Value type**	**Default value**	**Description**
id	string	-	The name of the vehicle type
accel	float	≥ 0	The acceleration ability of vehicles of this type in $m \cdot s^{-2}$

Continued on next page

decel	float	$\geq$ 0	The deceleration ability of vehicles of this type in $m \cdot s^{-2}$
apparentDecel	float	== *decel*	The apparent deceleration of the vehicle as used by the standard model (in $m \cdot s^{-2}$). The follower uses this value as expected maximal deceleration of the leader.
emergencyDecel	vClass specific	$\geq$ *decel*	The maximum deceleration ability of vehicles of this type in case of emergency in $m \cdot s^{-2}$
maxAccelProfile	list of speed-accel pairs	"0.0 accel, 2778 accel"	The maximal physically possible acceleration for the vehicle, depending on the speed (in $m \cdot s^{-1}$ $m \cdot s^{-2}$).
desAccelProfile	"0.0 accel, 2778 accel"	list of float $\geq$ 0	The maximal desired acceleration for the vehicle corresponding to the same index in *speedTable* in $m \cdot s^{-1}$ $m \cdot s^{-2}$

Continued on next page

startupDelay	float >= 0	0	The extra delay time before starting to drive after having had to stop. Not applied after a scheduled stop
tau	float	1	The driver's desired (minimum) time headway. Exact interpretation varies by model. For the default model (Krauss) this is based on the net space between leader back and follower front
sigma	float	0.5	The driver imperfection (0 denotes perfect driving)
length	float	5.0	The vehicle's length in m.
width	float	1.8	The vehicle's width in m.
mass	float	1500	The vehicle's empty mass in kg.
minGap	float	2.5	The empty space after leader in m.
maxSpeed	float	55.55	The vehicle's technical maximum velocity in $m \cdot s^{-1}$.

Continued on next page

vClass	class	"passenger"	An abstract vehicle class. These classes are used in lane definitions and allow/disallow the usage of lanes for certain vehicle types.
emissionClass	emission class	"$\mathrm{PC}_{GE}U4$"	An emission class. By default a gasoline passenger car conforming to emission standard Euro 4 is used.
carFollowModel	string	"Krauss"	The name of the model used for car following.
laneChangeModel	string	"LC2013"	The name of the model used for changing lanes.

Appendix B

SUMO2CHIMERE source code

```
def aggregate_to_cells(emis_file, cells_file,
outfile, in_crs='EPSG:4326', out_crs='EPSG:4326', export=False):
'''
Parameters
----------
emis_file: Text file containing the punctual data to be aggregated.
cells_file: Shapefile containing the cells where the punctual data must
be aggregated.
outfile: Absolute path of the csv file containing the aggregated data.
in_crs: Coordinate Reference System (CRS) of the input data.
out_crs: CRS of the aggregated (output) data.

Returns
------

'''

# Step 1: Read file containing punctual emissions
# and assign geometry
emis_df = pd.read_csv(emis_file)

if 'X' not in emis_df.columns or 'Y' not in emis_df.columns:
    raise ValueError('X and Y must be present in "emis_df" columns.')

emis_gdf = gpd.GeoDataFrame(emis_df,
geometry=gpd.points_from_xy(emis_df.X, emis_df.Y), crs=in_crs)
```

```
    # Step 2: Read file containing cells data
    # For now, only rasters or polygons are allowed
    raster_df = gpd.read_file(cells_file)
    if raster_df.crs == None:
        raise ValueError('''Your "cells_file" data has not associated CRS.
        Please, check your data and assign it a CRS
        before executing this script.''')
    print(raster_df)
    print(emis_gdf.crs)
    print(raster_df.crs)

    if emis_gdf.crs != raster_df.crs: # If CRSs mismatch,
    match the emissions CRS to that of the cells for a correct aggregation.
        emis_gdf = emis_gdf.to_crs(raster_df.crs)


    # Step 3: Assign cells to emissions and sum all emissions
    #within each cell
    merged_df = gpd.sjoin(emis_df, raster_df, how='right')
    merged_df['centroid'] = merged_df.geometry.centroid
    merged_df['X_centroid'] = merged_df['centroid'].x
    merged_df['Y_centroid'] = merged_df['centroid'].y
    out_df = merged_df.groupby(['X_centroid',
    'Y_centroid']).sum(numeric_only=True)

    # Step 4: If needed, convert the aggregated #data to the desired output crs.
    #Then, export the aggregated data.
    if out_df.crs != out_crs:
        out_df = out_df.to_crs(out_crs)

    out_df.to_csv(outfile, sep=';', decimal='.', header=True, index=True)


def modify_EMI(emisfiles, cellareas_file, EMI_file, outfile, emis_pol, pol,
activity_sector='SNAP7', daytypes, speciation_file='', vdist_file='',
convert_to_molec=True, hourly_corr=False, corr_factorsfile=''):
    '''
```

```
    Script that modifies CHIMERE's EMI file with data read from text file(s).
    This script assumes filenames of the emission data to have
    the following format:
    '*_<hour><id>.csv' where <hour> is the hour of the day
    for which the emissions are computed and
    <id> is the label of the scenario for each daytype.

    Parameters
    ----------
    - emisfiles : list
        List containing the absolute paths of text file(s) containing
        gridded emissions data (in kg!).

    - cellareas_file : str
        Text file containing the areas (in km2) of each cell in emisfiles.

    - EMI_file : str
        Absolute path of the EMI file(s) to be modified.

    - outfile : str
        Absolute path of the modified EMI file(s) path.

    - emis_pol : str
        String describing the pollutant of the emissions.

    - pol : str
        String describing the pollutant of the model.

    - activity_sector : str
        The activity sector the user is working with (i.e., 'SNAP7').

    - daytypes : dict
        Dictionary relating a prefix to each day of the week.
        Example: {1:'L', 2:'L', 3:'L', 4:'L', 5:'L', 6:'F', 7:'F'}

    - speciation_file (optional) : str
        Absolute path of the text file where the details of the speciation
        are given.
```

```
    - vdist_file (optional) : str
        Absolute path of the text file where the vertical distribution of
        emissions within model levels is especified.
        If no value given, all emissions will be inserted in the
        first vertical model level.

    - convert_to_molec : boolean
        Some EMI variables such as NO, NO2 and HONO are given in molec/cm2/s,
        which is not a common unit when working with emissions.
        If this option is set to True, conversion from kg to molec/cm2/s
        is done

    - hourly_corr : boolean
        If this option is set to True, correction factors are applied
        for each month.

    - corr_factorsfile (optional): str
        Filename of the file containing correction factors.

    '''

    # Step 0. Define parameters and read optional files
    N_av = 6.022e23

    MM_pol = molar_mass(pol) # Uses external module:
    #https://gist.github.com/elibroftw/22e3b4c1eb7fa0a6c83d099d24200f95


    if len(speciation_file)>0: ## Read speciation file (if given)
        speciation_df = pd.read_csv(speciation_file, engine='python', sep=None)
        speciation_factor =
        speciation_df[(speciation_df.SPECIE == emis_pol) &
                      (speciation_df.MODEL_SPECIE == pol) &
                      (speciation_df.ACTIVITY_SECTOR == activity_sector)]['FRAC']
                      * 0.01
        if activity_sector not in speciation_df['ACTIVITY_SECTOR'].unique():
            raise ValueError('''
```

```
            Your activity sector is not found within the speciation file.
            A speciation factor cannot be defined.
            ''')
        if emis_pol not in speciation_df['SPECIE'].unique():
            raise ValueError('''
            Your "emis_pol" is not found within the speciation file.
            A speciation factor cannot be defined.
            ''')
        if pol not in speciation_df['MODEL_SPECIE'].unique():
            raise ValueError('''
            Your "pol" is not found within the speciation file.
            A speciation factor cannot be defined.
            ''')

    else:
        speciation_factor = 1


    if len(vdist_file)>0: ## Read vertical distribution file.
    #If no value given, create DataFrame with only first vertical model level
        vdist_df = pd.read_csv(vdist_file, engine='python', sep=None)
        vdist_df['FRAC'] *= 0.01 # From % to 0-1 values
    else:
        vdist_df = pd.DataFrame()
        vdist_df['MODEL_VLEVEL'] = 0
        vdist_df['FRAC'] = 1

    ## Read file for monthly corrections
    if hourly_corr == True:
        corr_factors = pd.read_csv(corrfactors_file,
        sep=';', decimal='.', header=0).set_index('Unnamed: 0')


    # Step 1: Read emission file(s) and creates one unique emission file
    with all the hourly data.
    if type(emisfiles) != list:
        raise ValueError('''
        "emisfiles" must be a list, even when only 1 file is provided.
```

```
        ''')

    emis_df = pd.DataFrame() # DataFrame where all hourly data will be saved
    emisfiles_dt = {} # Identify the emisfiles corresponding to each daytype

    emisfiles_dt = {}
    hours = {}
    for i in range(7):
        # 1=Monday, ... 7=Sunday.
        emisfiles_dt[i+1] = [x for x in
        emisfiles if daytypes[i+1]==''.join([y for
        y in x.split('_')[-1] if not y.isdigit()]).split('.')[0]]
        # Finds only files corresponding to that scenario

    for i in range(7):
        hours[i+1] = [int("".join([y for y in x.split('_')[-4] if y.isdigit()]))
        for x in emisfiles_dt[i+1]]
        if max(hours[i+1]) > 24:
            raise ValueError('''
            hour values cannot be larger than 24.
            If your scenarios have more than 24 hours, please split them
            in groups no larger than 24h.
            ''')
        for h in hours[i+1]:
            if ''.join([str(h),daytypes[i]]) in emis_df.columns:
                continue # Avoid duplicated data
            df = pd.read_csv(emisfiles[j], engine='python', sep=None)
            df.columns = ['X_centroid','Y_centroid', ''.join([str(h),
            daytypes[i]])]
            df = df.set_index(['X_centroid','Y_centroid'])

            emis_df = pd.concat([emis_df,df], axis=1)

    emis_df = emis_df.reset_index(drop=False)


    # Step 2: Let's find the emissions coordinates to know what cells
    to modify in the EMI file.
```

```
emis_minlon = float(emis_df.X_centroid.min())
emis_maxlon = float(emis_df.X_centroid.max())
emis_minlat = float(emis_df.Y_centroid.min())
emis_maxlat = float(emis_df.Y_centroid.max())
print('Limits of the region with emissions')
print([emis_minlon, emis_maxlon, emis_minlat, emis_maxlat])


chimemi_xr = xr.open_dataset(EMI_file) # Read the EMI file to be modified
out_xr = chimemi_xr.copy() # Where we will save the modified data

## If lon and lat are not in refnc_xr dimensions,
## I need to get the indices for the domain limits in order to
## get the cells to modify.
if 'lon' not in list(chimemi_xr.dims.keys()):
    lon_vals = chimemi_xr.sel(type_day=0, Time=0, south_north=0).lon.values
    lat_vals = chimemi_xr.sel(type_day=0, Time=0, west_east=0).lat.values

    # Get the indixes of the last cell inside the emis domain
    lonmin_diff = lon_vals - emis_minlon
    i_min = int(np.argmin(np.abs(lonmin_diff)))
    if lonmin_diff[i_min] > 0:
        i_min -= 1

    lonmax_diff = lon_vals - emis_maxlon
    i_max = int(np.argmin(np.abs(lonmax_diff)))
    if lonmax_diff[i_max] < 0:
        i_max += 1

    latmin_diff = lat_vals - emis_minlat
    j_min = int(np.argmin(np.abs(latmin_diff)))
    if latmin_diff[j_min] > 0:
        j_min -= 1

    latmax_diff = lat_vals - emis_maxlat
    j_max = int(np.argmin(np.abs(latmax_diff)))
    if latmax_diff[j_max] < 0:
        j_max += 1
```

```
# Step 3: Let's modify the values of the EMI file!
## Read domain's cell areas file
cellareas_df = pd.read_csv(cellareas_file, engine='python', sep=None)

for vlev in vdist_df['MODEL_VLEVEL'].unique():
    if vdist_df[(vdist_df['MODEL_VLEVEL']==vlev)]['FRAC'].values[0] == 0:
        continue
    else:
        vert_factor =
        vdist_df[(vdist_df['MODEL_VLEVEL']==vlev)]['FRAC'].values[0]
    for dt in range(7):
        if len(hours[dt+1]) == 0:
            warnings.warn('''No hourly data for this daytype,
            skipping iteration.''')
            continue
        for h in hours[dt+1]: #range(24):
            label=''.join([str(h),daytypes[dt+1]])


            ## Read hourly data from emissions file
            hourly_df =
            emis_df.loc[:,['X_centroid','Y_centroid',
            label]].set_index(['X_centroid','Y_centroid'])

            ## Convert hourly data to [X,Y] matrix (substituying matrix)
            emis_2D = hourly_df.unstack().T
            # Y_centroid in rows, X_centroid in columns

            ## Apply speciacion factors
            emis_2D = emis_2D * speciation_factor

            ## Units conversion
            if convert_to_molec == True:
            ## Convert from kg to molecules/cm2/s
                emis_2D = emis_2D * N_av / (MM_pol * 1e10)
                ## Convert units (if necessary)
```

```
        emis_2D = emis_2D * 1000 / 3600
        ## Cell area
        cellarea_2D = chim_cellarea.values[j_min:j_max+1,
        i_min:i_max+1]

        emis_2D = emis_2D / cellarea_2D

    else: ## Convert from kg to g/km2/s
        emis_2D = emis_2D * 1000 / 3600
        ## Cell area
        cellarea_2D = chim_cellarea.values[j_min:j_max+1,
        i_min:i_max+1]

        emis_2D = emis_2D / cellarea_2D


    ## Multiply by vertical factor
        emis_2D = emis_2D * vert_factor

    ## Multiply by temporal factors, if needed
    if hourly_corr == True:
        emis_2D = emis_2D * corr_factors.loc[prefix,mon]


    ## Check that dimensions of the substituying matrix
    #and the matrix to be substitute match
    chimemi_xr_matrix = chimemi_xr.sel(type_day=dt,
    Time=h-1, south_north=slice(j_min,j_max+1),
    west_east=slice(i_min,i_max+1),bottom_top=0)[pol]

    emis_2D[emis_2D < 1e-4] = chimemi_xr_matrix.values
    # Where SUMO does not provide emissions,
    # keep the original EMI values
    if (emis_2D.shape[0] - chimemi_xr_matrix.shape[0] != 0) or
    (emis_2D.shape[1] - chimemi_xr_matrix.shape[1] != 0):
        raise ValueError('Matrices dimensions do not match.')
```

```
                ## Insert emis_2D values in original EMI file
                outnc_xr[pol][h-1,dt,vlev,j_min:j_max+1,
                i_min:i_max+1] = emis_2D.values
    outnc_xr.to_netcdf(outfile)
```

Appendix C

Estimating the effect of the COVID-19 pandemic on pollutant emissions in Europe

The estimation of the impact of mitigation measures or relevant events on emissions is very relevant for air quality modelling and policing making at every scale. This work presents the results of an estimation of the impacts of the COVID-19 pandemic on the emissions of several European countries, across every sector of activity, during 2020.

In this way, a fast and simple methodology that takes advantages of observed relationships between variables is developed to estimate the emissions factors corresponding to different sectors of activities, to provide a certain degree of independency to researchers that need this information for different purposes. This work does not present an entirely new methodology but simplifies existing ones and modify them when appropriate, avoiding both high computing resources and specific expertise.

Due to the broad range of sectors affected by restrictions associated to the COVID-19 pandemic, and the different responses of countries to it, very different impacts have been modelled for different cases. The largest emissions reductions were modelled for the aviation sector, with a reduction of 62.7% in average. Moreover, countries with the lightest restrictions presented lighter reductions, even increased emissions in some activity sectors such as public and manufacturing industry sectors.

Atmospheric Pollution Research 13 (2022) 101388

Contents lists available at ScienceDirect

Atmospheric Pollution Research

journal homepage: www.elsevier.com/locate/apr

Estimating the effect of the COVID-19 pandemic on pollutant emissions in Europe

Alejandro Rodríguez-Sánchez *, Marta G. Vivanco, Mark Richard Theobald, Fernando Martín

Atmospheric Modelling Unit, Environment Department, CIEMAT, Av. Complutense, 40, 28040, Madrid, Spain

ARTICLE INFO

Keywords:
Air pollution
Anthropogenic emissions
Pandemic
Lockdown
COVID-19

ABSTRACT

Changes in primary emissions due to the COVID-19 lockdowns in Europe for the year 2020 have been estimated by considering fully open-access and near-real-time measured activity data from a wide range of information sources and with simple computational techniques. The estimates consist on a dataset of reduction factors that are both time- and country-dependent and provided for the following source categories: energy industry (power plants), manufacturing industry, road traffic, aviation, shipping and other stationary combustion activities such as residential and commercial-institutional activities. Inspired in other authors' estimates for COVID reductions, the advantage of this methodology is that there is no use of machine learning, making this procedure more accessible to the general scientific community. We have followed a fast methodology that takes advantage of observed relationships between variables (e.g. temperature and energy demand) without needing special algorithms for finding those relationships. The comparison of our estimates with others from other authors indicate a reasonable agreement and pointing out that emissions dropped by a 17% on average in Europe, with large differences between sectors of activities and spatial heterogeneity. The most affected sector was aviation, with a spatial-averaged variation of −63% in emissions since the implementation of first restrictions with respect business-as-usual values. 2020 emission changes with respect to business-as-usual values in countries ranges from a −13% in Norway and Poland to a more than −20% in several Mediterranean countries as well as the United Kingdom. Two main periods of emission reductions have been identified.

CRediT author statement

Alejandro Rodríguez-Sánchez: Conceptualization, Methodology, Validation, Investigation, Visualization, Writing- Original draft preparation **Marta G. Vivanco**: Conceptualization, Writing- Reviewing and Editing, Supervision, Visualization. **Mark Richard Theobald**: Conceptualization, Writing- Reviewing and Editing, Visualization, Investigation, Validation. **Fernando Martin**: Writing- Reviewing and Editing.

1. Introduction

Since late February 2020 until the present day, most European countries have imposed lockdowns and mobility restrictions in order to prevent further spread of the COVID-19 pandemic, resulting in an unprecedented change in lifestyles. All non-essential activities were paralysed for several weeks in most countries at some point, resulting in a reduction in atmospheric anthropogenic emissions.

As a result, a drop in atmospheric pollutant concentrations was observed in several countries both by in-situ (Burns, J. et al., 2021; Putaud, J.P. et al., 2021) and satellite-based observations (Sun, K. et al., 2021; Fioletov, V et al., 2021). While these studies have assessed changes in pollutant concentrations, further understanding of the impacts of restriction measures upon air quality and climate requires the quantification of the reduction of anthropogenic emissions. To date, only three other studies (Guevara et al., 2020a and 2020b; Zheng et al., 2021) – of which the authors are aware – looking at the non-local quantification of emission changes due to the pandemic have been published. Two of those works focus on Europe (also the focus of this study), while the third one is focused on China. The other two studies that focused on emissions from European countries only covered the period between 21 February and July 31, 2020 at the latest, which does not cover emission variations due to changes in restrictions after the first COVID-19 outbreak. Neither covers a wide enough range to compare the 2020 emissions with previous years. In this study, the whole year of

Peer review under responsibility of Turkish National Committee for Air Pollution Research and Control.
* Corresponding author.
E-mail address: alejandro.rodriguez@ciemat.es (A. Rodríguez-Sánchez).

https://doi.org/10.1016/j.apr.2022.101388
Received 16 November 2021; Received in revised form 11 March 2022; Accepted 11 March 2022
Available online 22 March 2022

2020 is covered, allowing an evaluation of the COVID-19 pandemic on annual emissions from a non-local perspective.

As Guevara et al. (2020a, 2020b) points out, understanding and quantifying the impact of the COVID-19 lockdowns on European emissions and air quality is a difficult task due to the heterogeneous implementation of restrictions across different countries, including (i) different starting dates of the restrictions, (ii) diversity in the levels and type of restrictions, (iii) changes in time of the restriction levels, and (iv) different spontaneous responses by individuals. It's important to highlight that estimations of changes in anthropogenic emissions released to the atmosphere are required for diverse applications including economics and policy making (e.g. providing reference values for developing strategies), healthcare (e.g. for estimating health impacts of air pollution) and ecology (e.g. for estimating impacts to vegetation).

The chronology of national restriction levels in Europe is illustrated in Fig. 1, which shows stringency index trends computed by the Oxford COVID-19 Government Response Tracker (OxCGRT) for selected countries (Hale et al., 2021). The stringency index reports how the response of governments varied by combining several indicators (e.g. school closures, restrictions in movement, implementation of economic policies).

As can be seen, there were two main periods when moderate or severe restrictions were imposed in all countries, with little difference between them during the first COVID-19 outbreak (Sweden was the main exception in Europe not imposing restrictions but giving instead a series of national recommendations to their citizens), and more accentuated differences after the end of the first outbreak in early summer 2020.

In this work, we refer to the "first wave" and "second wave" of the coronavirus outbreak for those periods in which stringency index increases considerably. We consider the first wave as the period between February 21 – when Italy impose strict restrictions – and July 1, when all the countries have reduced stringency indexes. The start of the second wave is more difficult to define, due to lags between countries. Nevertheless, December 2020, January 2021 and February 2021 have significantly higher stringency indexes than previous months and therefore it can be considered that the second wave occurred during the winter months and the first three weeks of March 2021, after which the stringency index begins to drop in most countries.

Considering all of the above, the quantification of emission changes due to the COVID-19 lockdown requires the use of reduction factors that are, at least: (i) country-dependent, (ii) pollutant- and sector-dependent and (iii) time-dependent.

In this paper we describe a methodology to estimate day-, sector- and country-dependent emission reduction factors for most European countries using open-source data. These factors are used to quantify European primary emission reductions and the associated impacts upon air quality. In this work, an emission reduction factor is considered as a multiplicative factor to pre-pandemic emissions values: an emission reduction factor lower than 1 (or emissions lower than 100% of business-as-usual (BAU) values) indicates decreased emissions in 2020 with respect pre-pandemic values, whereas an emission reduction factor greater than 1 (emissions greater than 100% of BAU values) are associated with larger emissions than pre-pandemic ones.

Our emission reduction factors are calculated from data from a wide range of information sources, including open-access and near-real-time measured activity data, proxy indicators and other available reports.

This work, unlike previous studies, covers the whole of 2020 for the following anthropogenic source categories: energy industry, manufacturing industry, road transport, shipping and aviation. Furthermore, this study presents a faster, simpler and easily reproducible methodology as it does not use Machine Learning (ML) algorithms because, despite being widely used tools in scientific research, tuning a ML model can be a difficult and time-consuming task, thus complicating the emission reduction estimation process.

In summary, the main objective of the present work is to develop a methodology that allows the estimation of emission reductions due to the COVID-19 pandemic in an easy way, to provide a certain degree of independency to researchers that need this information for different purposes. We did not aim to create an entirely new methodology but simplify existing ones and modify them when appropriate, avoiding both high computing resources and specific expertise in techniques such as Machine Learning.

Section 2 describes the methods and datasets used to estimate the emission reduction factors for each of the pollutant sectors and selected countries. Section 3 discusses the results obtained and compares them to previous emission reduction factors calculated using other methodologies. Section 4 includes our main conclusions and perspectives for the future of emission reduction calculations.

2. Methodology

The approach followed to estimate emission reduction factors is based on that of Guevara et al. (2020a, 2020b). Data from a large range

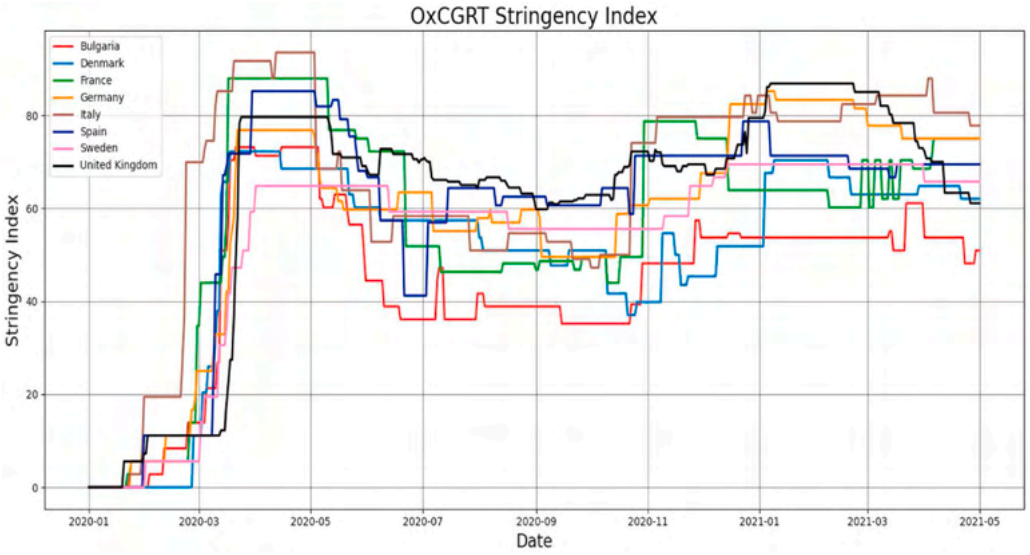

Fig. 1. Evolution of the stringency index computed by the Oxford COVID-19 Government Response Tracker (OxCGRT) for the period January 1, 2020 to May 1, 2021 for seven selected countries. Data available in Hale et al. (2021).

of information sources was gathered. As a result, a set of time- and sector-resolved emission reduction factors for European countries for the year 2020 has been estimated, considering the Gridded Nomenclature For Reporting (GNFR) classification of emission source sectors. As in Guevara et al. (2020a), we considered the following four GNFR sectors: GNFR_A (energy industry), GNFR_B (manufacturing industry), GNFR_F (road transport) and GNFR_H (aviation). In addition, other sectors potentially affected by the COVID-19 lockdown such as GNFR_C (other stationary combustion activities, specifically residential and commercial/institutional sectors) and GNFR_G (shipping) have been included, although the latter is only pollutant dependent, not country-dependent – due to the lack of physical borders in the sea. Some sectors such as agriculture, which is considered part of the GNFR_C category, have been considered as essential activities during the pandemic because of their importance to provide necessary services to the community. Because of that, we have assumed that emissions from these activities have not changed at all during the pandemic.

Regarding the spatial coverage of the dataset, we tried to include all the European countries with continuous data for the entire year of 2020. The only countries that did not meet this criterion are Malta, Luxembourg, Belarus, Bosnia and Herzegovina, North Macedonia, Turkey and Ukraine. Subsection 2.1 provides further information about the data sources and the countries with available data for each activity source sector.

We collected and processed daily time series representing the main activities of each sector, with the exception of GNFR_G (shipping), for which only weekly data were available (EMSA, 2021 We then combined the information in order to derive daily emission reduction factors as a function of country and sector.

2.1. Information sources and quality check

Our dataset includes information from a large variety of data sources.

For estimating GNFR_A and GNFR_B emission reduction factors, we have used data from the ENTSO-E transparency platform. ENTSO-E, the European Network of Transmission System Operators for Electricity, is the association for the cooperation of the European transmission system operators (TSOs) and is responsible for the secure and coordinated operation of Europe's electricity system (ENTSO-E, 2021). We collected hourly data of electricity demand for the EU-27 countries plus Norway and United Kingdom for the years 2017–2020 and computed the daily total values. Days with no data were assumed to be days with no variations with respect to business-as-usual values. Also temperature data from the Copernicus Climate Change Service (C3S, 2017) was used. Data from Switzerland was obtained from the national website (Confederation Suisse, 2021).

To compute the contribution of industry to the total electricity demand, the industry fraction to total energy demand data from Eurostat (2021) and Confederation Suisse (2021) were used.

Another source of information was the Google Mobility database (Google LLC., 2020). This dataset reports daily variations on mobility by country for different categories of places: public transport stations, grocery stores, parks, residential places, workplaces and recreation sites. Daily data for the EU-27 countries, Norway, North Macedonia, Turkey and United Kingdom was obtained for the period February 17, 2020 to January 1, 2021.

Its values for the different places were adjusted using the criterion of Guevara et al. (2020a, 2020b). These data were used to estimate GNFR_C and GNFR_F emission reduction factors.

Daily local traffic data from the cities of Madrid (Madrid Municipality Open Data portal, 2021) and Dublin (Transport Infrastructure Ireland, 2021) were used to improve the temporal resolution of TomTom based traffic emission reduction factors.

The emission reduction factors for the shipping sector were derived from the data on the impact of COVID-19 on European shipping traffic provided by EMSA (2021), which starts at week 15 of 2020. These data are not country dependent with a single value for all European waters.

Finally, we derived the reduction factors related to air traffic emissions during Landing and Take-Off cycles (LTO) in airports from daily statistics provided by EUROCONTROL (2021a, 2021b) for the whole of 2020. Again, we used data corresponding to the EU-27 countries, Norway, United Kingdom, Turkey and North Macedonia.

2.2. Energy industry

Following the methodology of Guevara et al. (2020a, 2020b), we assumed that energy from the industry sector follows the changes in electricity demand reported by the European Network of Transmission System Operators for Electricity (ENTSO-E), under the hypothesis that changes in electricity demand are closely related to changes in electricity generation. ENTSO-E centralizes the collection and publication of the electricity generation for each European member state and the United Kingdom. However, unlike in Guevara et al. (2020a, 2020b), we have not used machine learning algorithms to weather-normalize the electricity demand.

The use of electricity demand as an energy indicator is not a totally rigorous assumption, because other factors such as the use of heating or cooling systems also contribute to demand (Botzen Wouter et al., 2021; De Cian et al., 2007). The use of those systems is directly related to temperature; for this reason (in contrast to Guevara et al. (2020a, 2020b), who used machine learning techniques) we used electric demand data from a period with a similar meteorology to 2020, in order to minimize the impact of heating or cooling systems, and attribute the differences to the effect of COVID-19 restrictions on electricity consumption. With this consideration, we collected hourly data from 2018 to 2019 for each country, since this is the period (since 1950) with average and seasonal average temperatures most similar to those of 2020 (Table 1, Fig. S1). The season with the largest differences between the year 2020 and this reference period is winter, with winter 2020 being an exceptionally warm one. However, this season is the one with least impact of temperature on electric demand, as heating systems in Europe use little electricity – barely 5.9% of the energy used for heating is electricity (https://www.odyssee-mure.eu/publications/efficiency-by-sector/households/heating-energy-consumption-by-energy-sources.html, last accessed: October 2021)-. This means that it is expected that changes in emissions in winter 2020 due to restrictions related to the pandemic (especially in February) are notably larger than variations in emissions due to changes in the meteorology. As a result, we assume that mean emissions of 2018 and 2019 are representative of the emissions for 2020 when considering only the effect of weather on the emissions.

Taking into account these considerations, the emission reduction factor for the energy industry were calculated as in Guevara et al. (2021), as:

$$\boldsymbol{ERF}_{\boldsymbol{GNFR-A}}\,(\boldsymbol{d},\boldsymbol{c}) = \frac{\boldsymbol{ED}_{2020}(\boldsymbol{d},\boldsymbol{c}) - \boldsymbol{ED}_{\boldsymbol{ref}}\,(\boldsymbol{d},\boldsymbol{c})}{\boldsymbol{ED}_{\boldsymbol{ref}}(\boldsymbol{d},\boldsymbol{c})}$$

where $ERF_{GNFR-A}\,(d,c)$ is the emission reduction factor for energy industry for day "d" and country "c"; $ED_{2020}(d,c)$ is the electric demand

Table 1
Variation of mean temperatures for 2018 and 2018–2019 with respect to 2020. DJF refers to the period December-January-February; MAM to March-April-May; JJA to June-July-August and SON to September-October-December. Annual stands for the mean across all the months.

	DJF	MAM	JJA	SON	Annual
2020 temperature minus 2018 and 2019 averaged mean temperature (°C)	1.59	−0.21	−0.28	0.80	0.47
2020 mean temperature minus 2018 mean temperature (°C)	2.44	−0.24	−0.48	0.60	0.58

Data calculated from ERA5-Land dataset public data.

observed in 2020 for day "d" and country "c"; and $ED_{ref}(d,c)$ is the average of electric demand observed in 2018 and 2019 for day "d" and country "c" as representative of Business As Usual (BAU) electric demand.

As shown in Fig. S2 in the Supplement, although most of the variations between emission reduction factors computed using 2018 as a reference year and those using the mean emissions of 2018 and 2019 as the reference are small, there are some big differences. This is due to missing values, with Luxembourg and Cyprus being the countries with most missing data. For the days with missing data we have set the emission reductions to zero.

2.3. Manufacturing industry

The emission reduction factors for the manufacturing industry (category GNFR_B) are based on the emission reduction factors for the energy industry described in section 2.1. Following the criterion of Guevara et al. (2021), 25% of the total energy generation emission reductions have been attributed to the manufacturing industry sector, which is consistent with the 27% decrease in electricity use by the manufacturing sector reported by the electricity transmission system operator of France (RTE, 2020). Again, unlike Guevara et al. (2021), we have not used ML methods to process the original energy demand data.

The reduction of power demand attributable to the manufacturing industry sector was then translated into a total reduction in industrial activity using the national energy balances reported in Eurostat (2021):

$$\boldsymbol{ERF}_{GNFR-B}(\boldsymbol{d},\boldsymbol{c}) = \frac{0.25 * \boldsymbol{ERF}_{GNFR-A}(\boldsymbol{d},\boldsymbol{c})}{\boldsymbol{s}(\boldsymbol{c})}$$

where $ERF_{GNFR-B}(d,c)$ is the emission reduction factor for the manufacturing industry energy use for day "d" and country "c"; and $s(c)$ is the contribution of this sector to the total energy consumption for country "c".

2.4. Road transport

In order to compare methodologies, we have created an emission reduction factor based on TomTom (2021) monthly rush hour congestion data as well as the Google Mobility data (Google LLC., 2021). Both procedures have been found to be fast and provide good results. Therefore, TomTom data could be an open-source alternative to Google mobility data, the latter being used in Guevara et al. (2020a, 2020b), which was not available to the general public before the pandemic.

Furthermore, to improve temporal resolution, data from traffic counts have been included for countries where this type of data is freely available. To include these data, we have assumed that reductions in road mobility in the main city or cities of a country contribute the most to national reductions and so we have considered the traffic reductions in the most important cities of each country to be representative of the reductions for the entire country.

The procedure is illustrated in Fig. 2. Once the monthly emission reduction factors (ERF) for the traffic sector are calculated using TomTom (2021) monthly-based mobility data, we improved their temporal resolution in a certain country using the traffic count data from the main cities of the country (right part of Fig. 2). From the raw traffic count data, we derived daily and monthly reductions of traffic in 2020 with respect to business-as-usual values The monthly reductions are then subtracted from the daily reductions in order to obtain the daily reductions with respect to the monthly mean values (zero-centered daily variations of traffic). Finally, those daily reductions with a mean value of zero are added to the previously calculated monthly ERF to obtain the definitive daily ERF for this country. The result is a time series with daily time resolution – same as the traffic count data –, but with a monthly mean equal to the monthly emission reduction factors derived from TomTom (2021) data. These series have a bias with respect Google

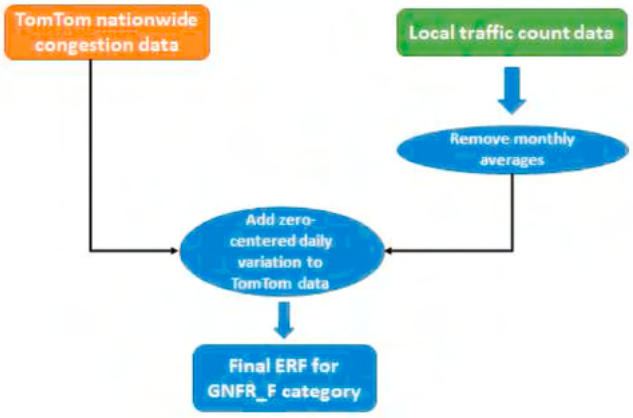

Fig. 2. Procedure to improve temporal resolution of original ERF for traffic sector using daily traffic count data.

mobility data that in part represents the contribution from the population of the rest of the country. This bias tends to be positive (we estimate larger reductions than other studies and the Google database), in part since mobility reductions in villages and small towns are smaller than in larger cities due to the lower availability of essential services and the lower spread of COVID-19 in less populated areas, especially at advanced stages of an outbreak (Coskun et al., 2021; Wong and Li, 2020).

This approach works well for countries such as Spain and Ireland, as illustrated in Fig. S3 and Fig. S4, where differences with estimates from Guevara et al. (2021) can be seen. In those figures, the green lines represent the initial ERF estimation and the blue lines are the updated ERF computed using the methodology described in Fig. 2. Unfortunately, not all European countries have openly available traffic count data, and therefore for most countries emission reduction factors were calculated on a monthly basis.

2.5. Aviation

Emission reduction factors for the aviation sector (GNFR_H) were derived from monthly and daily air traffic data published by EUROCONTROL (EUROCONTROL, 2021a, 2021b) classified by country, instead of using individual airport data as in Guevara et al. (2020a).

2.6. Shipping

For the shipping sector, emission reduction factors were derived from the weekly reports published by the European Maritime Safety Agency (EMSA, 2020). As there are no physical borders in the sea, a weekly emissions reduction factor for the whole of Europe was estimated using weekly vessel traffic data classified by type of vessel, as in Guevara et al. (2021):

$$\boldsymbol{ERF}_{GNFR-G}(\boldsymbol{w},\boldsymbol{c},\boldsymbol{v}) = \sum_{v=1}^{n} \boldsymbol{ERF}(\boldsymbol{w},\boldsymbol{v}) * \boldsymbol{C}(\boldsymbol{v},\boldsymbol{c})$$

where $\boldsymbol{ERF}_{GNFR-G}(\boldsymbol{w},\boldsymbol{c},\boldsymbol{v})$ is the resulting emission reduction factor for the shipping sector for the week "w", vessel type "v" and pollutant "c"; $\boldsymbol{ERF}(\boldsymbol{w},\boldsymbol{v})$ is the emission reduction factor for vessel type "v" and week "w"; and $\boldsymbol{C}(\boldsymbol{v},\boldsymbol{c})$ is the contribution of vessel type "v" to the total emissions of the shipping activities sector for pollutant "c". The contribution of each type of vessel to total European shipping emissions of each pollutant were obtained from Jalkanen et al. (2016).

2.7. Other stationary combustion activities

Finally, emission reduction factors were calculated for other

stationary combustion activities (GNFR_C), which includes commercial and institutional sector activities; residential activities; primary sector (agriculture, fishing, forestry, etc.) activities and other activities, whose contribution is small. Primary sector activities were considered as essential activities which means that lockdowns and other restrictive measures were not applied to them. Consequently, the emission reduction factors calculated in this work are associated with reductions in residential, institutional and commercial activities.

In order to estimate the variations in emissions associated with the aforementioned activities, the "Google COVID-19 Community Mobility Reports" (Google LLC, 2020) database was used. This dataset reports daily variations on mobility by country for different categories of places: public transport stations, grocery stores, parks, residential places, workplaces and recreation sites. Increasing (decreasing) mobility towards the different places is directly associated with increasing (decreasing) activities related to them. These variations are computed by Google for each weekday, using the 5-week period between January 3, 2020 and February 6, 2020 as a baseline.

Again, in order to compare with the study by Guevara, the same criterion was adopted to restrict daily variations of mobility towards places of residence to an upper limit of +10%, according to the data reported by Le Quére et al. (2020), which are in line with those reported by the thermostat fabricant Tado (2020). This is because the Google mobility database tends to overestimate changes in mobility (Guevara et al., 2021). Furthermore, mobility changes for journeys to commercial/institutional buildings were limited to a maximum reduction of 66.9%, with respect to the BAU scenario (Guevara et al., 2020a, 2020b).

Depending on the main economic activities of a country, the contribution of each sector to total emissions for the GNFR_C category differs considerably from one country to another in the EU. Taking this into account, the emission reduction factors of residential and commercial/institutional sectors are computed, as in Guevara et al. (2020a, 2020b), as a weighted average of the variations of these sectors from the Google database:

$$\boldsymbol{ERF}_{GNFR-C}(\boldsymbol{d},\boldsymbol{c},\boldsymbol{p}) = \boldsymbol{RF}_{res}(\boldsymbol{d},\boldsymbol{c})^{*}\boldsymbol{S}_{res}(\boldsymbol{c},\boldsymbol{p}) + \boldsymbol{RF}_{comm}(\boldsymbol{d},\boldsymbol{c})^{*}\boldsymbol{S}_{comm}(\boldsymbol{c},\boldsymbol{p})$$

where $ERF_{GNFR-C}(d,c,p)$ is the resultant emission reduction factor for GNFR_C activities for day "d", country "c" and pollutant "p"; is the mobility reduction factor associated with the residential sector for day "d" and country "c"; $S_{res}(c,p)$ is the contribution of the residential subcategory to the total emissions of the GNFR_C category for the country "c" and pollutant "p"; $RF_{comm}(d,c)$ is the mobility reduction factor associated with the commercial/institutional sector for day "d" and country "c"; and $S_{comm}(c,p)$ is the contribution of the commercial/institutional subcategory to the total emissions of the GNFR_C category for country "c" and pollutant "p".

The contribution of each subcategory to the total emissions of the GNFR_C category, as well as the total emissions for the GNFR_C category, is obtained from the emission data officially submitted by the Parties to the LRTAP Convention to the EMEP programme for the last five years (2015–2019). However, these data are highly dependent on how the different Parties submit their emission inventories to the EMEP programme (EMEP/CEIP, 2021). There are cases in which some subcategories have no emissions assigned to them for several reasons, such as that the country does not estimate emissions for that subcategory or the country includes emissions corresponding to one GNFR subcategory in another subcategory. Also it can be that a specific subcategory or process does not exist in a country. These cases in which emissions cannot or have not been estimated for a subcategory are a minority and it has been possible to calculate the contribution of each subcategory (residential and commercial/institutional) to the total emissions corresponding to GNFR_C activities.

3. Results and discussion

3.1. Energy industry

Fig. S5 shows a comparison between the emission reduction factors calculated for the energy industry in this study (hereinafter Rodríguez-Sánchez database) and in that of Guevara et al. (2020a) (hereinafter Guevara database) for Spain. It can be seen that the general trends are similar. The emission reduction factors obtained in this study have larger variations than those in the Guevara database. This could be due to the fact we have selected a two-year period as a baseline and so anomalies in one year are not fully compensated. The second reason is that our data is not weather normalised for the sake of rapidness and ease of calculation. This can amplify the effect of days of increased consumption occurring on one specific day and year. For example, the peaks observed in Spain during the last days of the year correspond to an unusually cold period that extended until late-January. As Spain is a relatively warm country, electric consumption increased 15% during first week of 2021 due to the activation of heating systems. However, differences between both databases' emission reduction factors are still small, with an absolute value of 1.08% for the case of Spain and 0.57% when averaging all countries' data.

From the 7-day moving average of the aforementioned data (Fig. S6), we can see that the values obtained with our methodology are consistent and agree quite well with estimates obtained using more complex methodologies.

Fig. 3 shows the computed emission reduction factors for the GNFR_A category for some European countries (Spain, France, Italy and Germany). In general, those countries behave quite similarly with Italy having the largest reductions during the first wave of COVID-19 pandemic and France showing a more pronounced reduction in emissions during November 2020, which is consistent with an abrupt increase in its stringency index in that month (Fig. 1).

As for the number of days for the period February 21, 2020 to December 31, 2020 below or above BAU emissions for the energy industry, there is a predominance of days with below average emissions, especially in Italy, as shown in Fig. 4. Small countries such as Cyprus and Luxembourg show the largest number of days with emissions above 125% and below 75% of business-as-usual values. The maximum possible value for the cumulative number of days exceeding these significant variations is 315 (21 February to 31 December).

3.2. Manufacturing industry

Figs. S7 and S8 illustrate the daily emission reduction factors and the 7-day moving average for the manufacturing sector. Again, our data fluctuate more than that obtained using complex methodologies but show the same trend. We see a slight underestimation of emission reduction factors for Spain with respect to the Guevara database. This translates in slightly larger differences than for the Energy industry sector between both databases: 3.30% in Spain and 2.01% for all countries' data. Very similar trends to those of GNFR_A category are found for the European countries highlighted on the previous section (not shown), with the previously mentioned exception of France in October and November 2020.

Greater emission reductions are observed in small countries such as Cyprus and Luxembourg, as for the energy sector (Fig. S9). This is expected as energy and manufacturing industries are closely related sectors in most countries.

3.3. Road transport

Fig. S10 shows the initial estimation of monthly emission reduction factors for road transport in Spain. As can be seen, the data for Spain in both databases agree quite well, with a more pronounced drop and recovery of road traffic emissions in the Guevara database. The absolute

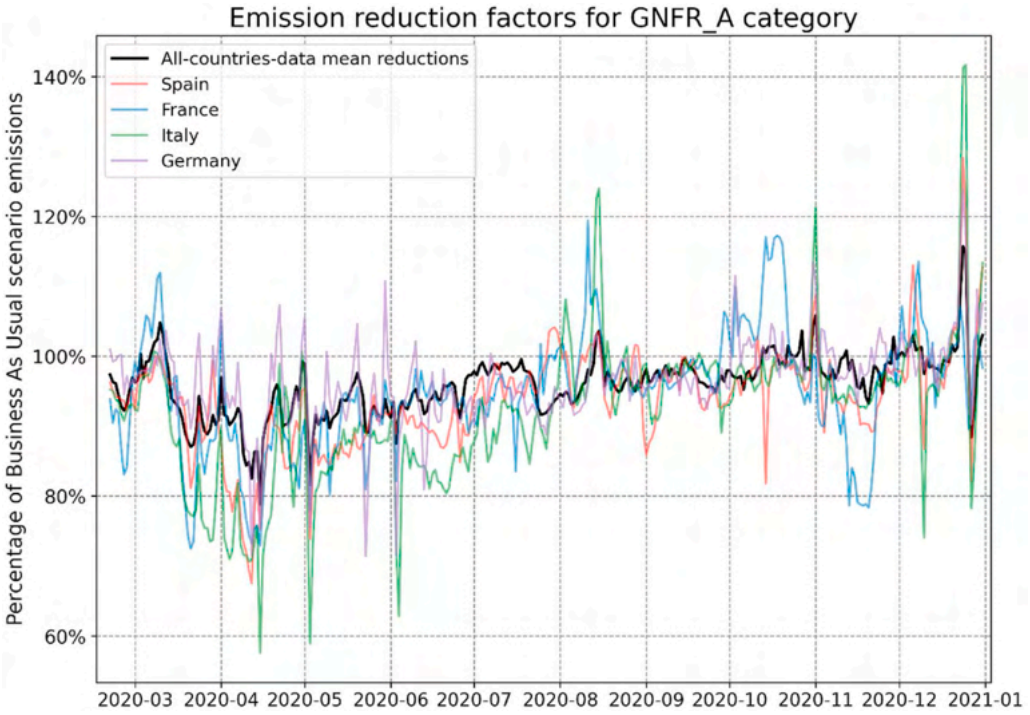

Fig. 3. Emission reduction factors calculated in this study for the energy industry for 2020 for some selected countries (France, Germany, Italy, Spain; and the mean of all countries in the study (black curve)).

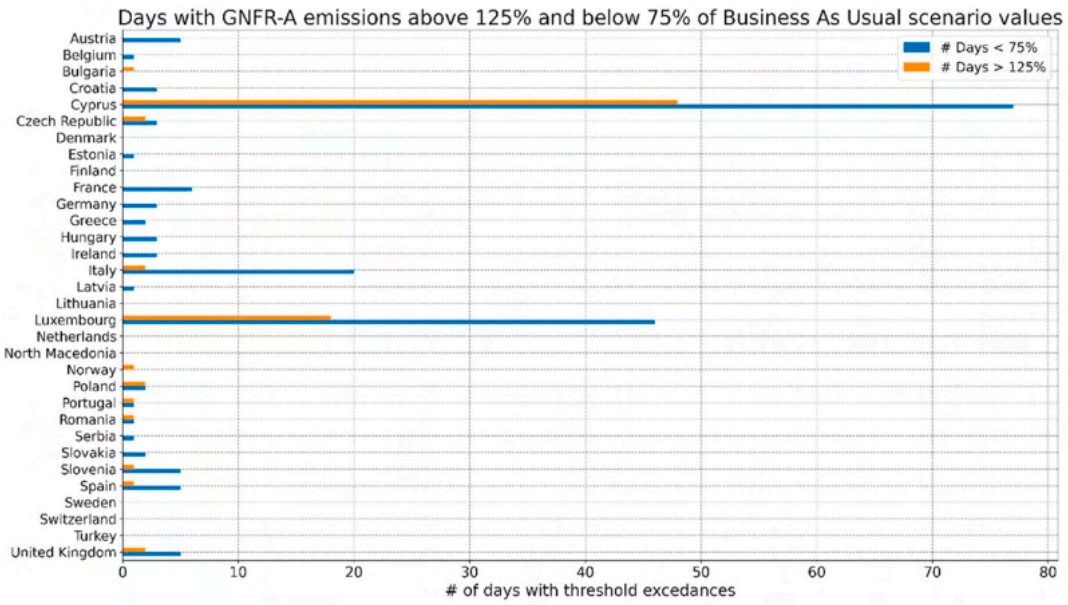

Fig. 4. Number of days with emissions for the energy industry above 125% of business-as-usual (BAU) values (orange) and below 75% of BAU values (blue).

value of the period-averaged difference between the monthly emission reduction factors of both databases for Spain is of 1.42% and of 3.50% for all the countries. For some countries, such as Spain, our data are more consistent with the Guevara database than with Google mobility transit data after the first COVID-19 wave, which tend to overestimate the emission reductions (Guevara et al., 2020a).

Transforming the monthly emission reduction factors into daily emission reduction factors results in good agreement with the Guevara database for the case of Spain, as shown in Fig. S3. Also, good results were obtained for the case of Ireland, using Dublin traffic count data to represent the daily traffic variation in this country (Fig. S4). These results suggest that this method represents a good alternative to estimate national road transport related emissions from monthly rush hour data (TomTom) and the available traffic counts.

In both cases the differences in emission reduction factors between weekdays and weekends grows notably during the second wave of the coronavirus pandemic, especially in the case of Spain were differences up to 60% are seen between consecutive days. This is a limitation of the methodology introduced: the lack of data from more cities gives more weight to the traffic variations in the capital cities of Madrid and Dublin and their local restrictions. In the case of Madrid, during the last months of 2020 and the beginning of 2021, relatively light restrictions were

applied to recreational activities: bars opened until curfew at midnight, 50% or more of capacity in bars and other recreational sites, etc.; while teleworking was by the time the predominant form of work. This make the difference between weekend traffic, which tend to increase, and weekday traffic, which stayed quite low, giving rise to abrupt changes in the emission reduction factors.

For several other countries we didn't find freely available data. Because of that reason and for the sake of consistency, Fig. 5 shows the monthly emission reduction factors obtained for all the countries included in this study. It can be identified the second wave of COVID-19 affecting road traffic during late autumn after a relatively normal summer.

3.4. Aviation

Fig. 6 shows the emission reduction factors used to calculate our monthly emission reductions for the aviation sector for Spain. This is the sector most affected by the COVID-19 pandemic. The figure shows how emissions dropped to almost zero in April and do not fully recover during the analysis period and have a peak in summer with emissions approaching 50% of business-as-usual values, only to drop again in autumn.

The daily data shown in Fig. S11 show more clearly the sudden recovery of emissions from the aviation sector during the months of July and August, except in some Eastern Europe countries where the recovery of flight numbers was much more gradual.

Fig. S12 shows the comparison between the emission reduction factors from the study and those of the Guevara database for Spain. As can be seen, the two datasets are reasonable consistent and we can assume that our data are valid for the whole year (yearly-averaged differences between both databases emission reduction factors are of 0.5% when considering all countries). As in road transport, the effect of the second wave of COVID-19 on the emissions related the aviation is visible, with emissions decreasing during autumn 2020 and recovering slightly by the end of the year for the Christmas holidays. The total annual emission reduction for the aviation sector in 2020 is 47% with respect to business-as-usual values and excluding the pre-lockdown period the reduction is more than 60%.

As one could expect, for almost all the 315 days of 2020 since the beginning of restrictions, the emissions related to the aviation sector were below 75% of the business as usual levels (Fig. S13) because of the dramatic decrease in commercial flight activities since March 2020.

3.5. Shipping

Fig. S14 shows the emission reduction factors for the shipping sector. Our data show larger emission reductions than those of the Guevara database, but again differences are quite small (maximum difference is 5% in the first week of May), which allows us to assume that our calculations are valid for the whole of 2020. Here, the differences between both datasets are of 2.05%.

Fig. S15 shows that there were no substantial differences between the different pollutants emitted by shipping, which indicates that all vessel types followed the same drop and recovery in their activities as each type vessel type has a particular contribution from each pollutant to total emissions. The only significantly different behaviour between pollutants is found in the last week of the year, where NOx emissions increased with respect to the previous week due to an increase of roll on-roll off cargo ship and chemical tanker traffic (EMSA, 2021).

3.6. Other stationary combustion activities

Fig. 7 shows the NO_X emission reduction factors for other stationary combustion activities across Europe. As for the road traffic data, we can see the first and the beginning of the second wave of the COVID-19 pandemic in the emission reduction factors, for most countries, particularly in France and Italy, where NO_X emissions dropped in November 2020 and again at the end of December 2020, corresponding to rises in the stringency index (Fig. 1). Less evident is the emissions variation at the end of 2020 in countries with much more steady stringency index such as Spain, where NO_X emissions corresponding to GNFR_C activities does barely drop in November and drop significantly less than for the countries with higher stringency index in the last week of December 2020 (Fig. 10).

Although for NO_X we see emission reductions due to the predominance of commercial/institutional sector -which reduced their activities- with respect to the residential sector -which increased their activities-, the picture is quite different for pollutants such as non-methane volatile

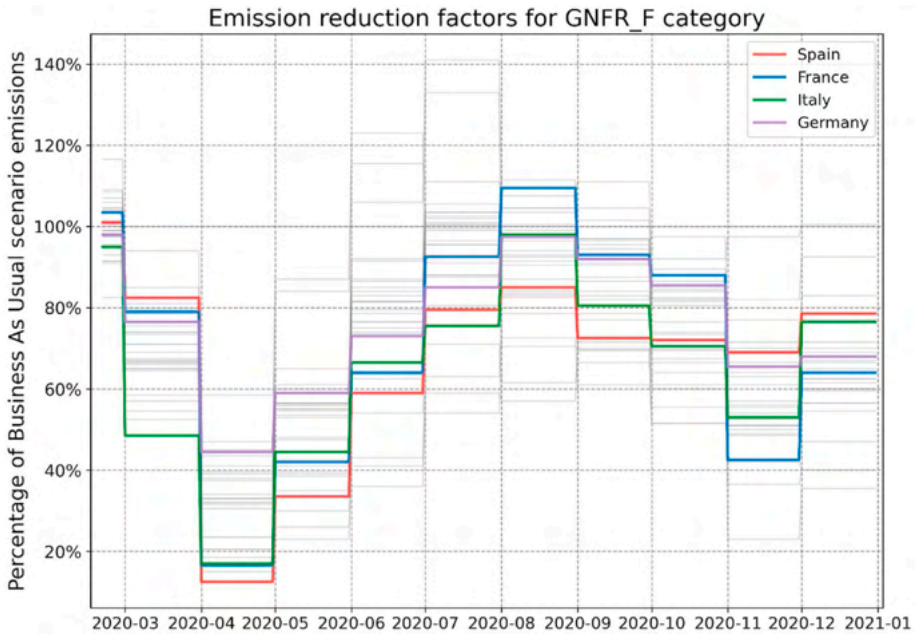

Fig. 5. Emission reduction factors calculated *for road transport during 2020 for all countries (grey) and some selected countries (colours): France, Germany, Italy and Spain.*

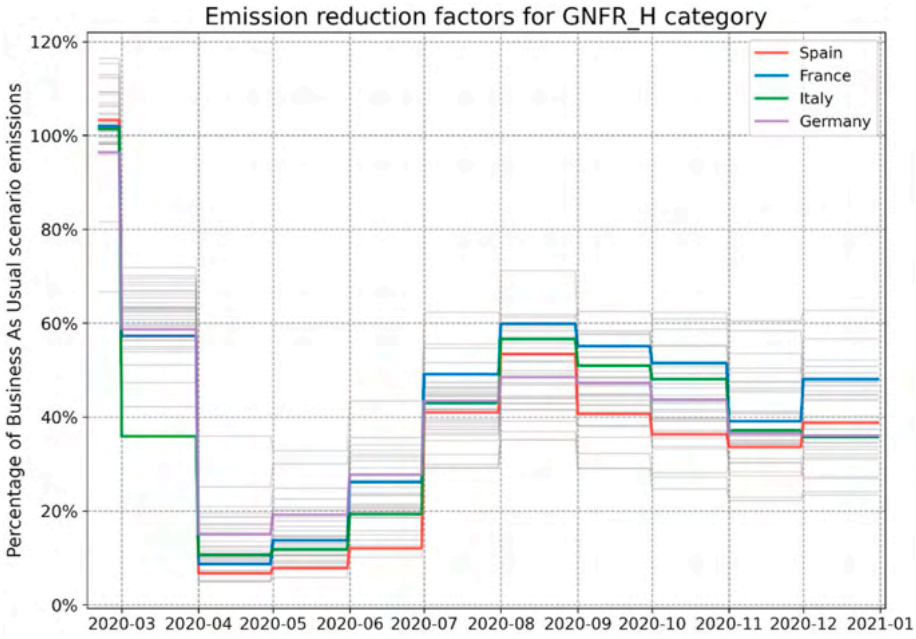

Fig. 6. Monthly emission reduction factors calculated for aviation during 2020 for all countries (grey) and some selected countries (colours): France, Germany, Italy and Spain.

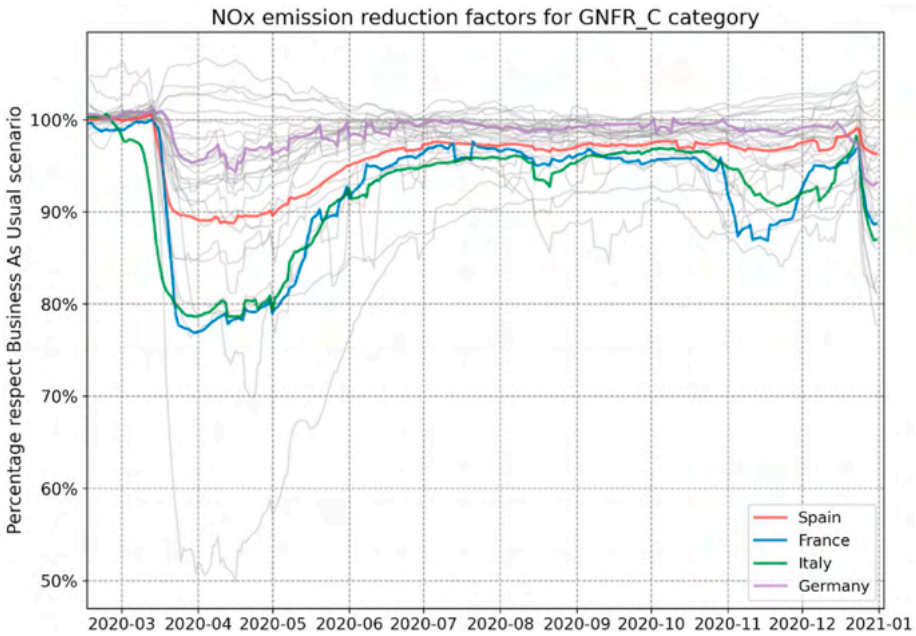

Fig. 7. Emission reduction factors for NO_X calculated for the GNFR-C category during the period February 21, 2020 to December 31, 2020 for selected countries. Some selected countries are highlighted in colours: France, Germany, Italy and Spain.

organic compounds (NMVOC). Fig. 8 shows the emission reduction factors related to commercial/institutional and residential sectors for NMVOC. There is a clear increase of emissions due to the period with more severe restrictions in most countries. This increase is clearly dominated by the contribution of the residential sector. Italy is the main exception to this rule, indicating that the institutional/commercial sector was more affected by restrictive measures than in other countries. This is confirmed in Figs. S16 and S17, which show the different direction of emission variations for NMVOC for the residential sector (more NMVOC emissions than usual due to increased activity) and the commercial/institutional sector (less emissions due to reduced activity).

Fig. S18 to Fig. S22 show the emission reduction factors for GNFR_C category obtained for each pollutant, as well as a comparison between the two databases for Spain. For NO_X, we calculate a slightly larger reduction than that in the Guevara database of about 2%, on average. The trend is the same between the two databases. For PM_{10} and CO, similar but slightly higher values were obtained than those using the more complex methodology of Guevara et al., (2020a). The values for $PM_{2.5}$ are very similar to those of the PM_{10} (not shown). For NH_3 our estimated emission reduction factors are slightly higher than the Guevara database for the period when both databases coincide. Nonetheless, the trend is the same and the data appear to be quite representative of the evolution of emissions during year 2020. For SO_x we observe a higher reduction of emissions during the first wave of the pandemic, by

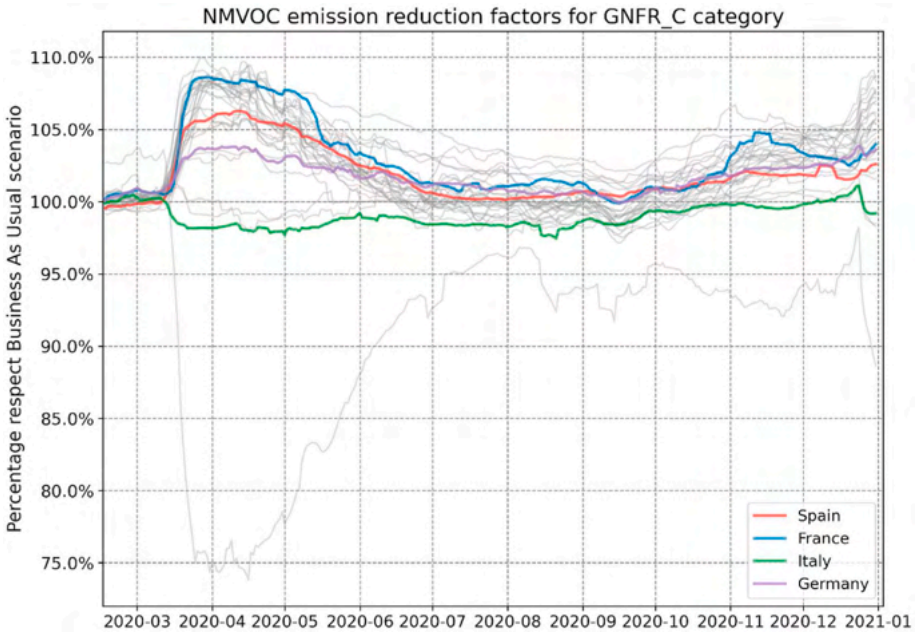

Fig. 8. Emission reduction factors for NMVOC calculated for other stationary combustion activities during the period January 1, 2020 to December 31, 2020 for selected countries. Some selected countries are highlighted in colours: France, Germany, Italy and Spain.

about 5% on average in Spain, with respect to the Guevara database. This difference reduces when the values return to near normal levels of activity but a slight overestimation of reductions is still apparent. In general, the sign of the small differences between both databases depends on the pollutant and the country. This is because differences in economic activities give rise to different contributions of commercial/institutional and residential activities to the GNFR_C category for each pollutant.

No days with emissions above 110% of business-as-usual values have been observed in any of the countries for any of the pollutants, while several countries have registered more than 100 days with emissions below 90% of BAU values for NH_3, NO_x and SO_x (Fig. 9). For NO_X, the case of United Kingdom is notable, with emissions for more than 140 days below the 90% threshold. This is associated with the more conservative policy of the United Kingdom regarding the lifting of restrictions until spring 2021. The United Kingdom was the first European country to introduce a second national lockdown in November 2020, reducing all activities – including commercial/institutional ones – to a minimum. Further information about the chronology of the United Kingdom lockdowns during 2020 can be found here: https://researchbriefings.files.parliament.uk/documents/CBP-9068/CBP-9068.pdf.

Also of note is the number of days with SO_x reductions in Portugal. However, in absolute values the reduction of SO_x emission from GNFR_C category is not relevant as most of the SO_x emissions of Portugal are

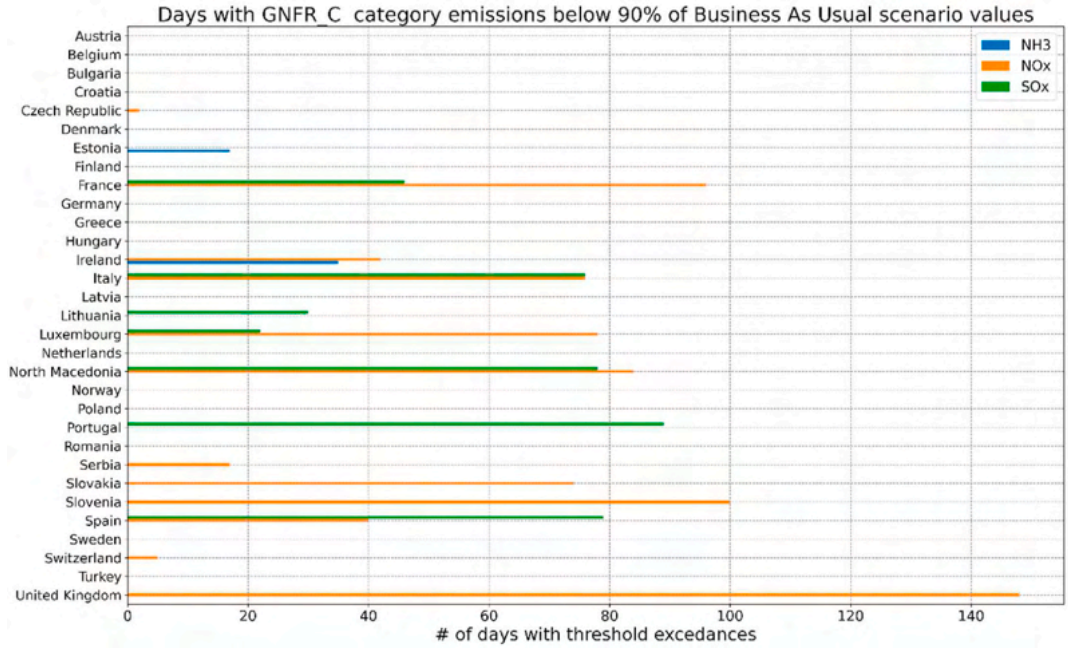

Fig. 9. Number of days with emissions from other stationary combustion activities below 90% of business-as-usual values for: CO (blue), NH_3 (orange), NMVOC (green), NO_x (red), PM_{10} (purple), $PM_{2.5}$ (brown) and SO_x (pink).

generated in the energy sector as illustrated in the national Informative Inventory Report (https://apambiente.pt/sites/default/files/_Clima/Inventarios/IIR2021.pdf).

Only emission reduction factors of NO_X, SO_X and NH_3 have days with significant emission reductions. For pollutants dominated by residential activities (i.e. NMVOC, PM_{10} and $PM_{2.5}$), no reductions were found.

3.7. Overall trends

Fig. 10 presents a summary of the emission changes for the period between February 21, 2020 and December 31, 2020 with respect to business-as-usual values for every country considered in the study and for all categories except GNFR_G, which has a single value representing all countries. For every country, aviation is the sector with the largest drop in emissions due to the mobility restrictions and drop in international tourism. This sector is followed by the road transport activities, which represent the second largest drop in emissions for all countries.

However, differing trends are observed for the industrial and public sectors. While for those sectors the mean reduction averaged over all countries was about 4% (Table 2), increases were found for both sectors in Denmark and Switzerland. From the available electricity consumption data from the Danish Government COVID-19 reference page (https://www.dst.dk/da/Statistik/covid-19-hurtige-indikatorer#erhverv), it can be seen that there were no significant changes between electricity consumption associated with manufacturing and public sector industries for Denmark during 2020 with respect to the previous year (Fig. S23). In fact, electricity consumption is greater after summer, which can explain an increase in emissions in this country. This agrees with the Stringency Index for Denmark, which has lower values for the second wave of COVID-19 than for the other European countries (Fig. 1), implying a lower reduction of emissions.

The GNFR_C category has the lowest emission variations for most of the countries (Table 2). Emissions in this category actually increased by 1%, on average, probably due to the increase from the residential sector more than compensating the emission reductions in the commercial/institutional sector as people spent more time in their homes in 2020 than on average.

Table 2
Time- and spatially-averaged emission reduction factors for each GNFR category.

Category	GNFR_A	GNFR_B	GNFR_C	GNFR_F	GNFR_G	GNFR_H
Variation with respect to BAU (%)	−4,07	−4,44	+1,14	−26,08	−15,81	−62,65

4. Conclusions

This paper presents a dataset of day-, sector- and country-dependent emission reduction factors that allow the quantification of the impact of the COVID-19 lockdown on European primary emissions. The reduction factors are provided for a period that covers the whole period with any restrictions during the year 2020, and for the six emission sectors that presumably contribute the most to emission reductions as a result of mobility restrictions, i.e. road transport, energy industry, manufacturing industry, aviation, shipping and other stationary combustion activities. Our emission reduction factors are based on a wide range of open-access information sources and near-real-time measured activity data, proxy indicators, and other available information. We have used a simple methodology that is easy to reproduce and does not require specific expertise nor substantial computational resources, but provides reasonable estimations of emission reduction factors.

The main findings and conclusions of this work are as follows:

- A simple methodology without the use of machine learning to weather-normalize the results is sufficient to estimate emission reduction factors with little deviations from more complex approaches. Moreover, we extend the estimates to the whole period of 2020 with any restrictions due to pandemic, which, to date, has not been done before.
- Emission reductions during the pandemic situation are clearly driven by national mobility restrictions.
- The largest emission reductions during the period 21 February to December 31, 2020 were in the aviation sector, with an emission reduction of 62.7%, on average, for the countries considered in this study.

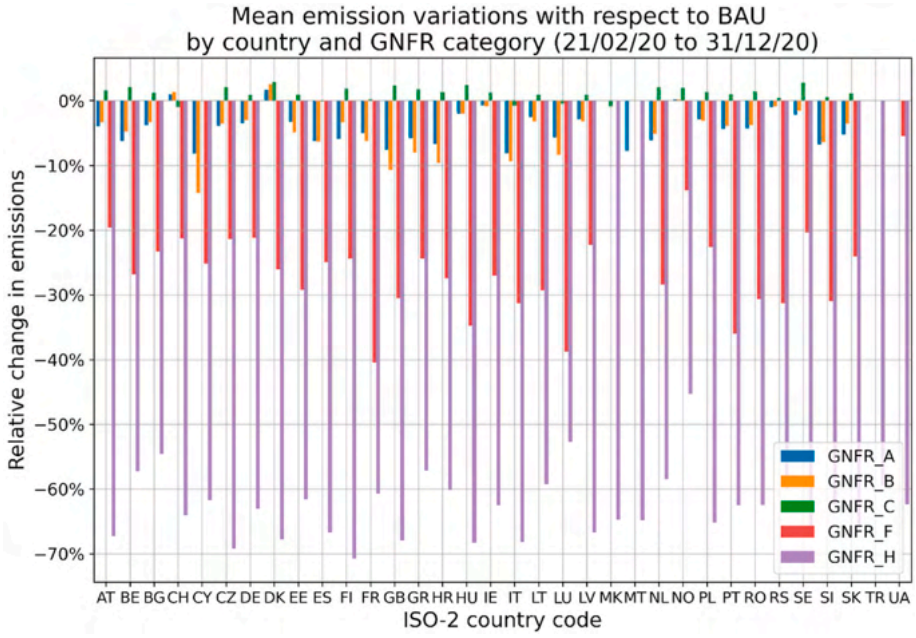

Fig. 10. Mean emission reduction factors for 2020 by sector category for all countries. Shipping (GNFR_G) is not included because there is a single value for all countries.

- Countries with the lightest restrictions were estimated to increase emissions in public and manufacturing industry sectors (i.e.: Denmark and Switzerland).
- Open-access data availability is key to the scientific community being able to regularly estimate emission variations due to changes in anthropogenic activities (e.g.: population increases in urban areas) and to elaborate pollution exposure mitigation strategies. Although great advances have been made recently, further effort is needed to extend open-access policies.

Data availability

The computed emission reduction factors per country, sector and day are provided in the Supplement Material.

Declaration of competing interest

The authors declare that they have no known competing financial interests or personal relationships that could have appeared to influence the work reported in this paper.

Acknowledgements

The authors acknowledge Marc Guevara for the provision of estimations of emission reductions for the period 21 February to July 31, 2020. We also acknowledge the Spanish Ministry for Ecological Transition and Demographic Challenge (METDC). This results are part of the I + D + i project Retos-AIRE, funded by the Spanish Ministry of Science and Innovation under the grant agreement AEI/10.13039/501100011033/.

Appendix A. Supplementary data

Supplementary data to this article can be found online at https://doi.org/10.1016/j.apr.2022.101388.

References

Botzen Wouter, W.J., Nees, T., Estrada, F., 2021. Temperature effects on electricity and gas consumption: empirical evicence from Mexico and projections under future climate conditions. Sustainability 305, 13. https://doi.org/10.3390/su13010305.

Burns, J., Hoffmann, S., Kurz, C., Laxy, M., Polus, S., Rehfuess, E., 2020. COVID-19 mitigation measures and nitrogen dioxide – a quasi-experimental study of air quality in Munich, Germany. Atmos. Environ. 246, 11808 https://doi.org/10.1016/j.atmosenv.2020.118089.

Confederation Suisse, 2021. Energy balances for Switzerland. Available at. https://www.eda.admin.ch/aboutswitzerland/en/home/wirtschaft/energie/energie-fakten-und-zahlen.html, 2021.

Copernicus Climate Change Service (C3S), 2021. ERA5: fifth generation of ECMWF atmospheric reanalyses of the global climate. Copernicus climate change service climate data store (CDS). https://cds.climate.copernicus.eu/cdsapp#!/home, 2017.

Coskun, H., Yildirim, N., Gündüz, S., 2021. The spread of COVID-19 virus through population density and wind in Turkey cities. Sci. Total Environ. 751, 141663. https://doi.org/10.1016/j.scitotenv.2020.141663.

De Cian, Enrica, Elisa, Lanzi, Roberto, Roson, 2007. The impact of temperature change on energy demand: a dynamic panel analysis," working papers. Fond. Eni Enrico Mattei 46.

EMEP/CEIP, 2021. Officially reported emission data. Available at. https://www.ceip.at/webdab-emission-database/reported-emissiondata, 2020.

EMSA, 2021. COVID-19 – impact on shipping. Available at. http://www.emsa.europa.eu/psc-main/new-inspection-regime/392-covid19-shipping.html, 2020.

ENTSO-E, 2021. Transparency platform. Available at. https://transparency.entsoe.eu/, 2020.

EUROCONTROL, 2021a. CO2 emissions by state. Oper. Airports 2020. https://asperformance.eu/data/.

EUROCONTROL, 2021b. Daily traffic variation - States. Available at. https://www.eurocontrol.int/Economics/DailyTrafficVariation-States.html?ectl-covid=, 2021.

Eurostat, 2021. Energy balances. Available at. https://ec.europa.eu/eurostat/web/energy/data/energy-balances, 2020.

Fioletov, V., McLinden, C.A., Griffin, D., Krotkov, N., Liu, F., Eskes, H., 2021. Quantifying urban, industrial, and background changes in NO2 during the COVID-19 lockdown period based on TROPOMI satellite observations. https://acp.copernicus.org/preprints/acp-2021-536/.

Google, L.L.C., 2021. Google COVID-19 community mobility reports. Available at. https://www.google.com/covid19/mobility/, 2020.

Guevara, et al., 2020a. Time-resolved emission reduction for atmospheric chemistry modelling in Europe during COVID-19 lockdowns. Atmos. Chem. Phys. 21, 773–797. https://doi.org/10.5194/acp-21-773-2021.

Guevara, et al., 2020b. D3: Report on Short-Term Emission Reduction Factors. ECMWF Copernicus Report CAMS/COP_066.

Hale, T., Angrist, N., Goldszmidt, R., Kira, B., Petherick, A., Phillips, T., Webster, S., Cameron-Black, E., Hallas, L., Majumdar, S., Tatlow, H., 2021. A global panel database of pandemic policies (Oxford COVID-19 Government Response Tracker). Nat. Hum. Behav. 5, 529–538. https://doi.org/10.1038/s41562-021-01079-8, 2021.

Jalkanen, J.P., Johansson, L., Kukkonen, J., 2016. A comprehensive inventory of ship traffic exhaust emissions in the European sea areas in 2011. Atmos. Chem. Phys. 16, 71–84. https://doi.org/10.5194/acp-16-71-2016.

Le Quéré, C., Jackson, R.B., Jones, M.W., Smith, A.J.P., Abernethy, S., Andrew, R.M., De-Gol, A.J., Willis, D.R., Shan, Y., Canadell, J.G., Friedlingstein, P., Creutzig, F., Peters, G.P., 2020. Temporary reduction in daily global CO2 emissions during the COVID-19 forced confinement. Nat. Clim. Change. https://doi.org/10.1038/s41558-020-0797-x.

Madrid Municipality Open Data portal, 2021. Available at. https://datos.madrid.es/portal/site/egob/menuitem.c05c1f754a33a9fbe4b2e4b284f1a5a0/?vgnextoid=33cb30c367e78410VgnVCM1000000b205a0aRCRD&vgnextchannel=374512b9ace9f310VgnVCM100000171f5a0aRCRD&vgnextfmt=default, 2021.

Putaud, J.-P., Pozzoli, L., Pisoni, E., Martins Dos Santos, S., Lagler, F., Lanzani, G., Dal Santo, U., Colette, A., 2021. Impacts of the COVID-19 lockdown on air pollution at regional and urban background sites in northern Italy. Atmos. Chem. Phys. 21, 7597–7609. https://doi.org/10.5194/acp-21-7597-2021.

Rte, 2020. Réseau de transport d'électricité: L'impact de la crise sanitaire (COVID-19) sur le fonctionnement du système électrique, available at. https://www.concerte.fr/system/files/concertation/ImpactsdelacrisesanitaireCOVID-19surlesyst%C3%A8me%C3%A9lectrique.pdf.

Sun, K., Li, L., Jagini, S., Li, D., 2021. A satellite-data-driven framework to rapidly quantify air-basin-scale NOx emissions and its application to the Po Valley during the COVID-19 pandemic. Atmos. Chem. Phys. 21, 13311–13332. https://doi.org/10.5194/acp-21-13311-2021.

Tado, 2020. Percent increase in home heating consumption. Available at. https://www.current-news.co.uk/news/lockdown-causes-british-households-heating-use-to-soar, 2020.

TII, 2021. Transport Infrastructure Ireland, p. 2021. https://data.tii.ie/.

TomTom, N.V., 2021. TomTom traffic index. Available at. https://www.tomtom.com/en_gb/traffic-index/, 2020.

Wong, D.W.S., Li, Y., 2020. Spreading of COVID-19: density matters. PLoS One 15 (12), e0242398. https://doi.org/10.1371/journal.pone.0242398.

Zheng, B., Zhang, Q., Geng, G., Chen, C., Shi, Q., Cui, M., Lei, Y., He, K., 2021. Changes in China's anthropogenic emissions and air quality during the COVID-19 pandemic in 2020. Earth System Science Data 13 (6), 2895–2907. https://doi.org/10.5194/essd-13-2895-2021. In press.

Appendix D

How do meteorological conditions impact the effectiveness of various traffic measures on NOx concentrations in a real hot-spot?

Science of the Total Environment 954 (2024) 176667

Contents lists available at ScienceDirect

Science of the Total Environment

journal homepage: www.elsevier.com/locate/scitotenv

How do meteorological conditions impact the effectiveness of various traffic measures on NO_X concentrations in a real hot-spot?

A. Rodríguez-Sánchez [a,*], J.L. Santiago [a], M.G. Vivanco [a], B. Sanchez [a], E. Rivas [a,b], A. Martilli [a], F. Martín [a]

[a] Environmental Department, CIEMAT, Avenida Complutense 40, 28040 Madrid, Spain
[b] Vicerrectorado de Investigación, Innovación y Doctorado, Universidad Politécnica de Madrid (UPM), Ramiro de Maeztu 7, 28040 Madrid, Spain

HIGHLIGHTS

- High-resolution NO_X maps in a hot-spot are estimated by a multimodel methodology.
- Modelled NO_X concentrations for every scenario are consistent with observations.
- The largest emissions did not lead to the highest concentrations due to meteorology.
- The Low Emissions Zone has little positive effect for the actual access restrictions.
- For the same emissions, meteorology affects mean concentrations up to a factor 2.

GRAPHICAL ABSTRACT

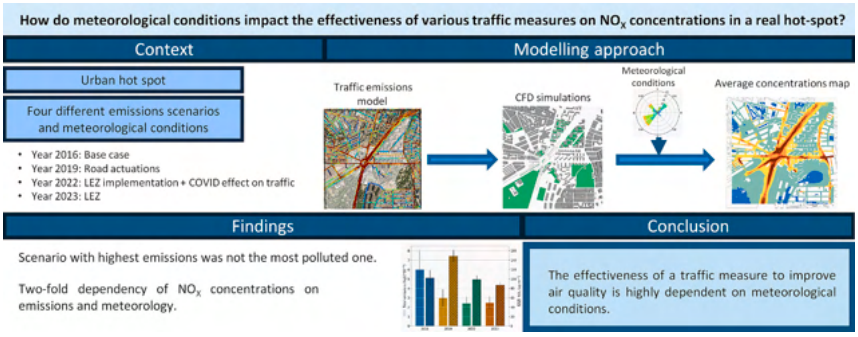

ARTICLE INFO

Editor: Anastasia Paschalidou

Keywords:
Urban air quality
Mitigation strategies
NO_X
Computational fluids dynamics model
Microscopic traffic modelling

ABSTRACT

Recently, air quality has become a major concern for policy makers around the world, which has led to the implementation of mitigation measures. In particular, in urban areas most measures affect the road transport sector, as this is one of the main contributors to air pollution in those areas. Recent studies have pointed out the need to determine the importance of external factors such as the meteorological conditions on the net effect on air quality of mitigation strategies. Due to the strong spatial variability of urban air pollution, high spatial resolution modelling is necessary. In this work, the impacts on emissions and nitrogen oxides (NO_x) concentrations of several mitigation strategies on a real air pollution hot spot in southern Madrid (Spain) are simulated at microscale under different meteorological conditions. The results show that the meteorological conditions affect local NO_x concentrations, and its net changes can be comparable to those due to emission reductions. In particular, meteorological conditions in 2019 induced higher NO_x concentrations than in 2016, despite the local emissions were reduced by 50 % from 2016 to 2019. On the other hand, the impact of the implementation of a Low Emissions Zone (LEZ) on NO_x concentrations is small and consistent with values found in other LEZs around Europe. However, this impact varies up to 70 % depending on the meteorological conditions. The impacts of a mitigation strategy are largely influenced by the meteorological conditions, and therefore the achievement of the target reduction of concentrations pursued by these measures will depend on the meteorological conditions.

* Corresponding author.
E-mail address: alejandro.rodriguez@ciemat.es (A. Rodríguez-Sánchez).

https://doi.org/10.1016/j.scitotenv.2024.176667
Received 4 July 2024; Received in revised form 19 September 2024; Accepted 30 September 2024
Available online 8 October 2024

1. Introduction

Despite the fact that emissions and concentration of air pollutants have fallen over the last few years, air pollution remains the largest environmental health risk in Europe (EEA, 2023) and so, air quality management is nowadays an important ongoing challenge. High pollution levels have been often observed in urban areas, where both emissions and population concentrate. Particularly, citizens living in large metropolitan areas are exposed to elevated concentrations of nitrogen dioxide (NO_2) mainly because of traffic emissions (EEA, 2021). Road transport is responsible of most nitrogen oxides (NO_x) emissions in Europe, and also accounts for an important part of the particulate matter (PM) emissions in that region (EEA, 2022; Thunis et al., 2023).

Meteorological conditions are one of the main factors that affect air quality, as they affect how pollutants are transported by or removed from the atmosphere. Precipitation can help dissipating heavier pollutants, whereas wind can disperse lighter ones (Kassomenos et al., 1998, 2014). Other parameters such as solar radiation and temperature can favour the removal or creation of pollutants by triggering chemical transformations of pollutants (Latini et al., 2002). Furthermore, in a city, interactions between the atmosphere and the urban obstacles (buildings, vegetation, etc.) induce complex flow patterns. Inside the urban canopy, the wind flow can be channelled and slowed down by urban obstacles depending on the wind speed and direction, which affects the distribution of air pollutants inside the streets (Dejoan et al., 2010; Parra et al., 2010; Santiago et al., 2013). This fact, joined to the irregular spatial distribution of anthropogenic emissions, produces high levels of pollution and strong gradients of pollutant concentrations in streets. Therefore, pollutant concentrations in the streets are affected by both the emissions and the meteorological conditions. Hence, accurate estimates of anthropogenic pollutant emissions to the atmosphere and high-resolution modelling of the wind flow properties (wind speed and direction) and of the dispersion of pollutants through the urban atmosphere is key to estimate the population's exposure to high air pollution levels (Santiago et al., 2021).

To improve the air quality, air pollution mitigation strategies are being developed and implemented around the world, especially in urban areas. Examples of these measures include the promotion of public transportation usage, ring road utilization, traffic flow improvements, speed limit reduction, and the low emission zones (LEZ). LEZs are areas where access for road vehicles is restricted, usually based on their emission classes. In Europe, there are >200 LEZs in operation (Holman et al., 2015). As in urban areas traffic is one important source of PM and the major source of NO_2 (Belis et al., 2013; Degraeuwe et al., 2017; Coelho et al., 2022), the implementation of LEZ could be an effective measure to reduce traffic related pollution and to improve urban air quality. Nonetheless, some studies question the efficiency of already existing LEZ in Europe because most of them do not apply to most vehicles (Holman et al., 2015) or their size is not big enough to dissuade people from using private transport (Moral-Carcedo, 2022).

However, despite their wide implementation, estimating the impact of mitigation measures remains a major challenge. Multiple studies have been carried out to assess the effects after the LEZ implementation using monitoring data and comparing the air quality before and after LEZ implementation (Boogaard et al., 2012; Panteliadis et al., 2014; Ellison et al., 2013). However, a simple comparison of concentrations neglects several factors other than LEZs that affect the concentrations of air pollutants such as the meteorology. This is considered by some studies (Gu et al., 2022; Ma et al., 2021), but an estimation of the effects of external factors as meteorology with high-spatial resolution at street level is still needed due to the heterogeneity of air pollutant concentrations in urban areas, which affects the spatial representativeness of air quality monitoring stations (Martin et al., 2015; Santiago et al., 2013). For that reason, the research questions to answer are: How can we properly evaluate the impacts of mitigation strategies? To what point are local mitigation measures effective to reduce air pollution at a local scale?

The aim of this work is to compare the impact of several air pollution mitigation strategies on a real hot-spot and explore the potential effect of meteorological conditions on their impact. Those strategies are the modification of the geometry of one main street in 2017 and the implementation of a LEZ in 2022. Their impacts are studied for a winter month, when air pollution problems are more likely to arise in Spain. To this end, a sophisticated methodology is developed to compute high-resolution NO_x maps for each scenario considered. The methodology consists of several steps: Firstly, high-resolution traffic-related NO_x emissions are computed for several scenarios (each study case corresponding to one mitigation strategy) using an emissions model coupled to a microscopic, time-discrete traffic simulator. Then, the NO_x dispersion over time is computed through Computational Fluid Dynamic (CFD) simulations. A numerical methodology based on the combination of a set of steady state CFD-RANS (Reynolds Averaged Navier-Stokes) simulations corresponding to the 16 wind rose sectors considering the actual wind conditions and the weekly traffic pattern emissions. Finally, the time series of NO_x concentrations are computed choosing at each simulated hour the CFD simulation corresponding to the wind direction in the research area given by a mesoscale meteorological model at that hour.

This procedure is done for 4 different periods, corresponding to February 2016, February 2019, February 2022 and February 2023. The whole methodology is explained in Section 2 and the choice of the aforementioned periods is explained in Subsection 2.2. The results are showed in Section 3, followed by a discussion of the limitations of this methodology in Section 4. A discussion of the results and the conclusions are presented in Section 5. The evaluation of each one of the components of the employed methodology is presented within the supplementary material.

2. Methodology description

To estimate the impact of each mitigation strategy on NO_x concentrations; high-resolution NO_x maps have been computed for winter conditions. This consists of two main steps for each study case: the computation of traffic-related NO_x emissions; and the dispersion through the modelling domain, which depends on the meteorological conditions. Sixteen hourly aggregated traffic emissions scenarios that represent the weekly traffic pattern are obtained using a microscopic traffic model for each simulated period. The resulting emissions are used as input data to a set of precomputed CFD simulations (one for each 16 wind directions), obtaining concentration maps for each wind direction and for each emission scenario. Then, a numerical methodology is applied to obtain the resulting time series of NO_x concentrations and the monthly-averaged concentration maps depending on the meteorological conditions. To this end, it is assumed that: under neutral or near-neutral conditions the air pollutant concentrations are inversely proportional to the wind speed; that NO_x acts as a non-reactive pollutant; and that thermal effects and the change of the wind flow patterns due to the thermal effects are neglected. The assumption of that thermal effects are neglected in this work comes from the fact that they are negligible in comparison with dynamical effects (without thermal effects) in winter conditions. The strong mean shear imposed by the presence of buildings in urban areas at microscale, makes that the atmosphere is often close to neutral stability, in particular in winter when the solar forcing is not very intense. It has been proved that this assumption works well under specific circumstances, such as those recently mentioned (Santiago et al., 2022; Rivas et al., 2019; Sanchez et al., 2017). The meteorological conditions for each case study are obtained from a mesoscale meteorological model. Finally, background concentrations from an urban background air quality monitoring station are added to the concentrations obtained with the numerical methodology (Parra et al., 2010; Sanchez et al., 2017; Santiago et al., 2013).

Below, a description of the area in which this work is focused

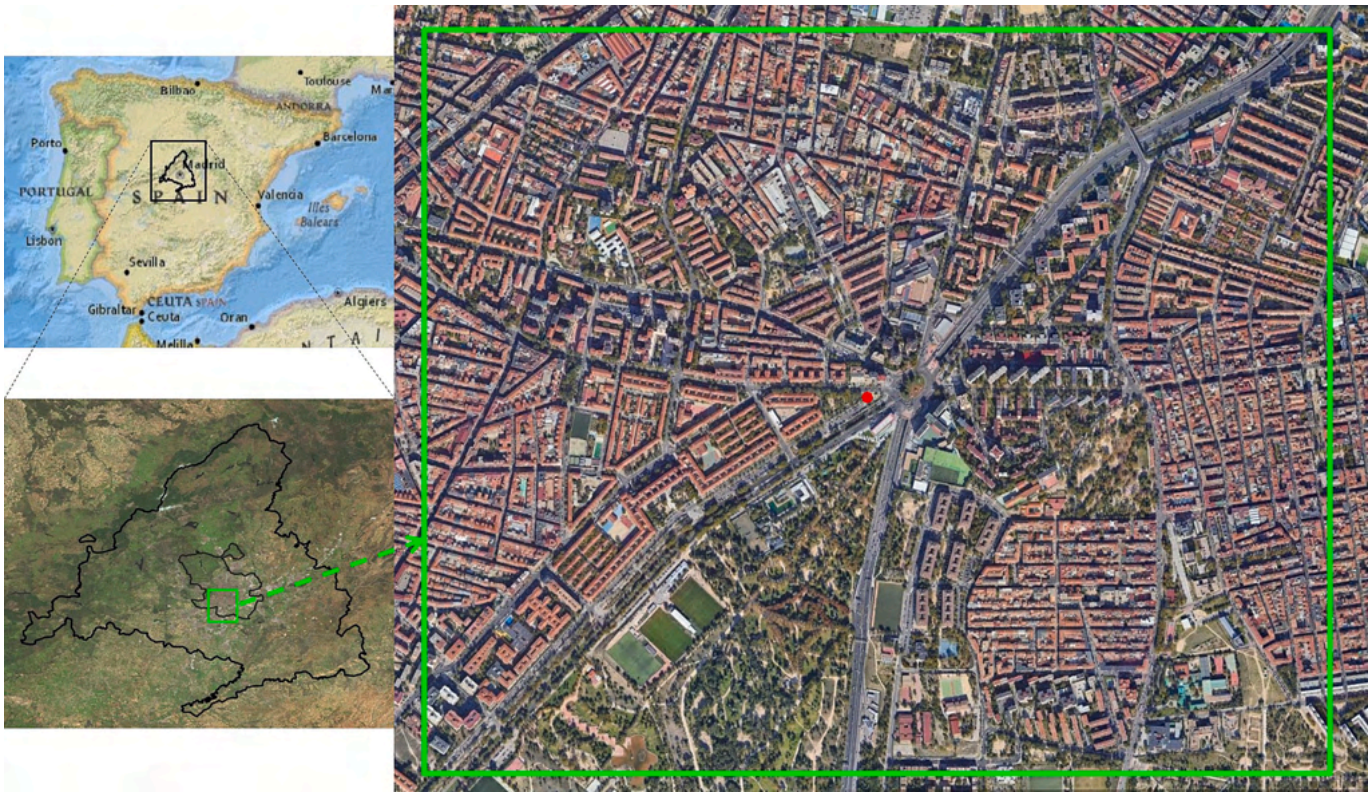

Fig. 1. Location of the research area of Plaza Elíptica at the south of Madrid. Location of Plaza Elíptica AQMS marked in red.

(Section 2.1) and a description of the studied scenarios (Section 2.2) are provided. Then, a detailed explanation of how the traffic-related emissions are obtained using a microscopic traffic simulation model (Section 2.3) is given. The dispersion of the emissions through the modelling domain is computed using CFD simulations, which description is shown in Section 2.4. In Section 2.5, the setup of the mesoscale meteorological model used in the numerical methodology is explained, followed by a description of the applied numerical methodology in Section 2.6.

2.1. Domain of study

The study is focused on Plaza Elíptica square, a heavily trafficked roundabout with a freeway crossing it through a tunnel at the south of Madrid city (Fig. 1). Even this is not a typical urban area, as it is widely open, this location is a highly polluted microenvironment, with a complex geometry and a heavy presence of pedestrians that makes this location a representative traffic hot-spot where urban air quality issues commonly occur. In fact, the air quality monitoring station (AQMS) located inside this area has exceeded the annual mean NO_2 concentration EU limit value (40 μg m^{-3}) for at least 15 consecutive years, being 2022 the first year below this limit since measures started in 2007.

2.2. Cases of study

In this work, four time periods are simulated corresponding to four different traffic-related situations around the study domain (2016, 2019, 2022 and 2023). For all of them, the month of February is selected to analyse due to it being a month with typically high air pollution levels in Madrid and it is a winter month with no bank holidays, meaning that a representative traffic weekly pattern can be found easier. The study periods are then as follows:

- February 2016: The traffic flows and the road network existent by this date are considered as the "base" case.
- February 2019: This case corresponds to the first mitigation strategy applied by the Madrid City Council to reduce air pollution in some streets near Plaza Elíptica. Within this strategy, the number of lanes of one main street inside the domain (Street 1 in Fig. 5) was reduced from 3 to 1 and its direction was reversed. Also, a bikelane was added replacing the rightmost lane.
- February 2022: Since December 2021 a LEZ was implemented affecting the area surrounding Plaza Elíptica roundabout. In addition, in early 2022 some mobility restrictions (pandemic-related) were still prevailing. This LEZ restricts access to gasoline vehicles previous to EURO 2 emission standard and diesel vehicles previous to EURO 3.
- February 2023: In this case, the only difference was the full recovery of road mobility after the pandemic.

Table 1
Nomenclature for the scenarios resulting from the combination of every emission configuration and every meteorological and background conditions.

	Met16Backg16	Met19Backg19	Met22Backg22	Met23Backg23
Em16	2016_Em16	2019_Em16	2022_Em16	2023_Em16
Em19	2016_Em19	2019_Em19	2022_Em19	2023_Em19
Em22	2016_Em22	2019_Em22	2022_Em22	2023_Em22
Em23	2016_Em23	2019_Em23	2022_Em23	2023_Em23

To assess the effect of these mitigation strategies and meteorology on NO_x, concentrations due to each local mitigation strategy are estimated for every year. To simplify the understanding of the workflow to the reader, Table 1 presents a summary of all the possible combined scenarios resulting from combining the emissions and the meteorological and background concentration conditions of each study period.

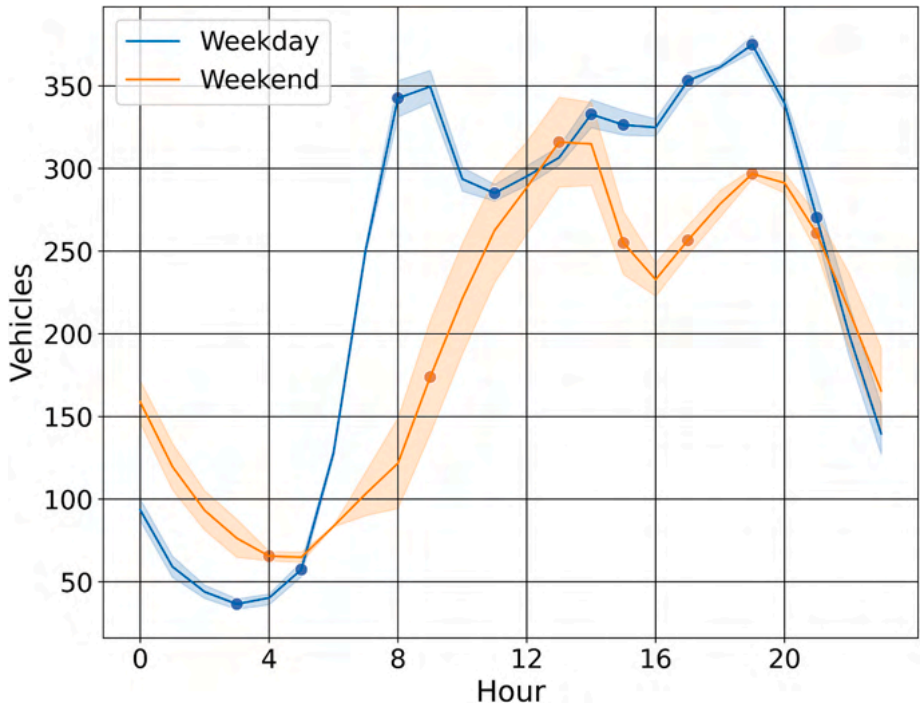

Fig. 2. Average measured traffic in Plaza Elíptica during February 2022 grouped by daytype (lines). Points represent the selected hourly traffic scenarios. Shaded area represents the standard deviation of measured traffic.

2.3. Computing traffic-related emissions

Traffic-related emissions are obtained by coupling an emission model to a microscopic traffic simulation model. The traffic simulation model used is SUMO (SUMO are the initials for Simulation of Urban Mobility), an open-source microscopic space-continuous and time-discrete traffic simulation model that allows intermodal simulation, including different motorized vehicle types, bicycles and pedestrians (Alvarez Lopez et al., 2018).

SUMO allows the creation of traffic flows from different types of input data. In this work we use traffic detector data to this end, using 80 % of the detectors for simulation purposes and the remaining 20 % for validation of simulations (check supplementary material for model evaluation). The road network is imported from OpenStreetMap (OSM) and inconsistencies with the real road network were manually corrected. In this case, we had no information about the traffic lights cycles. For this reason, we set most of the traffic lights in SUMO as type "actuated". This option allows smooth traffic flows by prolonging traffic phases whenever a continuous stream of traffic is detected. It switches to the next phase after detecting a sufficient time gap between successive vehicles. For the Plaza Elíptica square, the author collected in-situ data at several times and this information was used to manually adjust the traffic lights in the simulations to obtain realistic traffic flows towards the roundabout.

SUMO allows instantaneous emissions computation by coupling an emission model to the traffic simulation model. Among the available emission models in SUMO, the simplified version of the PHEM (Passenger Car and Heavy-duty Emission Model) model, PHEMlight v5 model, was chosen for this work due to two reasons: its more detailed vehicle fleet and for considering external factors as the road slope. SUMO includes its own classification of vehicle types. Each vehicle type is defined by the vehicle's physical parameters (i.e. length, colour or maximum velocity) and also by the car-following model's parameters (i.e. driver-related parameters). However, the emission model defines the emission parameters for each SUMO vehicle type. This means that vehicles are grouped into different categories according to their fuel type, vehicle dimensions and weight, and vehicle age and engine capacity. The composition of vehicles fleet is collected from vehicle registration data sets in Madrid (Madrid City Council, 2024).

In order to save computational resources, the same approach as in Quaassdorff et al. (2016) is applied, selecting some representative traffic scenarios to estimate the traffic evolution across a whole week, instead of simulating the complete period for each case of study. Sixteen 1-h length traffic scenarios representative of different traffic flow conditions are defined to complete the weekly traffic pattern. Fig. 2 shows the traffic cycle used for Em2022 scenarios. Each scenario has been performed using the traffic count data for the corresponding period, therefore each scenario has its own weekly cycle. However, the traffic weekly cycle does not change significantly between emission scenarios ($R \geq 0.995$ between all simulated scenarios), with the rush hours occurring at the same hours for all simulations. The traffic simulations were performed using as input data traffic count detectors from the network of traffic count detectors deployed by Madrid City Council. The time step selected for the simulations was 0.1 s. This choice was made in order to maximize the continuity of the emissions fields, as larger time steps lead to more travelled distance of a vehicle between time steps and, therefore, to larger distance between two emissions.

To estimate the uncertainty in emissions due to the limited available data to perform traffic simulations, for each period we have performed 10 simulations using the same input data but different seed, and then computed the mean emissions and the standard deviation of the dataset for each cell in the study area. That means that each of those 10 simulations corresponding to one study case has exactly the same traffic count detectors as input data, but 10 different set of routes assigned to each vehicle at the beginning of the simulations (i.e. 10 different initial conditions).

The uncertainty in the simulated traffic flow can arise from different issues. One important source of uncertainty is the lack of data regarding the traffic lights cycles. One traffic light cycle for weekdays and another for weekend days are assumed, but these cycles can fluctuate during the same day according to the traffic intensity upstream the traffic light. Another important source of uncertainty is the punctual nature of the traffic count detectors network. Since most streets lack traffic count detectors, several solutions are possible to create vehicle routes sets that

meet the spatial-temporal distribution of vehicles across the domain. This is why we have performed several simulations for each scenario to consider multiple solutions to this traffic-assignment problem. The validation of simulated traffic with measures shows high correlation values for all periods ($R \geq 0.98$), and low values for normalised mean squared error (NMSE) and fractional bias (FB). More details can be found in the supplementary material.

SUMO allows to compute emissions for each individual vehicle at every time step. This emission data is aggregated in time extracting 16 hourly-aggregated emission data for each vehicle and scenario (corresponding to the 16 emission scenarios that complete the weekly traffic pattern). Also, for each simulation, we aggregate the emission data in space, using 5 m × 5 m cells. Then both the mean emissions across the 10 simulations in each cell for each scenario and the standard deviation are computed. These gridded mean emissions (and their standard deviation) are then passed as input data to the CFD model.

2.4. Dispersion of traffic-related emissions

Once the traffic-related emissions are estimated, NO_x dispersion is simulated throughout the Plaza Elíptica domain using a Computational Fluids Dynamic (CFD) model. In this study, the CFD modelling approach consists of steady-state simulations based on the Reynolds-averaged Navier-Stokes (RANS) equations with the realizable k-ε turbulence closure scheme. The software used was the STARCCM+ from SIEMENS.

The CFD domain has been constructed considering recommendations of best practice guidelines (Franke et al., 2007; Di Sabatino et al., 2011). The domain size is approximately of 1300 m × 1300 m × 270 m, and features resolved include buildings, the tunnel traversing Plaza Elíptica square and vegetation. A mesh independency test has been performed using fine and coarse meshes, and the results concluded a clear mesh independence (Sanchez et al., 2017). The vegetation is included in green areas present inside the domain. It is considered as a porous medium and its dynamical effects are considered by introducing a momentum sink term and sink/source terms of turbulent kinetic energy (k) and its dissipation (ε) to the momentum, k and ε equations inside this region (Di Sabatino et al., 2011; Santiago et al., 2013). A leaf area density of 0.5 m^{-1} is considered for the trees. Inlet profiles of velocity, turbulent kinetic energy and dissipation of turbulent kinetic energy are imposed considering neutral inlet profiles, usually employed in CFD modelling (Rivas et al., 2019):

$$u(z) = \frac{u_*}{\kappa} ln\left(\frac{z + z_0}{z_0}\right) \tag{1}$$

$$\kappa = \frac{u_*^2}{\sqrt{C_\mu}} \tag{2}$$

$$\varepsilon = \frac{u_*^3}{\kappa(z + z_0)} \tag{3}$$

where u_* is the friction velocity, z_0 is the roughness length, C_μ is a model constant (=0.09) and κ is von Karman's constant (0.4). The roughness length of the ground is fixed as $z_0 = 0.03$ taking into account the first cell height close to ground, the relationship between equivalent sand-grain roughness height and aerodynamic roughness length, and the wall law limitation (Richards and Hoxey, 1993).

The NO_x emissions are obtained as explained in Section 2.2 and distributed into the traffic regions with resolution of <1 m. NO_x, as the sum of NO and NO_2, is considered non-reactive and it is modelled by means of a transport equation. Turbulence induced by the traffic is not considered in this work and for that, the diffusion of pollutants close to the source is underestimated. As it was used in (Sanchez et al., 2017), a low value of Schmidt number ($Sc = 0.3$) is selected, which implies a greater turbulent diffusion and is in the range of the optimum values of Sc (from 0.2 to 1.3) according to the various flow properties and geometries (Tominaga and Stathopoulos, 2007).

2.5. Mesoscale meteorological simulations

The meteorological parameters used in the methodology described in the next section have been derived from mesoscale simulations performed with the meteorological mesoscale model WRF (Weather Research and Forecasting) (Chen et al., 2011). This model has been run for four different years (2016, 2019, 2022 and 2023). For each one, the simulation starts at 0000 UTC of the January 21st and ends at midnight of the March 1st of the same year. The domain configuration consists of four nested domains, with horizontal resolutions of 27, 9, 3 and 1 km, with the finest domain encompassing a region with dimensions of 112 km (E-W) and 124 km (N-S), that includes the whole urban area of Madrid and surrounding satellite cities. The first domain was fed with input boundary data from ERA5 (Hersbach et al., 2020). The vertical resolution is 5 m in the lowest 50 m of the atmosphere. Above, the grid spacing gradually increases up to the top of the domain, located at 20 km. The higher resolution in the lowest 50 m is chosen to resolve the strong vertical gradients of mean variables and turbulent fluxes that are present in the Urban Roughness Sublayer and to take maximum advantage of the multilayer urban scheme used to represent the urban areas (BEP-BEM, Martilli et al., 2002; Salamanca et al., 2010). This scheme solves a separate energy budget for roof, walls and street, and computes the generation of heat in the buildings due to equipment, occupants and cooling/heating systems, and its exchange with the exterior. Detailed configurations can be found in Sanchez et al. (2017).

2.6. Numerical methodology

In this work, the NO_X (as $NO+NO_2$) is considered a non-reactive pollutant and its behaviour similar to a tracer because of the fast interconversion rate between NO and NO_2 (Sanchez et al., 2016, 2017). This assumption has been successfully considered at microscale in several studies (e.g., Sanchez et al., 2016, 2017; Jeanjean et al., 2017).

To estimate the NO_x concentration (hereafter referred to as $[NO_x]$) over time, it is necessary to carry out the following steps. Firstly, the 16 hourly emission scenarios for each year are simulated for each wind direction using the CFD model. Thereafter, the selection of the wind direction sector at every hour is derived from the outputs of mesoscale simulations in the grid cell corresponding to the microscale domain. Likewise, the corresponding emission scenario is selected for that hour following the traffic flow pattern previously described.

$$C_{sim}(t) = C_{sim}(WindSector(t)\,, EmisSc(t)\,) \tag{4}$$

The second step is the proper computation of $[NO_x]$ transforming the simulated concentration according to the actual wind speed. On the basis that the thermal and the chemical effects are neglected, the simulated concentration is inversely proportional to the actual wind speed. In this study we use the approach proposed by Sanchez et al. (2017) where $[NO_x]$ is transformed using the friction velocity at the canopy top as reference velocity instead of the wind speed. This is because at low wind speeds thermal effects become significant, failing our assumption of $[NO_x]$ being inversely proportional to wind speed and the use of the friction velocity minimizes this error. It is noteworthy that the value of the friction velocity is obtained from the mesoscale model and it accounts for not only dynamical effects of buildings but also thermal effects. Thus, several effects neglected in CFD simulations, such as the deviation from neutral conditions, are considered in a simplified way by means of this reference velocity. The height of the canopy top is considered as the roof height of the tallest building, and the friction velocity is given by the following expression,

$$u_* = \left[\left(< u'w' >\right)^2 + \left(< v'w' >\right)^2\right]^{\frac{1}{4}} \tag{5}$$

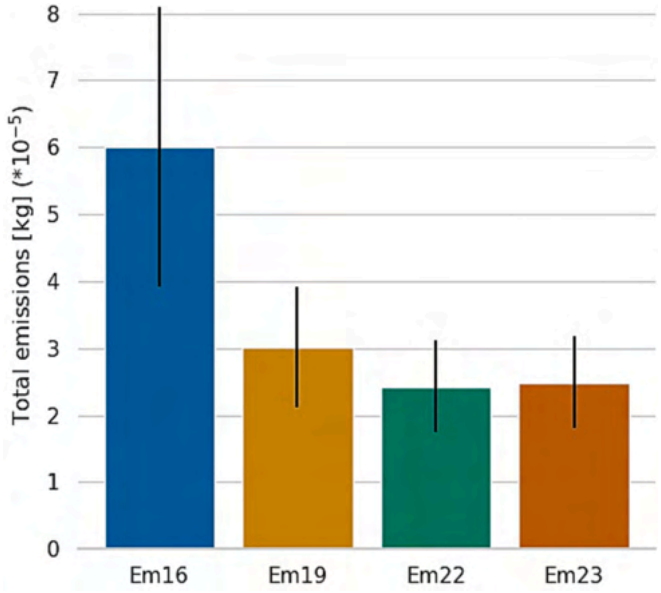

Fig. 3. Total emissions inside the study domain for each scenario. Error bars represent the standard deviation of modelled emissions.

Once the traffic-related concentrations are computed, it is essential to add to the result the background concentration since the CFD results only represent the local traffic contribution. The hourly background concentration is obtained from the urban background air quality monitoring station located at 1.5 km NW the research area.

Consequently, the computed [NO_x] at every hour is the result from the multiplication of $C_{sim}(t)$ and the ratio between the reference friction velocities at the canopy top from the CFD and from the mesoscale model, plus the background concentration:

$$C_{comp}(t) = \left.\frac{u_{*,CFD}(t)}{u_{*,WRF}(t)}\right|_{z=h_{canopy}} \cdot C_{sim}(t) + C_{backgroud}(t) \quad (6)$$

However, when the friction velocity given by WRF is below a given threshold (0.07 m s^{-1} in this work), the first term on Eq. (6) does change. In those cases, we do not select a specific wind direction, as for very low wind speeds the wind direction is highly variable. Instead, we take the average of all 16 wind directions and u* is limited to 0.07 m s^{-1}. That is, for cases of very low wind velocities, Eq. (6) is converted to:

$$C_{comp}(t) = \left.\frac{u_{*,CFD}(t)}{0.07}\right|_{z=h_{canopy}} \cdot \overline{C_{sim}^{16WD}}(t) + C_{backgroud}(t) \quad (7)$$

where,

$$\overline{C_{sim}^{16WD}}(t) = C_{sim}(EmisSc(t)) \quad (8)$$

To quantify the effect of changes in emissions, for each meteorological condition and background concentration every emission scenario is estimated, getting 4 different concentration values for the same meteorology and background concentrations. The same analysis has been performed removing the background concentrations, so by comparing the same scenarios for different years it is obtained the sole effect of meteorology on local-emissions-related [NO_x].

3. Results and discussion

3.1. Emissions evolution

The total monthly sum of local traffic emissions for each simulated scenario are shown in Fig. 3. The base case (Em16) has the largest values of NO_x emissions doubling those for the nearest scenario, which is Em19. The years 2022 and 2023 have very similar emissions (Em22 emissions are just 2 % lower than those in Em23 scenario, difference well below the standard deviation on emissions for each scenario). Therefore, we can assume that emission reductions due to remaining pandemic-related restrictions in mobility in 2022 were almost non-existent, and changes in

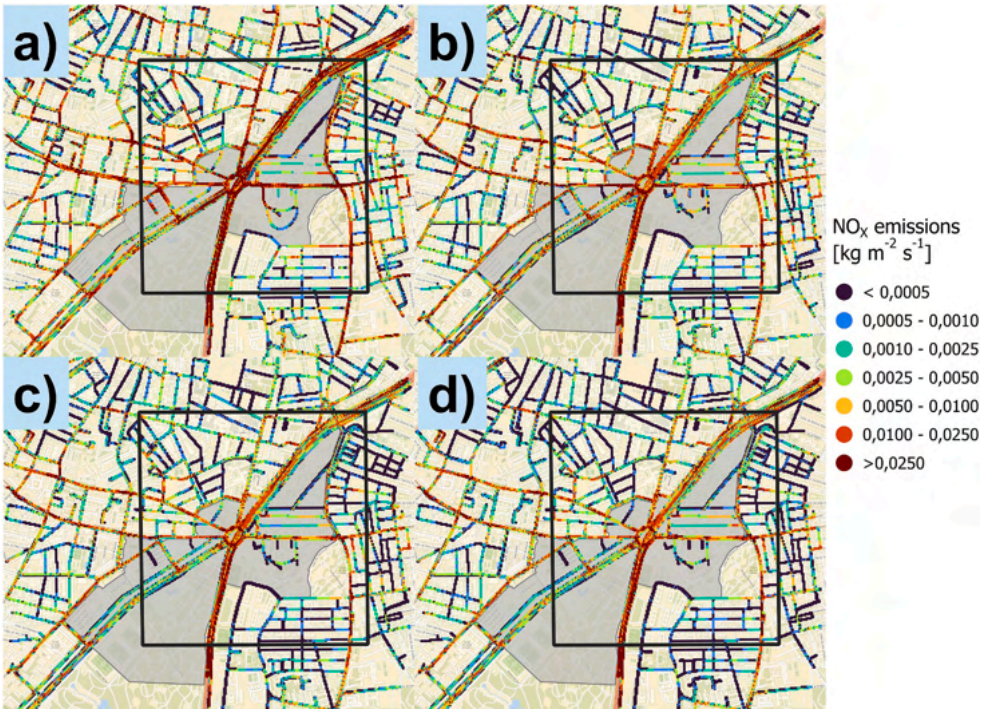

Fig. 4. Spatial distribution of total NO_x emissions across the domain corresponding to the following emission scenarios: a) Em16; b) Em19; c) Em22; d) Em23. Grey shadowed area indicates the surface affected by the LEZ. Black square represents the limits of the CFD domain.

Fig. 5. Domain employed for the CFD model with relevant streets highlighted in red and numbered from 1 to 8. Buildings are coloured in dark grey whereas vegetation is represented with green colour.

concentrations are mainly due to non-local contributions.

The spatial distribution of those emissions is shown in Fig. 4. Largest emissions are found inside the roundabout; across the highway traversing the roundabout; and those streets with entry or exit to the roundabout. Also, high levels of emissions are found in the street traversing the domain from south to north at the rightmost part of it (labelled as Street 5 in Fig. 5). This street is not as trafficked as the other mentioned streets, but it is one of the streets with the largest road grade inside the study area, which largely influences the road-traffic emissions (Wyatt et al., 2014).

Fig. 5 shows the CFD domain with some relevant street numbered from 1 to 8. These streets are of special interest as they are particularly affected by the mitigation strategies. In particular:

- Streets 1 and 2 are directly affected by the first mitigation strategy, in which street 1 direction is reversed and its number of lanes reduced from 3 to 1. This affects directly the traffic flows that traverses street 2 as it becomes the only one west-headed exit of the roundabout.
- Streets 3 to 8 are directly affected by the implementation of a LEZ. Streets 4, 6 and 7 are inside the LEZ, which means less vehicles are permitted to access them than before its implementation. On the other hand, streets 3, 5 and 8 are streets that surround the LEZ, and they are selected in order to study if the implementation of the LEZ affects the air quality inside those streets due to a possible redistribution of traffic flows.

Emissions have been declining progressively in time across most of the domain. Exceptions include:

- Between 2016 and 2019, emissions increase in Street 1, presumably due to change in road direction. Also in this period, emissions increase in Street 2 and Street 3.
- Emissions in Streets 3, 4,5 and 7 increase from 2019 to 2022.
- Emissions in Street 8 remain nearly constant across time.

3.2. Air quality time evolution

This section presents a comparison of monthly mean [NO_x] at pedestrian level (3 m height) in Plaza Elíptica for the scenarios 2016_Em16, 2019_Em19, 2022_Em22 and 2023_Em23. The nomenclature used in this section and hereafter for the different scenarios is shown in Table 1 (Subsection 2.2). All results are presented at a height of 3 m because it is the height of the intake systems of the air quality monitoring stations to measure pollutant concentrations employed for air quality assessment. Other similar studies used the same height (Santiago et al., 2021; Santiago et al., 2022; Sanchez et al., 2017). The [NO_x] timeseries used to compute the monthly mean values are evaluated at the Plaza Elíptica AQMS. A good agreement with the observed concentration values is obtained for each simulated period. More details can be found in the supplementary material.

Fig. 6 shows the monthly mean [NO_x] for the different cases of study. Strong spatial variability is present between scenarios, with local emissions being especially important across the main roads. In scenario 2016_Em16, concentrations above 100 μg m^{-3} are found across all main streets inside the domain. The roundabout and the highway traversing it are the most polluted areas with concentrations above 200 μg m^{-3} in large portions. Similar values are found near traffic light signals in

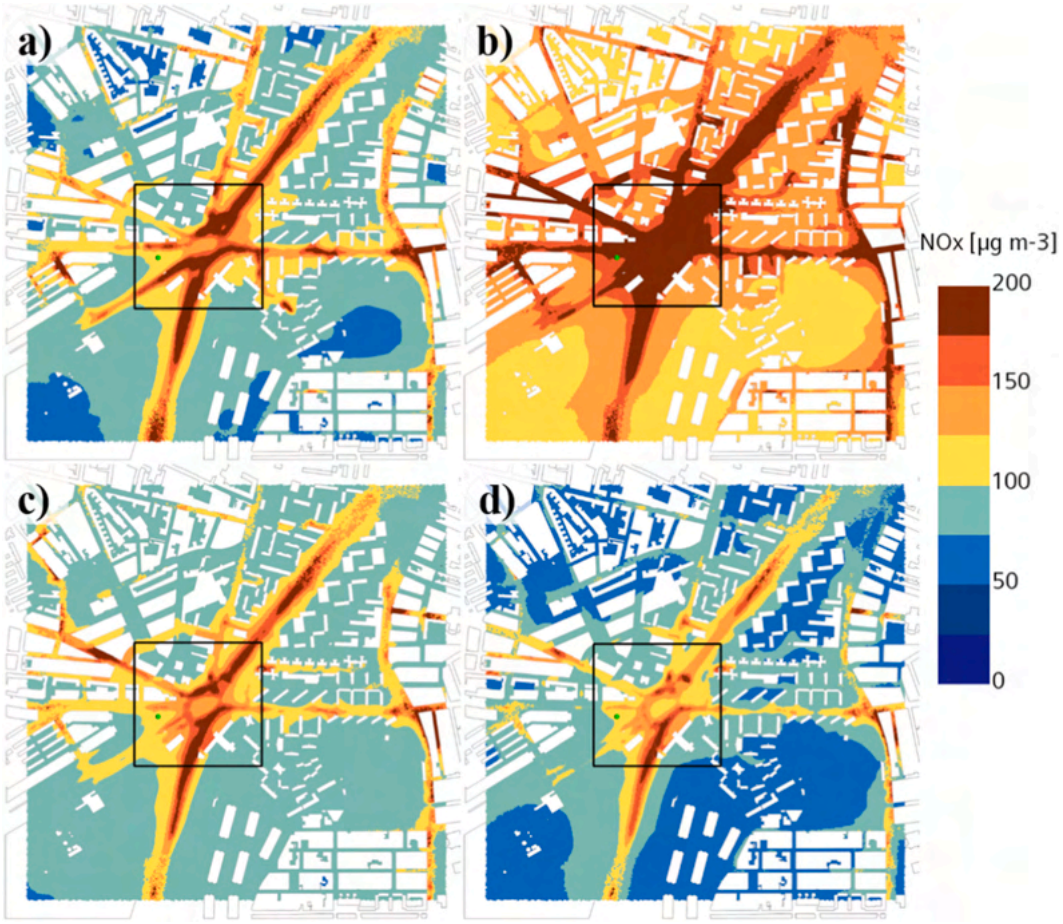

Fig. 6. Monthly mean NO_x concentration at pedestrian level (3 m above ground) in: a) 2016_Em16 scenario; b) 2019_Em19 scenario; c) 2022_Em22 scenario; and d) 2023_Em23 scenario. 300 m × 300 m study area highlighted in black.

Table 2
Separated contributions, total value and standard deviations of spatially averaged monthly mean NO_x concentrations for the CFD domain.

Scenario	Background [NO_X] [µg m^{-3}]	Local [NO_X] [µg m^{-3}]	Total [NO_X] [µg m^{-3}]	[NO_X] STD [µg m^{-3}]	Local contribution to [NO_X] (%)
2016_Em16	65.90	34.70	100.61	15.51	34.49
2019_Em19	109.00	39.26	148.26	12.51	26.48
2022_Em22	71.01	27.62	98.64	7.84	28.00
2023_Em23	63.56	23.28	86.84	6.10	26.81

streets 6 and 7. For the scenario 2019_Em19, concentration values are much higher than in 2016 across all the domain. Values exceeding 200 µg m^{-3} are obtained across most main roads. Concentrations between 125 and 150 µg m^{-3} are obtained in streets with little traffic. The concentrations are higher than 100 µg m^{-3} throughout the domain for that year. Modelled [NO_x] during 2022_Em22 scenario are quite similar to that of 2016_Em16 with some exceptions. Lower values of NO_x were obtained in 2022_Em22 scenario than in 2016_Em16 inside streets 1,4,5,6 and 7, but higher concentrations were modelled in streets 2, 3 and 8. The less polluted scenario is the 2023_Em23 one. In this scenario, there are barely areas with concentrations near or above 200 µg m^{-3}. Main roads across the domain present values of averaged NO_x around 100 µg m^{-3}, but less trafficked streets present values near 75 µg m^{-3}. An inner study area of 300 m × 300 m has also been studied because of the great traffic and pedestrian presence inside that area. There, concentrations are up to 40 µg m^{-3} higher in average than for the whole CFD domain in each scenario, but they follow the same temporal evolution.

Table 2 summarizes the spatially-averaged of monthly mean [NO_x] values for each case of study across every cell inside the CFD domain at a pedestrian level. A remarkable fact is that the 2019_Em19 scenario shows a much higher average concentration than the 2016_Em16 case, despite almost halving its local emissions. An important contributor to this result is the background concentration. Monthly mean [NO_x] of background in the 2019_Em19 scenario is 109 µg m^{-3}, whereas in the 2016_Em16 case its value is 65.8 µg m^{-3}. Nevertheless, this difference of 43.2 µg m^{-3} in the background does not fully explain the change in [NO_x] between those two scenarios. The local contribution to [NO_x] increases from 2016 to 2019 despite a 50 % reduction on emissions, fact that is accentuated in the 300 m × 300 m research area (Table S4). This behaviour suggests an influence of meteorology on local monthly-averaged NO_x concentrations. Background concentrations in this area mostly comes from urban traffic emissions, and traffic decreased across the whole city between 2016 and 2019 (not shown), so it seems that meteorology also affects total concentrations by increasing the pollutants concentrations reaching the study area from other parts of the city. Ruling out an increase of emissions as the cause of the increased air pollutant concentrations in 2019_Em19, the cause seems to be windier conditions (Fig. 7 and Fig. S2) and a greater stability (Fig. 9) in that period.

The differences in meteorological conditions are key to explain the apparently counterintuitive behaviour of the monthly mean [NO_x]. Fig. 7 shows the modelled windroses for each simulated scenario. The colours indicate the different wind speeds ranges, and the height of the bars indicates the relative frequency of each wind speed and direction. 2016 is the period with the highest frequency of wind speeds >2 m s^{-1}

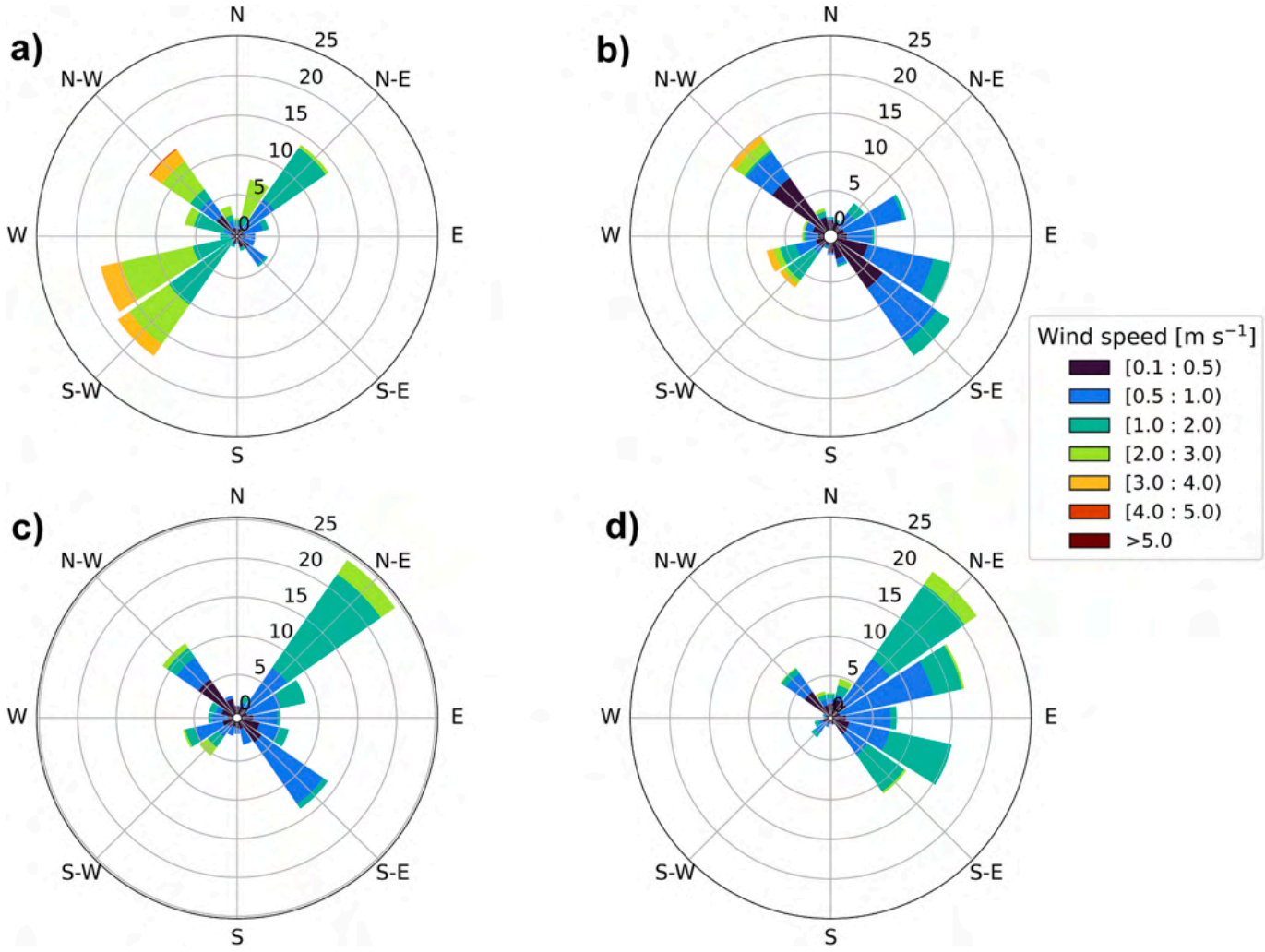

Fig. 7. Modelled wind roses for Plaza Elíptica AQMS for: a) 2016_Em16 scenario; b) 2019_Em19 scenario; c) 2022_Em22 scenario; and d) 2023_Em23 scenario. Labels in the radial direction indicate the relative frequency of observed wind speed, whereas the labels in the angular direction indicate the wind direction. Wind speed ranges are indicated by colours.

(34 %), while <23 % of observations registered wind speeds below 1 m s^{-1}. Every else scenario presents at least a 61 % of observations with wind speeds below 1 m s^{-1}. On the other hand, the 2019 scenario presents the highest proportion of observations below 0.5 m s^{-1} (36 %) and below 1 m s^{-1} (78 %).

Highest values of [NO_x] correspond to lower wind speeds, as low wind speeds reduces transport and dispersion of pollutants (Kassomenos et al., 1998, 2014). This explains why the 2016_Em16 is the second less polluted one despite its higher emission values. The 2016_Em16 and 2023_Em23 scenarios, which are the windiest ones, have each other >63 % and 70 % of observations respectively with [NO_x] < 100 μg m^{-3} at the Plaza Elíptica AQMS. On the other hand, the 2019_Em19 scenario -the one with lowest wind speed- has barely a 26 % of the observations with [NO_x] < 100 μg m^{-3}, and nearly a 9 % of the observations (~60 hourly values) registered values of [NO_x] > 400 μg m^{-3} (Fig. 8).

In addition, the atmospheric stability is analysed for each period through the parameter H_{canopy}/L_{urb}. This parameter represents the coefficient between buoyant and inertial forces (Santiago et al., 2014). L_{urb}, which is an urban length scale analogous to the Obukhov length, has been obtained from the mesoscale outputs following the formula:

$$L_{urb} = \frac{u_*^3}{\frac{g}{T_{ref}}\frac{Q_h}{\rho C_p}} \quad (9)$$

where ρ is the air density, g is the acceleration due to gravity, Q_h is the total heat flux from all urban surfaces divided by the plan area, C_p is the specific heat of air and T_{ref} is a reference temperature, which in this case is the temperature at the canopy top (H_{canopy}). The adimensional number H_{canopy}/L_{urb} is zero for neutral atmospheric conditions, meanwhile high values indicate a greater importance of buoyant forces and, therefore, atmospheric conditions further from the neutral case. Fig. 9 shows the time evolution of H_{canopy}/L_{urb} for each one of the simulated periods. February 2019 shows the highest number of days with large values of this parameter, followed by 2022. On the other hand, February 2016 atmospheric conditions were near to neutrality throughout most of the months, with only 4 days with at least one hourly value of H_{canopy}/L_{urb} > 10.

Returning to the analysis of monthly mean [NO_x], the 2022_Em22 scenario shows larger spatially averaged concentrations over the whole domain than the 2023_Em23 scenario (Fig. 6) despite its emissions being slightly lower. The former scenario presents a spatially a local-related concentration of 27.6 μg m^{-3} (just 7 μg m^{-3} –or 20 % lower than the 2016_Em16 scenario despite a 60 % reduction in local emissions), whereas the averaged local-related concentration in the latter one is of 23.3 μg m^{-3} (Table 2). All scenarios show the maximum concentrations near the roundabout and near the tunnel, with two maximum values at the south entry and the north exit of the tunnel; meanwhile the minimum values occur far from the emissions (in green zones and inside

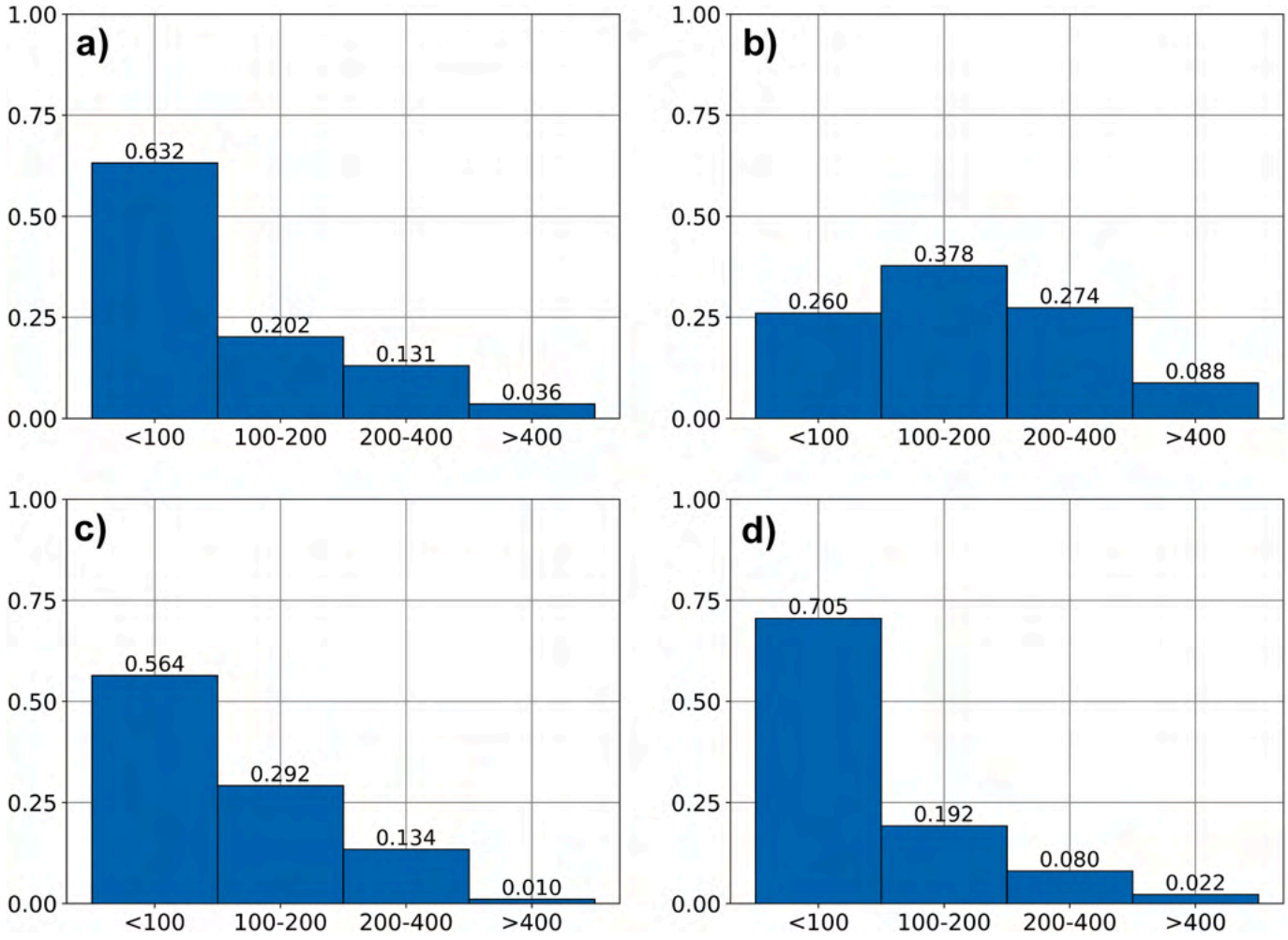

Fig. 8. Histograms of measured NO_X concentration [μg m^{-3}] in Plaza Elíptica AQMS for: a) 2016_Em16 scenario; b) 2019_Em19 scenario; c) 2022_Em22 scenario; and d) 2023_Em23 scenario.

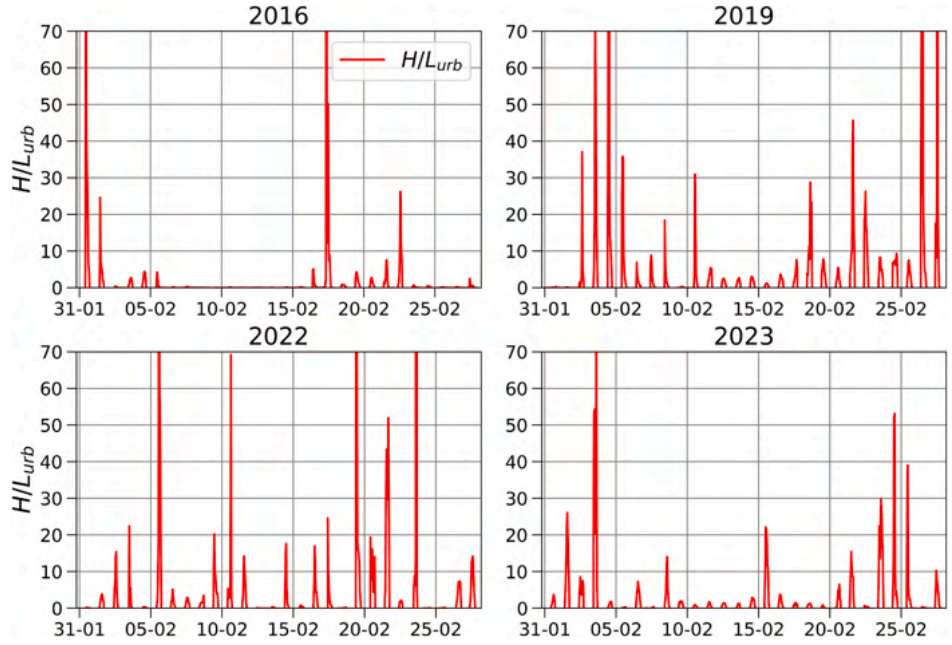

Fig. 9. Time series of hourly h_{canopy}/L_{urb} for the different simulated periods: a) February 2016; b) February 2019; c) February 2022; and d) February 2023.

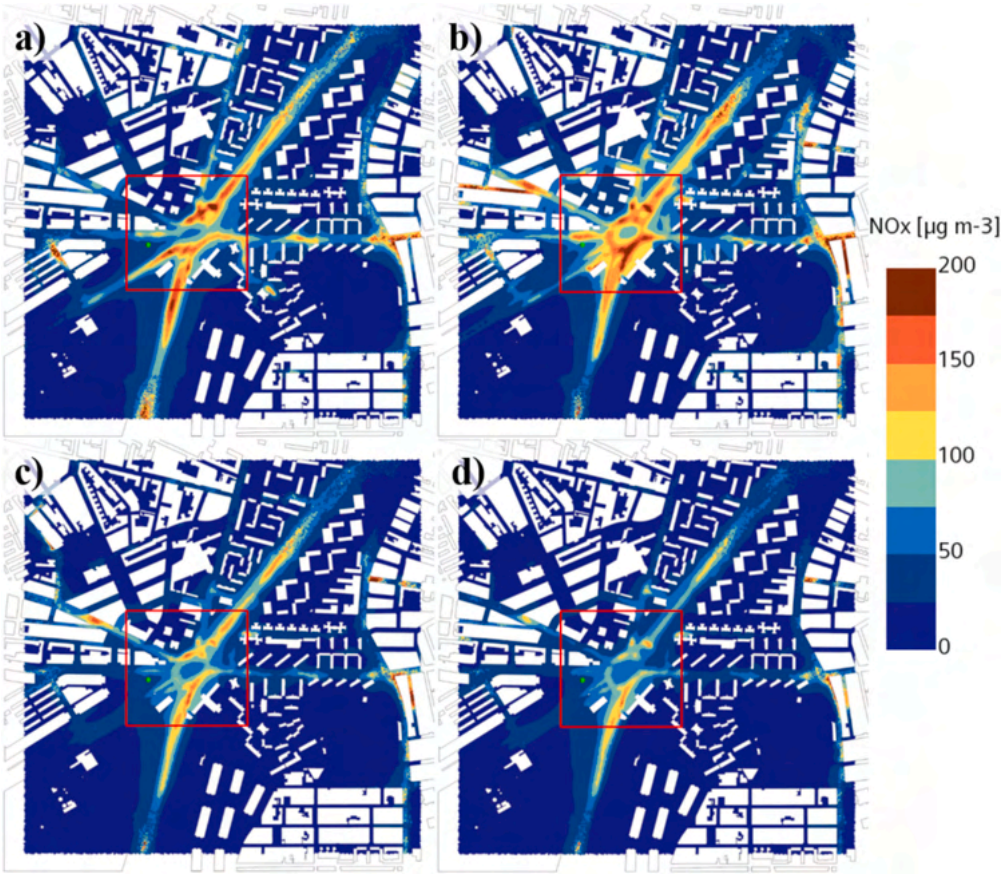

Fig. 10. Monthly mean NO_x concentration at pedestrian level (3 m above ground) due to local traffic emissions in: a) 2016_Em16 scenario; b) 2019_Em19 scenario; c) 2022_Em22 scenario; and d) 2023_Em23 scenario. 300 m × 300 m study area highlighted in red.

inner courtyards). This spatial distribution agrees with observed and modelled values in previous works (Borge et al., 2016; Sanchez et al., 2017). In the first study, an intensive measuring campaign of NO_2 and PM, along with meteorological parameters, is performed for a winter month (February 2015); while in the latter one NO_2 concentrations are computed using a numerical methodology and then evaluated with the observational campaign from Borge et al., 2016. Both works found the highest pollutant values at the entries and exits of the tunnel, with also high concentration values inside the roundabout and near traffic lights. The tunnel that traverses the roundabout has the heaviest traffic flows inside the domain, which explains why this area presents the highest levels of NO_x.

Focusing on the centre of the domain (the 300 m × 300 m study area), the results are in line with those from the whole CFD domain. The most relevant fact is the increase of local-related [NO_x] relative contribution in all study cases by a factor 1.5 (Table S4). This result is expected as this research area contains more areas with presence of local emissions than the whole CFD domain.

Finally, Fig. 10 shows the contribution of local traffic emissions to monthly-averaged [NO_x] for each scenario. Largest values are found inside the streets with largest emissions (discussed in Section 3.1). Note the increased values of local-related [NO_x] after the implementation of the first mitigation strategy inside Streets 2 and 8.

3.3. *Effect of local traffic measures and meteorological conditions on [NO_x]*

To assess the effects of local traffic measures and meteorology on [NO_x] at pedestrian level, concentrations due to each local mitigation strategy are estimated for the conditions (meteorology and background) corresponding to every year. Spatially averaged monthly mean concentrations for each case are shown in Fig. 11. The x-axis represents different meteorological and background conditions, meanwhile the colours represent each emission scenario. The meteorological conditions of February 2019 result in the highest values of the monthly mean [NO_x] from local emissions for each one of the emissions scenarios; meanwhile for all meteorological conditions, the emissions of Em16 gives the highest values of local [NO_x], as expected from the results explained in Section 3.1. Also, the largest emission reductions for each meteorology are obtained when comparing the Em22 and the Em16 scenarios, which is also as expected as they are the scenarios with the lowest and highest emissions respectively.

Table 3 summarizes the variation in the spatially averaged monthly mean NO_x concentrations across the CFD domain due to changes in emission, for each meteorological conditions scenario. Here it can be seen how the differences on monthly-averaged [NO_x] between emissions cases also depends on the meteorological conditions selected for the comparison. For example, let us consider the effectiveness of the implementation of the LEZ by comparing the monthly-averaged [NO_x] in the Em22 case with those of the Em19 case. If we do compare them using the Met16 as the reference meteorological conditions for both emissions scenarios, the reductions in monthly-averaged [NO_x] due to the implementation of the LEZ would have been of 6.14 µg m^{-3} in average across all the CFD domain. However, if we use the Met22 as the reference conditions, the reduction would have been of 10.41 µg m^{-3} –a 70 % larger reduction. These values are in line with previous studies based on observations of NO_X concentrations before and after the implementation of an LEZ (Boogaard et al., 2012; Ma et al., 2021). Boogaard et al. (2012) studied the variation in concentration for several pollutants before and after the implementation of LEZs in The

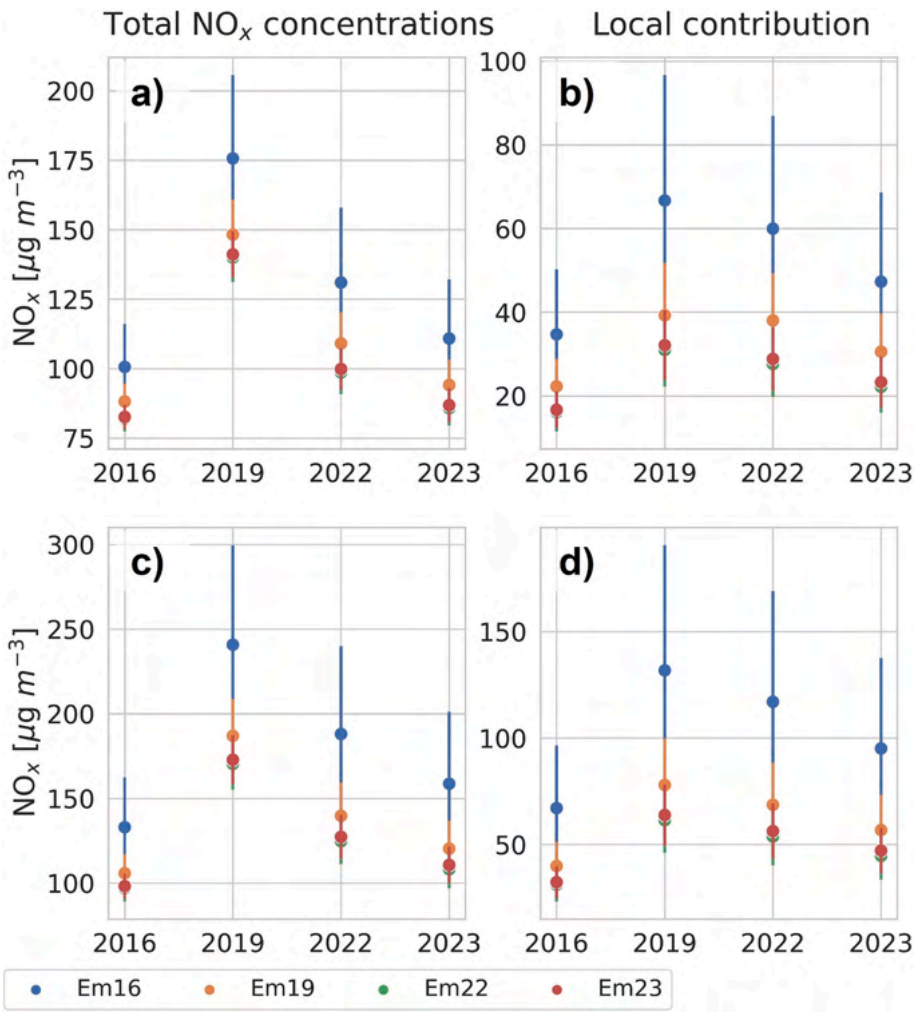

Fig. 11. a): Total (local + background) spatially averaged monthly mean NO_x concentrations across all cells inside the CFD domain. b): Local contribution to spatially averaged monthly mean NO_x concentrations across all cells inside the CFD domain. c): Same as a) but spatially averaged inside the 300 m × 300 m study area. d): Same as b) but spatially averaged inside the 300 m × 300 m study area.

Table 3
Net change of the spatially averaged monthly mean NO_x concentrations inside CFD domain in μg m^{-3}.

Variation in total spatially averaged monthly mean NO_x concentrations [μg m^{-3}] (% of local values/% of total values)						
	Em19 vs Em16	Em22 vs Em16	Em23 vs Em16	Em22 vs Em19	Em23 vs Em19	Em23 vs Em22
Met16	−12.43 (−35.8/ −12.4)	−18.57 (−53.5/ −18.5)	−18.02 (−51.9/ −17.9)	−6.14 (−27.6/ −7.0)	−5.59 (−25.1/ −6.3)	0.55 (3.4/ 0.7)
Met19	−27.43 (−41.1/ −15.6)	−35.71 (−53.5/ −20.3)	−34.58 (−51.9/ −19.7)	−8.28 (−21.1/ −5.6)	−7.15 (−18.2/ −4.8)	1.13 (3.6/ 0.8)
Met22	−21.94 (−36.6/ −16.7)	−32.35 (−53.9/ −24.7)	−31.15 (−51.9/ −23.8)	−10.41 (−24.2/ −9.5)	−9.21 (−24.2/ −8.4)	1.20 (4.4/ 1.2)
Met23	−16.73 (−35.4/ −15.1)	−25.10 (−53.1/ −22.6)	−24.01 (−50.8/ −21.7)	−8.37 (−27.4/ −8.9)	−7.28 (−23.8/ −7.7)	1.09 (4.9/ 1.3)

Netherlands using measurement campaigns. The absolute differences for NO_x ranged between −39.5 and +5.2 μg m^{-3}. Panteliadis et al. (2014) estimated the effect of LEZ in traffic-related NO_x concentrations in Amsterdam to be in the range of −9.34 and −1.57 μg m^{-3}, or −9.07 and −3.73 μg m^{-3} when adjusted the values to the type of day, wind direction and wind speed. For the London Ultra Low Emissions Zone (ULEZ), the reductions are quite similar. Reductions of up to −8.24 μg m^{-3} in [NO_x] were found by Ma et al. (2021).

Furthermore, the changes in [NO_x] due to changes in emissions represent up to the 54 % of the local traffic emission contribution to [NO_x] inside the CFD domain, and up to the 25 % of total [NO_x].

For the 300 m × 300 m study area, the impacts of the mitigation strategies are significatively larger due to the removal of significant areas with no emissions (e.g., parks and pedestrian areas), and also the difference between the same emissions comparison due to the choice of meteorological conditions increases, with values up to 35 μg m^{-3} (Table S5).

To analyse the spatial distribution of the aforementioned variations in monthly-averaged [NO_x] due to different meteorological conditions, Fig. 12 shows the distribution of the local contribution to monthly-averaged [NO_x]. Each column represents the same emissions conditions while each row represents a unique meteorological scenario. It shows the effect of both changes (emissions and meteorological conditions) on NOx concentrations due to local traffic emissions. The maps a), f), k) and p) correspond to the real conditions for each study period (i.e. to the scenarios 2016_Em16, 2019_Em19 and so on).

Again, for all scenarios the Met19 meteorological conditions result in the largest values of NO_x across the entire domain. The magnitude of the effect of mitigation strategies is clearly dependant on the meteorology.

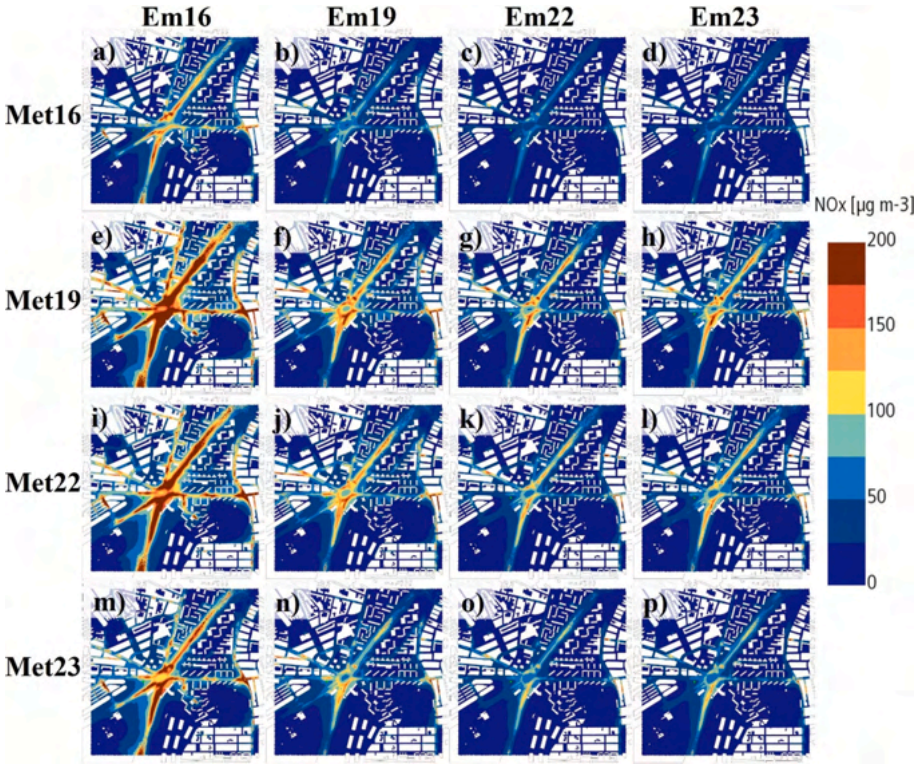

Fig. 12. Panel of monthly-averaged NO_x concentrations for the different scenarios. a) 2016_Em16; b) 2016_Em19; c) 2016_Em22; d) 2016_Em23; e) 2019_Em16; f) 2019_Em19; g) 2019_Em22; h) 2019_Em23; i) 2022_Em16; j) 2022_Em19; k) 2022_Em22; l) 2022_Em23; m) 2023_Em16; n) 2023_Em19; o) 2023_Em22; and p) 2023_Em23.

Table 4
Net and relative changes on local monthly-averaged NO_x concentrations inside the CFD domain.

Variation in local spatially averaged monthly mean NO_x concentrations [µg m^{-3}] (% of local values)						
	Met19 vs Met16	Met22 vs Met16	Met23 vs Met16	Met22 vs Met19	Met23 vs Met19	Met 23 vs Met22
Em16	31.99 (92.2)	25.27 (72.8)	12.59 (36.3)	−6.72 (−10.1)	−19.40 (−29.1)	−12.68 (−21.1)
Em19	16.99 (76.3)	15.76 (70.8)	8.29 (37.2)	−1.23 (−3.1)	−8.70 (−22.2)	−7.47 (−19.6)
Em22	14.85 (92.0)	11.49 (78.7)	6.06 (37.6)	−3.36 (−7.0)	−8.79 (−28.4)	−5.43 (−23.0)
Em23	15.43 (92.5)	12.15 (72.8)	6.60 (39.6)	−3.29 (−10.2)	−8.83 (−27.5)	−5.55 (−19.2)

For example, the spatial distributions of NO_x for the 2019_Em23 scenario and is for the 2016_Em16 scenario are similar. The 60 % reduction in emissions between both scenarios is nearly balanced by the meteorological conditions. In this case, the impact of meteorology and emission changes are similar for some strategies, but of opposite sign. Let us now consider another case. For the first implemented strategy (2019_Em19), the local contribution to NO_x increased in relation to the 2016_Em16 scenario, as described in previous sections. In this case, the NO_x reduction due to mitigation strategy is lower than the increase due to the meteorology. However, if we consider the same meteorological conditions for quantify the effect of this measures (i.e., if we compare 2019_Em19 with 2019_Em16 or 2016_Em19 with 2016_Em16), a large decrease in local-related NO_x concentrations is observed. This is an example of how the meteorological conditions can even reverse the sign of the impacts of a mitigation strategy on local air quality. This reversal doesn't occur when analysing the effects of the implementation of the LEZ, but even in this case the magnitude of the impacts of the strategy depends on the meteorological conditions selected for the comparison. When comparing the Em22 and Em19 scenarios with the same meteorological conditions (e.g. 2019_Em19 vs 2019_Em22), the reductions in monthly-averaged [NO_x] are less than those observed in reality (2019_Em19 vs 2022_Em22).

In Table 4 a quantification of the effect of the different meteorological conditions on the different emissions scenarios is shown. Local contributions to [NO_x] show a great variability with the meteorology, even changing by a factor almost 2 in some cases, as for example when comparing the meteorological conditions of February 2016 and February 2019 for every emission scenario. These changes in spatially averaged local [NO_x] are in some cases even greater than those due to changes in emissions presented in Table 3. When also considering the variations in the background concentrations, the variability is still quite large. Most scenarios show an increase of averaged NO_x >70 % when comparing the 2019 meteorological conditions with those of 2016, while a decrease of up to 38 % has been observed for the same emissions scenarios between the 2023 and the 2019 meteorological conditions (Table S6). For the 300 m × 300 m study area the results are similar (not shown).

Fig. 13 illustrates how would have changed the monthly-averaged [NO_x] for each meteorological condition and background concentrations (rows) if considering different emissions configurations (columns). For example, in the first row the reference is the scenario 2016_Em16; in the second one the reference is 2019_Em19, etc. For each row, only the effect of change in local emissions is observed as the background concentrations cancel out. The spatial distribution of the monthly-averaged [NO_x] net changes is highly heterogeneous, being larger near emissions. The scale on Fig. 13 is clipped to ±100 µg m^{-3}, although this value is

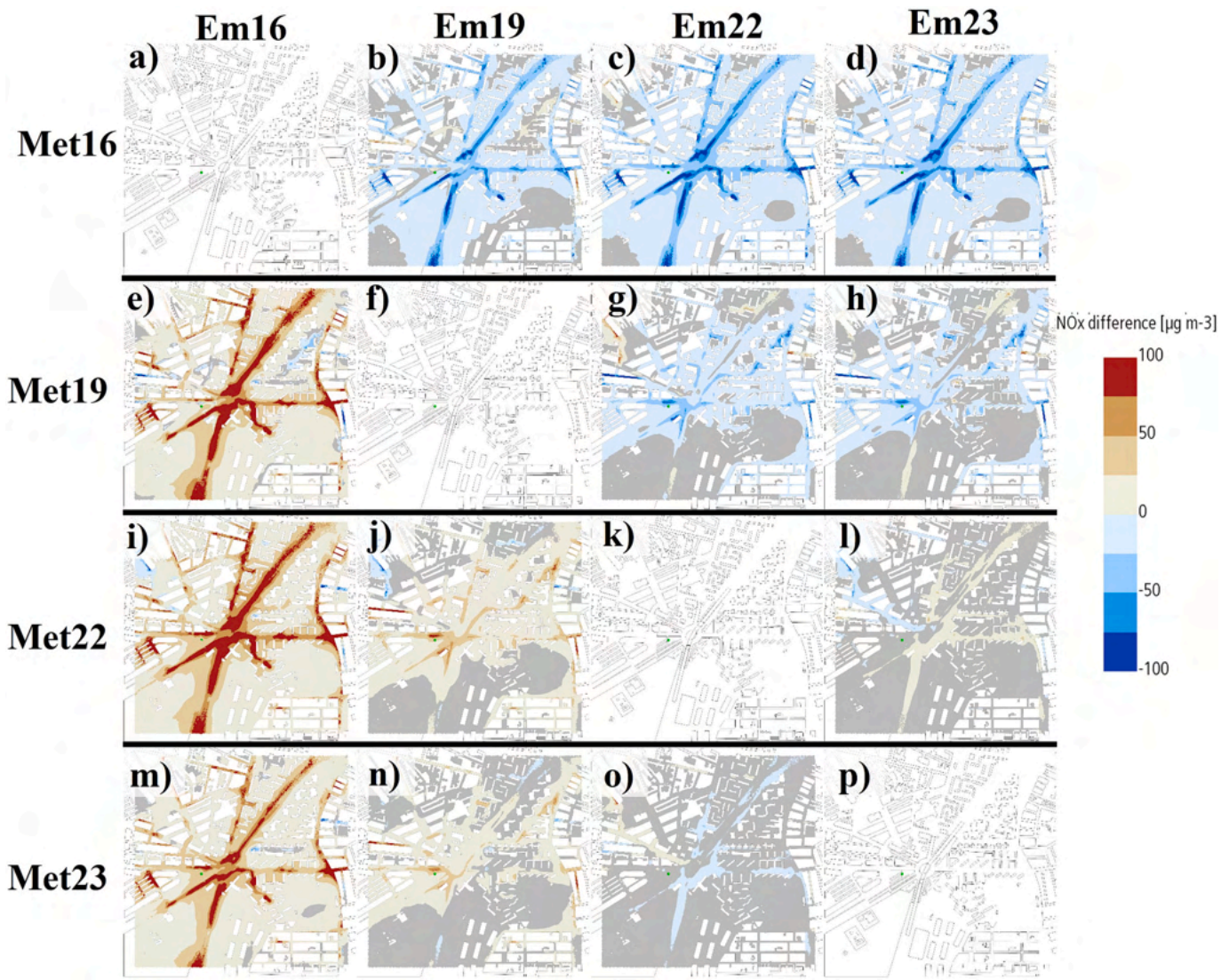

Fig. 13. Differences of monthly-averaged NO_x concentrations between scenarios. a) NO_X for 2016_Em16 scenario – NO_X for 2016_Em16 scenario; b) NO_X for 2016_Em19 scenario – NO_X for 2016_Em16 scenario; c) NO_X for 2016_Em22 scenario – NO_X for 2016_Em16 scenario; d) NO_X for 2016_Em23 scenario – NO_X for 2016_Em16 scenario; e) NO_X for 2019_Em16 scenario – NO_X for 2019_Em19 scenario; f) NO_X for 2019_Em19 scenario – NO_X for 2019_Em19 scenario; g) NO_X for 2019_Em22 scenario – NO_X for 2019_Em19 scenario; h) NO_X for 2019_Em23 scenario – NO_X for 2019_Em19 scenario; i) NO_X for 2022_Em16 scenario – NO_X for 2022_Em22 scenario; j) NO_X for 2022_Em19 scenario - NO_X for 2022_Em22 scenario; k) NO_X for 2022_Em22 scenario - NO_X for 2022_Em22 scenario; l) NO_X for 2022_Em23 scenario - NO_X for 2022_Em22 scenario; m) NO_X for 2023_Em16 scenario – NO_X for 2023_Em23 scenario; n) NO_X for 2023_Em19 scenario - NO_X for 2023_Em23 scenario; o) NO_X for 2023_Em22 scenario - NO_X for 2023_Em23 scenario; and p) NO_X for 2023_Em23 scenario - NO_X for 2023_Em23 scenario. Values between −5 and 5 µg m^{-3} are shadowed in grey. Note that maps in each row have been computed with the same meteorological conditions but different emissions scenarios (columns). In each row, the reference scenario is the scenario with real conditions for that year (e.g. 2016_Em16, 2019_Em19, and so on).

exceeded in some areas of the domain. For the meteorological conditions of 2016, all emissions configurations show significant emissions reductions inside the main roads of the research area with respect to those of the 2016 emission configuration. In this case, the magnitude of the changes near emissions is large enough to spread to regions far from emissions. For the meteorological conditions of 2019, only the emissions of 2016 yield to an increase in monthly-averaged [NO_x], albeit even this case shows areas with significant reductions (greater in absolute value than 5 µg m^{-3}). On the other hand, when comparing the emissions of 2022 and 2023 little areas with significant variations are found and they are limited to near emissions.

The same comparison exercise can be done but maintaining the emissions constant and changing the meteorological conditions. Fig. 14 illustrates the differences in monthly-averaged [NO_x] for 4 different meteorological conditions, using as reference the scenario with emissions and background corresponding to the year of the meteorological conditions. The meteorological conditions of February 2019 result in the largest concentrations for every emissions scenario both due to the increase on background concentrations and in local concentrations. The increases in local concentrations can be noticed by the stronger colours inside the main streets where most emissions occur inside the domain. On the other hand, the meteorological conditions of February 2016 result in the less polluted configurations for every emissions configuration, followed by the February 2023 meteorological conditions. The net differences between the less and most polluted configurations depend on the emissions scenario but, for most of them, in most polluted streets this difference exceeds the 75 µg m^{-3} value, as it happened when comparing different emissions for the same meteorology (Fig. 13) and as can clearly be seen comparing, for example, the 2016_Em19 and the 2019_Em19 scenarios. In zones far from emissions, the difference in monthly-averaged [NO_x] between different meteorological conditions is the difference between background concentrations. The spatial

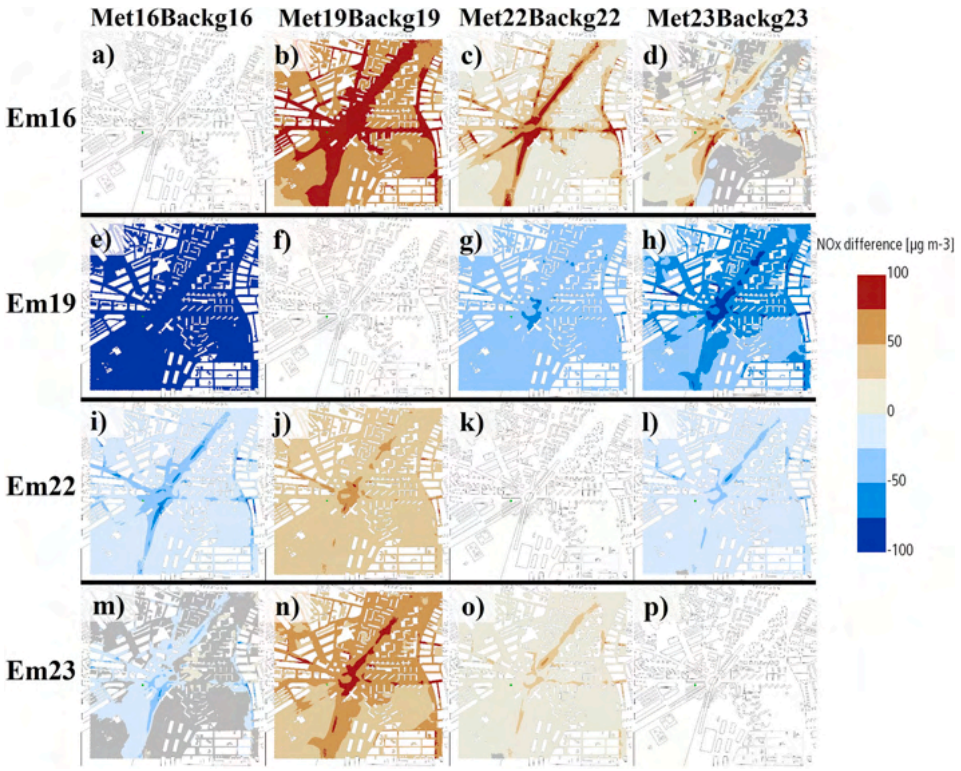

Fig. 14. Differences of monthly-averaged NO_x concentrations between scenarios. a) NO_X for 2016_Em16 scenario – NO_X for 2016_Em16 scenario; b) NO_X for 2019_Em16 scenario – NO_X for 2016_Em16 scenario; c) NO_X for 2022_Em16 scenario – NO_X for 2016_Em16 scenario; d) NO_X for 2023_Em16 scenario – NO_X for 2016_Em16 scenario; e) NO_X for 2016_Em19 scenario – NO_X for 2019_Em19 scenario; f) NO_X for 2019_Em19 scenario – NO_X for 2019_Em19 scenario; g) NO_X for 2022_Em19 scenario – NO_X for 2019_Em19 scenario; h) NO_X for 2023_Em19 scenario – NO_X for 2019_Em19 scenario; i) NO_X for 2016_Em22 scenario – NO_X for 2022_Em22 scenario; j) NO_X for 2019_Em22 scenario - NO_X for 2022_Em22 scenario; k) NO_X for 2022_Em22 scenario - NO_X for 2022_Em22 scenario; l) NO_X for 2023_Em22 scenario - NO_X for 2022_Em22 scenario; m) NO_X for 2016_Em23 scenario – NO_X for 2023_Em23 scenario; n) NO_X for 2019_Em23 scenario - NO_X for 2023_Em23 scenario; o) NO_X for 2022_Em23 scenario - NO_X for 2023_Em23 scenario; and p) NO_X for 2023_Em23 scenario - NO_X for 2023_Em23 scenario. Values between −5 and 5 µg m^{-3} are shadowed in grey. Note that maps in each row have been computed with the same emissions but different meteorological conditions and background concentrations. In each row, the reference scenario is the scenario with real conditions for that year (e.g. 2016_Em16, 2019_Em19, and so on).

distribution of the net changes in monthly mean [NO_x] due to changes in meteorological conditions differs from those due to changes in emissions because of the contribution of the background concentrations in the former one. Nonetheless, their magnitude is similar especially near emissions.

4. Limitations

The approach we propose here has some limitations:

- The results presented in this work only are for a winter month. However, these meteorological conditions tend to play an important role on air quality in Madrid. In addition, the conclusions about the effects of meteorology on air quality at pedestrian level can be extrapolated to other conditions. An analysis for considering the full year is one of the main future lines of this work.
- Regarding the turbulence treatment in CFD simulations, a LES model would be more accurate than a RANS model. But this work focuses on the average impact of mitigation strategies during a whole winter month and compares the relative concentration between scenarios, for which the RANS models are suitable enough as show in the model evaluation and in the previous work applied to the same area (Sanchez et al., 2017). In addition, considering the large number of scenarios analysed here, the calculation time required for a LES model would be very high.
- The background concentrations are obtained from an urban background air quality meteorological station, which could induce some errors for some wind directions. However, Sanchez et al. (2017) showed that this approach is appropriate.
- The assumptions of the numerical methodology (concentrations inversely proportional to wind speed) can induce errors in modelled concentrations. Nonetheless, the model evaluation of the present study and previous works (Rivas et al., 2019; Sanchez et al., 2017; Parra et al., 2010) have found this methodology is appropriate for the purpose of this study.

5. Discussion and conclusions

A multi-model methodology has been used to study the impacts of several local mitigation strategies in [NO_x] in a real hot spot in Madrid. The impact of meteorological conditions when analysing the effectiveness of the mitigation strategies is also investigated. The good outcomes when evaluating the traffic model results with observational data indicate a realistic representation of traffic flows inside the study domain. The reliability of the resulting emissions depends on the good representation of the vehicle float and the road network; the degree of detail of the input data; and the level of accuracy of the emission model. Meteorology provided by WRF model is also successfully evaluated using meteorological variables measured at AQMS. NO_x is computed by the numerical methodology based on CFD simulations. The analysis of the model performance shows a good fit in the time evolution of pollutants concentrations with independence of the simulated period.

Four different periods have been simulated to evaluate the impact of two different mitigation measures. The emissions inside the research area have gradually decreased since 2016, with no significant variation

between 2022 and 2023. However, this trend was not translated to monthly-averaged concentrations. The scenario corresponding to February 2019 showed the highest NO_x concentration values (149 μg m^{-3}) due to both higher background and local contributions to NO_x concentration. The higher local contribution in 2019 with less emissions indicates an impact of meteorology in monthly-averaged concentrations. Therefore, time averaged spatial distributions of NO_x concentrations shows a two-fold dependency on local emissions and meteorology. Local emissions are an important contributor to air pollution in urban areas, especially close to traffic emissions. Its contribution to total concentrations inside the research area ranges between 41 % and 51 % near Plaza Elíptica roundabout but can exceed 60 % under specific meteorological and emissions configurations. Conditions with low wind speed increase the importance of local emissions, as transport of pollutants from other regions is reduced. In addition, changes in meteorological conditions with the same emission configuration can alter the concentration of NO_x by a factor 2 and its impact on monthly-averaged NO_x concentrations can be comparable to the impacts due to changes in emissions, even surpassing then under specific conditions. By all these reasons, we state that a good evaluation of mitigation strategies should consider different meteorological situations. In addition, we have observed that the impact of local mitigation measures is limited by the non-local contribution of pollutants, which also depends on meteorological conditions. The spatial distribution of [NO_x] and its variations with different meteorological and emission scenarios is highly heterogeneous, and so high-resolution modelling is needed to properly capture the impacts of local air pollution mitigation strategies.

The original aim of the strategies analysed in this work was to reduce air pollutant concentrations at local scale. When removing the effect of meteorological conditions, it has been found that the net effect of the abatement measure consisting of changing road directions was a general improvement of air quality, but some increases in [NO_x] are noted near the actuated area. On the other hand, the LEZ of Plaza Elíptica seems to have little effect on [NO_x]. These results are in line with previous research performed on other LEZ zones in Europe (Gu et al., 2022; Boogaard et al., 2012; Ma et al., 2021). It is expected that its effect increases in following years with increasing access restrictions to the LEZ. In any case, meteorological conditions largely drive the net effect of abatement measures and therefore the achievement of the target reduction of concentrations pursued by these measures will depend on the meteorological conditions.

Therefore, typical meteorological conditions of the study area should be considered for the design of mitigation measures.

CRediT authorship contribution statement

A. Rodríguez-Sánchez: Writing – original draft, Visualization, Validation, Methodology, Investigation, Formal analysis, Conceptualization. **J.L. Santiago:** Writing – review & editing, Visualization, Methodology, Investigation, Formal analysis, Conceptualization. **M.G. Vivanco:** Conceptualization, Methodology, Visualization, Writing – review & editing. **B. Sanchez:** Writing – review & editing, Visualization, Software, Methodology, Conceptualization. **E. Rivas:** Writing – review & editing, Software, Methodology. **A. Martilli:** Writing – review & editing, Methodology, Conceptualization. **F. Martín:** Methodology, Conceptualization.

Declaration of competing interest

The authors declare that they have no known competing financial interests or personal relationships that could have appeared to influence the work reported in this paper.

Data availability

Data will be made available on request.

Acknowledgements

The authors acknowledge the Spanish Ministry for Ecological Transition and Demographic Challenge (METDC). These results are part of the I + D + i project Retos-AIRE, funded by the Spanish Ministry of Science and Innovation under the grant agreement AEI/10.13039/501100011033/ and of Project TED2021-132431B-I00 (TRANS-AIRE: Transition to cleaner air in Spain) funded by MCIN/AEI/10.13039/501100011033 and by the European Union NextGenerationEU/PRTR. This work was partially supported by the computing facilities of Extremadura Research Centre for Advanced Technologies (CETA-CIEMAT), funded by the European Regional Development Fund (ERDF). CETA-CIEMAT belongs to CIEMAT and the Government of Spain.

Appendix A. Supplementary data

Supplementary data to this article can be found online at https://doi.org/10.1016/j.scitotenv.2024.176667.

References

Alvarez Lopez, P., Behrisch, M., Bieker-Walz, L., Erdmann, J., Flötteröd, Y.-P., Hilbrich, R., Lücken, L., Rummel, J., Wagner, P., Wießner, E., 2018. Microscopic traffic simulation using SUMO. In: IEEE Intelligent Transportation Systems Conference (ITSC).

Belis, C., Karagulian, F., Larsen, B., Hopke, P., 2013. Critical review and meta-analysis of ambient particulate matter source apportionment using receptor models in Europe. Atmos. Environ. 69, 94–108. https://doi.org/10.1016/j.atmosenv.2012.11.009.

Boogaard, H., Janssen, N.A.H., Fischer, P.H., Kos, G.P.A., Weijers, E.P., Cassee, F.R., van der Zee, S.C., de Hartog, J.J., Meliefste, K., Wang, M., Brunekreef, B., Hoek, G., 2012. Impact of low emission zones and local traffic policies on ambient air pollution concentrations. Sci. Total Environ. 435–436, 132–140. https://doi.org/10.1016/j.scitotenv.2012.06.089.

Borge, R., Narros, A., Artíñano, B., Yagüe, C., Gómez-Moreno, F.J., de la Paz, D., Román-Cascón, C., Díaz, E., Maqueda, G., Sastre, M., Quaassdorff, C., Dimitroulopoulou, C., Vardoulakis, S., 2016. Assessment of microscale spatio-temporal variation of air pollution at an urban hotspot in Madrid (Spain) through an extensive field campaign. Atmos. Environ. 140, 432–445. https://doi.org/10.1016/j.atmosenv.2016.06.020.

Chen, F., Kusaka, H., Bornstein, R., Ching, J., Grimmond, C.S.B., Grossman-Clarke, S., Loridan, T., Manning, K.W., Martilli, A., Miao, S., Sailor, D., Salamanca, F.P., Taha, H., Tewari, M., Wang, X., Wyszogrodzki, A.A., Zhang, C., 2011. The integrated WRF/urban modelling system: development, evaluation, and applications to urban environmental problems. Int. J. Climatol. 31, 273–288. https://doi.org/10.1002/joc.2158.

Coelho, S., Ferreira, J., Rodrigues, V., Lopes, M., 2022. Source apportionment of air pollution in European urban areas: lessons from the ClairCity project. J. Environ. Manag. 320, 115899. https://doi.org/10.1016/j.jenvman.2022.115899.

Degraeuwe, B., Thunis, P., Clappier, A., Weiss, M., Lefebvre, W., Janssen, S., Vranckx, S., 2017. Impact of passenger car NOX emissions on urban NO2 pollution – scenario analysis for 8 European cities. Atmos. Environ. 171, 330–337. https://doi.org/10.1016/j.atmosenv.2017.10.040.

Dejoan, A., Santiago, J.L., Martilli, A., Martin, F., Pinelli, A., 2010. Comparison between large-eddy simulation and Reynolds-averaged Navier–Stokes computations for the MUST field experiment. Part II: effects of incident wind angle deviation on the mean flow and plume dispersion. Bound.-Layer Meteorol. 135, 133–150. https://doi.org/10.1007/s10546-010-9467-2.

Di Sabatino, S., Buccolieri, R., Olesen, H.R., Ketzel, M., Berkowicz, R., Franke, J., Schatzmann, M., Schlunzen, K., Leitl, B., Britter, R., Borrego, C., Costa, A., Castelli, S., Reisin, T., Hellsten, A., Saloranta, J., Moussiopoulos, N., Barmpas, F., Brzozowski, K., Goricsan, I., Balczo, M., Bartzis, J., Efthimiou, G., Santiago, J.L., Martilli, A., Piringer, M., Baumann-Stanzer, K., Hirtl, M., Baklanov, A., Nuterman, R., Starchenko, A., 2011. COST 732 in practice: the MUST model evaluation exercise. Int. J. Environ. Pollut. 44 (1–4), 403–418. https://doi.org/10.1504/IJEP.2011.038442.

Ellison, R.B., Greaves, S.P., Hensher, D.A., 2013. Five years of London's low emission zone: effects on vehicle fleet composition and air quality. Transp. Res. Part D: Transp. Environ. 23, 25–33. https://doi.org/10.1016/j.trd.2013.03.010.

European Environment Agency, 2021. Air Quality in Europe 2021. https://www.eea.europa.eu/publications/air-quality-in-europe-2021. (Accessed 1 July 2024).

European Environment Agency, 2022. Air quality in Europe 2022. https://www.eea.europa.eu//publications/air-quality-in-europe-2022. (Accessed 1 July 2024).

European Environment Agency, 2023. Europe's Air Quality Status 2023. https://www.eea.europa.eu/publications/europes-air-quality-status-2023. (Accessed 1 July 2024).

Franke, J., Hellsten, A., Schlünzen, H., Carissimo, B., 2007. Best practice guideline for the CFD simulation of flows in the urban environment. In: COST Action 732—Quality Assurance and Improvement of Microscale Meteorological Models (Hamburg, Germany).

Gu, J., Deffner, V., Küchenhoff, H., Pickford, R., Breitner, S., Schenider, A., Kowalski, M., Peters, A., Lutz, M., Kerschbaumer, Slama, R., Morelli, X., Wichmann, H.E., Cyrys, J.,

2022. Low emission zones reduced PM_{10} but not NO_2 concentrations in Berlin and Munich, Germany. J. Environ. Manag. 302, 114048. https://doi.org/10.1016/j.jenvman.2021.114048.

Hersbach, H., Bell, B., Berrisford, P., et al., 2020. The ERA5 global reanalysis. Q. J. R. Meteorol. Soc. 146, 1999–2049. https://doi.org/10.1002/qj.3803.

Holman, C., Harrison, R., Querol, X., 2015. Review of the efficacy of low emission zones to improve urban air quality in European cities. Atmos. Environ. 111, 161–169. https://doi.org/10.1016/j.atmosenv.2015.04.009.

Jeanjean, A.P.R., Buccolieri, R., Eddy, J., Monks, P.S., Leigh, R.J., 2017. Air quality affected by trees in real street canyons: the case of Marylebone neighbourhood in central London. Urban For. Urban Green. 22, 41–53. https://doi.org/10.1016/j.ufug.2017.01.009.

Kassomenos, P.A., Flocas, H.A., Lykoudis, S., Skouloudis, A., 1998. Spatial and temporal characteristics of the relationship between air quality status and mesoscale circulation over an urban Mediterranean basin. Sci. Total Environ. 217 (1–2), 37–57. https://doi.org/10.1016/S0048-9697(98)00167-3.

Kassomenos, P.A., Vardoulakis, S., Chaloulakou, A., Paschalidou, A.K., Grivas, G., Borge, R., Lumbreras, L., 2014. Study of PM10 and PM2.5 levels in three European cities: analysis of intra and inter urban variations. Atmos. Environ. 87, 153–163. https://doi.org/10.1016/j.atmosenv.2014.01.004.

Latini, G., Grifoni, R.C., Passerini, G., 2002. Influence of meteorological parameters on urban and suburban air pollution. WIT Trans. Ecol. Environ. 53.

Ma, L., Graham, D.J., Stettler, M.E., 2021. Environ. Res. Lett. 16, 124001. https://doi.org/10.1088/1748-9326/ac30c1.

Madrid City Council Open Data Portal, 2024. https://datos.madrid.es/portal/site/egobvol. (Accessed June 2024).

Martilli, A., Clappier, A., Rotach, M.W., 2002. An urban surface exchange parameterisation for mesoscale models. Bound.-Layer Meteorol. 104, 261–304. https://doi.org/10.1023/A:1016099921195.

Martin, F., Santiago, J.L., Kracht, O., Garcia, L., Gerboles, M., 2015. FAIRMODE spatial representativeness feasibility study. In: Report EUR 27385 EN. https://doi.org/10.2788/49487. ISBN 978-92-79-50322-1 (PDF), ISSN 1831–9424 (online).

Moral-Carcedo, J., 2022. Dissuasive effect of low emission zones on traffic: the case of Madrid Central. Transportation 51, 25–49. https://doi.org/10.1007/s11116-022-10318-4.

Panteliadis, P., Strak, M., Hoek, G., Weijers, E., van der Zee, S., Dijkema, M., 2014. Implementation of a low emission zone and evaluation of effects on air quality by long-term monitoring. Atmos. Environ. 86, 113–119. https://doi.org/10.1016/j.atmosenv.2013.12.035.

Parra, M., Santiago, J.L., Martín, F., Martilli, A., Santamaría, J., 2010. A methodology to urban air quality assessment during large time periods of winter using computational fluid dynamic models. Atmos. Environ. 44 (17), 2089–2097. https://doi.org/10.1016/j.atmosenv.2010.03.009.

Quaassdorff, C., Borge, R., Pérez, J., Lumbreras, J., de la Paz, D., de Andrés, J.M., 2016. Microscale traffic simulation and emission estimation in a heavily trafficked roundabout in Madrid (Spain). Sci. Total Environ. 566–567, 416–427. https://doi.org/10.1016/j.scitotenv.2016.05.051.

Richards, P., Hoxey, R., 1993. Appropriate boundary conditions for computational wind engineering models using the k-ε turbulence model. In: Computational Wind Engineering, vol. 1, pp. 145–153. https://doi.org/10.1016/0167-6105(93)90124-7.

Rivas, E., Santiago, J.L., Lechón, Y., Martín, F., Ariño, A., Pons, J.J., Santamaría, J.M., 2019. CFD modelling of air quality in Pamplona City (Spain): assessment, stations spatial representativeness and health impacts valuation. Sci. Total Environ. 649. https://doi.org/10.1016/j.scitotenv.2018.08.315.

Salamanca, F., Krpo, A., Martilli, A., Clappier, A., 2010. A new building energy model coupled with an urban canopy parameterization for urban climate simulations—part I. Formulation, verification, and sensitivity analysis of the model. Theor. Appl. Climatol. 99, 331–344. https://doi.org/10.1007/s00704-009-0142-9.

Sanchez, B., Santiago, J.-L., Martilli, A., Palacios, M., Kirchner, F., 2016. CFD modeling of reactive pollutant dispersion in simplified urban configurations with different chemical mechanisms. Atmos. Chem. Phys. 16, 12143–12157. https://doi.org/10.5194/acp-16-12143-2016.

Sanchez, B., Santiago, J.-L., Martilli, A., Martin, F., Borge, R., Quaassdorff, C., de la Paz, D., 2017. Modelling NOX concentrations through CFD-RANS in an urban hot-spot using high resolution traffic emissions and meteorology from a mesoscale model. Atmos. Environ. 163, 155–165. https://doi.org/10.1016/j.atmosenv.2017.05.022.

Santiago, J.L., Martin, F., Martilli, A., 2013. A computational fluid dynamic modelling approach to assess the representativeness of urban monitoring stations. Sci. Total Environ. 454–455, 61–72. https://doi.org/10.1016/j.scitotenv.2013.02.068.

Santiago, J.L., Krayenhoff, E.S., Martilli, A., 2014. Flow simulations for simplified urban configurations with microscale distributions of surface thermal forcing. Urban Clim. 9, 115–133. https://doi.org/10.1016/j.uclim.2014.07.008.

Santiago, J.L., Borge, R., Sanchez, B., Quaassdorff, C., de la Paz, D., Martilli, A., Rivas, E., Martin, F., 2021. Estimates of pedestrian exposure to atmospheric pollution using high-resolution modelling in a real traffic hot-spot. Sci. Total Environ. 755, 142475. https://doi.org/10.1016/j.scitotenv.2020.142475.

Santiago, J.L., Sanchez, B., Rivas, E., Vivanco, M.G., Theobald, M.R., Garrido, J.L., Gil, V., Martilli, A., Rodríguez-Sánchez, A., Buccolieri, R., Martin, F., 2022. High spatial resolution assessment of the effect of the Spanish national air pollution control programme on street-level NO_2 concentrations in three neighborhoods of Madrid (Spain) using mesoscale and CFD modelling. Atmosphere 13 (2), 248. https://doi.org/10.3390/atmos13020248.

Thunis, P., Pisoni, E., Zauli Sajani, S., Monforti-Ferrario, F., Bessagnet, B., Vignati, E., De Meij, A., 2023. Urban PM2.5 Atlas, Air Quality in European Cities, 2023 Report. Publications Office of the European Union, Luxembourg. https://doi.org/10.2760/63641 (JRC134950).

Tominaga, Y., Stathopoulos, T., 2007. Turbulent Schmidt numbers for CFD analysis with various types of flowfield. Atmos. Environ. 41 (37), 8091–8099. https://doi.org/10.1016/j.atmosenv.2007.06.054.

Wyatt, D.W., Li, H., Tate, J.E., 2014. Energy and environmental impacts of roadway grades. Transp. Res. Part D: Transp. Environ. 32, 160–170. https://doi.org/10.1016/j.trd.2014.07.015.

References

Abou-Senna, H., Radwan, E., Westerlund, K., Cooper, C.D., 2013. Using a traffic simulation model (vissim) with an emissions model (moves) to predict emissions from vehicles on a limited-access highway. Journal of the Air & Waste Management Association 63, 819–831.

Alalwan, H.A., Alminshid, A.H., Aljaafari, H.A., 2019. Promising evolution of biofuel generations. subject review. Renewable Energy Focus 28, 127–139. URL: https://www.sciencedirect.com/science/article/pii/S1755008418303259, doi:https://doi.org/10.1016/j.ref.2018.12.006.

Alvarez Lopez, P., Behrisch, M., Bieker-Walz, L., Erdmann, J., Flötteröd, Y.P., Hilbrich, R., Lücken, L., Rummel, J., Wagner, P., Wießner, E., 2018. Microscopic traffic simulation using sumo, in: 2019 IEEE Intelligent Transportation Systems Conference (ITSC), IEEE. pp. 2575–2582. URL: https://elib.dlr.de/127994/.

Arya, P.S., 2001. Introduction to micrometeorology. volume 79. 2 ed., Academic press.

Aumont, B., Chervier, F., Laval, S., 2003. Contribution of HONO sources to the NOx/HOx/O3 chemistry in the polluted boundary layer. Atmospheric Environment 37, 487–498. URL: https://www.sciencedirect.com/science/article/pii/S1352231002009202, doi:10.1016/S1352-2310(02)00920-2.

Bachlin, W., Bosinger, R., Brand, A., Schultz, T., 2006. Oberprufung des no-no2-umwandlungsmodells fur die anwendung bei imissionsprognosen fur bodennahe stickoxidfreisetzung. Gefahrstoffe-Reinhaltung der Luft 66(4), 154–157.

Barceló, J., Ferrer, J.L., García, D., Florian, M., Saux, E.L., 1998. Parallelization of Microscopic Traffic Simulation for Att Systems Analysis. Springer US, Boston, MA. pp. 1–26. URL: https://doi.org/10.1007/978-1-4615-5757-9_1, doi:10.1007/978-1-4615-5757-9_1.

Belis, C., Karagulian, F., Larsen, B., Hopke, P., 2013. Critical review and meta-analysis of ambient particulate matter source apportionment using receptor models in Europe.

Atmospheric Environment 69, 94–108. URL: https://www.sciencedirect.com/science/article/pii/S1352231012010540, doi:10.1016/j.atmosenv.2012.11.009.

Bieser, J., Aulinger, A., Matthias, V., Quante, M., Denier van der Gon, H., 2011. Vertical emission profiles for Europe based on plume rise calculations. Nitrogen Deposition, Critical Loads and Biodiversity 159, 2935–2946. URL: https://www.sciencedirect.com/science/article/pii/S0269749111002387, doi:10.1016/j.envpol.2011.04.030.

Bigazzi, A., Van Lint, J., Klunder, G., Stelwagen, U., Ligterink, N., 2010. Traffic data for local emissions monitoring at a signalized intersection, in: 13th International IEEE Conference on Intelligent Transportation Systems, pp. 210–215. doi:10.1109/ITSC.2010.5625302.

Boogaard, H., Janssen, N.A., Fischer, P.H., Kos, G.P., Weijers, E.P., Cassee, F.R., van der Zee, S.C., de Hartog, J.J., Meliefste, K., Wang, M., Brunekreef, B., Hoek, G., 2012. Impact of low emission zones and local traffic policies on ambient air pollution concentrations. Science of The Total Environment 435-436, 132–140. URL: https://www.sciencedirect.com/science/article/pii/S0048969712009229, doi:10.1016/j.scitotenv.2012.06.089.

Borge, R., Narros, A., Artíñano, B., Yagüe, C., Gómez-Moreno, F.J., de la Paz, D., Román-Cascón, C., Díaz, E., Maqueda, G., Sastre, M., et al., 2016. Assessment of microscale spatio-temporal variation of air pollution at an urban hotspot in madrid (spain) through an extensive field campaign. Atmospheric Environment 140, 432–445.

Botzen, W.W., Nees, T., Estrada, F., 2021. Temperature Effects on Electricity and Gas Consumption: Empirical Evidence from Mexico and Projections under Future Climate Conditions. Sustainability 13. doi:10.3390/su13010305.

Bougeault, P., Lacarrere, P., 1989. Parameterization of orography-induced turbulence in a mesobeta–scale model. Monthly Weather Review 117, 1872–1890.

Boulter, P., 2005. Ppr 065 a review of emission factors and models for road vehicle non-exhaust particulate matter. URL: https://uk-air.defra.gov.uk/library/reports?report_id=364.

Briffa, J., Sinagra, E., Blundell, R., 2020. Heavy metal pollution in the environment and their toxicological effects on humans. Heliyon 6, e04691. doi:10.1016/j.heliyon.2020.e04691. place: England.

Britter, R.E., Hanna, S.R., 2003. Flow and dispersion in urban areas. Annual Review of Fluid Mechanics 35, 469–496. URL: https://www.annualreviews.org/content/journals/

10.1146/annurev.fluid.35.101101.161147, doi:https://doi.org/10.1146/annurev.fluid.35.101101.161147.

Buccolieri, R., Santiago, J.L., Rivas, E., Sanchez, B., 2018. Review on urban tree modelling in cfd simulations: Aerodynamic, deposition and thermal effects. Urban Forestry Urban Greening 31, 212–220. URL: https://www.sciencedirect.com/science/article/pii/S1618866717304600, doi:https://doi.org/10.1016/j.ufug.2018.03.003.

Burns, J., Hoffmann, S., Kurz, C., Laxy, M., Polus, S., Rehfuess, E., 2021. COVID-19 mitigation measures and nitrogen dioxide – A quasi-experimental study of air quality in Munich, Germany. Atmospheric Environment 246, 118089. URL: https://www.sciencedirect.com/science/article/pii/S1352231020308219, doi:10.1016/j.atmosenv.2020.118089.

Cameron, G., Wylie, B., McArthur, D., 1994. Paramics-moving vehicles on the connection machine, in: Supercomputing '94:Proceedings of the 1994 ACM/IEEE Conference on Supercomputing, pp. 291–300. doi:10.1109/SUPERC.1994.344292.

Chang, J.C., Hanna, S.R., 2005. Technical descriptions and user's guide for the boot statistical model evaluation software package, version 2.0. Harmonisation within atmospheric dispersion modelling for regulatory purposes .

Chen, F., Kusaka, H., Bornstein, R., Ching, J., Grimmond, C., Grossman-Clarke, S., Loridan, T., Manning, K.W., Martilli, A., Miao, S., et al., 2011. The integrated wrf/urban modelling system: development, evaluation, and applications to urban environmental problems. International Journal of Climatology 31, 273–288.

Coelho, S., Ferreira, J., Rodrigues, V., Lopes, M., 2022. Source apportionment of air pollution in European urban areas: Lessons from the ClairCity project. Journal of Environmental Management 320, 115899. URL: https://www.sciencedirect.com/science/article/pii/S0301479722014724, doi:10.1016/j.jenvman.2022.115899.

Copernicus Climate Change Service (C3S), 2021. Transparency platform. https://cds.climate.copernicus.eu/datasets/reanalysis-era5-single-levels?tab=overview. Accessed on 12th September, 2025.

Coşkun, H., Yıldırım, N., Gündüz, S., 2021. The spread of COVID-19 virus through population density and wind in Turkey cities. Science of The Total Environment 751, 141663. URL: https://www.sciencedirect.com/science/article/pii/S0048969720351925, doi:10.1016/j.scitotenv.2020.141663.

Csikós, A., Varga, I., 2012. Real-time modeling and control objective analysis of motorway emissions. Procedia - Social and Behavioral Sciences 54, 1027–1036. URL: https:

//www.sciencedirect.com/science/article/pii/S1877042812042802, doi:https://doi.org/10.1016/j.sbspro.2012.09.818. proceedings of EWGT2012 - 15th Meeting of the EURO Working Group on Transportation, September 2012, Paris.

Dalpé, B., Masson, C., 2009. Numerical simulation of wind flow near a forest edge. Journal of wind engineering and industrial aerodynamics 97, 228–241.

De Cian, E., Lanzi, E., Roson, R., 2007. The Impact of Temperature Change on Energy Demand: A Dynamic Panel Analysis. Technical Report. URL: https://ageconsearch.umn.edu/record/9322/files/wp070046.pdf, doi:10.22004/ag.econ.9322.

Degraeuwe, B., Thunis, P., Clappier, A., Weiss, M., Lefebvre, W., Janssen, S., Vranckx, S., 2017. Impact of passenger car NOX emissions on urban NO2 pollution – Scenario analysis for 8 European cities. Atmospheric Environment 171, 330–337. URL: https://www.sciencedirect.com/science/article/pii/S1352231017307057, doi:10.1016/j.atmosenv.2017.10.040.

Dejoan, A., Santiago, J.L., Martilli, A., Martin, F., Pinelli, A., 2010. Comparison Between Large-Eddy Simulation and Reynolds-Averaged Navier–Stokes Computations for the MUST Field Experiment. Part II: Effects of Incident Wind Angle Deviation on the Mean Flow and Plume Dispersion. Boundary-Layer Meteorology 135, 133–150. URL: https://doi.org/10.1007/s10546-010-9467-2, doi:10.1007/s10546-010-9467-2.

Den Braven, K.R., Abdel-Rahim, A., Henrickson, K., Battles, A., 2012. Modeling vehicle fuel consumption and emissions at signalized intersection approaches : integrating field-collected data into microscopic simulation. URL: /view/dot/25382.

Di Sabatino, S., Buccolieri, R., Olesen, H., Ketzel, M., Berkowicz, R., Franke, J., Schatzmann, M., Schlunzen, K., Leitl, B., Britter, R., Borreco, C., Costa, A., Castelli, S., Reisin, T., Hellsten, A., Saloranta, J., Moussiopoulos, N., Barmpas, F., Brzozowski, K., Goricsan, I., Balczo, M., Bartzis, J., Efhimiou, G., Santiago, J., Martilli, A., Piringer, M., Baumann-Stanzer, K., Hirtl, M., Baklanov, A., Nuterman, R., Starchenko, A., 2011. Cost 732 in practice: the must model evaluation exercise , 403–418URL: https://www.inderscienceonline.com/doi/abs/10.1504/IJEP.2011.038442, doi:10.1504/IJEP.2011.038442.

Directive 2001/81/EC, 2001. Directive 2001/81/EC of the European Parliament and of the Council of 23 October 2001 on national emission ceilings for certain atmospheric pollutants. Technical Report. Official Journal of the European Union.

Directive 2008/50/EC, 2008. Directive 2008/50/EC, D. (2008). Ambient air quality and cleaner air for Europe. Technical Report. Official Journal of the European Union.

Directive 2014/23/EU, 2014. Directive 2014/23/eu of the european parliament and of the council of 26 february 2014 on the award of concession contracts text with eea relevance. Official Journal of the European Communities , 32014L0023.

Directive 2016/2284, 2016. Directive (EU) 2016/2284 of the European Parliament and of the Council of 14 December 2016 on the reduction of national emissions of certain atmospheric pollutants, amending Directive 2003/35/EC and repealing Directive 2001/81/EC. Technical Report. Official Journal of the European Union.

Directive (EU) 2024/2881, 2024. Directive (eu) 2024/2881 of the european parliament and of the council of 23 october 2024 on ambient air quality and cleaner air for europe (recast). Official Journal of the European Communities , 32024L2881.

Düring, I., Bächlin, W., Ketzel, M., Baum, A., Friedrich, U., Wurzler, S., 2011. Impact of realistic hourly emissions profiles on air pollutants concentrations modelled with CHIMERE. Atmospheric Environment 20, 67–73. URL: https://www.schweizerbart.de/papers/metz/detail/20/75684/A_new_simplified_NO_NO2_conversion_model_under_consideration_of_direct_NO2_emissions, doi:10.1127/0941-2948/2011/0491.

Ebel, A., Friedrich, R., Rodhe, H., 1994. Tropospheric modelling and emission estimation: Generation of european emission data for episodes (genemis) project, eurotrac annual report 1993, part 5. EUROTRAC Annual report .

EEA, 2016. Explaining road transport emissions - A non-technical guide. ISBN: 978-92-9213-723-6. Technical Report. European Environment Agency (EEA). URL: https://doi.org/10.2800/71804.

EEA, 2017. Air Quality in Europe-2017 Report. EEA Technical Report No 13/2017. ISBN: 978-92-9213-921-6. Technical Report. European Environment Agency (EEA). URL: http://www.eea.europa.eu/publications/air-quality-in-europe-2017.

EEA, 2021. Air Quality in Europe 2021. https://www.eea.europa.eu/publications/air-quality-in-europe-2021. Accessed on 29th August, 2025.

EEA, 2022. Air Quality in Europe 2022. https://www.eea.europa.eu/publications/air-quality-in-europe-2022. Accessed on 29th August, 2025.

EEA, 2023. Transport and environment report 2022. Technical Report. European Environment Agency (EEA). URL: https://www.eea.europa.eu/ds_resolveuid/32ddca81444147fdb729523b3a98fe91.

EEA, 2024. Europe's Air Quality Status 2024. EEA Technical Report No 06/2024. ISBN: 978-92-9480-650-5. Technical Report. European Environment Agency (EEA). URL: https://www.eea.europa.eu/publications/europes-air-quality-status-2024.

EEA, 2025. Europe's Air Quality Status 2025. EEA Technical Report No 06/2024. ISBN: 978-92-9480-710-6. Technical Report. European Environment Agency (EEA). URL: https://www.eea.europa.eu/en/analysis/publications/air-quality-status-report-2025.

Ellison, R.B., Greaves, S.P., Hensher, D.A., 2013. Five years of London's low emission zone: Effects on vehicle fleet composition and air quality. Transportation Research Part D: Transport and Environment 23, 25–33. URL: https://www.sciencedirect.com/science/article/pii/S136192091300059X, doi:10.1016/j.trd.2013.03.010.

EMEP, 2025. How to measure vehicle emissions. https://www.ceip.at/webdab-emission-database/emissions-as-used-in-emep-models. Accessed on 29th August, 2025.

EMEP/CEIP, 2020. Officially reported emission data. https://www.ceip.at/webdab-emission-database/reported-emissiondata. Accessed on 12th September, 2025.

EMEP/EEA, 2023. EMEP/EEA air pollutant emission inventory guidebook 2023 – Technical guidance to prepare national emission inventories. Publications Office of the European Union. doi:http://www.doi.org/10.2800/795737.

ENTSO-E, 2021. Transparency platform. https://transparency.entsoe.eu/. Accessed on 12th September, 2025.

EPA, 2025. Hydrogen in transportation. https://www.epa.gov/greenvehicles/hydrogen-transportation. Accessed on 17th September, 2025.

EUROCONTROL, 2021a. Co2 emissions by state. oper. airports 2020. https://ansperformance.eu/data/. Accessed on 12th September, 2025.

EUROCONTROL, 2021b. Daily traffic variation - states. https://www.eurocontrol.int/Economics/DailyTrafficVariation-States.html?ectl-covid=. Accessed on 12th September, 2025.

European Alternative Fuels Observatory, 2025. European union (eu27): Vehicles and fleet). https://alternative-fuels-observatory.ec.europa.eu/transport-mode/road/european-union-eu27/vehicles-and-fleet. Accessed on 29th August, 2025.

European Commission, 2025. How to measure vehicle emissions. https://wikis.ec.europa.eu/spaces/ULEV/pages/44142156/How+to+measure+vehicle+emissions.

European Institute of Innovation & Technology, 2025. Boosting electric vehicles charging infrastructure network in Europe. https://www.eit.europa.eu/news-events/news/boosting-electric-vehicles-charging-infrastructure-network-europe. Accessed on 29th August, 2025.

Eurostat, 2025. Electricity production, consumption and market overview. available online (18th july, 2025). Eurostat URL: https://ec.europa.eu/eurostat/statistics-explained/index.php?title=Electricity_production,_consumption_and_market_overview.

Eurostat, 2025. Energy balances - eurostat. https://ec.europa.eu/eurostat/statistics-explained/index.php?title=Energy_balance_-_new_methodology. Accessed on 12th September, 2025.

Fioletov, V., McLinden, C.A., Griffin, D., Krotkov, N., Liu, F., Eskes, H., 2022. Quantifying urban, industrial, and background changes in no_2 during the covid-19 lockdown period based on tropomi satellite observations. Atmospheric Chemistry and Physics 22, 4201–4236. URL: https://acp.copernicus.org/articles/22/4201/2022/, doi:10.5194/acp-22-4201-2022.

Franke, J., 2007. Best practice guideline for the CFD simulation of flows in the urban environment. Meteorological Inst.

Friedrich, R., 2000. GENEMIS: Generation of European Emission Data for Episodes, in: Borrell, P., Borrell, P.M. (Eds.), Transport and Chemical Transformation of Pollutants in the Troposphere: An Overview of the Work of EUROTRAC. Springer Berlin Heidelberg, Berlin, Heidelberg, pp. 375–386. URL: https://doi.org/10.1007/978-3-642-59718-3_18, doi:10.1007/978-3-642-59718-3_18.

Google, L.L.C., 2021. Google covid-19 community mobility reports. https://www.google.com/covid19/mobility/. Accessed on 12th September, 2025.

Goricsán, I., Balczó, M., Balogh, M., Czáder, K., Rákai, A., Tonkó, C., 2011. Simulation of flow in an idealised city using various cfd codes. International journal of Environment and Pollution 44, 359–367.

Granier, C., Darras, H., van der Gon, D., Doubalova, J., Elguindi, N., Galle, B., Gauss, M., Guevara, M., Jalkanen, J.P., Kuenen, J., Liousse, C., Quack, B., Simpson, D., Sindelarova, K., 2019. The Copernicus Atmosphere Monitoring Service global and regional emissions (April 2019 version). Technical Report. Copernicus Atmosphere Monitoring Service (CAMS) report. doi:10.24380/d0bn-kx16.

Gu, J., Deffner, V., Küchenhoff, H., Pickford, R., Breitner, S., Schneider, A., Kowalski, M., Peters, A., Lutz, M., Kerschbaumer, A., Slama, R., Morelli, X., Wichmann, H.E., Cyrys, J., 2022. Low emission zones reduced PM10 but not NO2 concentrations in Berlin and Munich, Germany. Journal of Environmental Management 302, 114048. URL: https://www.sciencedirect.com/science/article/pii/S0301479721021101, doi:10.1016/j.jenvman.2021.114048.

Guenther, A., Karl, T., Harley, P., Wiedinmyer, C., Palmer, P.I., Geron, C., 2006a. Estimates of global terrestrial isoprene emissions using megan (model of emissions of gases and aerosols from nature). Atmospheric Chemistry and Physics 6, 3181–3210. URL: https://acp.copernicus.org/articles/6/3181/2006/, doi:10.5194/acp-6-3181-2006.

Guenther, A., Karl, T., Harley, P., Wiedinmyer, C., Palmer, P.I., Geron, C., 2006b. Estimates of global terrestrial isoprene emissions using megan (model of emissions of gases and aerosols from nature). Atmospheric Chemistry and Physics 6, 3181–3210. URL: https://acp.copernicus.org/articles/6/3181/2006/, doi:10.5194/acp-6-3181-2006.

Guevara, M., Jorba, O., Soret, A., Petetin, H., Bowdalo, D., Serradell, K., Tena, C., Denier van der Gon, H., Kuenen, J., Peuch, V.H., Pérez García-Pando, C., 2021. Time-resolved emission reductions for atmospheric chemistry modelling in europe during the covid-19 lockdowns. Atmospheric Chemistry and Physics 21, 773–797. URL: https://acp.copernicus.org/articles/21/773/2021/, doi:10.5194/acp-21-773-2021.

Hale, T., Angrist, N., Goldszmidt, R., Kira, B., Petherick, A., Phillips, T., Webster, S., Cameron-Blake, E., Hallas, L., Majumdar, S., Tatlow, H., 2021. A global panel database of pandemic policies (Oxford COVID-19 Government Response Tracker). Nature Human Behaviour 5, 529–538. URL: https://doi.org/10.1038/s41562-021-01079-8, doi:10.1038/s41562-021-01079-8.

Hausberger, S., 2009. Emission factors from the model phem for the hbefa version 3 .

Hausberger, S., Krajzewicz, D., 2014. Extended simulation tool phem coupled to sumo with user guide. COLOMBO deliverable 4.2 , 1–55.

Hefny Salim, M., Heinke Schlünzen, K., Grawe, D., 2015. Including trees in the numerical simulations of the wind flow in urban areas: Should we care? Journal of Wind Engineering and Industrial Aerodynamics 144, 84–95. URL: https://www.sciencedirect.com/science/article/pii/S0167610515001178, doi:https://doi.org/10.1016/j.jweia.2015.05.004. selected papers from the 6th International Symposium on Computational Wind Engineering CWE 2014.

Hersbach, H., Bell, B., Berrisford, P., Hirahara, S., Horányi, A., Muñoz-Sabater, J., Nicolas, J., Peubey, C., Radu, R., Schepers, D., Simmons, A., Soci, C., Abdalla, S., Abellan, X., Balsamo, G., Bechtold, P., Biavati, G., Bidlot, J., Bonavita, M., De Chiara, G., Dahlgren, P., Dee, D., Diamantakis, M., Dragani, R., Flemming, J., Forbes, R., Fuentes, M., Geer, A., Haimberger, L., Healy, S., Hogan, R.J., Hólm, E., Janisková, M., Keeley, S., Laloyaux, P., Lopez, P., Lupu, C., Radnoti, G., de Rosnay, P., Rozum, I., Vamborg, F., Villaume, S., Thépaut, J.N., 2020. The era5 global reanalysis. Quarterly Journal of the Royal Meteorological Society 146, 1999–2049. URL: https://rmets.onlinelibrary.wiley.com/doi/abs/10.1002/qj.3803, doi:https://doi.org/10.1002/qj.3803, arXiv:https://rmets.onlinelibrary.wiley.com/doi/pdf/10.1002/qj.3803.

Holman, C., Harrison, R., Querol, X., 2015. Review of the efficacy of low emission zones to improve urban air quality in european cities. Atmospheric Environment 111, 161–169. URL: https://www.sciencedirect.com/science/article/pii/S1352231015300145, doi:https://doi.org/10.1016/j.atmosenv.2015.04.009.

Jalkanen, J.P., Johansson, L., Kukkonen, J., 2016. A comprehensive inventory of ship traffic exhaust emissions in the european sea areas in 2011. Atmospheric Chemistry and Physics 16, 71–84. URL: https://acp.copernicus.org/articles/16/71/2016/, doi:10.5194/acp-16-71-2016.

Jalkanen, J.P., Johansson, L., Kukkonen, J., Brink, A., Kalli, J., Stipa, T., 2012. Extension of an assessment model of ship traffic exhaust emissions for particulate matter and carbon monoxide. Atmospheric Chemistry and Physics 12, 2641–2659. URL: https://acp.copernicus.org/articles/12/2641/2012/, doi:10.5194/acp-12-2641-2012.

Johansson, L., Jalkanen, J.P., Kalli, J., Kukkonen, J., 2013. The evolution of shipping emissions and the costs of regulation changes in the northern eu area. Atmospheric Chemistry and Physics 13, 11375–11389. URL: https://acp.copernicus.org/articles/13/11375/2013/, doi:10.5194/acp-13-11375-2013.

Johansson, L., Jalkanen, J.P., Kukkonen, J., 2017. Global assessment of shipping emissions in 2015 on a high spatial and temporal resolution. Atmospheric Environment 167, 403–415. URL: https://www.sciencedirect.com/science/article/pii/S1352231017305563, doi:10.1016/j.atmosenv.2017.08.042.

Jurado, X., Reiminger, N., Vazquez, J., Wemmert, C., Dufresne, M., Blond, N., Wertel, J., 2020. Assessment of mean annual no2 concentration based on a partial dataset. Atmospheric Environment 221, 117087. URL: https://www.sciencedirect.com/science/article/pii/S1352231019307265, doi:https://doi.org/10.1016/j.atmosenv.2019.117087.

Kassomenos, P., Flocas, H., Lykoudis, S., Skouloudis, A., 1998. Spatial and temporal characteristics of the relationship between air quality status and mesoscale circulation over an urban Mediterranean basin. Science of The Total Environment 217, 37–57. URL: https://www.sciencedirect.com/science/article/pii/S0048969798001673, doi:10.1016/S0048-9697(98)00167-3.

Kassomenos, P., Vardoulakis, S., Chaloulakou, A., Paschalidou, A., Grivas, G., Borge, R., Lumbreras, J., 2014. Study of PM10 and PM2.5 levels in three European cities: Analysis of intra and inter urban variations. Atmospheric Environment 87, 153–163. URL: https://www.sciencedirect.com/science/article/pii/S1352231014000132, doi:10.1016/j.atmosenv.2014.01.004.

Kim, J.J., Baik, J.J., 2004. A numerical study of the effects of ambient wind direction on flow and dispersion in urban street canyons using the rng k– turbulence model. Atmospheric Environment 38, 3039–3048. URL: https://www.sciencedirect.com/science/article/pii/S1352231004001773, doi:https://doi.org/10.1016/j.atmosenv.2004.02.047.

Krauss, S., 1998. Microscopic modeling of traffic flow: Investigation of collision free vehicle dynamics. Deutsches Zentrum für Luft– und Raumfahrt URL: DoctoralDissertation.

Kuenen, J., Dellaert, S., Visschedijk, A., Jalkanen, J.P., Super, I., Denier van der Gon, H., 2022. Cams-reg-v4: a state-of-the-art high-resolution european emission inventory for air quality modelling. Earth System Science Data 14, 491–515. URL: https://essd.copernicus.org/articles/14/491/2022/, doi:10.5194/essd-14-491-2022.

Kurtenbach, R., Becker, K., Gomes, J., Kleffmann, J., Lörzer, J., Spittler, M., Wiesen, P., Ackermann, R., Geyer, A., Platt, U., 2001. Investigations of emissions and heterogeneous formation of HONO in a road traffic tunnel. Atmospheric Environment 35, 3385–3394. URL: https://www.sciencedirect.com/science/article/pii/S1352231001001388, doi:10.1016/S1352-2310(01)00138-8.

Latini, G., Cocci Grifoni, R., Passerini, G., 2002. Influence of meteorological parameters on urban and suburban air pollution. Air Pollution IX , 753–762.

Launder, B.E., Spalding, D.B., 1974. The numerical computation of turbulent flows. Computer methods in applied mechanics and engineering 3, 269–289.

Le Quéré, C., Jackson, R.B., Jones, M.W., Smith, A.J.P., Abernethy, S., Andrew, R.M., De-Gol, A.J., Willis, D.R., Shan, Y., Canadell, J.G., Friedlingstein, P., Creutzig, F., Peters, G.P., 2020. Temporary reduction in daily global CO2 emissions during the

COVID-19 forced confinement. Nature Climate Change 10, 647–653. URL: https://doi.org/10.1038/s41558-020-0797-x, doi:10.1038/s41558-020-0797-x.

Ley 7/2021, 2021. Ley 7/2021, de 20 de mayo, de cambio climático y transición energética. Boletín Oficial del Estado 121, 62009–62052.

Li, J., Sun, Z., Lenschow, D.H., Zhou, M., Dou, Y., Cheng, Z., Wang, Y., Li, Q., 2020. A foehn-induced haze front in beijing: observations and implications. Atmospheric Chemistry and Physics 20, 15793–15809. URL: https://acp.copernicus.org/articles/20/15793/2020/, doi:10.5194/acp-20-15793-2020.

Litman, T., 2013. Comprehensive evaluation of energy conservation and emission reduction policies. Transportation Research Part A: Policy and Practice 47, 153–166. URL: https://www.sciencedirect.com/science/article/pii/S0965856412001619, doi:https://doi.org/10.1016/j.tra.2012.10.022.

LMD, 2025. Chimere documentation. https://www.lmd.polytechnique.fr/chimere/docs/CHIMEREdoc_v2023.pdf. Accessed on 17th September, 2025.

Ma, L., Graham, D.J., Stettler, M.E.J., 2021. Has the ultra low emission zone in London improved air quality? Environmental Research Letters 16, 124001. URL: https://dx.doi.org/10.1088/1748-9326/ac30c1, doi:10.1088/1748-9326/ac30c1. publisher: IOP Publishing.

Madrid-City-Council, 2025. Madrid municipality bus fleet. available online (18th july, 2025) URL: https://www.emtmadrid.es/Empresa/Somos/NuestraFlota.

Madrid City-Council, 2025. Madrid municipality opendata portal. https://datos.madrid.es/portal/site/egob. Accessed on 12th September, 2025.

Martilli, A., Clappier, A., Rotach, M.W., 2002. An urban surface exchange parameterisation for mesoscale models. Boundary-Layer Meteorology 104, 261–304.

Martín, F., Santiago, J.L., Kracht, O., García, L., Gerboles, M., 2015. FAIRMODE Spatial representativeness feasibility study. Report number: Report eur 27385 en. Affiliation: European Commission Joint Research Centre Institute for Environment and Sustainability. .

Martín, F., Janssen, S., Rodrigues, V., Sousa, J., Santiago, J., Rivas, E., Stocker, J., Jackson, R., Russo, F., Villani, M., Tinarelli, G., Barbero, D., José, R.S., Pérez-Camanyo, J., Santos, G.S., Bartzis, J., Sakellaris, I., Horváth, Z., Környei, L., Liszkai, B., Kovács, , Jurado, X., Reiminger, N., Thunis, P., Cuvelier, C., 2024. Using dispersion models at microscale to assess long-term air pollution in urban hot spots: A FAIRMODE

joint intercomparison exercise for a case study in Antwerp. Science of The Total Environment 925, 171761. URL: https://www.sciencedirect.com/science/article/pii/S0048969724019041, doi:10.1016/j.scitotenv.2024.171761.

Martín, F., Rodrigues, V., Santiago, J., Sousa, J., Stocker, J., Janssen, S., Jackson, R., Russo, F., Villani, M., Tinarelli, G., Barbero, D., José, R.S., Pérez-Camanyo, J., Sousa-Santos, G., Tarrason, L., Bartzis, J., Sakellaris, I., Horváth, Z., Környei, L., Jurado, X., Reiminger, N., Masey, N., Hamilton, S., Rivas, E., Cuvelier, C., Thunis, P., 2025. Estimating the air quality standard exceedance areas and the spatial representativeness of urban air quality stations applying microscale modelling. Science of The Total Environment 988, 179824. URL: https://www.sciencedirect.com/science/article/pii/S0048969725014652, doi:10.1016/j.scitotenv.2025.179824.

McCrae, I., Barlow, T., Latham, S., 2006. Instantaneous vehicle emission monitoring. trl project report. PPR126 .

McTrans Center, 2025. Tsis-corsim (traffic software integrated system-corridor simulation). https://mctrans.ce.ufl.edu/tsis-corsim/. Accessed on 29th August, 2025.

Menut, L., Bessagnet, B., Khvorostyanov, D., Beekmann, M., Blond, N., Colette, A., Coll, I., Curci, G., Foret, G., Hodzic, A., Mailler, S., Meleux, F., Monge, J.L., Pison, I., Siour, G., Turquety, S., Valari, M., Vautard, R., Vivanco, M.G., 2013. Chimere 2013: a model for regional atmospheric composition modelling. Geoscientific Model Development 6, 981–1028. URL: https://gmd.copernicus.org/articles/6/981/2013/, doi:10.5194/gmd-6-981-2013.

Menut, L., Chiapello, I., Moulin, C., 2009. Predictability of mineral dust concentrations: The african monsoon multidisciplinary analysis first short observation period forecasted with chimere-dust. Journal of Geophysical Research: Atmospheres 114. URL: https://agupubs.onlinelibrary.wiley.com/doi/abs/10.1029/2008JD010523, doi:https://doi.org/10.1029/2008JD010523, arXiv:https://agupubs.onlinelibrary.wiley.com/doi/pdf/10.1029/2008JD010523.

Menut, L., Goussebaile, A., Bessagnet, B., Khvorostiyanov, D., Ung, A., 2012. Impact of realistic hourly emissions profiles on air pollutants concentrations modelled with CHIMERE. Atmospheric Environment 49, 233–244. URL: https://www.sciencedirect.com/science/article/pii/S1352231011012441, doi:10.1016/j.atmosenv.2011.11.057.

Ministerio Para la Transición Ecológica y Reto Demográfico, 2019. I Programa Nacional de Control de la Contaminación Atmosférica. Technical Report. Gobierno de

España. URL: https://www.miteco.gob.es/es/calidad-y-evaluacion-ambiental/temas/emisiones-a-la-atmosfera/emisiones-pncca-.html.

Ministerio Para la Transición Ecológica y Reto Demográfico, 2024. Actualización del Programa Nacional de Control de la Contaminación Atmosférica 2023-2030. Technical Report. Gobierno de España. URL: https://www.miteco.gob.es/content/dam/miteco/es/calidad-y-evaluacion-ambiental/sgalsi/atm%C3%B3sfera-y-calidad-del-aire/emisiones/pol-med/actualizacion_pncca2023_240115.pdf.

Moral-Carcedo, J., 2024. Dissuasive effect of low emission zones on traffic: the case of Madrid Central. Transportation 51, 25–49. URL: https://doi.org/10.1007/s11116-022-10318-4, doi:10.1007/s11116-022-10318-4.

Murakami, S., 1990. Numerical simulation of turbulent flowfield around cubic model current status and applications of k model and les. Journal of Wind Engineering and Industrial Aerodynamics 33, 139–152. URL: https://www.sciencedirect.com/science/article/pii/016761059090030G, doi:https://doi.org/10.1016/0167-6105(90)90030-G.

NCAR, . Wrf users guide documentation URL: https://www2.mmm.ucar.edu/wrf/users/wrf_users_guide/build/html/index.html.

NCEP/NOAA, 2025. Gfs numerical forecast system model. available online (28th july, 2025). NCEP/NOAA URL: https://www.emc.ncep.noaa.gov/emc/pages/numerical_forecast_systems/gfs.php.

Negrenti, E., 1999. The 'corrected average speed' approach in enea's tee model: an innovative solution for the evaluation of the energetic and environmental impacts of urban transport policies. Science of The Total Environment 235, 411–413. URL: https://www.sciencedirect.com/science/article/pii/S0048969799002491, doi:https://doi.org/10.1016/S0048-9697(99)00249-1.

Ntziachristos, L., Gkatzoflias, D., Kouridis, C., Samaras, Z., 2009. Copert: A european road transport emission inventory model, in: Athanasiadis, I.N., Rizzoli, A.E., Mitkas, P.A., Gómez, J.M. (Eds.), Information Technologies in Environmental Engineering, Springer Berlin Heidelberg, Berlin, Heidelberg. pp. 491–504.

Odyssee-Mure, 2025. Sectoral profile - households. https://www.odyssee-mure.eu/publications/efficiency-by-sector/households/heating-energy-consumption-by-energy-sources.html. Accessed on 12th September, 2025.

Oke, T.R., 1997. Urban environments. McGill–Queen's University Press.

Pamidimukkala, A., Kermanshachi, S., Rosenberger, J.M., Hladik, G., 2024. Barriers and motivators to the adoption of electric vehicles: A global review. Green Energy and Intelligent Transportation 3, 100153. URL: https://www.sciencedirect.com/science/article/pii/S2773153724000057, doi:10.1016/j.geits.2024.100153.

Panteliadis, P., Strak, M., Hoek, G., Weijers, E., van der Zee, S., Dijkema, M., 2014. Implementation of a low emission zone and evaluation of effects on air quality by long-term monitoring. Atmospheric Environment 86, 113–119. URL: https://www.sciencedirect.com/science/article/pii/S1352231013009801, doi:10.1016/j.atmosenv.2013.12.035.

Parra, M., Santiago, J., Martín, F., Martilli, A., Santamaría, J., 2010. A methodology to urban air quality assessment during large time periods of winter using computational fluid dynamic models. Atmospheric Environment 44, 2089–2097.

Passant, N., 2002. Speciation of uk emissions of non-methane volatile organic compounds. DEFRA,Oxon .

PTV Group, 2025. Ptv vissim. https://www.ptvgroup.com/es/productos/ptv-vissim. Accessed on 29th August, 2025.

Putaud, J.P., Pozzoli, L., Pisoni, E., Martins Dos Santos, S., Lagler, F., Lanzani, G., Dal Santo, U., Colette, A., 2021. Impacts of the covid-19 lockdown on air pollution at regional and urban background sites in northern italy. Atmospheric Chemistry and Physics 21, 7597–7609. URL: https://acp.copernicus.org/articles/21/7597/2021/, doi:10.5194/acp-21-7597-2021.

Quaassdorff, C., 2018. Development of a microscale traffic emission simulation system. application to madrid for the definition of air quality improvement measures. Universidad Politécnica de Madrid URL: DoctoralDissertation.

Quaassdorff, C., Borge, R., Pérez, J., Lumbreras, J., de la Paz, D., de Andrés, J.M., 2016. Microscale traffic simulation and emission estimation in a heavily trafficked roundabout in madrid (spain). Science of The Total Environment 566, 416–427.

Quaassdorff, C., Smit, R., Borge, R., Hausberger, S., 2022. Comparison of microscale traffic emission models for urban networks. Environmental Research Letters 17, 094030. URL: https://dx.doi.org/10.1088/1748-9326/ac8b21, doi:10.1088/1748-9326/ac8b21. publisher: IOP Publishing.

Real Decreto 102/2011, 2011. Real decreto 102/2011, de 28 de enero, relativo a la mejora de la calidad del aire. Boletín Oficial del Estado 25.

Real Decreto 39/2017, 2017. Real decreto 39/2017, de 27 de enero, por el que se modifica el real decreto 102/2011, de 28 de enero, relativo a la mejora de la calidad del aire. Boletín Oficial del Estado 24, 6918–6930.

Real Decreto-ley 29/2021, 2021. Real decreto-ley 29/2021, de 21 de diciembre, por el que se adoptan medidas urgentes en el ámbito energético para el fomento de la movilidad eléctrica, el autoconsumo y el despliegue de energías renovables. Boletín Oficial del Estado 305.

Reiminger, N., Jurado, X., Maurer, L., Vazquez, J., Wemmert, C., 2024. Modeling no2 concentrations in real urban areas using computational fluid dynamics: A comparative analysis of methods to assess no2 concentrations from nox dispersion results. Sustainable Cities and Society 103, 105286. URL: https://www.sciencedirect.com/science/article/pii/S2210670724001148, doi:https://doi.org/10.1016/j.scs.2024.105286.

Reynolds, O., 1895. Iv. on the dynamical theory of incompressible viscous fluids and the determination of the criterion. Philosophical Transactions of the Royal Society of London. (A.) 186, 123–164. URL: https://royalsocietypublishing.org/doi/abs/10.1098/rsta.1895.0004, doi:10.1098/rsta.1895.0004, arXiv:https://royalsocietypublishing.org/doi/pdf/10.1098/rsta.1895.0004.

Reşitoğlu, A., Altinişik, K., Keskin, A., 2015. The pollutant emissions from diesel-engine vehicles and exhaust aftertreatment systems. Clean Technologies and Environmental Policy 17, 15–27. URL: https://doi.org/10.1007/s10098-014-0793-9, doi:10.1007/s10098-014-0793-9.

Richards, P., Hoxey, R., 1993. Appropriate boundary conditions for computational wind engineering models using the k-ε turbulence model. Journal of wind engineering and industrial aerodynamics 46, 145–153.

Rivas, E., Santiago, J.L., Lechón, Y., Martín, F., Ariño, A., Pons, J.J., Santamaría, J.M., 2019. Cfd modelling of air quality in pamplona city (spain): Assessment, stations spatial representativeness and health impacts valuation. Science of The Total Environment 649, 1362–1380. URL: https://www.sciencedirect.com/science/article/pii/S004896971833287X, doi:https://doi.org/10.1016/j.scitotenv.2018.08.315.

Rodriguez-Rey, D., Guevara, M., Linares, M.P., Casanovas, J., Salmerón, J., Soret, A., Jorba, O., Tena, C., Pérez García-Pando, C., 2021. A coupled macroscopic traffic and pollutant emission modelling system for Barcelona. Transportation Research Part D: Transport and Environment 92, 102725. URL: https://www.sciencedirect.com/science/article/pii/S1361920921000274, doi:10.1016/j.trd.2021.102725.

Rodríguez-Sánchez, A., Vivanco, M.G., Theobald, M.R., Martín, F., 2022. Estimating the effect of the covid-19 pandemic on pollutant emissions in europe. Atmospheric Pollution Research 13, 101388. URL: https://www.sciencedirect.com/science/article/pii/S1309104222000745, doi:https://doi.org/10.1016/j.apr.2022.101388.

Román-Cascón, C., Yagüe, C., Ortiz-Corral, P., Serrano, E., Sánchez, B., Sastre, M., Maqueda, G., Alonso-Blanco, E., Artiñano, B., Gómez-Moreno, F., Diaz-Ramiro, E., Fernández, J., Martilli, A., García, A., Núñez, A., Cordero, J., Narros, A., Borge, R., 2023. Wind and turbulence relationship with NO2 in an urban environment: a fine-scale observational analysis. Urban Climate 51, 101663. URL: https://www.sciencedirect.com/science/article/pii/S2212095523002572, doi:10.1016/j.uclim.2023.101663.

Rotach, M.W., 1999. On the influence of the urban roughness sublayer on turbulence and dispersion. Atmospheric Environment 33, 4001–4008. URL: https://www.sciencedirect.com/science/article/pii/S1352231099001417, doi:https://doi.org/10.1016/S1352-2310(99)00141-7.

Roth, M., 2000. Review of atmospheric turbulence over cities. Quarterly Journal of the Royal Meteorological Society 126, 941–990. URL: https://rmets.onlinelibrary.wiley.com/doi/abs/10.1002/qj.49712656409, doi:https://doi.org/10.1002/qj.49712656409, arXiv:https://rmets.onlinelibrary.wiley.com/doi/pdf/10.1002/qj.49712656409.

Ryu, B.Y., Jung, H.J., Bae, S.H., 2015. Development of a corrected average speed model for calculating carbon dioxide emissions per link unit on urban roads. Transportation Research Part D: Transport and Environment 34, 245–254. URL: https://www.sciencedirect.com/science/article/pii/S1361920914001539, doi:https://doi.org/10.1016/j.trd.2014.10.012.

Sadler Consultants, Ltd., 2025. Urban Access Regulations in Europe. https://urbanaccessregulations.eu. Accessed on 29th August, 2025.

Salamanca, F., Krpo, A., Martilli, A., Clappier, A., 2010. A new building energy model coupled with an urban canopy parameterization for urban climate simulations—part i. formulation, verification, and sensitivity analysis of the model. Theoretical and applied climatology 99, 331–344.

Salmond, J.A., McKendry, I., 2009. Influences of meteorology on air pollution concentrations and processes in urban areas. Air Quality in Urban Environments 28, 23.

Sanchez, B., Santiago, J.L., Martilli, A., Martin, F., Borge, R., Quaassdorff, C., de la Paz, D., 2017. Modelling nox concentrations through cfd-rans in an urban hot-spot using

high resolution traffic emissions and meteorology from a mesoscale model. Atmospheric Environment 163, 155–165.

Sanchez, B., Santiago, J.L., Martilli, A., Palacios, M., Kirchner, F., 2016. Cfd modeling of reactive pollutant dispersion in simplified urban configurations with different chemical mechanisms. Atmospheric Chemistry and Physics 16, 12143–12157. URL: https://acp.copernicus.org/articles/16/12143/2016/, doi:10.5194/acp-16-12143-2016.

Santiago, J., Borge, R., Martin, F., de la Paz, D., Martilli, A., Lumbreras, J., Sanchez, B., 2017a. Evaluation of a cfd-based approach to estimate pollutant distribution within a real urban canopy by means of passive samplers. Science of The Total Environment 576, 46–58.

Santiago, J., Borge, R., Sanchez, B., Quaassdorff, C., de la Paz, D., Martilli, A., Rivas, E., Martín, F., 2021. Estimates of pedestrian exposure to atmospheric pollution using high-resolution modelling in a real traffic hot-spot. Science of The Total Environment 755, 142475. URL: https://www.sciencedirect.com/science/article/pii/S0048969720360046, doi:10.1016/j.scitotenv.2020.142475.

Santiago, J.L., Martilli, A., Martín, F., 2007. CFD simulation of airflow over a regular array of cubes. Part I: Three-dimensional simulation of the flow and validation with wind-tunnel measurements. Boundary-Layer Meteorology 122, 609–634. URL: https://doi.org/10.1007/s10546-006-9123-z, doi:10.1007/s10546-006-9123-z.

Santiago, J.L., Martín, F., Martilli, A., 2013. A computational fluid dynamic modelling approach to assess the representativeness of urban monitoring stations. Science of The Total Environment 454-455, 61–72. URL: https://www.sciencedirect.com/science/article/pii/S0048969713002532, doi:https://doi.org/10.1016/j.scitotenv.2013.02.068.

Santiago, J.L., Rivas, E., Sanchez, B., Buccolieri, R., Martin, F., 2017b. The impact of planting trees on nox concentrations: The case of the plaza de la cruz neighborhood in pamplona (spain). Atmosphere 8, 131.

Sanz, C., 2003. A note on k-ε modelling of vegetation canopy air-flows. Boundary-Layer Meteorology 108, 191–197.

Seinfeld, J.H., Pandis, S.N., 1998. Atmospheric chemistry and physics: from air pollution to climate change. John Wiley & Sons.

Shih, T.H., Liou, W.W., Shabbir, A., Yang, Z., Zhu, J., 1995. A new k-ε eddy viscosity model for high reynolds number turbulent flows. Computers & Fluids 24, 227–238.

Skamarock, W.C., Klemp, J.B., 2008. A time-split nonhydrostatic atmospheric model for weather research and forecasting applications. Journal of Computational Physics 227, 3465–3485. URL: https://www.sciencedirect.com/science/article/pii/S0021999107000459, doi:https://doi.org/10.1016/j.jcp.2007.01.037. predicting weather, climate and extreme events.

Smit, R., Brown, A., Chan, Y., 2008. Do air pollution emissions and fuel consumption models for roadways include the effects of congestion in the roadway traffic flow? Environmental Modelling Software 23, 1262–1270. URL: https://www.sciencedirect.com/science/article/pii/S1364815208000406, doi:https://doi.org/10.1016/j.envsoft.2008.03.001.

Smit, R., Dia, H., Morawska, L., 2009. Road traffic emission and fuel consumption modelling - trends new developments and future challenges, in: Demidov, S., , Bonnet, J. (Eds.), Traffic Related Air Pollution and Internal Combustion Engines., US: Nova Science Publishers, Inc.. pp. 29–68.

Smit, R., Kingston, P., Wainwright, D., Tooker, R., 2017. A tunnel study to validate motor vehicle emission prediction software in Australia. Atmospheric Environment 151, 188–199. URL: https://www.sciencedirect.com/science/article/pii/S1352231016309736, doi:10.1016/j.atmosenv.2016.12.014.

Smit, R., Smokers, R., Rabé, E., 2007. A new modelling approach for road traffic emissions: Versit+. Transportation Research Part D: Transport and Environment 12, 414–422.

Solazzo, E., Cai, X., Vardoulakis, S., 2008. Modelling wind flow and vehicle-induced turbulence in urban streets. Atmospheric Environment 42, 4918–4931. URL: https://www.sciencedirect.com/science/article/pii/S1352231008001799, doi:https://doi.org/10.1016/j.atmosenv.2008.02.032.

Spirić, V.T., Janković, S., Vraneš, A.J., Maksimović, J., Maksimovic, N., 2012. The impact of air pollution on chronic respiratory diseases. Polish Journal of Environmental Studies 21, 481–490. URL: https://www.pjoes.com/The-Impact-of-Air-Pollution-on-Chronic-r-nRespiratory-Diseases,88776,0,2.html.

Stull, R.B., 1988. An introduction to boundary layer meteorology. Kluwer Academic Publishers.

Sun, K., Li, L., Jagini, S., Li, D., 2021. A satellite-data-driven framework to rapidly quantify air-basin-scale no_x emissions and its application to the po valley during the covid-19 pandemic. Atmospheric Chemistry and Physics 21, 13311–13332. URL: https://acp.copernicus.org/articles/21/13311/2021/, doi:10.5194/acp-21-13311-2021.

Thorpe, A., Harrison, R.M., 2008. Sources and properties of non-exhaust particulate matter from road traffic: A review. Science of The Total Environment 400, 270–282. URL: https://www.sciencedirect.com/science/article/pii/S004896970800658X, doi:10.1016/j.scitotenv.2008.06.007.

Thunis, P., Pisoni, E., Zauli Sajani, S., Monforti-Ferrario, F., Bessagnet, B., Vignati, E., De Meij, A., 2023. Urban PM2.5 atlas – Air quality in European cities – 2023 report. Publications Office of the European Union. doi:10.2760/63641.

TII, 2021. Transport infrastructure ireland. https://data.tii.ie/. Accessed on 12th September, 2025.

TomTom, N.V., 2025. Tomtom traffic index. https://www.tomtom.com/en_gb/traffic-index/. Accessed on 12th September, 2025.

Tutuianu, M., Bonnel, P., Ciuffo, B., Haniu, T., Ichikawa, N., Marotta, A., Pavlovic, J., Steven, H., 2015. Development of the World-wide harmonized Light duty Test Cycle (WLTC) and a possible pathway for its introduction in the European legislation. Transportation Research Part D: Transport and Environment 40, 61–75. URL: https://www.sciencedirect.com/science/article/pii/S1361920915001030, doi:10.1016/j.trd.2015.07.011.

Versteeg, H.K., Malalasekera, W., 2007. An Introduction to Computational Fluid Dynamics: The Finite Volume Method. Pearson Education.

Verwer, J.G., 1994. Gauss–seidel iteration for stiff odes from chemical kinetics. SIAM Journal on Scientific Computing 15, 1243–1250. URL: https://doi.org/10.1137/0915076, doi:10.1137/0915076.

WHO, 2018. Burden of disease from household air pollution for 2016. v3 April 2018. Technical Report. World Health Organization (WHO). URL: https://cdn.who.int/media/docs/default-source/air-pollution-documents/air-quality-and-health/hap_bod_results_may2018_final.pdf.

WHO, 2021. What are the WHO Air quality guidelines? Technical Report. World Health Organization (EEA). URL: https://www.who.int/news-room/feature-stories/detail/what-are-the-who-air-quality-guidelines.

WHO, 2024. Sustainable development goal indicator 3.9.1: mortality attributed to air pollution. Technical Report. World Health Organization (WHO). URL: https://www.who.int/publications/i/item/9789240099142.

Wong, D.W.S., Li, Y., 2020. Spreading of COVID-19: Density matters. PLOS ONE 15, e0242398. URL: https://doi.org/10.1371/journal.pone.0242398, doi:10.1371/journal.pone.0242398. publisher: Public Library of Science.

Yakhot, V., Orszag, S.A., 1986. Renormalization group analysis of turbulence. I. Basic theory. Journal of Scientific Computing 1, 3–51. URL: https://doi.org/10.1007/BF01061452, doi:10.1007/BF01061452.

Zheng, B., Zhang, Q., Geng, G., Chen, C., Shi, Q., Cui, M., Lei, Y., He, K., 2021. Changes in china's anthropogenic emissions and air quality during the covid-19 pandemic in 2020. Earth System Science Data 13, 2895–2907. URL: https://essd.copernicus.org/articles/13/2895/2021/, doi:10.5194/essd-13-2895-2021.

Zhu, G., Tian, Y., Liu, M., Zhao, Y., Wang, W., Wang, M., Li, Q., Xie, K., 2023. Comprehensive competitiveness assessment of ammonia-hydrogen fuel cell electric vehicles and their competitive routes. Energy 285, 129471. URL: https://www.sciencedirect.com/science/article/pii/S0360544223028657, doi:https://doi.org/10.1016/j.energy.2023.129471.